Design and Synthesis of Terpyridine Functionalised Supramolecular Architectures

Jason M. Delente, M.Sc.
January 2021

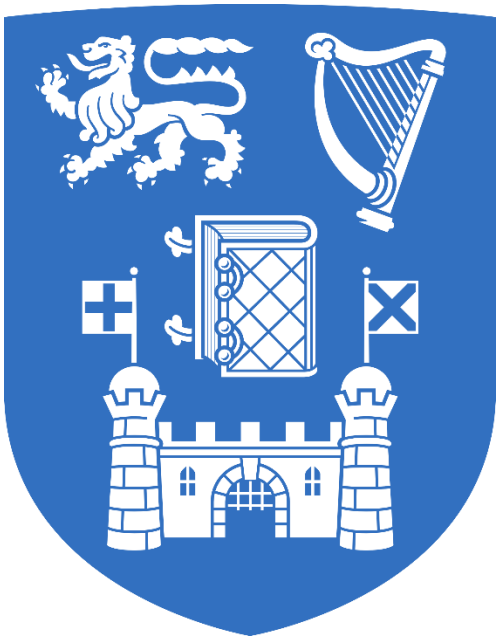

Trinity College Dublin
The University of Dublin

Based on research carried out under the direction of
Prof. Thorfinnur Gunnlaugsson

A thesis submitted to the School of Chemistry, Trinity College Dublin, The University of Dublin, for the degree of Doctor of Philosophy

Declaration

I declare that this thesis has not been submitted as an exercise for a degree at this or any other university and it is entirely my own work. I agree to deposit this thesis in the University's open access institutional repository or allow the Library to do so on my behalf, subject to Irish Copyright Legislation and Trinity College Library conditions of use and acknowledgement.

Signed: _____

Jason M. Delente

Abstract

Coordination-driven supramolecular assembly is an extremely useful tool to generate architectures of increased complexity and functionality, such as metallo-supramolecular gels and emissive materials. Interest in the terpyridine motif to realise such aims has continuously grown through the years due to its capacity to act as a key structural unit in the design of metallo-organic structures by binding strongly to many different metal ions. This thesis, entitled "Design and Synthesis of Terpyridine Functionalised Supramolecular Architectures" describes the synthesis and characterisation of different building blocks adorned with the 2,2′:6,2″-terpyridine (TPy) motif, and their uses to form *d*- and *f*-metal complexes and higher order self-assembled structures.

Chapter 1 introduces the principles of supramolecular chemistry, with a particular focus on the use of 2,2′:6,2″-terpyridines and 1,8-naphthalimides, and their uses in the formation of complexes and naphthalimide Tröger's bases. The unusual shape of Tröger's bases, and the properties that arise from this structure, are discussed, followed by several examples of lanthanides complexes featuring these motifs. A short review summarises the effects of the size of the lanthanide radii on the stability constants of the subsequent complexes. Recent examples of self-assembly of benzene-1,3,5-tricarboxamide scaffolds (BTA) are discussed with a focus on the formation of soft materials. The chapter is concluded by highlighting the research explored in the following chapters.

Chapter 2 describes the functionalisation of the naphthalimide moiety through the imide using 4′-(4-aminophenyl)-2,2′:6′,2″-terpyridine. The coordination of this ligand to various *d*-metal ions is described including the full characterisation of the resulting complexes. A brief comparison of the spectroscopic properties of the ligand and its corresponding Zn(II), Co(II), Fe(II) and Cd(II) complexes is discussed followed by a description of their electrochemical properties.

Chapter 3 discusses the use of the aforementioned 4′-(4-aminophenyl)-2,2′:6′,2″-terpyridine adorned 4-amino-1,8-naphthalimide to synthesise the corresponding 4-amino-1,8-naphthalimide Tröger's base (**TBNap-TPy**), and its full characterisation. The spectroscopic properties of **TBNap-Tpy** are discussed along with its aggregation-induced emission (AIE) properties. The use of **TBNap-TPy** as a fluorescent sensor for various nitroaromatics is described, and the capacity of **TBNap-TPy** to discriminate phenolic and non-phenolic nitroaromatics is demonstrated, including a detailed analysis of the interactions

between **TBNap-TPy** and picric acid using UV-Vis absorption, emission, and IR spectroscopy, as well as DFT calculations, are described along with the effects of the presence of various anions. In addition, the limit of detection of picric acid and the effect of pH on the detection of picric acid are discussed. The synthesis and characterisation of a covalent organic polymer containing the TBNap moiety are described along with a detailed study of its use as a sensor for picric acid. This polymer is compared to the AIE active **TBNapTPy**. The synthesis of coordination polymers using $Zn(BF_4)_2$, $Fe(BF_4)_2$ and $Co(BF_4)_2$, and their characterisation, is discussed followed by their morphology studies. Finally, the spectroscopic and electrochemical properties of the ligand and the corresponding polymers are described.

Chapter 4 focuses on the synthesis and uses of 1,3,5-benzene tricarboxamide functionalised with terpyridine (**BTA-TPy**) to generate supramolecular architectures able to form soft materials. A solution study of **BTA-TPy** in the presence of various Ln(III) ions (Ln = La, Sm, Eu, Gd, Tb, Yb and Lu) using UV-vis absorption and emission titrations is described, with an emphasis on the effect of the lanthanide contraction on the binding constants, determined through non-linear regression analysis. The formation of gels using **BTA-TPy**, and their modification using the aforementioned Ln(III) ions is described, focusing on the effects on their physical properties through morphological and rheological studies. The modification of the gel by diffusion of a ruthenium complex is also discussed in this chapter.

Chapter 5 describes the design and synthesis, through several approaches, of a novel 1,3,5-benzene tricarboxamide functionalised with terpyridine using chiral amino-acids as spacer groups. While the desired tripodal molecule could not be obtained, the procedure for the formation of the TFA salt of L-Alanine-4’-(4-aminophenyl)-2,2':6',2''-terpyridine is described, along with its full characterisation, setting a platform for the functionalisation of 4′-(4-aminophenyl)-2,2′:6′,2″-terpyridine with various amino acids.

The conclusions are presented in Chapter 6, while Chapter 7 outlines the experimental details of the work presented herein. This is followed by literature references and appendices to support the preceding chapters.

Acknowledgements

First and foremost, I would like to sincerely thank my supervisor Prof. Gunnlaugsson for giving me the opportunity to do research in his group with such a degree of freedom, his constant support and enthusiasm over the last four years.

Thank you to the generous financial support from the Science Foundation Ireland (SFI) and AMBER. And a massive thanks to Inspiring Generations Doctoral Support Fund which allowed me to finish m PhD in great conditions despite the situation.

Secondly, I must thank my various collaborators throughout my PhD. Prof Wolfgang Schmitt and Mr Kevin Byrne for their carrying out the gas adsorption experiments, Prof Graeme W. Watson and Dr. Deivasigamani Umadevi for the DFT calculations, Dr. Ronan Daly and Dr. Niamh Willis-Fox from the Institute For Manufacturing (IFM) department of engineers at Cambridge University for hosting me for two weeks and their help with rheology measurements.

I must also thank the Experimental and Technical staff within the School of Chemistry, particularly Dr John O'Brien for helping me with all the NMR and Dr Manuel Ruether for introducing me to so many different techniques, solving my problems when I couldn't get the TGA or Fluorolog working and the numerous impromptu liquid nitrogen refill. Dr Brendan Twamley for his help with X-ray crystallography, and Dr Gary Hessman for his help with mass spectrometry and the long hours looking for the elusive Tröger's base macrocycle.

I can't be more grateful to the "drinky-pooh" group for all these pints (and knowledge) exchanged, and to have made the last year much more enjoyable. Massive thanks to all the members of the Gunnlaugsson group, past and present, for the support, chats, and proof-reading throughout the past few years. I must first thank the three legendary post-docs that have truly influenced the chemist and human that I have become during this PhD. Oxana, thank you for being such a great mentor and friend, for always being willing to help solve my chemistry problems, introducing me to the BTA chemistry and teaching me pretty much everything I know about lanthanides. Thank you for everything you do for the group, I have seen what the lab become when you are not around and I must say you make it a better place! Raju, thank you to have introduced me to the great world of Tröger's bases and nitroaromatics, to always willing to help, the numerous week-end chats in the office and the big bottle of picric acid. You are a great mentor and your PhD students are lucky to have

you. Chris, thank you for sharing your view about the academic world, scientific rigour, and to have helped so much during my internship and my first months in the group. Your students are very lucky to have you as a mentor and I hope we will get a chance to meet again for more drinky-pooh.

To me auld flower Eoin, for making Charlyne and I feel home in Ireland, for all the memories and to make us discover Mayo, the best county in Ireland. I truly hope that one day, when the curse will be over Mayo will win the All-Ireland and you will be able to finally fit in your swimsuit. Bjørn, thank for hum… I don't know? Ooooh. But also for showing what true determination means, Eoin is right about you, you are a god amongst men! À Steve, Grumpy Daddy merci pour toute ton aide avec le fluorolog, et surtout les nombreuses vidéos marrantes tout au long de l'écriture. Muchas gracias Sandra gilipollas for the very brief introduction to the beautiful world of biochemistry and ruthenium chemistry. I hope to see you again soon even if you betrayed to go to smelly Pfizer. I also want to thank Dermot for sharing all your sexy knowledge, your support to combine this document and the numerous chats. Hannah for trying so hard to diffract my "crystals". Isabel and Bruno for the basketball breaks. Elena for briefly introducing me to biochemistry. Amy and Sachi for sharing all your knowledge about SEM. Adam (the second most senior post-doc of the group) thank you for all your help with my chemistry, in particular the electrochemistry, all the corrections, but also for sharing all your Pokemon Go knowledge, and the numerous after community days lunches. Thank you to Sam for sharing all his knowledge about computers, to Dawn, Anna and Gearóid for your help in the lab. Tumpa "boss" I hope that my SEM stuff will be of great use, Helen for the very brief time that we shared the fumehood, I hope you'll have a great time in the group. To my 4th year buddy, Emanuele, thank you for the numerous chats, the music in the lab and always willing to annoy Adam with me, I hope that you will be happier now that it is over. Thank you to the visiting students who were a great addition to the group, especially Jacobo, mad lad and Adrián.

Thank you to the present PhD members of the TG group. June for trying every rubbish "crystals" I gave you, sorry about this and the corrections. Deirdre for all your help with the crystal structures and the corrections. To Patrick thank you for the proof reading, Tómas good luck with the transfer writing and Laura for the four years ahead, it will be challenging but also a great experience! Good luck Connie for the Master, I believe you are in good hands.

To all the non-TG and non-chemistry friends, thanks for always being there, you truly made this easier.

Last but not least! Merci à Papa et Maman, pour votre soutien inconditionnel durant toutes ces années, je ne serais jamais arrivé aussi loin sans vous et il n'y a aucun mot pour exprimer à quel point je suis reconnaissant pour tout ce que vous avez fait pour moi. Dire que je voulais m'arrêter à Bac +2 ! Promis cette fois c'est fini pour de bon. Lulu, le seul propriétaire de forêts ardéchoises avec un permis bateau que je ne connais. Merci pour ton soutien, pour toujours avoir veillé sur moi malgré le fameux événement du rondin de bois que tu as essayé de me jeter dessus afin d'être enfant unique (j'ai des preuves en vidéo !). Tu m'as toujours inspiré avec tes nombreuses passions et j'espère pouvoir faire de même maintenant que j'ai fini les études. J'ai hâte de venir vous voir Fanny et toi quand nous pourrons voyager à nouveau ! Charlyne, merci pour ton soutien et ta patience pendant ces dernières années. D'avoir écouté mes lamentations et constamment su comment me remonter le moral et me remotiver quand les choses devenaient difficiles, en particulier ces dernières semaines. Merci pour ton aide avec le décryptage et les modifications des corrections et pour les nombreuses heures de relecture, je n'aurais jamais réussi sans toi. Ces dernières années ont été une sacrée aventure et j'ai vraiment hâte de commencer ce nouveau chapitre avec toi.

Abbreviations

°C	Degree Celsius
1D	One dimensional
2D	Two dimensional
3D	Three dimensional
Å	Angstrom
a.u.	Arbitrary unit
ADP	Adenosine diphosphate
AFM	Atomic force microscopy
AIE	Aggregation-induced emission
Amino-Nap	4-Amino-1,8-naphtalimide
AML	Advanced Microscopy Laboratory
AMP	Adenosine monophosphate
APCI	Atmospheric pressure chemical ionization
ATP	Adenosine triphosphate
br	Broad
BSA	Bovine serum albumin
BTA	1,3,5-benzenetricarboxamide
btp	2,6-bis(1,2,3-triazole-4-yl) pyridine
c	Concentration
CD	Circular Dichroism
cm	Centimeter
COP	Covalent organic polymer
CP-MAS	Cross-polarization magic angle spinning Carbon-13 nuclear magnetic resonance
CR	Charge recombination
CS	Charge separation
DFT	Density functional theory
DNA	Deoxyribonucleic acid
DPA	Di(2-pyridylmethyl)-N'-(p-aminophenyl) ethylene
dpa	Dipicolinic acid
E	Energy
EDPA	*N*,*N*-di(2-pyridylmethyl)-*N*'-(p-aminophenyl)ethylene diamine
EDX	Energy-dispersive X-ray spectroscopy
eq	Equivalent
ESI	Electrospray ionization
eV	Electron volt
FITR	Fourier-transform infrared spectroscopy
g	Gram
h	Hour
HMBC	Heteronuclear multiple bond correlation
HRMS	High-resolution mass spectroscopy
HRP	Helix reversal penalty
HSQC	Heteronuclear single quantum coherence spectroscopy
hν	Energy (photon)
hνex	Excitation energy

ICP	Infinite coordination polymer
IFE	Inner filter effect
IR	Infrared
ISC	Intersystem crossing
ITC	Internal charge transfer
K	Kelvin
KSV	Stern-Volmer constant
l	Liter
LMWG	Low-molecular weight gelator
Ln	Lanthanides
LOD	Limit of detection
M	Molar
m/z	Mass to charge ratio
M:L	Metal to ligand ratio
mg	Milligrams
MHz	Megahertz
min	Minute
mL	Millilitre
MLCT	Metal to Ligand charge transfer
mM	Millimolar
MMP	Mismatch penalty
MOF	Metal-organic framework
mol	Mole
MRI	Magnetic resonance imaging
ms	Millisecond
mV	millivolt
NAC	Nitroaromatic compound
NIR	Near Infrared
nm	Nanometer
NMR	Nuclear magnetic resonance
ns	Nanosecond
OPETA	Oligo(phenylene ethynylene) tricarboxamide
Pa	Pascal
PA	Picric acid
PBS	Phosphate buffered saline
PET	Photoinduced electron transfer
pH	-log $[H^+]$
pKa	-log Ka (where Ka is the acidity constant)
ppb	Parts per billion
ppm	Parts per millions
ps	Picosecond
rt	Room temperature
s	Second
SANS	Small-angle neutron scattering
SDS	Sodium dodecyl sulfate
SEM	Scanning electron microscopy
S_n	Singlet state
TB	Tröger's base
TBNap	4-amino-1,8-Naphthalimide Tröger's base
TEM	Transmission electron microscopy

TGA	Thermogravimetric analysis
TLC	Thin layer chromatography
Tn	Triplet state
TPy	2,2’,6’,2’’-terpyridine
TREN	Tris(2-aminoethyl)-amine
tta	2-thenoyltrifluoroacetone
UV	Ultraviolet
UV-vis	Ultraviolet-visible
V	Volt
VT NMR	Variable temperature nuclear magnetic resonance
wt %	Weight percentage
ε	Extinction coefficient
λ	Wavelength
λem	Emission wavelength
λex	Excitation wavelength
λmax	Maximum absorbance or intensity at corresponding wavelength
μg	Microgram
μm	Micrometre
μM	Micromolar
μs	Microseconds
τD_2O	Lifetime in deuterated water
τH_2O	Lifetime in non-deuterated water

Notes on Publications

Sections of this work have been published in peer-reviewed journals prior to submission of this thesis.

Chapter 2 and 3, sections of this chapter were described in the article “Aggregation induced emission (AIE) active 4-amino-1,8-naphthalimide-Tröger's base for the selective sensing of chemical explosives in competitive aqueous media” co-authored with Deivasigamani Umadevi, Sankarasekaran Shanmugaraju, Oxana Kotova, Graeme W. Watson and Thorfinnur Gunnlaugsson, (*Chem. Commun*., 2020, **56**, 2562-2565).

Chapter 3, a section of this chapter was published in the article “Hyper-crosslinked 4-amino-1,8-naphthalimide Tröger’s base containing pyridinium covalent organic polymer (COP) for discriminative fluorescent sensing of chemical explosives” co-authored with Deivasigamani Umadevi, Kevin Byrne, Wolfgang Schmitt, Graeme W. Watson, Thorfinnur Gunnlaugsson and Sankarasekaran Shanmugaraju, (*Supramol. Chem.*, 2020, **32**, 508-517).

Table of Contents

“Happiness can be found even in the darkest of times, when one only remembers to turn on the light.”—Albus Percival Wulfric Brian Dumbledore, OM (First Class), Grand Sorc., D. Wiz., Chf. Warlock of the magenmagot, Supreme Mugwump.
Harry Potter and the Prisoner of Azkaban, Alfonso Cuaron, 2004 adapted from Rowling, J. K., author. *Harry Potter and the Prisoner of Azkaban.* London: Bloomsbury, 1999.

Chapter 1— Introduction

1.1 Introduction

Over the past number of decades, supramolecular chemistry has been intensively studied and has been the centre of the attention in the chemistry world with the Nobel Prize awarded to Donald J. Cram,[1] Jean-Marie Lehn, and Charles J. Pedersen in 1987 for their work on the development of crown ethers, cryptands,[2] and cavitands,[3] respectively. This opened the door to the development of a wide range of complex functional structures[4,5] used in interdisciplinary research in chemistry and biology. Applications of such structures include the enantioselective recognition of DNA[6] and use as anticancer agents,[7,8] as well as chemical computing applications such as "on-off" switch systems that use ion recognition for the formation of supramolecular logic gates.[9] These systems can be used in information-handling, to form molecular machines, molecular sensors and also for gas adsorption, to name a few. This development led to another Nobel Prize being awarded to Jean-Pierre Sauvage, Sir James Fraser Stoddart and Bernard L. Feringa in 2016 for the design and synthesis of molecular machines.[10-14]

Using supramolecular synthetic approaches based on complementary interactions, non-covalent bonding and metal templates, it has been possible to synthesise complex architectures such as rotaxanes, catenanes, and molecular borromean rings (an assembly of three interlocked macrocycles which upon breaking any macrocycle allows the others to disassociate) which were difficult to prepare using only covalent chemistry and more importantly, these systems are capable of undergoing reversible morphological changes.[15] Metallo-supramolecular architectures have become extremely common. Their coordination-driven architecture using simple linkers and coordination sites is a very powerful tool to obtain assemblies of increased complexity and functionality[16] such as metallo-supramolecular gels,[16,17] emissive materials using lanthanides,[18,19] self-healing gels,[19] interpenetrated cages,[16] to name a few. Obviously, the choice of the coordination site is crucial in the formation of such functional molecules that could show selectivity toward metal ions and a plethora of examples can be found in the literature, but chelate complexes derived from a polypyridine functionalities have been extensively used in this field, namely, bipyridine (bpy),[20] terpyridine (TPy)[21] and phenanthroline (phen).[22]

The objectives of this PhD thesis was to design and develop ligands that could self-assemble into higher-order supramolecular structures with a particular focus on the use of 4-amino-1,8-naphthalimide (Amino-Nap), its corresponding 4-amino-1,8-naphthalimide Tröger's base (TBNap) and 1,3,5-benzenetricarbonyl tricarbomaxide (BTA) building blocks. This

thesis' main objective is centred on the formation of highly ordered assemblies through the aspect coordination of *d*- and *f*-metal ions using 2,2′:6′,2″-terpyridine (TPy) and to explore the properties and the applications of the resulting supramolecular materials obtained through a wide range of spectroscopic, physical and imaging techniques. With this in mind, this introductory chapter will focus on: the recent advances on the formation of ligand containing TPy moieties used to form supramolecular polymers; the latest developments in naphthalimide and Tröger's Base chemistry; a brief overview of the BTA used to form soft-material and the interest of incorporating *d*- and *f*-metal ions into such assemblies.

1.2 Terpyridine

2,2′:6,2″-Terpyridine, also referred to as terpyridine (or TPy), was discovered by Morgan and Burstall in the early 1930s.[23] Since then, the number of publications based on the TPy motif (Figure 1-1) has continuously increased, which can be explained by the fact that it is a key structure in the design of metallo-organic structures. The terpyridine structure is composed of three co-planar nitrogen donor atoms usually behaving as a tridentate ligand. In the solid-state, to minimise the interactions between the nitrogen lone pair and the Van der Waals interactions between $H_{3,3',5',3''}$ atoms, the three rings adopt a *transoid* configuration as shown in Figure 1-1A. However, when bonded to metal ions, the TPy rings occupy a cis-cis configuration.[24] Because of its clamp-like structure, it forms very stable octahedral complexes with *d*-metal ions,[25-28] and higher coordination with *f*-metal ions.[29] This ability to bind strongly to metal ions makes TPy a great building block for supramolecular chemistry with the view of making complex molecular architectures. Usually, the type of complexes encountered is of the form $[M(TPy)_2]$, which possess a centre of symmetry at the metal ion as shown in Figure 1-1B, yielding an achiral complex. This possibility of forming achiral complexes when using symmetrical substitution of the terpyridine motif is of considerable advantage when aiming toward forming multinuclear species, as the use of other motifs such as phen and bipy, will result in the formation of different diastereoisomers leading to the presence of different environments, and of course, different properties.[30]

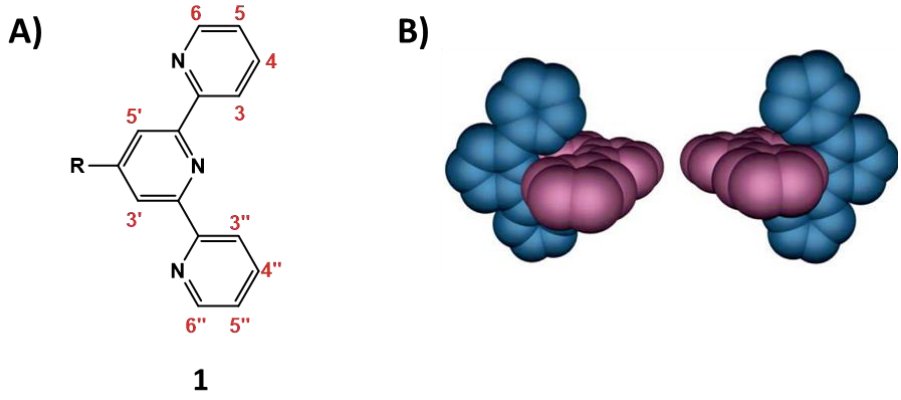

Figure 1-1 A) Structure and numbering of TPy (**1**), B) achiral $[M(TPy)_2]$ species with a symmetrical ligand.[30]

The UV-visible spectrum of free TPy molecules is composed of π-π^* transitions around 280 nm while upon the formation of complexes with various *d*-metal ions, a new band appears between 300-350 nm corresponding to the conformational change of the pyridine rings from the *transoid* configuration in the free ligand to the *cis* configuration in the complex.[31] The Fe(II) and Ru(II) bis(terpyridine) complexes display the most significant changes in their absorption spectra with the appearance of a metal-to-ligand charge-transfer (MLCT) band in the visible region that gives rises to the colour of the complexes.[32] The emission properties of the TPy moiety are dependent on the substitution of the binding unit, while Zn(II) and Cd(II) bis(terpyridine) complexes are luminescent due to their full *d*-orbitals and therefore cannot participate in electron transfer processes. The Fe(II) and Ru(II) analogues are usually non-emissive. In the case of the Fe(II) bis(terpyridine) complexes, this can be explained by the fact that their *d*-shells are partially filled and thus can induce quenching of the excited state through electron or energy transfer mechanisms.[33] The poor spectroscopic properties of the $[Ru(TPy)_2]^{2+}$ complexes have been extensively studied and are explained by the fact that the bite angle of the rigid TPy moiety gives rise to a distorted octahedral geometry upon complexation, leading to a reduction of the ligand field strength of TPy and a decrease in the energy of the *d*-*d* metal-centred triplet state (^{3}MC). The ^{3}MC is thermally accessible from the ^{3}MLCT which favours non-radiative decay to the ground state.[32-34]

Several approaches have been described to improve the photophysical properties of $[Ru(TPy)_2]^{2+}$ complexes such as modifying the energy difference between the ^{3}MLCT and the ^{3}MC.[35] Incorporation of an electron-withdrawing group at the 4-position of the central pyridine ring leads to a stabilisation of the ^{3}MLCT state, thus lowering the thermal population of the ^{3}MC state which increases the luminescence lifetime of the complex.[36] This is observed for the ruthenium complex **2**, in which one of the terpyridine moieties is

substituted in the 4-position with a mesylate group, and displays a lifetime of 36 ns.[36] It is also possible to use an electron-donating group to destabilise the ^{3}MC state, and as demonstrated by Maestri *et al*., the use of a terpyridine functionalised with an electron-withdrawing group and a second one functionalised with an electron-donating group to form a heteroleptic complex leads to a further increase in the excited state lifetime, such as in the case of **3**, which displayed a lifetime of 50 ns.[36]

A second approach corresponds to the substitution of the terpyridine moiety with an aromatic group. In the ground state, 4-phenyl substituted TPy molecules display a twist of approximately 30° between the 4-phenyl and central pyridine rings, however; in the excited state, the rings are co-planar.[37,38] Thus, the electron delocalisation which stabilises the ^{3}MLCT excited state is extended, as demonstrated for complex **4** which displays an excited state lifetime of 1 ns against 250 ps for $[Ru(TPy)_2]^{2+}$.[39,40] This approach was further explored by Fang *et al*. who successfully extended the electron delocalisation in the ground state by functionalising the TPy in the 4-position with a pyrimidine group.[41] The 2-pyrimidyl moiety can form hydrogen bonds between its two nitrogen atoms and the hydrogen atoms of the central pyridine rings of the TPy, thus achieving ground state co-planarity with an angle of 4.5° compared to 28.3° for a phenyl substituted TPy.[41] The corresponding ruthenium complex displayed an excited state lifetime of 8 ns, while the combination of the co-planarity strategy and the stabilisation of the ^{3}MLCT state through the use of an electron-withdrawing group such as a cyano group in the para position of the pyrimidyl substituent led to an excited state lifetime of 200 ns for complex **6** (Figure 1-2).[41]

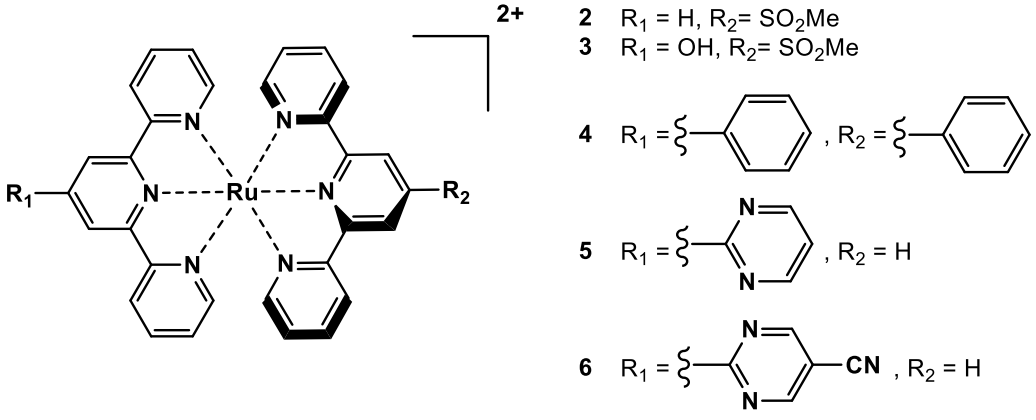

Figure 1-2 Structures of room temperature emissive terpyridine ruthenium complexes **2**-**6**. Structures reproduced from references.[36,41]

A third approach consists of reducing the angular strain of the TPy in the complex by introducing a methylene spacer between the central pyridine ring and one of the other pyridine rings. This increases the flexibility of the pyridine rings during the complexation

and destabilises the *d-d* states leading to an excited state lifetime of 17 ns for complex **7** (shown in Figure 1-3).[42]

Finally, a fourth strategy is the use of a second chromophore which possess a non-emissive triplet state of similar energy to the emissive ^{3}MLCT state. This leads to the creation of an equilibrium between the two states and induces an increased excited state lifetime.[35] Complex **8** (shown in Figure 1-3) displays this character, whereby the ligand is composed of a TPy functionalised with 5-(9-anthryl)-pyrimid-2-yl and combines the bichromophoric approach along with the extended electron delocalisation. The emission of **8** displayed a bi-exponential decay, with the shortest lifetime corresponding to the decay of the initially formed ^{3}MLCT state. The second lifetime is due to the ^{3}MLCT radiative decay obtained by the equilibrium between the ^{3}MLCT and the triplet anthracene states, yielding a lifetime of 1806 ns.[43]

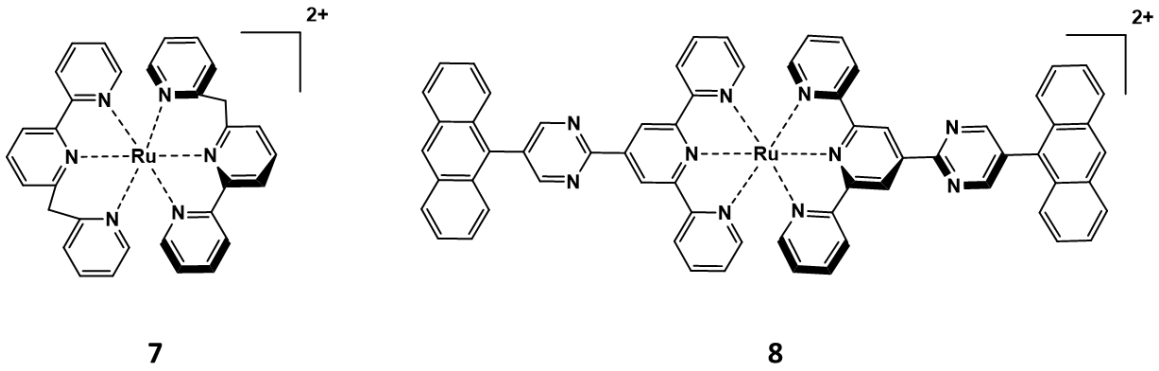

7 **8**

Figure 1-3 Structures of room temperature emissive terpyridine ruthenium complexes **7** and **8**.

Terpyridine metal complexes have been widely explored and possess a great range of potential applications, such as the multicomponent gels synthesised by Biswas *et al*. using zinc complexes **9** and **10** in combination with luminogens such as acridine yellow (**11**), ethidium bromide (**12**), or azido- BODIPY (**13**). Mixtures of various combinations: **9-12**, **9-13**, **10-11**, **10-12** and **10-13**, successfully formed multicomponent gels when exposed to Cl^- ions upon the addition of HCl as seen in Scheme 1-1. The gels were studied by AFM, SEM and TEM, demonstrating different arrangements, dimension of fibres and shapes for each gel. Spectrophotometric analysis of the interactions between each component revealed that upon addition of HCl, the NO_3^- ions coordinated to the Zn complexes were replaced by Cl^- ions. The emission study revealed that each gel was emissive and had a longer excited state lifetime than the corresponding individual components in solution. Cytotoxicity studies were performed against breast cancer cell line and showed that only **10-11** was cytotoxic. The gels **9-13**, **10-11**, **10-12** and **10-13** penetrated the cells and localised in the cytoplasm displaying

a strong emission. These results suggested that the incorporation of luminogens in the gel make them suitable for cellular imaging due to their non-cytotoxicity and bright emission fluorescence.[44]

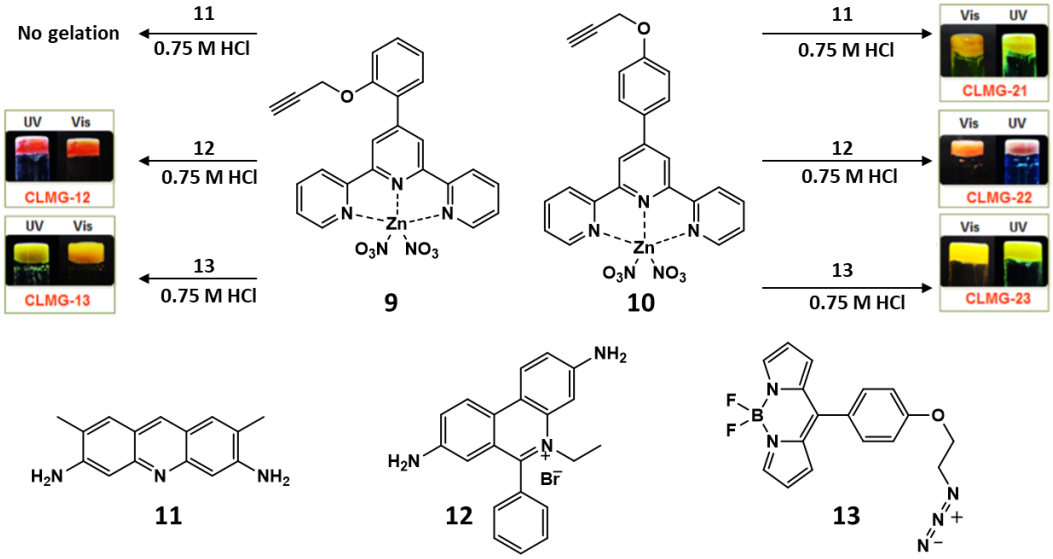

Scheme 1-1 Formation of multicomponent gels using the Zn(II) complexes **9** and **10** upon addition of the luminogens **11**, **12** and **13** with their corresponding photography under UV light. Reproduced from reference.[44]

Another example of applications for TPy complexes was demonstrated by Rupp *et al*. who synthesised the ligands **14-17** (shown in Scheme 1-2A) in low to moderate yields. Heteroleptic ruthenium complexes **14Ru-17Ru** were formed by reaction of **14-17** with [Ru(TolylTPy)]Cl_3. Their PF_6^- salts were isolated and characterised by single crystal X-ray diffraction, NMR, elemental analysis and mass spectrometry. The photophysical properties of the complexes were studied, revealing that all the complexes were emissive at room temperature and that their emission intensities were partially quenched in the presence of oxygen. The electrochemical and DFT studies of each complex indicated the potential for these complexes to be used as photosensitisers to produce hydrogen. This hypothesis was tested by using $[Co(dmgH)_2(H_2O)_2](BF_4)_2$ (where $dmgH^-$ = dimethylglyoximato) as catalyst and triethanolamine as the sacrificial electron donor. This experiment demonstrated that the four complexes could be used as photosensitisers with a half-life ranging from 2-6 h, with **14Ru** and **16Ru** being the most stable. While these complexes displayed less activity than some previously reported Ru(II) complexes, they highlighted the use of **14Ru-17Ru** as photosensitisers under both blue and red light irradiation which allows them to use a broader range of the solar spectrum for hydrogen production.[45]

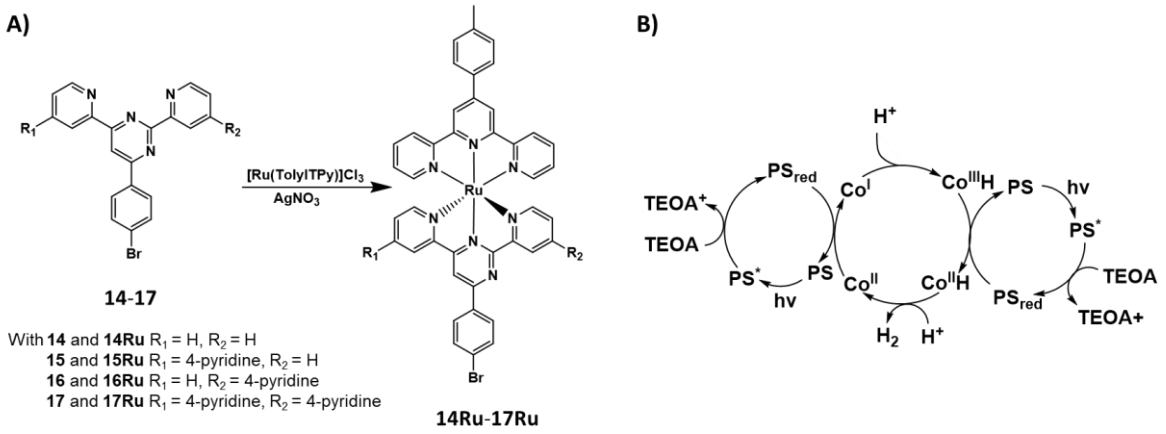

Scheme 1-2 A) Synthesis of **14Ru-17Ru** and B) Proposed photocatalytic cycle for photocatalytic hydrogen evolution using Co(II) catalyst. Reproduced from reference.[45]

Rajah *et al*. synthesised the ruthenium complex **18** (shown in Figure 1-4) composed of a bis(terpyridine) ruthenium complex appended with phenyl picolinic acid in the 4-position of one TPy moiety. This complex can be used as a ditopic ligand to form *d-f* complexes; the formation of which was monitored by ^{1}H NMR spectroscopy. Upon addition of Lu(III) ions, the Lu(**18**)$_3$ complex was formed in solution, while further addition of Lu(III) ions resulted in the successive formation of Lu(**18**)$_2$ and Lu(**18**) complexes. UV-vis and emission spectroscopy studies showed that upon coordination of various Ln(III) ions such as Lu(III), Yb(III), Er(III) and Nd(III), the emission intensity of the ^{3}MLCT state of the Ru(II) complex displayed moderate to no quenching. While the sensitisation of Yb(III), Er(III), and Nd(III)-centred emission could be observed, the studies of energy transfer through a combination of transient absorption spectroscopy and excited state lifetime measurements demonstrated the presence of an energy transfer from the ^{3}MLCT state and the 4*f** excited states. These results also highlighted the influence of the distance between the two metal ions and therefore the importance of the spacer between the TPy and the second binding unit.[46]

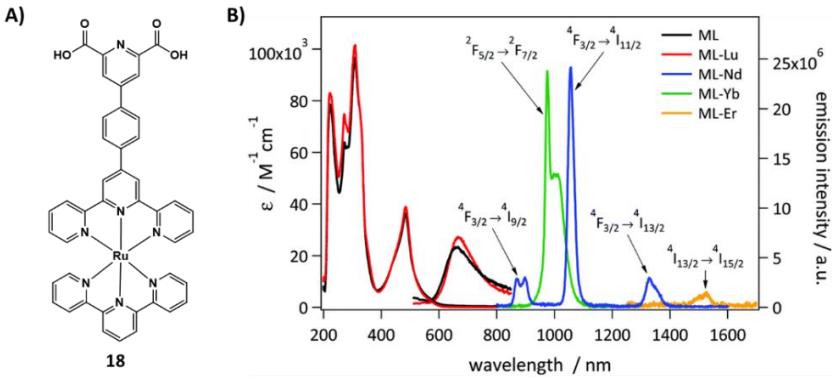

Figure 1-4 A) Structure of **18** and B) UV-vis absorption and emission spectra (λ_{ex} = 485 nm) of **18**–Ln complexes where Ln = Lu, Nd, Yb or Er. Reproduced from reference.[46]

As demonstrated by the aforementioned examples, depending on the desired application, the use of a spacer between two or more terpyridine units to form a multitopic ligand is of paramount importance.[47] The spacers used in this work will be described in the following paragraphs along with some of the complexes formed with such compounds.

1.3 1,8-Naphthalimide

Supramolecular chemistry is in part based on the use of simple "building blocks" to build more complex structures. Nowadays, a wide range of these molecular units have been developed and studied such as polymers,[48] inorganic complexes[49] and organic molecules.[4] One of these building blocks that has received increasing interest in the past decade is the 1,8-naphthalimide or benzo[de]isoquinolin-1,3-dione **19** motif. As shown in Figure 1-5, it is a planar molecule composed of two conjugated rings fused to a third ring which includes an imide functionality. Many derivatives are substituted in the 3 or 4 position, such as 4-amino-1,8-naphthalimide **20** and are widely used, where their spectroscopic properties can be tuned by their chemical functionalisation.[50,51]

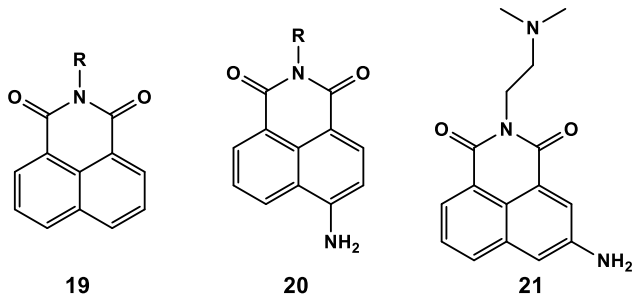

Figure 1-5 4-Nitro-1,8-naphthalimide (**19**), 4-amino-1,8-naphthalimide (**20**), Amonafide (**21**)

The 4-nitro-1,8-naphthalimides possess high energy excited states, as the nitro functional group and the imide moiety are electron-withdrawing. The reduction of this moiety to give the 4-amino-1,8-naphthalimide derivative results in a 'push-pull' based internal charge transfer (ICT) excited state, caused by the electron-donating amine and the electron-withdrawing imide,[52] as shown in Figure 1-6.

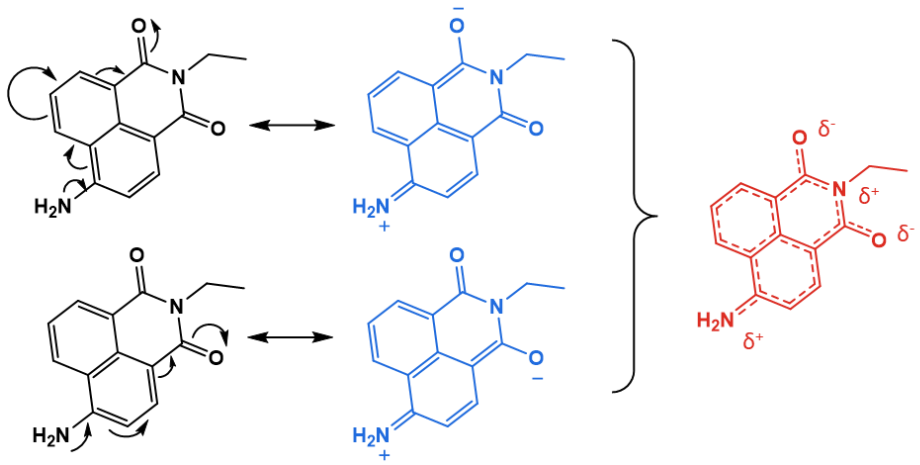

Figure 1-6 4-Amino-1,8-naphthalimide structures, and schematic representation of the ICT excited state within the 4-amino-1,8-naphthalimide fluorophore caused by a 'push-pull' action. Reproduced from reference.[52]

Molecules possessing the 1,8-naphthalimide motif have found applications as fluorescent brighteners, fluorescent bio-probes, solar energy collectors[52] and as laser dyes.[53] They are also used as specific binding agents, anti-cancer and fluorescent cellular imaging agents.[7] For example, Amonafide (**21**) (shown in Figure 1-5), which is a derivative of 1,8-naphthalimide substituted in position 3 was synthesised by Braña *et al*. and displayed interesting behaviour in animal tumours and subsequestly, entered clinical trials.[54]

Another appealing property of naphthalimides is their ability to target biomolecules. As shown in functionalisation studies, several derivatives of 1,8-naphthalimides have been reported as good candidates for photochemotherapeutic inhibition of viruses.[55,56] Their spectroscopic properties have also been used to synthesise numerous anion sensors.[57,58] The advantage of this family of molecules is their relatively easy synthesis on a large scale in high purity.[7] Recent examples of naphthalimide complexes that have been synthesised and showed interesting properties are di(2-pyridylmethyl)amine (DPA) and *N*,*N*-di(2-pyridylmethyl)-*N'*-(p-aminophenyl)-ethylenediamide (EDPA) functionalised naphthalimides synthesised by Xiyou *et al*.[59] Compound **22** was shown to have logic gate operations using Cu^{2+} and Zn^{2+} as the chemical input. Zn^{2+} ions can also interact with both coordination sites. When coordinating to the receptor at the imide position, the zinc ion blocks the photoinduced electron transfer (PET) which restores the quenched emission while coordination to the receptor at the 4-amino position blocks the ICT process usually occurring, leading to a shift in the absorption spectrum. Addition of Cu^{2+} also blocks the PET process when coordinated to the imide receptor but leads to a significant decrease in the fluorescence of the complex. Pope *et al*. recently synthesised several rhenium complexes

such as compound **23-30** as viable cellular imaging agents, demonstrating that the most lipophilic derivative (**29**) showed the best cellular uptake.[60]

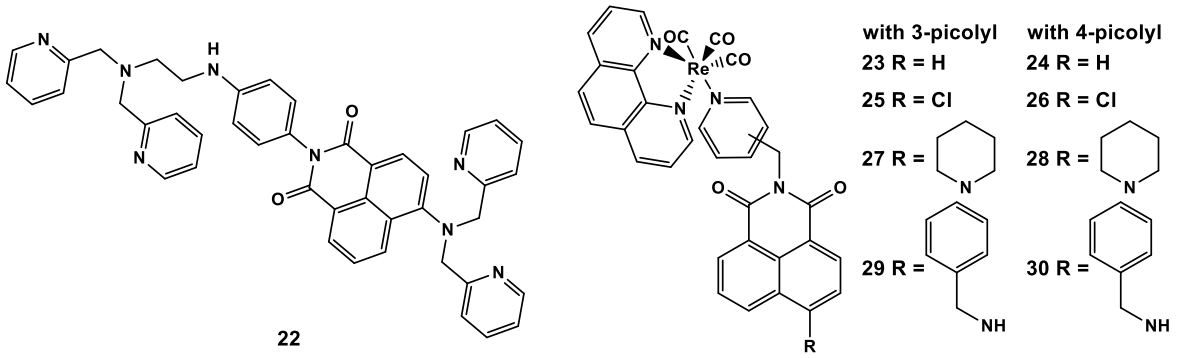

Figure 1-7 Structure of A) DPA-EDPA naphthalimide **22**, B) rhenium complex of 1,8-naphthalimide derivative **23-30**. Reproduced from references.[59,60]

More recently De Bettencourt-Dias *et al*. reported the synthesis of 1,8-naphthalimide ligand able to coordinate lanthanide ions, to sensitise the Ln(III)-centred emission and generate $^1O_2$.[61] The ligands used shown in Figure 1-8 are composed of the naphthalimide building block and a binding unit, 4-aminopyridine-2,6-dicarboxamide in the case of **Nap-cbx** (**31**) and 4-aminopyridine-2,6-diethyl ester in the case of **Nap-dpe** (**32**). Titration of the ligands in a solution of $Eu(NO_3)_3$ evidenced the formation of 1:1, 1:2 and 1:3 metal to ligand species. Fitting of these titrations allowed the determination of the binding constant of each species for both ligands, with $\log_{\beta 1:1} = 8.02 \pm 0.07$, $\log_{\beta 1:2} = 14.01 \pm 0.24$ and $\log_{\beta 1:3} = 19.00 \pm 0.20$ for the **32-Eu** complexes and $\log_{\beta 1:1} = 8.64 \pm 0.12$, $\log_{\beta 1:2} = 14.67 \pm 0.11$ and $\log_{\beta 1:3} = 19.80 \pm 0.24$ for the **31-Eu** complexes which are similar values to other lanthanide complexes using these binding units. They continued by forming 1:3 M:L complexes using Eu(III), Nd(III), Gd(III) and Yb(III) ions. The study of their photophysical properties in DCM:CH_3CN revealed the successful sensitisation of Eu(III), Yb(III) and Nd(III)-centred emission with a quantum yield of sensitised Eu(III)-centred emission of 8.3% for $[Eu(\mathbf{32})_3]^{3+}$ and 16.7% for $[Eu(\mathbf{31})_3]^{3+}$ while the quantum yields of the Yb(III) and Nd(III) complexes could not be determined due to the weak emission of the complexes. Interestingly, all the complexes and the ligand displayed generation of $^1O_2$. This was demonstrated by the monitoring of the phosphorescence at 1270 nm which is attributed to $^1O_2 \rightarrow {}^3O_2$ transition. This was further confirmed by the increase in the Ln(III)-centred emission of the complexes when measured in degassed solutions with the absence of the transition at 1270 nm.[61]

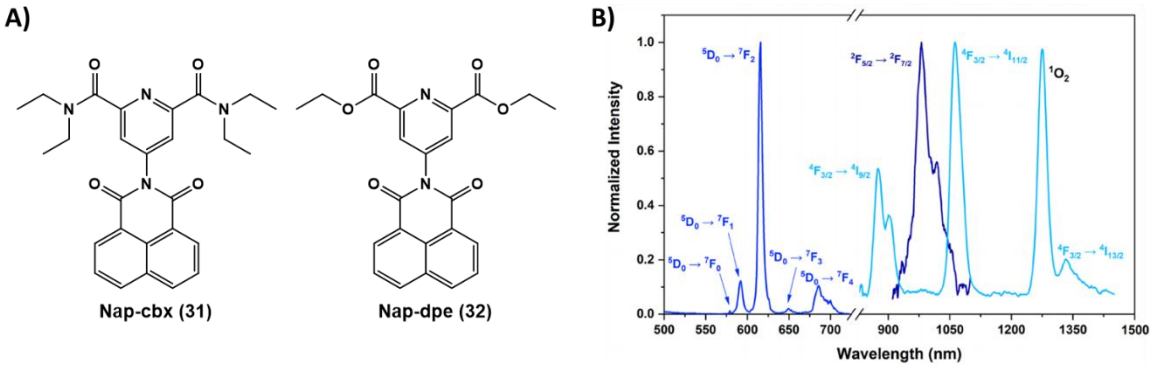

Figure 1-8 A) Structure of **Nap-cbx** (**31**) and **Nap-dpe** (**32**), B) normalized emission spectra of the [**Ln(31)**$_3$]$^{3+}$ complexes (Ln = Eu(III) (blue), Nd(III) (light blue), and Yb(III) (navy)). Reproduced from reference.[61]

The Patra research group synthesised an emissive Eu(III) probe in high yield using two different ligands, the first one being a composed of a naphthalimide functionalised at the imide position with a terpyridine (**33**) and the second one being 2-thenoyltrifluoroacetone (tta) as shown in Figure 1-9A.[62] Titration of [Eu(tta)$_3$(H$_2$O)$_2$] in a solution of **33** showed the formation of 1:1 complex [Eu(tta)$_3$(**33**)]. Spectroscopic studies of the complex in Tris buffer revealed a weak emission band attributed to the ligand and demonstrated the successful sensitisation of the Eu(III)-centred emission. DFT calculations were used to further demonstrate that both the naphthalimide ligand (**33**) and tta can efficiently transfer energy from there triplet state to the Eu(III) ions. Using time-resolved spectroscopy Gupta *et al.* determined the hydration state of the complex to be 0, which implies that the coordination sphere of the Eu(III) ion contains only the ligands. Following these results, the emission was monitored as a function of the pH, revealing that the Eu(III)-centred emission was quenched at pH < 4 due to the protonation and displacement of the β-diketone tta and at pH > 9 due to the dissociation of tta, while this phenomenon was found to be fully reversible over at least four cycles. Displacement based anion experiments also revealed that the Eu(III)-centred emission was quenched in the presence of F^-, HCO_3^- and citrate anions (shown in Figure 1-9C) due to the displacement of tta ligand, thus demonstrating a lack of specificity for a particular anion. This was an encouraging result for use of this complex as a platform to develop more specific sensors by the modification of the ligands. Due to the known ability of naphthalimide to bind to DNA, a DNA binding study was carried out through the monitoring of the absorption of the complex upon the addition of CT-DNA and the results suggested a groove binding or partial intercalation interaction. Ethidium bromide displacement assay and time-resolved spectroscopy confirmed the strong binding of the complex to CT-DNA. These results overall suggest that the complex [Eu(tta)$_3$(**33**)] represent a good base for the further development of an intracellular pH probe.[62]

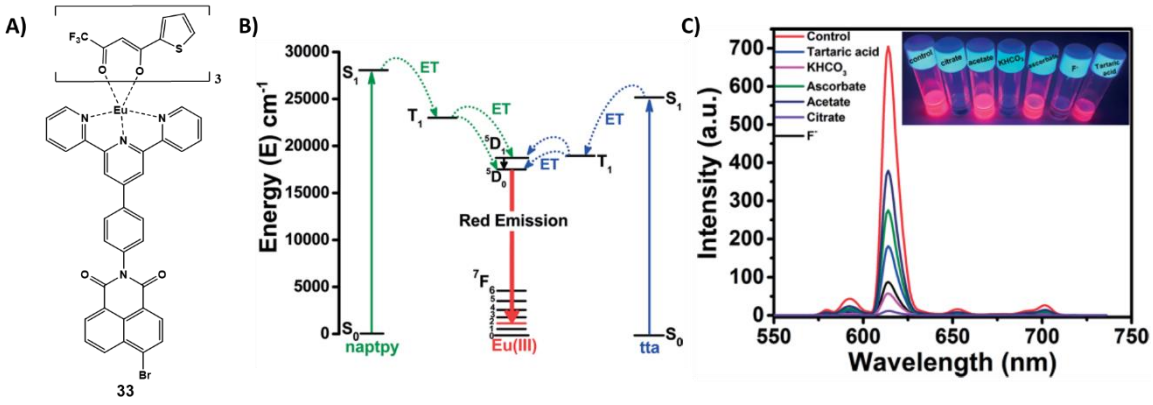

Figure 1-9 A) Structure of [Eu(tta)$_3$(**33**)], B) Energy-transfer diagram for the tta and **33** ligands occurring in [Eu(tta)$_3$(**33**)] and C) Luminescence spectral changes of [Eu(tta)$_3$(**33**)] in the presence of various ions and inset: image of the solutions under a UV lamp. Reproduced from reference.[62]

Another use of the naphthalimide moiety is in the formation of TBNap which is part of the Tröger's base family. This structure forming a larger building block has been of great interest in supramolecular chemistry and some examples are discussed in the next paragraph.

1.4 Tröger's Base

The very first Tröger's Base (TB), also known as 6H,12H-5,11-methano dibenzo[*b,f*][1,5]diazocine, was synthesised by Julius Tröger in 1887,[63] however the correct chemical structure was elucidated and published by Spielman in 1935 by carrying out different reactions on the TB and analysing the resulting products.[64] The original conditions for the formation of TB involved the condensation of *p*-toluidine and dimethoxymethane in HCl.[63] Through the years, many research groups have developed procedures for the synthesis of TB analogues, with the general strategy employing formaldehyde (often formed *in-situ* through the use of precursors such as paraformaldehyde, methenamine or dimethoxymethane), and a derivative of aniline in acidic conditions (often trifluoroacetic acid and is used as solvent).[65] The mechanism was elucidated by Wagner (Scheme 1-3) which further demonstrated the possibility to use aniline derivatives to form TB.[66,67]

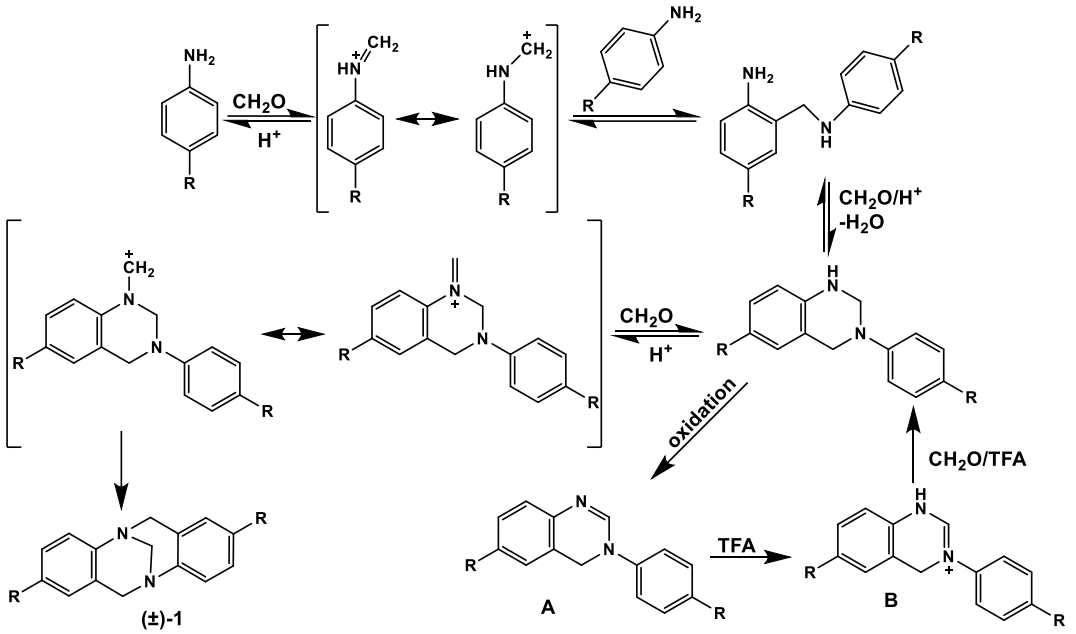

Scheme 1-3 Mechanism of formation of Tröger's Base proposed by Wagner and Farrar.[66] Reproduced from reference.[68]

The chiral nature of the TB due to the two tertiary bridgehead N-atoms of the diazocine ring was revealed by the Nobel prize laureate Vladimir Prelog who successfully separated the two enantiomers.[69] Prelog further demonstrated that the optically pure isomers are stable at room temperature but racemization takes place in dilute acidic conditions, making the enantiomeric separation difficult. The crystal structure of the first TB was reported by Larson and Wilcox,[70] and were followed by many other research groups.[71-74] Due to its C_2 symmetry with a Λ-like structure with a dihedral angle ranging from 80 to 120 degrees depending on the substituents of the phenyl ring, this scaffold is of great interest for the formation of supramolecular architectures such as the metallocage reported by the Wärnmark research group which upon using the racemic mixture of **34** with [1,3-Bis(diphenylphosphino)propane]palladium(II) triflate forms exclusively the heterochiral dimer **(*R, R, S, S*)-35** (shown in Scheme 1-4), thus demonstrating diastereoisomer self-discrimination during the formation of the metallo-macrocycle. [75]

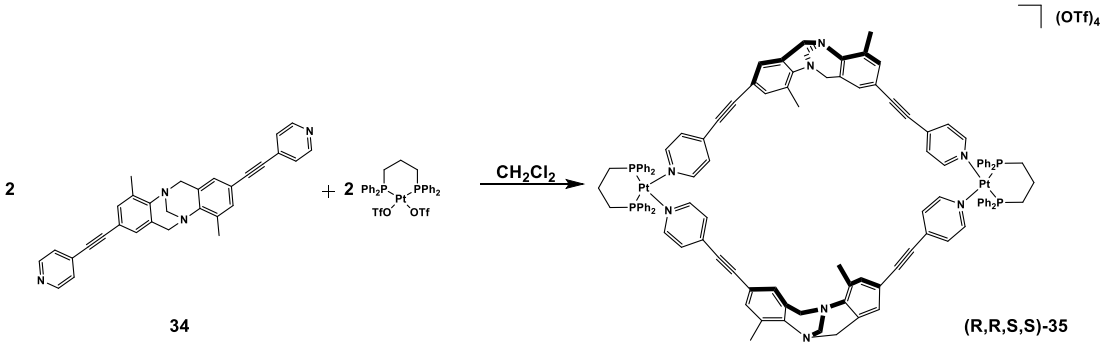

Scheme 1-4 Synthesis of the heterochiral dimer **(R, R, S, S)-35**. Reproduced from reference.[75]

Pardo *et al*. reported the structure of molecular tweezers, of which the synthesis led to the formation of both the syn- and anti-isomers of only one of the two stereoisomers possible, thus demonstrating that the cyclisation reaction is stereoselective. They also demonstrated that the syn-isomer (**36**) was the more thermodynamically stable. The X-ray structures revealed that for the syn-isomer, the two arms are almost parallel and that the bridging benzene ring is nearly perpendicular to the one situated at the end of the arm as shown in Figure 1-10B. Thus opening up the way for the formation of more complex TB structures.[76]

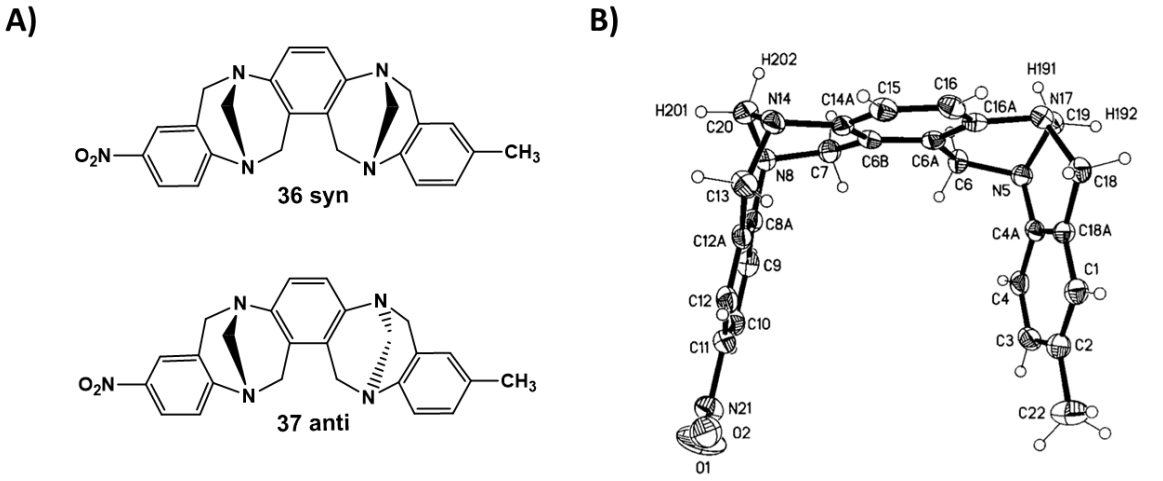

Figure 1-10 A) Scheme of syn- (**36**) and anti-isomers (**37**) of TB tweezers, B) ORTEP representation of **36** (the syn-isomer). Reproduced from reference.[76]

Another example of the use of the particular shape of the TB motif is the formation of a molecular bowl by Mosca *et al*.[77] were both **38** (shown in Figure 1-11A) and **39** are composed of three TB and the size of the cavity is controlled by the motif used for the core, a benzene ring, and a triphenylene core, respectively. Interestingly, using X-ray diffraction on **38.DCM** (shown in Figure 1-11B) and **39.NB** (nitrobenzene), they demonstrated that the size of the cavity formed by the three arms can vary to maximise the host-guest interactions by a modification of the angle between the naphthalene and the plane of either the phenylene or triphenylene. Thus both molecular bowls could be used as a turn-off sensor for the detection of nitroaromatics such as TNT, NB, 2,4-DNT and 2,6-DNT.[77]

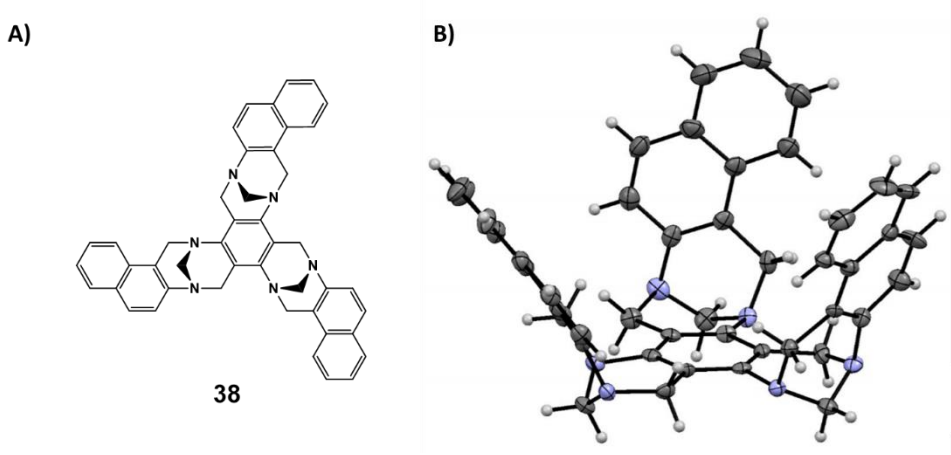

Figure 1-11 A) Structural formula of **38**, B) Structure of **38**. Reproduced from reference.[77]

Talianová *et al*. recently developed a series of asymmetric coumarin TB derivatives with cyanine substituents, through a multiple-step synthesis yielding the desired TBs in high yields. The evaluation of their spectroscopic properties revealed that emission of **40** and **41** are independent of pH while **42** emission intensity drastically decreases when the pH increases. Biological studies of the three TB highlighted their ability to penetrate cells and particularly the lysosomes of several cell lines as seen in Figure 1-12B, and that **40** has a better photostability and higher intensity in the cell than **41** and **42** and also displayed a more stable luminescence than the commercially available lysosomal probes LT-B and LT-G. Evaluation of the cytotoxic activity of the three TB demonstrated that a concentration of 4 μM for **40** and **41** and 1 μM for **42** lead to cell viability of 80%, thus allowing the use of the three dyes as cellular imaging agents in the nanomolar concentration, therefore demonstrating the interest of TBs as cellular imaging agents.[78]

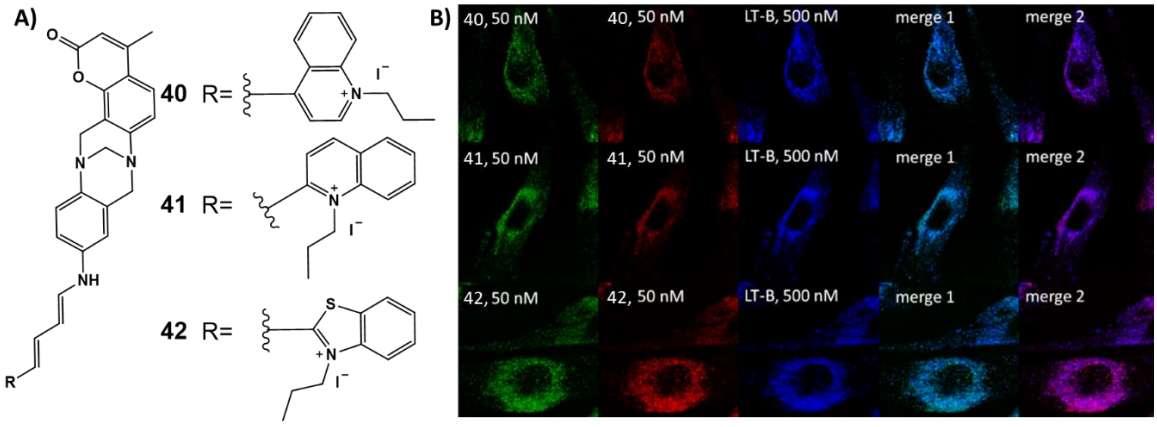

Figure 1-12 A) Scheme of TB **40**, **41** and **42**, B) Lysosomal localization of fluorescent probes **40**-**42**. In cell line HF-P4 were co-labelled with the probes **40**-**42** and specific commercial lysosomal probe LysoTracker Blue DND-22 (LT-B). Reproduced from reference.[78]

Another area of interest for the use of TB is the formation of metal-organic-frameworks (MOFs). Jeon *et al*. reported two infinite coordination polymers (ICP)

composed of a TB derivatised with coordination units able to form a zigzag polymer in presence of zinc. Interestingly these two polymers formed fluorescent ICP particles of micrometre size upon diffusion of diethyl ether in DMF. These particles demonstrated high robustness as they were stable in a variety of solvents and in dry conditions too.

The formation of those particles was further studied with time-dependent SEM. To do so, the ligand **43-CO_2** and $Zn(OAc)_2$ were mixed in DMF and following the addition of diethyl ether, aliquots of the solution were analysed. SEM analysis revealed that seeds agglomerated and formed spherical aggregates with a rough surface within 10 minutes. After which, the surface of the particles became smoother leading to a perfect sphere within 60 minutes as seen in Figure 1-13B. Thus, the formation of the particles consists of an oligomerization step with the formation of ICP upon coordination of **43-CO_2**, followed by nucleation, both aggregation and fusion of particles to form bigger spheres followed by a smoothing of the surface. The ability of the ICP particles to uptake gas was evaluated and revealed modest uptake of H_2 (77.0 cm^3 g^{-1}, 0.69 *wt* % for **43-CO_2-A**), and (63.4 cm^3 g^{-1}, 0.56 *wt* % for **43-CO_2-B**), however, they displayed a significantly lower uptake for N_2 thus revealing the capacity of **43-CO_2** to selectively uptake gases.[79]

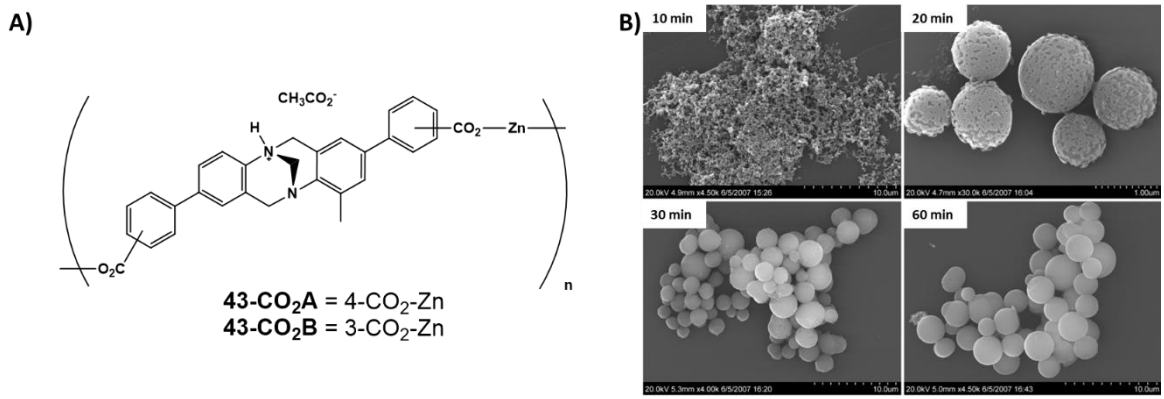

Figure 1-13 A) Scheme of **43-CO_2A** and **B**. B) SEM images monitoring the formation of ICP particle of **43-CO_2B** at 10 min, 20 min, 30 min and 60 min. Reproduced from reference.[79]

The Tao research group have synthesised and reported pyridinium TB derivatives (**44-X**, shown in Figure 1-14A) with X= S for $C_6H_4SO_3^-$,[80] I for I^-,[81] N for NO_3^- or H for $Hg(SCN)_4^{2-}$,[82] which displayed aggregation-induced emission (AIE) upon addition of counter solvent (toluene in these cases) to the acetonitrile solution of the compound. The AIE effect was rationalised by a combination of decreased rate of enantiomerisation and a decreased efficiency of vibrational quenching due to the steric interactions taking place during the aggregation, as well as the presence of a twisted configuration which suppresses quenching interactions due to a higher intermolecular distance which was highlighted by

crystallographic analysis. Those factors are reinforced by strong internal charge transfer (ICT) with the positively charged pyridyl ring potentially acting as an electron-acceptor and the two amides of the diazocine ring acting as the electron donors.[80] **44-S**, **44-I** and **44-N** interactions with bovine serum albumin (BSA) were studied in buffer solution and revealed that when mixing, only **44-X** did not yield an increase in fluorescence. However, the addition of sodium dodecyl sulfate (SDS) which is an ionic surfactant to the BSA solution leads to a fluorescence enhancement during the titration of the BSA/SDS solution into the aqueous solution of **44-X**. These results evidenced that **44-X** molecular configurations do not allow the compounds to enter the binding sites of the folded protein to form aggregates. While the addition of a small quantity of SDS denatures the protein and opens-up the binding site of BSA thus allowing **44-X** to interact with BSA through hydrophobic and electrostatic interactions which leads to the enhancement of the AIE effect as seen in Figure 1-14B. These results demonstrated that the Λ-like structure combined with the smart design of TB derivatives can lead to exciting luminescent properties which can be further used for biological imaging.[81]

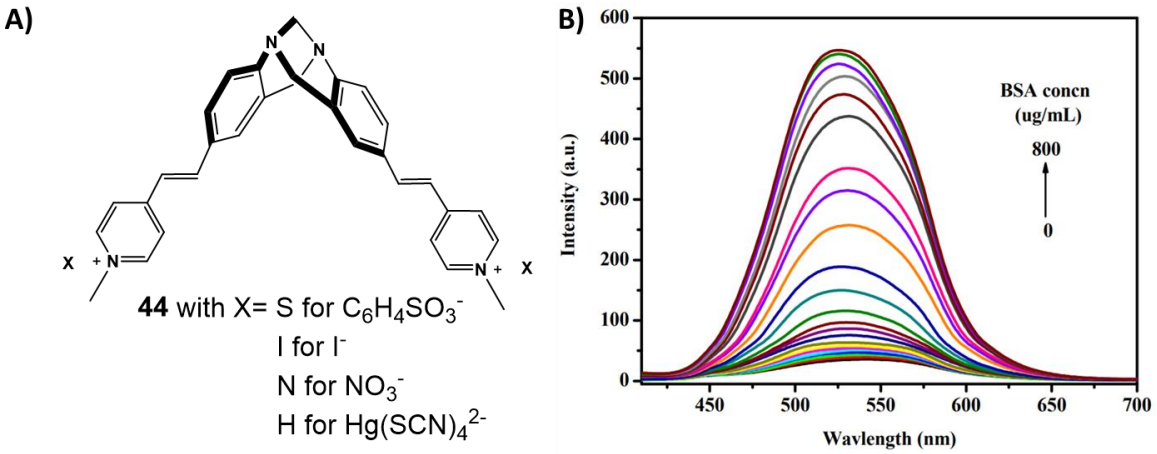

Figure 1-14 A) Scheme of **44-X**, B) Fluorescence enhancement of **44-I** (10 µM in aqueous PBS containing 0.05% w/v SDS, pH = 7.0) in the presence of different amounts of BSA (from 0 to 900 µg/mL). Reproduced from reference.[81]

The combination of the interesting luminescence properties of TB and the numerous applications of Nap described previously, drew the interest of Deprez *et al*. who synthesised the first series of 4-amino-1,8-naphthalimide-containing Trögers bases (TBNap) in 2005 (shown in Scheme 1-5).[83] The dimerization of the Amino-Nap to the TBNap was achieved through heating formaldehyde in presence of the desired Nap in hydrochloric acid and ethanol solution. A careful UV-vis and emission analysis of this series revealed that the electronic absorption spectra of TBNap are relatively insensitive to the solvents while the emission spectra displayed a significant shift of λ_{max} as a function of the solvent polarity.

Similarly, the quantum yield of the compounds are highly dependent on the solvent too. These results were attributed to the Amino-Nap luminescent properties which are highly dependent on the solvent, while the various substitution on the imide positions demonstrated very little to no influence on the spectroscopic properties of TBNap.[83] Concomitantly, the Gunnlaugsson group was working on similar TBNaps and that work will also be reviewed herein.

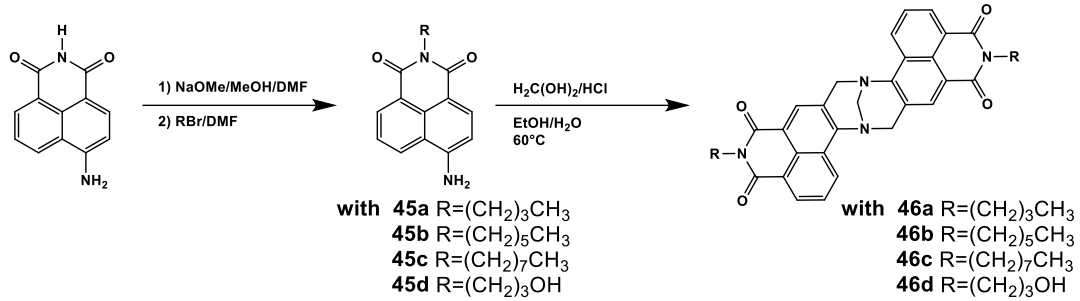

Scheme 1-5 First synthesis of TBNap carried out by Deprez. Reproduced from reference.[83]

More recently, Zhao *et al*. took advantage of the almost orthogonal geometry of the two naphthalimide moieties in the TB to study the ability of **47** (shown in Figure 1-15A) for the formation of spin-orbital charge transfer intersystem crossing, which corresponds to an electron transfer from the singlet state to the triplet state.[84] This can lead to many applications such as photocatalysis and photodynamic therapy; hence, the importance of the development of such systems and the understanding of the mechanisms involved. Using transient absorption spectroscopy, Zhao *et al*. demonstrated that spin-orbital charge transfer intersystem crossing was taking place through charge separation (CS) followed by charge recombination (CR) which induces intersystem crossing (ISC). Transient absorption analysis was further used to demonstrate a lifetime of 46 μs for the triplet state and the intersystem crossing efficiency showed a dependence on the solvent polarity. Through a combination of spectroscopy experiments and DFT calculations, Zhao *et al*. were able to determine the simplified Jablonski diagram of **47** which is shown in Figure 1-15B.

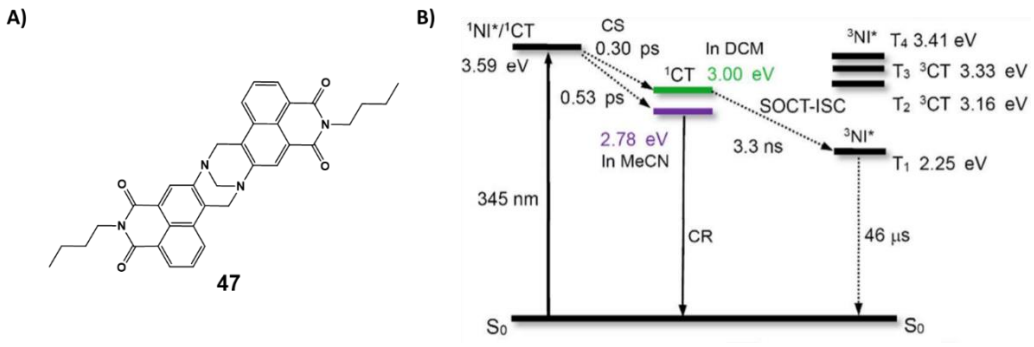

Figure 1-15 A) Structure of **47** used by Zhao *et al*. and its simplified Jablonski diagram as determined through spectroscopy experiment, DFT calculations and orbital analysis. Reproduced from reference.[84]

Another class of compounds which possess very interesting photophysical properties and have been extensively studied over the last fifty years are the lanthanides complexes. The following paragraph describes several examples of lanthanide complexes and their properties as well as the requirement for the successful sensitisation of the lanthanide-centred emission. This is followed by a short review of the effect of the size of the lanthanide radius on the stability constant of the complex.

1.5 Lanthanides

Since the discovery of the first lanthanide element, sesquioxide yttria (Y_2O_3) discovered in 1794 by the Finnish chemist Gadolin,[85] scientists have been hugely attracted by the discovery of new rare-earth elements with Promethium being the last addition to the lanthanoid family in 1947. Following their discovery and the progress made to separate and purify them, lanthanides have been widely used in screens, lasers,[86] optical fibres,[87] magnets,[88] catalyst,[89] security inks and contrast agent for MRI to name a few applications.[90-94] While a lot of these applications are achieved using mostly the formation of cluster and nanoparticles, over the last 30 years, the development of new areas in lanthanide chemistry have been taking place with an increase in the use of lanthanides in supramolecular chemistry leading to the formation of macrocycles, heterometallic *d-f* compounds, coordination polymers and many other examples.[95,96]

The lanthanides (Ln) are comprised of 15 elements and compose the first row of the *f*-block of the periodic table with the actinides being the second. As described by Dr. Cotton in his book "Lanthanide and actinide chemistry",[97] lanthanides exhibit several features that differentiate them from *d*-metals, they possess a wide range of coordination numbers from 6 to 12 and are widely used in their +3 oxidation state. Ln(III) ions adopt the $[Xe]4f^n$ (n=0-14) electronic configuration and are gradually filled; however, due to the decrease in energy of the 4f orbitals at atomic number 57 (Lanthanum), the f orbitals penetrate the xenon core and are well shielded by the filled 5s, 5p and 6s sub-shells.[98] This shielding of the 4f orbital results in their non-participation to the coordination of the ions and therefore, their magnetic and spectroscopic properties are largely (but not entirely) uninfluenced by the ligand, making their distinct photophysical characteristic highly interesting.

Due to the shielding of the 4f sub-shell by 5s, 5p and 6s sub-shells, the 4f orbitals are not involved into the chemical bonding during the formation of complexes and this results in a very small Stokes shift upon excitation contrary to purely organic chromophores which

lead to sharp line-like absorption (with very low probabilities and rarely visible) and emission bands through f-f transition as shown in Figure 1-16.[99] Using a combination of empirical and experimental studies, Heinrich Dieke successfully determined the energy levels of each rare earth elements and their emissive state in the crystals of $LaCl_3$ and thus provided an excellent tool for the determination of the bands observed during the spectroscopic experiments. This paved the way for many more studies of the lanthanides energy levels and an example of the partial energy diagrams for the lanthanide aquo ions determined by Carnall *et al*. is shown in Figure 1-16B.[100-102]

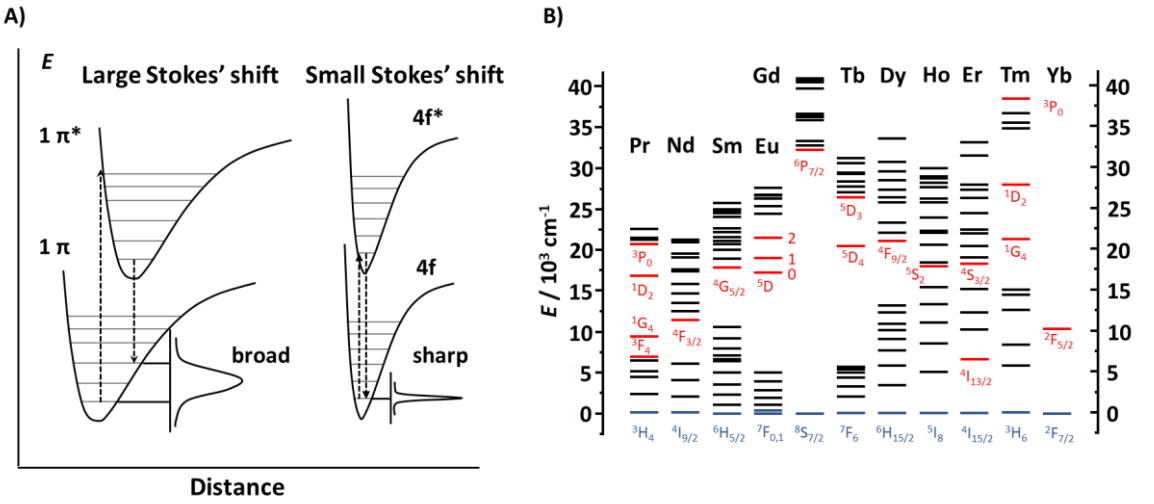

Figure 1-16 A) Configurational coordinate diagram for emission from (left) an organic chromophore and (right) a lanthanide ion. B) Partial energy diagrams for the lanthanide aquo ions with the main luminescent levels drawn in red, while the fundamental levels are in blue. Images reproduced from references.[99,103]

The term symbol used to describe the different energy levels in Figure 1-16B corresponds to $^{2S+1}L_J$ with S the total spin quantum number, L the total orbital angular momentum quantum number and J the total angular quantum number which indicate the relative orientation of the spin and the orbital momenta. The spin selection rule states that the total spin cannot change ($|\Delta S| = 0$), the change in the orbital angular momentum can be $|\Delta L| = 0, \pm 1$, and the change in the orbital angular momentum can be $|\Delta J| = 0, \pm 1$.[104] In addition to the spin selection rule other rules are operative. Laporte's selection rule states that the initial and final wavefunctions must change in parity, which means that the *f-f* transitions are forbidden by electric dipole mechanism. However, when the lanthanide ion is under the influence of a ligand-field, non-centrosymmetric interactions allow the mixing of electronic states of opposite parity into the 4*f* wavefunctions, which relaxes the selection rules and lead to the transition to be partially allowed and gives rise to the electric dipole (ED) transitions. The major electronic states mixing contributing to their intensity are $4f_n$ configuration with opposite parity $4f_{n-1}\ 5d_1$.[105] Some transitions called hypersensitive or

pseudo-quadrupolar transitions because they apparently follow the selection rules of electric quadrupole transitions (for example $^5D_0 \rightarrow {}^7F_2$ for Eu(III)) are ED transitions that are highly sensitive to small changes in the Ln(III) environment. Another type of allowed transitions are the magnetic dipole (MD) transitions, but their intensity is weak. However, in 4*f*–4*f* spectra they often have intensity of the same order of magnitude as induced electric dipole transitions. Quadrupolar transitions are also parity allowed, but they are much weaker than MD transitions so that they are usually not observed.[99]

Because the absorption coefficients of Ln(III) ions are very low ($\varepsilon < 1\ M^{-1}\ cm^{-1}$) due to the low probability of 4f→4f transitions since they are forbidden by the electric dipole selection rule, the direct excitation of the lanthanide ion is extremely inefficient. One way to overcome this issue is to use the antenna effect (also known as sensitisation) first described by Weissman and shown in Figure 1-17.[106,107] The indirect excitation of the Ln(III) ion occurs through excitation of the singlet ground state of the antenna (S_0), generating a higher vibrational level singlet excited state (S_1). This excited state can be deactivated to the ground state either through a non-radiative pathway (vibrational or collisional quenching) or by fluorescence ($S_1 \rightarrow S_0$). Alternatively, intersystem crossing (ISC) can take place and transfer the energy from S_1 into the excited triplet state (T_1) of the antenna. If the T_1 does not undergo deactivation to the ground state either through a non-radiative pathway or by phosphorescence ($T_1 \rightarrow S_0$), the energy transfer can take place from T_1 to the lanthanide ion through intramolecular energy transfer of the antenna which is followed by metal-centred emission or *via* a range of non-radiative deactivation.[98,106,108,109] However, it is important to note that this energy transfer path is not the only one involved and that other processes can take place when using a *d*-metal ion complex as the antenna.[109,110]

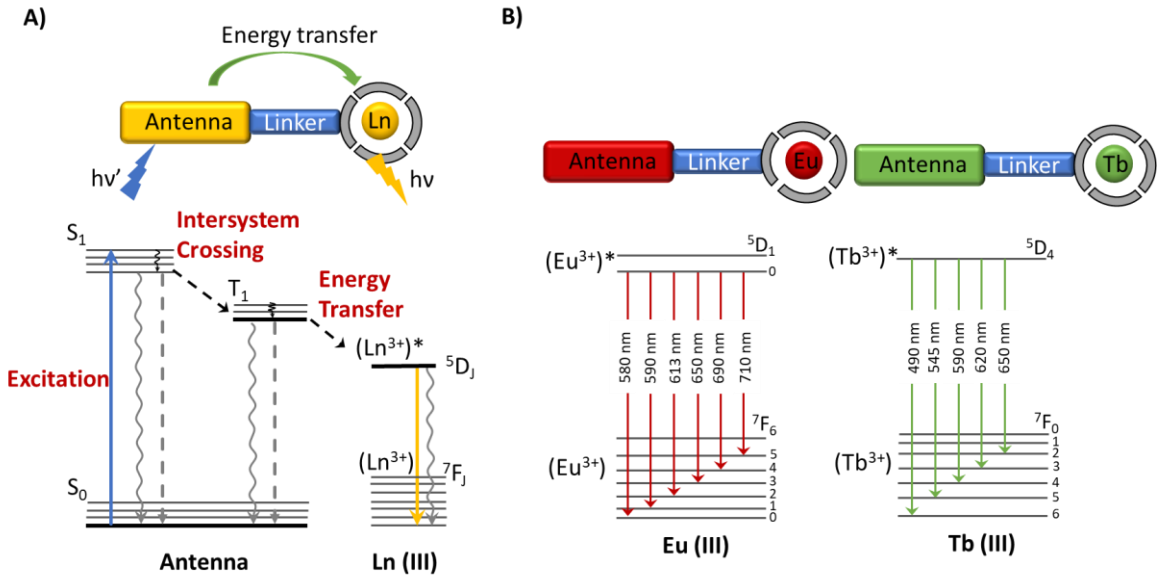

Figure 1-17 A) Schematic representation of the antenna effect with a simplified Jablonski diagram representing the sensitisation pathway for Ln(III) ion through the antenna effect. The blue line corresponds to energy absorption, wiggly arrows correspond to non-radiative deactivation process, dashed lines correspond to emissive radiative decay from the ligand, the yellow line corresponds to emissive (fluorescence or phosphorescence) radiative decay from lanthanide ion. B) Luminescent 4f−4f transitions of europium and terbium complexes and commonly observed emission wavelengths to emit red and green light, respectively. Images reproduced from reference.[108]

Once the energy transfer into the excited state of the Ln(III) ion has been achieved, lanthanide ion-centred emission can take place through different transitions. The first one is fluorescence, which is a spin-allowed transition with no changes in the spin multiplicity ($\Delta S = 0$), which occurs in a short time frame ($<10^{-6}$ s). The second one is through phosphorescence which is spin-forbidden due to a change in multiplicity ($\Delta S \neq 0$), which occurs in a longer time frame than fluorescence ($>10^{-6}$ s). The lanthanide-centred emission can also be achieved by a combination of both fluorescence and phosphorescence.[103] The f-f emission lines of lanthanides ions cover the entire spectrum, starting in the UV with Gd(III), in the visible with Pr(III), Sm(III), Eu(III), Tb(III), Dy(III), and Tm(III), and in the near-infrared region with Pr(III), Nd(III), Ho(III), Er(III), and Yb(III).[85]

A way to maximise the Ln-centred emission is to design the ligand such as its triplet state energy is close to one of the higher excited states of the metal ion, however, it is important to keep a minimum difference of 2500-3500 cm^{-1} between the triplet energy level of the ligand and the emissive state of the Ln(III) ion to avoid the occurrence of back transfer.[109] Another deactivation pathway of the excited state of the lanthanide corresponds to the vibrational quenching of the excited state by coordinated or diffusing solvent molecules possessing O-H, N-H and C-H groups, and particularly, water molecules. This phenomenon was first observed by dissolving lanthanide (III) salts in D_2O rather than in

water revealing a much brighter emission for Eu(III) and Tb(III) ions.[111] These results further demonstrated that both emission intensity and lifetime of Ln(III) ions are considerably decreased in the presence of water. This is observed for emissive Ln(III) ions but is particularly true for the lanthanides possessing a small energy gap between their emissive state and their highest sub-level of the ground state. This effect is used to determine the coordination environment of Ln(III) ions and to determine the hydration level state (also known as q-value) of the ion, which corresponds to the number of water molecules present in the inner coordination sphere of the ion and that are therefore coordinating it. This work was first developed on the Eu(III) ions by Horrock *et al*.[112,113] To determine the q-value it is necessary to measure the lifetime of the complex both in water and deuterated water, assuming that O-D oscillators have little to no contribution to the deactivation and that the other non-radiative decay pathways are the same in water and deuterated water. The relationship used to determine the q-value is:

$$q = A \times (\Delta k_{obs} - B)$$

$$\text{With } \Delta k_{obs} = k_{H_2O} - k_{D_2O} = \frac{1}{\tau_{H_2O}} - \frac{1}{\tau_{D_2O}}$$

Where A and B correspond to parameters depending on both the Ln(III) ion studied and the ligand used as antenna. A is used to describe the inner sphere contribution to the quenching while B is used to describe both the outer-sphere contribution of diffusing solvent molecule and corrective factor taking into account the presence of other deactivating vibrations. It is important to note that these relationships require the determination of both A and B parameters using a family of structurally related ligands of known hydration state.[114]

Several strategies have been developed to minimise the deactivation pathways of Ln(III) emission, such as the use of rigid coordination environment to avoid high-energy vibrations. Using ligands with a high number of coordinating units is also a good strategy to shield the Ln(III) ion from solvent molecules and collisional quenching. In this quest of highly emissive Ln(III) complexes, numerous coordinating units have been used. Different chelating units are used for the formation and sensitisation of lanthanide complexes, ranging from macrocycles to podands using various types of coordinating units such as carboxylic acids, pyridine and other carbonyl groups. One scaffold that attracted particular attention is the cyclen macrocycle unit,[115] known as a strong coordinating site for Ln(III) ions, it requires the use of a chromophore to sensitise the Ln(III) ion. A recent example presented by the Borbas research group,[116] inspired by the early work of Williams and Parker,[117] demonstrated the design and synthesis of **48-51** (shown in Figure 1-18A) and that by

modifying the substitution of the antenna and removing N-H oscillator from the close proximity of the Ln(III) ion, it was possible to improve both the Eu(III) and Tb(III) emission quantum yields up to 11.6% and 45% in water, respectively.[116]

Various research groups have been studying the use of coumarin derivatives as antenna for the sensitisation of lanthanides,[118-120] and the Guasque research group was the first group to report a study in which the coumarin derivatives (**52**, shown in Figure 1-18B) are directly bound to the Ln(III) ions. They obtained crystals of the Sm, Eu, Tb, and Dy complexes demonstrating the coordination of the Ln(III) ions by X-ray diffraction, revealing that the coumarin derivative binds to the lanthanide ions in a similar fashion to the β-diketonates. Three **52** compounds coordinated the lanthanides through the alkoxide group and the carbonyl of the ketone, while two other coordination sites are filled by two solvent molecules. Photophysical studies of these four complexes lead to the determination of absolute quantum yield of 0.5%, 11.6%, 29.2% and 21.9% for [Sm(**52**)$_3$(H_2O)(EtOH)], [Eu(**52**)$_3$(H_2O)(EtOH)], [Tb(**52**)$_3$(H_2O)(EtOH)], and [Dy(**52**)$_3$(H_2O)(EtOH)] respectively, and subsequently, they reported one of the most luminescent dysprosium complexes in ethanolic solution.[121]

Taking advantage of the coordination properties of bipyridine and carboxylic acids, the Feng research group developed an antenna (**53**) (shown in Figure 1-18C) capable of forming 3:2 M:L complexes in the presence of Tb(III) and Dy (III) ions and 1:2 M:L complex with Sm(III) ions, which display high solid-state luminescence with long lifetime and high quantum efficiency.[122]

Bis and tridentate pyridine-based chelating ligands have been widely used for the formation of emissive lanthanide complexes and a large library of dipicolinic acid derivatives have been synthesised by several research groups. Notably, the Gunnlaugsson group has greatly contributed to the study of this moiety and this will be discussed in a following chapter. In 2016, the Mazzanti research group reported the development of pyridine-bis-tetrazolate scaffold appended with different substituents on the para position such as triazoles and an alkyne shown in Figure 1-18D. The formation of complexes in the presence of Eu(III) and Tb(III) ions was studied both in solution and in the solid-state allowing for a clear understanding of the coordination environment of the Ln(III) ions. The study of the spectroscopic properties of the complexes revealed that the substitution of the triazole through the N-position, as done for **54** and **55**, does not modify significantly the properties of the complexes. While the use of an alkyne anisole derivative (**56**) showed

excellent results for the shift of the absorption window, making it an ideal candidate for the sensitisation of Eu(III) ions through two-photon excitation.[123]

Yang *et al.* reported a compound composed of a D-gluconic amide acetal derivative and amino-terpyridine linked together by an alkyl chain of various length. Interestingly, Yang *et al.* studied the formation of gel for **57** (shown in Figure 1-18E) in various solvents and discovered that they were able to form gels in anisole, chlorobenzene and tetrachloroethylene and further modified the gel by drop-casting on the top of the gel a solution of Eu(III) and Tb(III) ions in acetonitrile. The resulting gels were studied by spectroscopy and demonstrated the successful sensitisation of Eu(III) and Tb(III) ions by the terpyridine after coordination, however, using only MALDI-TOF mass spectrometry they determined the M:L ratio to be 1:1. It is also interesting to note a drastic change in the xerogel morphology upon diffusion of the lanthanides ions.[124]

The Jung research group reported a bis-terpyridine derivative with alanine moiety (**58**, shown in Figure 1-18F), interestingly this compound was able to form gels in DMSO:H_2O mixtures (7:3) with and without lanthanides ions (Eu and Tb). The gels displayed luminescence for both ligand and lanthanide-centred emission, while AFM studies demonstrated that the concentration of Eu(III) and Tb(III) ions governed the size of the helical pitch length, reducing it from 48.9 nm to 30.7 nm for the Tb gel and 48.9 nm to 39.1 nm for the Eu gel in the presence of 1 equivalent of Ln(III) ion. Another interesting observation is the clear enhancement of the strength of the gel upon coordination of the terpyridine to Tb(III) and Eu(III) ions. A slightly stronger gel was obtained when using Tb(III) than when using Eu(III) with an increase in the G' and G" values of 2.2- and 1.6-folds, respectively, compared to the gel formed by **58**.[125]

The Pikramenou research group reported an imidodiphosphonate binding unit (**59**, shown in Figure 1-18G),[126] inspired by the work of Kulpe *et al.*,[127] that chelate Ln (III) ion through the oxygen atoms of the two phosphine oxides. Using the potassium salt of **59** they were able to synthesis and form Ln(**59**)$_3$ with Eu, Tb, Dy, Sm, Gd, Er, Nd, and Yb ions. They were able to obtain crystals suitable for X-ray diffraction for all the complexes and demonstrated the binding of 3 deprotonated units **59** and one solvent molecule (ethanol in this case) for all the complexes except with the Yb(III) ions which was rationalised by the important decrease in size of the ion resulting in stronger interaction with the ligand and therefore, a better shielding of the Yb(III) ion. Gratifyingly, each visible light-emitting complex demonstrated a long luminescent lifetime (up to 3.1 ms for Tb(III) ion) in dry

acetonitrile, while Nd(III) and Yb(III) complexes displayed emission in the near-infrared (NIR).

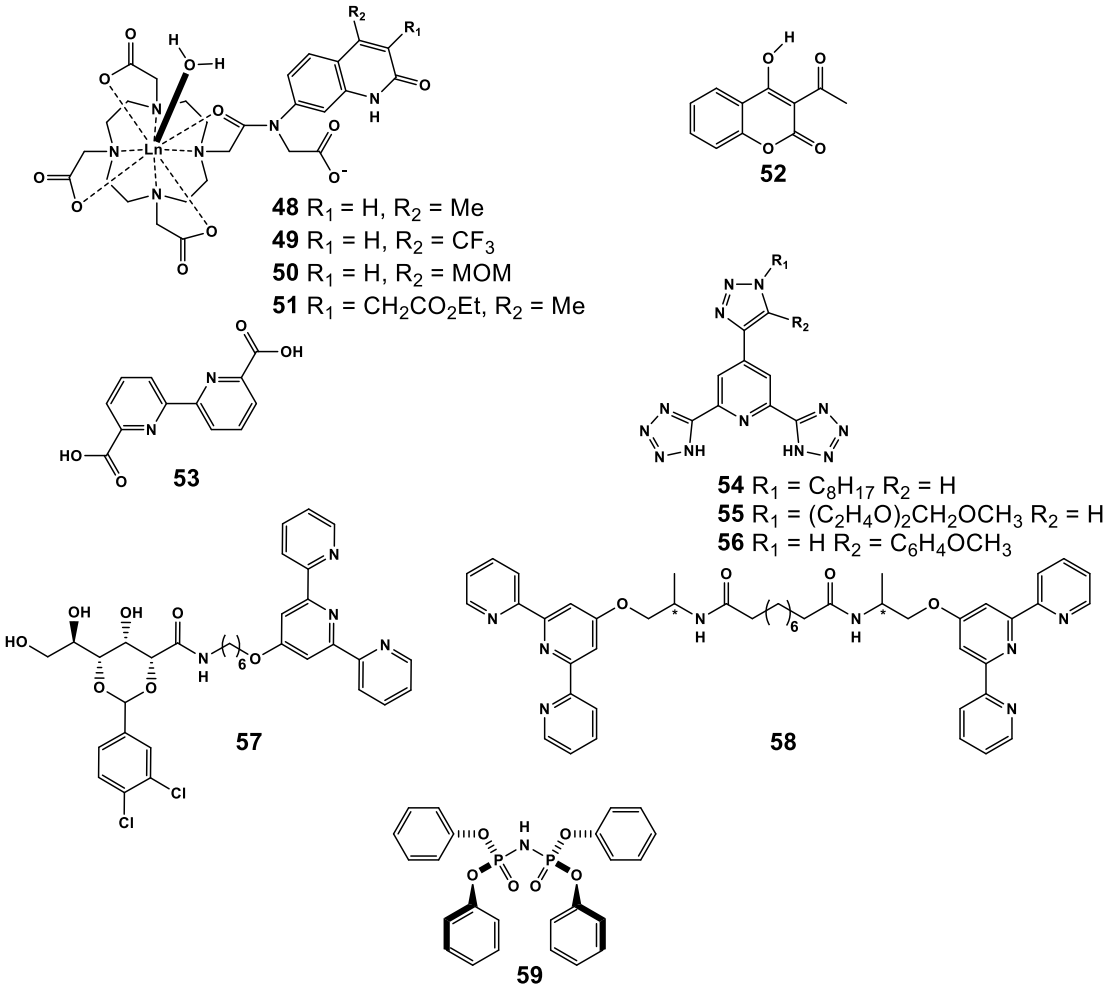

Figure 1-18 Various structures of lanthanide coordinating molecules acting as sensitisers. Structure reproduced from references.[116,121-126]

The last example, reported by the Pikramenou research group highlighted the influence of the size of the lanthanide, which resonates with the lock and key principles which is vastly used in biology to describe molecules that can only be chemically active if they are attached to a receptor. This principle was further used by chemists Izatt, Lamb, Christensen and Haymore, who first reported in 1977 the stability constants of the series of Ln(III) ions with 18-crown-6 (**60**) which were measured by calorimetric titrations revealing that the stability constant of the 18-crown-6 complex with Ln(III) ions smaller than Gd(III) could not be measured.[128] Desreux, Massaux, Delchambre and Duyckaerts further developed this research and compared the stability constant to the one previously reported by Izatt *et al.*[129] They successfully determined the stability constant of the complexation of the 14 lanthanides ions by 4,4'(5')-di-tert-butylbenzo-18-crown-6 (**61**) and demonstrated a nearly linear relationship with the inverse of the ionic radii. Thus highlighting that the largest

lanthanide ions (La^{3+}) form more stable complexes with the crown ether than any other lanthanide, and that the stability constant decreases along with the ionic radius as shown in Figure 1-19B.

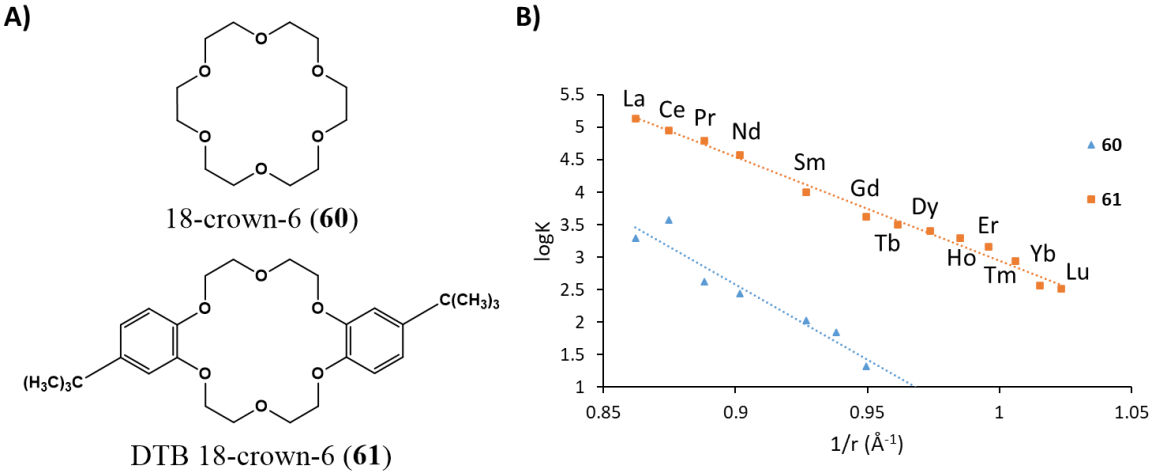

Figure 1-19 A) Structure of 18-crown-6 (**60**) and DTB-18-crown-6 (**61**). B) Stability constants of 18-crown-6 (**60**, determined by calorimetric titration in methanol), and DTB-18-crown-6 (**61**, determined by competitive potentiometric titration with Ag^{I} in acetonitrile) versus the reciprocal of the ionic radii of lanthanides. Reproduced from references.[128,129]

Pilloud and Bünzli explored the effect of the macrocycle size of the crown ether on the formation of complexes with Ln(III) ions.[130] This demonstrated that the complexation of the lanthanide ion by macrocyclic ligands is dependent on the fit between the ionic diameter and the dimension of the ligand cavity and its flexibility. When comparing crown ether to their corresponding podands (composed of ethylene glycol units), they have shown that the coronates demonstrated higher stability constants, especially for smaller ions as shown in Figure 1-20B, highlighting the interest of a preorganised binding unit. They also showed that the 15-crown-5 (**63-C**) is more suitable to form complexes with smaller Ln(III) ions while 18-crown-6 (**64-C**) is better for larger ions.[130] These results must be taken with care as the macrocycles adapt their conformation to coordinate smaller ions, leading to very similar values for **63-C** and **64-C** and in some cases it was possible to fit the data to the formation of 1:2 M:L complexes. It is possible to counter this trend by rigidifying the cycle by adding benzyl rings; however, the overall stability constants are greatly decreased.[131] Further modifications of macrocyclic receptors have been carried out using a pendant arm. This resulted in stronger complexation due to the binding unit used on the pendant arm but no significant size effect was observed along the lanthanide row, thus demonstrating the limitation of restricted flexibility in the coordinating molecule.

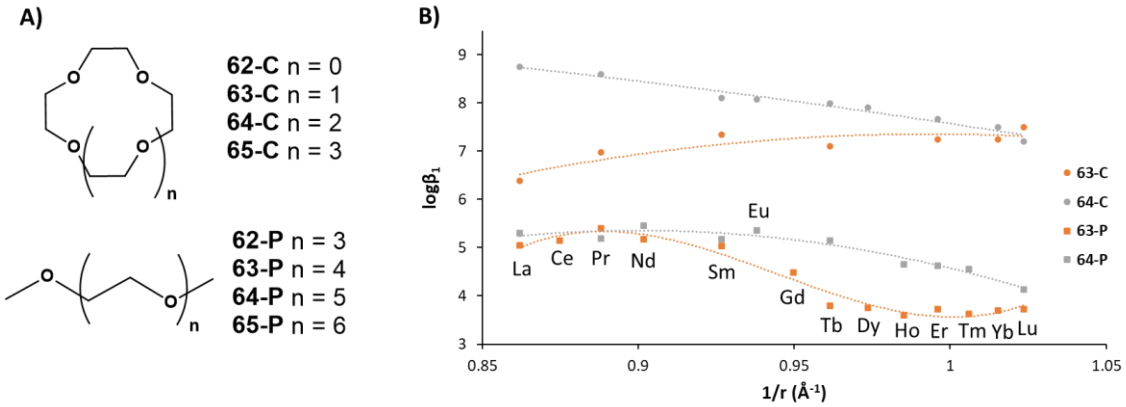

Figure 1-20) A) Structure of the crown ether and the corresponding podants used for the study. B) The plot of the cumulative binding constants for the formation of lanthanides complexes with **63-C**, **63-P**, **64-C**, **64-P** (in propylene carbonate) as determined by potentiometric titration versus the reciprocal of the ionic radii for a coordination number of 9. Reproduced from data obtained in references.[130,132,133]

To improve the selectivity of the complexation of lanthanides, a novel approach was undertaken: the use of a flexible ligand specifically designed to form stabilising non-covalent intermolecular interactions to further stabilise the final complex, called the induced fit concept.[131] The first ligand exhibiting intermolecular interactions strong enough to affect the thermodynamic trend was reported by Grenthe.[134] The dipicolinic acid (**66**), once deprotonated, form stable triple helicate complexes around Ln(III) ions, with two lightly different configurations along with the lanthanide series since the triple helicate is slightly distorted for larger lanthanide ions (Ce-Eu).[135] The ligand displayed a cumulative formation constant ($\log\beta_3$) for $[Ln(\mathbf{66}\text{-}2H)_3]^{3-}$ that follows the electrostatic trend, which is an increase of $\log\beta_3$ along with the lanthanide series for the large Ln(III) ions (La-Tb). However, as shown in Figure 1-21, for smaller lanthanides ions (Tm-Lu) the $\log\beta_3$ decrease which can be attributed to the electrostatic repulsion of the carboxylate groups that are being brought together by the coordination of the smaller lanthanide ion.[131]

Piguet and Bünzli studied the diethyl pyridine-2,6-dicarboxylate (**67**) and they reported that the cumulative formation constants $\log\beta_1$, $\log\beta_2$ and $\log\beta_3$ follow the electrostatic trend along with the radius contraction of the Ln(III) ions.[136] *N*,*N*,*N'*,*N'*-Tetraethylpyridine-2,6-dicarboxamide (**68**) was studied in the presence of various lanthanides and also resulted in the formation of triple-helical complexes.[137] This was further confirmed by the obtention of pure crystals of $[Ln(\mathbf{68})_3](TfO)_3$ for Sm, Eu, Gd, Tb and Lu while larger lanthanide resulted in a mixture of 1:2 and 1:3 M:L complexes. Similarly to **66** and **67**, the lanthanide ions are nonacoordinated with the six oxygen atoms of the carbonyl and the three nitrogens of the pyridine. UV-vis absorption titration of **68** upon addition of Ln(III) ions in acetonitrile resulted in the observation of the formation of 1:1, 1:2 and 1:3

M:L species. The cumulative formation constants obtained for **68** also resulted in the classical electrostatic interactions. However, the author recognised that the uncertainty on the value prevents the detection of small effects. More importantly, the ^{1}H NMR studies have shown that the symmetry obtained in the triple-helical complexes with the smaller lanthanides is altered for the bigger lanthanides which is in agreement with the weaker coordination of the pyridine with the larger lanthanides ions due to its slight torsion to accommodate the ion.[137]

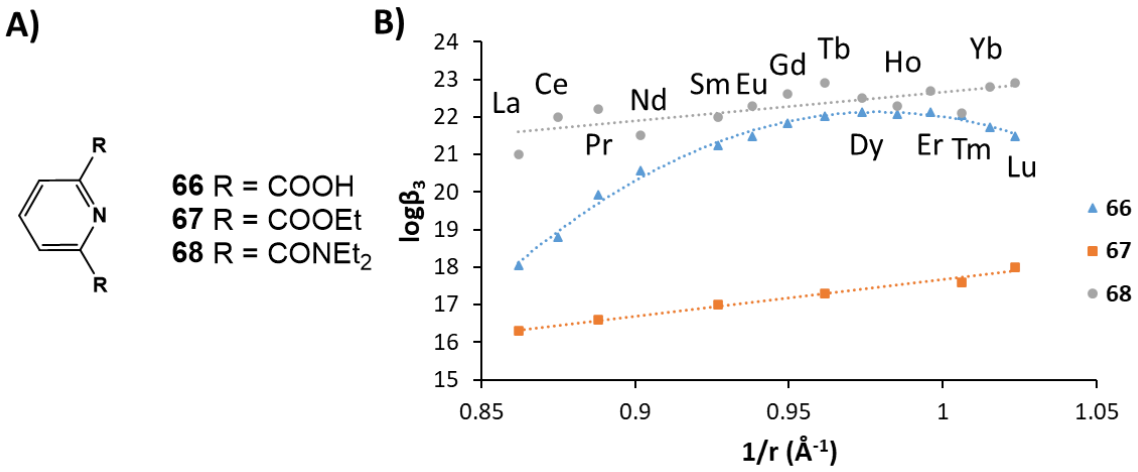

Figure 1-21 A) Structure of ligands **66-68**. B) The plot of the cumulative binding constants for the formation of lanthanide triple helicates with ligands **66** (in water), **67** (in acetonitrile) and **68** (in acetonitrile) as determined by spectroscopic titration versus the reciprocal of the ionic radii for a coordination number of 9. Reproduced from reference.[106,136,137]

Having established that the modification of the two carbonyl groups did not improve the size discrimination of **66-68** with the Ln(III) ions, Piguet and Bünzli developed 2,6-bis(1-methyl-benzimidazol-2-yl)-pyridine (**69**) and derivatised it using several lengths of chains in the R_2 position as shown in Figure 1-22A.[138] By the means of X-ray crystallography, NMR studies and UV-vis spectroscopic studies of the different complexes formed by **69** with La, Nd, Eu, Gd, Tb, Ho, Yb and Lu, it was proven that **69** assembled in a triple-helical manner around the lanthanide ions by coordinating it through nine heterocyclic nitrogens. X-ray crystallographic studies of the $[Eu(\mathbf{69})_3]^{3+}$ demonstrated a short distance between the benzimidazole rings of each strand and revealed strong intramolecular stacking, demonstrating the use of intramolecular interactions to favour the medium-sized lanthanides.

Spectroscopic titrations of **69** assembled with $Ln(ClO_4)_3$ in acetonitrile demonstrated the formation of 1:1, 1:2 and 1:3 M:L species and the cumulative binding constants further confirmed the observations made through the study of X-ray crystals structures, a lower stability for the complexes with the smaller lanthanides ions Ho(III), Yb(III) and Lu(III) was

determined. These results were further confirmed by competitive potentiometric titrations with Ag(I), demonstrating that the stability constants for the formation of $[Ln(\mathbf{69})_3]^{3+}$ are slightly lower than the one determined by spectroscopy but follow the same trend. Similarly to **69** and **70**, a decrease in the binding constant was observed for the smaller lanthanides demonstrating that the replacement of the methyl groups bound to the benzimidazole arms by lipophilic groups did not interfere on the self-assembly of the ligand around the ion.[138]

Addition of a bulky aryl group,3,5-dimethoxybenzyl in this case on the benzimidazole gave **71** which displayed an improved antenna effect relative to **69**. The stability constants for the formation of complexes were determined through competitive potentiometric titrations with Ag(I) and Ln(III) and showed almost no variation upon the changes in the ionic radius of the ions. Petoud *et al*. rationalized it by the presence of the bulky group resulting in a strong steric interaction with H_A when the two rings move from the transoid-transoid (free ligand) to cisoid-cisoid conformation upon complexation. Additionally, upon complexation, the formation of $[Ln(\mathbf{71})_3]^{3+}$ occurs. Each ligand is brought closer together and the dimethoxybenzyl groups are pushed together, therefore, hindering the formation of tight coordination environment around the lanthanide ion.[139] The influence of the substituents on the central pyridine of **71** was studied by the addition of an electron-withdrawing group (**72**) or an electron-donating group (**73**). The stability constants were also determined by the competitive potentiometric method with Ag(I) and Ln(III) and it was revealed that in the case of **72**, no 1:3 M:L complexes were observed either in solution or in the solid-state. However, both spectroscopic and potentiometric titrations revealed the formation of 1:1 and 1:2 complexes with Eu(III) ions, displaying a much lower stability constant than **69**. In the case of **73**, the ligand bearing an electron-donating group, the stability constants obtained were nearly as high as the one obtained for **69** and adhere closely to the trend that **69** displayed for the size discrimination effect as shown in Figure 1-22B. This highlights the importance of the substituent on the central pyridine ring which directly influences the electron density of the ring and therefore the strength of the N-Ln(III) interactions.[139]

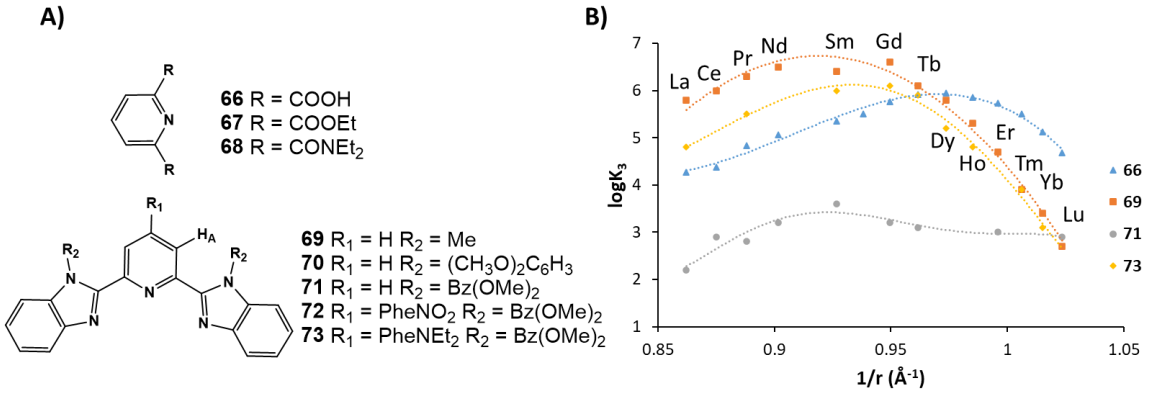

Figure 1-22A) Structure of ligands **66**-**73**. B) The plot of the third stability constants for the formation of lanthanide triple helicates with ligands **66**, **69**, **71** and **73** as determined by competitive potentiometric titration at 25 °C, I = 0.1 M, versus the reciprocal of the ionic radii for a coordination number of 9. Reproduced from reference.[139]

Renaud *et al*. also studied the effect of covalently linking three binding units (in this case **68**) to a core moiety of tris(2-aminoethyl)-amine (TREN). The resulting ligand **74** (shown in Scheme 1-6) was studied in the presence of various Ln(III) ions in acetonitrile. The fitting of the data obtained through spectrophotometric titration of **74** with $Ln(ClO_4)_3$ revealed the formation of 1:1 M:L complexes for Ln(III) ions of moderate to small-size (Nd (III)-Lu(III) ions) while the formation of both 1:1 and 1:2 M:L complexes was evidenced for Ln (III) ions of large to moderate-size (La(III)-Pr(III) ions). Interestingly the values of the cumulative formation constant of the 1:1 complexes $\beta_{1:1}$ did not follow the classical electrostatic trend that was observed for the non-clipped triple-helical complexes formed with **68**. Indeed, a minor decrease in the stability of the complexes formed with the smaller lanthanides ions was observed. This effect can be assigned to the clipping of the three binding units, which preorganise the binding unit leading to a structural control, along with improved thermodynamic stability and kinetic inertness of the lanthanide complexes.[140]

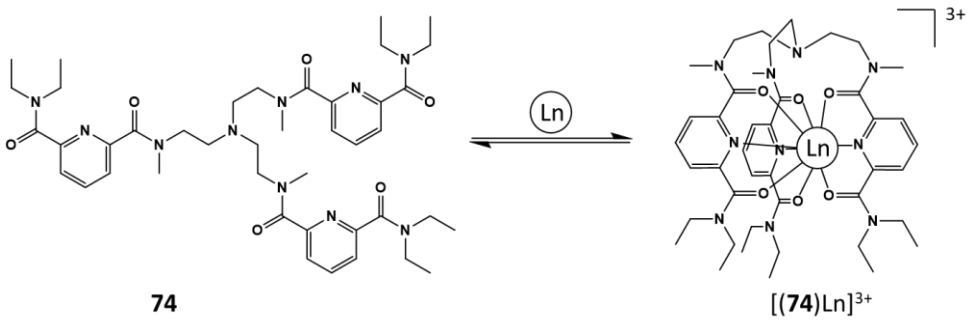

Scheme 1-6 Structure of the free ligand **74** and its corresponding lanthanide complex. Reproduced from reference.[140]

While TREN was used as the core for the formation of the tripodal ligand **74**, other moieties can be used for the formation of tripodal ligands. One that has attracted significant

attention, due to its easy functionalisation and ability to self-assemble, is the benzene-1,3,5-tricarboxamide which is described in the following paragraph.

1.6 Self-Assembly of the Benzene-1,3,5-Tricarboxamide Scaffolds

As described in the previous paragraphs, supramolecular chemistry allows the formation of extremely ordered structures through multiple interactions by simply designing a single molecule in such a way that a combination of weak interactions (H-bonding, π-π stacking, electrostatic interactions and hydrophobic interactions) and in some cases, metal complexation between each molecule will thermodynamically favour such organisation. The recent advances in this area have allowed scientists to develop new materials with tunable properties called soft materials. The notion of soft material brings together two major features: complexity and flexibility as explained by de Gennes.[141] The first feature, complexity, is clear because even using small and simple molecules, complex architectures are achieved in soft materials. The second feature, flexibility, is achieved by the material adapting itself to the environment through various physical modifications, change of shape and viscosity, with the most discernable being a change of organisation at the molecular scale which can result in a drastic change of the properties and functionality of the material.[142] Polymers, colloids, liquid crystals and gels are all part of the soft material family. Gels have attracted the interest of the scientific community over the last few years, and are defined as non-fluid colloidal networks or polymer networks that are expanded throughout their whole volume by a fluid. In the case of supramolecular gels, this polymer network is formed through the physical aggregation of polymer chains, caused by hydrogen bonds, π-π stacking, and electrostatic interactions to name just a few.[143]

A class of soft-materials composed of a molecule called low molecular weight gelators (LMWGs) have gained research interest and are classified as hydrogels when formed in water and organogels when formed in organic solvents. A wide variety of building blocks have been used to develop LMWGs like ureas, porphyrins, sugars and amino acids leading to the development of stimuli-responsive gels. The nature of the stimuli can be temperature, pH or chemical.[144-146] Despite an increasing number of building blocks used to form supramolecular gels a lot of them require multi-step synthesis limiting their application and their potential commercialisation. A privileged moiety in this area is benzene-1,3,5-tricarboxamide (BTA). The first BTA molecule was reported in 1915 by Curtius using benzene tricarboxylic acid as starting material yielding a C-centred BTA.[147] Nowadays, a

vast variety of starting materials allowing milder reactions conditions are commercially available such as 1,3,5-benzenetricarbonyl trichloride, using other starting materials it is also possible to obtain N-centred BTA (shown in Figure 1-23). Meijer *et al.* demonstrated that the N-centred BTA display weaker hydrogen bonding caused by the higher barrier for the rotation of the $C_{aromatic}$-N_{amide} bond compared to the C-centred BTA.[148]

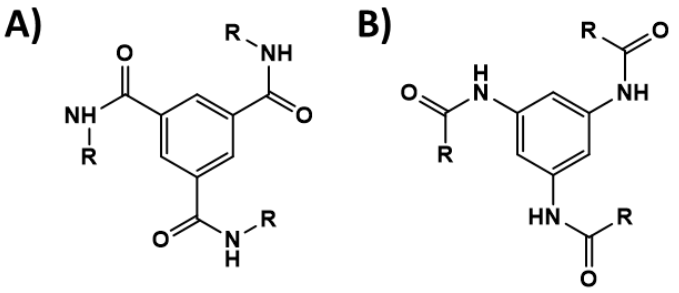

Figure 1-23 General structure of A) a C-centred BTA and (b) N-centred BTA.

Over the past few years, BTA molecules have been widely studied and derivatised using numerous groups such as alkyl, aryl, amino acids and oligopeptides amongst others.[149] These molecules have been investigated in a large variety of applications ranging from hydrogels to nucleating agent for polymers.[150,151] Depending on the application desired, the side-chain functionalisation is very important. Using long alkyl side chains induces liquid crystalline behaviour while bulky aliphatic side chains lead to crystalline solids. Introduction of a chiral moiety into the side chain usually leads to the formation of helical aggregates that have been extensively studied by Meijer *et al.*[152] Those aggregations and their mechanisms have been characterised using spectroscopic techniques such as circular dichroism and UV-visible absorption studies. Meijer demonstrated that C-centred BTAs self-assemble in solution owing to a strong threefold H-bonding into helical aggregates. Circular dichroism (CD) of these molecules showed a strong Cotton effect, around 220 nm, when a chiral centre is present in the molecule which confirms the helical nature of the assembly.[153]

Meijer *et al.* have also shown that the mechanism of formation of helical aggregates using BTAs includes a nucleation phase followed by an elongation phase, they have then studied the effect of substitution on the chiral centre of a self-assembled helix.[152] To do so they substituted the methyl at the chiral centre of the side chain by a deuterium atom (**75a** and **75b**) and studied the difference between the deuterated *R* and *S* alone, and in the presence of the other chiral molecules (**76a** and **76b**) that are shown in Figure 1-24.

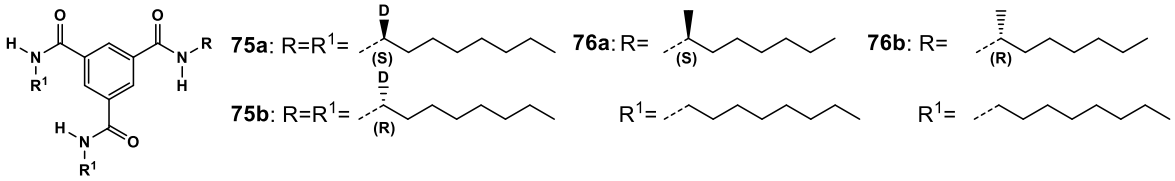

Figure 1-24 BTAs **75**and **76** used by Meijer *et al*. to study the effect of chirality on substitution. Reproduced from reference.[152]

UV-vis absorption and CD spectroscopy revealed that **75a** can form helical supramolecular polymers in dodecane. However, the net helicity also corresponding to the diastereoisomeric excess is of 0.38 (where a net helicity of 1 corresponds to a complete aggregation in either *P* or *M* helicity) thus both *M* and *P* helicity are present in solution with one slightly favoured. The sergeant and soldier study, using **75a** as the soldier and **76a** or **76b** as the sergeant, revealed that **76a** only needs to represent 6% of the molecule in solution to direct all the helical sense to *M* while **76b** needs to be accounted for 10% to direct all the helical sense to *P*. This demonstrates that the initial helicity in excess for **75a** is *M* and that when the sergeant is added to a solution containing chiral assemblies, to be able to dictate the helical sense, it is necessary to overcome both the helix reversal penalty (HRP) and the mismatch penalty (MMP) which occurs due to the presence of stacks in unpreferred helicity. This has demonstrated the importance of the substitution at the chiral centre upon the formation of helical aggregates and in particular, that even an isotope substitution can result in a significant alteration of the overall helicity. The absence of Cotton effect in the CD signals of **75a** in methylcyclohexane demonstrated that the structure of the solvent is crucial in the self-assembly process, thus revealing also the importance of the environment in which the systems are studied.[152]

Bouteiller *et al.* synthesised BTA derivatives from (L)-methionine (**77**), (L)-phenylalanine (**78**) and (L)-norleucine (**79**) dodecyl esters shown in Figure 1-25A. Using small-angle neutron scattering (SANS), they demonstrated that **77** and **78** were able to assemble at room temperature into rigid rods of a cross-section equivalent to one molecule and at 70 °C into dimers while **79** assembles into dimers at room temperatures. Infrared spectroscopy revealed that the NH and C=O of the amide groups are involved in hydrogen bonding for the formation of stacks for **77** and **78**, while for the dimer, the NH of the amide is interacting with the C=O of the ester for **79**. The transition from the stacked form to the dimeric form could be evidenced through concentration and temperature dependant IR studies, showing that at 60 °C the dimer is the only form present in solution while at 20 °C the dimer is only accounting for *ca*. 20% of the material present. Circular dichroism

measurements in several conditions demonstrated that both the stacked form and the dimers are CD active while the monomers are silent as shown in Figure 1-25B. It also revealed that the stacked form is preferentially right-handed helices in cyclohexane and exhibit only one maximum while the dimers exhibited three maxima. Overall this study demonstrated that the self-assembly of BTAs is strongly dependent on the nature of the amino-ester, the solvent used and the concentration.[154]

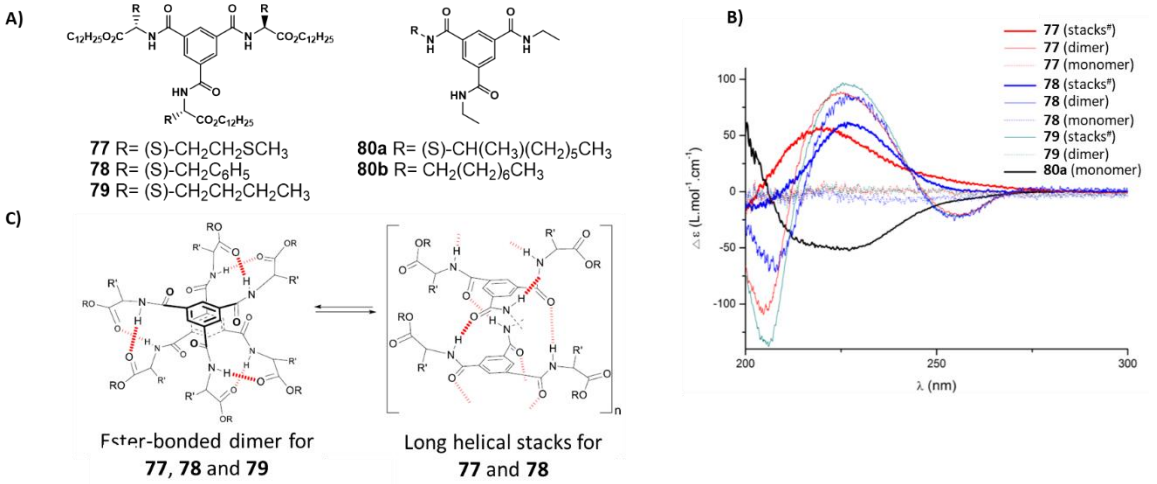

Figure 1-25 A) Structure of **77**, **78**, **79**, **80a** and **80b**. B) CD spectra of ester BTAs and **80**. C) Structures for the dimer and the long helical assemblies formed by ester BTAs. Reproduced from reference.[154]

Sanchez *et al*. synthesised a series of oligo(phenylene ethynylene) tricarboxamides (OPETAs), each of them composed of three (**81**), two (**82**) or one (**83**), stereogenic centres at the side chain (Figure 1-26A). OPETAs display similar behaviour to BTAs and form supramolecular polymers through a combination of π-stacking and the formation of triple array H-bonding interactions between the amides. The CD study of both absolute configuration *R* and *S* for each compound revealed similar patterns, thus demonstrating that the presence of multiple chiral centres in the tripodal compounds does not further influence the chirality of the supramolecular assembly than when the molecule only bears one chiral centre. However, the sergeant and soldier experiments shown in Figure 1-26E-G demonstrated that the number of chiral centres on the molecule influences the ability of the compound to dictate the chirality of the supramolecular assembly composed of an achiral compound (**84**), with the strongest results displayed by **81** which possess three chiral centres. From these experiments, they were able to estimate the HRP, revealing that **81** displays the highest helices reversal penalty and therefore that it is the one hindering the formation of domains with inverse helicity the most, so when the number of chiral centre on one monomer is increased, it increases the capacity of OPETAs to transfer the chiral information and to achieve a fully amplified chiral state.

The majority rule experiment, which consists of using different ratios of both enantiomers and recording the evolution of the CD signals as a function of the enantiomeric excess, allowed (in combination with variable temperature CD), for the determination of the MMP for each compound. This demonstrated that the MMP increases when the number of stereogenic centres in the molecule decreases; therefore, when the number of stereogenic centres decreases in a monomeric unit, its ability to achieve a fully amplified chiral state decreases too. This observation is in agreement with the effect observed from the sergeant and soldier experiment; however, this is the opposite to what was described for BTAs. These results were rationalised by previous studies and computational experiments demonstrating that in the case of BTAs, the angle between two monomeric units is of ≈ 65° thus the side chains are spatially far from each other and only produce weak interactions. While for OPETAs, it was found that the angle between two monomeric units is of ≈ 18° and therefore the side chains experience steric interactions with the surrounding side chains (Figure 1-26B and C). Therefore, this work has highlighted the importance of the size of the core of the self-assembling unit on the final helical polymer.

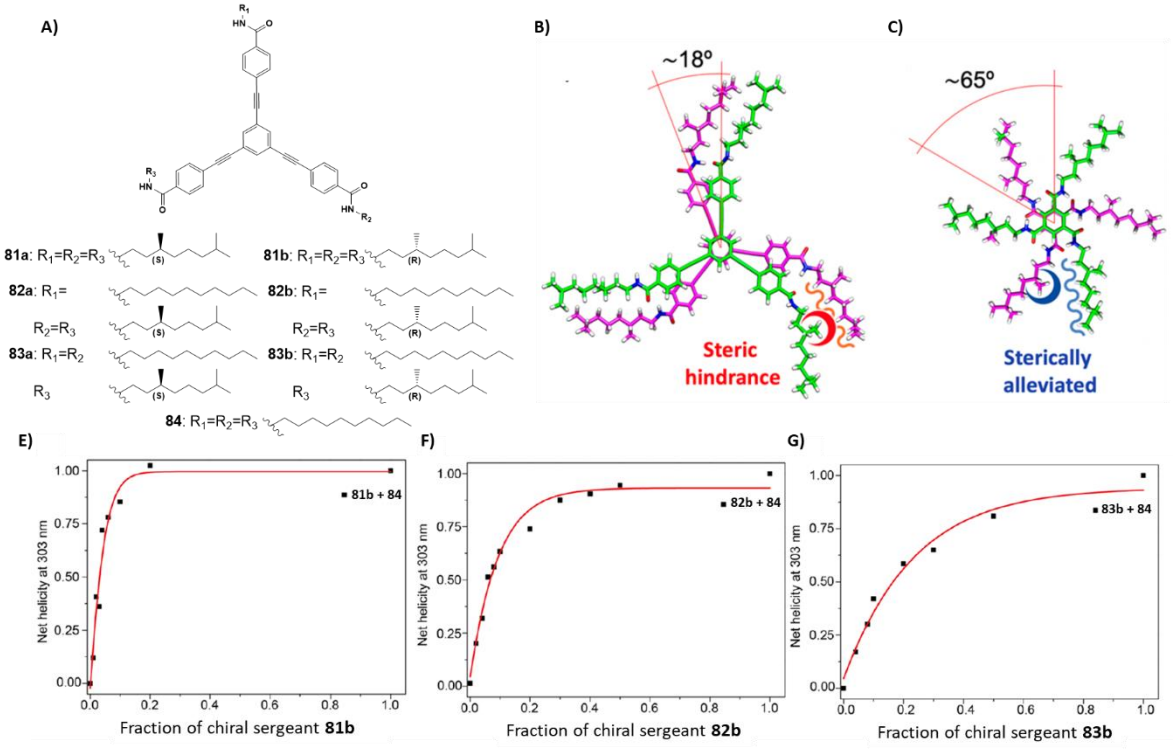

Figure 1-26 A) Structures of oligo(phenylene ethynylene) tricarboxamides 1−3. B) Schematic illustration of the steric hindrance effect occurring for OPETA **81b** and C) the analogous BTA. E-G) Sergeant and soldier experiments for achiral **84** upon mixing with chiral **81b** (E), **82b** (F), and **83b** (G). Reproduced from reference.[155]

Only a few examples of BTAs functionalised with terpyridine are found in literature, taking advantage of the terpyridine moiety and its ability to bind metals. One of these have

gained the attention of several research groups and was first synthesised by the Gunnlaugsson research group. It is composed of a BTA core and a propane chain, which is used as the spacer to link the terpyridine moieties to the core, as shown in Figure 1-27. **85** has shown interesting behaviour both alone and in presence of metals. The work done by the Gunnlaugsson group will be presented in a following chapter while the immediate proceeding section will remain focused on the work of other research groups.

Jung and coworkers have shown the possibility of forming chiral arrangements of achiral gold nanoparticles as shown in Figure 1-27. To do so, they used **85**, previously developed by the Gunnlaugsson group, as a gelator in DMSO:H_2O in the presence of a chiral component (**86**) allowing them to take advantage of the sergeant/soldier property of such assembly leading to the formation of specifically handed helixes. CD study of the gel in the presence of a various amount of **86a** or **86b** demonstrated that addition of 1 equivalent of the chiral component induces the maximum of CD intensity because all the chiral molecules are incorporated in the hydrogel while further addition of the chiral molecules leads to a decrease in CD intensity because the presence of **86** as a free component disrupts the formation of the nanofibres. Further investigations have shown that the chiral agent served as a template for Au(I) ions to spatially control the organisation of the nanoparticles at the surface of the nanofibers and that depending on the UV-photoreduction time of gold, the helically coupled plasmon absorption can be tuned throughout a range of the visible spectrum.[26]

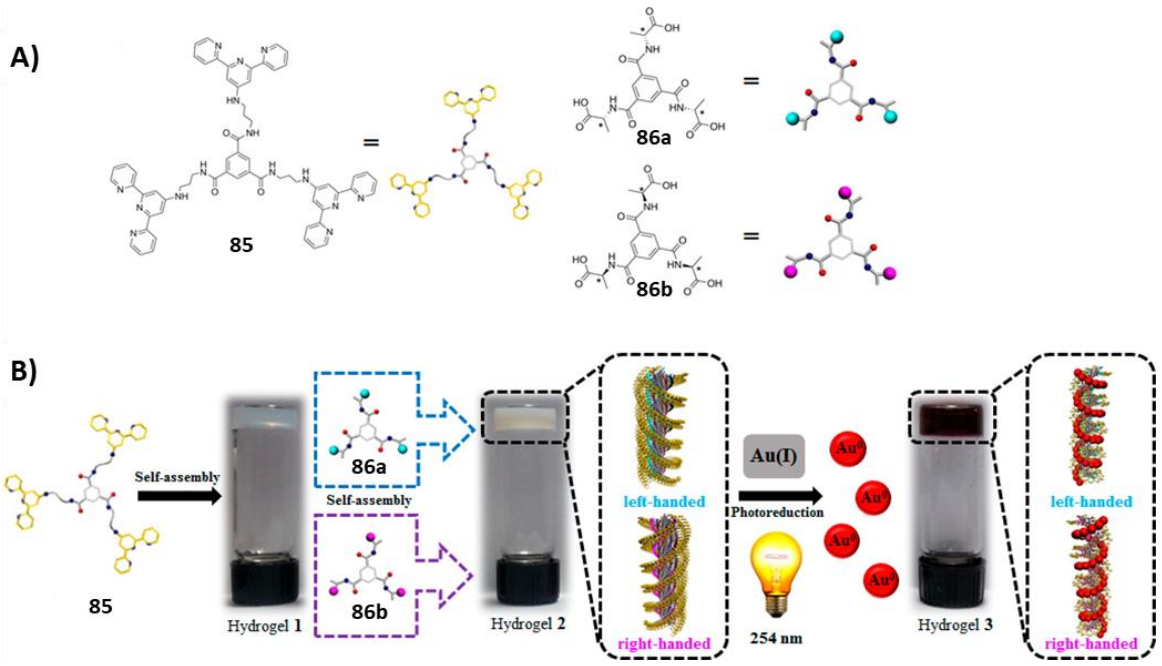

Figure 1-27 A) Structures of the gelator **85** and the two chiral agents (**86a** and **86b**). B) Formation of gel and chiral fibres as well as the chiral assembly of gold nanoparticles. Reproduced from reference.[26]

In 2015, Jung and coworkers demonstrated the use of **85** as a sensor for Zn(II) ions.[156] Indeed, in a DMSO:H_2O (1:99 *v/v*) mixture, the emission of the terpyridine moieties in compound **85** is quenched due to the aggregation of the compound in fibres as shown in Figure 1-28, bottom A. However, in the presence of Zn(II), the compound exhibits a strong emission with a maximum of emission at a 2:3 M:L ratio. Interestingly, the addition of other *d*-metal ions or various anions does not change the emission of the complex formed with Zn(II). TEM imaging showed that when **85** aggregates it forms fibrillar structures, while in presence of Zn(II) the compound forms spherical structures as shown in Figure 1-28, bottom B. While in the presence of other *d*-metals, only fibrillar structures could be observed. The "turn-on" effect of Zn(II) on **85**, is rationalised by the fact that without Zn(II), the terpyridines can freely rotate which can non-radiatively deactivate the excited species, while coordination of the terpyridine units by zinc blocks this rotation.

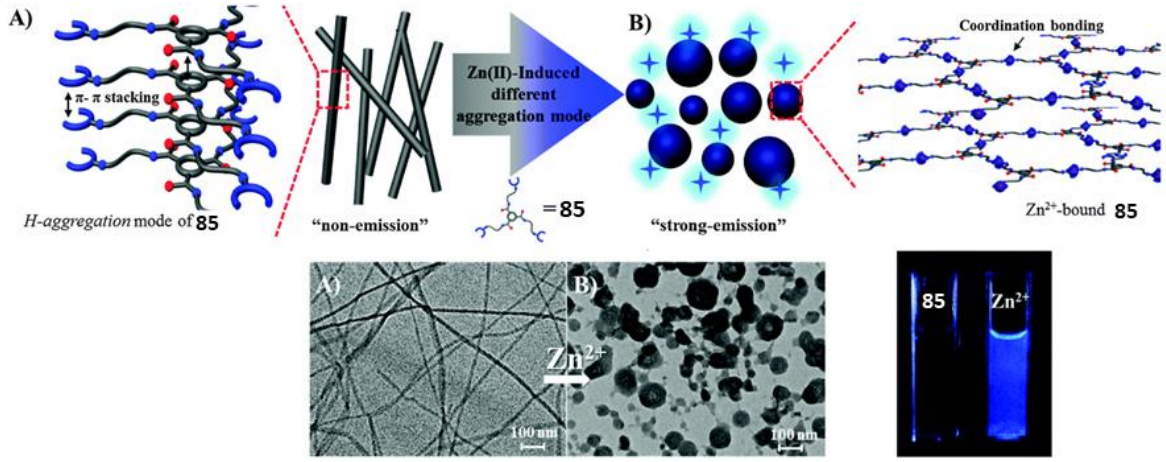

Figure 1-28 A) The aggregation mode of compound **85** alone and B) in presence of Zn(II) ions. Bottom line: TEM showing the aggregation mode of compound **85** A) alone and B) in the presence of Zn(II) ions and the bottom right picture shows the emission of the compound alone and in presence of Zn(II) ions under UV-light. Reproduced from reference.[156]

Jung and coworkers also formed a Tb(III) complex with **85** and showed that upon increasing the water content of the methanolic solution, the formation of fibres was observed and the complex emission considerably decreased, partly due to the aggregation caused quenching effect ("turn-off" of the chromophore). This quenching was also rationalized by the water molecules coordinating the Tb(III) ion and resulting in non-radiative energy transfer through O-H vibrations. Studies of the luminescence lifetime of the Tb-centred emission of **85-Tb** both in D_2O and H_2O allowed them to calculate the hydration number of the complex using the Horrocks equation previously described using 4.2 as the value for the parameter A, which describes the contribution of the inner-sphere to the quenching. This

revealed that **85** coordinates Tb(III) through one terpyridine unit and the coordination sphere of the Tb(III) ion is completed with 3 NO_3^- anions and 3 water molecules.

Following these results, they investigated the ability of **85-Tb** to bind biologically relevant anions which would decrease the number of water molecules bound to the Tb(III) ion and enhance its luminescence. The strongest "turn-on" effect visible on the Tb(III)-centred emission occurred through the addition of nucleotides and in particular, adenosine triphosphate (ATP). The binding of ATP to the Tb(III) ion was demonstrated through ^{1}H NMR with the proton peaks of the adenine group being shifted to the high field in the presence of **85-Tb** which is attributed to the formation of π-π stacking interactions with the terpyridine ring. The water peak which was broad without ATP was shifted and sharpened in presence of **85** indicating the dissociation of the water molecule from the Tb(III) ions by the addition of ATP. This observation was confirmed by the shift of the phosphate peaks in the ^{31}P NMR and their broadening in the presence of **85-Tb** which confirms the coordination of Tb(III) through the oxygen atoms of ATP as shown in Figure 1-29. The response of the complex has been demonstrated to be preferential to ATP over AMP and ADP, which can be rationalized by a lower number of oxygen atoms able to coordinate the Tb(III) ion and hinder the possibility of the adenine to form π-π stacking interactions with the terpyridine ring. The self-assembly of the complex with ATP showed stability over a pH range from 6 to 9, meaning that the complex is stable under physiological pH and that ionic strength does not affect the luminescence properties. More importantly, they have shown the capability of the complex to quantify the amount of ATP by measuring the luminescence intensity using calibrated luminescence lifetimes and that the complex could also be used effectively as a probe to monitor ATP levels for enzymatic *in vivo* reactions.[157]

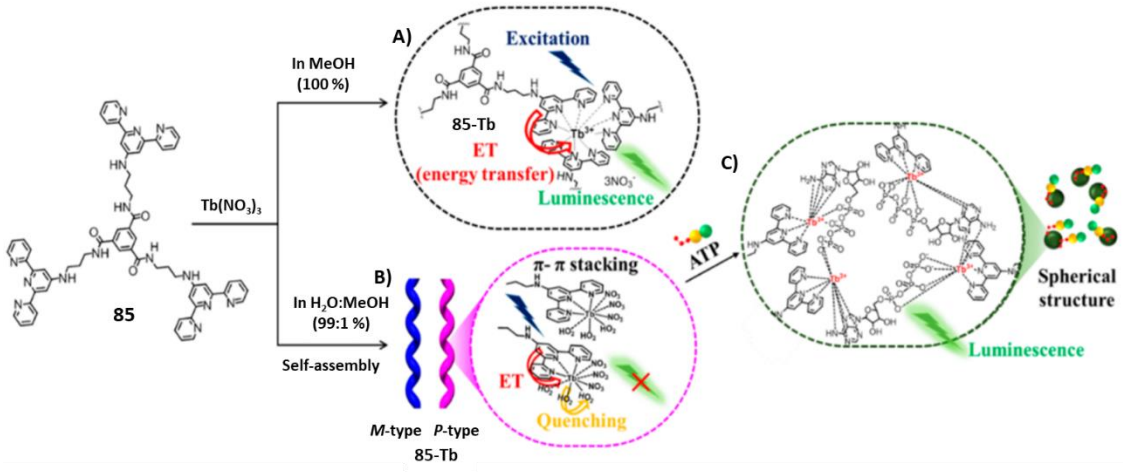

Figure 1-29 Schematic representation of the "turn-on" luminescence sensing mechanism of supramolecular assembly **85-Tb** for ATP: A) in MeOH (turn-on), B) in H_2O: MeOH mixture (turn-off), and C) in presence of ATP (turn-on). Reproduced from reference.[157]

Recently Hou *et al.* synthesised another BTA functionalised with terpyridine by using an alkoxy chain as the linker. The luminescent properties of **87** in the presence of Eu(III) and Tb(III) ions were studied and revealed the successful sensitisation of the Ln(III)-centred emission as well as the possibility to tune the colour of the emission from red to green by varying the ratio of Eu(III) and Tb(III) ions in the formation of the complex. The influence of the presence of different anions in solution on the luminescent properties of the complexes was investigated and interestingly revealed that for both **87-Eu** and **87-Tb**, the Ln(III)-centred emission decreases in presence of $H_2PO_4^-$. In the case of **87-Eu$_1$Tb$_1$**, as shown in Figure 1-30C, the Eu(III)-centred emission increases and the Tb(III)-centred emission decreases leading to a change of the colour of the emission from yellow to green. Further study of the sensing mechanism led to the conclusion that the amide close to the core of the molecule is involved in the coordination of the Ln(III) ions and when $H_2PO_4^-$ is present, the amide is not involved in the coordination anymore and instead, becomes involved in the formation of hydrogen bonds with the anion thus leading to a change in the coordination environment of Ln(III) ions. This change in the coordination is thought to promote the energy transfer from Tb(III) ion to Eu(III) ion leading to the increase in the luminescence of the Eu(III)-centred emission and the decrease of the Tb(III)-centred emission.[158]

By taking advantage of the tunability of the colour of the polymer emission depending on the ratio of Eu(III) and Tb(III) ions used and the excitation wavelength used, the Li research group also demonstrated the use of **87-Eu$_1$Tb$_{12}$** as a white light emitter.[159]

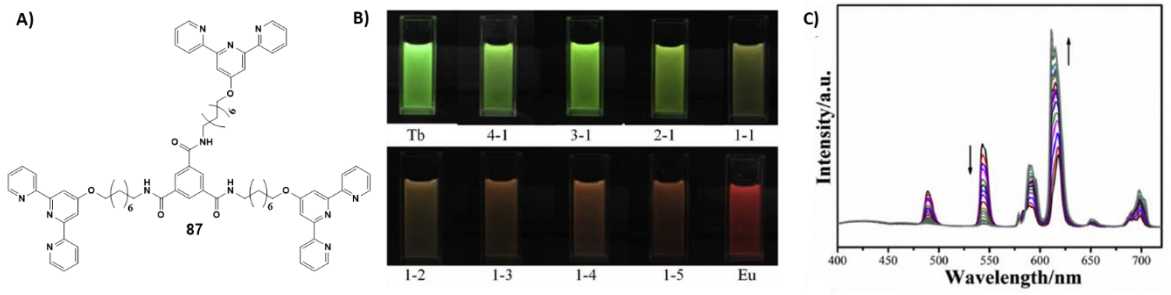

Figure 1-30 A) Structure of **87**. B) Photograph of **87-Ln** with different Tb:Eu ratio in DMF under UV lamp irradiation. C) Luminescence spectra of **87-Eu$_1$Tb$_1$** upon the addition of upon titration with $H_2PO_4^-$ (0-4 equiv.) in DMF solution (1×10^{-5} M, λ_{ex} = 328 nm). Reproduced from reference.[158]

The Gunnlausson research group have also developed expertise and contributed to the area of supramolecular chemistry through the development of sensors, polymers, and luminescent lanthanide complexes to name a few, using the building blocks and metals previously discussed. The remaining part of this chapter aims to outline the work described

in this thesis while the contribution of the Gunnlaugsson group to the synthesis and studies of these building blocks will be summarised at the beginning of the relevant chapters.

1.7 Work Described in this Thesis

The work described in this thesis furthers, and address the synthesis and characterisation of I) terpyridine functionalised naphthalamide, 4-amino-1,8-naphthalimide Tröger's base, their coordination with various *d*-metals and the spectroscopic and electrochemical properties of the resulting material being investigated while the influence of the self-assembly of II) BTA on the coordination to lanthanide ions is explored along with the synthesis of chiral BTA.

Chapter 2 presents the synthesis of a terpyridine functionalised naphthalimide followed by the characterisation of the ligand alone and the formation of complexes using *d*-metals with the study of their photophysical and electrochemical properties.

Chapter 3 discusses the synthesis and characterisation of a terpyridine functionalised 4-amino-1,8-naphthalimide Tröger's base, with the ability to produce aggregation-induced emission and its use as a nitroaromatics sensor along with a comparison with a TBNap covalent organic polymer used for the same application. The uses of **TBNapTPy** to form linear polymers with *d*-metals will be addressed along with the study of the associated photophysical and electrochemical properties.

Chapter 4 analyses the self-assembly study of **85** in solution followed by a spectroscopic investigation of the influence of this self-assembly on the coordination of lanthanide ions as a function of the ionic radius of the lanthanides. The formation and characterisation of hydrogels using **85** as a low-molecular-weight gelator are also discussed, followed by the modification of those gels using lanthanides ions or a second component such as a ruthenium polypyridyl complex.

Chapter 5 depicts the synthesis of amino-functionalised terpyridine moieties and the attempts to form a chiral tris-terpyridine BTA molecule along with the full characterisation of the successfully synthesised compounds.

The conclusions are presented in Chapter 6, while Chapter 7 outlines the experimental details of the work presented herein, followed by the references and additional information.

Chapter 2— Synthesis and Study of 4'-Phenyl-2,2′:6′,2″-Terpyridine Functionalised 4-Amino-1,8-Naphthalimide and its Metal Complexes

2.1 Introduction

One of the more established research areas within the Gunnlaugsson group has been based on the development of naphthalimide sensors. The first naphthalimide sensor designed and synthesised in the Gunnlaugsson group was based on the fluorophore-spacer-receptor principle with two compounds, **88** and **89**, being composed of a 4-amino-1,8-naphthalimide moiety as the fluorophore and a thiourea functionality as the receptor **88** and **89** as shown in Figure 2-1A.[160] Spectroscopic studies of the two compounds revealed that in the presence of AcO^-, $H_2PO_4^-$ and F^- the emission was significantly reduced (Figure 2-1B). This was rationalized by the presence of an inefficient induced PET in the absence of anions in solution which once added, form a complex with **88** or **89** and the PET becomes efficient and the emission is quenched. The binding of the anions to the compounds was investigated by ^1H NMR and showed that AcO^-, $H_2PO_4^-$ form 1:1 complexes while F^- forms 1:2 complexes. Monitoring of the absorbance as a function of the concentration of F^- revealed that at high concentrations of F^-, the formation of a new band at 536 nm was observed concomitantly with the disappearance of the band centred at 444 nm, thus indicating hydrogen bonding or deprotonation of the 4-amino moiety of the Amino-Nap centres.[160]

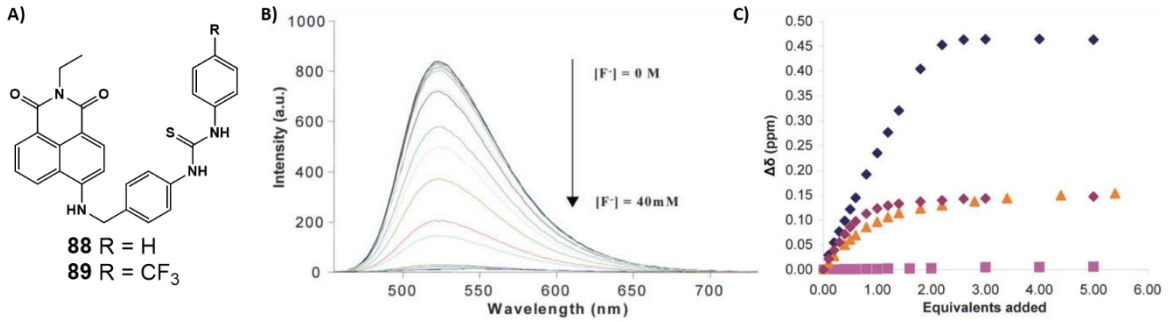

Figure 2-1A) Structure of **88** and **89**, B) changes of the emission of **88** upon addition of F^- and C) the chemical shift of one of the aromatic protons of **88** upon titration of several anions: F^- (blue diamond), AcO^- (red diamond); $H_2PO_4^-$ (orange triangle); Cl^- (pink square). Reproduced from reference.[160]

This system was further modified to shorten the spacer by removing the phenyl ring, and the receptor included either a urea moiety or thiourea to give compounds **90**, **91** and **92** (shown in Figure 2-2A).[161] Titration of AcO^- and $H_2PO_4^-$ ions demonstrated only minor changes in the absorption and emission spectra for the three compounds, while the presence of F^- showed significant changes in the absorbance with a bathochromic shift of the ICT band for the three compounds as shown in Figure 2-2B, for **90**. The emission spectra of **90** and **91** were significantly affected by the presence of F^- ion leading to the quenching of the emission in both cases while the emission of **92** was only quenched to *ca*. 20%, thus demonstrating that the thiourea is a stronger hydrogen bond donor.

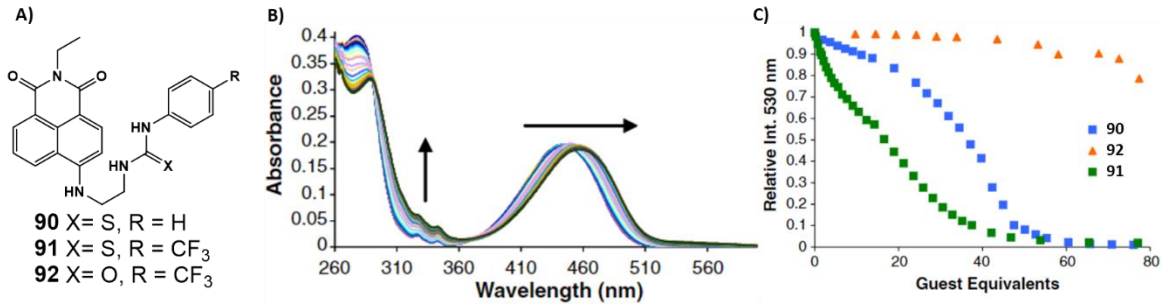

Figure 2-2 A) Structure of **90**, **91** and **92**, changes in the B) absorption of **90** and C) emission spectra at λ = 530 nm of **90**, **91** and **92** upon the addition of F^-. Reproduced from reference.[161]

Further experiments were carried on this system by linking the spacer and the receptor to the naphthalimide at the imide position as shown for **93** and **94** shown in Figure 2-3A. Veale *et al*. aimed to induce an electron-charge density at the imide position which leads to a PET quenching mechanism upon binding of the anion.[162] Similarly to the results previously observed, the addition of AcO^- and $H_2PO_4^-$ ions to a solution of **93** and **94** only showed minor changes in the absorption spectra and the addition of F^- at high concentration resulted (shown in Figure 2-3B) in similar changes for **93** to those observed for **89** while they were not visible for **94** due to the lack of 4-amino protons. Studies of the emission spectra of **93** and **94** upon the addition of AcO^- and $H_2PO_4^-$ ions revealed a moderate quenching of the emission with the formation of 1:1 complexes. Interestingly the addition of F^- led to a *ca*. 90% and only *ca*. 50% quenching of **93** and **94** respectively, revealing the influence of the substitution of the 4-amino position.

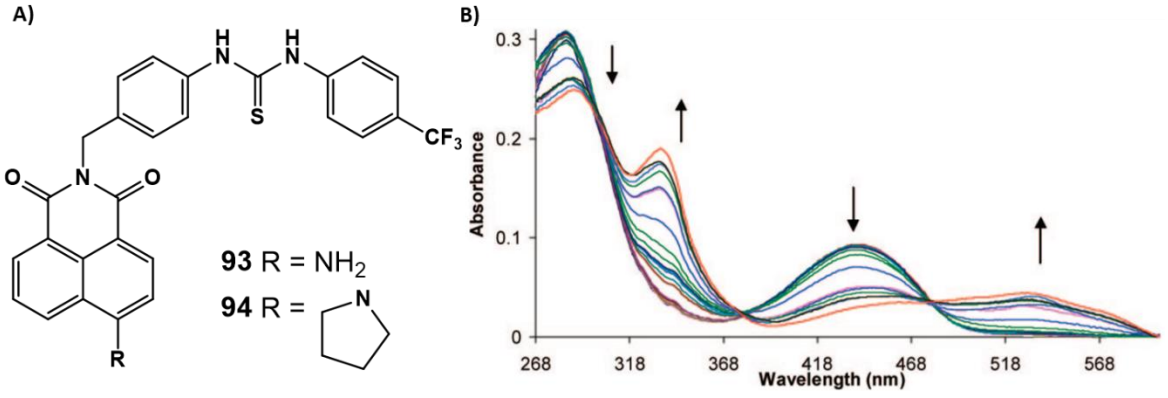

Figure 2-3 A) Structure of **93** and **94**, B) changes in the absorption spectra of **93** upon the addition of F^- ions. Reproduced from reference.[162]

Associated structures, **95** and **96** shown in Figure 2-4A, were synthesised in good yields. Spectroscopic studies of the two compounds as a function of the pH revealed a hypsochromic shift of the ICT band of **95** with decreasing pH and this was rationalised by the protonation of the amine in the sensor in acidic conditions, while **96**, which has a slightly longer spacer, only displayed a small decrease in absorbance when the pH was lowered. In

both cases however, monitoring of the emission as a function of the pH demonstrated a strong, fully reversible increase of the emission upon acidification which was attributed to the suppression of the PET mechanism. Taking advantage of the iminodiacetate, the coordination to various metal ions was attempted. It revealed that in presence of Zn(II) ions, both **95** and **96** did not display changes in their absorption spectra but instead, showed an increase in emission due to the coordination of Zn(II) ions which is rationalised by the suppression of the PET due to an increase in the oxidation potential of the receptor upon binding to Zn(II) ions. The binding constants were determined to be logβ = 3.9 and logβ = 4.0 for **95** and **96**, respectively. Binding of other metal ions was attempted and most of them only displayed minor changes with Cd(II) ions being the most competitive one with binding constants determined to be logβ = 2.0 and logβ = 1.8 for **95** and **96**, respectively, thus demonstrating that the two sensors show good potential for sensing of Zn(II) ions in biological systems.[163,164]

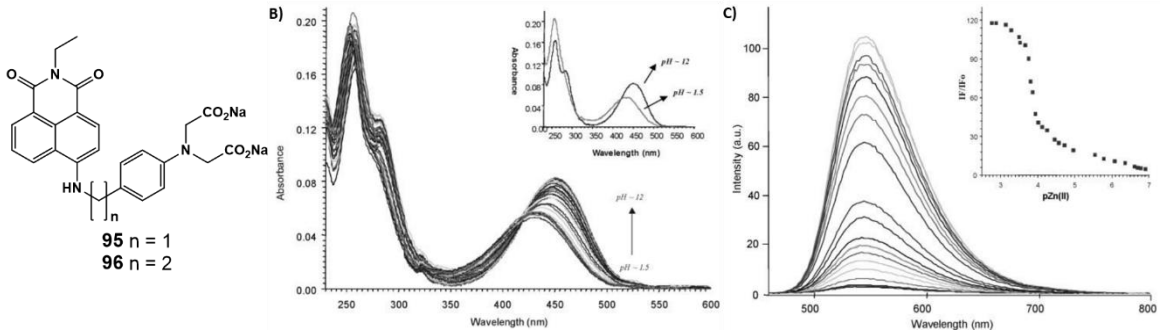

Figure 2-4 A) Structure of **95** and **96**, B) changes in the absorption of **95** in the function of pH and inset show the absorption spectra at pH 1.5 and 12, C) Changes in the emission of **95** in the function of the concentration of Zn(II) ions and inset the changes at 550 nm as a function of −log[Zn(II)]. Reproduced from references.[163,164]

Another example developed in the Gunnlaugsson group corresponds to the functionalisation of a naphthalimide in the 3-position by a trifluoromethyl aryl urea which demonstrates a significant change of its fluorescence in the presence of fluoride anion *via* deprotonation of the urea receptor.[165]

Inspired by Baitalik and co-workers[166] who used a ruthenium complex as an anion sensor, Gunnlaugsson *et al.* used a naphthalimide polypyidyl complex **97** (shown in Figure 2-5A) to sense the fluoride anion. The mechanism of this system is such that the anion recognition interferes with the energy transfer from the naphthalimide to the Ru(II) MLCT excited state leading to the quenching of the red Ru-centred emission. This sensor has been tested with Br^-, Cl^-, AcO^-, $H_2PO_4^-$ and F^- all of which have shown changes in the absorption and emission spectrum.[167]

These compounds were first synthesised because ruthenium (II) complexes with intercalating groups and chromophores have been used for targeting DNA. Using the well-known photophysical properties of the naphthalimide and its ability to intercalate into DNA, they have synthesised the first example of a naphthalimide derivative **97** able to cleave DNA. They have also demonstrated that the presence of the electron-deficient nitro group at the 4-position of the naphthalimide alters the ability of the compound to bind to DNA. The absorption spectrum of the amino-naphthalimide shows a single band in the visible region due to both the amino-naphthalimide ICT and the MLCT of the metal complex. Excitation at this wavelength, however, only gives rise to the MLCT-based emission at 635 nm as it is possible to see in Figure 2-5B, thus demonstrating that both the naphthalimide and the bipyridine contribute to the Ru(II)-centred emission. The complex was expected to interact with DNA using electrostatic and π-stacking interactions as well as intercalation of the naphthalimide moiety. Those interactions have been highlighted by DNA titrations in 10 mM phosphate buffer at pH 7.0, leading to significant changes in the absorption and emission spectra as shown in Figure 2-5C. Using agarose gel electrophoresis, it has been shown that both the nitro-naphthalimide and the amino-naphthalimide can cleave DNA upon irradiation but at P/D 10, the supercoiled DNA has been completely converted by the amino-naphthalimide, showing that it is a significantly better DNA cleaver than its corresponding nitro derivative.[168]

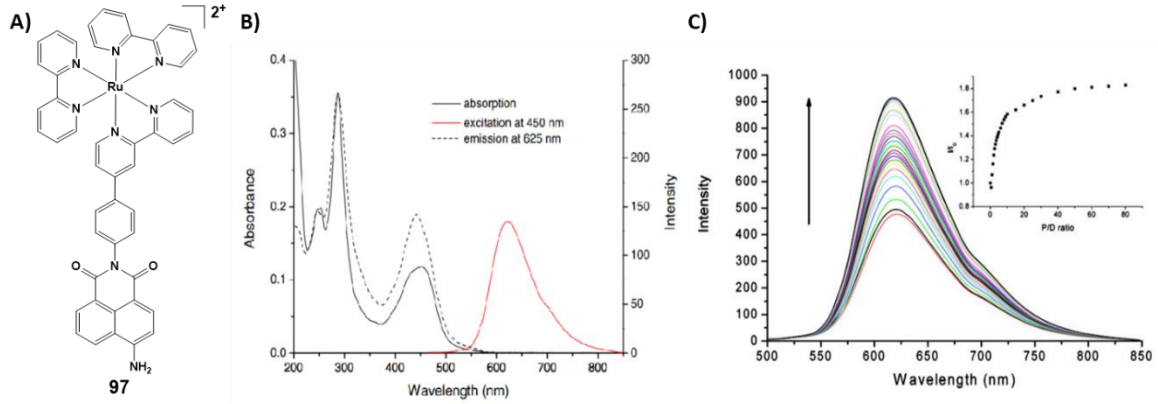

Figure 2-5 A) Structure of **97**, B) absorption, emission and excitation spectrum of **97** and C) changes in the emission spectrum of **97** with an increasing concentration of st-DNA (0-670 μM). Reproduced from reference.[168]

Veale *et al*. also synthesised a tris(2-aminoethyl)amine (TREN) based 4-amino-1,8-naphthalimide **98** (shown in Figure 2-6A) which displayed minor changes in the absorption spectra as a function of the pH, while the emission was highly sensitive to the pH.[169] Indeed, its emission intensity was the highest at pH < 4 due to the protonation of all the amine of the TREN moiety thus hindering PET. As pH was increased, the successive deprotonation of

the amino groups gave rise to a successive increase in efficiency of the PET quenching. It was also demonstrated that upon the addition of various *d*-metals, only the presence of Cu(II) ions affected the spectroscopic properties of **98**. Interestingly, titrations of Cu(II) ions at two different pH revealed a higher extent of the quenching for the titration at pH 7.4 and the fitting of both titrations revealed that at pH 5.6 the formation of 1:2 (Cu(II): **98**) was the predominant species and at pH 7.4 the formation of 1:1 (Cu(II): **98**) was the predominant species as shown in Figure 2-6B concomitantly with a higher quenching of the emission, thus demonstrating the effect of the pH on the sensing of Cu(II) ions.

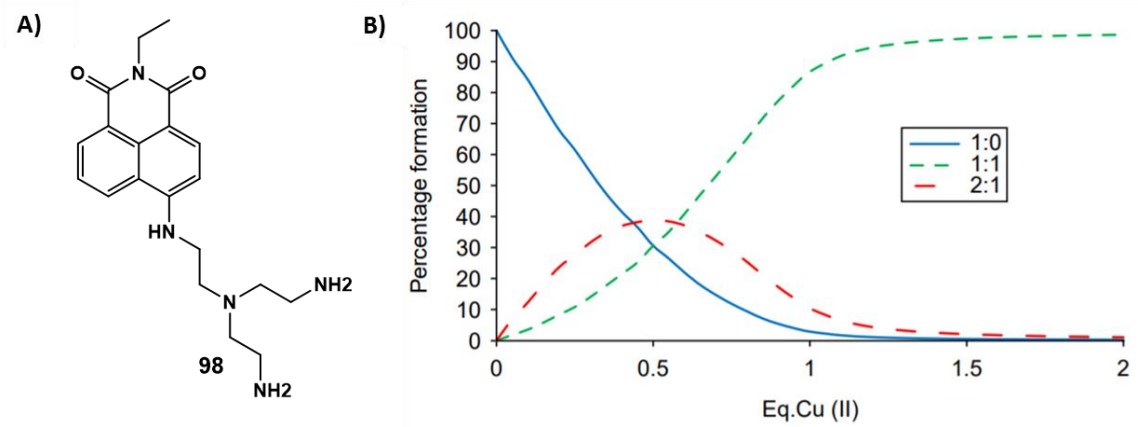

Figure 2-6 A) Structure of **98** and B) speciation-distribution diagram obtained through the fitting of the titration of Cu(II) ions in the presence of **98** at pH 7.4. Reproduced from reference.[169]

Kitchen *et al*. explored the effect of the imide substitution of 4-nitro-1,8-naphthalimide by substituting 4-aminopyridine and 3-aminopyridine and quaternised the pyridine using benzyl bromide to obtain single crystals of X-ray diffraction quality. Complexation of the two ligands with different Cu(II) salts in 1:2 (M:L) ratios afforded single crystals of X-ray diffraction quality, leading to the discovery of very different coordinations. Indeed, with $Cu(OAc)_2$ dinuclear acetate bridged systems were obtained while reactions with $Cu(CF_3SO_3)_2$ and $Cu(ClO_4)_2$ led to the formation of mononuclear systems, thus revealing the importance of subtle changes such as the counter ion and even a small modification of the coordinating unit.[170]

Lovitt *et al*. studied further the use of a coordinating unit at the imide position of 1,8-naphthalimide by using 2- 3- and 4-picolylamine shown in Figure 2-7A.[171] Coordination of **99**, **100** and **101** to Mn(II), Co(II) and Ni(II) chloride led to single crystals suitable for X-ray diffraction while the use of **102** led to the formation of strong gels upon coordination to Mn(II), Co(II) (shown in Figure 2-7B) and a weak gel in the presence of Ni(II) chloride. Further attempts to form gels using **102** using 1:1 and 1:2 (M:L) ratio with Co(II) were successful along with the formation of mixed metallo gel using Co(II)/Ni(II) and

Co(II)/Mn(II). To understand the influence of the 4-amino functionalisation on the gelation, piperidine was used to form **105** which was also able to form gels upon coordination to Mn(II), Co(II). While the use of **103** and **104** did not lead to the formation of gels or good quality crystals demonstrating the influence of the position of the pyridine at the imide position. Thermogravimetric analysis of the gels formed by **102** revealed a weight percentage (*wt* %) between 1.5% and 1.7% for each gel and SEM demonstrated that the gel is formed through a densely packed fibrous network. Rheological studies of the gels demonstrated their ability to recover after undergoing the gel-sol transition while the chemical modification of the gel through the addition of a competing coordination unit, another *d*-metal, a π-rich species or the sequestration of chloride anions led to the destruction of the gels.

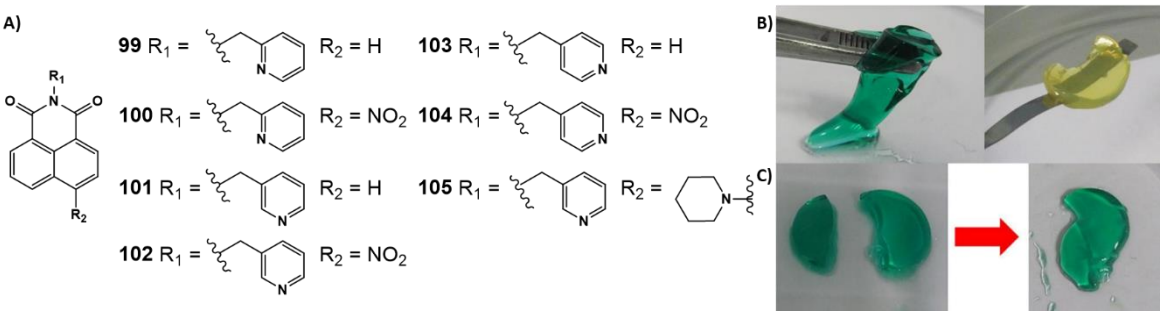

Figure 2-7 A) Structures of **99**-**105** and B) pictures of **102** gels with Co(II) (left) and Mn (II) (right) C) the recovery of the Co(II) gel after incision. Reproduced from reference.[171]

This work was extended to 4-oxonaphthalimide by Hawes *et al*. through the functionalisation of the naphthalimide at the 4-position by 4-hydroxybenzoic acid to form **106** shown in Figure 2-8A.[172] A gel could be formed by dissolving **106** in the presence of K_2CO_3 in water and conditions screening revealed that only 2.5 mg of **106** and 6 eq. of K_2CO_3 were necessary to induce gelation; however, the thermal stability was greatly reduced with a sol-gel transition at 38 °C against 81 °C when using 10 mg of **106**. SEM studies showed the presence of thick branching fibrils (Figure 2-8B). The robustness of the gel was assessed by rheological measurement demonstrating a rapid recovery of the solid-like behaviour of the gel after shearing over multiple cycles. The uses of other bases to dissolve **106** in water highlighted the key role of K_2CO_3 to lead to the presence of K^+ ions in solution to reduce the carboxylate-carboxylate interactions which have proven to be essential for the formation of the hydrogel.

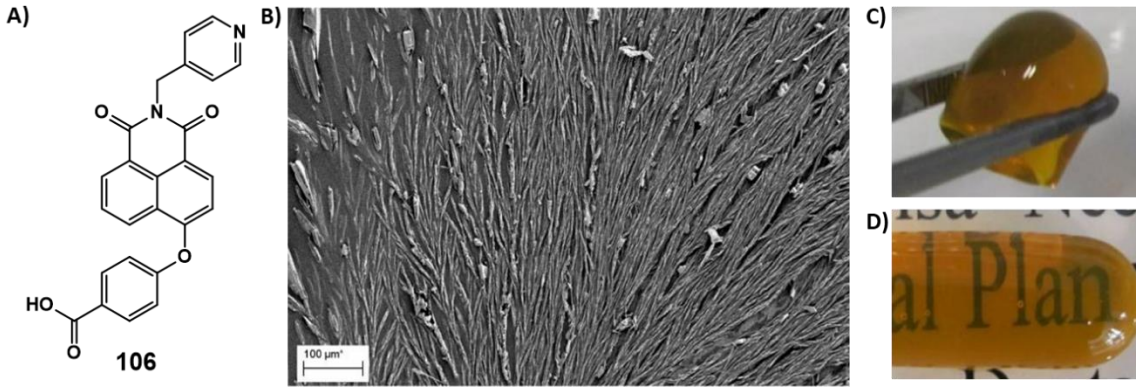

Figure 2-8 A) Structure of **106**, B) SEM picture of the xerogel, pictures of the gel showing C) robustness and D) transparency. Reproduced from reference.[172]

As described in the previous examples, the photophysical properties of 1,8-naphthalimides have been extensively studied for use in a wide range of applications. Depending on the desired application, functionalisation at the imide position and the 4-position is of paramount importance. While a variety of urea and thiourea anion sensors were synthesised and studied by the Gunnlaugsson research group,[160-162] only a few examples of naphthalimides functionalised with coordinating units were reported by the Gunnlaugsson group, but nevertheless these showed very interesting properties, such as the luminescent ruthenium complex (**97**) which demonstrated the ability to interact with DNA and to cleave it,[173] and the work by Lovitt *et al*. where picolylamines were used to functionalise naphthalimides and form gels upon coordination to various *d*-metal ions.[171]

In this chapter, the functionalisation of the naphthalimide moiety through the imide using 4′-(4-aminophenyl)-2,2′:6′,2″-terpyridine is described. Coordination to various *d*-metal is also explored in this chapter along with a brief study of their spectroscopic and electrochemical properties.

2.2 Synthesis and Characterisation of 4-Amino-1,8-Naphthalamide and *d*-Metal Ion Complexes

2.2.1 Synthesis and characterisation of 4-amino-1,8-naphthalimide

The 4-amino-1,8-naphthalamide adorned with the phenyl-terpyridine moiety **AminoNap-Tpy** (**107**) was synthesised from commercially available 2-acetylpyridine, 4-nitrobenzaldehyde and 4-nitro-1,8-naphthalic anhydride, in a few steps.

Formation of 4′-(4-nitrophenyl)-2,2′:6′,2″-terpyridine was carried out using the procedure described by the Brudvig research group,[174] and shown in Scheme 2-1, consisting

of the formation of the chalcone precursor **108**, using 2-acetylpyridine and 4-nitrobenzaldehyde in 69% yield, and the formation of the desired 2-pyridinylpyridinium iodide salt **109** in 32% yield. The 4′-(4-nitrophenyl)-2,2′:6′,2″-terpyridine (**110**) was synthesised using **108** and **109** in the Kröhnke reaction in the presence of ammonium acetate, in methanol; a 4 h reflux led to the precipitation of a white compound which was isolated to give **110** in 75% yield. The reduction of the nitro group of **110** was achieved through catalytic hydrogenation using 10 *wt* % Pd/C under 3 atm of H_2 in DMF. Filtration of the resulting mixture through celite and removal of the solvent under reduced pressure gave **111** as a yellow solid in 89% yield. All the intermediates were characterised by ^{1}H NMR (see appendix), and all were in good agreement with the data previously reported in the literature.[174-176]

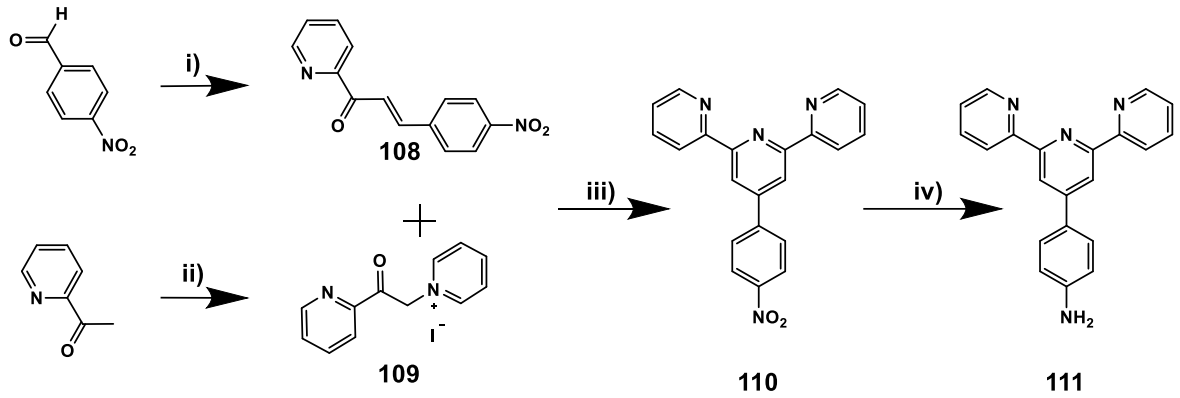

Scheme 2-1 Synthesis of 4′-(4-aminophenyl)-2,2′:6′,2″-terpyridine from 2-acetylpyridine and 4-nitrobenzaldehyde, i) 2-acetylpyridine, NaOH, MeOH, 32%; ii) I_2, pyridine, Ar, reflux, 69%; iii) NH_4OAc, MeOH, reflux 4 h, Ar, 75%; iv) 20% Pd/C, DMF, H_2, 24 h, 89%.

Single crystals of X-ray diffraction quality of **111** were obtained by evaporation of the ether solvent used to triturate **111**. The crystallography analysis was carried, out and the data solved and refined by Ms Deirdre McAdams and Dr. Brendan Twamley (TCD). The diffraction data was solved and refined in the orthorhombic space group $Pca2_1$. The asymmetric unit contains one molecule (Z = 4) and, as shown in Figure 2-9, the terminal pyridine rings are orientated along with the interannular bond in a *transoid* arrangement, which is, typically observed for terpyridine moieties,[177] an angle of *ca*. 29° can be observed between the phenyl ring and the central pyridine ring. The interannular C-C bond lengths [1.480(6)-1.491(5) Å], C-C [1.368(6)-1.396(6) Å] and C-N [1.332(6)-1.350(5) Å] in the pyridyl units are comparable to those previously reported for **111** and similar structure.[38,177,178] While no hydrogen bonding interactions could be observed, one of the terminal pyridine rings forms a π-π association with the central pyridine ring of another molecule of **111** with a centroid-centroid distance of 3.914 Å, a shift distance of 1.469 Å and

an angle of 7.047° between them demonstrating that the rings are not co-planar. As shown in Figure 2-9B, the bulk structure displayed a herringbone-type packing arrangement.

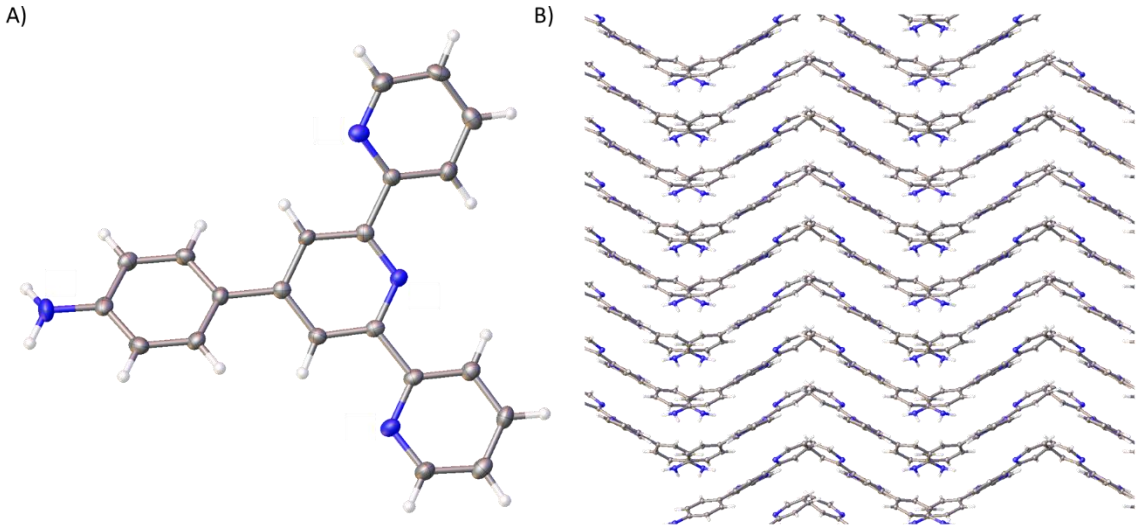

Figure 2-9 A) Crystal structure of ligand **111**. Thermal ellipsoids are shown at the 50% probability level. Nitrogen atoms are marked in a blue colour. B) Supramolecular architecture of **111** viewed normal to the 100 plane. Displacement parameters shown at 50% probability.

The functionalisation of the 4-amino-1,8-naphthalic anhydride by **111** at the imide position was carried out following a modified procedure commonly used in the Gunnlaugsson research group,[171] and is shown in Scheme 2-2.

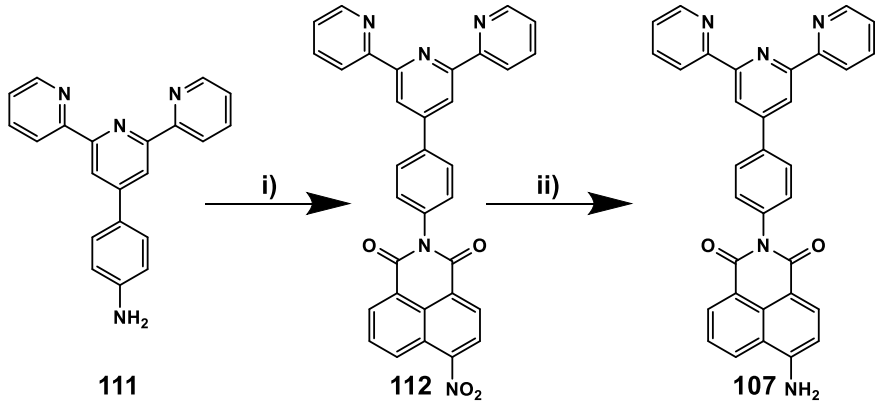

Scheme 2-2 Synthesis of **AminoNap-TPy** i) 4-nitro-1,8-naphthalic anhydride, AcOH, reflux, 40%; ii) 20% Pd/C, DMF, H_2, 12 h, 95%.

4-nitro-1,8-naphthalic anhydride and **111** were dispersed in acetic acid in a pressure vessel and the resulting mixture refluxed for 24 h. Neutralisation of the reaction mixture led to the precipitation of a beige solid which was isolated and triturated in warm ethyl acetate to give the desired product **112** in 39% yield. The successful synthesis of **112** was demonstrated by HRMS (MALDI) with the presence of the $[M+H]^+$ ion (*m/z* = 550.1532). It was further confirmed by ^1H NMR (DMSO-d_6, 600 MHz, as shown in Figure 2-10) with

the singlet corresponding to the $H_{3',5'}$ resonances being shifted from 8.64 ppm to 8.81 ppm and the disappearance of the NH_2 signal at 5.61 ppm (see appendix).

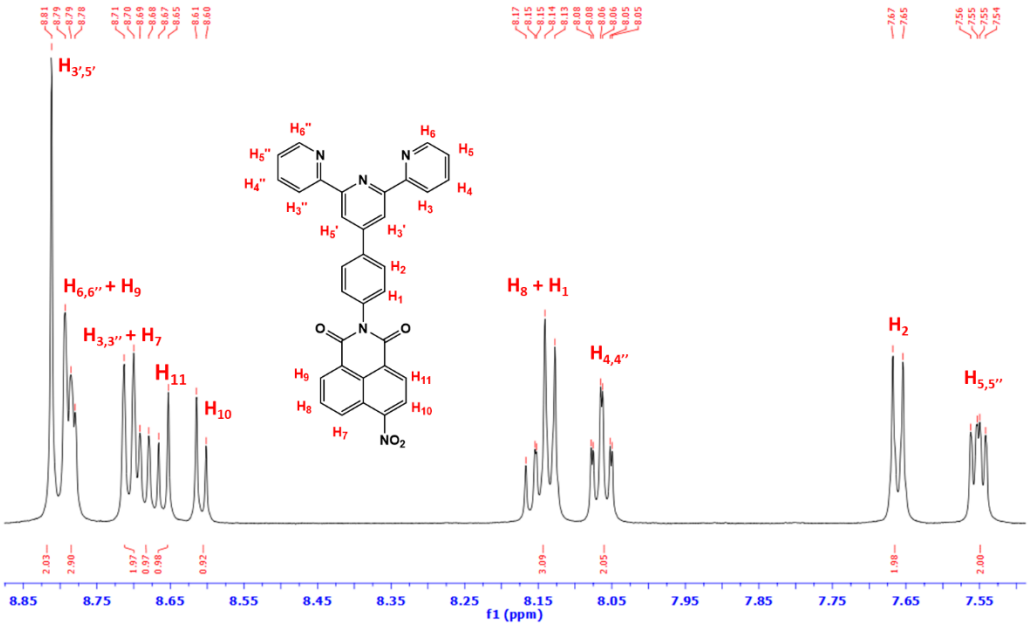

Figure 2-10 ^{1}H NMR (DMSO-d_6, 600 MHz) of the highlighted aromatic region of **112**. Full spectrum shown in Figure A. 5 in the appendix.

Single crystals of X-ray diffraction quality of **112** were obtained from the evaporation of the ethyl acetate used to triturate the product. The crystallography was carried out and the data solved and refined by Dr. Hannah Dalton, in the monoclinic space group $P2_1/c$. The asymmetric unit contains one molecule (Z = 4), similarly to its precursor **111**, and as shown in Figure 2-11, the terminal pyridine rings are orientated in a *transoid* arrangement which is typically observed for terpyridine moieties.[177] An angle of *ca*. 42° can be observed between the phenyl ring and the pyridine while an angle of *ca*. 69° can be measured between the naphthalimide moiety and the phenyl spacer. The interannular C-C bond lengths [1.485(4)-1.495(4) Å], C-C [1.374(6)-1.393(5) Å] and C-N [1.333(4)-1.349(4) Å] in the pyridyl units are comparable with those previously reported for **111** and similar structures.[38,177,178] Weak intermolecular hydrogen bonding interactions are observed between C(28)-H(28) ··O(3) corresponding to H_6 and the oxygen of the carbonyl group of the imide, C(31)-H(31) ··O(1) corresponding to H_3 and the oxygen of the nitro group and C(34)-H(34) ··O(1) corresponding to $H_{3''}$ and the oxygen of the nitro group. They displayed a C···O distances of 3.277(4), 3.396(5) and 3.364(5) Å, respectively and correspond to C-H···O angles of 140.3°, 131.8° and 130.3°. As seen in Figure 2-11B, π-π associations are also observed between the terminal pyridine rings and the rings of the naphthalimide moiety with a centroid-centroid distance of [3.529-3.725 Å], a shift distance of [1.036-1.577 Å] and

an angle of [3.498-4.208°]. Within the bulk structure, the molecules are closely orientated with alternating head to toe arrangements.

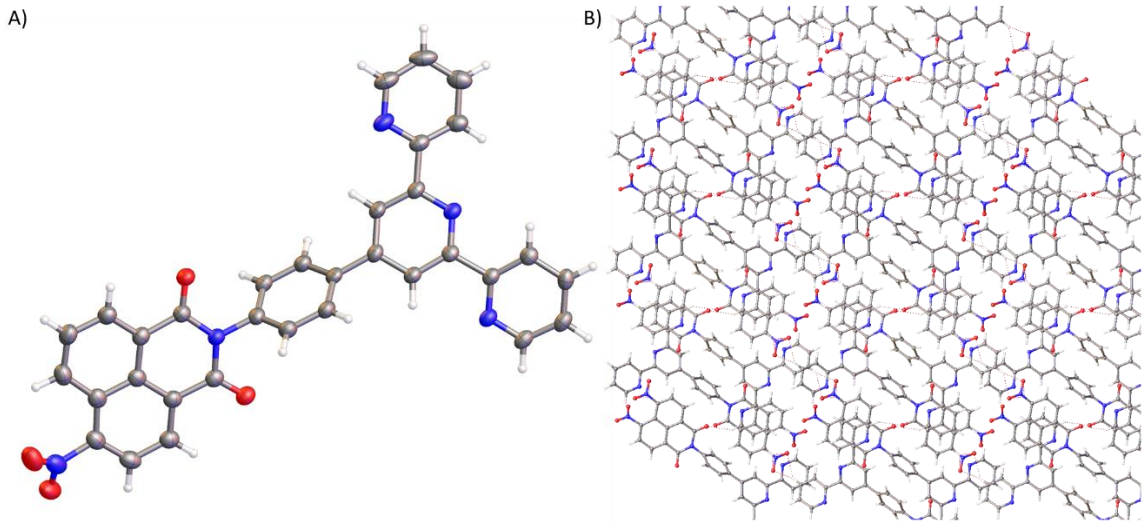

Figure 2-11 A) Crystal structure of **112**. Thermal ellipsoids are shown at the 50% probability level. Nitrogen atoms are marked in a blue colour and oxygen atoms are marked in red colour. B) Supramolecular architecture of **112**. Displacement parameters shown at 50% probability.

The reduction of the nitro group of **112** was achieved through catalytic hydrogenation using Pd/C under 3 atm of H_2 in DMF. Filtration of the resulting mixture through celite and removal of the solvent under reduced pressure gave **107** as a mustard coloured solid in 95% yield. The formation of the desired product was confirmed by HRMS (ESI) with the presence of the $[M\text{-}H]^-$ ion (*m/z* = 518.1616) and by elemental analysis (see Experimental Chapter). The structure was further confirmed by ^1H NMR in DMSO-d_6 with the shift of the doublet corresponding to H_{10} from 8.61 ppm to 6.90 ppm which is due to the reduction of the electron-attracting nitro group to the electron-donating amine as seen in Figure 2-12.

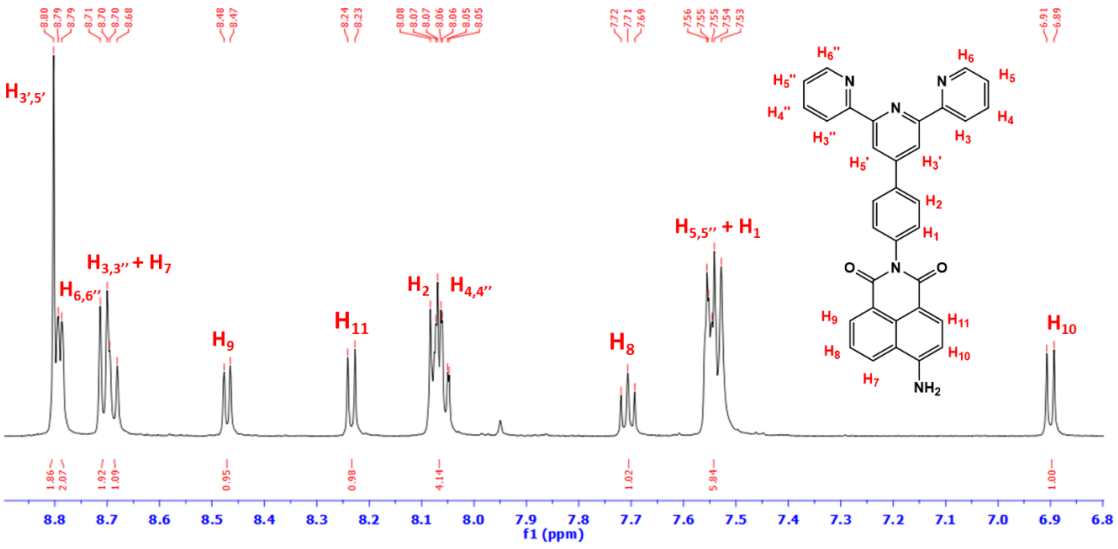

Figure 2-12 ^1H NMR (DMSO-d_6, 600 MHz) of the highlighted aromatic region of **107**. Full spectrum shown in Figure A. 10 in the appendix.

The IR spectrum of **107** reveals two bands at 3470 and 3316 cm^{-1} corresponding to the N−H stretching and N−H bending at 1584 and 1518 $cm^{-1}$and C=O stretching at 1690 and 1650 cm^{-1} corresponding to the carbonyls of the imide as shown in Figure 2-13.

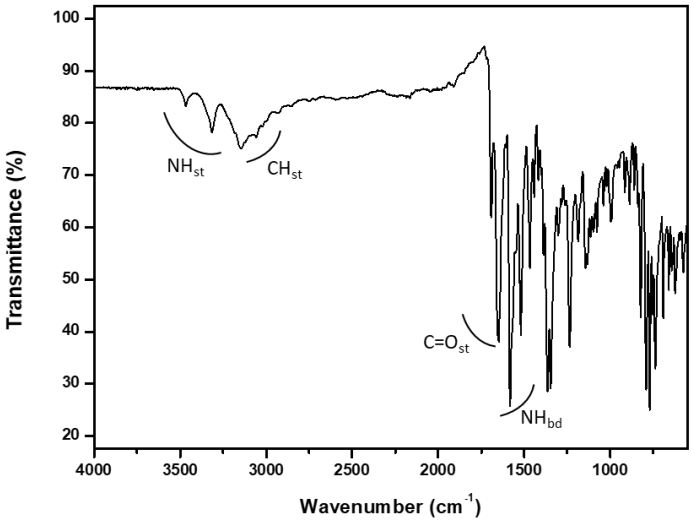

Figure 2-13 FTIR spectrum (4000-550 cm^{-1}) of **107**.

Having fully characterised the ligand **107**, the formation of *d*-metal ion complexes using **107** was carried out and is described in the following section.

2.2.2 Synthesis of *d*-metal complexes

The formation of *d*-metal ion complexes using **107** was attempted. Although several different sets of conditions (concentration, solvent, metal ions and counterions) were screened, unfortunately none of them gave single crystals of suitable quality for X-ray diffraction analysis. The successful formation of *d*-metal ion complexes was achieved by dissolving **107** and the desired metal salts ($Zn(BF_4)_2$, $FeCl_2$, $Cd(NO_3)_2$ and $Co(NO_3)_2$) in a 1:2 (M:L) ratio in 1 mL of DMF in glass vials with PTFE-lined caps and the reactions were carried out in a heat block at a controlled temperature of 75 °C, then they were cooled down at rt over 4 h. After 12 h the solvent was removed under reduced pressure and trituration of the solid obtained, followed by filtration, gave the desired complexes in yields of 98% for [**107**$_2$($Zn(BF_4)_2$)], 80% for [**107**$_2$($FeCl_2$)], 80% for [**107**$_2$($Cd(NO_3)_2$)] and 79% for [**107**$_2$($Co(NO_3)_2$)]. The successful formation of [**107**$_2$($Zn(BF_4)_2$)] was demonstrated by HRMS (ESI) with the presence of the $[M]^{2+}$ ion (*m/z* = 551.1342) and by elemental analysis (see Experimental Chapter). Coordination was further confirmed by ^1H NMR in DMSO-d_6 with the observation of a shift in the resonances corresponding to the terpyridine moiety, resulting from coordination of the Zn(II) ions. By contrast, the signals of the naphthalamide remain relatively unchanged (Figure 2-14).

The successful formation of [**107**$_2$(Cd(NO$_3$)$_2$)] was demonstrated by HRMS (MALDI) with the presence of the $[M]^+$ ion (m/z = 1152.2424) and by elemental analysis (see Experimental Chapter). The ^{1}H NMR in DMSO-d$_6$ of [**107**$_2$(Cd(NO$_3$)$_2$)] further demonstrated the coordination of Cd(II) ions, as the signals corresponding to the terpyridine moiety broadened and shifted, leading to the exact assignment of each signal being difficult. This contrasted with the naphthalimide signals which remained sharp as seen in Figure 2-14. The ^{1}H NMR in DMSO-d$_6$ of [**107**$_2$(FeCl$_2$)] shown in Figure 2-14 only reveals very broad signals leading to the exact assignment of each resonance difficult due to the presence of paramagnetic Fe(II) ions. However, it is possible to identify some similarities in the position of the signals with the previously described complexes, notably with the Zn(II) complex. By such a comparison, and using the integration for some of the resonances, the naphthalimide or the terpyridine protons could be partly assigned. The successful formation of the complex was further evidenced by HRMS (ESI) with the presence of $[M]^{2+}$ ion (m/z = 547.1376) and by elemental analysis (see Experimental Chapter).

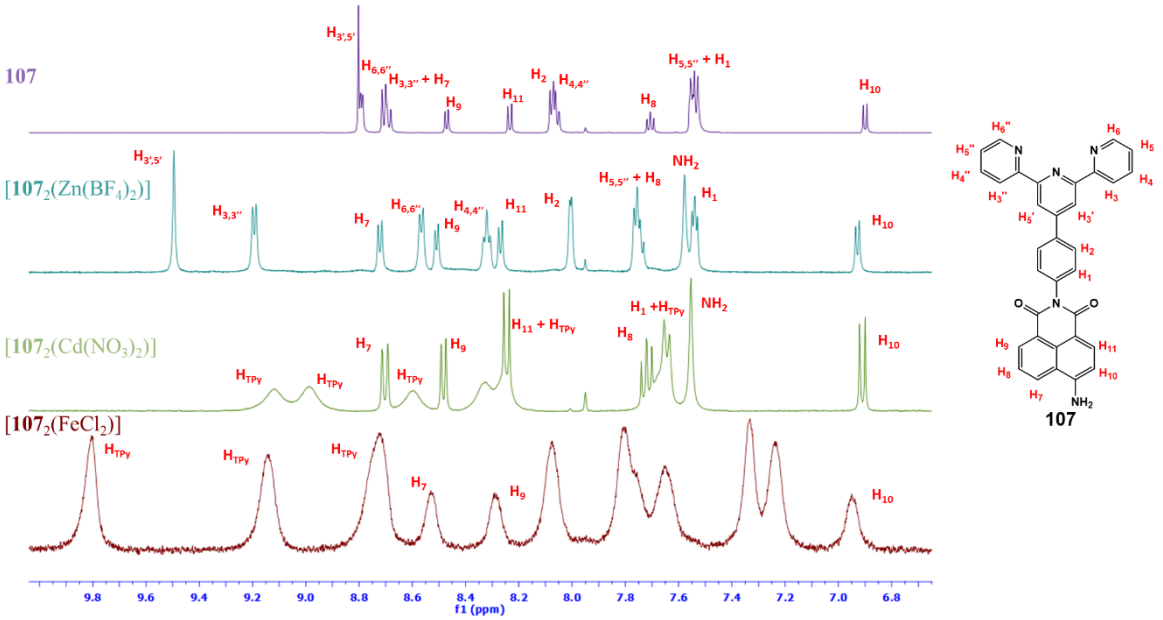

Figure 2-14 ^{1}H NMR (DMSO-d$_6$, 600 MHz) of the highlighted aromatic region of **107**, [**107**$_2$(Zn(BF$_4$)$_2$)], [**107**$_2$(FeCl$_2$)] (400 MHz), [**107**$_2$(Cd(NO$_3$)$_2$)] (400 MHz) and structure of **107** with the corresponding numbering of the protons.

The IR spectra of the different complexes was compared using **107**, are shown in Figure 2-15, and reveals that all have similar structures with two weak bands around 3500 cm^{-1} corresponding to the N−H stretches and several bands between 3300-3000 cm^{-1} accounting for the C−H stretches. All the complexes also displayed C=O stretching between

1690 and 1600 cm^{-1} corresponding to the carbonyls of the imide along with the bands corresponding to the N−H bending between 1350 and 1300 cm^{-1}.

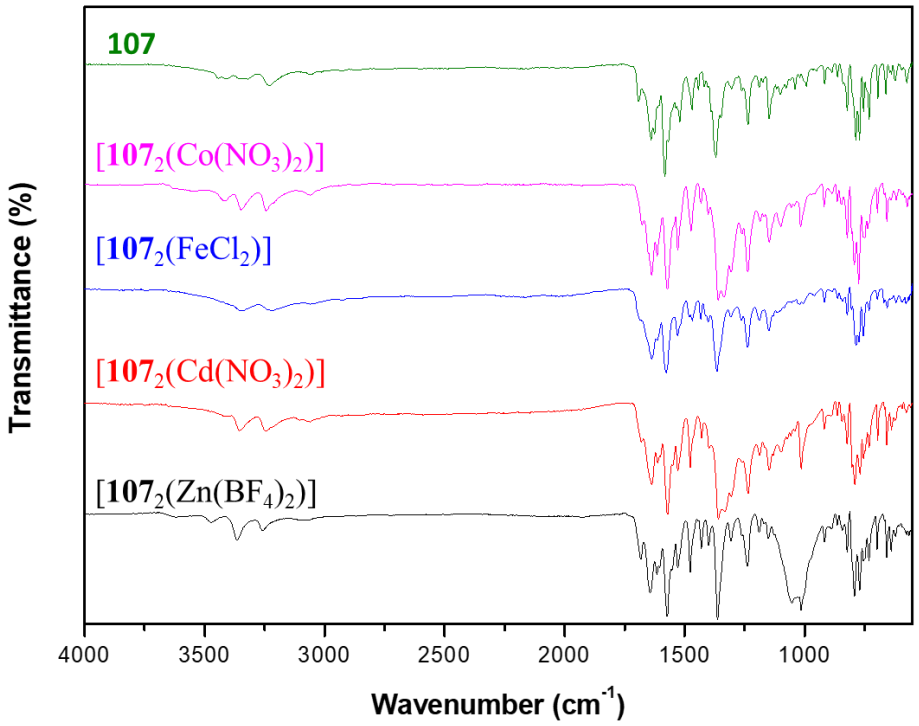

Figure 2-15 FTIR spectrum (4000-550 cm^{-1}) of **107**, [**107**$_2$(Co(NO$_3$)$_2$)] , [**107**$_2$(FeCl$_2$)], [**107**$_2$(Cd(NO$_3$)$_2$)] and [**107**$_2$(Zn(BF$_4$)$_2$)].

To mitigate the effects of the counterion which, as shown by Kitchen *et al.*,[170] can influence the solubility and crystal packing, the syntheses of complexes using commercially available Fe(BF$_4$)$_2$ and Co(BF$_4$)$_2$ were also attempted. Similar reaction conditions to the formation of [**107**$_2$(Zn(BF$_4$)$_2$)] were used. However, as seen in Figure 2-16, in both cases, while most of the sample corresponded to the desired products, a small quantity of free ligand could be observed. Consequently, the reaction time was increased to 72 h, but this did not result in any changes in the outcomes. Different protocols were attempted, such as the use of the direct addition of the metal salt, or the preparation of a solution containing the metal ion followed by a dropwise addition in a solution of **107**; varying the concentration of the reaction mixture; performing the reactions in glass vials with PTFE-lined caps or a round-bottomed flask using a magnetic stirrer, none of which led to the formation of the pure complexes.

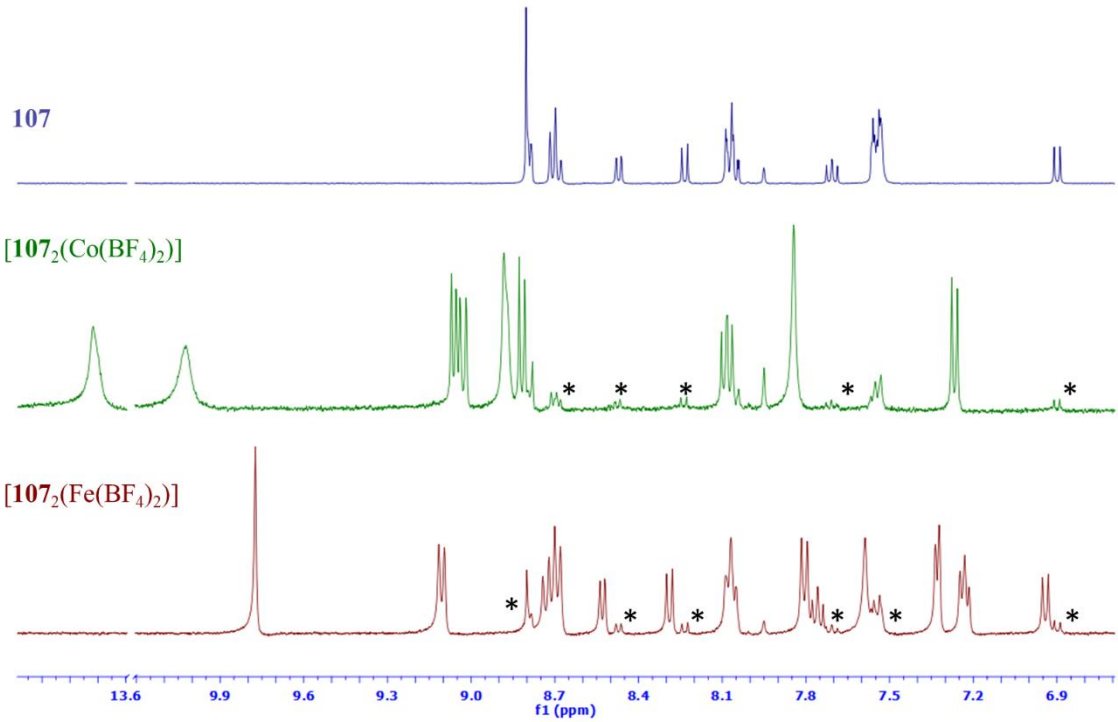

Figure 2-16 ^{1}H NMR (DMSO-d$_6$, 600 MHz) of the highlighted aromatic region of **107**, [**107**$_2$(Co(BF$_4$)$_2$)] (400 MHz) and [**107**$_2$(Fe(BF$_4$)$_2$)] (400 MHz) with traces of free ligand indicated by *.

Attempts to purify the complexes by column chromatography, reprecipitation, and crystallisation were hindered by the poor solubility of the complexes and did not yield the pure complexes. Therefore, it was decided that **107**, [**107**$_2$(Zn(BF$_4$)$_2$)], [**107**$_2$(FeCl$_2$)], [**107**$_2$(Cd(NO$_3$)$_2$)] and [**107**$_2$(Co(NO$_3$)$_2$)], which were isolated in high purity would be used for the spectroscopic and cyclic voltammetry studies that were subsequently carried out, and used to serve as a comparison with the TBNap polymers described in the following Chapter.

2.3 Spectroscopic Study

Having successfully synthesised and characterised **107** and its corresponding complexes, a brief study of their spectroscopic properties was carried out. The spectroscopic studies were carried out in DMF solution at a concentration of 1×10^{-5} M. The absorption spectra of **107** and the corresponding complexes, shown in Figure 2-17, revealed that all the complexes displayed ligand centred π→π* transitions at *ca*. 280 nm and around 325 nm along with the broad band centred at 430 nm which corresponds to the ICT and appears to be unaffected by the coordination of metal ions through the terpyridine moieties of these systems. As shown in Figure 2-17, [**107**$_2$(FeCl$_2$)] also displayed a band centred at 575 nm due to the dπ(Fe(II))→π*(TPy) MLCT transition which is responsible for the purple colour of the solution.

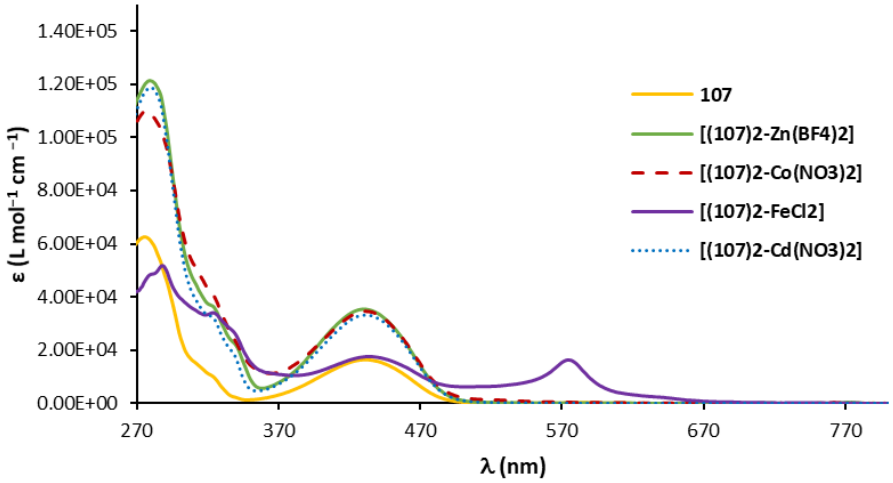

Figure 2-17 Absorption spectra of **107**, [**107**$_2$(Co(NO$_3$)$_2$)], [**107**$_2$(FeCl$_2$)], [**107**$_2$(Cd(NO$_3$)$_2$)] and [**107**$_2$(Zn(BF$_4$)$_2$)] in DMF (c = 1 × 10^{-5} M).

Excitation at λ_{ex} = 430 nm led to the observation of a broad emission band with λ_{max} = 520 nm for **107**, [**107**$_2$(Zn(BF$_4$)$_2$)], [**107**$_2$(Co(NO$_3$)$_2$)] and [**107**$_2$(Cd(NO$_3$)$_2$)] with the cadmium complex being the most emissive one and the zinc complex being almost as emissive as the ligand alone as seen in Figure 2-18. While [**107**$_2$(Co(NO$_3$)$_2$)] is less emissive and [**107**$_2$(FeCl$_2$)] can be considered as non-emissive, this can be explained by the fact that in the case of Co(II) and Fe(II) ions their *d*-shells are partially filled while in the case of Zn(II) and Cd(II) ions the *d*-orbitals are full.

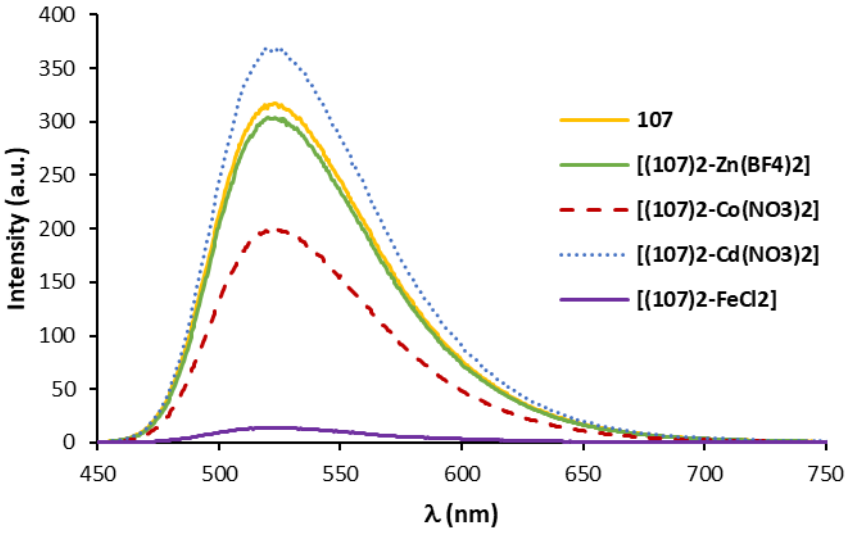

Figure 2-18 Emission spectra of **107**, [**107**$_2$(Co(NO$_3$)$_2$)], [**107**$_2$(FeCl$_2$)], [**107**$_2$(Cd(NO$_3$)$_2$)] and [**107**$_2$(Zn(BF$_4$)$_2$)] in DMF (c = 1 × 10^{-5} M), λ_{ex} = 430 nm.

The measurements of the excitation spectra of **107**, [**107**$_2$(Co(NO$_3$)$_2$)], [**107**$_2$(Cd(NO$_3$)$_2$)] and [**107**$_2$(Zn(BF$_4$)$_2$)] revealed very similar spectra to the absorption spectra previously recorded, although the intensity of the excitation spectra of [**107**$_2$(FeCl$_2$)]

was at very low intensity, as seen in Figure 2-19, due to the lack of any significant emission from the complex. Nevertheless, the principal bands could be observed, thus demonstrating the purity of this complex.

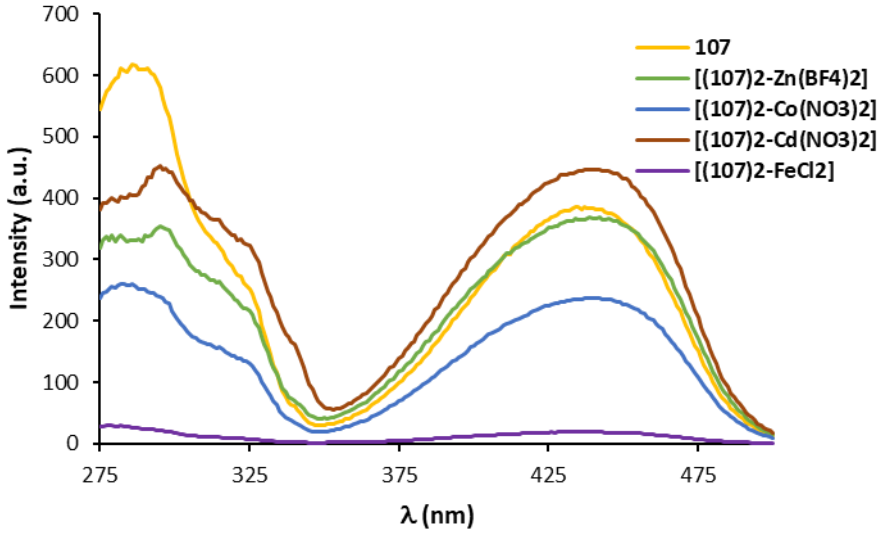

Figure 2-19 Excitation spectra (λ_{em} = 520 nm) of **107**, [**107**$_2$(Co(NO$_3$)$_2$)], [**107**$_2$(FeCl$_2$)], [**107**$_2$(Cd(NO$_3$)$_2$)] and [**107**$_2$(Zn(BF$_4$)$_2$)] in DMF (c = 1 × 10^{-5} M).

2.4 Cyclic Voltammetry

Cyclic voltammetry is a technique that measures the current response upon a voltage sweep between two values at a fixed rate and is reversed once the voltage reaches a maximum or minimum voltage. This technique is used to investigate the reduction and oxidation process of the species in solution. The scan rate of the sweep controls how fast the potential is scanned, which greatly influences the size of the diffusion layer of the species formed in solution and thus the current response measured, this phenomenon is used to probe whether the current response is due to a freely diffusing species or an absorbed analyte on the surface of the electrode.[179] Experimentally, an electrolyte solution is prepared by dissolving a salt in the desired solvent to reduce the resistance of the solvent. Three electrodes are necessary for this experiment: the working electrode is the electrode where the electrochemical phenomena are taking place; the counter electrode completes the electrical circuit which starts with the working electrode, and when a reaction occurs at the working electrode the current begins to flow and an opposite reaction occurs at the counter electrode; lastly, the third electrode used is the reference electrode, which is used as a reference point against which the potential of the other electrode can be measured.

Cyclic voltammetry studies of [**107**$_2$(Co(NO$_3$)$_2$)], [**107**$_2$(FeCl$_2$)] and [**107**$_2$(Zn(BF$_4$)$_2$)] were carried out at an approximate concentration of 1 × 10^{-3} M in CH$_3$CN

to serve as a comparison with the TBNap polymer described in the following chapter. Due to time constraints and material difficulties the studies of **107** and [**107**$_2$($Cd(NO_3)_2$)] were not carried out. The ferrocene/ferrocenium redox couple was used as the internal standard, and potentials were referenced against these. A gold electrode was used as the working electrode while platinum wires were used for both the reference electrode and the counter electrode.

As seen in Figure 2-20, the cyclic voltammogram of [**107**$_2$($Zn(BF_4)_2$)] displayed two quasi-reversible reductions, the first one with an onset at approximatively −1.94 V and the second one with an onset at approximatively −2.16 V. Upon examination of the CV trace of the reverse sweep, waves are observed, the onsets of which are at −2.41 V and −2.06 V. When reducing the electrochemical window to −2.10 to 0.00 V the second oxidation wave was still present thus demonstrating that the oxidation starting at −2.06 V is not due to an electrochemical side product arising from the second reduction.

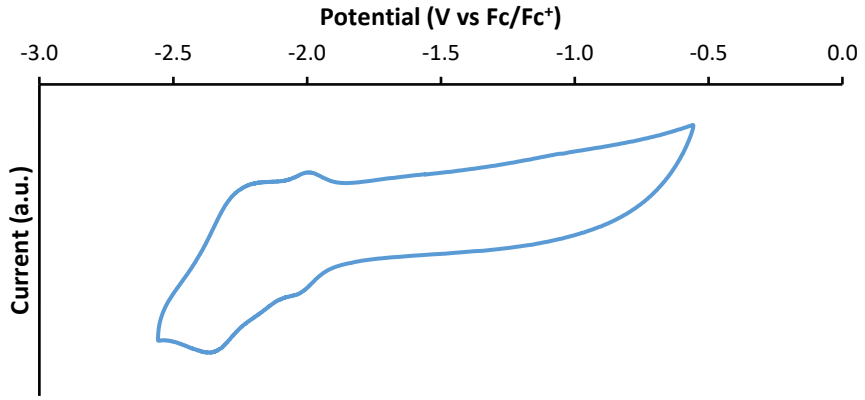

Figure 2-20 Voltammogram of [**107**$_2$($Zn(BF_4)_2$)] under N_2 at 100 mV/s, scanned in the negative direction in 0.1 M [NBu_4][PF_6] CH_3CN solution. The Fc/Fc^+ couple was used as an internal standard and the voltammogram is referenced against this couple.

As seen in Figure 2-21, the cyclic voltammogram of [**107**$_2$($Co(NO_3)_2$)] displayed two quasi-reversible reductions, the first one with an onset at approximatively −1.03 V and the second one with an onset at approximatively −1.84 V. The two corresponding oxidations can be observed on the reverse scan with onset potentials of −2.16 V and −1.33 V. The first redox couple can be attributed to the redox metal-based process corresponding to the Co(II)/Co(I) couple.[180] While the second redox couple observed can be attributed to a ligand-based process due to its similarity in the onset potentials observed with [**107**$_2$($Zn(BF_4)_2$)].

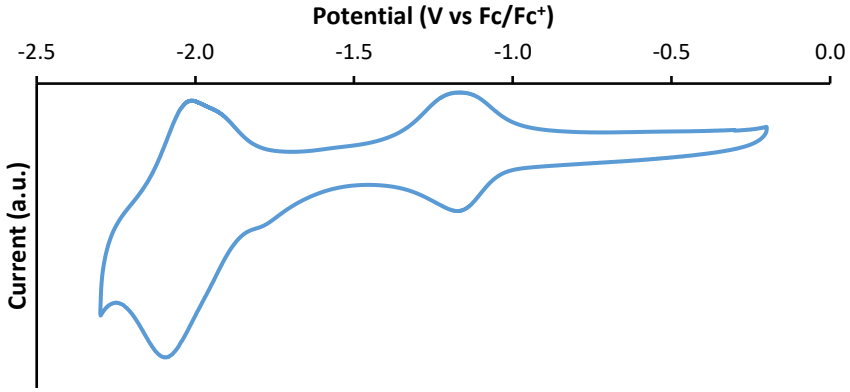

Figure 2-21 Voltammogram of [**107**$_2$(Co(NO$_3$)$_2$)] under N_2 at 100 mV/s, scanned in the negative direction in 0.1 M [NBu$_4$][PF$_6$] CH_3CN solution. The Fc/Fc^+ couple was used as an internal standard and the voltammogram is referenced against this couple.

As seen in Figure 2-22, the cyclic voltammogram of [**107**$_2$(FeCl$_2$)] displayed 3 quasi-reversible reductions at onset potentials of 0.99 V, −1.18 V and −1.50 V while three oxidations are visible on the reverse scan at onset potentials of −1.82 V, −1.45 V and 0.78 V. The first oxidation at approximatively 0.80 V can be attributed to the metal-based process corresponding to the Fe(III)/Fe(II) redox couple.[180] Interestingly, the two other redox couples observed do not correspond to the ones previously observed for [**107**$_2$(Co(NO$_3$)$_2$)] and [**107**$_2$(Zn(BF$_4$)$_2$)] and thus further investigation would be required to ascribe the nature of these redox processes. When increasing the scan range another irreversible oxidation is visible at an approximate onset of 0.93 V, which can be attributed to the oxidation of the chloride ion into chlorine.[181] A third quasi-reversible reduction is visible at an onset potential of −2.20 V and the corresponding oxidation with an onset potential of −2.40 V while the two other oxidations observed in the smaller potential range are not as visible (see appendix).

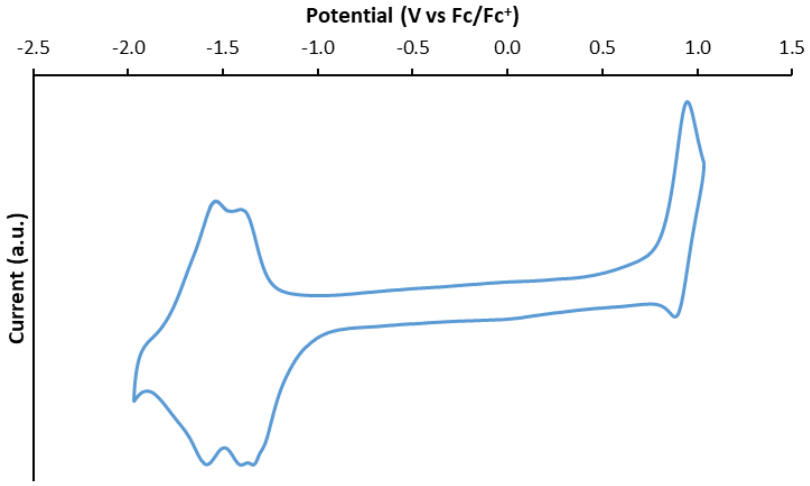

Figure 2-22 Voltammogram of [**107**$_2$(FeCl$_2$)] under N_2 at 100 mV/s, scanned in the negative direction in 0.1 M [NBu$_4$][PF$_6$] CH_3CN solution. The Fc/Fc^+ couple was used as an internal standard and the voltammogram is referenced against this couple.

2.5 Conclusion and Future Work

In this chapter, a novel terpyridine covalently attached to a 4-nitro- (**112**) and 4-amino-1,8-napthalimide (**107**) were successfully synthesised and fully characterised. Their ability to coordinate *d*-metal ions was investigated, while the formation of crystals suitable for X-ray diffraction could not be achieved for the complexes, crystal structures of the precursors **111** and **112** could be obtained. The spectroscopic properties of the ligand and its corresponding complexes with Zn(II), Cd(II), Fe(II) and Co(II) were explored along with their electrochemical properties using cyclic voltammetry which demonstrated the influence of the metal and the counter ion used on the different properties of the complex obtained.

Future work would involve other methods to obtain pure complexes with the tetrafluoroborate counterions to be able to more ideally compare the electrochemical data obtained, coupled with theoretical calculations on the electronic structure of the complexes and electrochemical measurements of the ligand alone to accurately discern the nature of redox waves. Finally, the use of **107** to form the corresponding Tröger's base, giving a ditopic ligand and explore its ability to form macrocycles or linear polymers upon coordination of *d*-metals will be discussed in Chapter 3.

Chapter 3— Synthesis and Study of 4-Amino-1,8-Naphthalimide-Tröger's Base and its Metal Complexes

3.1 Introduction

The first examples of TBNap synthesised in the Gunnlaugsson group are **113-115** which are shown in Figure 3-1A. The synthesis of these compounds was carried out by using paraformaldehyde in neat TFA, which is until now, the most efficient way to synthesise TBNap derivatives from 4-amino-1,8-naphthalimide derivatives. Similarly to their amino-Nap derivatives, **113-115** and TBNap in general display a high fluorescence due to their ICT which is caused by the "push-pull" mechanism described earlier in this thesis for the naphthalimides. Relative to their corresponding 4-amino-1,8-naphthalimides, TBNap derivatives have their ICT band in the absorption spectrum slightly blue-shifted due to the diazocine ring being less available to take part in the ICT. During pH titration of **113-115**, only one pK_a per compound was observed and was attributed to the terminal amines functionalising the TBNap on the imide positions. Contrary to their amino-Nap derivatives, **113-115**, absorption spectra displayed significant changes upon modification of the pH while their emission spectra had only minors changes indicating that the PET normally taking place for Nap derivative is not active for **113-115**. Titration of **113-115** in presence of calf thymus DNA (*ct*-DNA) demonstrated a relationship between the pK_a and the binding affinity with DNA. Indeed **115** displayed the lowest pK_a for the terminal amine and also displayed the lowest binding constant while **113** displayed both the highest pK_a and binding constant. More importantly, the binding constant of the precursors **Amino-Nap-113-115** was determined and it was highlighted that the TBNap moieties have a drastically improved binding affinity to DNA. Cellular uptake studies were carried out and showed that the three TBNap derivatives crossed the cell membrane within 24 hours and are localised in the nucleus and the cytoplasm (Figure 3-1B). Cell viability studies demonstrated that both **113** and **114** are much more toxic than their Nap precursors.[182,183]

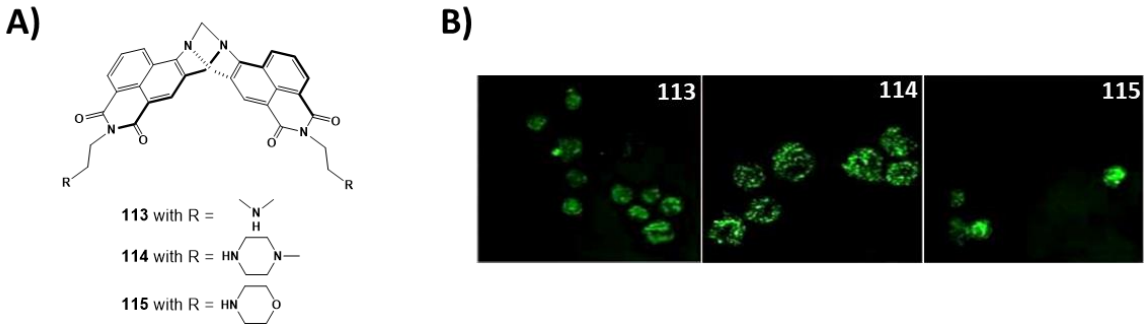

Figure 3-1 A) Structure of **113-115**. B) Cellular imaging pictures, taken after 24h of **113-115**showing localization in the nucleus by fluorescence arising from **113-115** (10 µM). Reproduced from references.[182,183]

Murphy *et al*. synthesised a series of 3-amino-1,8-naphthalimide Tröger's bases (**116-120**, shown in Figure 3-2) in moderate to high yields: **116** (54%), **117** (79%), **118** (54%), **119** (36%) and **120** (61%). Spectroscopic studies of **116-120** revealed that the ICT band of the absorption spectra were only slightly affected by the polarity of the solvent and thus that the diazocine ring can delocalise its electron pair into the naphthalimide while the 3-amino-1,8-naphthalimide precursors displayed a significant shift in the ICT band upon changes of the solvent polarity. The emission spectra of **116-120** displayed a bathochromic and hypochromic shift with increasing solvent polarity which is a similar behaviour to the one observed for the Nap precursors. At low to medium ionic strength, the absorption spectra of **116-120** (except **118**) exhibited significant modification upon addition of *ct*-DNA while at higher ionic strengths, the absorption spectra displayed changes to a lesser extent revealing that electrostatic interactions between **116-120** (except **118**) and *ct*-DNA are taking place. Further studies of the interactions with *ct*-DNA using the emission spectra of **116-120** (except **118**) demonstrated similar results to the absorption spectra that were further supported by ethidium bromide displacement assays. The interactions between **116-120** (except **118**) and *ct*-DNA were investigated using both circular and linear dichroism, which suggested that TBNap binds to *ct*-DNA in a bimodal fashion, with one Nap unit acting as a groove binder while the second one intercalates between the base pairs of DNA. The cellular uptakes of **116-120** were evaluated and demonstrated rapid uptakes in HeLa cells except for **118** and confocal microscopy revealed that the compounds are concentrated in the cytoplasm but do not penetrate the nucleus like their 4-amino-1,8-naphthalimide counterparts. More importantly, **116**, **117**, **119** and **120** induced cellular apoptosis after two hours of treatment demonstrating the therapeutic possibilities of these TBNaps.[184]

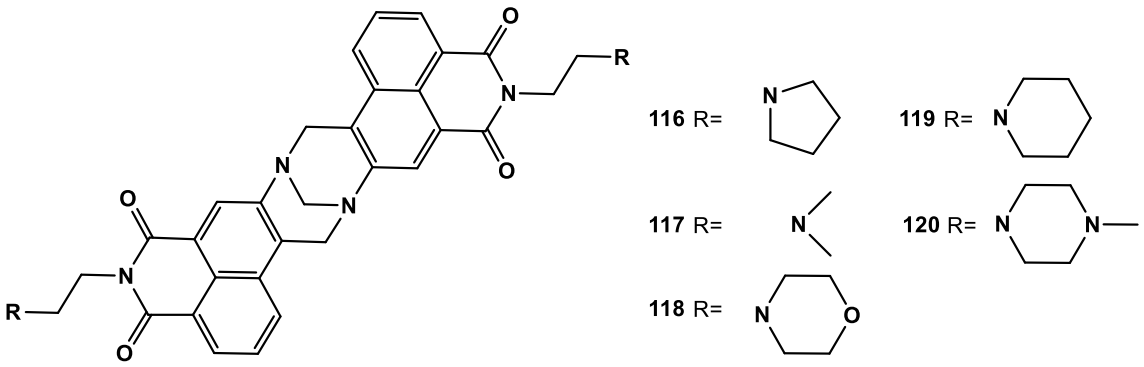

Figure 3-2 Structures of **116-120**. Reproduced from reference.[184]

Based on previous successes, Elmes *et al*. developed Ru(II)–polypyridyl-1,8-naphthalimide Tröger's bases **121-122** by reacting the Amino-Nap precursors with TFA and formaldehyde. Afterwards, the Tröger's bases were reacted with $Ru(bpy)_2Cl_2$ under

microwave irradiation to yield the desired complexes in reasonable yield (63-68%) (Figure 3-3A). Existing in the chloride salt form, both complexes containing the Tröger's bases were water-soluble and subsequently, their interactions with DNA were characterised in phosphate buffer as previous results from the group showed strong binding affinity of Tröger's bases towards DNA.[182] Contrary to what was expected, the two complexes showed very little change in their absorption and emission spectra compared to their Amino-Nap precursors. However, DNA denaturation experiments revealed significant changes in the melting behaviour of *st*-DNA demonstrating interactions between *st*-DNA and **121-122** which is highly dependent on the ionic strength of the medium. Further cellular studies in HeLa cells proved a rapid uptake of the complexes by the cells with a visible effect within two hours after the treatment and full uptake after four hours. The uptake was mainly concentrated in the cytoplasm and the complexes were harmless to the cells over a wide range of concentrations allowing this family of complexes to be used as imaging agents as shown in Figure 3-3B.[173]

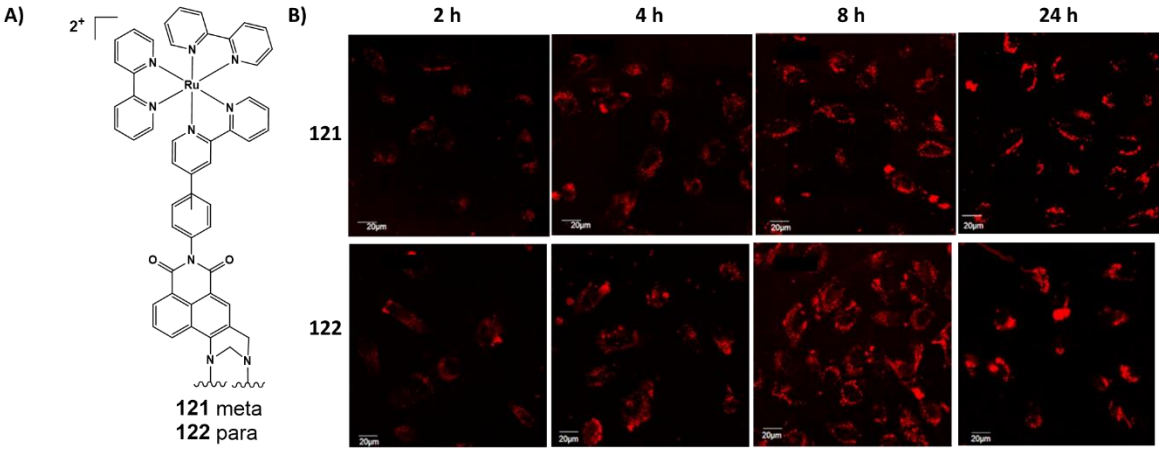

Figure 3-3 A) Structures of **121-122**. B) Time-dependent localisation of **121-122** in HeLa cells after 2, 4, 8 and 24 hours. Reproduced from reference.[173]

Traditionally, TBNap synthesised by the Gunnlaugsson research group were used as a racemic mixture; however, Banerjee *et al*. reported a method to resolve the enantiomers of two TBNap racemic mixtures using Sephadex C25 as the stationary phase and a chiral eluent sodium (−)-dibenzoyl-L-tartarate as the mobile phase.[6] The successful resolution and the enantiomeric purity of (±)-**123** and (±)-**124** (**Error! Reference source not found.**A) were determined using circular dichroism (CD) spectroscopy, which also demonstrated that each enantiomer was stable over a long period in buffer solution at pH 7.0. Further studies of DNA binding for the racemic mixture and the separated enantiomers of **123** and **124** revealed very little difference in the binding constants between each enantiomer and the racemic

mixture. However, when increasing the ionic strength up to 150 mM, the difference of affinity for the (-)-enantiomers was drastically increased with a binding constant being three times higher than that of the (+)-enantiomer. Additionally, this work reported the first solid-state analysis of the TBNap structure, thus confirming the orthogonal position of the two naphthalimide moieties (**Error! Reference source not found.**B).

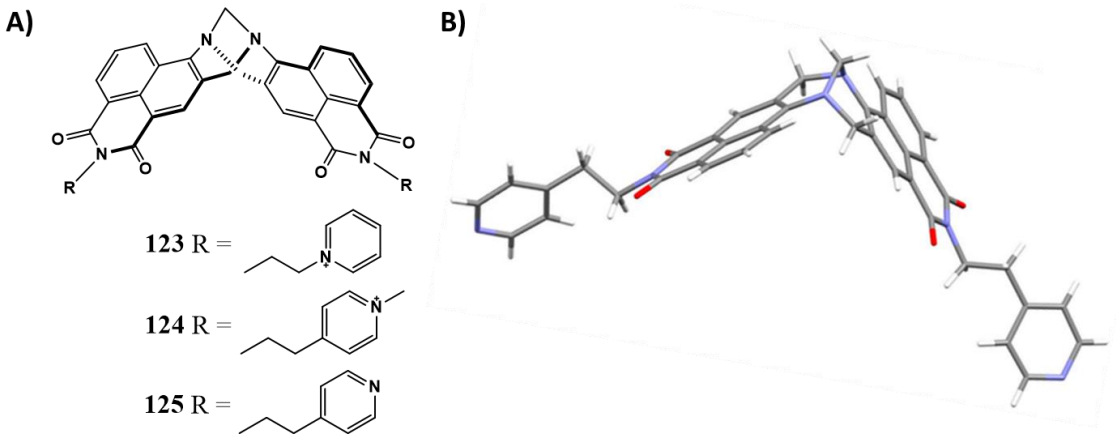

Figure 3-4 A) Structures of **123-125**. B) X-ray crystal structure of **125**, showing the orthogonal nature of the two naphthalimide units. Reproduced from reference.[6]

More recently, our research group has developed TBNap structure capable of detecting picric acid in competitive media. To take advantage of coordination polymer properties, Shanmugaraju *et al*. designed a TBNap functionalised with phenyl dicarboxylic acid, allowing to use the four carboxylic acid moieties to coordinate zinc ions and resultingly form a coordination polymer **126-Zn** shown in Figure 3-5A. X-ray powder diffraction revealed that the coordination polymer is amorphous, while thermogravimetric analysis (TGA) revealed the presence of solvent trapped within the network. SEM and AFM studies of **126-Zn** showed that the solid obtained is composed of spherical particles aggregated together which form a porous structure. When dispersed in water, **126-Zn** possesses a strong and broad emission band at 530 nm upon excitation. Interestingly, **126-Zn** is more emissive in water than its precursor **126**, making it an ideal candidate for sensing in aqueous media. Therefore, the selective and discriminative sensing of nitroaromatics in water was studied, revealing that **126** can discriminate between phenolic and non-phenolic nitroaromatics, with the highest quenching efficiency for picric acid as shown in Figure 3-5B. Satisfyingly, competitive experiments revealed that the quenching response was equally efficient for picric acid in the presence of structurally related analytes. Fitting of the changes in intensity using a Stern-Volmer plot demonstrated a Stern-Volmer constant of $43.7 \times 10^3\ M^{-1}$, with a limit of detection of 26.3 ppb. Another advantage of this system for the detection of

nitroaromatic in water is that it showed good recyclability over several cycles making **126-Zn** suitable for long-term on-field sensing of nitroaromatics.

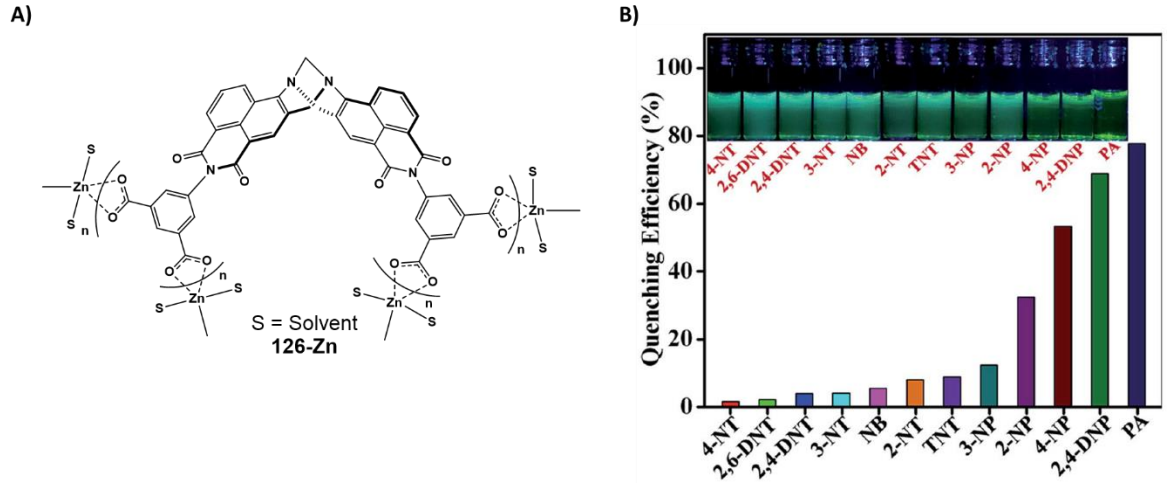

Figure 3-5 A) Structure of **126-Zn**. B) The extent of fluorescence quenching of **126-Zn** observed upon the addition of various analytes. Inset: the colour changes observed under UV-lamp. Reproduced from reference.[185]

Shanmugaraju *et al.* have also reported a new methodology, consisting of a one-pot reaction enabling the synthesis of a family of *N*-alkyl-1,8-naphthalimide based Tröger's bases *via* a nucleophilic displacement approach using **127** as the common precursor (Figure 3-6). The limits of this reaction were explored and showed that aliphatic primary amines, acyclic-tertiary amine substrates, cyclic-tertiary amines, aromatic pyridyl, hydroxylamines, gave the desired product in moderate to high yields while using aniline for the nucleophilic displacement was unsuccessful potentially because aromatic primary amines such as aniline are weaker nucleophiles than aliphatic amines.

The effect of the substituent on the phenyl ring of **127** was also investigated and by synthesising the aniline TBNap derivative using the traditional 4-amino-1,8-naphthalimide derivatives. By submitting the aniline TBNap derivative to similar conditions than **127** for the nucleophilic displacement previously described, the reaction yielded the desired product but in drastically lower yield thus demonstrating that the methyl ester substituents on the *N*-aryl moieties are essential to generate a sufficient electron-deficiency at the imide carbonyl group of the TBNap to achieve a complete heterocyclic ring cleavage using primary aliphatic amine nucleophiles. It has also been demonstrated that the corresponding anhydride can be obtained by simply reacting **127** with aqueous potassium hydroxide, opening the way to a huge number of functionalisations.[186]

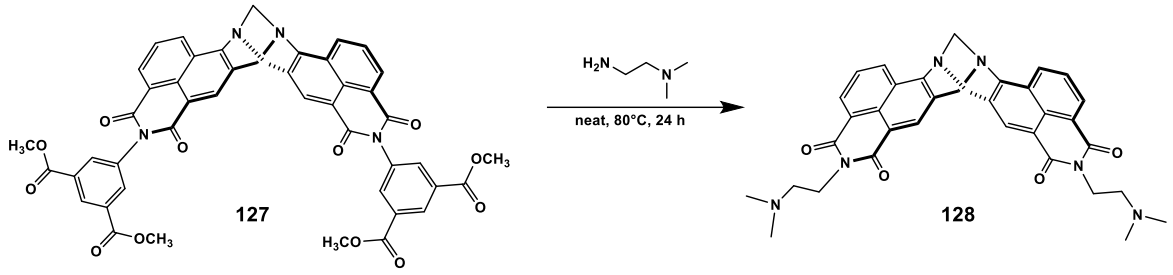

Figure 3-6 Nucleophilic displacement approach using **127** as a precursor. Reproduced from reference.[186]

A TBNap dipyridyl derivative (**129**) was synthesised and reported by Shanmugaraju *et al*. which was further used to form coordination polymers possessing intrinsic cavities due to the cleft-shape of the TBNap motif.[187] Coordination of **129** to cobalt ions in DMF led to crystals suitable for X-ray diffraction which revealed the formation of a one-dimensional coordination polymer (**129-Co-CP**) in a zig-zag motif (Figure 3-7B) with a calculated accessible volume for solvent molecules of approximatively 175 $Å^3$ per [$CoCl_2$(**129**)] units, while slow evaporation from the reaction mixture of **129-Cd-CP** led to single crystals that were further studied by X-ray diffraction (Figure 3-7C and D). In this case, the cadmium ion is coordinated by four pyridyl groups leading to a more compact structure than the **129-Co-CP** counterpart. Various analysis (TGA, powder diffraction and CPMAS-^{13}C NMR analysis) demonstrated degradation of the coordination polymer upon desolvation. SEM of the two coordination polymers revealed that **129-Co-CP** consists of rods while **129-Cd-CP** is composed of rectangular-shaped particles.

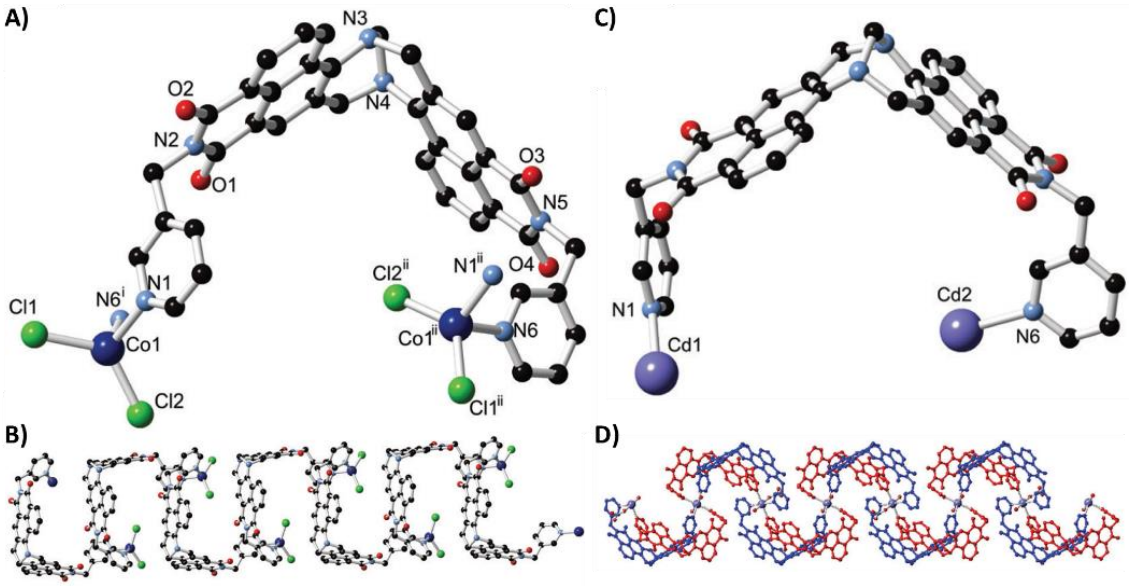

Figure 3-7 A) Structure of complex **129-Co-CP** with partial labelling scheme. B) Extended structure of a single chain of complex **129-Co-CP** viewed parallel to the crystallographic *b* axis. C) A representative example of ligand geometry in complex **129-Cd-CP** (one of two unique ligand molecules shown, for clarity) with partial atom labelling scheme. D) Extended structure of a single chain of **129-Cd-CP** with symmetry-related TBNap groups coloured together, showing the two overlapping zig-zag chains present within the structure. Reproduced from reference.[187]

Compound **125**, which derivatives were previously studied and demonstrated the ability to bind to DNA,[6] was further used with Ru(II)–curcuminato complex (**Ru-Cur**), which is a known anticancer active compound,[188] in the aim to improve cellular uptake and the anticancer potency. The formation of the complex between **125** and **Ru-Cur** was carried out successfully in giving **125-Ru-Cur** (Figure 3-8A).[189] The photophysical properties of **125-Ru-Cur** were evaluated, demonstrating the presence of both the ICT and MLCT bands in the absorption spectrum while the emission was slightly red-shifted compared to its precursor **125**. The cellular uptake of **125-Ru-Cur** and **125** was studied and demonstrated that both TBNaps were penetrating cells within 60 minutes, displaying a bright green fluorescence and mainly localised in the cytoplasm (Figure 3-8B). The cell viability was also examined and highlighted high toxicity for **125-Ru-Cur** with an IC_{50} of 4.9 μM, which is much higher than both **125** and **Ru-Cur** alone with IC_{50} of 25 μM and 16 μM, respectively (Figure 3-8C). This demonstrates that **125-Ru-Cur** is a good candidate to be used as a theranostic agent against cancer cells.

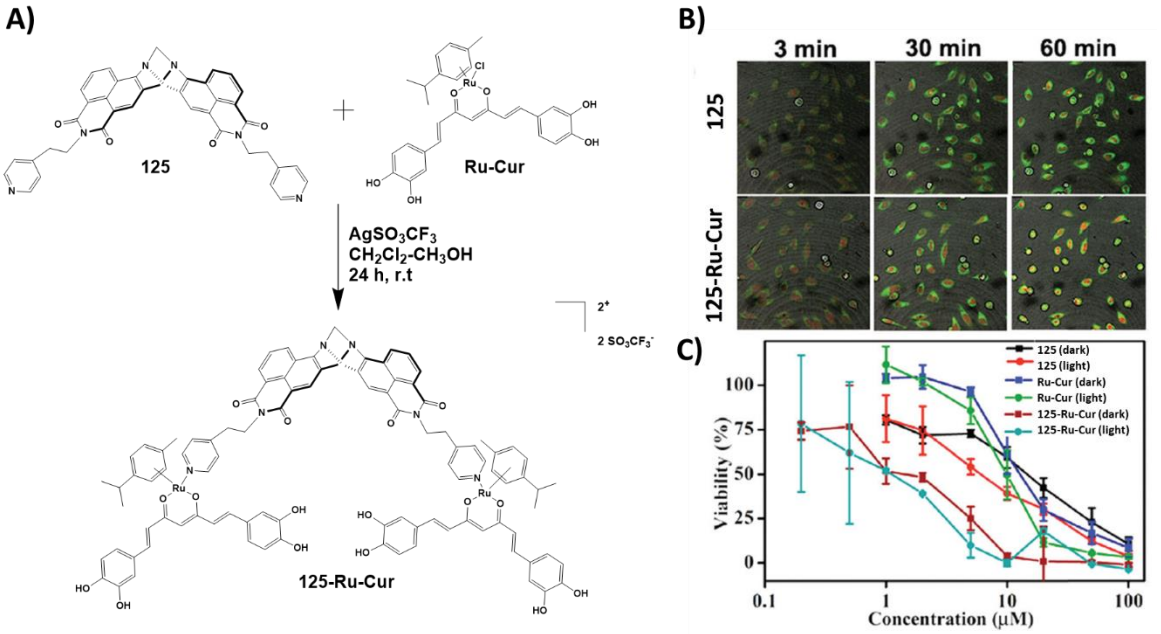

Figure 3-8 A) Synthesis of **125-Ru-Cur** from **125** and **Ru-Cur**. B) Confocal live-cell images of **125** (5 mM) and **125-Ru-Cur** (1 mM) within HeLa cells after 3 - 60 min of incubation. C) The antiproliferative effect of **125**, **Ru-Cur** and **125-Ru-Cur** on HeLa cells in dark and in light. Reproduced from reference.[189]

As described in the previous examples, the 4-amino-1,8-naphthalimide Tröger's bases (TBNap) can be very useful for supramolecular chemistry to form various structures such as metallo-cages,[75] molecular tweezers,[190] and metal-organic-frameworks (MOFs).[79] In an effort to develop this chemistry further, the Gunnlaugsson group has designed, synthesised and studied TBNaps with potential applications as imaging agents,[173] DNA

intercalators,[6] theranostic agents,[189] and sensors of NACs in aqueous media,[185] which were precedently discussed.

In this chapter, the knowledge surrounding the TBNap motif is further expanded through the development of a terpyridine adorned TBNap with an extensive study of its spectroscopic properties. Notably, this chapter provides a description of the first example of AIE-active TBNap and its application as a potential sensor of NACs. This work was described in the article "Aggregation induced emission (AIE) active 4-amino-1,8-naphthalimide-Tröger's base for the selective sensing of chemical explosives in competitive aqueous media" co-authored with Deivasigamani Umadevi, Sankarasekaran Shanmugaraju, Oxana Kotova, Graeme W. Watson and Thorfinnur Gunnlaugsson, (*Chem. Commun*., 2020, **56**, 2562-2565). The synthesis, spectroscopic and electrochemical studies of a series of *d*-metal zig-zag polymers using the terpyridine adorned TBNap is also discussed. This is followed by the study of a covalent organic polymer composed of the TBNap motif, which was synthesized and characterised by Asst. Prof. Sankarasekaran, as a sensor of NACs in aqueous media. This work was described in the article "Hyper-crosslinked 4-amino-1,8-naphthalimide Tröger's base containing pyridinium covalent organic polymer (COP) for discriminative fluorescent sensing of chemical explosives" co-authored with Deivasigamani Umadevi, Kevin Byrne, Wolfgang Schmitt, Graeme W. Watson, Thorfinnur Gunnlaugsson and Sankarasekaran Shanmugaraju, (*Supramol. Chem.*, 2020, **32**, 508-517).

3.2 Synthesis and Characterisation of 4-Amino-1,8-Naphthalimide-Tröger's Base

The 4-amino-1,8-naphthalamide Tröger's base adorned with phenyl-terpyridine moiety **TBNap-Tpy** (**130**) was synthesised from the commercially available 2-acetylpyridine, 4-nitrobenzaldehyde and 4-nitro-1,8-naphthalic anhydride, in a few steps. Formation of 4′-(4-nitrophenyl)-2,2′:6′,2″-terpyridine and its corresponding 4-amino-1,8-naphthalimide were described in Chapter 2. The condensation of **107** with paraformaldehyde to obtain the desired Tröger's base **130** was carried out using methods developed in our laboratory and is shown in Scheme 3-1. The compound **107** and paraformaldehyde were stirred overnight in TFA, followed by the dropwise addition of the reaction mixture to a solution of aqueous ammonia. Extraction of the aqueous phase with DCM, and washes of the organic phase with a saturated solution of sodium bicarbonate and water, followed by the removal of the solvent under reduced pressure, led the desired product as an orange powder in 77% yield.[185]

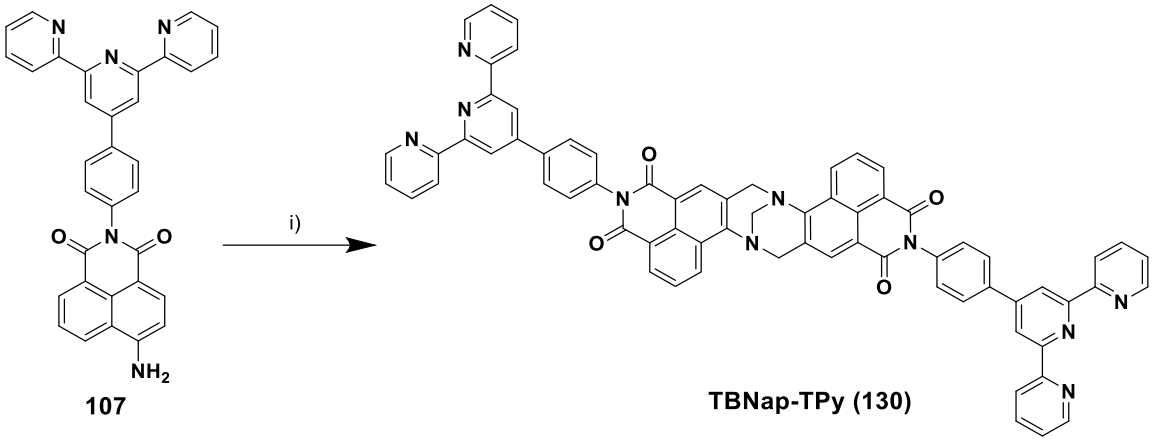

Scheme 3-1 Synthesis of **TBNap-TPy** (**130**) from **107**, i) TFA, H_2CO, 12 h, 77%.

The successful formation of **130** was demonstrated by HRMS-MALDI with the presence of $[M-H]^+$ ion (*m/z* = 1075.3445) and more importantly by elemental analysis with the formula $C_{69}H_{42}N_{10}O_4 \cdot 0.13CH_3Cl \cdot 0.01DMF \cdot 1.9H_2O$. The ^1H NMR (600 MHz) in DMSO-d_6 confirmed the formation of the Tröger's base moiety with the presence of the two well-defined doublets at 5.23 and 4.74 ppm corresponding to the methylene protons of the diazocine ring (Figure 3-9).[183]

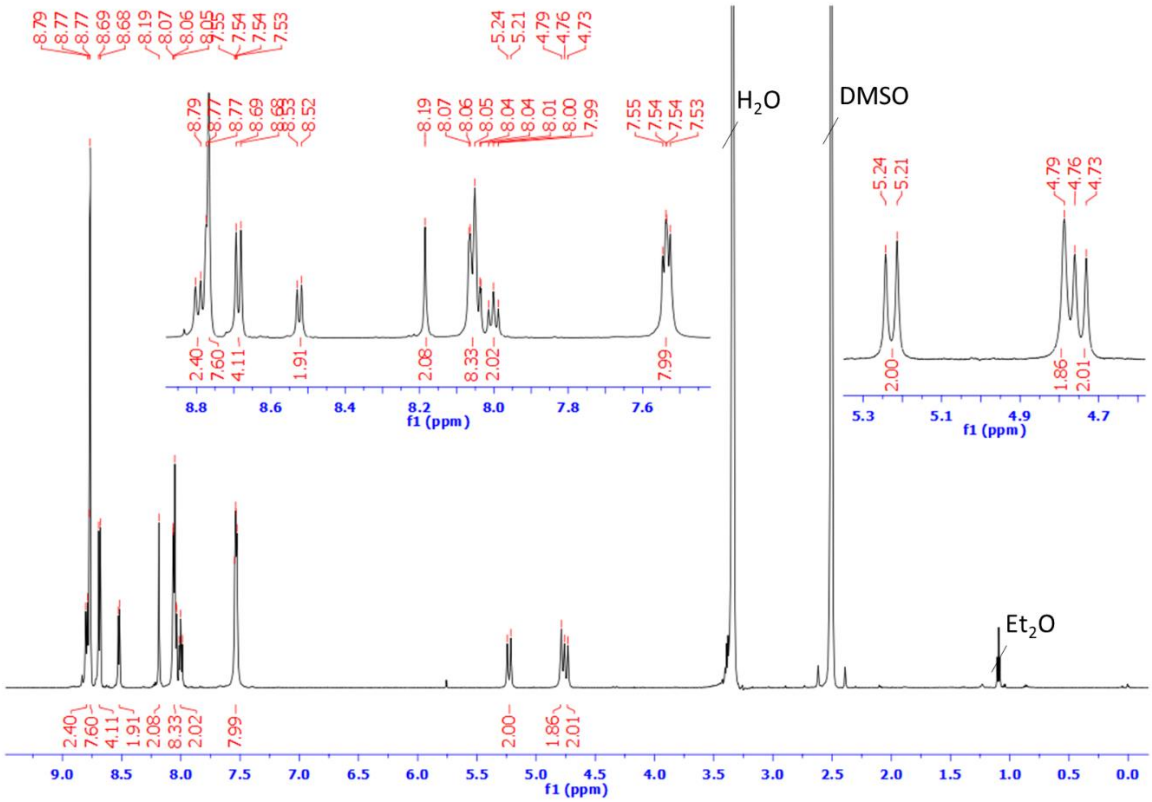

Figure 3-9 The ^1H NMR spectra (600 MHz, DMSO-d_6) of **130**. Inserts: zoom on the aromatic region of the ^1H NMR spectra from 7.4-9.0 ppm and 4.6-5.3 ppm.

The IR spectrum of **130** reveals two strong bands at 1705 cm^{-1} and 1665 cm^{-1} accounting for the C=O stretching on the naphthalimide moieties and a strong signal at 1240 cm^{-1} due to C−N stretching of the Tröger's base unit (Figure 3-10).

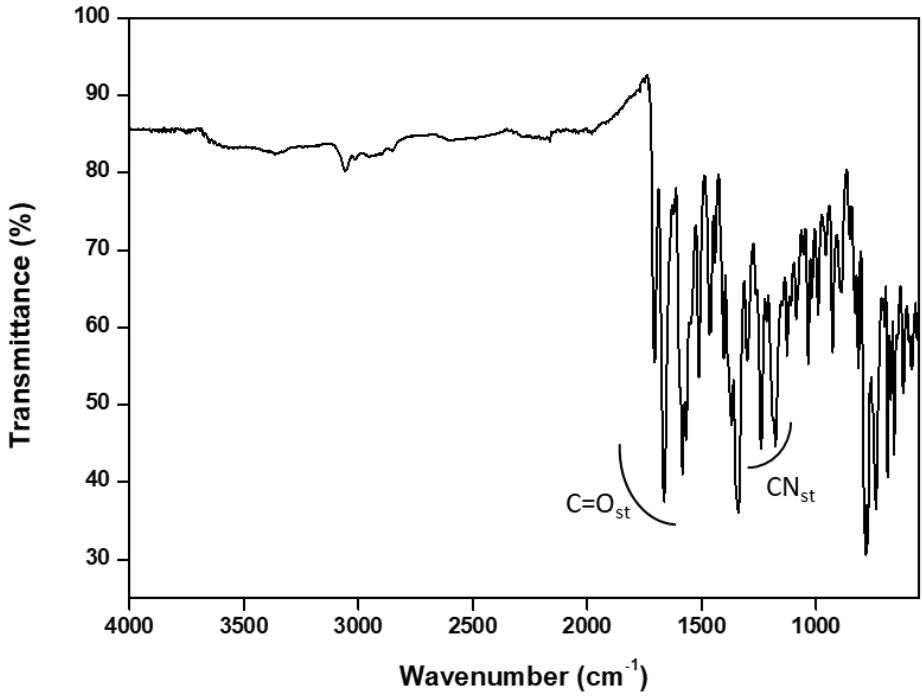

Figure 3-10 FTIR spectrum (550-4000 cm^{-1}) of **130**.

Having fully characterised **130**, its spectroscopic properties were next analysed with the aim of exploring its behaviour in solution.

3.3 Spectroscopic Study

The luminescence behaviour of **130** in solution was studied with the use of various organic solvents and mixture of organic-aqueous solutions. As expected from the previously studied 4-amino-1,8-naphthalamide,[182,184,187] the presence of a redshift of the emission spectrum upon increasing polarity can be observed in Figure 3-11B, which is an indicator of the presence of internal charge transfer (ICT) state due to the push-pull nature of the donating amine and the withdrawing diimide. This is typical for AminoNaps and the same phenomenon for TBNaps was demonstrated, however, the diazocine ring reduces the strength of the push-pull interactions leading to a small blue shift in the TBNap emission *vs.* the Nap emission (see appendix).[182-184]

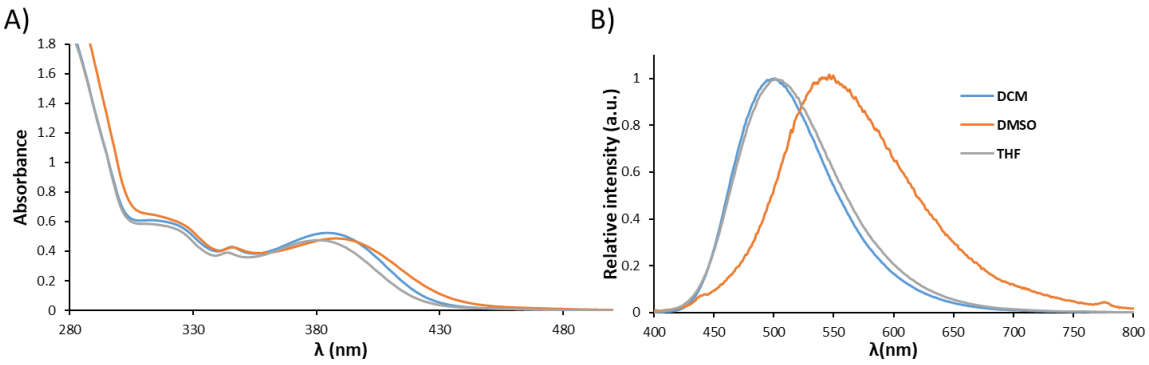

Figure 3-11 A) absorption spectra and B) normalised emission spectra of **130** in DCM, DMSO, THF. (c= 2.5×10^{-5} M), λ_{ex}= 388 nm for DCM and DMSO, λ_{ex}= 380 nm for THF.

The spectra of the ligand in DMSO (Figure 3-11A) is dominated by ligand-centred π→π* transitions centred at 278 nm (ε = 98919 ± 388 cm^{-1} M^{-1}), 319 nm (ε = 27929 ± 146 cm^{-1} M^{-1}), 346 nm (ε = 18864 ± 142 cm^{-1} M^{-1}), and the ICT Tröger's base band centred at 388 nm (ε = 21303 ± 134 cm^{-1} M^{-1}).[6,183,191] A dilution study on **130** in DMSO was carried out in the range of 25-0.25 µM, revealing a linear relationship for the absorption against concentration while a slightly parabolic relationship for the intensity in correlation to the concentration could be observed, presumably due to a combination of inner filter effect and aggregation.

Since the two phenyl-terpyridine moieties decorating the Tröger's base possess a free rotation, we had anticipated that upon addition of a counter solvent, a change in the spectroscopic properties of **130** would be observed. To investigate this, mixtures of organic-aqueous solutions were analysed. Upon addition of deionised water to a solution of **130** in DMSO, an enhancement in the fluorescence was observed. This is most likely due to enhanced aggregation of **130** and the 'switching-on' effect of the AIE; the effect is clearly visible even to the naked eye as demonstrated in the insert of Figure 3-12. Upon excitation of the ICT band (λ_{ex} = 388 nm) in DMSO, a broad fluorescence emission was observed with λ_{max} at 540 nm. Upon addition of H_2O, no significant shift was observed in the λ_{max}. However, a significant 3-fold enhancement was observed in the emission intensity (Figure 3-12) with maximum intensity being observed at 30% H_2O (λ_{max} = 530 nm). Once the water content increased beyond this point, the emission intensity slowly decreases, stabilising between 80-90% of H_2O as demonstrated in Figure 3-12B.

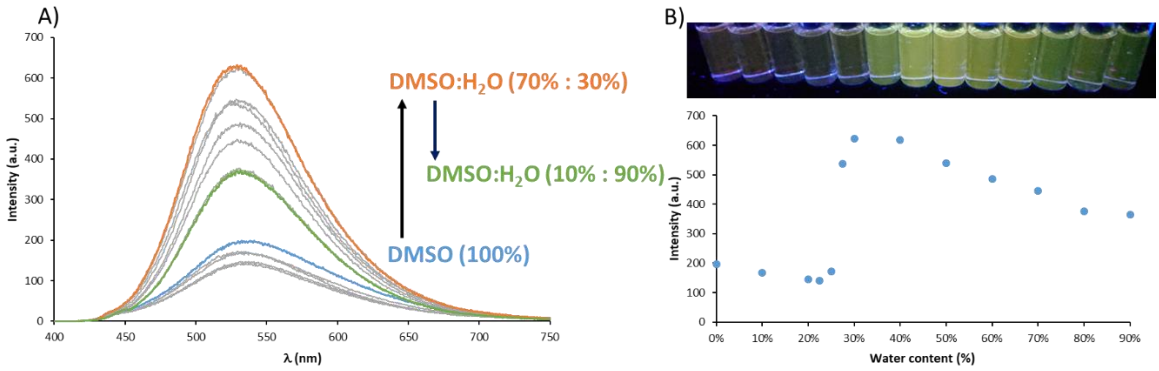

Figure 3-12 A) Emission spectra of **130** in DMSO (c= 4.6 × 10^{-6} M) at different percentage of water content (λ_{ex} = 388 nm). B) Intensity plot of **130** (c = 4.6 × 10^{-6} M) in DMSO upon addition of water at λ_{max} at 540 nm. Insert: Visible colour changes observed under a UV lamp (λ_{ex} = 360 nm).

This effect was further studied by measuring the changes in the absorption and excitation spectrum of **130** (c = 4.6 × 10^{-6} M) at various percentages of H_2O in DMSO (Figure 3-13A). No visible changes were observed upon increasing the water content on the absorption spectrum; however, it is possible to observe a shift in the excitation spectrum (λ_{em} = 540 nm) on the band corresponding to the ICT of the Tröger's base from 450 nm to 390 nm accounting for a change of the conformation of the molecule in solution when the water content was changed from 20% to 40% (Figure 3-13B).[165]

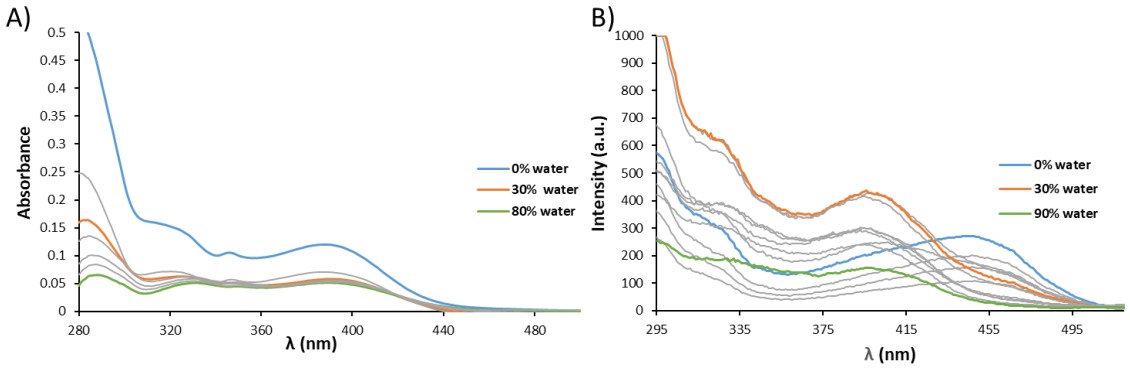

Figure 3-13 A) absorption spectra of **130** in DMSO (c = 4.6×10^{-6} M) at different percentage of water content. B) Excitation spectra (λ_{em} = 540 nm) of **130** in DMSO (c = 4.6×10^{-6} M) at different percentage of water content.

In the absorption spectrum (Figure 3-13A), no significant changes were observed in the ground state upon addition of H_2O compared to that seen in DMSO. In contrast, the fluorescence excitation spectrum exhibited a significant shift from 450 nm to 400 nm for the ICT transition when the H_2O content increased from 0% to 30% (Figure 3-13B). These changes are reflecting the aggregation of **130** in the more polar protic solution. To gain further insight into the aggregation effects, their associated morphological features were studied using Scanning Electron Microscopy (SEM).

3.4 Morphological Study

SEM was used to probe the aggregate formation at various DMSO:H_2O fractions. The samples were prepared by drop-casting the DMSO or DMSO/Water mixture (4.79×10^{-5}M) of **130** on silica wafers, dried both in ambient conditions and under high-vacuum for few hours, then coated with Pd/Au before the imaging. The SEM was carried out using the facilities of the Advanced Microscopy Laboratory (AML) in Trinity College Dublin. As presented in Figure 3-14, the SEM analysis of **130** in pure DMSO demonstrates the formation of amorphous aggregates with the presence of a random distribution of spherical particles. As the water content increased, the number of spherical aggregates increased, becoming the predominant structural feature when the water content reaches 30%. The spherical aggregates were measured using the image processing software ImageJ and have a size ranging from 48 nm to 300 nm.[192,193] Upon increasing the water content above 30%, the spherical aggregates are destroyed, forming amorphous aggregates which demonstrate the influence of the solvent on the self-assembly of **130**.[194] While the imaging showed good reproducibility, it was also possible to observe that the concentration used in the stock solution of **130** before drop-casting showed a small influence on the formation of the spheres and their quantity.

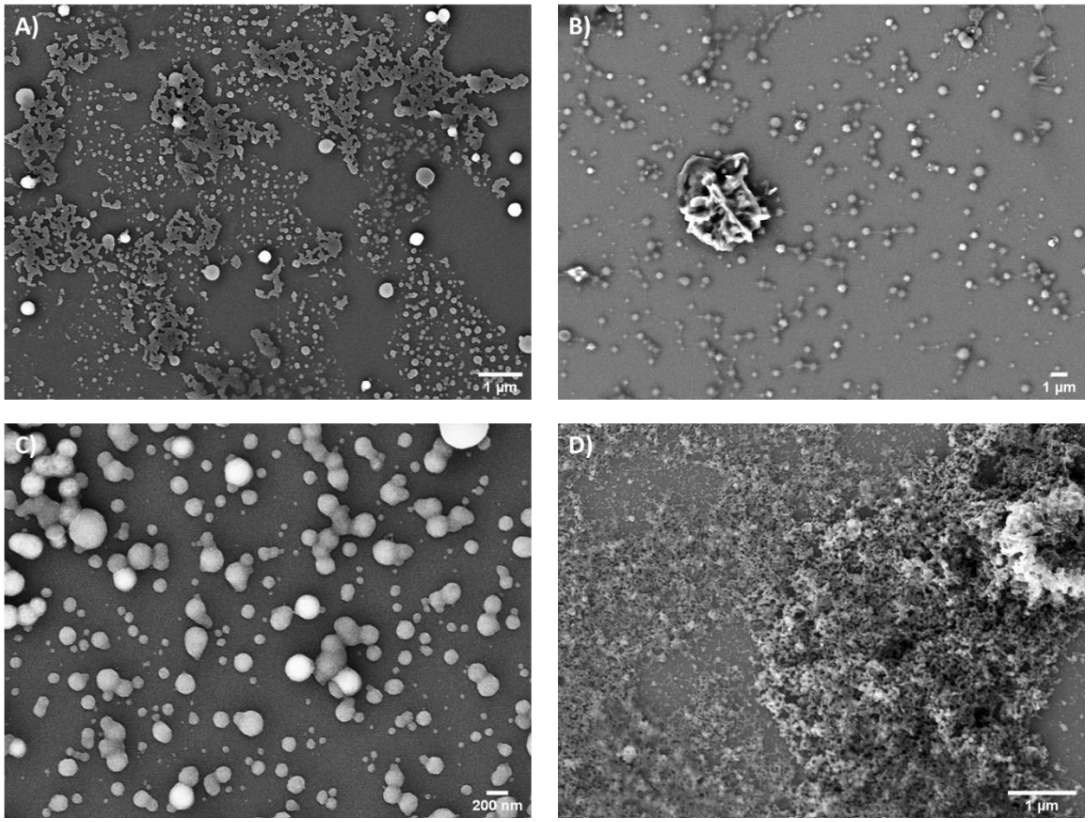

Figure 3-14 Scanning electron microscopy images of **130** in A) DMSO (scale bar 1 µm), B) 22.5% water (scale bar 1 µm), C) 30% water (scale bar 200 nm), D) 90% water (scale bar 1 µm).

Having synthesised, characterised and imaged **130** in various solvents and solvent mixtures, the application of this compound as a sensor of electron-deficient nitroaromatic compounds was next investigated.

3.5 Detection of Chemical Explosives in Competitive Aqueous Media

Poly-nitroaromatic compounds (NACs) are secondary chemical explosives; some of which, such as picric acid (PA), are extensively used in industry. PA is considered an environmental pollutant and potentially toxic to living organisms.[195] It has high solubility in water (≈14 $g.L^{-1}$), and as such, is stored and transported in water across the world to minimize the danger of explosion. The continuous exposure to saturated vapours of PA can cause severe and irreparable health issues like liver and kidney failure and neurological damages. As such, PA is a highly desirable target for chemosensing in competitive media.[196-198] While several examples of fluorescent sensors for NACs exist, there still remains a need to develop a suitable and reliable fluorescence sensor for the trace detection of NACs in competitive media.[185,199-201] Over the past few years, using 4-amino-1,8-naphthalimide Tröger's base motifs (TBNaps), the Gunnlaugsson research group have developed a variety of materials for the discriminative detection of NACs such as PA, including organic polymers and coordination networks.[185,202] It has been shown that these structures can sense PA with both high sensitivity and selectivity where the sensing action was monitored through observing the luminescent "on-off" and "off-on" switching properties in water. The objective of this work is to take advantage of the self-assembly of **130** observed in DMSO:H_2O mixture producing an enhanced luminescence from **130** to achieve a higher sensitivity due to the dynamic nature of the self-assembly. This work also represents the first example of a TBNap prone to AIE with use as a NACs sensor.

3.5.1 Detection of NACs using AIE sensor

3.5.1.1 Detection of picric acid

Several examples of luminescent sensors taking advantage of the AIE have been designed and have demonstrated their ability to compete with metal-organic frameworks (MOFs) and coordination polymers for sensing of NACs. These AIE sensors have shown both good sensitivity and selectivity, as well as enabling such sensing in a more competitive medium such as aqueous media.[197,203,204] Once the optimum emission properties for **130** were established to be in DMSO:H_2O mixture, the potential application of this system as a

luminescent sensor for pollutants in water, such as PA, which was used as a prototype of NACs, was investigated by monitoring the changes in the ICT emission of **130**. It was foreseen that increasing the electron density on the imide side of TBNaps, by incorporating the phenyl-terpyridine moieties, would potentially lead to enhancement of electrostatic interactions with electron-deficient NACs.

To demonstrate the ability of **130** for the detection of nitroaromatics, a fluorescent titration of **130** in presence of PA was performed in DMSO:H_2O (70%:30%). The absorption spectra were recorded but no significant changes in the ICT band were observed. The changes in the ICT centred **130** emission upon the increasing concentration of PA are shown in Figure 3-15. As can be seen, no noteworthy changes in λ_{max} were observed, while significant quenching in the TBNap fluorescence was observed between 0-74.1 µM of PA. The quenching propensity was thus next analysed using the Stern-Volmer equation:

$$\frac{I_0}{I} = 1 + K_{SV}[Q]$$

Where I_0 is the initial fluorescence intensity at λ_{max} = 540 nm before the addition of analyte, I is the fluorescence intensity in the presence of analyte, [Q] is the molar concentration of analytes, and K_{SV} is the Stern–Volmer constant. The result of the Stern-Volmer plot is shown in Figure 3-15B and an upward curvature can be observed, indicating that at least both static and dynamic quenching are involved and are further investigated in the following paragraph. Nevertheless, the linear region of these changes was fitted to a Stern-Volmer plot and gave Ksv = 4.06 ± 0.4 × 10^4 M^{-1} (this value was obtained from the average of 3 titrations), which is comparable to what has been observed for similar systems.[185] Furthermore the presence of both static and dynamic quenching was analysed using the equation:

$$\frac{I_0}{I} = (1 + K_{SV}[Q])(1 + K_S[Q])$$

Where K_s is the stability constant of the complex formed by the analyte and the fluorophore. Therefore by plotting (I_0/I-1)/[Q] against the concentration of analyte (PA in this case) a linear plot should be obtained if only static and dynamic quenching were involved.[205] However a parabolic relationship was observed (as shown in the appendixes) thus indicating that other mechanisms might be involved in the quenching.

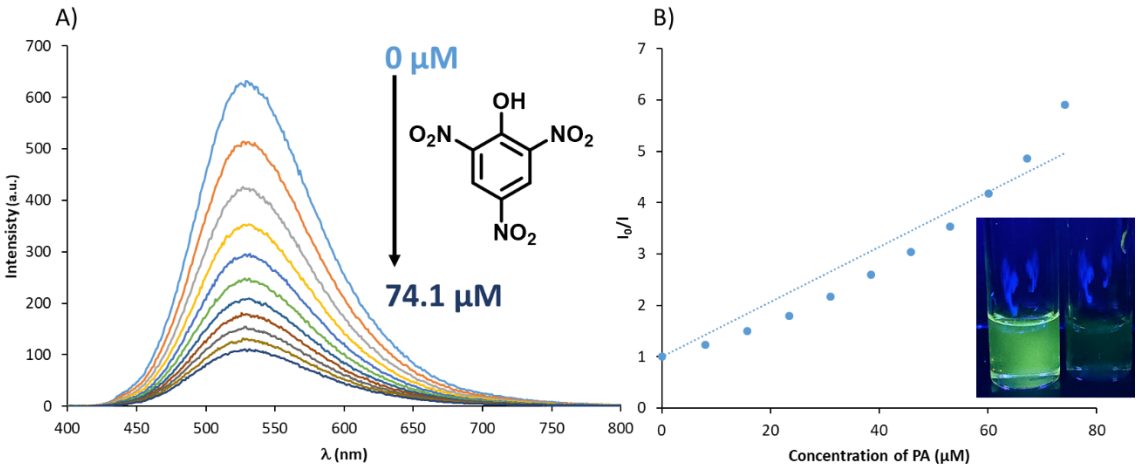

Figure 3-15 A) Fluorescence quenching observed for **130** (c = 4.6×10^{-6} M) upon addition of PA (0→74.1 µM) in DMSO:H_2O (70%:30%) solution. B): The corresponding Stern-Volmer plot for the quenching. *Insert*: Visible colour changes observed before (left) and after (right) addition of PA (74.1 µM) under a UV lamp (λ_{ex} = 360 nm).

3.5.1.2 Study of the static and dynamic quenching

From the results described above, the upward curvature observed in the Stern-Volmer plot indicates that several mechanisms for the detection of PA could be involved. The first one consist of Förster Resonance Energy Transfer which corresponds to the excited donor energy transfer to an acceptor through a non-radiative pathway. The second one could be due to the spectral overlap between the absorption spectra of PA and the excitation spectra of **130** is the inner filter effect. The third one is the formation of hydrogen bonds between the AIE active **130** and PA leading to either the formation of a ground state electrostatic complex or the disruption of the self-assembly observed for **130** leading to a decrease of the emission intensity. To evaluate the potential of energy transfer and/or filter effect a superposition of the normalised absorption spectrum of PA and the excitation and emission spectra of **130** can be seen in Figure 3-16. It appears clearly from these spectra that the inner filter effect is playing an important role in absorbing part of the excitation light but it is important to note a spectral overlap between the fluorescence spectrum of **130** and the absorption spectra of PA, confirming the possibility of energy transfer.[185,206] Moreover, as shown in the appendixes, 2,4-DNP displays a similar absorption spectrum to PA and therefore, a similar overlap with the excitation spectrum of **130** however as described later, the addition of 2,4-DNP only give rise to a quenching efficiency of **130** of 66% compared to 83% for PA. This demonstrates that the inner filter effect is not the only mechanism responsible for the quenching of the emission of **130**.

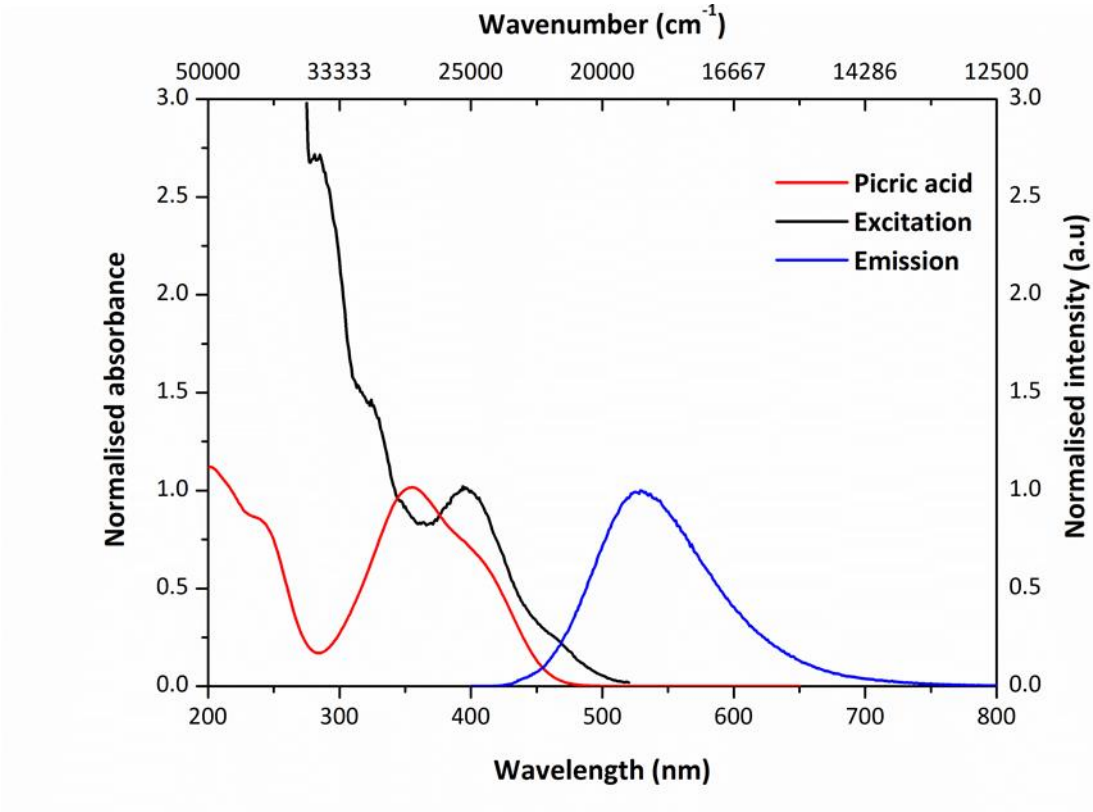

Figure 3-16 Normalised absorption spectra of picric acid in H_2O, excitation (λ_{em} = 540 nm) and fluorescence (λ_{ex} = 388 nm) spectrum of **130** in DMSO:H_2O (30%:70%).

To further study the mechanism of fluorescence quenching, the time-resolved fluorescence decay at different concentration of PA was recorded. The time-resolved decay of **130** in DMSO was best fitted to a bi-exponential decay, the calculated lifetimes are 0.89 ns and 8.46 ns. Similarly, the time-resolved decay of **130** in the 70:30 DMSO:H_2O mixture (Figure 3-17A) were best fitted to bi-exponential decay, which showed that upon addition of PA, the excited state lifetimes were decreasing respectively from 2.52 ns to 1.85 ns for τ_1, and 7.44 ns to 6.20 ns for τ_2 (the decays and their fit are shown in the appendices); thus revealing the interaction of PA to **130** in the excited state.[185]

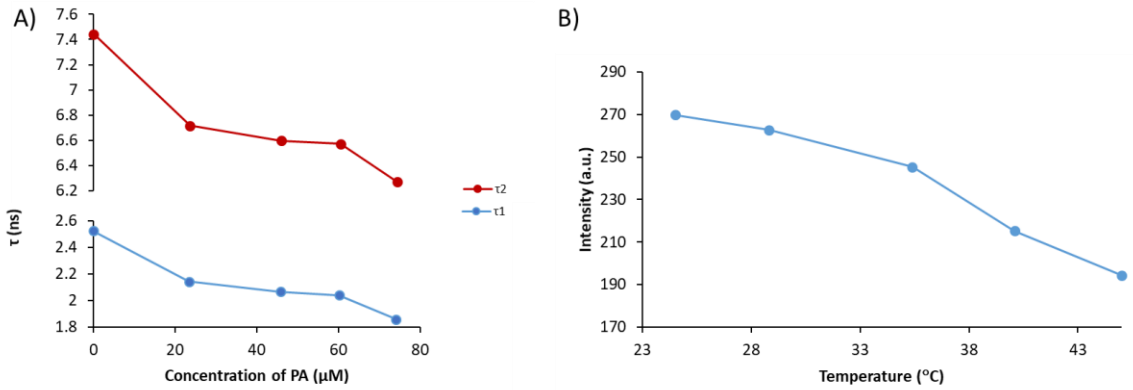

Figure 3-17 A) The fluorescence decay profiles of **130** upon addition of PA (0-74 μM) in DMSO:H_2O (70%:30%). B) Its temperature-dependent emission profile in the presence of PA (38.5 μM).

The temperature dependence quenching of the **130** emission in the presence of PA was analysed as demonstrated in (Figure 3-17B). It revealed that in the presence of 38.5 µM of PA (Figure 3-17B) the quenching efficiency was 59% at 24.5 °C while being dramatically increased to 70% at 45 °C. This can be accounted for by two phenomena; i) enhancement in dynamic quenching upon raising the temperature, due to the enhanced rate of collision between **130** and PA, and ii) the potential destruction of the **130** emissive aggregates.[185,207]

3.5.1.3 Investigation of the interactions between **130** and PA

To gain further insight into the interactions between **TBNap-TPy** and PA, a ^{1}H NMR titration was carried out in DMSO-d_6 at 1.11×10^{-3} M. This titration was also attempted in DMSO-d_6:D_2O (70%:30%) to be as close as possible to the actual sensing conditions; however, the concentration necessary to achieve this titration was leading to the formation of aggregates accompanied by a significant broadening of the signal on the ^{1}H NMR spectrum. The gradual addition of PA from 0 to 10 equivalents to the DMSO-d_6 solution of **130** ($c = 1.11 \times 10^{-3}$ M) resulted in a significant downfield shift for the proton resonance of $H_{5,5''}$, $H_{4,4''}$, $H_{3,3''}$, $H_{6,6''}$ and $H_{3',5'}$ corresponding to the protons of the terpyridine moieties. This suggests the presence of intermolecular hydrogen-bonding as well as π-π stacking interactions between PA and the terpyridines. On the other hand, H_{10}, $H_{10'}$ and H_{12} corresponding to the Tröger's base moiety as well as the protons corresponding to the naphthalimide did not show any changes in chemical shift (Figure 3-18).

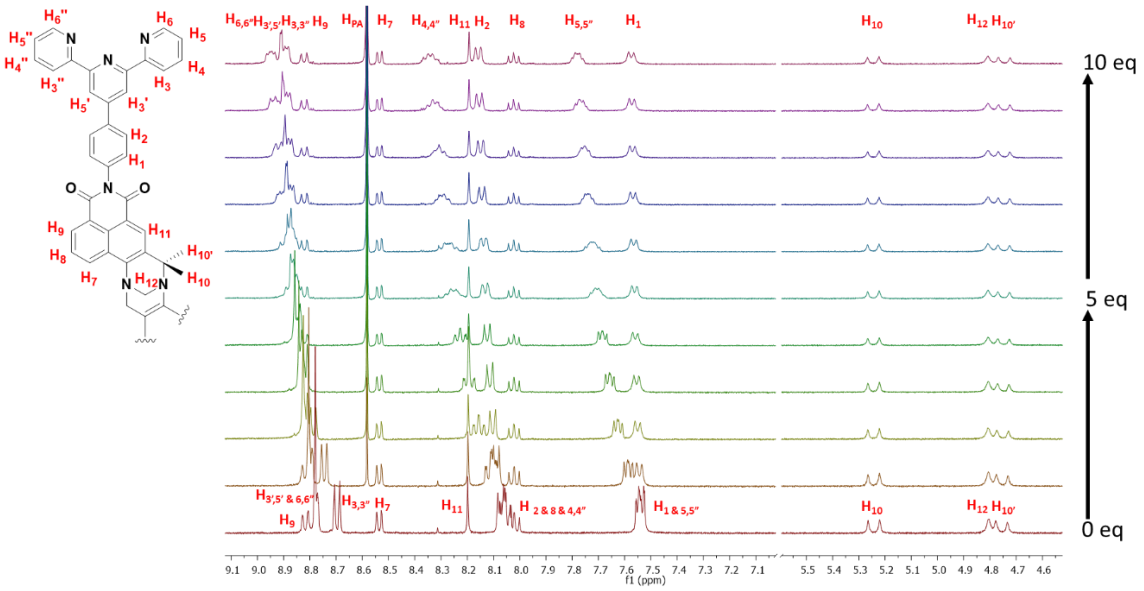

Figure 3-18 The change in the ^{1}H NMR of spectra (400 MHz, DMSO-d_6) of **130** ($c = 1.11 \times 10^{-3}$ mol.L^{-1}) upon mixing picric acid at a gradual increase in concentration over 0→10 equivalents.

The presence of intermolecular hydrogen-bonding was further investigated by recording the FT-IR spectra of the solid samples of PA and **130** before and after mixing it with PA. To do so, PA and **130** were dissolved together in DCM and the solvent was left to dry. It can be seen on the IR spectrum of PA (Figure 3-19), the sharp signal at 3100 cm^{-1} corresponding to the OH stretching but once PA (2 eq.) is mixed with **130** (1 eq.) this signal is not visible anymore in the IR spectrum confirming the existence of strong intermolecular hydrogen-bonding interactions between **130** and PA.[202]

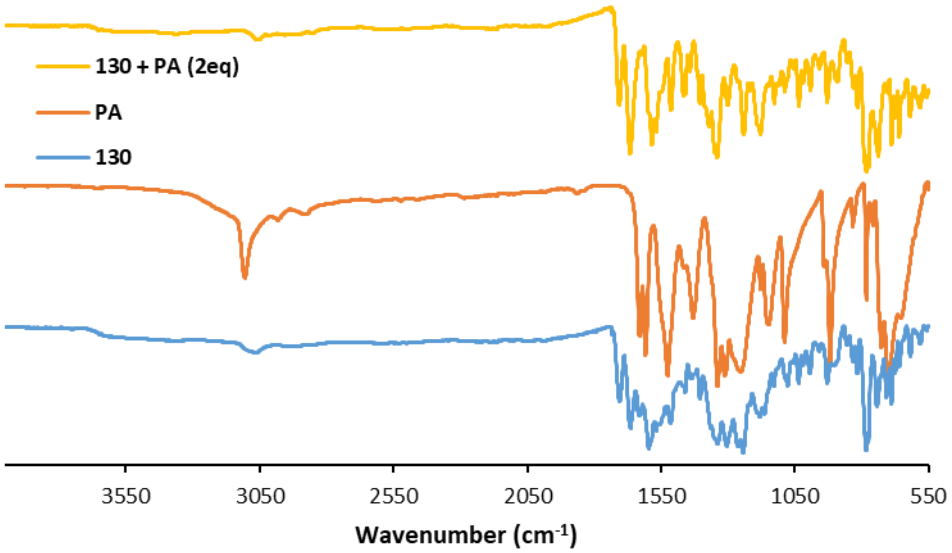

Figure 3-19 The FTIR spectrum (550-4000 cm^{-1}) of **130** (blue), PA (orange) and **130** in presence of 2 equivalents of PA (yellow).

To substantiate these arguments, density functional theory (DFT) analysis was performed by Dr. Deivasigamani Umadevi from the Watson computational chemistry group at Trinity College Dublin, using the M06-2X/6-311G(d,p)[208] method to highlight the potential interactions between **130** and PA using the model system. All the calculations were done by using the Minnesota M06-$2X_5$ functional and the 6-311G(d,p) basis set. All the calculations were done by using Gaussian 09 package.[209] The M06-2X method was chosen, as it has been shown to be better when compared to the more popular B3LYP alternatives when modelling nonbonding interactions.[210] The model system used to represent **130** is shown in Figure 3-20A and the binding energy (BE) was calculated using the equation below:

$$BE = (E_{TB} + E_{PA}) - E_{TB+PA}$$

With E_{TB} being the total energy of **130** and E_{PA} the total energy of PA. While E_{TB+PA} corresponds to the total energy of the complex formed by **130** and PA. The binding energy

was then corrected for basis set superposition error (BSSE) using the counterpoise correction method. The results of the calculations of the frontier molecular orbitals are shown in Figure 3-20B and demonstrate that the LUMO is essentially localised in the imide region of **130** while the HOMO is more localised in the Tröger's base and naphthalene region of the molecule. These results highlight that the TBNap moiety is electron-rich.

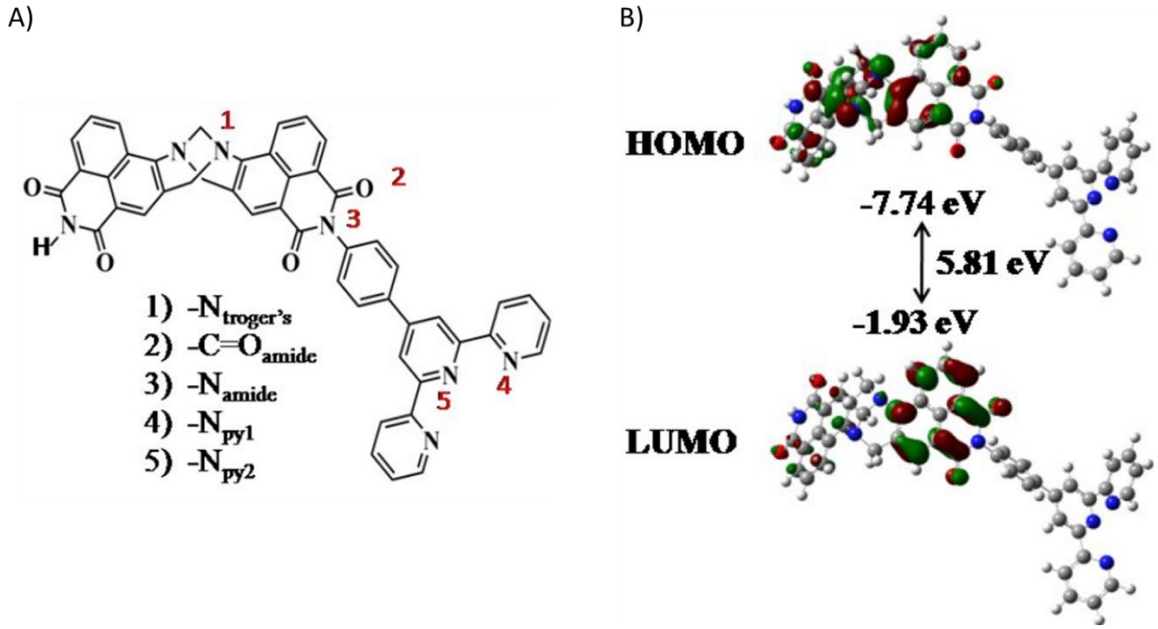

Figure 3-20 A) The model system used to represent **130** and the possible sites of interactions with PA and B) the frontier molecular orbital with their corresponding energy values of **130** model system.

Further analysis revealed five possible sites of interactions with PA on **130** (Figure 3-21A). These sites are the Lewis basic nitrogen of TBNap (-$N_{Tröger's}$), the carbonyl group of the imide (-COO_{imide}), the nitrogen of the imide (-N_{iimide}), the nitrogen of the central pyridine of the terpyridine moiety (-N_{Py2}) and the nitrogen of the side pyridine of the terpyridine (-N_{Py1}). Calculations showed that no stable interactions were observed at the (-N_{iimide}), however intermolecular interactions with PA at -$N_{Tröger's}$, -COO_{imide}, -N_{Py2} and -N_{Py1} were calculated to reach 8.45, 15.90, 18.46 and 23.87 kcal.mol^{-1} respectively. The nearest distance calculated for the interactions between each site and PA as shown in Figure 3-21 are 1.6 Å at -$N_{Tröger's}$, 1.8 Å at -COO_{imide}, 1.5 Å at -N_{Py1} and 1.9 Å at -N_{Py2}. The optimized geometries indicate a mixture of π-π stacking and hydrogen-bond interactions at -COO_{imide} and -N_{Py2} while only hydrogen bonding is taking place at -$N_{Tröger's}$ and -N_{Py1}. The higher binding energies calculated for the interactions at the terpyridine moieties confirmed the observed changes in the ^{1}H NMR spectra (Figure 3-18) and the enhanced sensing capacity of TBNap adorned with terpyridine moieties.

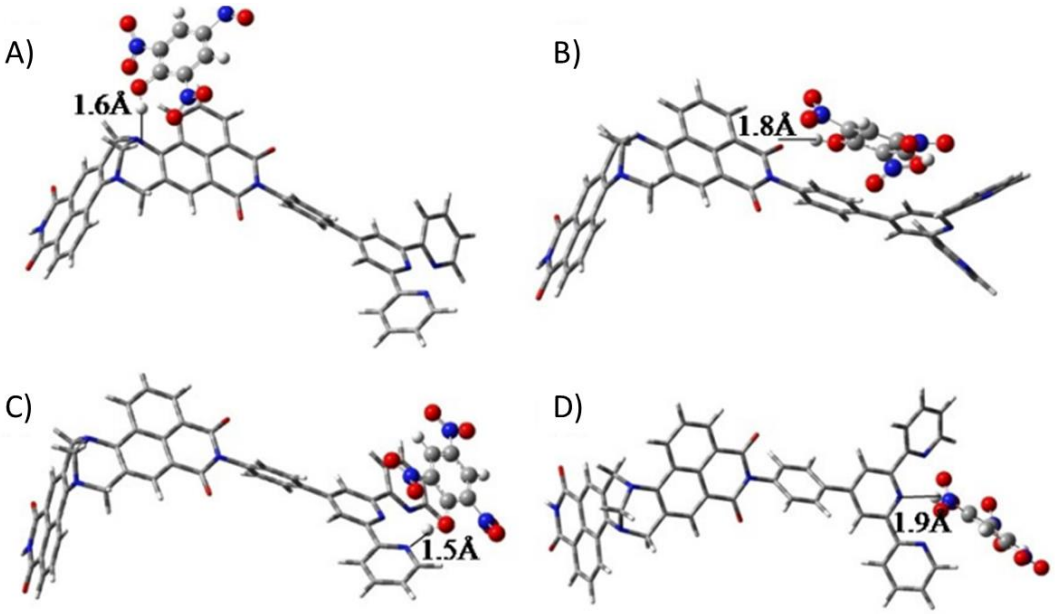

Figure 3-21 Optimized structures, nearest intermolecular distances of the **130** complexes with PA at A) -$N_{Tröger's}$, B) -C=O_{imide}, C) -N_{Py1} and D) -N_{Py2} sites. (The structure of **130** is given in tube representation for clarity).

3.5.1.4 Selectivity, competitivity and sensitivity towards NACs

To use **130** as an AIE sensor for PA in aqueous media, it was necessary to study the selectivity and sensitivity of **130** towards structurally related NACs. The selectivity of **130** was evaluated by carrying out fluorescence titrations using other NACs such as dinitrophenols (DNT) and nitrophenols (NP): 2,4-DNP, 2-NP, 3-NP, 4-NP, and the related dinitrotoluene (DNT) and nitrotoluene (NT): TNT, 2,4-DNT, 2,6-DNT, 2-NT, 3-NT, 4-NT and nitrobenzene (NB) and by calculating their quenching efficiency (Figure 3-22).

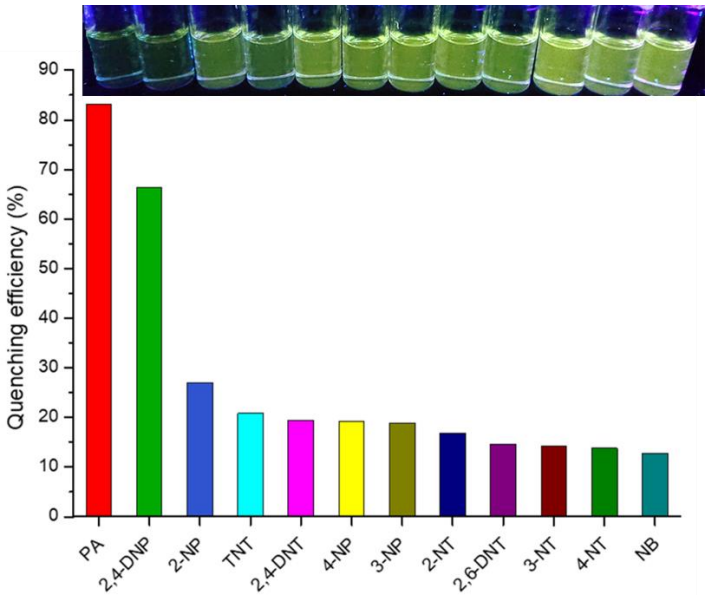

Figure 3-22 Quenching efficiency of various nitroaromatic at 74.1 μM in DMSO:H_2O (70%:30%) mixture. *Insert*: visual colour changes under a UV lamp (λ_{ex} = 360 nm).

These titrations (shown in the appendices) revealed that highest quenching efficiency was indeed obtained for PA with 83% after reaching 74.1 μM of PA in solution leading to the quenching of the AIE intensity; this being followed by 2,4-DNP which gave rise to 66% quenching at the same concentration (Figure 3-22). Furthermore, analysis of these changes using the Stern-Volmer equation showed linear regression from which K_{sv} was determined from (Table 3-1) with the error on each values corresponding to the standard deviation for the fitting of at least the duplicated titration. As shown in Appendix A.33, the Stern-Volmer plot only gives a linear response in the range 0 – 45.8 μM for the titration of PA, therefore this concentration range was used to calculate its corresponding Stern-Volmer constant. From this screening, it was obvious that the phenolic based nitroaromatics exhibited the highest quenching efficacy. This is partly explained by the presence of the phenol group being able to form strong intermolecular interactions with the nitrogen of the terpyridine combined with π-π stacking as demonstrated by the results of the DFT calculations as well as intermolecular interactions with the Lewis basic nitrogen of the Tröger's base motif.[185] Gratifyingly, the PA quenching could also be seen with the naked eye under a UV lamp irradiation (λ_{ex} = 360 nm) as demonstrated as an insert in Figure 3-15.

Table 3-1The Stern-Volmer constants K_{SV} of various nitroaromatics for the fluorescence quenching of **130**.

Analytes	**K_{SV} (M^{-1}) × 10^3**
PA	**40.6 ± 1.7**
2,4-DNP	**25.0 ± 0.4**
2-NP	**5.05 ± 0.1**
TNT	**3.19 ± 0.09**
2,4-DNT	**3.03 ± 0.08**
4-NP	**2.91 ± 0.07**
3-NP	**2.62 ± 0.2**
2-NT	**2.60 ± 0.05**
2,6-DNT	**2.38 ± 0.06**
3-NT	**2.19 ± 0.05**
4-NT	**1.96 ± 0.08**
NB	**1.04 ± 0.1**

The high selectivity of **130** towards phenolic nitroaromatics, and more specifically PA was further confirmed by performing competitive fluorescence studies, where a concentration of 74.1 μM of each of the NACs was added to a solution of **130** (green bar, Figure 3-23). This was followed by the addition of 74.1 μM of PA. The results (shown as

blue bars in Figure 3-23) clearly demonstrates that in all cases the **130** emission was further quenched upon addition of PA thus confirming the high selectivity of **130** towards PA.

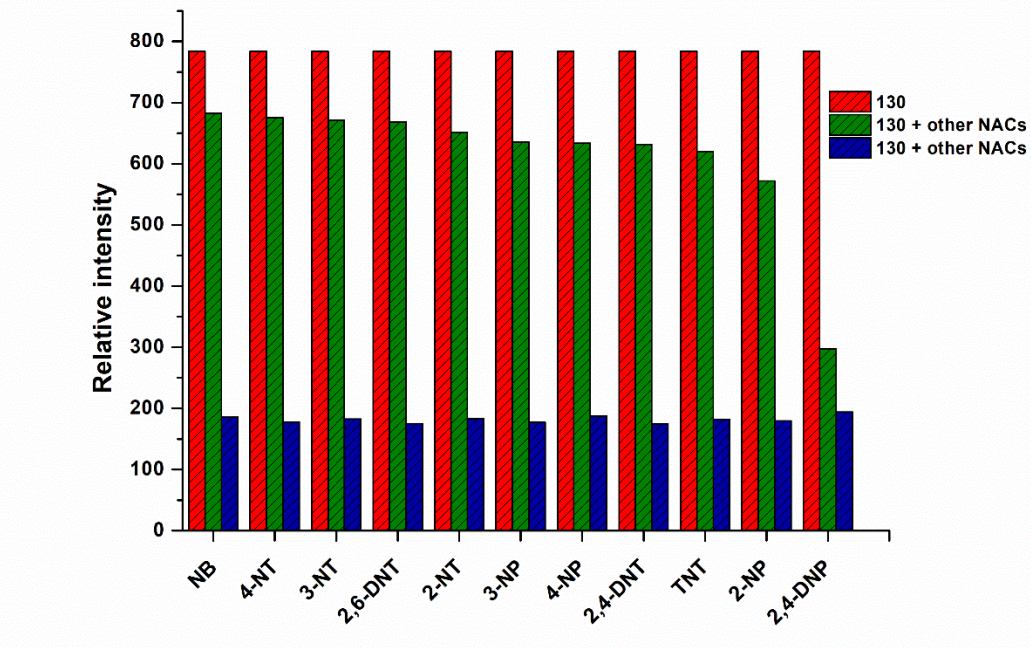

Figure 3-23 Competitive selective affinity of **130** (c = 4.6 × 10^{-6} M) towards different nitroaromatics in the presence of PA (74.1 µM) in DMSO:H_2O (70%:30%) mixture.

A sensitivity experiment was carried out by using a diluted solution of PA and proceeding to a titration (Figure 3-24). The limit of detection for PA in DMSO:H_2O (70%:30%) was calculated using the following equation:

$$Limit\ of\ detection\ (LOD) = \frac{3\sigma}{K} = 8.75\ *\ 10^{-8}\ \text{mol.}\,\text{L}^{-1} = 20.0\ ppb$$

Where σ (3.95) is the standard deviation of the initial emission intensity of **130** in DMSO:H_2O (70%:30%) before the addition of PA and *K* is the slope of the linear curve. The results showed that the **130** AIE response could be affected by a concentration of PA as low as 20 ppb. This result was calculated as the average of the triplicate.

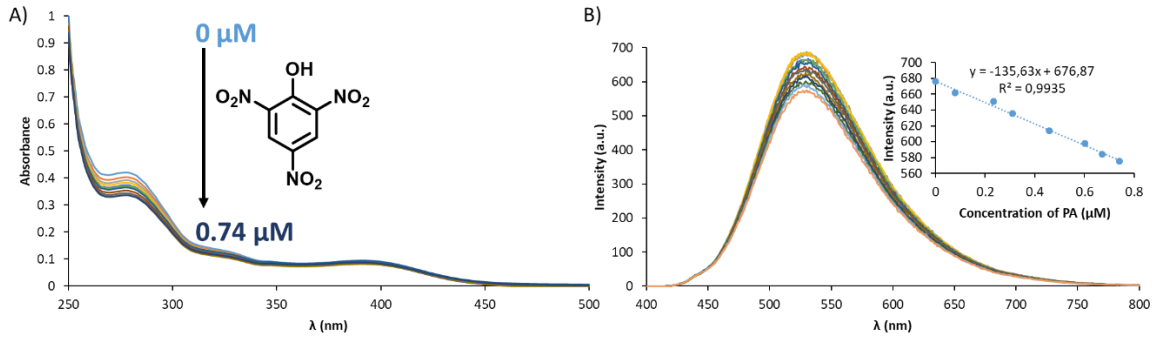

Figure 3-24 A) Absorption and B) emission spectra (λ_{ex} = 388 nm) of the sensitivity experiment of **130** in DMSO:H_2O (70%:30%) (c = 4.6 × 10^{-6} M) in the presence of PA (0-0.74 µM). Insert: Intensity plot in function of the concentration of PA.

Moreover, this level of sensitivity is under the allowed limit of NACs in drinking water established by the US EPA.[185] The response time towards PA was also evaluated at different PA concentrations and showed that upon addition of PA, the emission changes had equilibrated within a minute (Figure 3-25); the response time is independent of the concentration of PA employed.

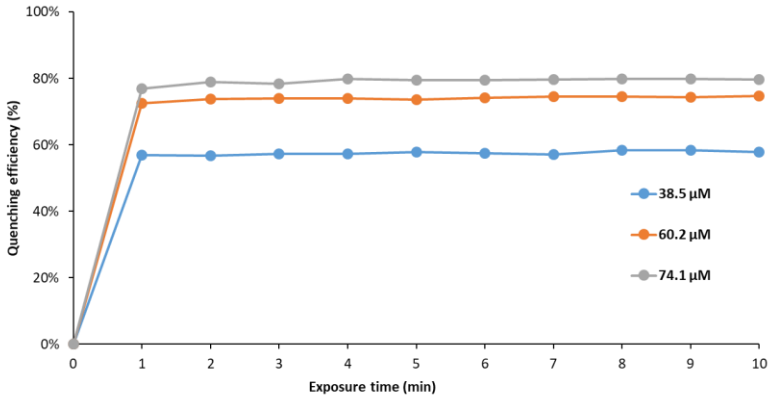

Figure 3-25 Time response of **130** (c = 4.6 × 10^{-6} M) upon contact of various concentration of PA in DMSO:H_2O (70%:30%) mixture.

3.5.1.5 Selectivity and competitivity towards ions

These overall results being very encouraging and demonstrating that **130** could potentially be used as a fluorescent AIE sensor for on-site detection of PA in the presence of various other common ions at an approximate concentration of 74 µM. This corresponds to the maximal concentration of PA which was tested (Figure 3-26). It demonstrated that **130** was insensitive to most ions, however, its fluorescence was quenched in presence of transition metals such as cadmium, zinc, nickel, copper, cobalt and iron due to the well-known chelating ability of the terpyridine moiety towards *d*-metals.

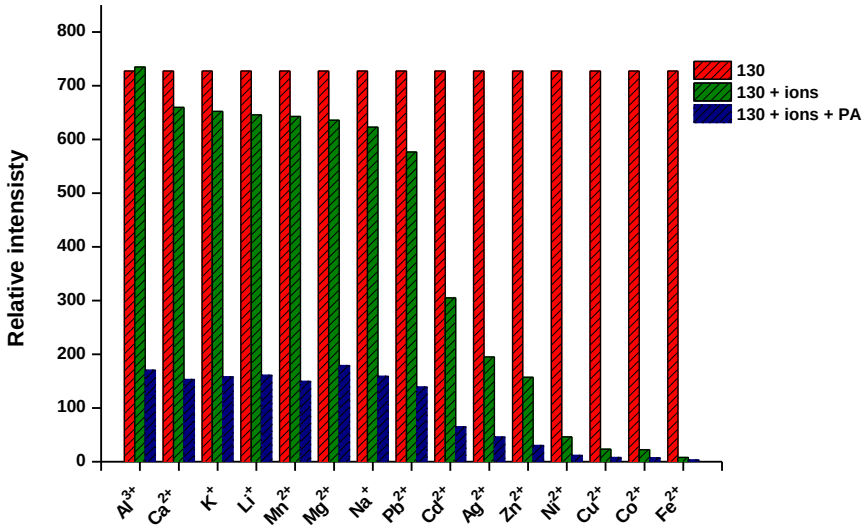

Figure 3-26 Competitive selective affinity of **130** (c = 4.6 × 10^{-6} M) towards different ions in the presence of PA (74.1 µM) in DMSO:H_2O (70%:30%) mixture.

Chelation of the metal by **130** was confirmed by visible changes in the absorption spectrum (Figure 3-27) starting by ≈ 8 nm shift in the ligand-centred π→π* transition at 280 nm and the sharpening of the same transition for $Zn(NO_3)_2$, $Ni(Cl)_2$, $FeSO_4$, $Cu(NO_3)_2$, $Co(NO_3)_2$ complexes. As a result of the coordination of the TPy, a significant increase in the absorption of the ligand-centred π→π* transitions centred 330 nm. Finally, in the case of $FeSO_4$ a characteristic band at 575 nm can be observed which is the result of spin allowed d_π(Fe(II))→π*(TPy), corresponding to metal-to-ligand charge-transfer (MLCT) transitions.[178]

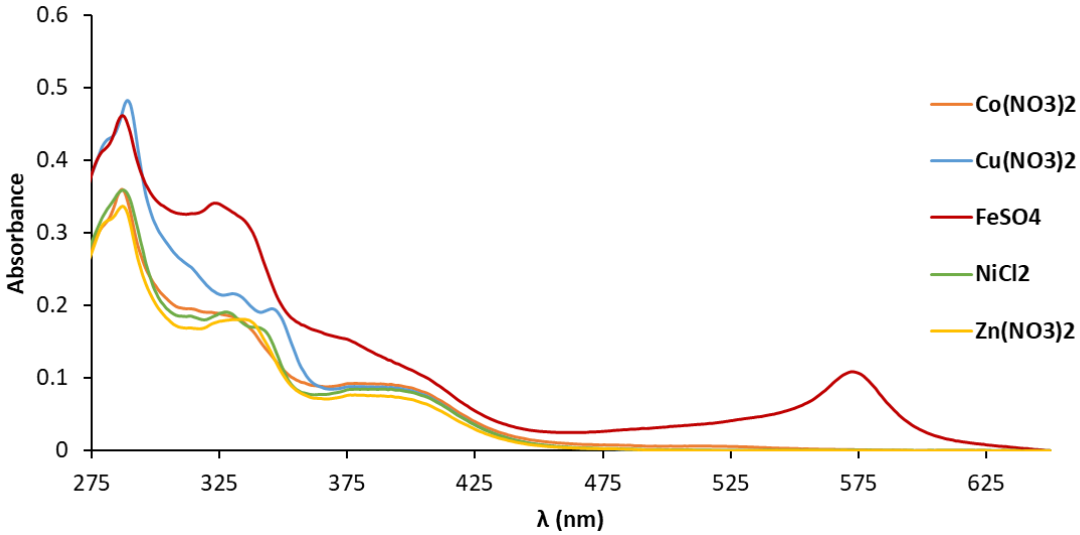

Figure 3-27 Absorption spectrum of **130** (c = 4.6 × 10^{-6} M) in presence of $Zn(NO_3)_2$, $Ni(Cl)_2$, $FeSO_4$, $Cu(NO_3)_2$, $Co(NO_3)_2$ and $Cd(NO_3)_2$ (74.1 μM) in DMSO:H_2O (70%:30%) mixture.

3.5.1.6 Effect of pH on the sensing of PA

To fully investigate **130** ability to detect picric acid in water and understand its limitations, the effect of pH on the sensing mechanism was next analysed. To obtain a meaningful measurement of pH, the studies were performed in a solvent mixture of DMSO:H_2O (1%:99%). The initial pH of **130** in DMSO:H_2O (1%:99%) was 6.4 and as it can be seen in Figure 3-28, the Stern-Volmer plot of the titration in DMSO:H_2O (1%:99%; orange dots) is very close to the titration in DMSO:H_2O (70%:30%) with a Stern-Volmer constant of K_{SV} = 3.9 × 10^4 M^{-1} suggesting that the sensing mechanisms in the two different ratios of solvent are roughly the same, but that the initial fluorescence intensity is much higher in DMSO:H_2O (70%:30%) as already demonstrated in Figure 3-12. In basic conditions (pH = 11.0; grey dots) however, the quenching is significantly lower, demonstrating a drastic effect of basic pH on the interactions between **130** and PA yielding to a Stern-Volmer constant of K_{SV} = 2.1 × 10^4 M^{-1}. Inversely, the quenching efficiency of PA in acidic conditions (pH = 2.4) was

greatly increased yielding a Stern-Volmer constant of $K_{SV} = 11.2 \times 10^4\ M^{-1}$. These results reinforce the hypothesis that the quenching efficiency of PA towards **130** is partly due to intermolecular hydrogen bonding interactions.

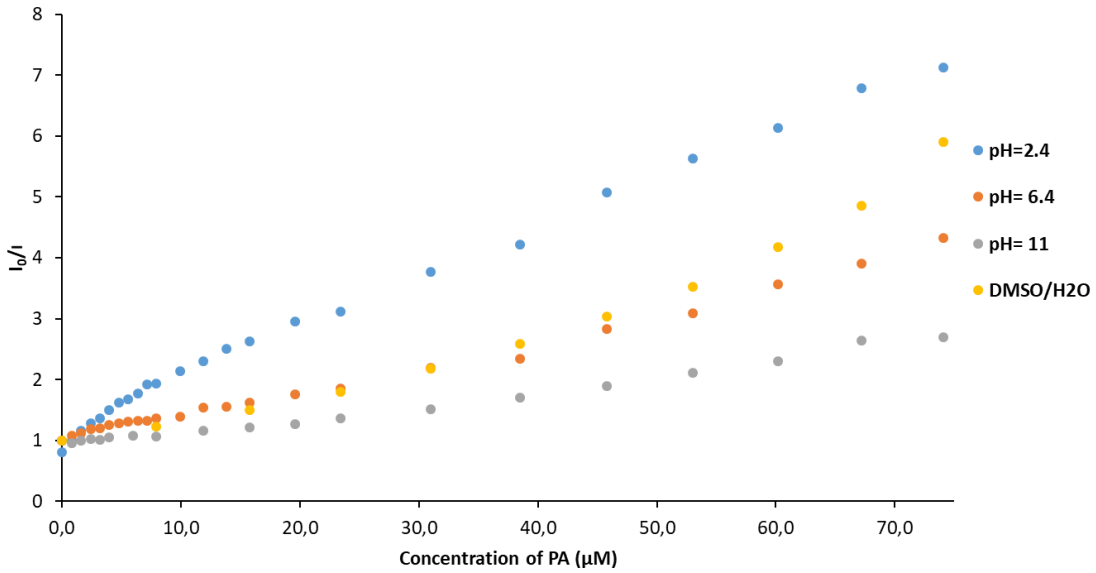

Figure 3-28 Relative changes in emission intensity (λ_{ex} = 388 nm) of **130** (c = 4.6×10^{-6} M) towards PA in DMSO:H_2O (1%:99%) mixture at different pH = 2.4 to 11 of the media compared to DMSO:H2O (30%:70%).

3.5.1.7 Conclusion

To conclude, it was demonstrated that **130**, by a combination of inner filter effect, dynamic and static quenching could selectively probe the presence of PA in water even in the presence of other ions and structurally related analytes, while not being notably affected by the changes of pH in the acidic region. A drawback lies within the conditions necessary for AIE. This requires dissolving **130** in DMSO followed by the addition of water and does not allow for the recovery of **130** after the detection of NACs, i.e. to wash it and use it again. This AIE system lacks recyclability which could be achieved using polymers or MOFs bearing the TBNap scaffold.

3.5.2 Detection of NACs using covalent organic polymer

A type of material that has gained huge interest in research for sensing and detection of various analytes are polymers which include both a metal-organic framework (MOF) and covalent organic polymer (COP) moieties. COPs just like MOFs, are composed of repeating motifs but only contain organic functional groups, usually leading to lighter materials than MOFs, as they are not composed of heavy elements. They are also generally very robust as they are principally composed of C-C and C-N bonds. In the same way that it is possible to finely tune the pore size and the surface area of MOFs, it is possible, by careful design of

the repeating unit, to achieve similarly desirable outcomes with COPs. Most COPs are used for gas storage[211] and catalysis.[212] The luminescent properties of COPs, combined with the ability to tune their pore sizes, make them ideal candidates for sensing applications.[213] Using electron-rich, conjugated fluorophores as one of the COP building blocks leads to the formation of large π-conjugated networks which are capable of acting as excellent electron donors and exhibit increased sensitivity toward electron acceptor analytes such as nitroaromatics.[214,215] Bearing this in mind, a 4-amino-1,8-naphthalimide Tröger's base COP (**TBNap-COP**, **131**) was synthesised and characterised by Asst. Prof. Sankarasekaran from the Gunnlaugsson research group (Scheme 3-2). It was anticipated that using a TBNap moiety would lead to a good selectivity and sensitivity towards phenolic-nitroaromatics due to the presence of Lewis basic nitrogens as demonstrated in the previous paragraph. Moreover using 1,3,5-tris(bromomethyl)benzene to form the crosslinked polymer would lead to the quaternarization of the pyridine groups, therefore yielding the formation of bromine counter ions. Presence of these ionic species helps to prevent any π-π stacking interactions taking place and thus facilitating the formation of a very stable fine suspension of **131** in water.

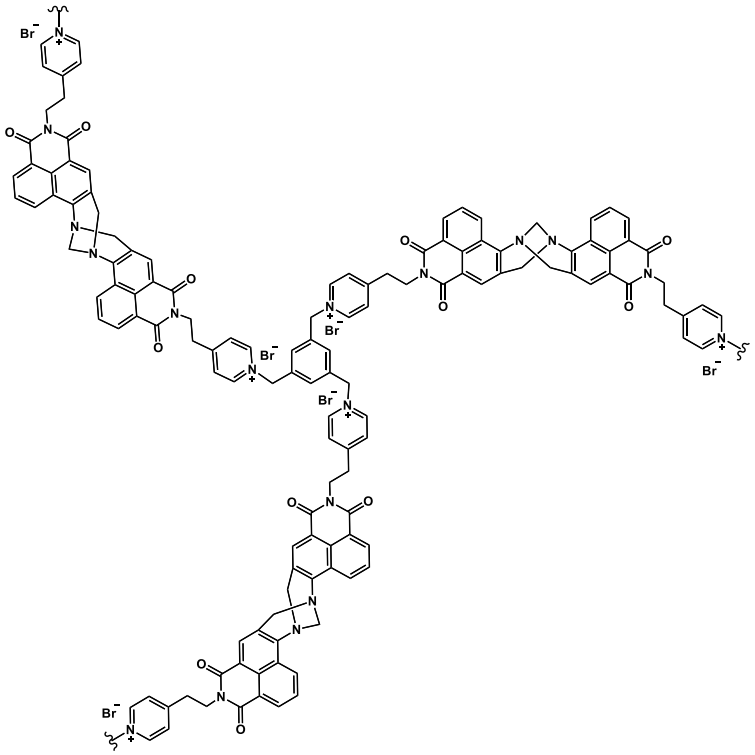

Scheme 3-2 Structure of **131**.

The polymer **131** was synthesised in 68% yield using the anhydride TBNap and the commercially available 1,3,5-tris(bromomethyl)benzene by heating in DMF for 3 days. The successful formation of **131** was confirmed by ^{1}H NMR, solid-state CP-MAS ^{13}C NMR, FT-

IR, and elemental analysis. The ^{1}H NMR spectrum in DMSO-d_6 revealed the presence of the Troger's base moiety with the doublet at 5.19 ppm and the merged singlet and doublet at 4.71–4.66 ppm accounting for the methylene protons of the diazocine ring (see in the appendices). Notably, the pyridyl ^{1}H signals of **131** are significantly down field shifted (~3.14 ppm) upon quaternization. The solid-state CP-MAS ^{13}C-NMR spectrum (shown in the appendices) further confirmed the presence of the TBNap unit, with a resonance at 164 ppm corresponding to the carbonyl groups, and two further resonances at 64 ppm and 57 ppm ascribed to the CH_2 of the diazocine ring.[185,216] The FT-IR spectrum of **131** showed two signals at 1691 cm^{-1} and 1654 cm^{-1} corresponding to the C=O stretching frequencies of the carbonyl groups of the naphthalimide moiety, two strong transitions at 1259 cm^{-1} and 1231 cm^{-1} accounting for the C-N stretching of the diazocine ring of the Troger's base.[185,202,216] The elemental analysis revealed that the sample is composed of $[C_{141}H_{108}Br_6N_{18}O_{12}].3CH_2Cl_2.4CH_3OH.DMF$. While the thermogravimetric analysis (TGA) of **131** under N_2 showed a weight loss of 4% at 200 °C, representing the loss of solvent trapped within the polymeric network. **131** was found to be stable up to ~270 °C, demonstrating good thermal stability (see in the appendices).

3.5.2.1 Spectroscopic study of **131**

To obtain a fine suspension in water, 2.5 mg of the polymer were sonicated in 10 mL of deionised water for 30 minutes and the solution was let to settle for 3 days before collecting the supernatant which was used for the following studies. The solution of **131** displayed a very weak absorption, however, the main features could be visualised with π→π* transitions centred at 275 nm and the ICT Tröger's base band centred at 370 nm (Figure 3-29A). Upon excitation at 370 nm, **131** exhibited a broad emission signal ranging from 420 nm to 670 nm with a maximum of intensity at 490 nm (Figure 3-29B).

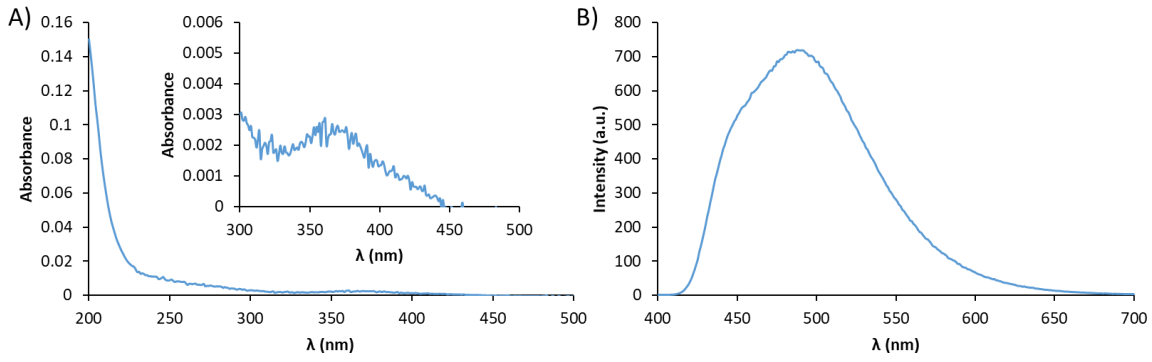

Figure 3-29 A) Absorption, insert: expansion of the 300-450 nm region, and B) fluorescence (λ_{ex} = 370 nm) spectra of **131** dispersed in water.

The excitation spectrum of **131** in water, presented in Figure 3-30, displayed 3 bands, at 242 nm, 276 nm and 303 nm accounting for the π→π* transitions due to the numerous aromatic cycle in the polymer. Two other bands could be observed with one at 356 nm corresponding to the ICT of the Tröger's base band and another one at 420 nm could be observed.

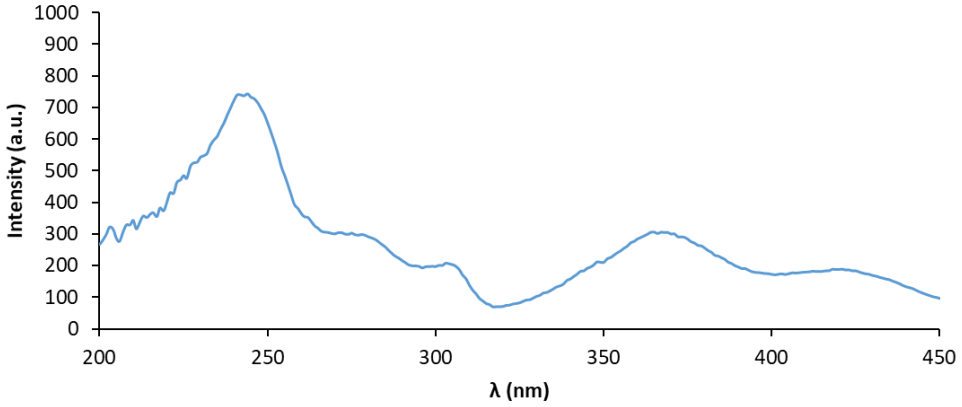

Figure 3-30 Excitation spectrum of **131** in water (λ_{em} = 490 nm).

To study the ability of **131** to detect nitroaromatics, a fluorescent titration of **131** in water in the presence of PA was performed. The absorption spectra were recorded but no significant changes in the ICT band were observed. The changes in the ICT centred emission of **131** upon increasing concentration of PA are shown in Figure 3-31. As it can be seen, no significant changes in λ_{max} were observed, while significant quenching in the TBNap fluorescence was observed between 0-90.9 µM of PA. Gratifyingly the fluorescence quenching could be observed by the naked eye under a UV lamp (λ_{ex} = 360 nm) as demonstrated in Figure 3-31.

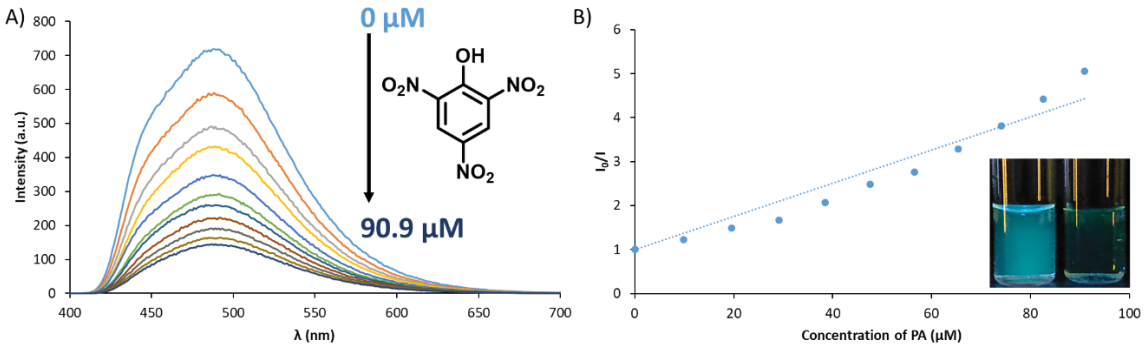

Figure 3-31 A) Fluorescence quenching of **131** upon addition of PA (0-90.9 µM; λ_{ex} = 370 nm). B) The corresponding Stern-Volmer plot. Insert: Visible colour changes observed before (left) and after (right) addition of PA (90.9 µM) under UV lamp (λ_{ex} = 360 nm).

The result of the Stern-Volmer plot is shown in Figure 3-31B, clearly depict an upward curvature meaning that both dynamic and static quenching are occurring.

Nevertheless, the linear region (from 0 to 65.4 μM) of these changes was fitted to a trendline and the average of the triplicates gave $K_{sv} = 3.27 \pm 0.13 \times 10^4\ M^{-1}$, which is comparable to what has been observed for similar systems.[185,216]

Furthermore the presence of both static and dynamic quenching was analysed using the equation:

$$\frac{I_0}{I} = (1 + K_{SV}[Q])(1 + K_S[Q])$$

Where K_s is the stability constant of the complex formed by the analyte and the fluorophore. Therefore by plotting $(I_0/I\text{-}1)/[Q]$ against the concentration of analyte (PA in this case) a linear plot should be obtained if only static and dynamic quenching were involved.[205] As seen in Figure 3-32, a linear plot is obtained, thus demonstrating the presence of both static and dynamic quenching during the sensing process.

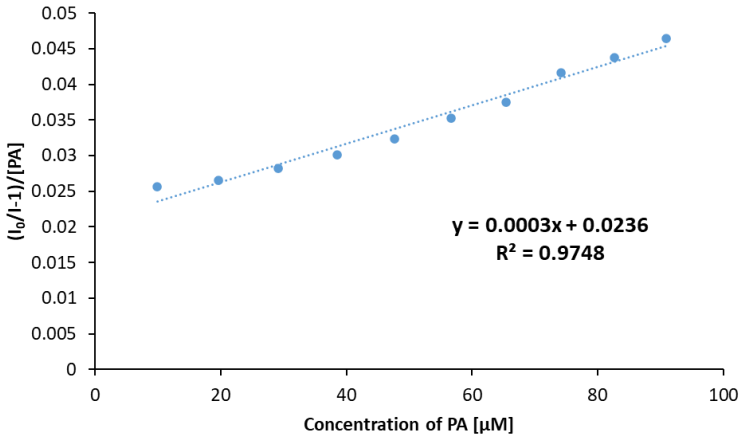

Figure 3-32 The Stern-Volmer plot of $(I_0/I\text{-}1)/[PA]$ against the concentration of PA.

3.5.2.2 Study of the quenching mechanisms

Similarly to what was observed for **130**, the quenching of fluorescence upon addition of PA can involve several mechanisms. The first mechanism consists of energy transfer from the excited donor to an acceptor through a non-radiative pathway. The second one which could be due to the spectral overlap between the absorption spectra of PA and the excitation spectra of **131** is the inner filter effect (IFE). The third is the formation of hydrogen bonds between the Lewis basic nitrogen of the Tröger's base and the phenol group of PA leading to the formation of a ground state electrostatic complex resulting in a decrease of the emission intensity. To evaluate the potential of energy transfer and/or filter effect, a superposition of the normalised absorption spectrum of PA and the excitation and emission spectra of **131** can be seen in Figure 3-33. It appears clearly from these spectra that the IFE is playing an important role in absorbing a part of the excitation light but it is important to note a spectral

overlap between the fluorescence spectrum of **131** and the absorption spectra of PA confirming the possibility of an energy transfer between the two components. Moreover, 2,4-DNP displays a similar absorption spectrum to PA and therefore a similar overlap with the excitation spectrum of **131**. As described later, the addition of 2,4-DNP only gave rise to a quenching efficiency of the emission **131** of 62% compared to 80% for PA. Thus demonstrating that the IFE is not the only mechanism responsible for the quenching of the emission of **131**.

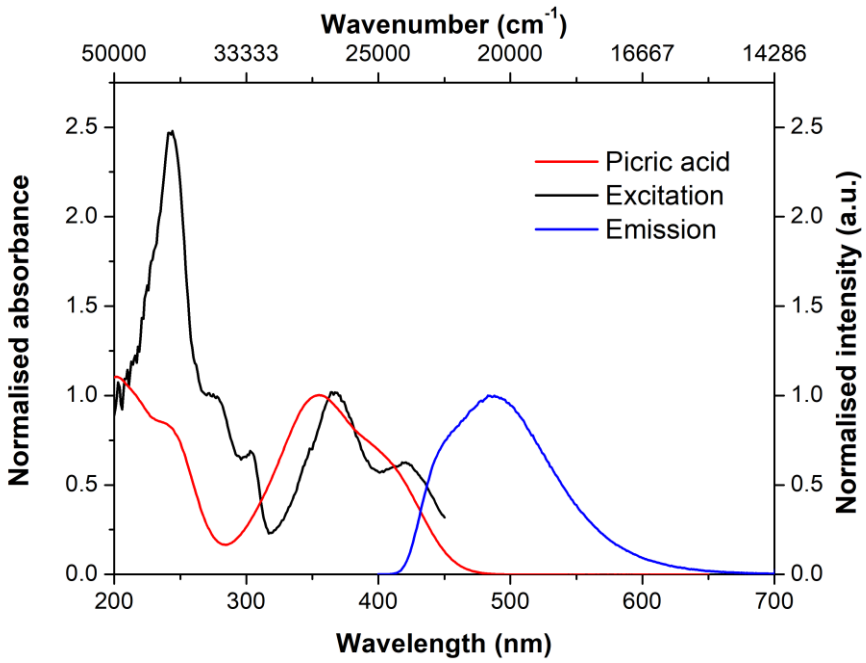

Figure 3-33 Normalised absorption spectra of picric acid, excitation (λ_{em} = 490 nm) and fluorescence (λ_{ex} = 370 nm) spectrum of **131** in H_2O.

To fully understand the impact of the IFE through the entire titration, the IFE correction was calculated using the equation:

$$I_{corr} = I_{obs} \times 10^{\frac{A_{ex}+A_{em}}{2}}$$

Where I_{corr} is the corrected fluorescence intensity, I_{obs} the measured maximum intensity, A_{ex} and A_{em} correspond to the absorbance values of **131** in presence of PA at the excitation wavelength and the maxima of emission, respectively.[217,218] The value for I_{corr} can be found in Table A.1 in the appendices and was used to determine the contribution of the IFE to the quenching efficiency. The contribution of the IFE was determined to be responsible for ~56% of the observed quenching efficiency in presence of 90.9 μM of PA (Figure 3-34). Thus, demonstrating that the inner filter effect is not the only mechanism responsible for the

quenching of the emission intensity of **131** and that the remaining 24% of fluorescence quenching involves other mechanisms.

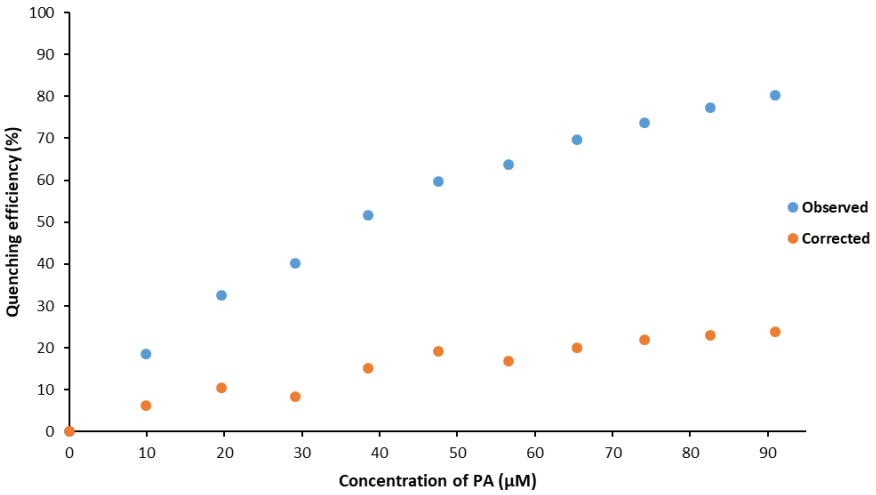

Figure 3-34 Observed and corrected quenching efficiencies of PA at various concentrations on **131** in water.

As described by Lakowicz and Albrecht,[219] the presence of an upward curvature indicates that both static and dynamic quenching are taking place during the sensing. To demonstrate the presence of dynamic quenching the fluorescence was recorded as a function of temperature in the presence of PA at 47.6 µM (Figure 3-35A). At 25 °C the quenching efficiency increases from 57% to 61% at 55 °C which is a lesser increase in quenching efficiency than the previously observed for **130**. In the case of **131**, the fine suspension formed in water is composed of a robust covalently bound polymer and therefore, an increase in the quenching efficiency would mainly be attributed to an increase in the rate of collision between **131** and PA. While **130** was forming supramolecular assemblies that could be disrupted by external stimuli. This result further confirmed that the observed fluorescence quenching follows the dynamic quenching mechanism. To investigate the role of static quenching on the quenching mechanism, the time-resolved fluorescence decay at different concentrations of PA were recorded.

The time-resolved decay of **131** suspended in H_2O was fitted to a bi-exponential decay, the calculated lifetimes, which were obtained from the average of triplicates measurements, are 3.97 ns for τ_1 and 10.61 ns for τ_2. Upon addition of PA to the suspension, the lifetimes of the polymer decreased to 3.16 ns and 9.98 ns for τ_1 and τ_2, respectively, at a concentration of 90.9 µM of PA (Figure 3-35B). This demonstrates that PA is forming a complex with the excited state of **131** and that therefore static quenching is occurring.[185]

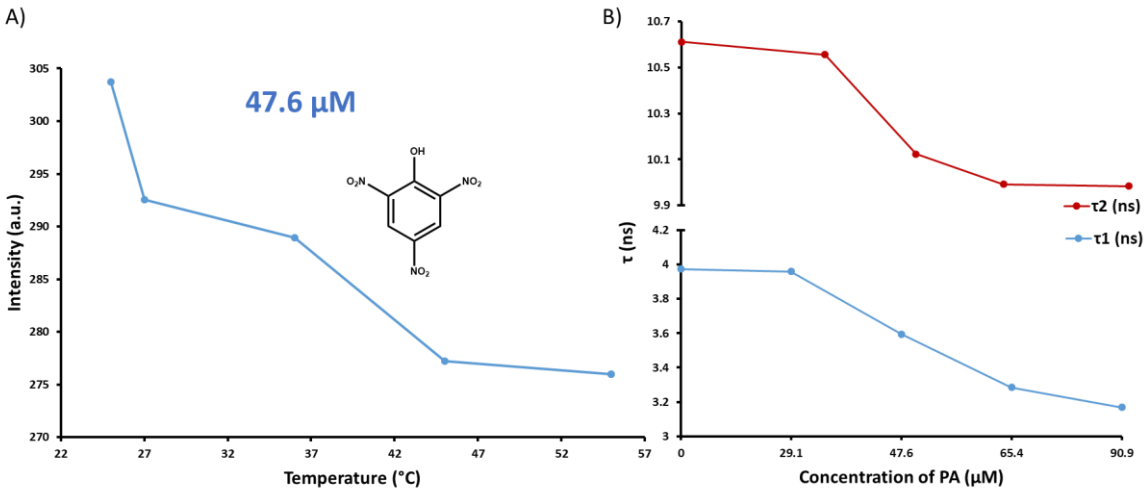

Figure 3-35 A) The temperature-dependent emission profile of **131** in the presence of PA (47.6 µM). B) The fluorescence decay profiles of **131** upon addition of PA (0-90.9 µM).

3.5.2.3 Effect of pH on the sensing of PA

To fully investigate the ability of **131** to detect picric acid in water and understand its limitations, the effect of pH on the detection mechanism was investigated. The initial pH of **131** in H_2O was 6.2. It can be observed in Figure 3-36 that in basic conditions (pH = 11.7; grey dots) the quenching efficiency is drastically decreased ($K_{SV} = 1.86 \pm 0.06 \times 10^4\ M^{-1}$) while in acidic conditions (pH= 2.3; blue dots) the quenching efficiency is only slightly decreased ($K_{SV} = 2.35 \pm 0.05 \times 10^4\ M^{-1}$). These results substantiate the idea that the quenching mechanism between PA and **131** is partly due to intermolecular hydrogen bonding interactions.

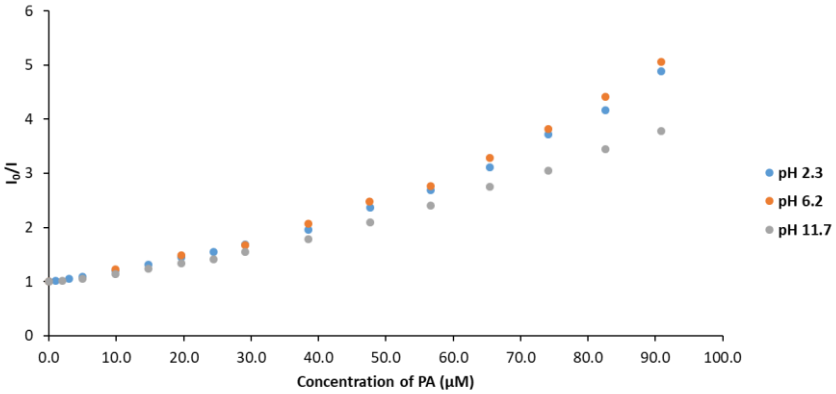

Figure 3-36 Stern-Volmer plot of the fluorescence quenching of **131** in H_2O in the presence of PA (0-90.9 µM) at various pH.

To corroborate these arguments, density functional theory (DFT) analysis was again performed by Dr. Deivasigamani Umadevi. One monomer unit was considered as a model to represent the polymer and the geometry optimisations were performed using the M06-2X12 hybrid functional of Truhlar and Zhao with 6-31+G(d) basis set. All the calculations

were utilized in the Gaussian 09 package.[209] The results of the calculation are shown in Figure 3-37 and highlight the optimised geometry and the frontier orbitals of PA, the picrate anion and the **131** model system. It demonstrates that the highest occupied molecular orbital (HOMO) of **131** is mainly located on the Tröger's base moiety while the lowest unoccupied molecular orbital (LUMO) density is more localised in the pyridinium moiety. The calculated energy of the HOMO and the LUMO of the **131** model systems are −10.548 eV and −5.704 eV, respectively, while the HOMO and LUMO of the picrate anion are −4.490 eV and 1.351 eV, respectively. This suggests that charge transfer can occur from the HOMO of the picrate anion to the LUMO of **131** and therefore supports the proposed static quenching mechanism at low concentration of PA.

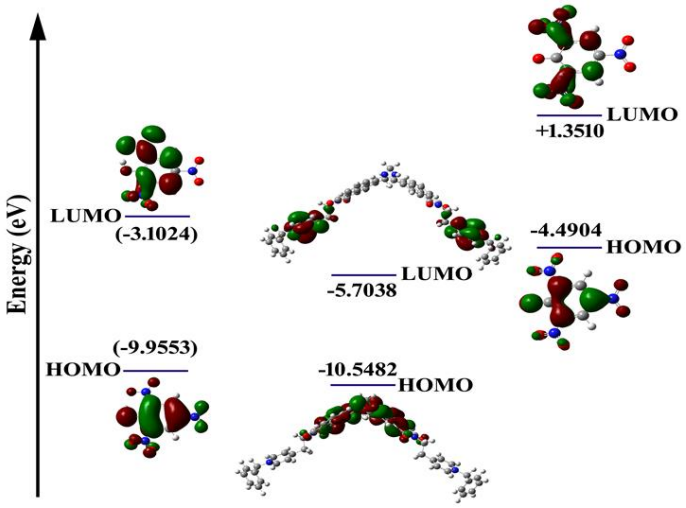

Figure 3-37 Pictorial representation of the calculated HOMO and LUMO of picric acid, **131** and the picrate ion.

3.5.2.4 Sensitivity and competitivity towards NACs

A sensitivity experiment was carried out by using a diluted solution of PA and proceeding to a titration (Figure 3-38). The limit of detection for PA in H_2O was calculated using the following equation:

$$Limit\ of\ detection\ (LOD) = \frac{3\sigma}{K} = 5.41\ *\ 10^{-8}\ \text{mol.}\,\text{L}^{-1} = 12.4\ ppb$$

Where σ (2.74) is the standard deviation of the initial emission intensity of **131** in H_2O before the addition of PA and *K* is the slope of the linear curve. The results showed that the **131** response could be affected by a concentration of PA as low as 12 ppb which is lower than the allowed limit of NACs in drinking water established by the US EPA.[185]

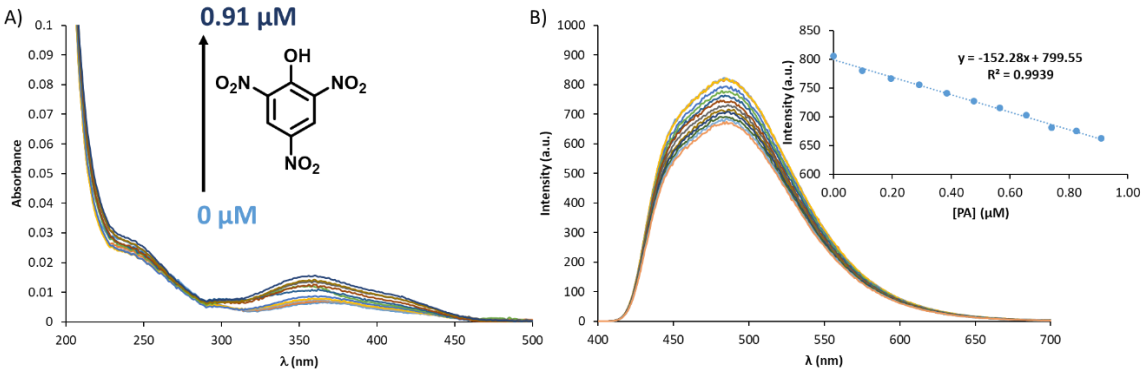

Figure 3-38 Sensitivity experiment of **131** in H_2O in the presence of PA (0-0.91 µM). Insert: Intensity plot in function of the concentration of PA.

The response time towards PA was also evaluated at different PA concentrations and showed that upon addition of PA, the emission changes had equilibrated within a minute (Figure 3-39) and the response time is independent of the concentration of PA in solution which makes **131** an ideal candidate for on-site detection of PA.

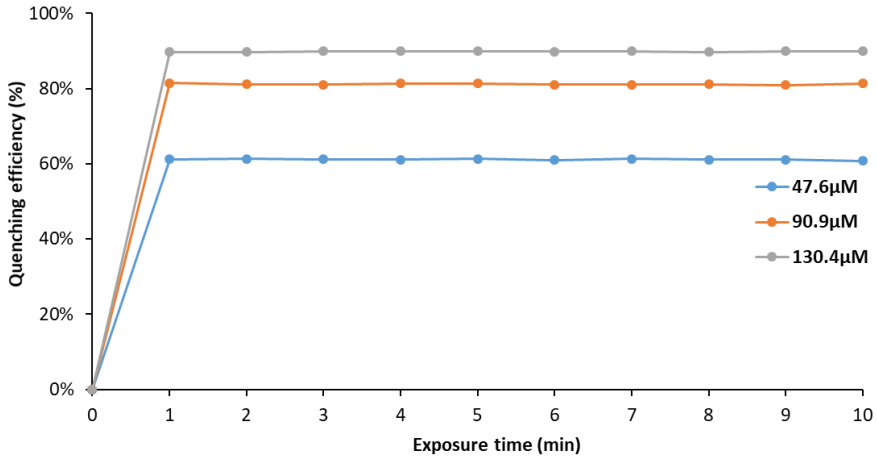

Figure 3-39 Time response of **131** upon contact with various concentration of PA in H_2O.

The selectivity of **131** was challenged by carrying out a competitivity experiment with structurally related nitroaromatics such as 2,4-DNP, 2-NP, 3-NP, 4-NP, TNT, 2,4-DNT, 2,6-DNT, 2-NT, 3-NT, 4-NT and NB. First, the "competitive" nitroaromatics (90.9 µM) was added to the suspension of **131** (green bar, Figure 3-40), then the same concentration of PA was added (blue bar, Figure 3-40), the quenching efficiency was calculated and reported in Figure 3-40. From this experiment, it is evident that phenolic nitroaromatics displayed the highest quenching efficiency. As in the case of **130**, this can be explained by the presence of the phenol group being able to form stronger intermolecular interactions with the Lewis basic nitrogen of the Tröger's base motif.[185] Gratifyingly, **131** exhibited high selectivity toward PA, being able to discriminate between this analyte and other phenolic nitroaromatics with

the closest being 2,4-DNP and 4-NP displaying a quenching efficiency of 62% and 38%, respectively.

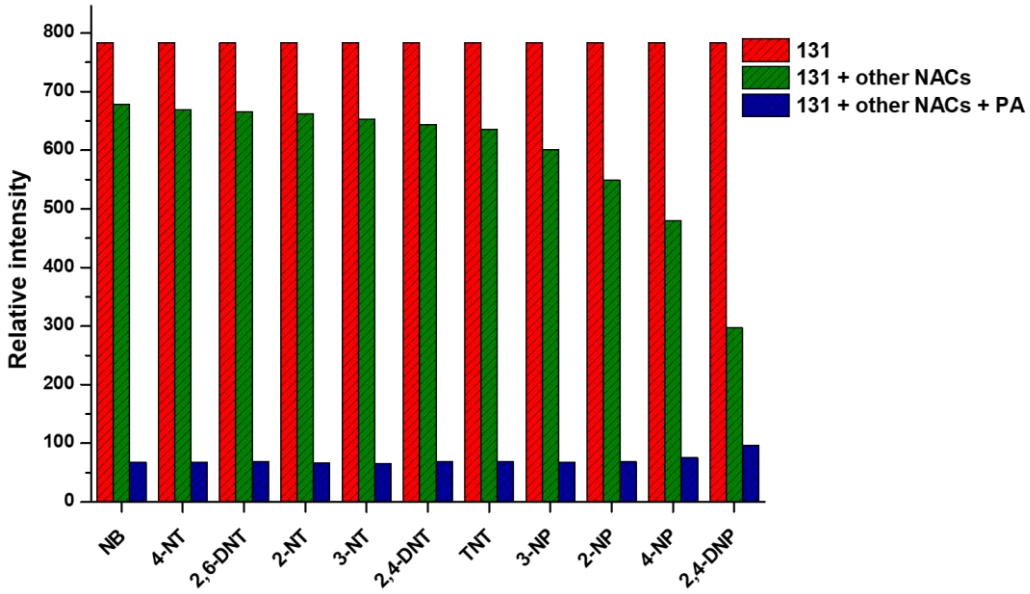

Figure 3-40 Competitive selective affinity of **131** towards different nitroaromatics in the presence of PA (90.9 μM) in H_2O.

Furthermore, analysis of the changes in the fluorescence displayed by **131** using the Stern-Volmer equation showed linear regression, from which K_{sv} was determined from (Table 3-2). As demonstrated in Figure 3-31, the Stern-Volmer plot of PA is characterised by a strong upward curvature in the higher concentration range and gives a linear response in the range 0-65.4 μM and therefore, this concentration range was used to calculate the Stern-Volmer constant. The results obtained confirmed the trend observed in Figure 3-40 with PA and 2,4-DNP displaying the highest Stern-Volmer constants followed by all the other phenolic nitroaromatics while the smallest Stern-Volmer constants being displayed by the non-phenolic nitroaromatics. All the Stern-Volmer constants were obtained from the average of at least duplicated titrations and the error indicated on the Stern-Volmer constants corresponds to the standard deviation of the fitting for a linear trendline.

Table 3-2 The Stern-Volmer constants K_{SV} of various nitroaromatics for the fluorescence quenching of **131**.

Analytes	**K_{SV} (M^{-1}) x 10^3**
PA	32.7 ± 1.3
2,4-DNP	17.4 ± 0.2
4-NP	6.80 ± 0.07
2-NP	4.78 ± 0.05
3-NP	3.29 ± 0.09
TNT	2.74 ± 0.07
2,4-DNT	2.53 ± 0.08
3-NT	2.30 ± 0.05
2-NT	2.09 ± 0.06
2,6-DNT	2.09 ± 0.04
4-NT	2.04 ± 0.05
NB	1.86 ± 0.05

3.5.2.5 Selectivity and competitivity towards ions

Following these encouraging results, the robustness of the detector was analysed *via* the sensing of PA in the presence of other competing ions. This was carried out by adding various ions to the aqueous suspension of **131** (red bar, Figure 3-41) to reach a concentration of 90.9 µM and studying the effect on the fluorescence (green bar, Figure 3-41). Finally, PA (90.9 µM) was added (blue bar, Figure 3-41) and the fluorescence of the solution was evaluated. As seen in Figure 3-41, only a minor change in the fluorescence could be observed upon addition of different ions such as transitions metals, with the highest response displayed by silver ions with a quenching efficiency of ≈ 23%. Gratifyingly, the quenching efficiency of PA in the presence of various ions is ≈ 77% compared to ≈ 81% in ideal conditions, proving the robustness of **131** as a sensor for PA in aqueous media.

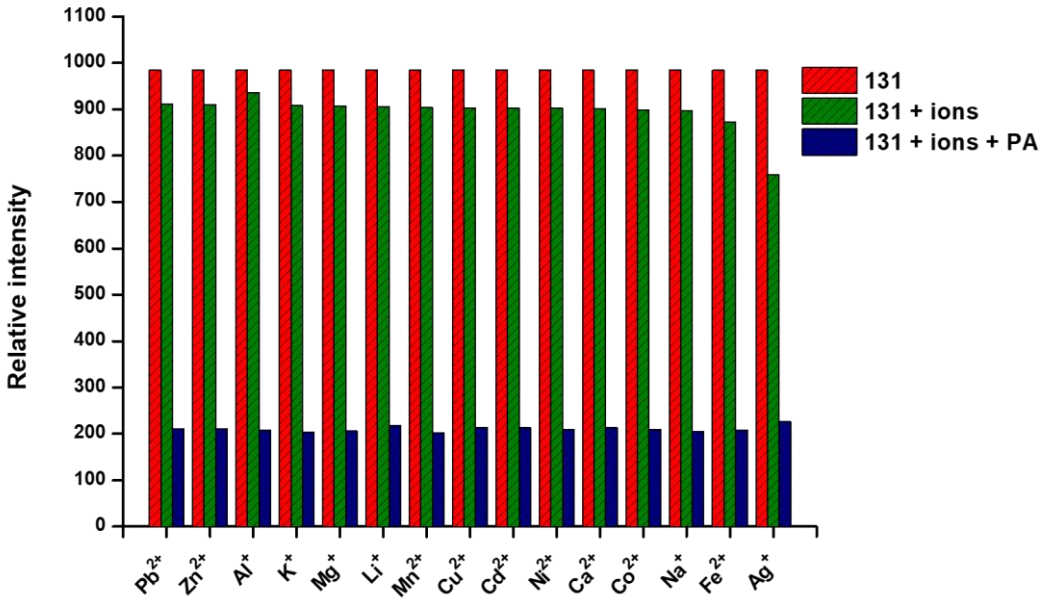

Figure 3-41 Competitive selective affinity of **131** towards different ions in the presence of PA (90.9 μM) in H_2O.

3.5.2.6 Conclusion

To conclude, the study of **131** has revealed that by a combination of inner filter effect, dynamic and static quenching, the covalent polymer can selectively discriminate PA in competitive media over an important range of pH with good sensitivity. The recyclability of the aqueous suspension of **131** was examined, however it was not possible to collect the suspension after addition of PA by centrifugation, wash it with ethanol and water to separate it from the analyte to reuse it, as has been displayed previously with a COF developed by the Gunnlaugsson research group.[202]

3.5.3 Comparison of the sensing performances of the AIE system and the COP

Two different systems were developed based on the same common motif, the 4-amino-1,8-naphthalimide Tröger's base. However, due to the great differences of the functionalisation at the imide positions, the two systems have shown different behaviours in solution. While the first system using **130** is used in a solvent mixture (DMSO: H_2O), **131** is used directly in water. The use of only one solvent has a certain advantage, but the need to leave the solution to settle for 3 days proves to be an inconvenience.

Evaluation of the quenching of the emission of both systems by the addition of PA demonstrated that a concentration of 74.1 μM results in 83% quenching of the emission of **130** while a concentration of 90.9 μM of PA was necessary to quench 80% of the emission of **131**. This result was further confirmed by estimation of the Stern-Volmer constants of 40.6×10^3 M^{-1} and 32.7×10^3 M^{-1} for **130** and **131**, respectively. Competitive selective

affinity experiments revealed that both systems were well able to discriminatively detect PA in the presence of various structurally related NACs; however, PA displayed a slightly higher quenching of **131** emission in the presence of other NACS than for **130** when comparing Figure 3-23 and Figure 3-40. The sensitivity experiments revealed a limit of detection of PA of 20 ppb for **130** against 12 ppb for **131**, demonstrating that while **130** will show a higher change in its luminescence in the presence of PA, the emission of **131** will be able to detect a lower quantity of PA in solution. Both systems displayed excellent time responses with the emission being stabilised within a minute in the presence of PA. Competitive selective affinity experiments in the presence of various ions, including *d*-metals, demonstrated that **131** ability to detect PA was only slightly affected by the presence of competing ions. While the emission of **130** was strongly quenched in the presence of various *d*-metal, greatly hindering its ability to detect PA in solution. Finally, the evaluation of the pH on the detection of PA revealed that Stern-Volmer constants of both systems are drastically reduced in basic pH due to the hindering of the hydrogen bonding interactions between the detectors and the analyte. However, the Stern-Volmer constant for the detection of PA by **130** is greatly improved in acidic conditions while the Stern-Volmer constant of **131** is slightly decreased, thus demonstrating that **130** has a better ability to detect PA in a wide range of pH.

Overall both systems possess advantages and inconveniences, while none of them has a significant advantage over the other it appears clearly that the two systems can complement each other, as it has been demonstrated that the strengths of one counter the weaknesses of the other. Since a previous example of TBNap based coordination polymer has displayed great potential for on-site sensing of PA and has shown the possibility to be recycled and reused several times for the sensing of PA,[185] it was decided to explore the use of **130** in the formation of coordination polymer and to explore their properties. These studies are described in the following paragraph.

3.6 Synthesis, Characterisation and Studies of 4-Amino-1,8-Naphthalamide-Tröger's Base Complexes

3.6.1 Synthesis and Characterisation of 4-amino-1,8-naphthalimide-Tröger's Base Complexes

Having studied the properties of the ligand **130** in solution and its potential use as an on-site detector of NACS, it was decided to explore its use in the formation of coordination polymers and to explore their properties. The coordination of **130** with various *d*-metals ($Zn(BF_4)_2$, $Fe(BF_4)_2$ and $Co(BF_4)_2$) was carried out by dissolving **130** in DMF followed by the addition of 1 equivalent of the desired metal in a sealed vial with a PTFE-lined cap and the mixture was heated in a dry block heater at 80 °C for 48 h. The removal of the solvent under reduced pressure, followed by the sonication and filtration of the solid obtained yielded the desired polymers (shown in Scheme 3-3) in high yields: 97% for [**130**($Zn(BF_4)_2$)], 92% for [**130**($Fe(BF_4)_2$)] and 96% for [**130**($Co(BF_4)_2$)].

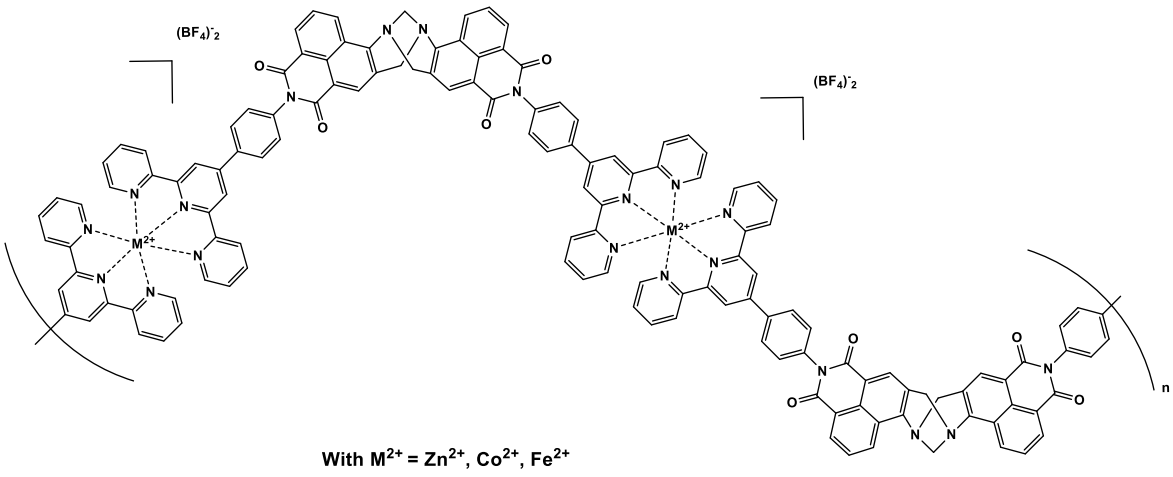

Scheme 3-3 Structure of the polymer [**130**($M(BF_4)_2$)] with M= Zn^{2+}, Co^{2+} or Fe^{2+}.

While none of the crystallisations attempted yielded crystals of suitable quality for X-ray diffraction, the full characterisation of the polymers was carried out by ^1H and CP-MAS ^{13}C-NMR, FT-IR and elemental analysis and can be seen in the experimental Chapter and appendixes. The ^1H NMR in DMSO-d_6 confirmed the successful coordination of the metal ions by the terpyridine with the shift and the broadening of the signals as seen in Figure 3-42. Importantly, the signal demonstrating that the Tröger's base motif is present in the

polymer are visible in the region of 6.0-4.7 ppm, corresponding to the methylene protons of the diazocine ring.[185,202]

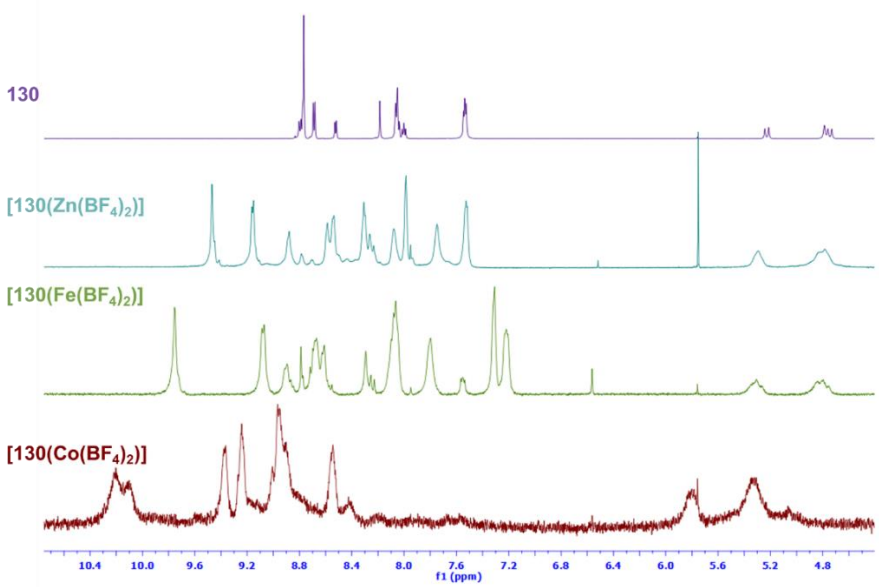

Figure 3-42 ^{1}H NMR (DMSO-d_6, 600 MHz) of the highlighted aromatic region of **130**, [**130**(Zn$(BF_4)_2$)], [**130**(Fe$(BF_4)_2$)] and [**130**(Co$(BF_4)_2$)] (400 MHz).

Since only the analysis of [**130**(Zn$(BF_4)_2$)] by ^{13}C{^{1}H} NMR gave a satisfying result, this spectrum was compared to the CP-MAS ^{13}C-NMR spectra that were recorded by Dr. Manuel Ruether and are shown in Figure 3-43. The solid-state CP-MAS ^{13}C-NMR further confirmed the presence of the TBNap unit, with a broad band ranging from 160 to 110 ppm covering the carbonyl carbons resonance and the resonance for most of the peaks observed in the ^{13}C{^{1}H} NMR of [**130**(Zn$(BF_4)_2$)]. The resonances observed between 55 and 40 ppm are assigned to the carbons of the methylene group of the diazocine ring.

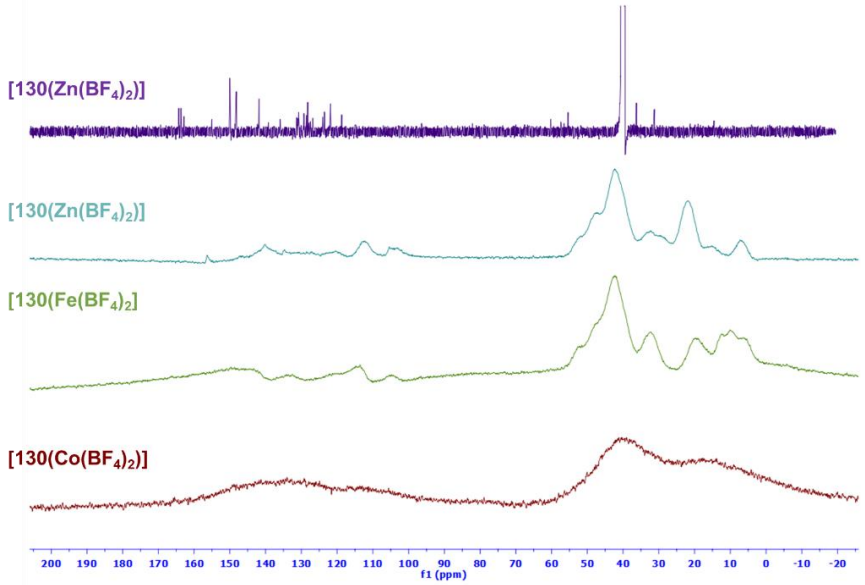

Figure 3-43 ^{13}C{^{1}H} NMR (DMSO-d_6, 151 MHz) of [**130**(Zn$(BF_4)_2$)] (purple) and solid-state CP-MAS ^{13}C-NMR (201.2 MHz) spectrum of [**130**(Zn$(BF_4)_2$)], [**130**(Fe$(BF_4)_2$)] and [**130**(Co$(BF_4)_2$)].

The FT-IR analysis of the three polymers revealed, as shown in Figure 3-44, that their IR spectra are very similar to their precursor **130** excepted for the presence of a strong broad band at 1029 cm^{-1}, which was also observed in the case of [**107** ($Zn(BF_4)_2$)] (see Chapter 2) and is due to the presence of the BF_4^- counter ion.[220] It possible to observe for the three polymers the presence of two strong bands in the region of 1700-1600 cm^{-1} corresponding to the C=O stretching on the naphthalimide moieties and a strong signal at 1240 cm^{-1} due to C−N stretching of the Tröger's base unit.

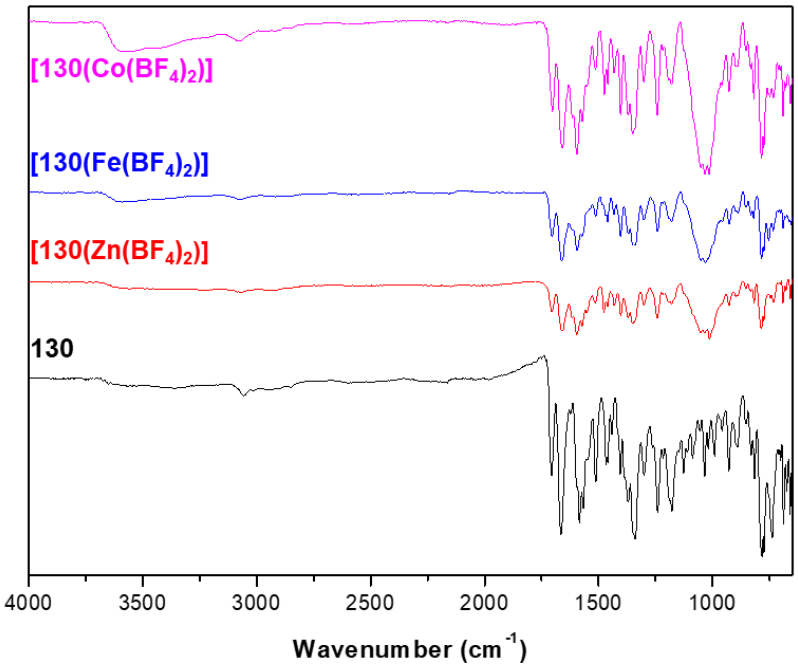

Figure 3-44 FTIR spectrum (4000–650 cm^{-1}) of **130**, [**130**($Zn(BF_4)_2$)], [**130**($Fe(BF_4)_2$)] and [**130**($Co(BF_4)_2$)].

TGA analysis of the ligand **130** and [**130**($Zn(BF_4)_2$)] were carried out; however, due to time constraints, [**130**($Fe(BF_4)_2$)] and [**130**($Co(BF_4)_2$)] could not be analysed. The thermogram of **130** shown in Figure 3-45A, demonstrated a weight loss of 6% until 400 °C, which can be attributed to the evaporation of solvent trapped in the solid, while the sample was found to be stable up to 457 °C demonstrating good thermal stability. Using similar conditions, the TGA of [**130**($Zn(BF_4)_2$)] revealed a continuous and steady weight loss throughout the entire temperature range as shown in Figure 3-45B, while the decrease of the temperature rate from 10 °C/min to 5 °C/min did not improve the results. The blue curve in Figure 3-45B, which corresponds to the TGA of [**130**($Zn(BF_4)_2$)] carried out with a scan rate of 10 °C/min, with a temperature hold of 30 minutes at 80 °C, demonstrated the presence of a large quantity of solvent within the amorphous sample with a weight loss of *ca*. 10% during the 30 minute temperature hold. Despite the temperature hold a thermogram of satisfying quality of [**130**($Zn(BF_4)_2$)] to estimate its thermal stability could not be obtained. It would

require keeping the sample under high vacuum heated in an oil bath for a few hours to try to remove as much solvent as possible before carrying out the thermogravimetric analysis; however, due to time constraints, it was not possible to carry out this experiment.

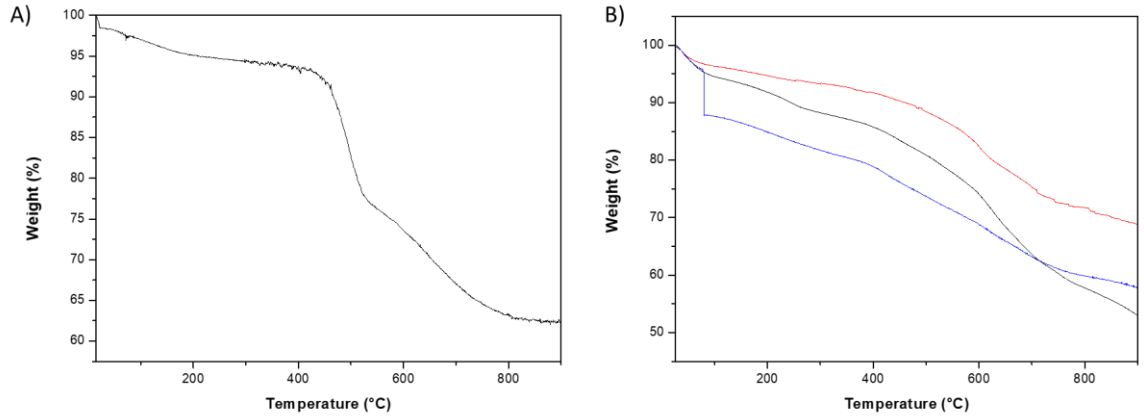

Figure 3-45 Thermogravimetric analysis of A) **130** and B) [**130**($Zn(BF_4)_2$)] at an increase of temperature of 10 °C/min (black), 5 °C/min (red) and 10 °C/min with a temperature hold of 30 minutes at 80 °C (blue).

Having fully characterised the different polymers, the morphology along with their spectroscopic and electrochemical properties were studied and are described in the following paragraphs.

3.6.2 Morphological study

SEM was used to probe the morphology of **130** and its polymers. The samples were prepared by drop-casting the DMF solutions (0.5 mg/mL) of **130** or the corresponding polymers [**130**($Zn(BF_4)_2$)], [**130**($Fe(BF_4)_2$)] and [**130**($Co(BF_4)_2$)] on silica wafers, before drying the sample for several days in ambient conditions and then under high-vacuum for several hours, then coated with Pd/Au before the imaging. The SEM was carried out using the facilities of the Advanced Microscopy Laboratory (AML) in Trinity College Dublin. As seen in Figure 3-46, two distinct morphologies could be observed within the same sample. The first morphology was comprised of spherical aggregates in a size range of 0.44-2.25 μm, with the majority of the spheres falling in the higher part of this range. The formation of the spheres was successfully reproduced and interestingly was the predominant form in the sample when increasing the concentration of the DMF solutions to 1 mg/mL. The second morphology observed, which was predominant in the samples prepared with the DMF solutions of 0.5 mg/mL of **130**, corresponds to the bowl-like shape observed in Figure 3-46C and D and had a size range of 2.2-4.5 μm.

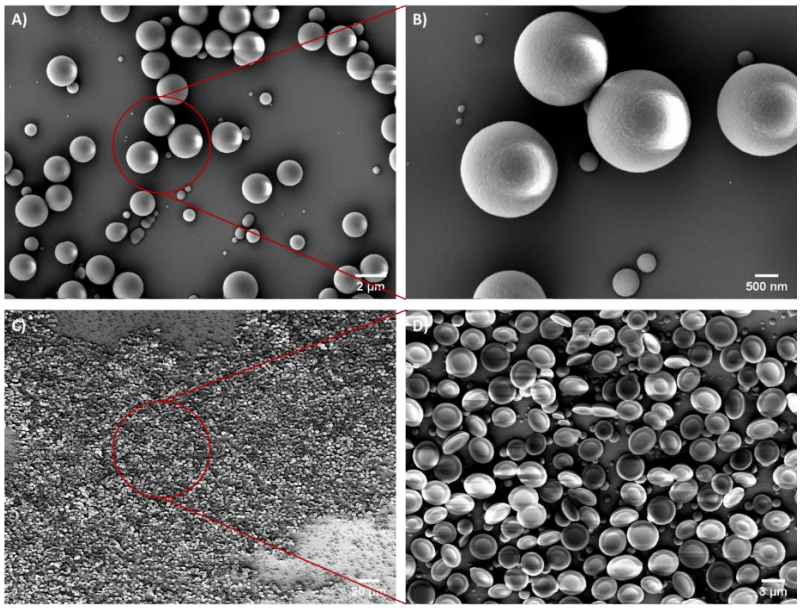

Figure 3-46 Scanning electron microscopy images of **130** of A) (scale bar 2 µm) and B) (scale bar 500 nm) spherical aggregates, C) (scale bar 20 µm) and D) (scale bar 3 µm) bowl-like aggregates obtained from a DMF solution (c = 0.5 mg/mL).

The SEM of [**130**($Zn(BF_4)_2$)] revealed that the presence of the Zn(II) ions induced a drastic change in the morphology with the formation of a very porous network of filaments of 100-600 nm with large cavities as shown in Figure 3-47. This morphology was demonstrated to be fully reproducible at higher concentrations by using a DMF solution of [**130**($Zn(BF_4)_2$)] of 1 mg/mL. The presence of the large cavity could indicate the ability of the material to store solvent or gas, which is in good agreement with the large quantity of solvent observed during the thermogravimetric analysis.

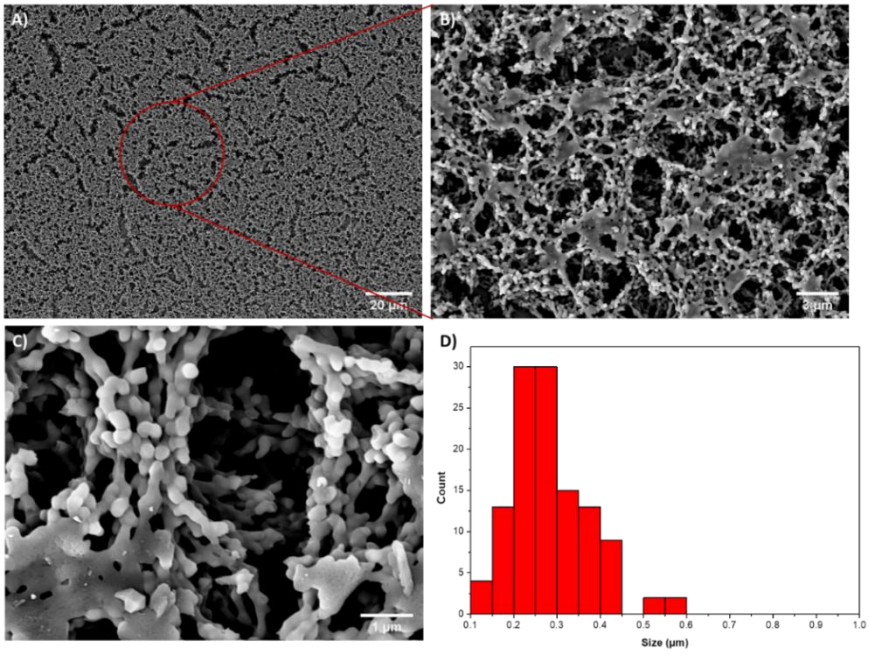

Figure 3-47 Scanning electron microscopy images of [**130**($Zn(BF_4)_2$)] of A) scale bar 20 µm, B) scale bar 3 µm, C) 1 µm of the porous structure and D) histogram of the size of the filament measured.

The SEM of [**130**($Fe(BF_4)_2$)] and of [**130**($Co(BF_4)_2$)], which are shown in Figure 3-48, revealed that unlike the Zn(II) polymer, the Fe(II) and Co(II) polymers only form amorphous aggregates when prepared in similar conditions using either 1 mg/mL or 0.5 mg/mL. Thus demonstrating the influence of the metal ion used to form the polymer on the overall structure of the material obtained.

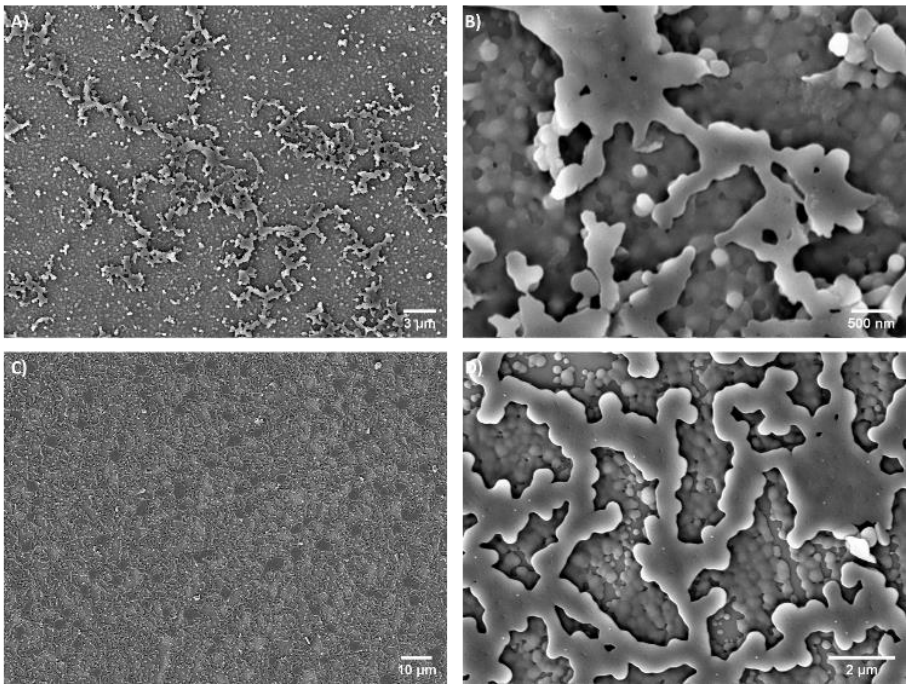

Figure 3-48 Scanning electron microscopy images of [**130**($Fe(BF_4)_2$)] A) scale bar 3 µm and B) 500 nm and of [**130**($Co(BF_4)_2$)] C) scale bar 10 µm and D) 2 µm.

Having characterised the morphology of the different polymers and compared them to the ligand, the spectroscopic properties of the polymers were studied and are described in the following paragraph.

3.6.3 Spectroscopic study

The luminescence behaviour of **130** in solution, which was already studied in several solvents and was previously described, was also studied in DMF to serve as a reference for the studies of the polymers. As expected, the presence of the ICT band at 388 nm can be observed in the absorption spectra in Figure 3-49A, with excitation into this band leading to a broad emission band centred at 538 nm. The dilution study on **130** in DMF revealed a slightly parabolic relationship for the emission intensity in correlation to the concentration, presumably due to a combination of inner filter effect and aggregation. Finally, the study of the excitation spectra in the function of the concentration in DMF revealed that the band

corresponding to the ICT is slightly shifted in the excitation spectra and this is potentially due to the formation of aggregates in DMF.

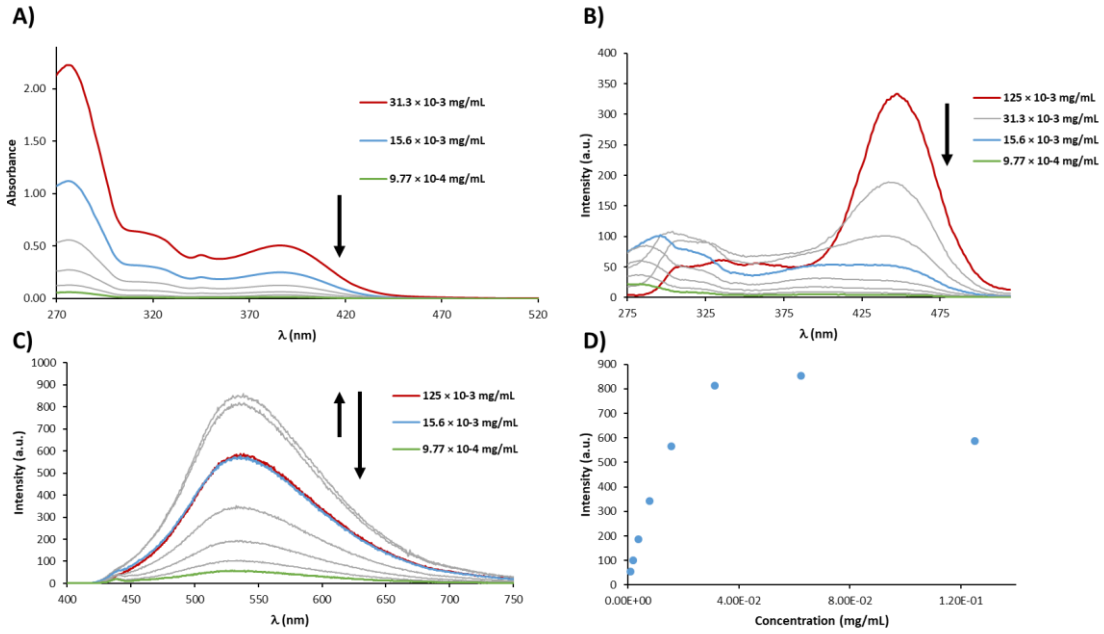

Figure 3-49 Changes in A) the absorption, B) the excitation (λ_{em} = 540 nm), C) the emission (λ_{ex} = 388 nm) spectra and D) the corresponding intensity profile at λ_{max}= 538 nm of **130** in DMF upon dilution.

The dilution study of [**130**($Zn(BF_4)_2$)] in DMF is shown in Figure 3-50, and revealed in the absorption spectra the presence of more pronounced bands at 325 and 420 nm which is due to the coordination of the Zn(II) ions while the ICT band remains unaffected. The broad emission band centred at 540 nm for the ligand appears to be shifted to 520 nm but is not shifted upon dilution. The excitation spectrum displays similar bands to the absorption; however, at higher concentration (c = 125 × 10^{-3} mg/mL) the band corresponding to the ICT band is at 413 nm compared to 388 nm in the absorption, although upon dilution shifts to 388 nm, thus demonstrating the presence of aggregates at high concentrations.

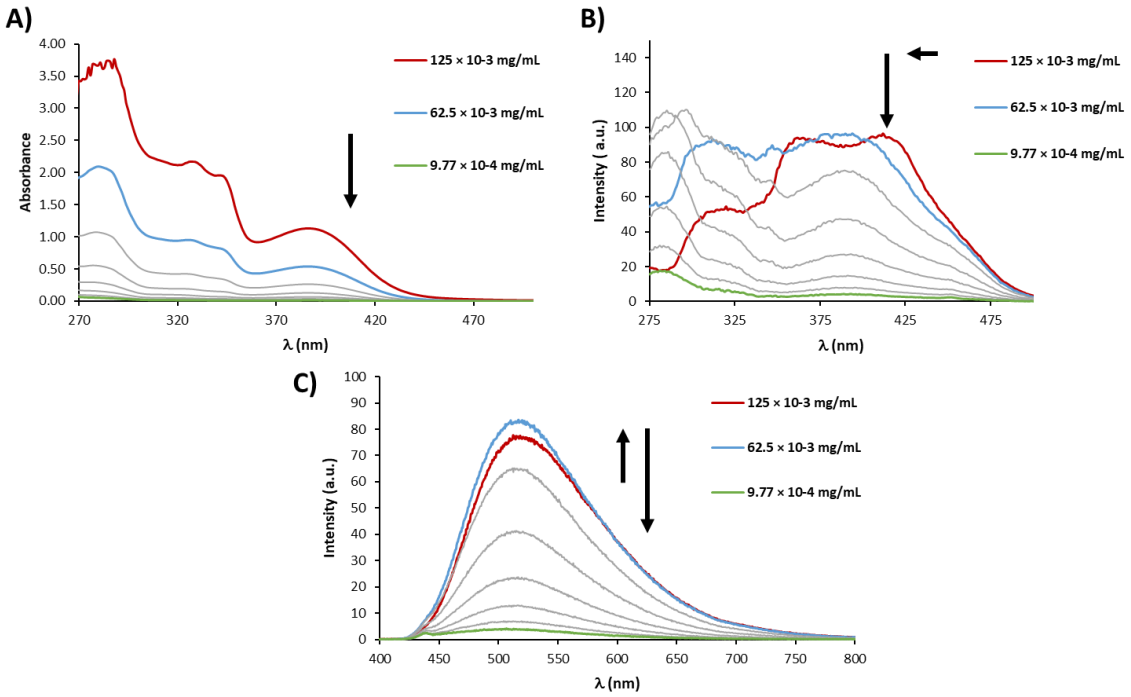

Figure 3-50 Changes in A) the absorption, B) the excitation (λ_{em} = 520 nm) and C) the emission (λ_{ex} = 388 nm) spectra of [**130**($Zn(BF_4)_2$)] in DMF upon dilution.

The dilution study of [**130**($Fe(BF_4)_2$)] in DMF shown in Figure 3-51 revealed the presence of a sharp band at 325 nm which is due to the coordination of Fe(II) ions. The ICT band is slightly shifted to 378 nm and there is a sharp band at 574 nm which corresponds to the d_π(Fe(II)) → π*(terpy) metal-to-ligand charge-transfer (MLCT) transition.[178] The emission obtained from the excitation at λ_{ex} = 380 nm led to a very weak emission which is shown in the appendix. The excitation spectra obtained, despite being very low in intensity, nevertheless displayed similar bands to the absorption spectra except for the band corresponding to the ICT band which is centred at 444 nm and shifted progressively to 400 nm upon the dilution. This could indicate the potential destruction of aggregates formed by [**130**($Fe(BF_4)_2$)] upon dilution.

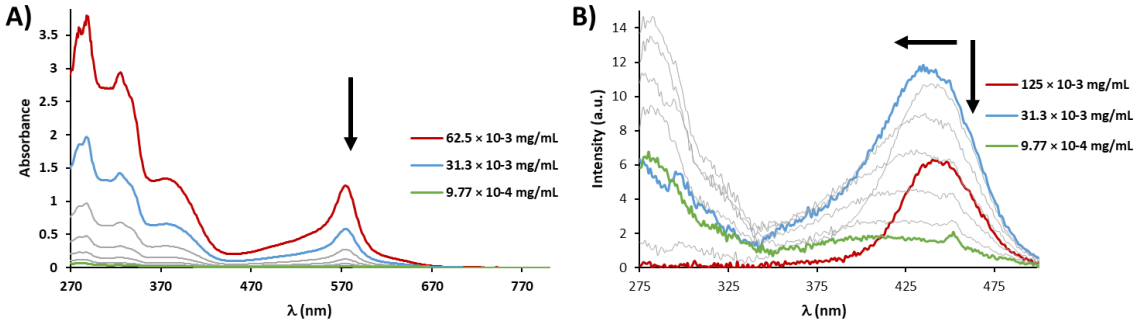

Figure 3-51 Changes in A) the absorption and B) the excitation (λ_{em} = 520 nm) spectra of [**130**($Fe(BF_4)_2$)] in DMF upon dilution.

The dilution study of [**130**($Co(BF_4)_2$)] in DMF shown in Figure 3-52 revealed very similar absorption, excitation and emission spectra to the ligand. Indeed, excitation at 388 nm led to the formation of a broad emission band centred at 540 nm. The excitation spectra displayed similar bands to the absorption spectra, again except for the band attributed to the ICT which appeared to be centred at 446 nm at higher concentration and upon dilution displayed a hypsochromic shift to 390 nm at the lower concentration.

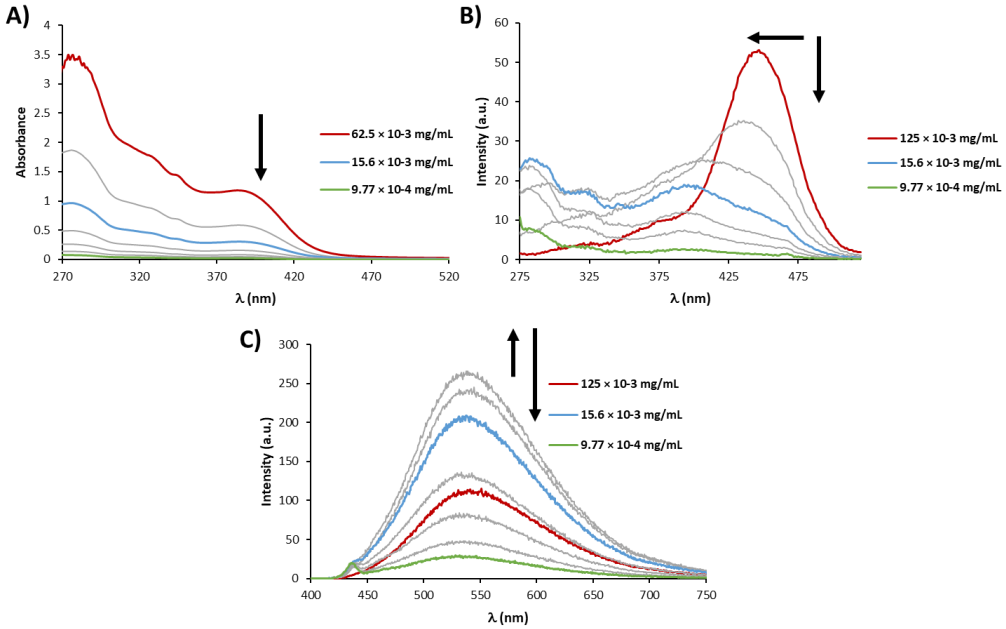

Figure 3-52 Changes in A) the absorption, B) the excitation (λ_{em} = 540 nm) and C) the emission (λ_{ex} = 388 nm) spectra of [**130**($Co(BF_4)_2$)] in DMF upon dilution.

Having characterised the spectroscopic properties of **130** and its corresponding polymers in DMF, their electrochemical properties were studied and are described in the following paragraph.

3.6.4 Cyclic voltammetry

Cyclic voltammetry studies of **130** and the corresponding polymers [**130**($Zn(BF_4)_2$)], [**130**($Fe(BF_4)_2$)] and [**130**($Co(BF_4)_2$)] were carried out at an approximate concentration of 1 mg/mL in dry DMF. The ferrocene/ferrocenium redox couple was used as the internal standard, and potentials were referenced against these. A glassy carbon electrode was used as the working electrode while platinum wires were used for both the reference electrode and the counter electrode. A comparison of the cyclic voltammogram of **130** and the corresponding polymers [**130**($Zn(BF_4)_2$)], [**130**($Fe(BF_4)_2$)] and [**130**($Co(BF_4)_2$)] is shown in Figure 3-53, and a detailed description of each voltammogram is given in the following paragraphs.

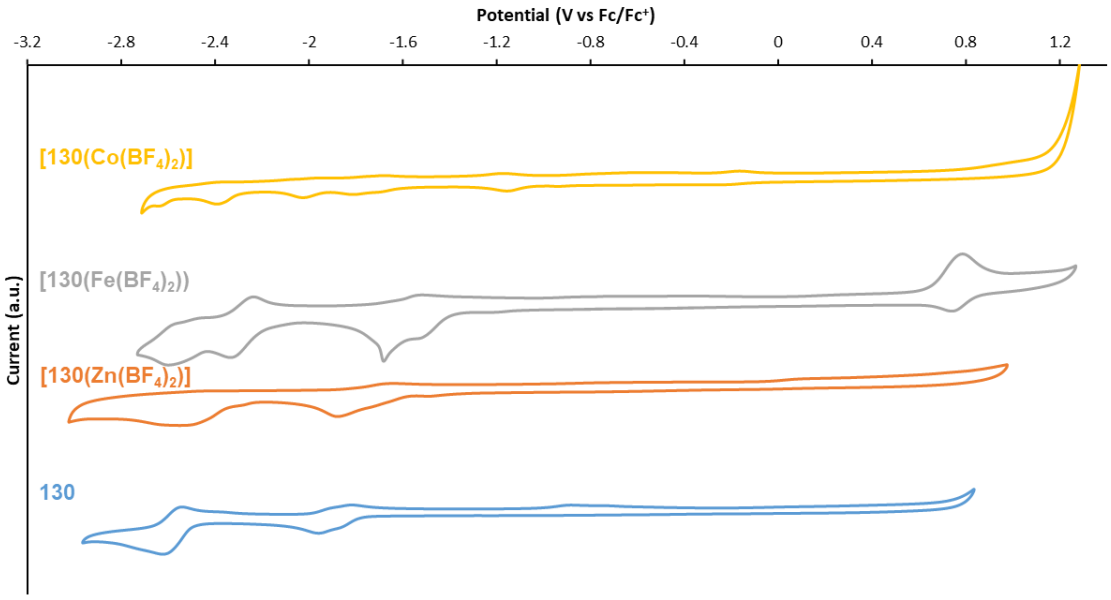

Figure 3-53 Voltammograms of **130** and the corresponding polymers [**130**($Zn(BF_4)_2$)], [**130**($Fe(BF_4)_2$)] and [**130**($Co(BF_4)_2$)] under N_2 at 100 mV/s, scanned in the negative direction in 0.1 M [NBu_4][PF_6] DMF solution. The Fc/Fc^+ couple was used as an internal standard and the voltammogram is referenced against this couple.

As seen in Figure 3-54, the cyclic voltammogram of **130** displayed two quasi-reversible reductions at onset potentials of −1.76 and −2.46 V, respectively, and the two corresponding oxidations can be seen on the reverse potential sweep at onset potentials of −2.70 and −1.98 V. A third oxidation can be observed at an onset potential of −1.05 V but when the scanned potential range is reduced the oxidation disappeared indicating that it is an electrochemical side-product.

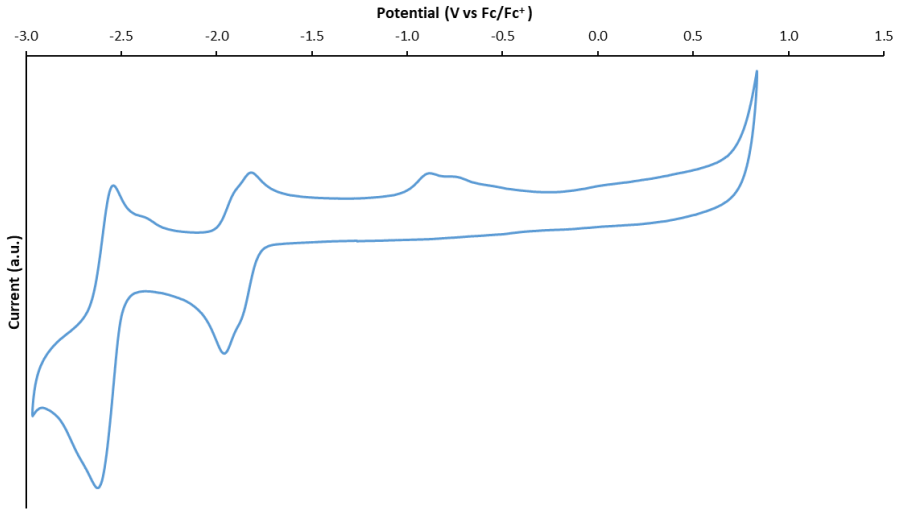

Figure 3-54 Voltammogram of **130** under N_2 at 100 mV/s, scanned in the negative direction in 0.1 M [NBu_4][PF_6] DMF solution. The Fc/Fc^+ couple was used as an internal standard and the voltammogram is referenced against this couple.

The cyclic voltammogram of [**130** ($Zn(BF_4)_2$)], shown in Figure 3-55, displayed two reductions, the first one being quasi-reversible with an onset potential of –1.57 V, on the reverse potential sweep an oxidation at an onset potential of −1.87 V can be observed. However, when the potential sweep is decreased to –2.40-0.00 V the oxidation is not visible, which means that it is due to the formation of an electrochemical side product. The second reduction being an irreversible reduction at an onset potential of −2.33 V, the reduction wave being particularly wide would suggest that several reductions are occurring at the same potential. These reductions could be attributed to both ligand-based and metal-based processes.

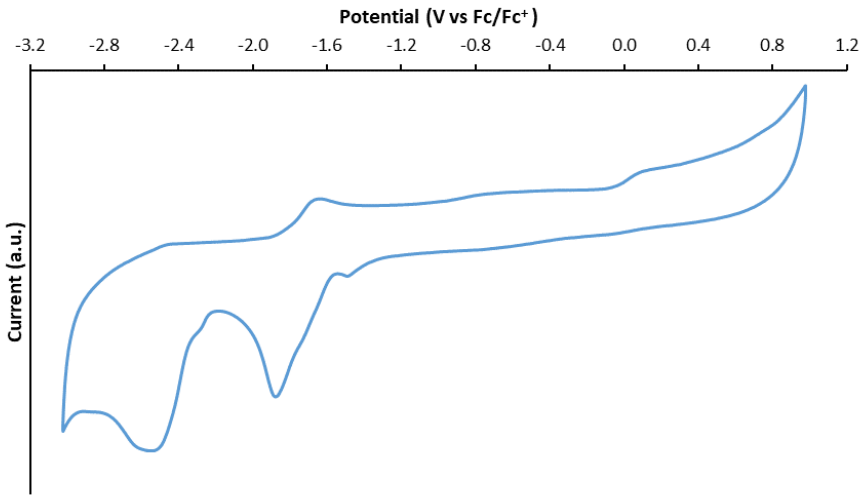

Figure 3-55 Voltammogram of [**130**($Zn(BF_4)_2$)] under N_2 at 100 mV/s, scanned in the negative direction in 0.1 M [NBu_4][PF_6] DMF solution. The Fc/Fc^+ couple was used as an internal standard and the voltammogram is referenced against this couple.

As seen in Figure 3-56, the cyclic voltammogram of [**130**($Fe(BF_4)_2$)], the complex shows one quasi-reversible oxidation at an onset of 0.63 V. The reverse wave can be observed at 0.83 V. This process is characteristic of the Fe(II)/Fe(III) redox couple.[180] There are also three reductions, with their onsets appearing at −1.38, −2.16 and −2.45 V, and the corresponding oxidations at −1.68, −2.35 and−2.64 V. The second redox couple at approximatively −1.53 V could be attributed to a ligand-based process due to the similarities of the onset potentials with the ones observed for **130**. The third redox couple at approximatively −2.25 V do not correspond to the ones previously observed and thus further investigation would be required to ascribe the nature of these redox processes; while the fourth redox couple at −2.54 V could be attributed to a ligand-based process due to its correspondence with one of the redox couples observed in the voltammogram of **130**.

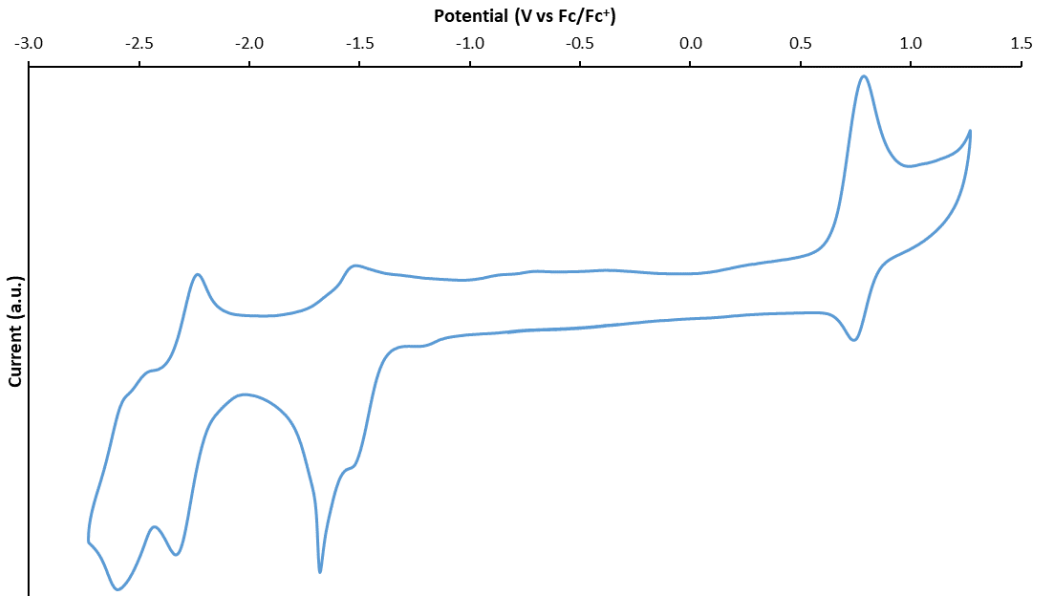

Figure 3-56 Voltammogram of [**130**($Fe(BF_4)_2$)] under N_2 at 100 mV/s, scanned in the negative direction in 0.1 M [NBu_4][PF_6] DMF solution. The Fc/Fc^+ couple was used as an internal standard and the voltammogram is referenced against this couple.

The cyclic voltammogram of [**130**($Co(BF_4)_2$)], shown in Figure 3-57 revealed the presence of six quasi-reversible reductions at onset potentials of −0.11 V, −1.05 V, −1.64V, −1.95 V, −2.28 V and −2.58 V. Their reverse waves can be observed at onset potentials of −2.45 V, −2.14 V, −1.80 V, −1.27 V and −0.26 V. The redox couple at approximatively −0.18 V is a metal-based process corresponding to the Co(III)/Co(II) couple while the redox couple at approximatively −1.16 V is attributed to the metal-based process corresponding to the Co(II)/Co(I) couple.[180] The redox couples at −1.72 V can be attributed to a ligand-based process due to its similarity with the potential of a redox couple observed for **130**. The reduction with the lower potential (−2.58 V) is potentially a ligand-based process due to its similarity with the potential of a redox couple observed for **130**, however, its proximity with the cathodic end of the solvent window resulted in the impossibility to observe the corresponding oxidation. The two remaining redox couples at −2.04 V and −2.36 V do not correspond to the ones previously observed and thus further investigation would be required to ascribe the nature of these redox processes.

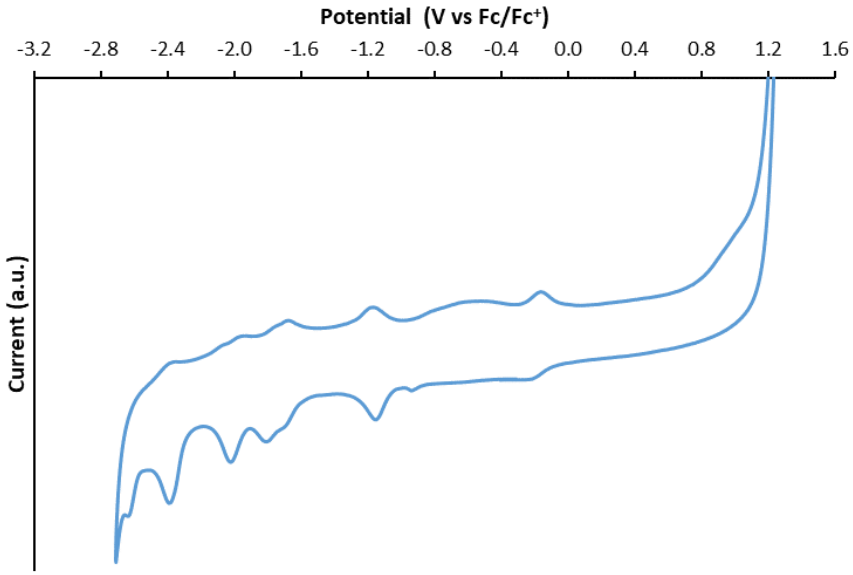

Figure 3-57 Voltammogram of [**130**($Co(BF_4)_2$)] under N_2 at 100 mV/s, scanned in the negative direction in 0.1 M [NBu_4][PF_6] DMF solution. The Fc/Fc^+ couple was used as an internal standard and the voltammogram is referenced against this couple.

3.7 Conclusion and Future Work

To summarise, two novel naphthalimide Tröger's bases have been synthesised and fully characterised. The first, a 4-amino-1,8-naphthalimide Tröger's base functionalised with phenyl-terpyridine moieties has been studied in a variety of solvents and the ability of this system to give rise to AIE in DMSO:H_2O mixtures has been investigated. Taking advantage of this property, the possibility to use **130** as a fluorescent sensor of various nitroaromatics was further demonstrated. **130** has also shown the capacity to discriminate phenolic and non-phenolic nitroaromatics due to the intermolecular hydrogen-bonding taking place between **130** and the hydroxy group of phenolic nitroaromatics. This system has shown an affinity for the sensing of PA and 2,4-DNP, exhibiting a Stern-Volmer constant of $40.6 \pm 1.7 \times 10^3$ M^{-1} and $25.0 \pm 0.4 \times 10^3$ M^{-1}, respectively. Further studies were carried out to understand the interactions between **130** and PA, with a ^1H NMR titration demonstrating that the protons of the terpyridine moieties were involved suggesting the presence of intermolecular hydrogen-bonding as well as π-π stacking interactions between PA and the terpyridines moieties. This finding was further confirmed by FT-IR with the disappearance of the signal corresponding to the hydroxy group of PA upon mixing PA with **130**. These results were substantiated by DFT calculations performed by Dr. Deivasigamani Umadevi, highlighting four interaction sites on **130**, the nitrogen atoms of the terpyridine moieties being the ones displaying the strongest intermolecular interactions. Modelling of these interactions

confirmed also that both intermolecular hydrogen-bonding, as well as π-π stacking interactions, were taking place. Competitivity experiments for the selective sensing of PA showed that **130** can discriminate PA from a variety of other nitroaromatics and that the presence of ions has little effect on the fluorescence sensing, except for transitions metals, which results in the quenching of **130** upon coordination to the terpyridine moieties. Finally, the effect of pH on the sensing mechanism was evaluated, an acidic pH resulted in a stronger fluorescence quenching while sensing in basic medium resulted in a lower sensitivity. The limit of detection was established to be 20 ppb which is lower than the allowed limit of NACs in drinking water established by the US EPA.[185,201,202] These overall results demonstrate that **130** could potentially be used as a fluorescent AIE sensor for the on-site detection of PA.

The second, a 4-amino-1,8-naphthalimide Tröger's base covalent organic polymer (**131**) was synthesised and characterised by Asst. Prof. Sankarasekaran from the Gunnlaugsson research group and the spectroscopic study of the COP suspended in water was carried out. **131** displayed a strong blue fluorescence with a maximum intensity at 490 nm. Taking advantage of this strong fluorescence, it was demonstrated that **131** could be used to detect the presence of PA in water by quenching of its fluorescence. More importantly, **131** exhibited the ability to discriminate between phenolic and non-phenolic nitroaromatics due to the intermolecular hydrogen-bonding taking place between **131** and the hydroxy group of phenolic nitroaromatics. This system has shown an affinity for the sensing of PA and 2,4-DNP, exhibiting a Stern-Volmer constant of $32.7 \pm 1.3 \times 10^3\ M^{-1}$ and $17.4 \pm 0.2 \times 10^3\ M^{-1}$, respectively. Competitivity experiments for the selective sensing of PA showed that **131** can discriminate PA from a variety of other nitroaromatics and that the presence of ions has very little, to no effect on the fluorescence sensing. The effect of pH on the sensing mechanism was evaluated, an acidic pH resulted in a slight decrease of fluorescence quenching ($K_{SV} = 2.35 \times 10^4\ M^{-1}$) while sensing in basic medium resulted in a drastic decrease of sensitivity ($K_{SV} = 1.86 \times 10^4\ M^{-1}$) suggesting again that hydrogen-bonding is involved in the sensing mechanism. The limit of detection was established to be 12 ppb which is lower than the allowed limit of NACs in drinking water established by the US EPA.[185,201,202] The sensing mechanism was further studied by DFT calculations performed by Dr. Deivasigamani Umadevi from the Watson computational chemistry group, highlighting the possibility of charge transfer occurring from the HOMO of the picrate anion to the LUMO of **131** and therefore supports the proposed static quenching mechanism at low

concentration of PA. These overall results demonstrate that **131** could potentially be used as a fluorescent sensor for the on-site detection of PA in water.

The coordination of **130** with various *d*-metals ($Zn(BF_4)_2$, $Fe(BF_4)_2$ and $Co(BF_4)_2$) was carried out and led to the formation of linear polymers that were fully characterised. The morphology study of **130**, [**130**($Zn(BF_4)_2$)], [**130** ($Fe(BF_4)_2$)] and [**130** ($Co(BF_4)_2$)] revealed the formation of two different morphologies for **130** which depended on their concentration in DMF; the bowl-like shape was favoured at 0.5 mg/mL while the spherical aggregates were favoured at a concentration of 1 mg/mL. It was also demonstrated that [**130**($Zn(BF_4)_2$)] formed a porous network of filaments, while both [**130**($Fe(BF_4)_2$)] and [**130**($Co(BF_4)_2$)] only formed amorphous aggregates. The studies of the spectroscopic properties of **130**, [**130**($Zn(BF_4)_2$)], [**130**($Fe(BF_4)_2$)] and [**130**($Co(BF_4)_2$)] in DMF demonstrated that [**130**($Zn(BF_4)_2$)] is the most luminescent polymer, followed by [**130**($Co(BF_4)_2$)], while [**130**($Fe(BF_4)_2$)] is non-emissive and it also revealed the formation of aggregates at higher concentration. Finally, their cyclic voltammograms were compared to the one of **130** and revealed the influence of the metal ion on their electrochemical properties. As future work, the full thermogravimetric analysis of the different polymers should be carried out along with the gas uptake of [**130** ($Zn(BF_4)_2$)] which was shown to be highly porous. Finally, the use of [**130** ($Zn(BF_4)_2$)] as a potential detector of PA in aqueous solution will be investigated. Due to the excellent results demonstrated by **130** and the zinc coordination polymer reported by Dr. Sankarasekaran Shanmugaraju,[185] it is predicted that [**130** ($Zn(BF_4)_2$)] could display improved detection properties compared to **130**, notably by displaying a more competitive affinity for PA against the presence of *d*-metals and could be potentially used for several sensing cycles.

Chapter 4— Cross-Linking the Fibers of a Supramolecular Gel from a Tripodal Terpyridine-Based Ligand through Its Multicomponent Gels

4.1 Introduction

Over the years, the Gunnlaugsson research group has developed expertise in the formation of luminescent lanthanide complexes using various antennae ranging from dipicolinc acid (dpa) to form healable metallogels,[19] 2,6-bis(1,2,3-triazol-4-yl)pyridine (btp) which could also be used for the formation of luminescent metallogels,[221] while the two previous building blocks could be incorporated into polymers,[222] used for the creation of luminescent logic gates,[223] and the formation of triple-stranded helicates.[224,225] The use of naphthyl derivatives for the creation of Langmuir-Blodgett film was also demonstrated,[226,227] as well as the use of cyclen for the development of potential MRI agents.[228] The terpyridine unit has also been used extensively in the Gunnlaugsson group in the conjugation to the BTA core for the formation of Ln(III) luminescent complexes and self-assembly and the following paragraph will focus on these examples along with the use of the BTA moiety for the formation of soft-materials.

As stated previously, the Gunnlaugsson group was the first to develop compound **85** and were interested in the ability of the compound to achieve metal-directed gelation to form more ordered structures with added functionality. In this system, the terpyridine unit has two roles. The first being the coordinating unit of Ln(III) ions, and the second to serve as an antenna and sensitise the excited state of Ln(III)-centred emission. Interactions of $EuCl_3$ with the ligand **85** were studied using various spectroscopic techniques in methanol (Figure 4-1). A clear bathochromic shift of the band at 280 nm was observed in the absorption spectrum of **85** (Figure 4-1A) upon addition of europium with the appearance of a shoulder at 320 nm, indicative of coordination of Eu(III) ions to the ligand which was confirmed by MS-analysis. Addition of Eu(III) ions significantly quenches ligand-centred emission (Figure 4-1B) due to the formation of complexes between the terpyridine moieties and Eu(III) ions leading to an energy transfer from the ligand to the excited state of Eu(III) ions with simultaneous enhancement of Eu(III)-centred emission (Figure 4-1C).[29]

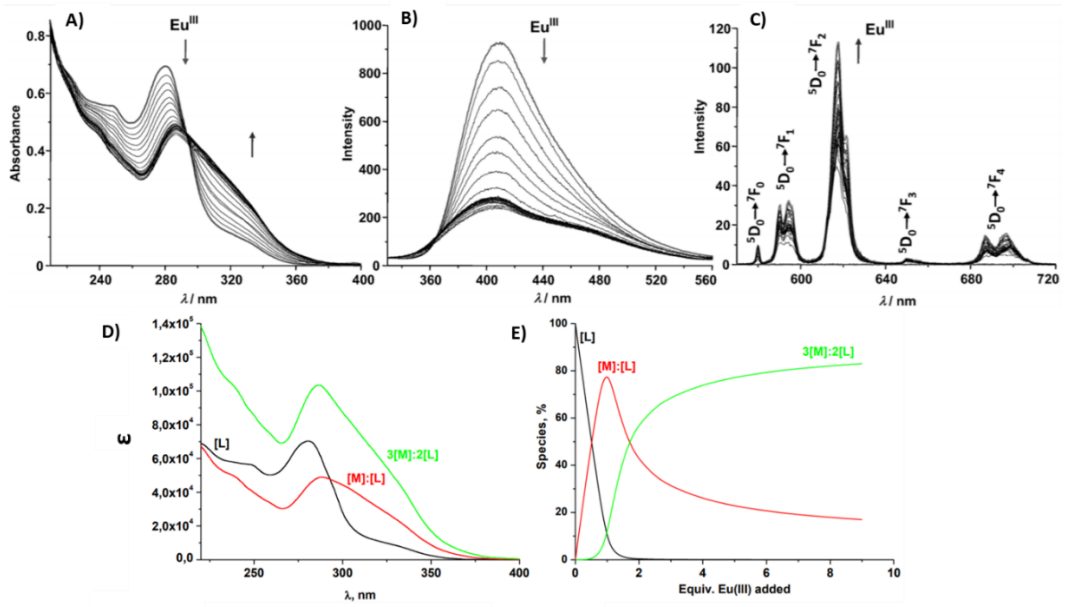

Figure 4-1 The changes observed in A) absorption, B) fluorescence and C) phosphorescence spectra of the ligand **85** upon titration with $EuCl_3$, D) recalculated absorption spectra and E) speciation-distribution diagram of the absorption titration. Reproduced from reference.[29]

Titration of **85** with $EuCl_3$, followed by the fitting of the data using non-linear regression analysis software also demonstrated that after the addition of 0.5 eq. of Eu(III) ions, a 3:2 (Eu(III) ions: **85**) species started to form with the amount of 1:1 complex decreasing (Figure 4-1E), indicating the possibility of achieving a higher stoichiometry and to form even more complex assemblies. The tripodal ligand **85** was used to form gels in MeOH:H_2O (30:70) with a *wt* % of 0.3% that was determined by TGA. Finally, the formation of a metallo-gel was undertaken between **85** and $EuCl_3$ in a 5:95 ratio of H_2O:MeOH (Figure 4-2C). Methanol was used as a co-solvent to help the solubility of the ligand **85**. Various ratios of Eu(III) ions and the ligand were tested and the best result was produced by the 3:1 (Eu(III) ions:**85**) ratio at 9 *wt* % of **85-EuCl₃** solid component. In the aim of studying the morphology of the gel, dried samples for both organo- and metallo-gels were prepared and SEM and TEM analyses showed a considerably more fibrous material for the metallo-gel (Figure 4-2B) demonstrating the effect of the metal.[29]

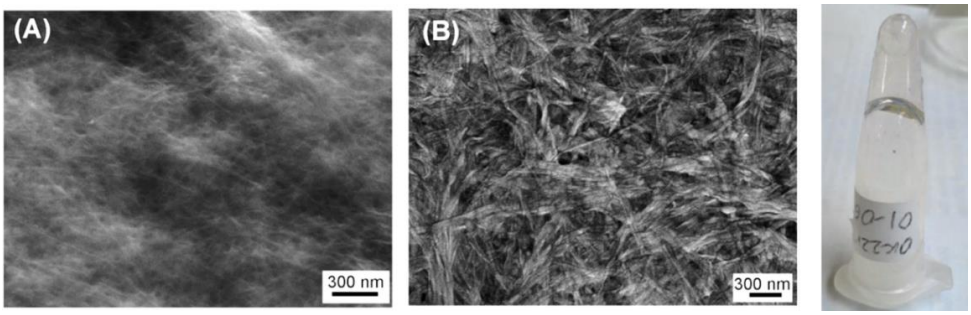

Figure 4-2 SEM images of the gel formed by A) the ligand **85**, B) the complex **85-EuCl₃** and C) picture of the metallo-gel. Reproduced from reference.[29]

Since common gelators such as gelatin and agarose are used as a platform to grow crystals, the Gunnlaugsson group used the gel formed by **85-EuCl$_3$** and also by the ligand **85** itself to grow crystals. The use of supramolecular chemistry in this area is recent but quite promising as these assemblies are reversible and can be tuned by external stimuli. The observation of the growth of the nanowires in this work was serendipitous and they were found to be NaCl which was confirmed by thermogravimetric analysis of the ligand along with further microscopic analyses of the wires. Their origin is believed to be due to the small amount of NaCl impurities present in the original ligand powder. The wires were studied by SEM, TEM as well as EDX analyses confirming the elemental composition of the wires observed in Figure 4-3. The same gels were used as matrices to grow potassium chloride and potassium iodide wires leading to the formation of wires with different morphologies as seen in Figure 4-3.[21]

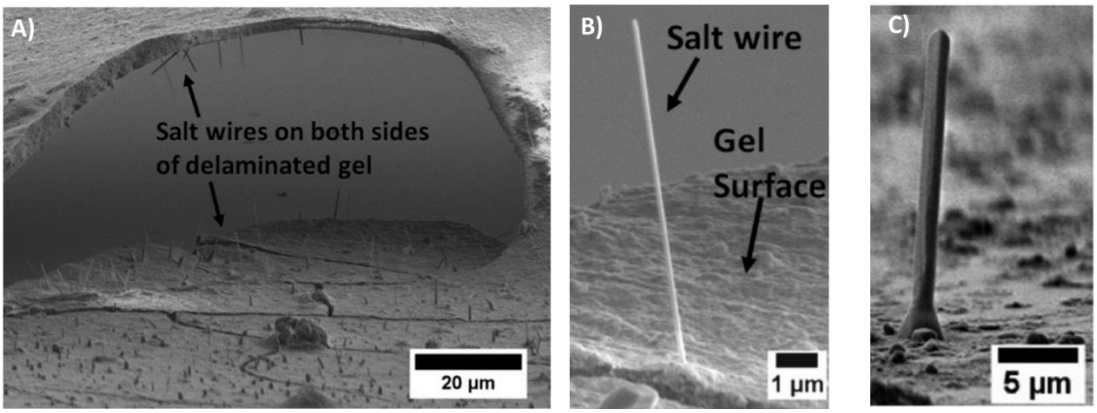

Figure 4-3 SEM images of A) NaCl wires observed growing on both sides of the dried gel film, B) small individual NaCl wire grown from the gel matrix, and similarly grown C) large KI wire. Reproduced from reference.[21]

This work was further continued and in 2015 the Gunnlaugsson group showed that reaction of the ligand **85** with *d*-metals such as Fe(II), Ni(II), Cu(II), Zn(II) and Ru(III) resulted in the formation of other metallo-gels, where metals again acted as "supramolecular glue" bringing ligand fibres closer together. To do so, **85** was used to form 0.3 *wt* % gels in MeOH:H_2O and the *d*-metals were added as an aqueous solution on the top of the gel and were let to diffuse through the gel generating a colour change (Figure 4-4A). The effect of the diffusion of metal ions on the gel morphology was studied by SEM and revealed that the presence of *d*-metals led to the fibres increasing from ≈ 20 nm to ≈ 50 nm in width in the case of Fe(II), Ni(II), Zn(II) and Ru(III) ions, thus demonstrating that the *d*-metal could act as a second component to drastically modify the properties of the gel.[17]

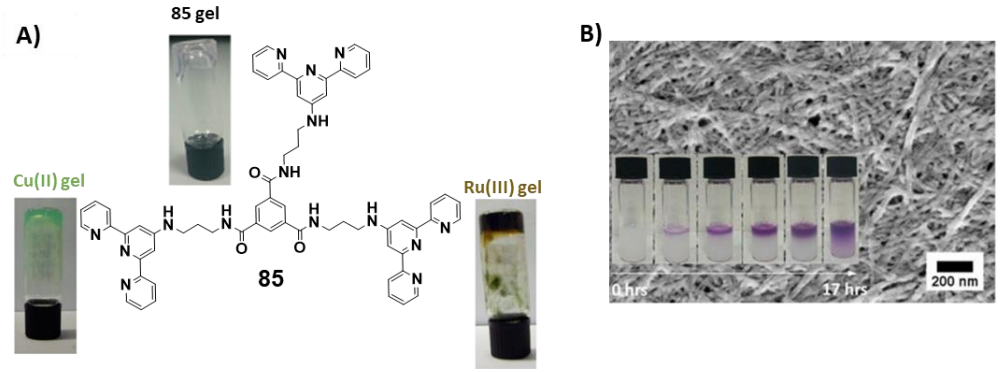

Figure 4-4 A) Structure of **85** and pictures of gels formed by the ligand alone, in the presence of Cu(II) and Ru(III) ions. B) SEM image of the gel with Fe(II), inset: diffusion of Fe(II) ions into **85** gel for 17 h. Reproduced from reference.[17]

As part of his doctoral research, Dr. Savyasachi synthesised a variety of BTA functionalised with terpyridine shown in Figure 4-5A, using both enantiomers of different amino acids as the linker in the aim to study the influence of the chiral centres on the self-assembly. The titrations of **133 (*R*/*S*)** with $Eu(CF_3SO_3)_3$ revealed the successive formation of 1:1, 2:1 and 3:1 M:L complexes, as shown schematically in Figure 4-5B, when carried out at 5×10^{-6} M. However, when titrating $Eu(CF_3SO_3)_3$ into a solution of **133 (*R*/*S*)** at 1×10^{-5} M, the successive formation of 1:1 and 3:2 M:L complexes could be observed, thus demonstrating the effect of the self-assembly of the ligand upon coordination of Eu(III) ions.

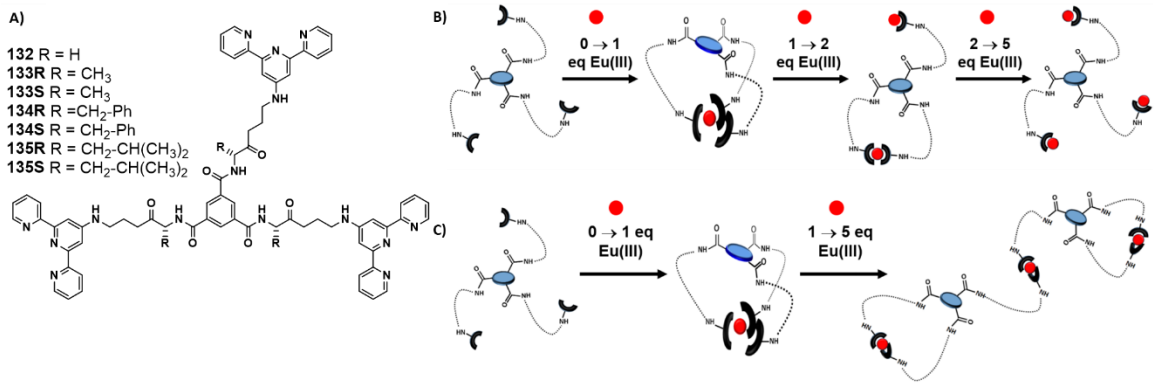

Figure 4-5 A) Structure of the chiral BTAs **132-135** synthesised by Dr. Savyasachi. Schematic representation of the complexes **133-Eu** formed through the titration at a concentration of **133** at B) 5×10^{-6} M and C) 1×10^{-5} M.

By using different amino acids (alanine, phenylalanine, glycine and leucine) the aim was to achieve various morphologies to shed light on the influence of the chiral moieties on the self-assembly of each compound. Another interest in the presence of the chiral amino acid, other than directing the self-assembly and inducing chirality at the supramolecular scale, was to add supplementary hydrogen bonding sites to the molecule compared to the precursor **85** that was used as a LMWG. However, gelation test of **132**, **133**, **134** and **135** in a variety of organic solvent with and without water revealed that only the glycine derivative

(**132**) was able to form a strong gel in CH_3CN:H_2O (6:4) mixture with a critical gelation concentration of 0.5 *wt* %. Interestingly, the gel formed by **132** displayed thixotropic behaviour, as upon addition of physical stress, the gel started to flow but upon rest, the gel reformed and a similar behaviour could be observed upon heating and cooling of the gel. Microscopy studies (SEM and TEM) of the gel revealed the presence of entangled fibres of *ca*. 30-50 nm and assemblies of several fibres into larger bundles. Finally, the rheological measurement carried out on the gel formed by **132** in CH_3CN:H_2O (6:4) mixture showed that the gel has an initial storage modulus of 1040 Pa and a cross-over point, which corresponds to the amplitude where the gel starts behaving like a liquid, of *ca*. 4%. The gel also displayed good recovery capacity by being able to recover several times its solid-like behaviour after undergoing a stress inducing the liquid-like behaviour.

SEM analysis of the viscous solution obtained with **133**-**135** revealed the formation of microspheres, with the best monodispersity achieved with both enantiomers of **133** in CH_3CN:H_2O mixtures. The mechanism of formation of the microsphere was investigated through a combination of fluorescence spectroscopy and microscopy experiments, which demonstrated that the microsphere formation is driven by the formation of hydrogen bonds between each molecule and that it can be hindered by the presence of other hydrogen bonding molecules such as urea. Further modification of the microsphere with Ln(III) ions was studied, demonstrating the formation of linear chains between the microspheres upon addition of Eu(III) or Tb(III) ions. In addition to the morphological changes of the microspheres induced by the Ln(III) ions, the photophysical properties of the microspheres were also modified, with the terpyridine coordinating the Ln(III) ions and acting as an antenna, allowing the sensitisation of the Ln(III)-centred emission.

BTA functionalised with alkyl chains of three different lengths with a terminal acid or ester **136**-**142** shown in Figure 4-6A, were successfully synthesised in good yield and studied by Dr. Lynes.[229] Single crystals of suitable quality for X-ray diffraction were obtained for **136**, **137**, **140** and **141**. **137** crystalised in the classical helical packing arrangement for BTAs while **136** displayed unusual loop interactions with the two amides of the same chain engaging in hydrogen bonding with the adjacent molecules. Further studies using dynamic scattering calorimetry and polarised optical microscopy of **136** and **137** revealed phases changing during the heating-cooling processes indicative of potential liquid crystal behaviour, however, the carboxylic acid derivatives did not have this behaviour. This is presumed to be due to the structural arrangement of the ester derivatives. The carboxylic acids **140** and **141** did not form the classical helical arrangement due to the presence of the

carboxylic acid competing for the formation of hydrogen bonds. Instead, they formed structures that contain solvent channels which are unstable when the solvent is removed leading to a loss of crystallinity.

Gelation studies of the different acids and ester demonstrated that the esters **136** and **137** did not form gels while the corresponding acids **139** and **141** were able to form gels with the best conditions being a mixture of THF:H_2O (1:2) with *ca*. 2.4 *wt* % and 5 *wt* % respectively. The rheological measurement revealed a solvent loss upon compression of the gel formed by **139**, thus increasing the weight percentage to 25%. The gel formed by **139** displayed a storage modulus of 3.12×10^6 Pa and a cross-over point at 0.78% while no dependence of the storage modulus was shown during the frequency sweep. Recovery test demonstrated that the gel formed by **139** could return to its original strength after being exposed to high stress.[229]

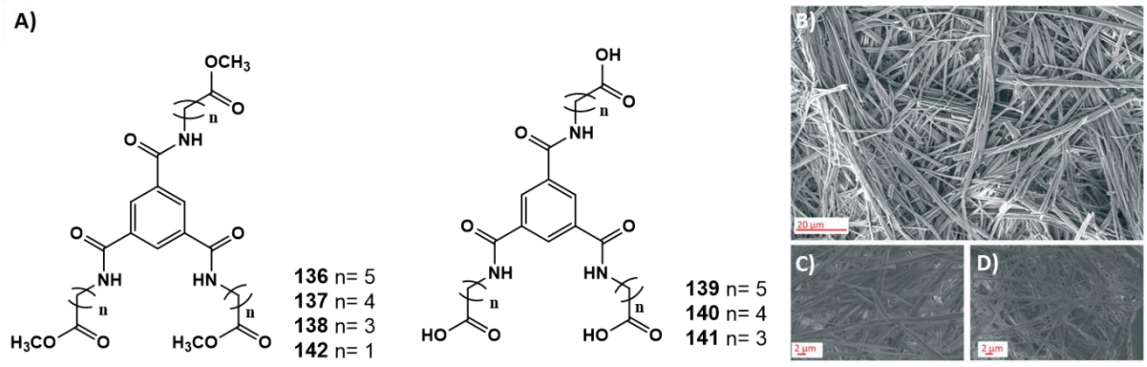

Figure 4-6 A) Structure of BTA derivative **136**-**142**. SEM images of xerogels of A) **139**, C) **140** and D) **141**. Reproduced from reference.[229]

Other BTA derivatives were prepared by Dr. Lynes such as **142** and **143** (shown in Figure 4-7A) to form coordination polymers. Despite the several hydrogen bonding sites available, **143** was unable to form gels in a variety of solvents. However, due to its terminal carboxylic groups, complexation to *d*-metal ions, in particular, Cd(II) ions was evaluated. The reaction of **143** with $Cd(NO_3)_2$ in DMF:H_2O yielded single crystals of the coordination polymer $[Cd_3(\mathbf{143}{-}H_3)_2(DMF)_2]\cdot 5H_2O\cdot 2DMF$, which upon gas uptake studies, demonstrated an excellent CO_2 capacity (17 *wt* %) at 278 K, which is due to the structural arrangement of the coordination polymer as evidenced by X-ray crystallography.[230]

Further extension of the arms of **143** with glycine or an alanine methyl ester was undertaken to form **144** and **145** respectively, and their corresponding carboxylic acids, **146** and **147** (shown in Figure 4-7B). Studies of these new tripodal compounds revealed that none of them were able to crystallise, however, gelation studies revealed that **144** was able to form a gel in MeOH at 1.75 *wt* % with SEM revealing the formation of long needle-like

fibres upon drying. The ester derivative **145** failed to form a gel and instead, formed a very viscous solution in MeOH at 3 *wt* % and SEM studies showed the presence of fibres in the xerogel. Finally, the carboxylic acid **147** was able to form a gel in H_2O, following the solubilisation of the compound through the addition of base followed by the gelation occurring through the addition of acid. TGA analysis demonstrated that the gel was formed with a *wt* % of 3.7% and SEM study revealed a similar morphology to its precursor **145.**[231]

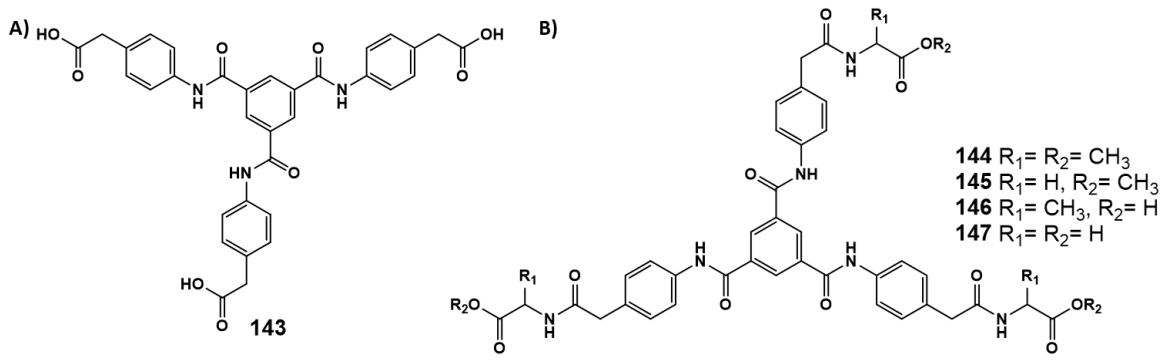

Figure 4-7 Structures of BTA derivatives A) **143** and B) **144-147**. Reproduced from reference.[231]

Dr. Lynes also explored the possibility to form a polymeric network using 1,3,5-benezenetricarbonyl as a core moiety, ethylenediamine as a spacer and 4-tert-butyl-2,6-diformylphenol to form a Schiff base. The interactions of the BTA-Schiff base polymer with Cu(II), Zn(II) and Co(II) were studied through a variety of techniques such as EDX, SEM, IR, spectroscopy and X-ray powder diffraction. These studies revealed that the polymer interacts with Cu(II) and Co(II) ions through a particular binding mode while a different one is responsible for the interactions with Zn(II) ions.[231]

As previously discussed, the tripodal ligand **BTA-TPy** (**85**) was developed in our laboratory, its study has revealed that **85** self-assembles through a combination of π-π stacking and three-fold hydrogen bonding between the BTA cores leading to the formation of fibres which ultimately lead to supramolecular polymers.[17,21,29] It has also been demonstrated that **85** is a low-molecular-weight gelator (LMWG), and forms gels in methanol-water mixtures as well as in dimethyl sulfoxide-water mixtures.[17,26,29] Another advantage of **85** is the presence of three terpyridines which are well known chelating units; forming strong complexes with *d*-metals but that can also be used as antennae for *f*-metal ions. The Gunnlaugsson research group, took advantage of it to demonstrate the possibility to cross-link the supramolecular fibres formed by **85** in the gel by diffusion of *d*-metals (Fe(II), Ni(II), Co(II), Zn(II) and Ru(III)), which resulted in a drastic modification of the colour of the gel and the morphology of the fibres.[17] It was also demonstrated by the Gunnlaugsson research group that **85** could sensitise Eu(III) emission, and that the complex

[Eu-**85**]$^{3+}$ was also capable of forming gels in methanol-water mixtures, therefore allowing to tune the properties of the gel. Besides modifying the luminescent properties of the gel, diffusion of *d*- or *f*-metal ions also results in the modification of the rheological properties of the resulting gels, which corresponds to the viscosity of the soft-material in different conditions. The control of those properties is essential through the use of the gel depending on its applications. For example, it might be crucial to be able to pass the gel through a syringe needle, a printer nozzle, without becoming fully liquid after the extrusion process, while being of a low enough viscosity to freely flow through the nozzle without blocking it. Thus the capacity of fine control of the rheological properties of a gel is highly desirable.

In this chapter, attention is drawn to the effect of the ionic radius of Ln(III) ions (known as the Lanthanide contraction) on the stability constants of the complexes, the luminescent properties of the material, the morphology of the gels as well as their rheological properties. Indeed as discussed in Chapter 1, the ionic radius of Ln(III) ions decreases by approximately 20% along the lanthanides row of the periodic table and as demonstrated by Piguet, Bünzli and others this decrease in size lead to different stability of the complexes.[106,134,136-139,232] These stability constants can be tuned according to different parameters such as the binding cavity size, the rigidity of the binding units and its functionalisation, allowing to perform size-discrimination upon binding to the Ln(III) ions.[106] An example of this effect was of particular interest to this work where Renaud *et al*. used *N*,*N*,*N*',*N*'-tetraethylpyridine-2,6-dicarboxamide and studied its interaction with Ln(III) ions using UV-vis absorption and ^{1}H NMR titrations. They determined that the stability constants of the 1:1, 1:2 and 1:3 M:L complexes increase when the ionic radius decreases which is the typical electrostatic trend.[137] However, by covalently linking the three ligands using covalent binding to a flexible tripod [(tris(2-aminoethyl)amine)] they demonstrated that the stability constants of the 1:1 complexes decreased as the ionic radius decreases.[140] Therefore the use of a tripodal linker between the coordinating units can be used to modify the interactions with the lanthanides, so by using a tripodal moiety able to form gels there should be a possibility to modify the binding constants of the complexes formed in the gels as a function of the ionic radius and potentially the rheological properties of the gel.

In this chapter, **85** was studied in solution in the presence of Ln(III) ions (Ln = La, Sm, Eu, Gd, Tb, Yb and Lu) through the UV-vis absorption and emission titrations, the fits of the changes, determined using non-linear regression analysis, and the comparison of the binding constants obtained as a function with the change of the ionic radii will be presented. The formation and modification of gels using **85** and the aforementioned Ln(III) ions were

also undertaken and the effect on their morphology and spectroscopic properties were studied and are discussed in this chapter as well. The modification of the **85** gels using $[Ru(phen)_2\mathbf{148}]^{2+}$ through its diffusion, and exploration of the properties of the resulting gel is also discussed.

4.2 Synthesis and Characterization of BTA-TPy (85)

The design of the ligand **85** is based on the benzene-1,3,5-tricarboxamide (BTA) core conjugated to three terpyridine (tpy) units *via* carboxamide spacers and it was synthesised in two steps (Scheme 4-1) from the commercially available 1,3,5-benzenetricarbonyl trichloride, 1,3-diaminopropane and 4′-chloro-2,2′:6′,2″-terpyridine using a procedure previously developed in the Gunnlaugsson research group.[17,21,29] *N*-[2,2';6',2'']Terpyridin-4'-yl-propane-1,3-diamine (**149**) was obtained by refluxing overnight 4′-chloro-2,2′:6′,2″-terpyridine in 1,3-diaminopropane, and was obtained as a white solid in 66% yield. The product (**149**) was reacted with 1,3,5-benzenetricarbonyl trichloride in dry DCM overnight resulting in the formation of a white solid that was filtered and washed with DCM yielding the pure desired compound in 90% yield.

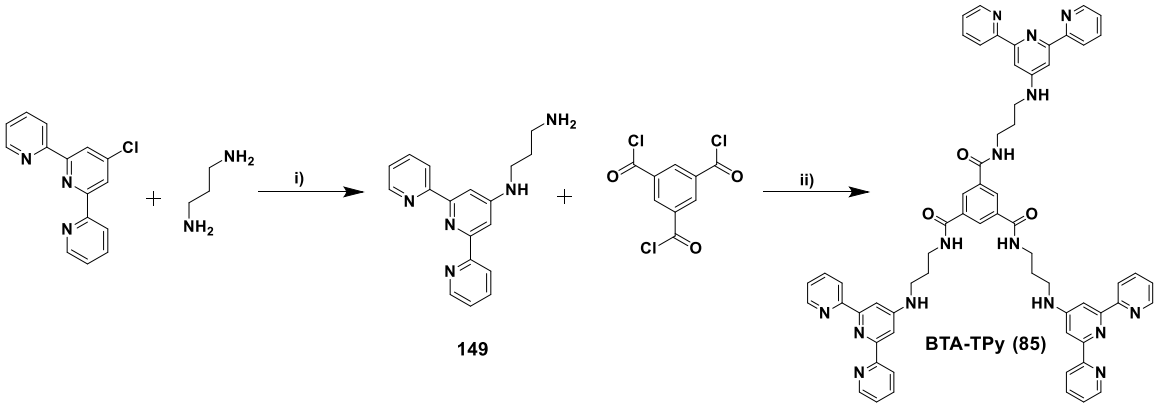

Scheme 4-1 Synthesis of **85** from 4′-chloro-2,2′:6′,2″-terpyridine: i) 120 °C, 12 h, 66%; ii) dry DCM, rt, 12 h, 90%.

The successful formation of **85** was demonstrated by HRMS-ESI with the presence of the $[M-H]^+$ ion (*m/z* = 1072.4835) and more importantly by elemental analysis with the formula $C_{63}H_{57}N_{15}O_3$ 1.3NaCl CH_2Cl_2 $2H_2O$ (the full characterisation and the data are available in the experimental sections and appendixes). The ^1H NMR in DMSO-d_6 confirmed the formation of the desired compound with the presence of a singlet at 9.14 ppm accounting for the amide group, the singlet at 7.68 ppm corresponding to the benzene core and the presence of the 3 sets of protons of the alkane chains at 3.59, 3.48 and 1.97 ppm (Figure 4-8).

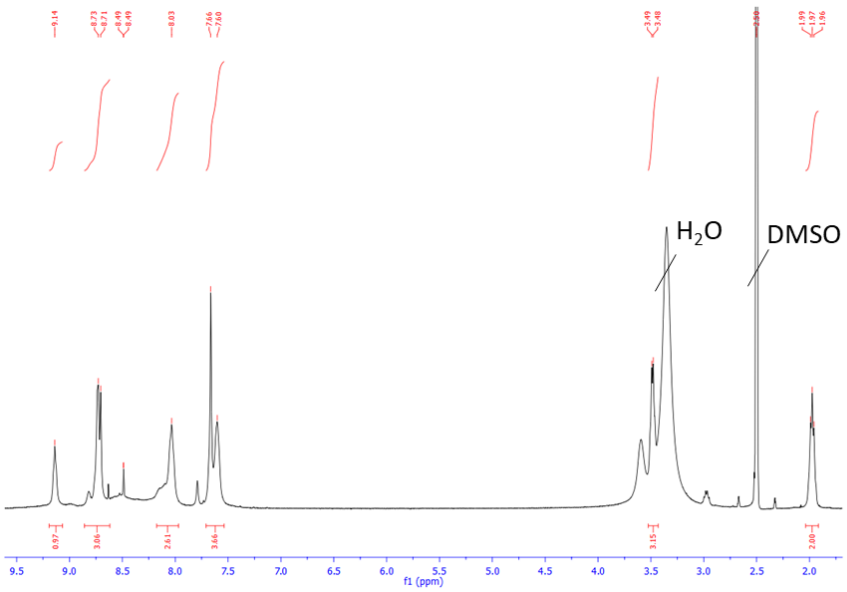

Figure 4-8 The ^{1}H NMR spectrum (400 MHz, DMSO-d_6) of **85**.

However, the signals in Figure 4-8 are very broad due to the formation of aggregates in DMSO and the strong tendency of the compound to self-assemble. This issue was overcome by doing a temperature-dependent ^{1}H NMR (VT NMR) experiment leading to a better splitting and sharpening of the signals as shown in Figure 4-9 when reaching higher temperatures.

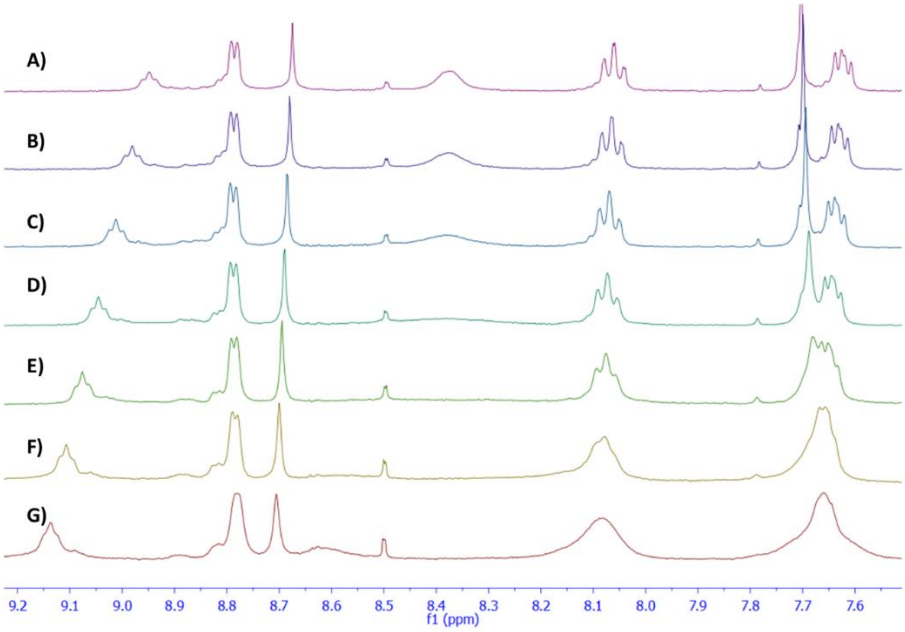

Figure 4-9 Temperature-dependent ^{1}H NMR spectra (VT NMR) (400 MHz, DMSO-d_6) of **85** (c = 2.60 × 10^{-3} M) at A) 80 °C B) 70 °C, C) 60 °C, D) 50 °C, E) 40 °C, F) 30 °C and G) 20 °C.

Alternatively, the dilution of the sample into deuterated methanol resulted in much sharper NMR signals and a better splitting of the signals as shown in Figure 4-10.

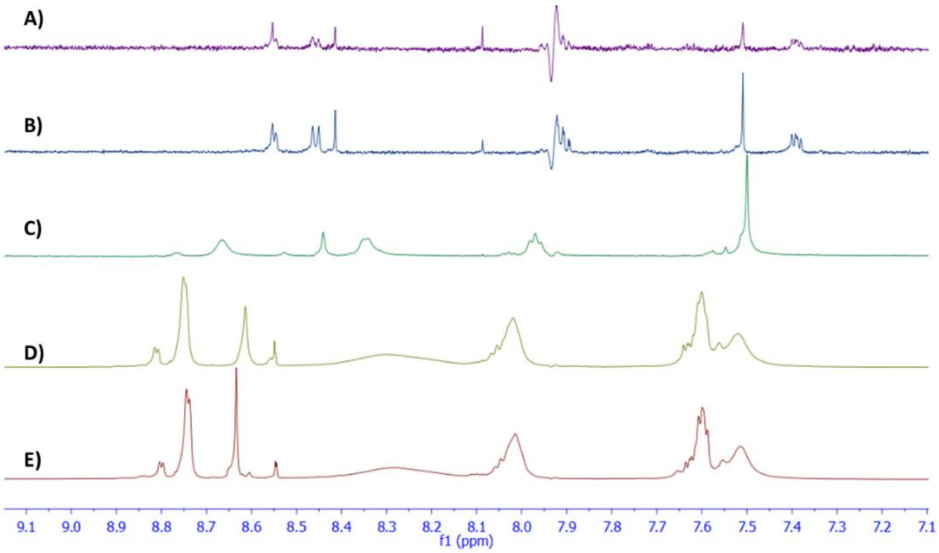

Figure 4-10 The ^{1}H NMR spectra of **85** (600 MHz, CD_3OD) at A) 0.5×10^{-5} M, B) 1.0×10^{-5} M, C) 1.0×10^{-4} M, 1.0×10^{-3} M and E) 2.0×10^{-3} M.

The IR spectrum of **85** confirmed the formation of the amide with the presence of N–H stretching at 3438 cm^{-1}, N–H bending at 1580 cm^{-1} and C=O stretching at 1635 cm^{-1} corresponding to the fingerprint of an amide and carbonyl bonds (Figure 4-11).

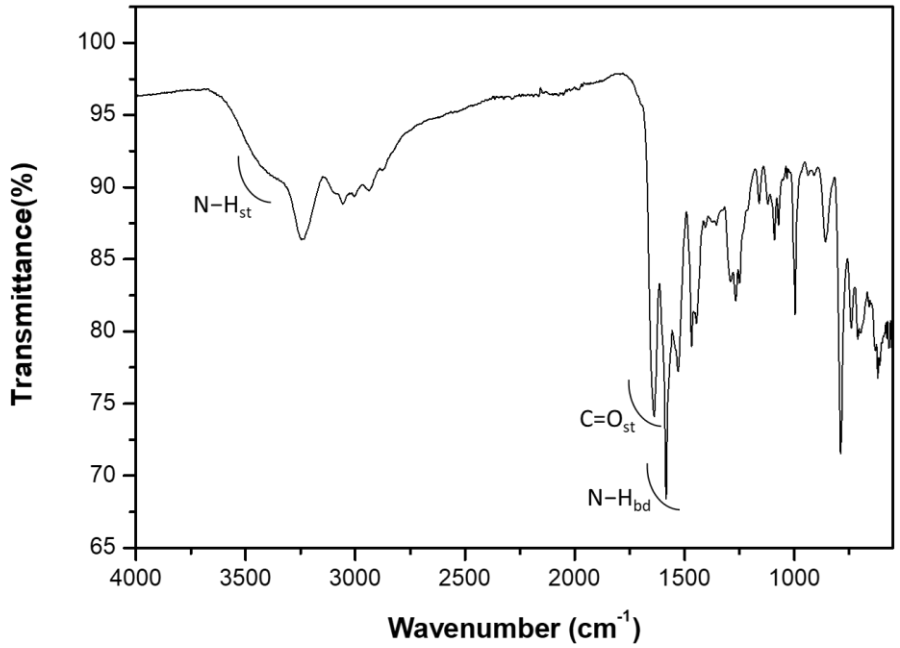

Figure 4-11 FTIR spectrum (4000 – 550 cm^{-1}) of **85**.

Having fully characterised **85**, its spectroscopic properties were next analysed with the aim of exploring its photophysical properties and behaviour in solution, alone and in the presence of *f*-metals.

4.3 UV-vis Absorption and Luminescence Emission Studies of 85 in Solution

4.3.1 Dilution study of 85

The absorption spectrum of **85** (c = 5.45 × 10^{-6} M) which was recorded in MeOH is shown in Figure 4-12 (blue), and displays a band centred at λ_{max} = 280 nm corresponding to the terpyridine $\pi \rightarrow \pi^*$ transition.[29] Excitation at 280 nm gave rise to a fluorescence emission with λ_{max} = 430 nm (Figure 4-12, grey). The excitation spectrum (Figure 4-12, orange) was structurally similar to the absorption spectrum. However, the main bands are slightly red-shifted. This effect could be the result of stacking interaction between molecules of the ligand or the formation of supramolecular polymers. Therefore, a dilution study was carried out to confirm the formation of inter-ligand interactions and the purity of the compound.

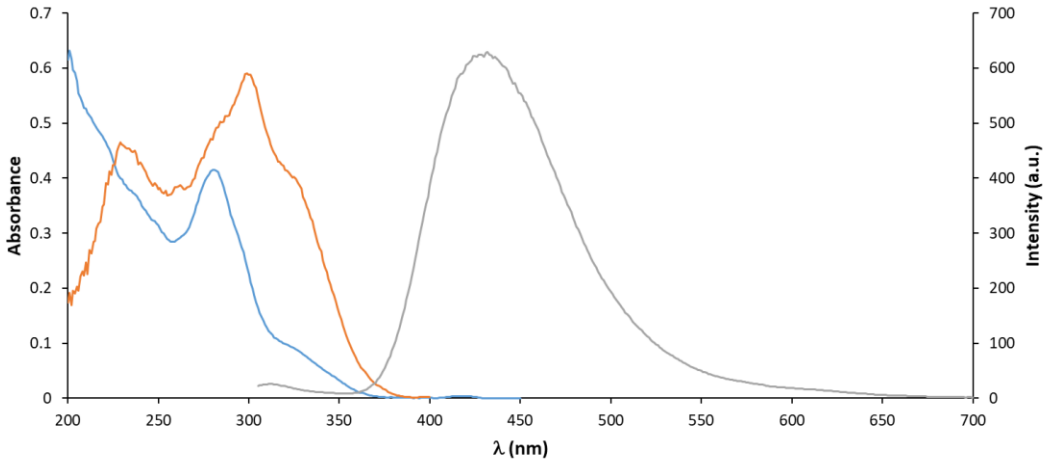

Figure 4-12 Absorption (blue), excitation (orange, λ_{em} = 420 nm) and fluorescence (grey, λ_{ex} = 280 nm) spectra in MeOH (c = 5.45 × 10^{-6} M) of **85**.

A dilution study of **85** in MeOH was carried out in triplicate between 25.00 × 10^{-6} – 0.64 × 10^{-6} M (Figure 4-13) revealing that all the absorption bands change linearly *vs* concentration only below 2.58 × 10^{-6} M (Figure 4-13C). Above this concentration, most likely the aforementioned formation of the self-assembly aggregates, through dimerisation of the molecules by intermolecular three-fold hydrogen bonding between BTA moieties and possibly π-π stacking between the terpyridine moieties, begins to occur. This is in good agreement with the self-assembly demonstrated by carrying out the ^{1}H NMR dilution experiments (Figure 4-10) though these were at much higher concentrations.[29]

As the linear changes in the absorption spectrum of the ligand *vs* concentration were observed in the range of (2.58–0.64) × 10^{-6} M it was considered as a range where the ligand behaves as a single molecule. Hence, this range was selected to determine the molar

extinction coefficient value of λ_{max} = 280 nm and it was estimated as $\varepsilon = 75.4 \pm 1.1 \times 10^3$ M^{-1} cm^{-1} which is in good agreement with the previously reported value.[29] The dilution study demonstrated a significant change in the shape of the excitation spectrum of the ligand accompanied by a blue-shift of the main bands leading to the excitation spectrum bands perfectly matching the absorption spectrum for a concentration of 2.58×10^{-6} M or lower (Figure 4-13B, D, E). Indeed when comparing the absorption and the excitation spectra of the ligand on the linear range of the changes it is possible to see that the principal bands of both spectra are perfectly aligned for both the absorption and the excitation spectra shown on Figure 4-13 (C and D), and thus demonstrating that above 2.58×10^{-6} M the ligand is already beginings to self-associate and form supramolecular polymers and that below this concentration the compound is behaving as a single molecule.

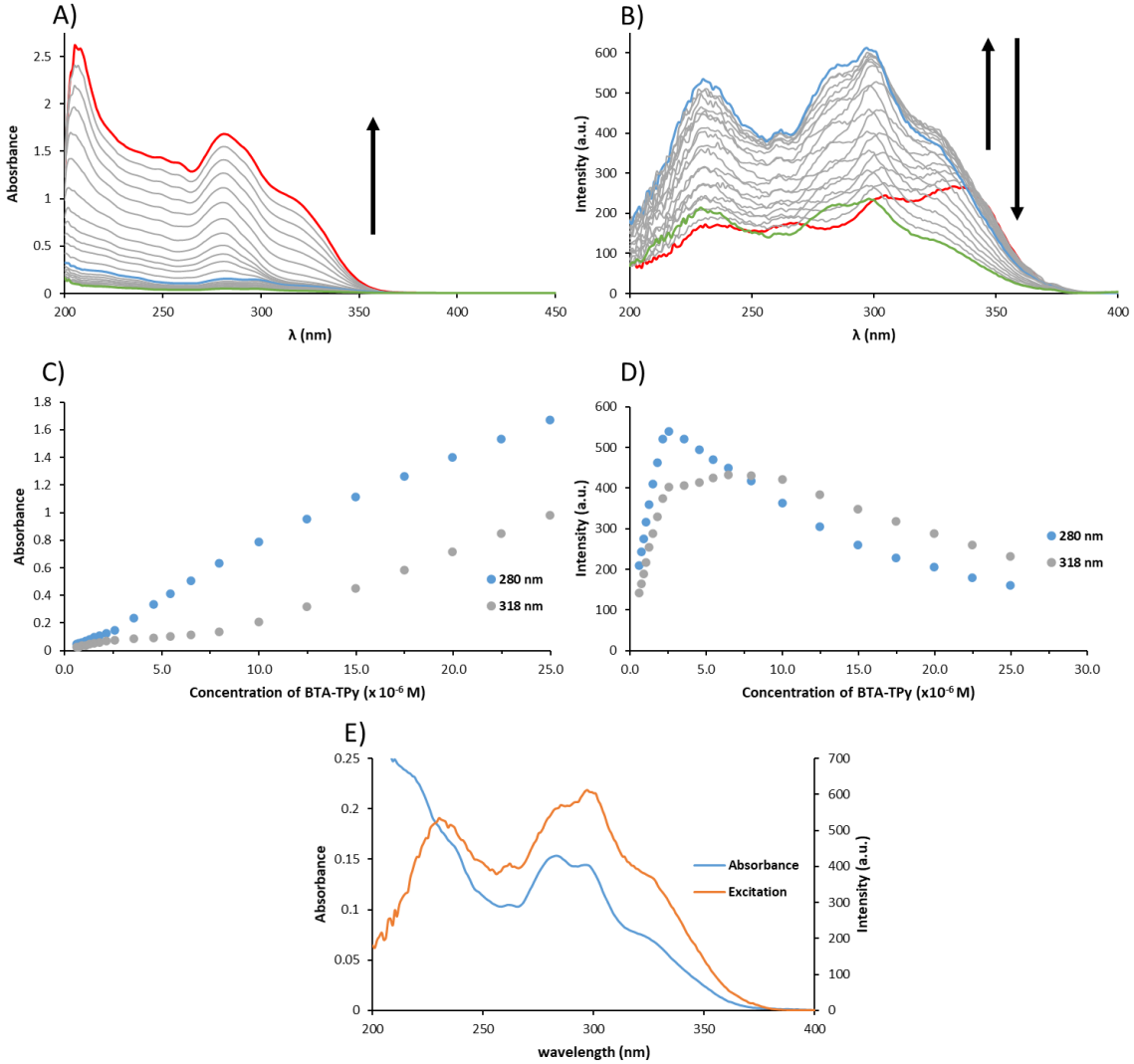

Figure 4-13 Changes in the A) absorption and B) excitation intensity (λ_{em} = 420 nm) upon dilution of **85** in MeOH ((25.00–0.64) × 10^{-6} M) with 25.00 × 10^{-6} M in red, 2.60 × 10^{-6} M in blue and 0.64 × 10^{-6} M in green. C) Absorption and D) excitation profile in function of concentration for λ = 280 and 318 nm. E) Absorption and excitation intensity (λ_{em} = 420 nm) of **85** in MeOH (2.58 × 10^{-6} M).

The dilution study revealed also that the emission intensity increases when diluting the compound from 25.0 × 10^{-6} M to 2.58 × 10^{-6} M is mostly due to the inner filter effect since in this range of concentration **85** is highly absorbing as shown in Figure 4-13. Interestingly, it is possible to see in Figure 4-14, a λ_{max} shift from 423 nm to 433 nm between 25.0 × 10^{-6} M and 2.58 × 10^{-6} M while λ_{max} remains constant between 2.58 × 10^{-6} M and 0.64 × 10^{-6} M which is presumably due to destruction of polymeric units formed at higher concentration.

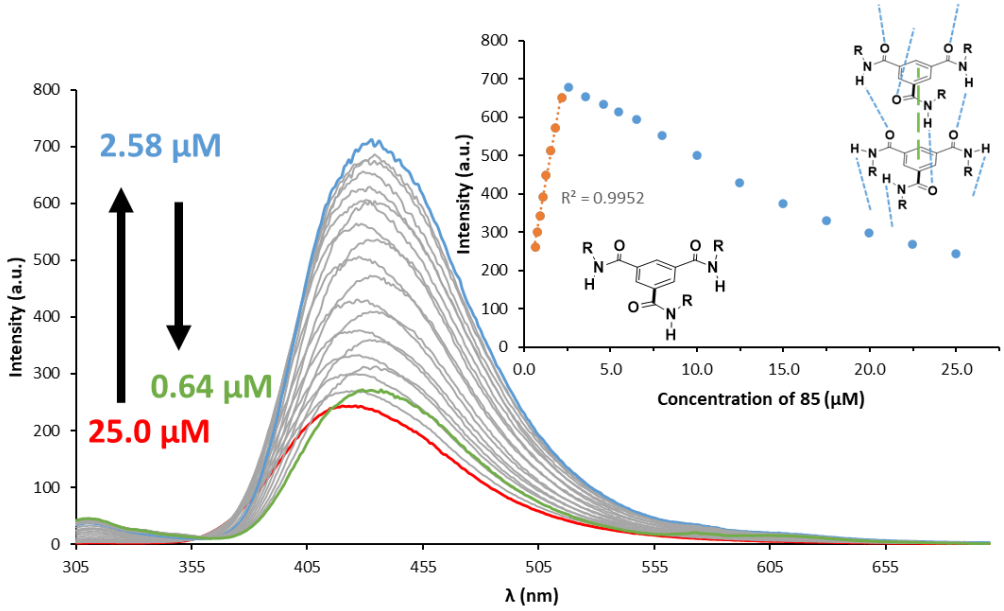

Figure 4-14 Changes in the fluorescence intensity (λ_{ex} = 280 nm) of **85** upon dilution in MeOH ((25.00–0.64) × 10^{-6} M). Insert: Fluorescence intensity at 423 nm in function of the concentration with a proposed model of interactions (hydrogen bonding represented by a blue dashed line, π-π stacking represented by a green dashed line).[29]

The intensity profile shown as an insert in Figure 4-14, for λ = 423 nm, confirms that in the range of 2.58 × 10^{-6} M to 0.64 × 10^{-6} M the decrease of the fluorescence intensity is linear and could indicate that within this range **85** is in solution as a single molecule. While in the range of 25.00 × 10^{-6} M to 2.58 × 10^{-6} M, the decrease of intensity would indicate the presence of the inner filter effect and the formation of supramolecular polymers through three-fold hydrogen bonding and π-π stacking as shown in the insert in Figure 4-14 which corroborates with previously obtained results.[29] Interestingly, another terpyridine tripodal compound synthesised in the Gunnlaugsson group that contains an alanine unit between the core and the arm of the tripod displayed similar behaviour.[233] However, the maximum of the concentration where the compound is behaving as a single molecule is below 6.5 × 10^{-6} M, demonstrating that expanding the arm of the tripod, even with moieties capable of hydrogen bonding results in a decrease of the capacity of the ligand to aggregate in solution.[233]

To further investigate the formation of supramolecular polymers at high concentration, the absorbance of **85** at 1.0 × 10^{-5} M in MeOH was recorded at various temperatures. As seen in Figure 4-15, upon increasing the temperature from 10 °C to 60 °C the band at 320 nm is decreasing in absorbance, while the band centred at λ_{max} = 280 nm remains the same. However, when cooling the sample from 60 °C to 10 °C the changes in the shoulder at 320 nm are minor and the band centered at λ_{max} = 280 nm increases, demonstrating an irreversible change in the aggregation formation as a function of temperature. This could be due to the formation of a self-assembly that is kinetically trapped and is not necessarily reversible over the time of the experiment, but further experiments would be required to demonstrate it.

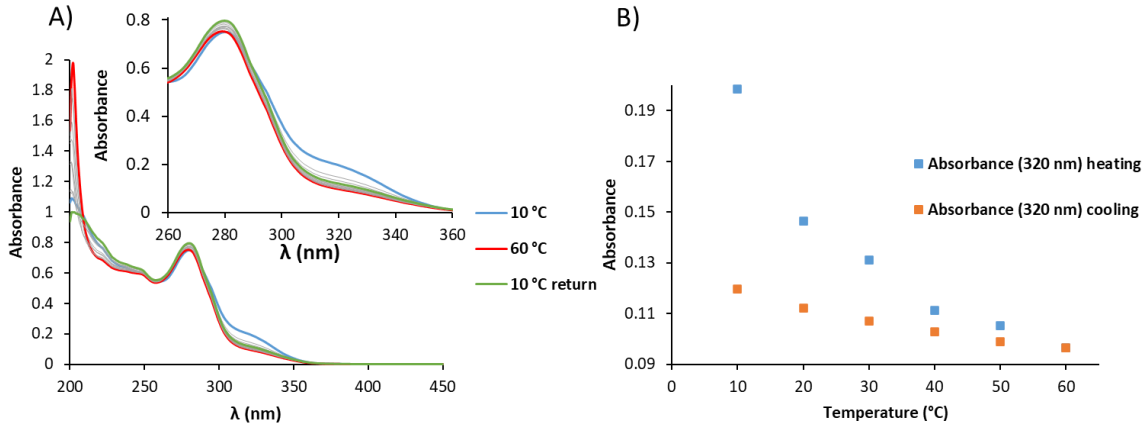

Figure 4-15 A) Changes in the absorption spectra of **85** (c = 1.0 × 10^{-5} M) in MeOH in the function of the temperature. B) Plot of the absorption at λ = 320 nm in the function of the temperature during both the heating and cooling processes.

The study of the fluorescence spectra as a function of temperature reveals a 5 nm hypsochromic shift upon the entire heating-cooling process, demonstrating an opposite response than upon the dilution of the sample, revealing a potential change in the assembly (see appendix). Interestingly, the excitation spectra did not show any significant changes in the band position as a function of the temperature (see appendix).

As the objective of this Chapter is to investigate and elucidate the relationship between the phenomenon observed in solution and in the gel states it was decided to use a solution of **85** at the concentration of 1.0 × 10^{-5} M in MeOH, for the following spectroscopic studies in the presence of various lanthanides (Ln = La, Sm, Gd, Eu, Tb, Yb, Lu). This concentration was used in the previously published work where the self-assembly between **85** with Eu(III) was investigated allowing for the direct comparison to that study.[29] Here, on one hand, it was possible to relate to the previous work and compare the binding constant values for the range of different lanthanides *vs* their ionic radius, but also thanks to the

dilution study performed here where the formation of polymeric units of **85** could be seen and determine more precisely the range where the aggregation between ligand molecules begin. Therefore, it will be possible to relate these solution studies to what can be observed in the gel state.

The seven lanthanide(III) ions were selected in a way that the entire row of the lanthanide was covered, with La(III) being the largest lanthanide, Sm(III), Eu(III), Gd(III) and Tb(III) are the intermediate-sized lanthanides while Yb(III) and Lu(III) represent the smallest ones.[234] As described in Chapter 1, Piguet, Bünzli and others have demonstrated that for some binding unit, size discrimination is displayed when studying the binding constants of the complexes *vs* the ionic radius and it was decided to investigate if the **85** is capable of size discrimination and if it is possible to affect the properties of the gel to a varying degree depending on the size of the Ln(III) ion used.

For all the titrations described in this chapter the $LnCl_3 \cdot 6H_2O$ were used but the notation $LnCl_3$ will be used through the discussion to simplify the description. The first titration presented in this chapter is the titration with $EuCl_3$ which emits in the red part of the electromagnetic spectrum, and often yields highly emissive complexes, which was carried out first to control that we obtain a similar value of binding constant than the ones previously reported.[29] Then the titration of the other luminescent lanthanide ions which represent the mid-sized lanthanide(III) ions such as $TbCl_3$ which emit in the green part of the visible range, similarly to Eu(III) ions often yield a highly emissive complex, and $SmCl_3$, which emits in the orange part of the visible spectrum will be described, followed by $GdCl_3$ which is rarely successfully sensitized. The titration with the $LaCl_3$ and $LuCl_3$, which are non-emissive Ln(III) ions and represent respectively the largest and the smallest ionic radius of the lanthanide series, are being described, followed by the results of the titration of $YbCl_3$ which is NIR-emissive and is the second smallest ionic radius in the lanthanide series.

A summary and a comparison of the cumulative binding constants obtained for each titration *vs* the ionic radius of the Ln(III) ions are then discussed.

4.3.2 UV-vis absorption and luminescence emission titrations of 85 in MeOH solution with $EuCl_3$

The trivalent europium ion can be characterised by its intense emission in the red region of the electromagnetic spectrum. It also has a relatively large energy gap and is, therefore, less prone to non-radiative deactivation. The very sharp emission bands, notably its hypersensitive transition $^5D_0 \rightarrow {}^7F_2$ and the relative intensity of each band allow to better

understand the coordination environment of the ion. Eu(III) ion sensitization has attracted a significant amount of research in the past, leading to the development of highly stable and luminescent complexes which display long emission lifetime in the ms-range which is of great interest for biological study, sensing array,[235] the fabrication of lasers,[87] white light-emissive complexes,[18,236] LEDs, and many other applications.[104] Metal directed self-assembly studies of **85** were carried out by titrating the ligand with $EuCl_3$ in MeOH at a concentration of 1×10^{-5} M ($EuCl_3 \cdot 6H_2O$ was used but to simplify the notation $EuCl_3$ is used throughout the text to explain the results of the titrations). A sample of 2.5 mL of ligand at 1×10^{-5} M was prepared and titrated against known volumes of standard solutions of $EuCl_3$ between 0 to 9 equivalents. Both UV-vis absorption and luminescence spectra were recorded after each addition and the titration was repeated in triplicate to ensure reproducibility. In all measurements, an excess of metal ion was added to ensure the saturation of all the binding sites following the procedure described previously.[29]

The changes in the absorption spectrum of the ligand upon binding to Eu(III) ions in MeOH at 1×10^{-5} M are shown in Figure 4-16. The addition of Eu(III) ions to **85** resulted in a hypochromic and bathochromic shift of 5 nm for the band centred at 280 nm and attributed to $\pi \rightarrow \pi^*$ transition of the terpyridine moiety. Simultaneously, the band centred at 280 nm shifted and broadened with the increase in absorbance of the shoulder at 325 nm indicating the coordination of the terpyridines by Eu(III) ions. The binding isotherm of the different wavelengths (Figure 4-16B) displays a plateau after the addition of 1 equivalent of Eu(III) ions indicating the changes of the equilibrium in solution and the evolution of the formation of different species. All the changes observed in the absorption spectra are in good agreement with the data already published confirming the reproducibility of the titration.[29]

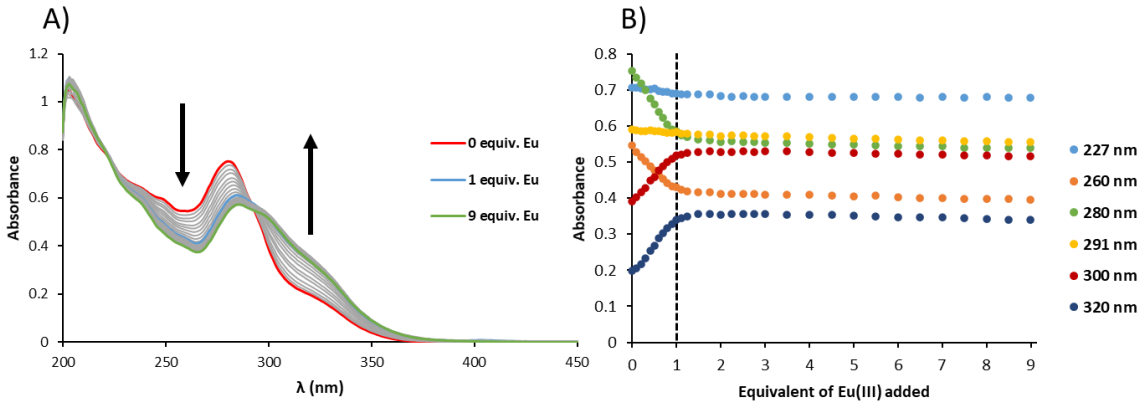

Figure 4-16 A) Changes in the absorption spectrum of **85** (1×10^{-5} M) upon titrating with $EuCl_3$ (0→9 eq) in MeOH at 22 °C. B) Binding isotherms for the complexation of **85** at various wavelengths.

While following the changes in the absorption of the ligand, the changes in the fluorescence spectra of **85** upon addition of $EuCl_3$ were also monitored. The excitation at λ = 280 nm which corresponds to the terpyridine band gave rise to a fluorescence emission with λ_{max} = 425 nm. The sequential addition of Eu(III) ions leads to a decrease in the fluorescence intensity until the addition of 1 equivalent of metal ions as can be seen in the isotherm plot (Figure 4-17B), and is also accompanied by a bathochromic shift to λ_{max} = 435 nm after addition of 1 equivalent of $EuCl_3$. Further addition of Eu(III) ions produce an increase in the fluorescence intensity until the addition of 9 equivalents. By comparing these results to those obtained previously,[29] it is possible to see that the fluorescence follows the same trend with a decrease of fluorescence intensity until the addition of 1 equivalent followed by an increase of intensity. However, the extent of this fluorescence quenching is considerably lower in the case herein.

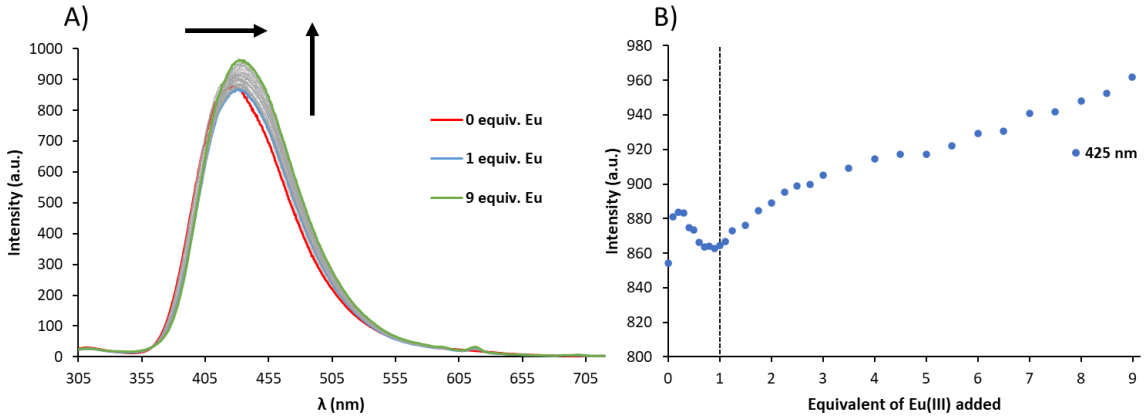

Figure 4-17 A) Changes in the fluorescence spectrum (λ_{ex} = 280 nm) of **85** (1×10^{-5} M) upon titrating with $EuCl_3$ (0→9 eq) in MeOH at 22 °C. B) Binding isotherm for the complexation of **85** at 425 nm.

Generally, the quenching of the fluorescence of the ligand upon addition of Eu(III) ions is an indication that sensitization of the metal-centred $^5D_0$ excited state occurs, through energy transfer from the ligand upon coordination of Eu(III) to the terpyridine moieties. The fact that here the fluorescence quenching is much lower could be interpreted as a less efficient energy transfer. This may occur due to a discrepancy in the number of subunits within supramolecular polymers formed between **85** molecules in solution which leads to the difference in the energy transfer processes happening between ligand molecules and Eu(III) ions, but this will need to be investigated in more detail later in this chapter.[237,238]

The excitation spectra of **85** (λ_{em} = 420 nm) upon addition of Eu(III) ions were also recorded and confirmed the trend followed by the fluorescence intensity which is a decrease of intensity from 0 to 1 equivalent of Eu(III) followed by an increase until the addition of 9

equivalent of Eu(III) ions. The fluorescence excitation spectra upon addition of $EuCl_3$ is available in the appendix.

The phosphorescence emission spectra were also recorded as the delayed Ln-emission upon excitation at λ_{ex} = 280 nm and the results are shown in Figure 4-18. Upon addition of $EuCl_3$, a gradual increase in the Eu(III)-centred emission was observed until the addition of 1 equivalent of Eu(III) ions, allowing the observation of the $^5D_0 \rightarrow ^7F_{0\text{-}4}$ transitions respectively at 580, 595, 618, 650 and 697 nm especially with the hypersensitive transition $^5D_0 \rightarrow ^7F_2$ being the most intense band because it obeys the selection rules.[104] The spectra recorded do not allow a detailed analysis to be performed but several elements can be extracted from it. Gratifyingly, the presence of the $^5D_0 \rightarrow ^7F_0$ indicates that the Eu(III) ion occupies a site with C_{nv}, C_n or C_s symmetry which is often the case for low symmetry complexes.[104] Also, it is important to note that the $^5D_0 \rightarrow ^7F_0$ transition appears as a single sharp symmetric band, possibly suggesting that the Eu(III) ions have all the same coordination environment. The $^5D_0 \rightarrow ^7F_1$ transition appears to be split in two which confirms the C symmetry around an axis going through the complex.[104] The changes in the intensity are in good agreement with the observed trend in the fluorescence spectra indicating that the energy transfer from the terpyridine to the Eu(III) is less efficient after the addition of more than 1 equivalent of metal ion. This could be explained by the formation of a less emissive species. This could be due to the coordination of MeOH inducing O−H vibrational quenching.

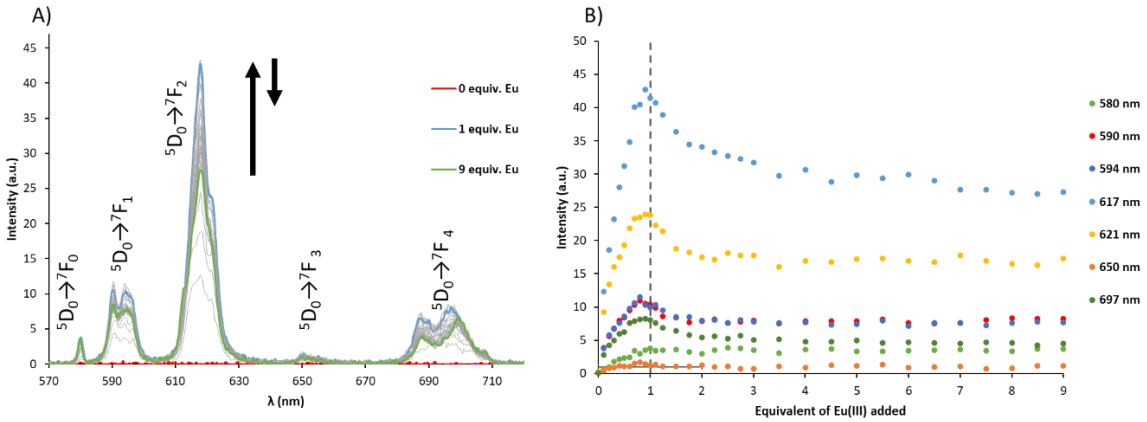

Figure 4-18 A) Changes in the phosphorescence emission spectrum (λ_{ex} = 280 nm) of **85** (1×10^{-5} M) upon titrating with $EuCl_3$ (0→9 eq) in MeOH at 22 °C. B) Binding isotherms for the complexation of **85** at various wavelengths.

Moreover, the observations made on the changes in the Eu(III)-centered emission are in good agreement with the previous observations.[29] The excitation spectra of phosphorescence emission recorded on the more intense band at λ = 618 nm resulted in an

identical spectrum to the absorption spectra as can be observed in the appendix. This confirms that the excitation of the Eu(III)-centred emission occurs through the energy transfer from the ligand which is acting as an antenna.[99]

The excitation spectra were recorded during the entire titration and are shown in the appendix. No obvious shift in the wavelengths of the bands was observed, while the relative intensity of the excitation spectra decreased through the addition of 0 to 1 equivalent of Eu(III) ions and slightly increased over the addition of the remaining 8 equivalents.

Through the titration of **85** with $EuCl_3$, the Eu(III)-centered luminescence lifetime was determined by fitting the Eu(III) excited state decay profiles of the most intense peak (λ = 618 nm) to a biexponential decay and the calculated values are summarised in Table 4-1 and corresponds to the average of triplicate measurements with the errors on the lifetimes corresponding to the standard deviation of the three values obtained. The initial lifetime after the addition of 0.1 equivalent of Eu(III) ions were estimated as 0.58 ms and 1.52 ms for τ_1 and τ_2 respectively while the addition of more equivalents of Eu(III) ions resulted in a gradual decrease of the lifetime reaching 0.24 and 0.49 ms for τ_1 and τ_2 respectively after the addition of 9 equivalents of Eu(III) ions. The gradual decrease of the lifetime of the Eu(III)-centred luminescence decays over the addition of the Eu(III) ions may be attributed to a change in the coordination environment of the Eu(III) ion with the binding of solvent molecules upon the dechelation of terpyridine units.[99] This assumption is further supported by the results, described in the following paragraph, of the fitting of the changes observed through the titration by non-linear regression analysis, allowing to determine the formation of the species in solution through the titration.

Table 4-1 Lifetime values of Eu(III)-centred luminescence decays during the titration of **85** (1×10^{-5} M) with $EuCl_3$ in MeOH.

Equivalent of Eu(III)	τ_1, ms	A_1 (%)	τ_2, ms	A_2 (%)
0.1	0.58 ± 0.01	24.8	1.52 ± 0.01	75.2
0.5	0.50 ± 0.01	40.6	1.24 ± 0.01	59.4
1	0.44 ± 0.01	44.5	0.89 ± 0.01	55.5
1.5	0.38 0.01	39.1	0.73 ± 0.02	60.9
3	0.35 ± 0.02	39.5	0.64 ± 0.02	60.5
6	0.29 ± 0.02	23.1	0.54 ± 0.01	76.9
9	0.24 ± 0.03	13.8	0.49 ± 0.01	86.2

4.3.3 Non-linear regression analysis of the UV-vis, fluorescence and Eu(III)-centred emission titrations data

An apparent stoichiometry of 1:1 (metal to ligand) could be observed during the titration but the evolution of the fluorescence and phosphorescence intensities suggested that even after the addition of 3 equivalents of Eu(III) ions other M:L complexation ratios were occurring. To gain further insight into the stoichiometry of the species in the solution, the changes in absorption, fluorescence and phosphorescence were analysed using a non-linear regression analysis program SPECFIT.[239-242] By using a combination of matrix manipulation, the equilibrium constant equations, the law of mass action and non-linear least square regression method, the global stability constant β (also known as a binding constant for the formation of complexes) were determined. For example, the binding constant $\beta_{n:m}$ corresponds to the global stability constant of a complex M_nL_m composed of n metals (M) and a number m of ligands (L) that is formed following the equilibrium equations:

$$nM + mL \overset{\beta_{n:m}}{\rightleftharpoons} M_nL_m \quad \text{where } \beta_{n:m} = \frac{[M_nL_m]}{[M]^n[L]^m}$$

It can be detailed in stepwise equilibrium equations describing $\beta_{n:m}$ as the product of the stepwise constants: $\beta_{n:m} = K_{1:1} \times K_{1:2} \times \ldots \times K_{n:m}$.

$$M + L \rightleftharpoons ML \quad \text{where } K_{1:1} = \frac{[ML]}{[M][L]}$$

$$ML + M \overset{K_{2:1}}{\rightleftharpoons} M_2L \quad \text{where } K_{2:1} = \frac{[M_2L]}{[ML][M]}$$

$$\vdots$$

$$M_{n-1}L_m + M \overset{K_{n:m}}{\rightleftharpoons} M_nL_m \quad \text{where } K_{n:m} = \frac{[M_nL_m]}{[M_{n-1}L_m][M]}$$

Normally the stability constants are quoted as logarithmic values as $\log\beta_{n:m}$, and therefore will be quoted in this way in this Thesis.

The first step in the process of fitting the data using non-linear regression analysis is to determine the number of species in solution at any given time. To do so, the number of significant eigenvectors is determined by analysing the changes in the spectra using the evolving factor analysis. This suggested that 3 species are absorbing in solution through the titrations. The first binding model proposed to fit the data was the formation of 1:1, 2:1 and 3:1 M_x:L_y species but the convergence of the data was not achieved in this case suggesting

that this equilibrium was not occurring in solution. This can be explained by the fact that at 1×10^{-5} M, **85** is forming supramolecular polymers as we have shown above, and therefore, we can expect more complex self-assemblies being formed in solution as was proposed previously for this system such as the formation of 1:1 and 3:2 species.[29] Moreover, Dr. Savyasachi demonstrated in his PhD thesis within the Gunnlaugsson group, for similar tris-terpyridine tripodal compounds, that to obtain a formation of the 1:1, 2:1 and 3:1 species, it was necessary to carry out the titration in the concentration range where the molecule was dilute enough to be in solution as a single molecule which is in the range of 10^{-6} M which also corroborates with our dilution experiment (Figure 4-13).[233] The changes in the absorption spectra were then fitted to the formation of 1:1 and 3:2 M:L complexes using the metal as a coloured species giving satisfactory fit of the calculated data to the experimental binding isotherm as shown in Figure 4-19B.

The convergence of the fit for the proposed binding model was determined by the recalculated spectra, the correspondence of the experimental to the calculated binding isotherms and convergence parameters mainly SigmaY (a table of the SigmaY values is available in the appendix for all the titrations presented in this Chapter). The recalculated absorption spectra are shown in Figure 4-19A and they correspond to the experimental data confirming the formation of 1:1 and 3:2 M:L complexes as well as the presence of **85** with the most pronounced absorption band at 280 nm while broadening of this band was observed for the 1:1 and 3:2 complexes with a more pronounced shoulder at 325 nm.

The speciation-distribution diagram (Figure 4-19C) describes the evolution of each species in solution through the addition of Eu(III) ions. As can be seen here upon the addition of $EuCl_3$, the formation of Eu:L species is the dominant event occurring, reaching a maximum formation of 81% at 1 equivalent of Eu(III). This is in agreement with the previously published results.[29] The addition of more than 1 equivalent of Eu(III) ions results in the formation of a second species, the previously mentioned Eu_3:L_2, with the simultaneous consumption of Eu:L species, demonstrating the possibility to shift the equilibrium process towards the formation of second species by increasing the concentration of Eu(III) ions reaching a maximum of 81% of Eu_3:L_2 after addition of 9 equivalents of $EuCl_3$.

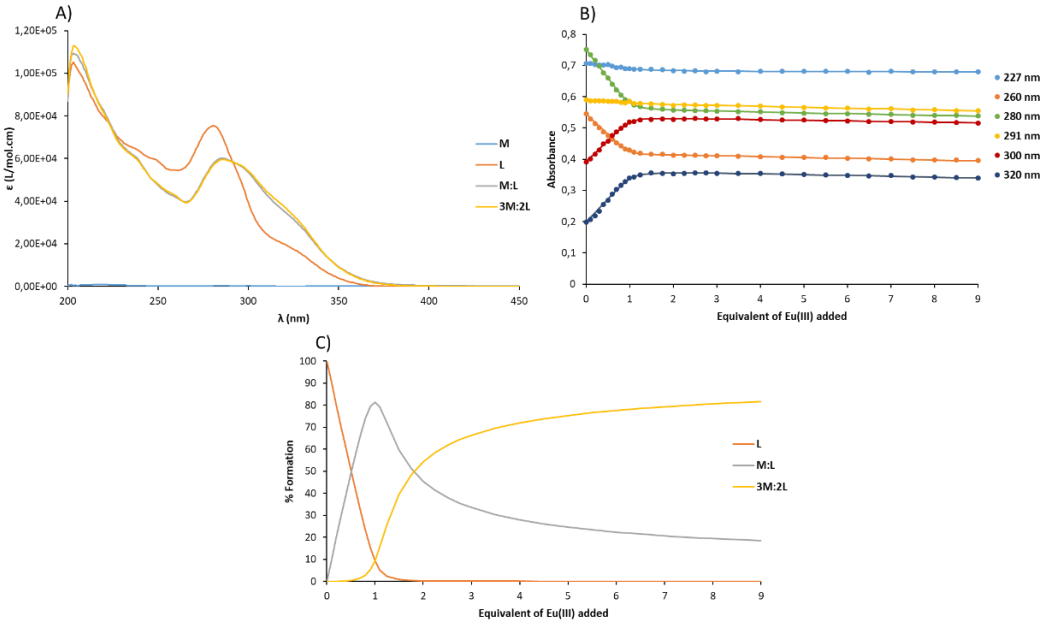

Figure 4-19 A) Recalculated absorption spectra, B) experimental binding isotherms (dots) for the UV-vis titration and their corresponding fit (line), C) speciation-distribution diagram obtained from the fitting of UV-vis titration of **85** (1×10^{-5} M) with $EuCl_3$ in MeOH at 22 °C using SPECFIT.

Using the data collected and the result of the non-linear regression analysis, the binding constants were obtained as the cumulative values for these species obtained. In the case of Eu:L species, the corresponding binding constant is $\log\beta_{1:1} = 7.5 \pm 0.3$ while for Eu_3L_2 species the binding constant obtained was determined as $\log\beta_{3:2} = 25.5 \pm 0.6$. Gratifyingly, the values obtained through the triplicate experiment for the binding constants are in good agreement with the previously reported values which are $\log\beta_{1:1} = 7.3 \pm 0.2$ and $\log\beta_{3:2} = 24.9 \pm 0.5$ demonstrating a good reproducibility.[29]

Non-linear regression analysis was also carried out on the fluorescence emission data obtained during the titration. The evolving factor analysis determined the presence of at least two emissive species in solution. The data obtained were fitted to the same stoichiometric species than for the absorption data which described the formation of 1:1 and 3:2 M:L complexes. The obtained recalculated spectra in Figure 4-20A, shows the 3:2 species with higher intensity of ligand-centred fluorescence and the shift in fluorescence maxima for the 1:1 and 3:2 complexes being in good agreement with the experimental data. The changes in the fluorescence emission spectra were fitted again to the formation of 1:1 and 3:2 M:L complexes and it resulted in a satisfying fit of the recalculated to the experimental data (Figure 4-20B). The speciation-distribution diagram obtained (Figure 4-20C), depicts the formation of 1:1 species upon addition of Eu(III) ions until 1.2 equivalents reaching a maximum of 99%. This is followed by the consumption of the 1:1 stoichiometry to form the

3:2 complexes until the addition of 9 equivalents of Eu(III) ions is reached, with a maximum of 12% formation. The discrepancy in speciation-distribution diagrams between the analysed data from absorption and fluorescence titrations can be explained by the presence of the quenching processes occurring between **85** ligand and Eu(III) ions which is reflected in the course of the fluorescence titration rather than the changes in the absorption one. The non-linear regression analysis programme can not fully analyse these processes, and hence, the variation in the percentage of formed species inevitably occurs. However, the binding constant obtained for this fitting gave $\log\beta_{1:1} = 7.7 \pm 0.5$ and $\log\beta_{3:2} = 23.4 \pm 0.7$, for the 1:1 and 3:2 complexes, respectively these again are very close to the values obtained with the fitting of the absorption data, as well as previously reported results confirming the validity of such global analysis approach.

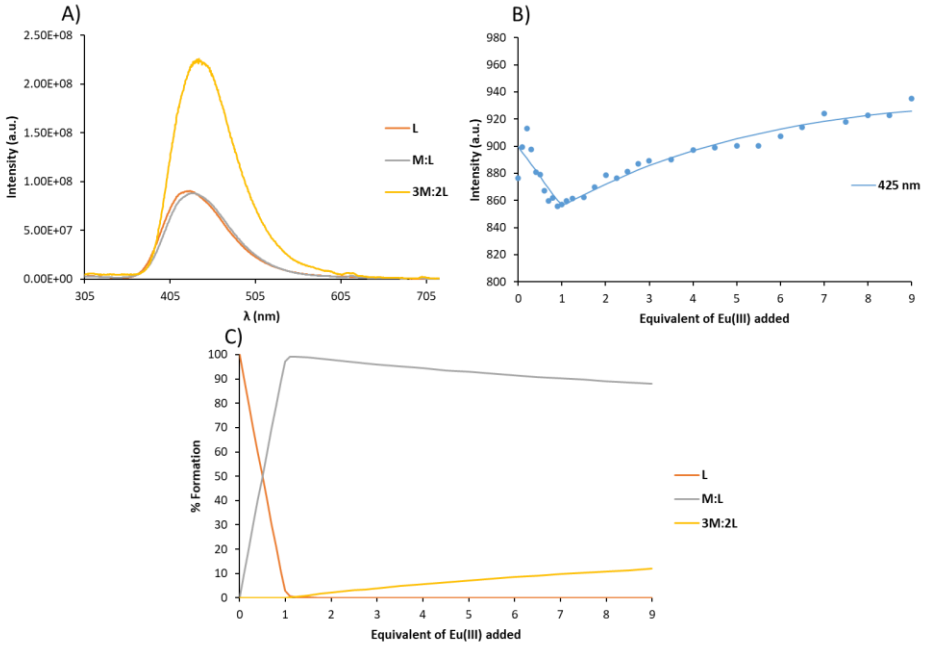

Figure 4-20 A) Recalculated fluorescence spectra, B) experimental binding isotherms (dots) for the fluorescence titration and their corresponding fit (line), C) speciation-distribution diagram obtained from the fitting of the fluorescence titration of **85** (1×10^{-5} M) with $EuCl_3$ in MeOH at 22 °C using SPECFIT.

Following the successful fitting of the fluorescence data, the analysis of the Eu(III)-centred emission was attempted. The evolving factor analysis determined the presence of three emissive species during the titration. The data from the phosphorescence titration were successfully fitted to the formation of 1:1 and 3:2 M:L complexes by using the ligand as coloured species. The recalculated spectra obtained from the fitting were in good agreement with the experimental data (Figure 4-21A). They also show that the 1:1 species were more emissive for the Eu(III)-centred emission than the 3:2 species which is in good correlation

with the results obtained from the fluorescence titration, where 1:1 species displayed a lower intensity of fluorescence due to a better energy transfer from **85** to the Eu(III) centre.

The changes in the phosphorescence spectra were also fitted to the formation of the 1:1 and 3:2 complexes, and gave a satisfying fit from the recalculated data to the experimental data. The speciation-distribution diagram follows the same trend as the one obtained from the fitting of the absorption data. Indeed, the predominant species until the addition of 1 equivalent of Eu(III) ions was the 1:1 complex reaching a maximum of 46%. While soon after the addition of one equivalent of Eu(III), a drastic increase in the formation of 3:2 species was observed simultaneously to the consumption of 1:1 species until the addition of 9 equivalents of Eu(III) ions; reaching a maximum of 94% for the 3:2 species and 6% of 1:1. The binding constant obtained for this fitting $\log\beta_{1:1} = 6.7 \pm 0.1$ and $\log\beta_{3:2} = 25.9 \pm 0.3$ for the 1:1 and 3:2 complexes, respectively. The value obtained for the formation of 1:1 species is slightly lower than the one obtained from the fitting of fluorescence and absorption spectra but this phenomenon was already observed previously, and again, can be attributed to the presence of alternative quenching processes reflected in the changes within Eu(III)-centred emission titration data that were not fully considered by the non-linear regression analysis software. Gratifyingly, the binding constants obtained are very close to the previously reported results and the very prominent changes observed in Eu(III)-centred emission allows for further insight into the binding processes occurring within this system.

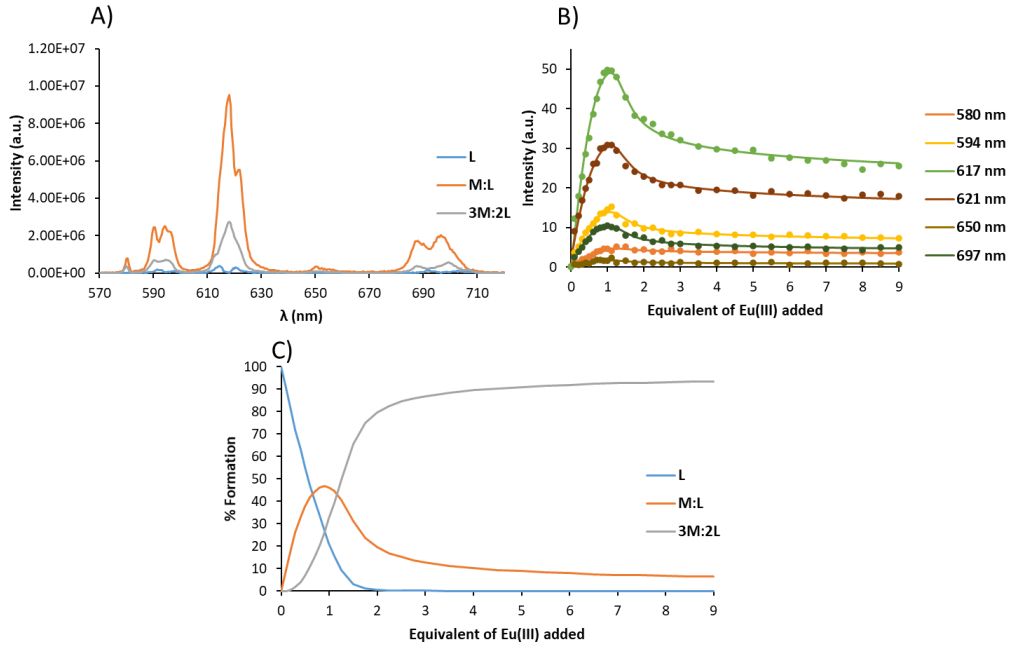

Figure 4-21 A) Recalculated Eu(III)-centred emission spectra, B) experimental binding isotherms (dots) for the phosphorescence titration and their corresponding fit (line) at various wavelength, C) speciation-distribution diagram obtained from the fitting of the Eu(III)-centred emission titration of **85** (1×10^{-5} M) with $EuCl_3$ in MeOH at 22 °C using SPECFIT.

By comparing the results obtained from the fitting of absorption, fluorescence and phosphorescence titrations, it is possible to see that a similar trend is followed in the three cases with first the predominant formation of 1:1 species until the addition of 1 equivalent of Eu(III) ions followed by the formation of 3:2 complexes simultaneously with the consumption of 1:1 species until the addition of 9 equivalents of Eu(III) ions. Because of the discrepancies in the speciation-distribution diagrams obtained from the fitting, it is not possible to draw a conclusion on the extent of the formation of each species during the titration. However, the binding constants obtained with the fitting of each experiment, which are summarised in Table 4-2, agreed closely (except for the formation of 1:1 species with the phosphorescence fitting) on the stability of each species formed in solution and are also in agreement with the previously reported data.[29]

Table 4-2 The summary of the binding constants obtained through fitting the data from absorption and emission titrations of **85** (c= 1×10^{-5} M) with $EuCl_3$ in MeOH at 22 °C using SPECFIT.

	Absorbance		**Fluorescence**		**Phosphorescence**	
	$\log\beta_{1:1}$	$\log\beta_{3:2}$	$\log\beta_{1:1}$	$\log\beta_{3:2}$	$\log\beta_{1:1}$	$\log\beta_{3:2}$
$EuCl_3$	7.5 ± 0.3	25.5 ± 0.6	7.7 ± 0.5	23.4 ± 0.7	6.7 ± 0.1	25.9 ± 0.3

Following the encouraging results obtained by the reproducibility of the titration of **85** in MeOH with $EuCl_3$, it was decided to proceed to the titrations and fitting of the data obtained with other luminescent lanthanide ions such as $TbCl_3$ and $SmCl_3$ and $GdCl_3$ whose emission is rarely successfully sensitized. Subsequently followed by the titrations of the $LaCl_3$ and $LuCl_3$, which are non-emissive Ln(III) ions, followed by the results of the titration with $YbCl_3$ which is NIR-emissive. The results from those titrations are described below.

4.3.4 UV-vis absorption, luminescence and non-linear regression analysis of 85 titrations with $TbCl_3$ in solution

The trivalent terbium ion can be characterised by its line-like emission in the green region of the electromagnetic spectrum. Tb(III) has a relatively large energy gap and is, therefore, less prone to non-radiative deactivation, and along with Eu(III) ion, are the two most luminescent lanthanides in the visible range. The Tb(III) ion sensitization has attracted a significant amount of research, leading to the development of highly stable and luminescent complexes, with high sensitivity toward dissolved oxygen, which display long emission lifetimes of great interest for biological studies,[243,244] acting as oxygen sensors[245] and emissive layers in OLEDs to only name a few.[246]

Metal directed self-assembly studies of **85** were carried out by titrating the ligand with $TbCl_3$ in MeOH at a concentration of 1×10^{-5} M ($TbCl_3 \cdot 6H_2O$ was used but to simplify the notation $TbCl_3$ is used through the text to explain the results of the titrations). A sample of 2.5 mL of ligand at 1×10^{-5} M was prepared and titrated against known volumes of standard solutions of $TbCl_3$ between 0 to 9 equivalents. Both UV-vis absorption and luminescence spectra were recorded after each addition and the titration was triplicated to ensure reproducibility. In all measurements, an excess of metal ion was added to ensure the saturation of all the binding sites.

As shown in Figure 4-22A, the addition of $TbCl_3$ to the solution of **85** resulted in a hypochromic and bathochromic shift with the simultaneous broadening of the band centred at 280 nm and attributed to the $\pi \rightarrow \pi^*$ transition of the terpyridine moiety. The shoulder forming at 325 nm during the addition of Eu(III) ions shown previously is also observed in this case with the addition of Tb(III) ions confirming the coordination of the terpyridine moieties by metal ions. Similarly to the titration with Eu(III), the binding isotherms of the changes in the absorption spectra of **85** here (Figure 4-22D) displays a plateau after the addition of 1 equivalent of Tb(III).

The excitation at λ = 280 nm which corresponds to the terpyridine band gave rise to a fluorescence emission with λ_{max} = 425 nm. Upon addition of Tb(III) ions, a bathochromic shift to λ_{max} = 430 nm together with a decrease in the fluorescence intensity was observed until 1 equivalent of Tb(III) ions is added (Figure 4-22B). Simultaneously it was possible to observe an increase in the intensity at 490, 545, 595 and 622 nm bands which correspond to the $^5D_4 \rightarrow {}^7F_{6-3}$ transitions of Tb(III) ions. These changes can be further analysed by looking at the experimental binding isotherms shown in Figure 4-22E. Further addition of Tb(III) from 1 up to 9 equivalents led to another 5 nm bathochromic shift of the λ_{max} along with an increase in intensity while the $^5D_4 \rightarrow {}^7F_{6-3}$ transitions of Tb(III) reach a plateau.

The delayed Tb(III)-centred emission was also recorded upon excitation at λ_{ex} = 280 nm and the results are shown in Figure 4-22C. Upon addition of Tb(III) to the solution of **85**, the apparition of sharp bands at 490, 545, 595 and 622 nm which corresponds to the $^5D_4 \rightarrow {}^7F_{6-3}$ transitions of Tb(III) ions was observed until the addition of 1 equivalent of Tb(III) ions, after which a plateau was reached.

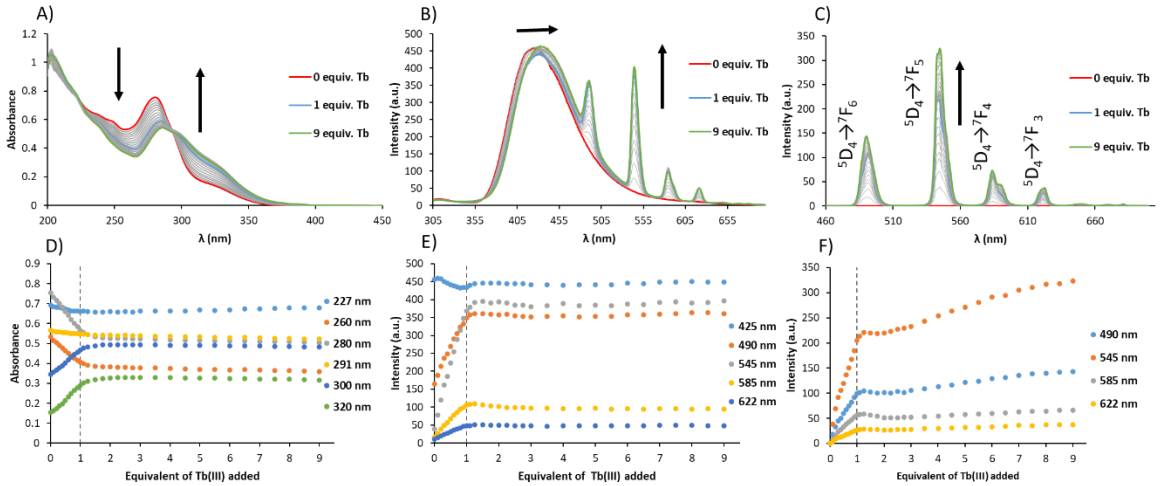

Figure 4-22 Changes in A) the absorption, B) fluorescence, C) Tb(III)-centred emission spectra of **85** (1×10^{-5} M) upon titrating with $TbCl_3$ (0→9 eq) in MeOH at 22 °C. Experimental D) absorption, E) fluorescence and F) Tb(III)-centred emission binding isotherms for the complexation of **85** at various wavelengths upon addition of $TbCl_3$.

Following the titration, fitting of the data using non-linear regression analysis was carried out using SPECFIT. The number of significant eigenvectors determined by analysing the changes in the absorption spectra is of potentially four species absorbing in solution. The changes in the absorption spectra were then fitted to the formation of 1:1 and 3:2 M:L complexes giving satisfying fits of the calculated data to the experimental binding isotherm as shown in Figure 4-23B.

The recalculated absorption spectra are shown in Figure 4-23A corresponds to the experimental one and confirms the formation of 1:1 and 3:2 M:L complexes with **85** being the species absorbing more at 280 nm, while this band is being broadened for the 1:1 and 3:2 complexes with an increase in the absorbance of the shoulder at 325 nm. The speciation-distribution diagram (Figure 4-23C) follows the same trend as seen in the $EuCl_3$ titration with the formation of 1:1 species being the principal event, reaching a maximum of 81% at 1 equivalent of Tb(III). Addition of more equivalents of Tb(III) ions resulted in the formation of 3:2 species with the consumption of 1:1 species reaching a maximum of 82% of Tb_3L_2 at 9 equivalents addition. The binding constants obtained for this fit are $\log\beta_{1:1} = 6.6 \pm 0.3$ and $\log\beta_{3:2} = 22.3 \pm 0.5$ for the 1:1 and 3:2 complexes respectively.

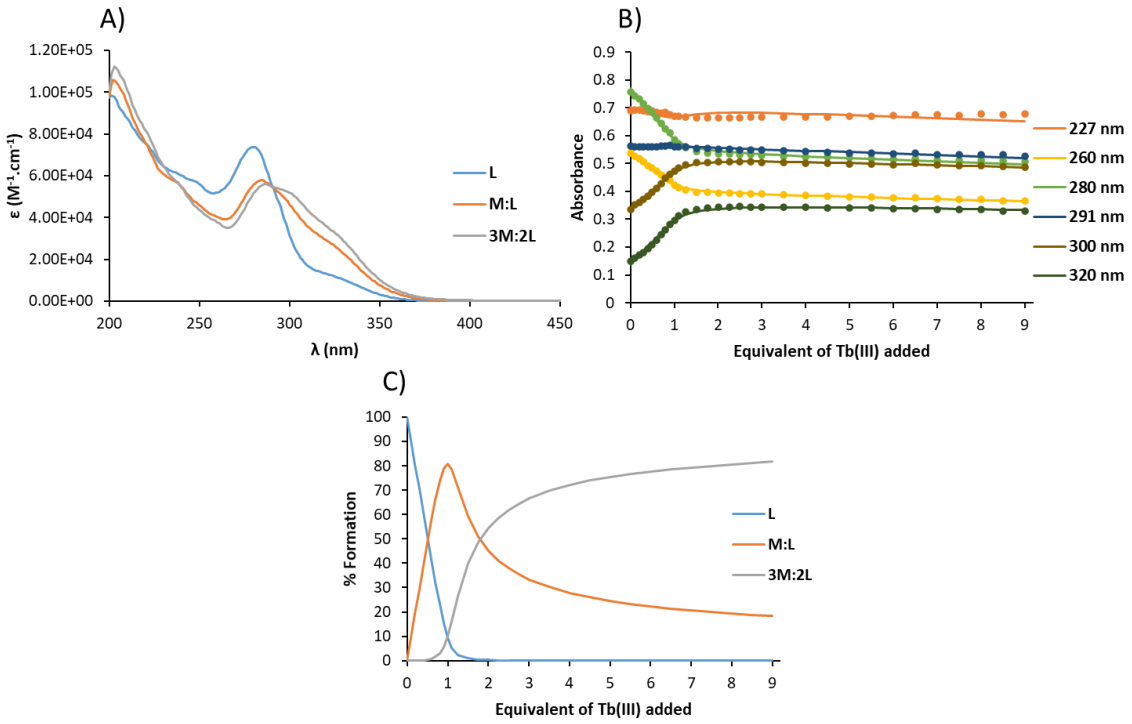

Figure 4-23 A) Recalculated spectra of absorption of L, M:L and 3M:2L, B) binding isotherms (dots) and their corresponding fit (line) and C) the corresponding speciation distribution diagram obtained from the fitting of UV-vis titration of **85** (1×10^{-5} M) with $TbCl_3$ in MeOH at 22 °C using SPECFIT.

Non-linear regression analysis of the changes in the fluorescence was carried out and the number of significant eigenvectors determined by analysing the changes in the fluorescence spectra is four. The experimental data was best fitted when the binding model for the formation of 1:1 and 3:2 M:L complexes was proposed. The recalculated spectra shown in Figure 4-24A are in good agreement with the experimental data, which is further confirmed by the binding isotherms showing an excellent correlation between the experimental data and the recalculated one. Similarly to the $EuCl_3$ titration, the speciation-distribution diagram obtained by fitting of the fluorescence changes is showing some discrepancies compared to the one obtained by fitting of the absorption data. However, it confirms that the main event during the addition of the first equivalent of Tb(III) ions is the formation of the 1:1 TbL complex, reaching a maximum of 97% after addition of 1 equivalent of $TbCl_3$. Further addition of Tb(III) ions resulted in a small decrease in the percentage of 1:1 species simultaneously with the formation of the 3:2 complex, reaching a yield of 86 and 14% for TbL and Tb_3L_2 species respectively. The binding constants obtained for this fitting are $\log\beta_{1:1} = 7.7 \pm 0.3$ for TbL and $\log\beta_{3:2} = 23.4 \pm 0.5$ for Tb_3L_2.

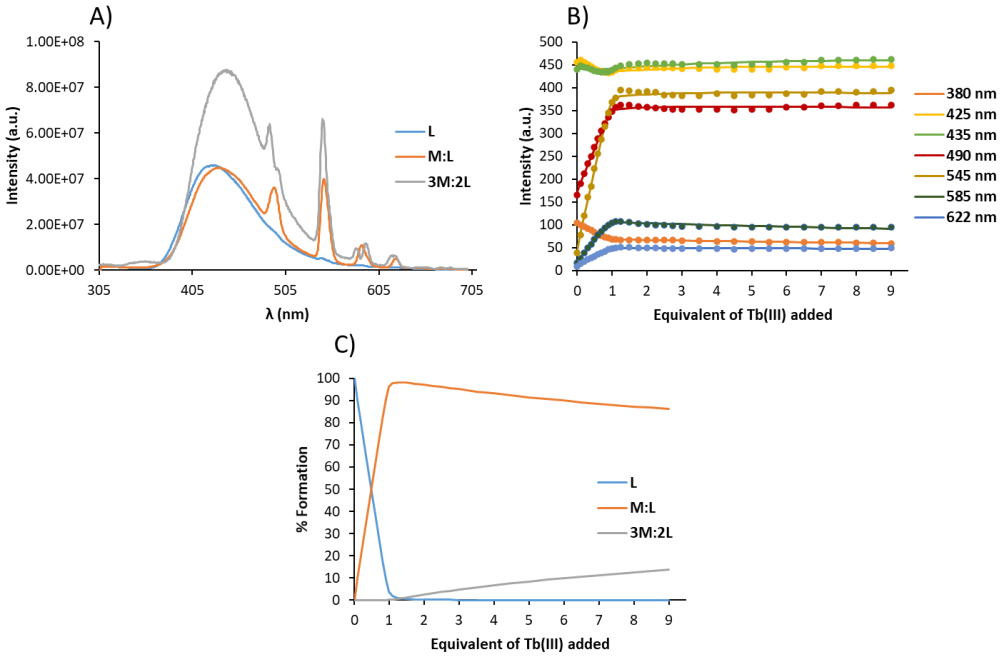

Figure 4-24 A) Recalculated spectra of fluorescence of L, M:L and 3M:2L, B) binding isotherms (dots) and their corresponding fit (line) and C) the corresponding speciation distribution diagram obtained from the fitting of fluorescence titration of **85** (1×10^{-5} M) with $TbCl_3$ in MeOH at 22 °C using SPECFIT.

The analysis of the changes using SPECFIT for the Tb(III)-centred emission spectra using evolving factor analysis revealed the presence of a maximum of four emissive species in solution. Using the metal and the ligand as coloured species gave a satisfying fit of the recalculated to the experimental data as seen in Figure 4-25A. The spectra of 1:1 and 3:2 species are shown in the recalculated spectra (Figure 4-25A) where it is also possible to observe that even if the ligand was considered as coloured its signal is as low as the baseline and that the metal could mostly be considered as noise.

The recalculated spectra are also in good agreement with the results obtained for the phosphorescence, with the TbL species having an emission more intense than Tb_3L_2 species (Figure 4-25B). The speciation-distribution diagram obtained is also very similar to the one obtained with the titration of Eu(III) ions, with the formation of 1:1 complex being the major event until the addition of 1 equivalent of $TbCl_3$, reaching 40% concomitantly with the formation of 3:2 species at 39%. The addition of more $TbCl_3$ led to an increase in the formation of Tb_3L_2 and the consumption of TbL to reach respectively 99% and 1% at the addition of 9 equivalents of Tb(III) ions (Figure 4-25C). Similarly to the Eu(III) ions titration, the discrepancy in the speciation-distribution diagrams can be explained by the presence of the quenching process occurring between **85** and Tb(III) ions. The binding constants obtained for this fitting are $\log\beta_{1:1} = 7.8 \pm 0.3$ for TbL and $\log\beta_{3:2} = 28.5 \pm 0.7$ for Tb_3L_2.

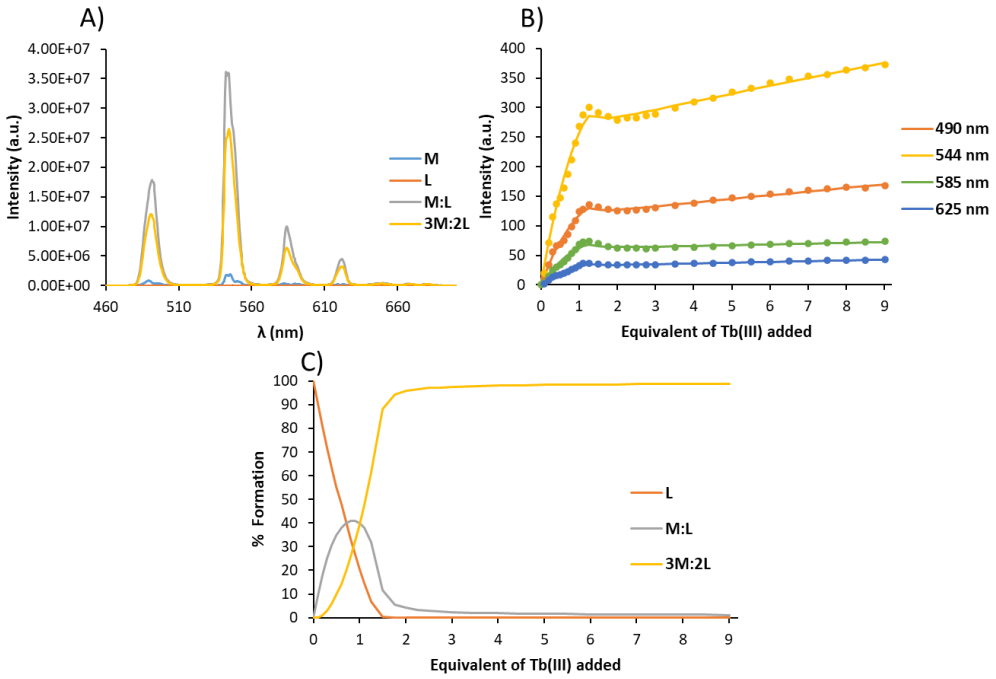

Figure 4-25 A) Recalculated spectra of Tb(III)-centred emission of L, M:L and 3M:2L; B) binding isotherms (dots) and their corresponding fit (line) for the Tb(III)-centred emission spectra with C) the corresponding speciation-distribution diagram obtained from the fitting of Tb(III)-centred emission titration of **85** (1×10^{-5} M) with $TbCl_3$ in MeOH at 22 °C using SPECFIT.

The behaviour observed for the absorption and the Tb(III)-centred luminescence during this titration displayed the same trend as the one previously reported by J. H. Jung *et al.*[157] However, no binding constant nor non-linear regression analysis was carried out in the previously reported work, therefore, no further comparison could be done. The binding constants obtained by the fitting of the absorption, fluorescence and Tb(III)-centred emission titration with $TbCl_3$ are summarised in Table 4-3.

Table 4-3 The summary of the binding constants obtained through fitting the data from absorption and emission titrations of **85** (c= 1×10^{-5} M) with $TbCl_3$ in MeOH at 22 °C using SPECFIT.

	Absorbance		**Fluorescence**		**Phosphorescence**	
	$\log\beta_{1:1}$	**$\log\beta_{3:2}$**	**$\log\beta_{1:1}$**	**$\log\beta_{3:2}$**	**$\log\beta_{1:1}$**	**$\log\beta_{3:2}$**
$TbCl_3$	6.6 ± 0.3	22.3 ± 0.5	7.7 ± 0.3	23.4 ± 0.5	7.8 ± 0.3	28.5 ± 0.7

Having successfully determined the stoichiometry of the different Tb(III) complexes, their speciation-distribution diagram and their binding constants, the titrations and fitting of the data obtained with Sm(III) ions were carried out and are described in the following paragraph.

4.3.5 UV-vis absorption, luminescence and non-linear regression analysis of 85 titrations with $SmCl_3$ in solution

Sm(III) ions are significantly less studied than Eu(III) and Tb(III). However, this ion presents the advantage of being a dual-emitter with emission bands in the orange region of the electromagnetic spectrum but also in the NIR. The major drawback with luminescence properties of this ion is its small energy gap between its emitting state and the next lower state, often leading to an absolute quantum yield smaller than 3% in solution.[247-249] Despite the low quantum yield, samarium complexes find their application as analytical sensors,[109] and in OLEDs.[250,251]

The self-assembly study of **85** in presence of lanthanides ions was pursued by titrating the ligand with $SmCl_3$ in MeOH ($SmCl_3 \cdot 6H_2O$ was used but to simplify the notation $SmCl_3$ is used through the text to explain the results of the titrations). A sample of 2.5 mL of ligand at the concentration of 1×10^{-5} M was prepared and titrated as described before for Tb(III) and Eu(III) against known volumes of the standard solution of $SmCl_3$ between 0 to 9 equivalents to ensure the saturation of all the ligand binding sites. Both UV-vis absorption and the luminescence spectra were recorded after each addition and the titration was triplicated to ensure reproducibility. The results are shown in Figure 4-26. It can be seen from the data obtained that the changes in the absorption spectra upon addition of Sm(III) ions resulted in very similar changes to the ones previously observed with both Tb(III) and Eu(III). Most of the changes occurred before the addition of 1 equivalent of Sm(III) ions and reached a plateau for the remaining of the titration as seen in Figure 4-26D.

The changes in the fluorescence spectra were similar to these obtained upon titration with Tb(III), namely a decrease in the intensity simultaneously with a bathochromic shift of λ_{max} by 5 nm upon addition of 1 equivalent of $SmCl_3$. The following addition of the remaining 8 equivalents of $SmCl_3$ resulted in a small increase in the intensity without changes in the position of λ_{max} as shown in Figure 4-26B and E respectively. Gratifyingly, upon the addition of $SmCl_3$ to the solution of **85**, it was possible to observe the appearances of the $^4G_{5/2} \rightarrow {}^6H_{5/2\text{-}11/2}$ transitions on the fluorescence spectra while the $^4G_{5/2} \rightarrow {}^6H_{13/2}$ and $^4G_{5/2} \rightarrow {}^6F_{3/2\text{-}9/2}$ which are in the NIR were not observed

The excitation spectra were recorded for the full titration (see in the appendix), no obvious shift in the wavelengths of the bands could be observed while the relative intensity of the excitation spectra decreased through the addition of 0 to 1 equivalent of Sm(III) ions and slightly increased over the addition of the remaining 8 equivalents.

Upon addition of Sm(III) ions to the solution of **85**, it was possible to observe Sm(III)-centred emission with the appearance of the $^4G_{5/2} \rightarrow {}^6H_{5/2\text{-}11/2}$ at 564, 600, 644 and 707 nm. The increase in the phosphorescence intensity reached its maximum at 0.8 equivalents of Sm(III) ions added with the following gradual decrease until the addition of 9 equivalents, this result was demonstrated to be reproducible through the repetition of the experiment.

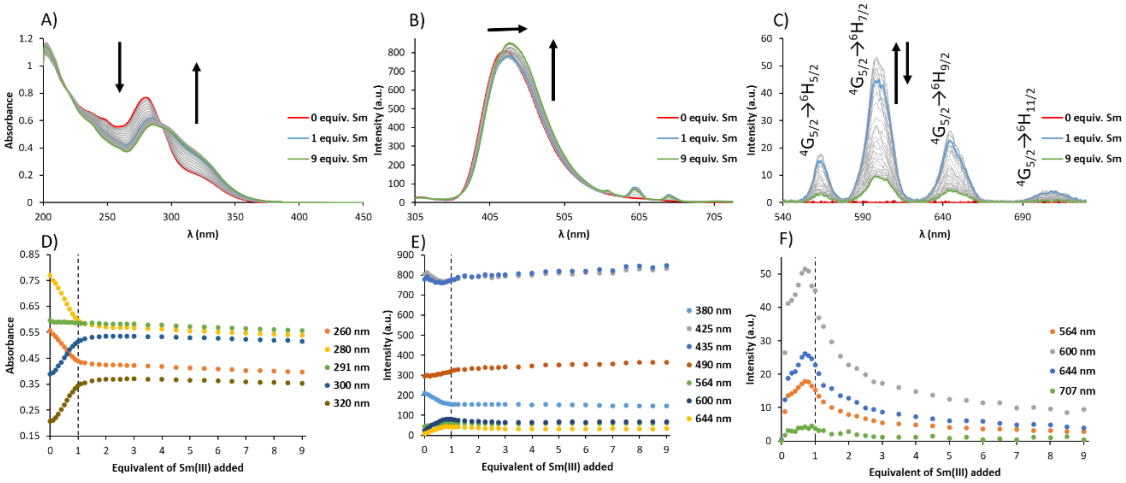

Figure 4-26 Changes in A) the absorption, B) fluorescence, C) Sm(III)-centred emission spectra of **85** (1×10^{-5} M) upon titrating with $SmCl_3$ (0→9 eq) in MeOH at 22 °C. Experimental D) absorption, E) fluorescence and F) Sm(III)-centred emission binding isotherms for the complexation of **85** at various wavelengths upon addition of $SmCl_3$.

The analysis of the changes in the absorption spectra using evolving factor analysis suggested the presence of three absorbing species. The fitting of the data obtained was carried out, as before, using the non-linear regression analysis software SPECFIT and the results are discussed in the following paragraph.

The recalculated absorption spectra for the 1:1 and 3:2 species were determined (Figure 4-27A) and are in good agreement with the experimental data. The convergence of the fit was demonstrated by the value of SigmaY (see table in appendix) and also demonstrated by the excellent superposition of the recalculated data to the experimental data (Figure 4-27B). The speciation-distribution diagram obtained, reveals that the formation of SmL is the predominant event for the entire titration but that the maximum of 92% was reached at 1.5 equivalents of Sm(III) ions added. The formation of Sm_3L_2 starts at 1 equivalent of Sm(III) ions in solution, and reaches its maximum of 29%, after addition of 9 equivalents of $SmCl_3$ (Figure 4-27C). The cumulative binding constants obtained from this fitting were $\log\beta_{1:1} = 6.8 \pm 0.1$ and $\log\beta_{3:2} = 22.3 \pm 0.3$ for the formation of SmL and Sm_3L_2 respectively and are the average obtained through several titrations and fittings. These values

are close to the ones obtained for the Tb(III)ions while being lower than the ones obtained for the Eu(III).

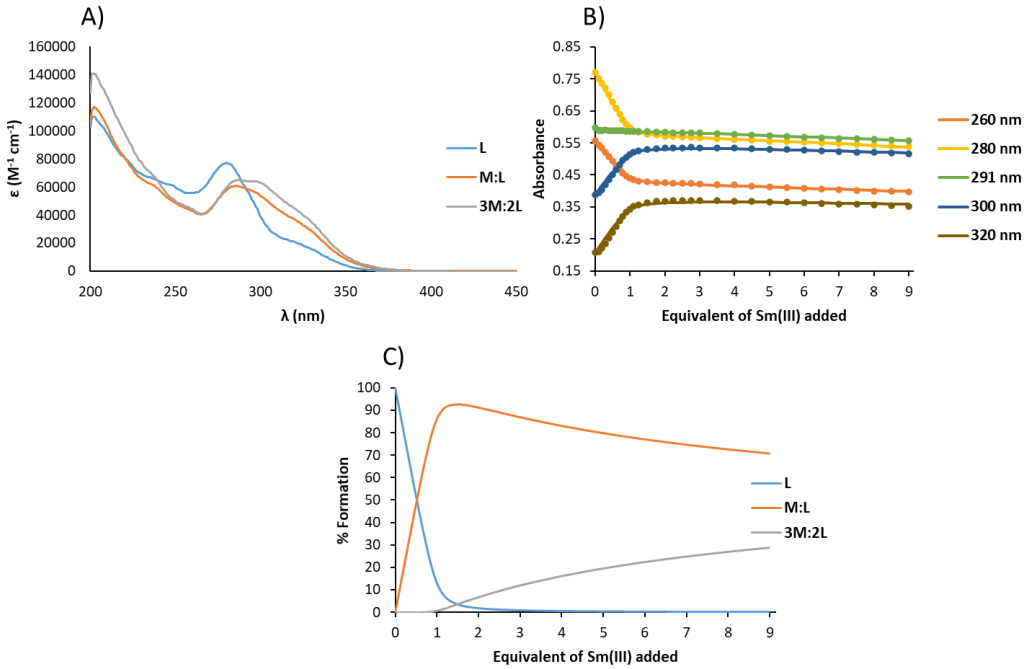

Figure 4-27 A) Recalculated spectra of absorption of L, M:L and 3M:2L, B) binding isotherms (dots) and their corresponding fit (line) and C) the corresponding speciation-distribution diagram obtained from the fitting of UV-vis titration of **85** (1×10^{-5} M) with $SmCl_3$ in MeOH at 22 °C using SPECFIT.

The analysis of the changes in the fluorescence emission spectra using evolving factor analysis suggested the presence of three emissive species as before. The fitting of the emission changes to the formation of 1:1 and 3:2 M:L species revealed similar results to the previous lanthanide titrations with the recalculated spectra showing good correlation with the experimental data in terms of the shift of λ_{max}, which is further confirmed by the recalculated binding isotherms being closely aligned to the experimental one (Figure 4-28B).

The speciation-distribution diagram was found to be in a good agreement with the one obtained using the absorption data. As shown in Figure 4-28C, the formation of 1:1 complex is the main event taking place during the titration, reaching its maximum of 98% at 1.25 equivalents of $SmCl_3$ added while the formation of 3:2 species reaches a maximum of 16% after addition of 9 equivalents of Sm(III) ions. The binding constants obtained with the fitting of the fluorescence data were $\log\beta_{1:1} = 7.6 \pm 0.6$ and $\log\beta_{3:2} = 23.6 \pm 0.8$ and are higher than the ones obtained through the fitting of the absorption because they are two different processes, and in the fluorescence some quenching processes are taking place and are not reflected in the absorption spectra, as a result the values of the binding constants vary from the fit obtained in the absorption.

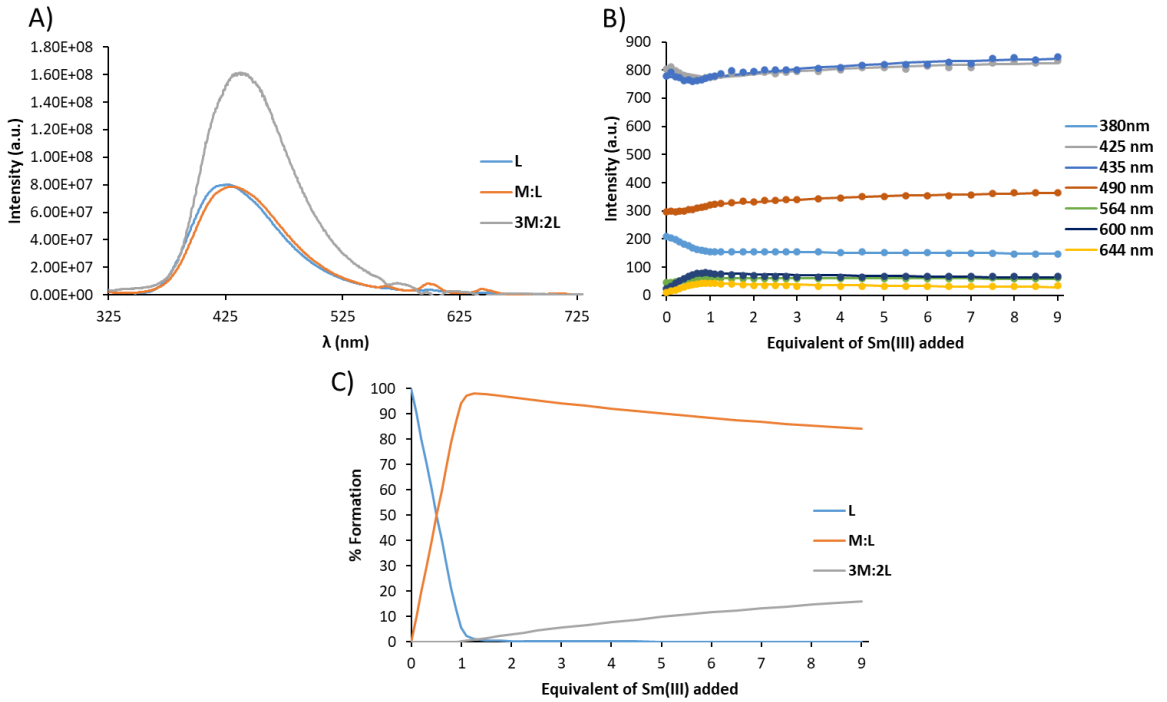

Figure 4-28 A) Recalculated spectra of fluorescence, B) binding isotherms (dots) and their corresponding fit (line) and C) the corresponding speciation-distribution diagram obtained from the fitting of fluorescence titration of **85** (1×10^{-5} M) with $SmCl_3$ in MeOH at 22 °C using SPECFIT.

The analysis of the changes in the Sm(III)-centred emission spectra in phosphorescence mode using evolving factor analysis suggested the presence of two emissive species. Fitting of the phosphorescence titrations was successful for the duplicate experiments. The recalculated spectra shown in Figure 4-29A, revealed that the 1:1 species shown the most efficient Sm(III)-centred emission which was in good agreement with the results obtained with other lanthanide ions. The binding isotherms of the recalculated data were slightly off but remained within an acceptable error margin. However, the speciation-distribution diagram describes the formation of 3:2 species as the dominant event in the titration, reaching a plateau after addition of 2 equivalents of $SmCl_3$ while the formation of 1:1 species reaches its maximum of only 1.5% at 0.8 equivalent of Sm(III) ions added. The binding constants obtained with the fitting of the phosphorescence data were $\log\beta_{1:1} = 4.7 \pm 0.5$ and $\log\beta_{3:2} = 22.1 \pm 0.2$.

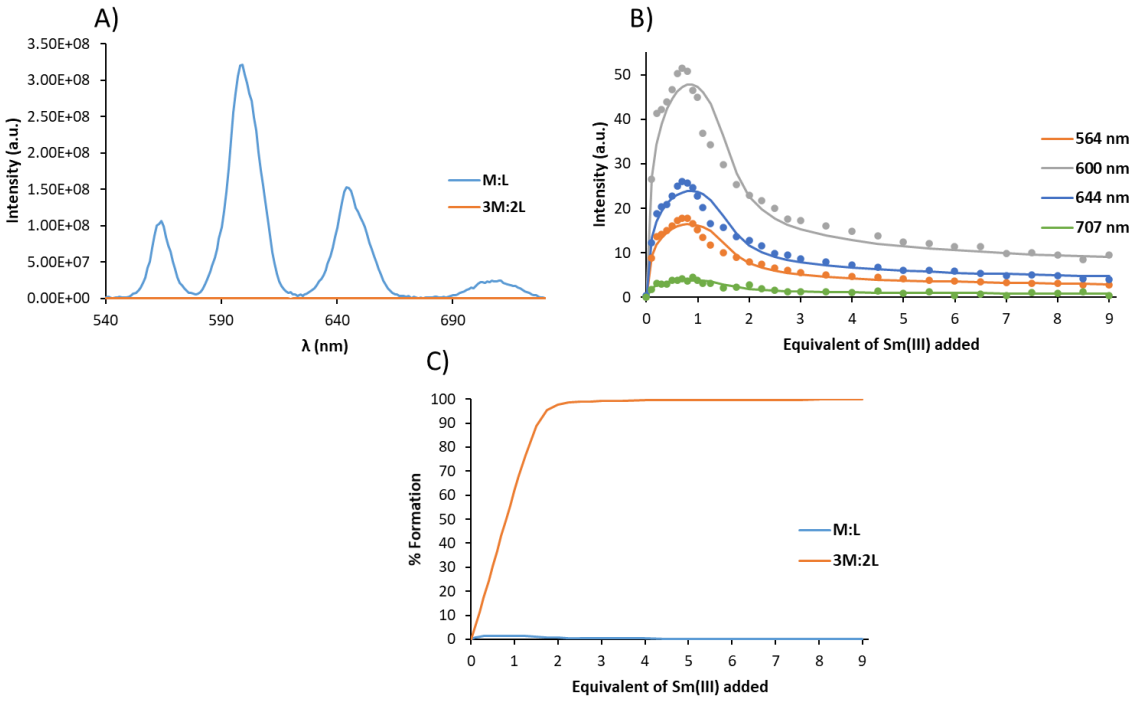

Figure 4-29 A) Recalculated spectra of Sm(III)-centred emission, B) binding isotherms (dots) and their corresponding fit (line) and C) the speciation-distribution diagram obtained from the fitting Sm(III)-centred emission titration of **85** (1×10^{-5} M) with $SmCl_3$ in MeOH at 22 °C using SPECFIT.

The binding constants obtained by the fitting of the absorption, fluorescence and Sm(III)-centred emission titration of **85** with $SmCl_3$ were summarised in Table 4-4. The values obtained for the cumulative binding constants through the fitting of the absorption and fluorescence data were in good correlation with the previously described binding constants for other lanthanides ions in this thesis, but these obtained by fitting of phosphorescence appeared much lower than expected relative to the other values obtained previously which was further supported by the discrepancies in the speciation-distribution diagram obtained. This also could be the result of quite low intensity of Sm(III)-centred emission due to the difference in its electronic structure compared to Eu(III) and Tb(III).[109]This could also be due to the presence of other quenching processes that are not reflected in the absorption and fluorescence spectra. Hence, these values were considered less reliable.

Table 4-4 The summary of the binding constants obtained through fitting of the data from absorption and emission titrations of **85** ($c = 1 \times 10^{-5}$ M) with $SmCl_3$ in MeOH at 22 °C using SPECFIT.

	Absorbance		**Fluorescence**		**Phosphorescence**	
	$\log\beta_{1:1}$	**$\log\beta_{3:2}$**	**$\log\beta_{1:1}$**	**$\log\beta_{3:2}$**	**$\log\beta_{1:1}$**	**$\log\beta_{3:2}$**
$SmCl_3$	6.8 ± 0.1	22.3 ± 0.3	7.6 ± 0.6	23.6 ± 0.8	4.7 ± 0.5	22.1 ± 0.2

Having successfully determined the stoichiometry of the different Sm(III) complexes, their speciation-distribution diagrams and binding constants, the titrations and fitting of the data obtained with Gd(III) ions were carried out and are described in the following paragraph.

4.3.6 UV-vis absorption, luminescence and non-linear regression analysis of 85 titration with $GdCl_3$ in solution

One of the main applications of Gd(III) ions is to absorb neutrons in nuclear reactors. Contrast agents for magnetic resonance imaging (MRI) is another application for which Gd(III) ions are widely used, due to their unique electronic configuration ($[Xe]4f^7$), possessing seven unpaired electrons conferring Gd(III) ions paramagnetic properties with a high magnetic moment.[252] Due to its ionic radius being part of the mid-size range with Eu(III), Tb(III) and Sm(III), and its ability to emit in the UV region of the electromagnetic spectrum, it was chosen for this study.

The self-assembly study of **85** in presence of lanthanide ions was continued by titrating the ligand with $GdCl_3$ in MeOH at a concentration of 1×10^{-5} M ($GdCl_3 \cdot 6H_2O$ was used but to simplify the notation $GdCl_3$. A sample of 2.5 mL of ligand at 1×10^{-5} M was prepared and titrated against known volumes of standard solutions of $GdCl_3$ between 0 to 9 equivalents. Both UV-vis absorption and luminescence spectra were recorded after each addition and the titration was triplicated to ensure reproducibility. In all measurements, an excess of metal ion was added to ensure the saturation of all the binding sites. The addition of $GdCl_3$ to the solution of **85** gave rise to a hypochromic and bathochromic shift synchronously with the broadening of the band centred at 280 nm and the increase in the absorbance of the shoulder at 325 nm (Figure 4-30A). The binding isotherm of the absorption titration of Gd(III) ions shown in Figure 4-30C, display the same trend as the previous titration with a plateau being reached after addition of 1 equivalent of Gd(III) ions.

The excitation at λ = 280 nm which corresponds to the terpyridine band gave rise to a fluorescence emission with λ_{max} = 425 nm. Upon addition of Gd(III) ions, a bathochromic shift to λ_{max} = 430 nm together with a small decrease in the fluorescence intensity is observed (Figure 4-30B) until 1 equivalent of Gd(III) ions is added. This change was further confirmed by the experimental binding isotherm shown in Figure 4-30D. Further addition of Gd(III) ions up to 9 equivalents led to an increase in intensity.

The fluorescence excitation spectra were recorded for the full titration and are shown in the appendices, similarly to the previous Ln(III) ions no obvious shift in the wavelengths

of the bands could be observed while the relative intensity of the excitation spectra decreased through the addition of 0 to 1 equivalent of Gd(III) ions and slightly increased over the addition of the remaining 8 equivalents.

The Gd(III)-centred emission was also recorded upon excitation at λ_{ex} = 280 nm and the results are shown in the appendices. Upon addition of Gd(III) ions to the solution of **85**, the appearance of the band centred at 312 nm which corresponds to the $^{6}P_{7/2} \rightarrow {}^{8}FS_{7/2}$ transition of Gd(III) ions can be observed after addition of 2 equivalents with the intensity increasing until the addition of 9 equivalents as shown in the binding isotherm in the appendices. However, the intensity observed for the Gd(III)-centred emission is too small to be significant and was not used for the fitting of the data by non-linear regression analysis. Titrations in similar conditions of Gd(III) ions without the ligand demonstrated also an increase in intensity suggesting that **85** is not sensitizing Gd(III)-centred emission.

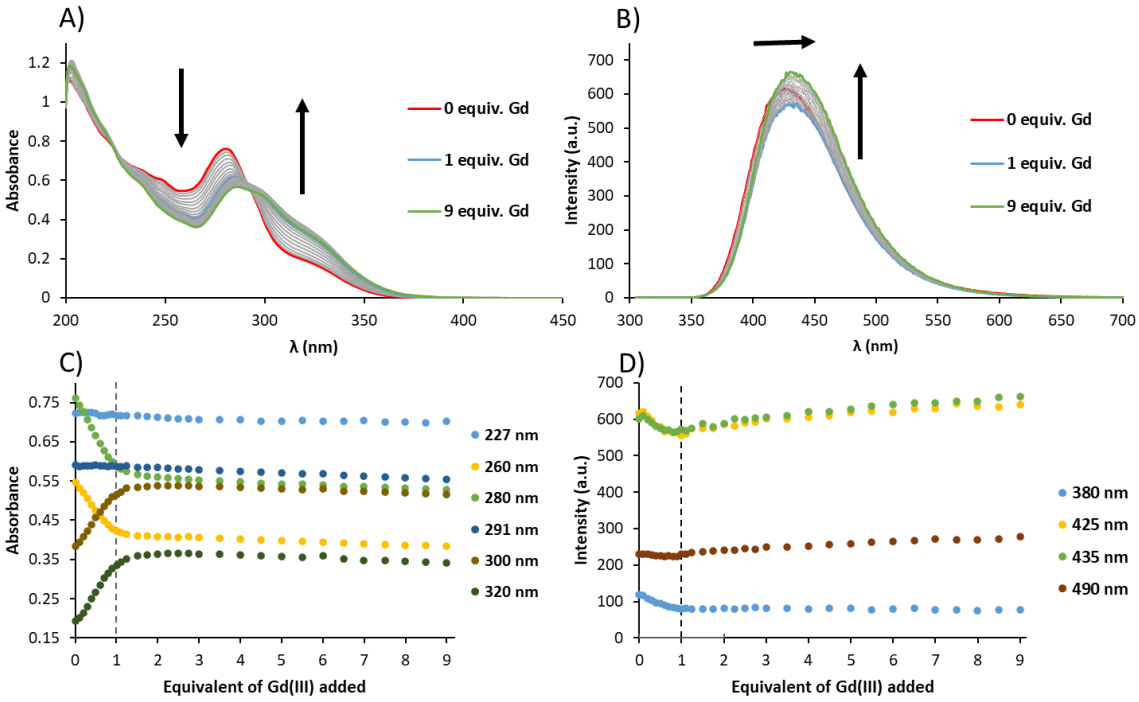

Figure 4-30 Changes in A) the absorption, B) fluorescence upon titrating with $GdCl_3$ (0→9 eq) in MeOH at 22 °C. Experimental C) absorption, D) fluorescence binding isotherms for the complexation of **85** at various wavelengths upon addition of $GdCl_3$.

The analysis of the changes in the absorption spectra using evolving factor analysis suggested the presence of three absorbing species through the titration as in the case of the other ions. The fitting of the data obtained by non-linear regression analysis was successfully carried out using SPECFIT and revealed a similar behaviour to the previous lanthanide titrations described in this chapter. Indeed, fitting of the absorption spectra changes revealed the formation of 1:1 and the expected 3:2 M:L species and their corresponding absorption

spectra were recalculated (Figure 4-31A). The good fit of the recalculated data to the experimental data is further confirmed by the isotherm diagrams shown in Figure 4-31B. Despite the absorption showing similar behaviour to the previous titrations, the speciation-distribution diagram obtained from the fitting of the data revealed that the formation of GdL complexes reached a maximum of 88% after addition of 1 equivalent of Gd(III) ions and it was the main event taking place here. The formation of Gd_3L_2 also occurred but remain minor, reaching a maximum of 5% after addition of 9 equivalents of Gd(III) ions. The binding constant obtained for the fitting of the absorption data are $\log\beta_{1:1} = 6.5 \pm 0.1$ for GdL and $\log\beta_{3:2} = 20.8 \pm 0.5$ for Gd_3L_2.

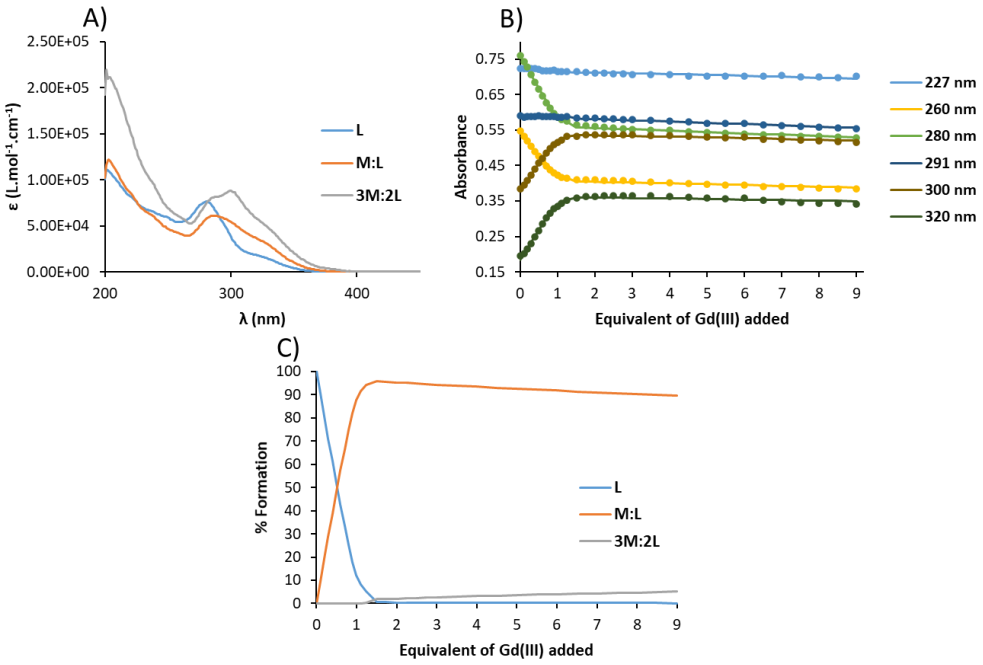

Figure 4-31 A) Recalculated spectra of absorption of L, M:L and 3M:2L, B) binding isotherms (dots) and their corresponding fit (line) and C) the corresponding speciation-distribution diagram obtained from the fitting of UV-vis titration of **85** (1×10^{-5} M) with $GdCl_3$ in MeOH at 22 °C using SPECFIT.

The analysis of the changes in the fluorescence spectra using evolving factor analysis suggested the presence of at least two emissive species. The recalculated fluorescence spectra of the 1:1 and 3:2 species formed during the titration are shown in Figure 4-32A, revealing that the 3:2 complex is the most luminescent. The binding isotherm highlights the correctness of the fit relative to the experimental data. The speciation-distribution diagram obtained with the fitting of the fluorescence data is in good agreement with the one obtained for the fitting of the absorption. As it can be seen in Figure 4-32C, the main event of the titration is the formation of 1:1 species, reaching a maximum of 95% after addition of 1 equivalent of Gd(III) ions. The formation of 3:2 species started at 1 equivalent of Gd(III) ions added, so after the formation of 1:1 complex it reached its maximum, and upon addition

of 9 equivalents of Gd(III), reached 22%. The binding constant obtained for the fitting of the fluorescence data were $\log\beta_{1:1} = 7.6 \pm 0.4$ for GdL and $\log\beta_{3:2} = 23.9 \pm 0.6$ for Gd_3L_2.

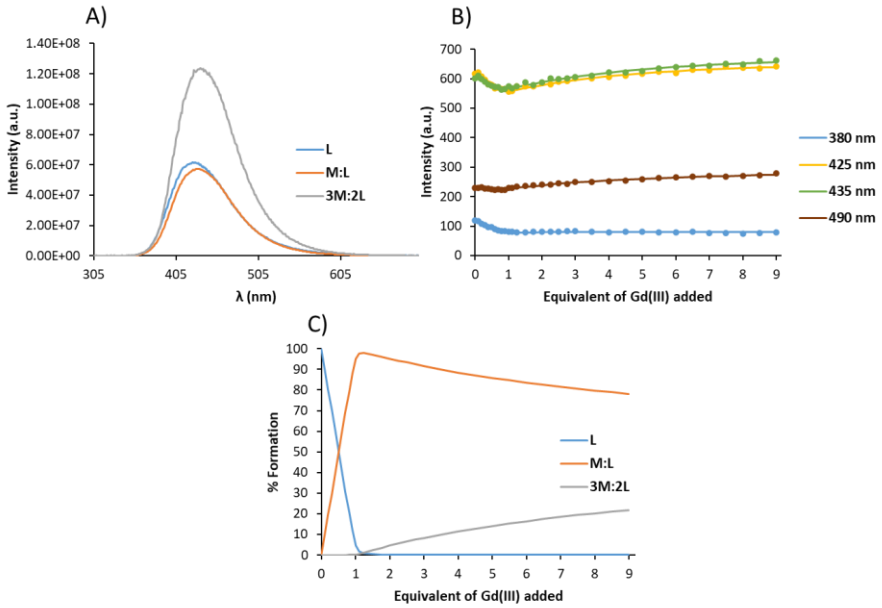

Figure 4-32 A) Recalculated spectra of fluorescence, B) binding isotherms (dots) and their corresponding fit and C) the corresponding speciation-distribution diagram obtained from the fitting of the fluorescence titration of **85** (1×10^{-5} M) with $GdCl_3$ in MeOH at 22 °C using SPECFIT.

The binding constants obtained by the fitting of the absorption and fluorescence titration of **85** in presence of $GdCl_3$ are summarised in Table 4-5.

Table 4-5 The summary of the binding constants obtained through fitting of the data from absorption and emission titrations of **85** (c= 1×10^{-5} M) with $GdCl_3$ in MeOH at 22 °C using SPECFIT.

	Absorbance		**Fluorescence**	
	$\log\beta_{1:1}$	**$\log\beta_{3:2}$**	**$\log\beta_{1:1}$**	**$\log\beta_{3:2}$**
$GdCl_3$	6.5 ± 0.1	20.8 ± 0.5	7.6 ± 0.4	23.9 ± 0.6

Since the stoichiometry of the different Gd(III) complexes, their speciation-distribution diagram and their binding constants were successfully determined, the titrations and fitting of the data obtained with the non-emissive La(III) ions were carried out and are described in the following paragraph.

4.3.7 UV-vis absorption, luminescence emission and non-linear regression analysis of 85 titration with $LaCl_3$ in solution

Lanthanum is used as an alloy in hydride batteries,[253] in optical fibres,[254] and scintillators.[255] Lanthanum is non-luminescent and unlike other lanthanides has an electronic configuration of [Xe] $5d^1$ $6s^2$, thus has no electrons in the *f* orbitals. For this chapter La(III) ion was selected

because it is the largest lanthanide(III) ion and its use in the titration will give a good representation of the behaviour of **85** in presence of large lanthanide(III) ions.

The self-assembly study of **85** in presence of lanthanide ions was pursued by titrating the ligand with $LaCl_3$ in MeOH at a concentration of 1×10^{-5} M ($LaCl_3 \cdot 7H_2O$ was used but to simplify the notation). As before these titrations were executed by using a sample of 2.5 mL of ligand at 1×10^{-5} M was prepared and titrated against known volumes of standard solutions of $LaCl_3$ between 0 to 9 equivalents to ensure the saturation of all the ligand binding sites. Both UV-vis absorption and luminescence spectra were recorded after each addition and the titration was triplicated to ensure reproducibility. From the absorption spectra it is possible to see (Figure 4-33A) that upon addition of $LaCl_3$, the band at 280 nm is considerably broadened, while the increase in the absorbance of the shoulder at 325 nm is much more prominent than previously observed with other lanthanides. It is also interesting to note that the experimental binding isotherms obtained display much smoother changes in the absorption at the various wavelengths than previously observed. The changes are also reaching a plateau much later for several wavelengths such as 280, 300 and 320 nm which potentially could be the evidence of a difference in the coordination of La(III) ions by the terpyridine moieties or less drastically, a significant difference in the binding constant which could result in a need of a higher quantity of La(III) ions in solution to reach the saturation of all the binding sites.

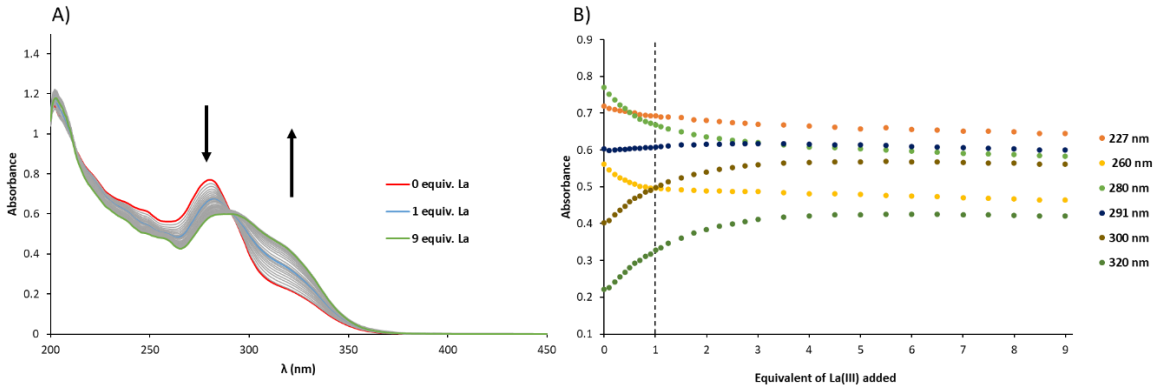

Figure 4-33 A) Changes in the absorption spectra of **85** (1×10^{-5} M) upon titrating with $LaCl_3$ (0→9 eq) in MeOH at 22 °C. B) Experimental absorption binding isotherms for the complexation of **85** at various wavelengths upon addition of $LaCl_3$.

The changes in the fluorescence spectra were also slightly different than previously observed in this thesis. Indeed, as seen in Figure 4-34A, the addition of 1 equivalent of La(III) ions to the solution of **85** produces a shift of λ_{max} from 420 nm to 430 nm while increasing the intensity. The shift in λ_{max} is not pursued with the further addition of La(III) ions, but the emission intensity increases through the entire titration as shown in Figure

4-34A and B. Unlike previous observation, during this titration the fluorescence intensity increased throughout the entire titration, as there is no possibility of energy transfer from the ligand to the La(III) ions, therefore the energy transfer that is usually taking place with other emissive lanthanide(III) ions leading to the decrease in the fluorescence intensity is not taking place here. Moreover, the coordination of the terpyridine units to La(III) ions restricts their free rotation again leading to an enhancement of the ligand-centred emission.[219]

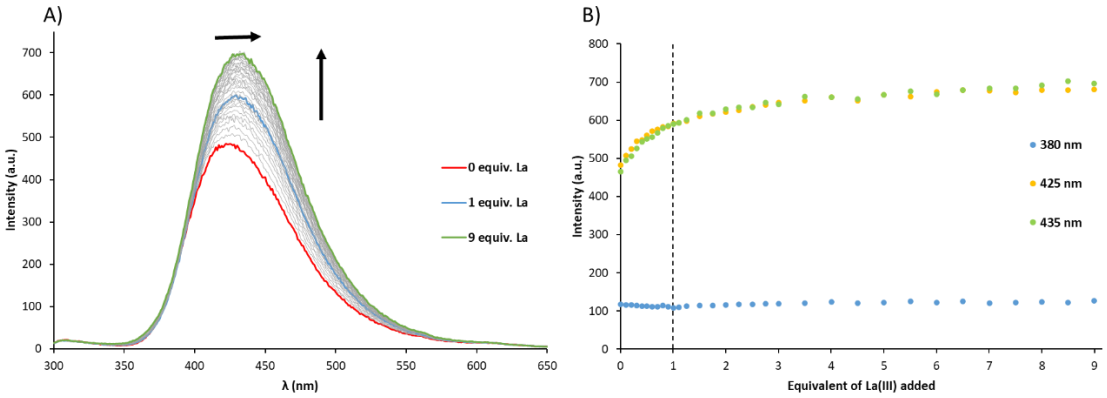

Figure 4-34 A) Changes in the fluorescence spectra of **85** (1×10^{-5} M) upon titrating with $LaCl_3$ (0→9 eq) in MeOH at 22 °C. B) Experimental fluorescence binding isotherms for the complexation of **85** at various wavelengths upon addition of $LaCl_3$.

The fluorescence excitation spectra were recorded for the full titration of $LaCl_3$ and are shown in the appendices, unlike the previous Ln(III) ions the relative intensity of the excitation spectra increased through the entire titration of La(III) ions (0 to 9 equivalents) while no obvious shift on the wavelengths of the bands could be observed as in previous cases.

The analysis of the changes in the absorption spectra using evolving factor analysis suggested the presence of three absorbing species as in previous cases. The results of the fitting of the absorption changes using non-linear regression analysis software SPECFIT are shown in Figure 4-35. The recalculated absorption spectra (Figure 4-35A) displays the absorption profile of 1:1 and 3:2 M:L species, revealing that the shoulder at 325 nm is much more pronounced for the 3:2 species. The good quality of the fit is demonstrated by the exact superposition of the recalculated binding isotherm with the experimental binding isotherm. The speciation-distribution diagram obtained from this fitting (Figure 4-35C), indicates that the first species formed corresponds to 1:1 complex, which reaches a maximum of 64% after addition of 1.5 equivalents of La(III) ions. Concomitantly, the 3:2 species is being formed and becomes the dominant species in solution after addition of 5 equivalents of La(III) ions to reach a maximum of 60% after addition of 9 equivalents of $LaCl_3$. The binding constants

obtained from the fitting of the absorption data are $\log\beta_{1:1} = 5.5 \pm 0.1$ and $\log\beta_{3:2} = 20.6 \pm 0.2$ for LaL and La_3L_2 species respectively. The binding constants obtained, in particular for the 1:1 complex are the lowest one observed with the different Ln(III) ion titrated and this is a result commonly observed when studying the effect of the size of the lanthanide ions on the binding constants, this is following the classical electrostatic trend with the larger lanthanides displaying lower binding constants which is due to the reduced charge density on the larger Ln(III) ions.[136]

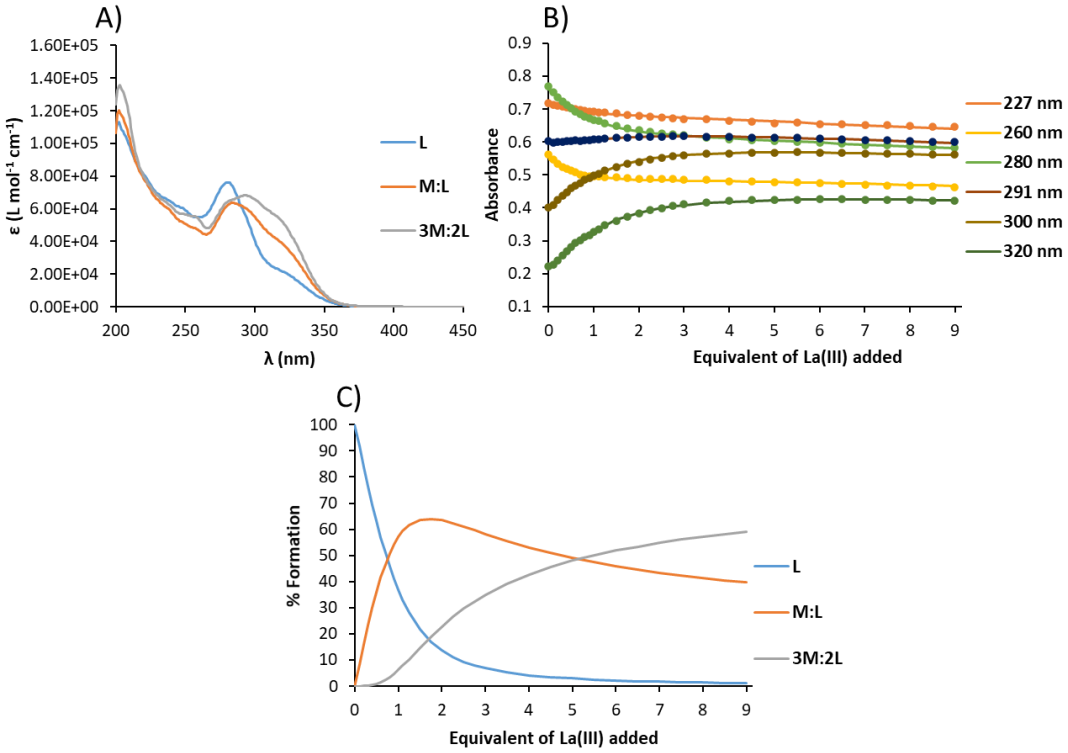

Figure 4-35 A) Recalculated spectra of the absorption of L, M:L and 3M:2L, B) binding isotherms (dots) and their corresponding fit (line) and C) the corresponding speciation-distribution diagram obtained from the fitting of the UV-vis titration of **85** (1×10^{-5} M) with $LaCl_3$ in MeOH at 22 °C using SPECFIT.

The analysis of the changes in the fluorescence spectra using evolving factor analysis suggested the presence of at least two emissive species in solution. The recalculated spectra obtained through the fitting of the fluorescence data were in a good agreement with the experimental data and show a similar λ_{max} shift between the free ligand and the complexed species (Figure 4-36A). The good quality of the fit was demonstrated by the exact superposition of the recalculated binding isotherm with the experimental binding isotherm. However, the speciation-distribution diagram shows significant differences in the extent of the formation of species but the trends are similar to the one obtained for the fitting of absorption data. Indeed, the main event during the titration was the formation of 1:1 species; reaching a plateau after addition of 1.5 equivalents of La(III) ions with 90% formation. In

the same time, the formation of 3:2 species was described as a minor event, reaching a maximum of 5% after addition of 9 equivalent of La(III) ions. The binding constant obtained from the fitting of the fluorescence data were $\log\beta_{1:1} = 6.1 \pm 0.2$ and $\log\beta_{3:2} = 20.0 \pm 0.4$ for LaL and La_3L_2 species respectively.

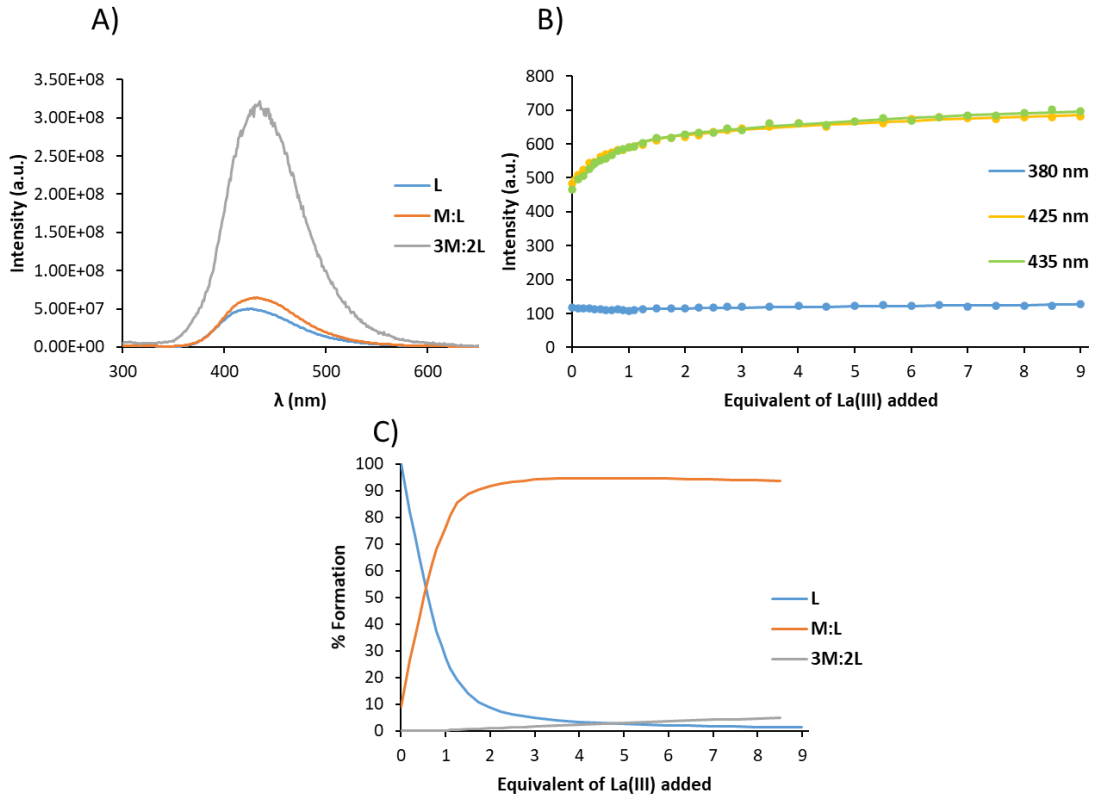

Figure 4-36 A) Recalculated spectra of the fluorescence of L, M:L and 3M:2L, B) binding isotherms (dots) and their corresponding fit (line) and C) the corresponding speciation-distribution diagram obtained from the fitting of the fluorescence titration of **85** (1×10^{-5} M) with $LaCl_3$ in MeOH at 22 °C using SPECFIT.

The binding constants obtained from the fitting of both the absorption and fluorescence data are summarised in Table 4-6 and were in good agreement with one another despite the discrepancies observed in the calculated speciation-distribution diagrams.

Table 4-6 The summary of the binding constants obtained through fitting of the data from absorption and emission titrations of **85** ($c = 1 \times 10^{-5}$ M) with $LaCl_3$ in MeOH at 22 °C using SPECFIT.

	Absorbance		**Fluorescence**	
	$\log\beta_{1:1}$	**$\log\beta_{3:2}$**	**$\log\beta_{1:1}$**	**$\log\beta_{3:2}$**
$LaCl_3$	5.5 ± 0.1	20.6 ± 0.2	6.1 ± 0.2	20.0 ± 0.4

Having successfully determined the stoichiometry of the different La(III) complexes, their speciation-distribution diagram and their binding constants, it was possible to observe that the binding constants calculated for the La(III) complex are lower than the ones obtained

for smaller lanthanides ions such as Sm(III) and Eu(III) which is in good agreement with the classical electrostatic trend due to a lower charge density expected for the larger ions.[136] The titrations and fitting of the data obtained with Lu(III) ions were carried out and are described in the following paragraph.

4.3.8 UV-vis absorption, luminescence emission and non-linear regression analysis of 85 titration with $LuCl_3$ in solution

With the electronic configuration of lutetium being [Xe] $6s^2$ $4f^{14}$ $5d^1$, the *f* orbital is full, which does not allow for Lu(III) metal-centred emission, therefore, its use is limited and its main application is in its lutetium oxyorthosilicate form as a scintillation detector for positron emission tomography.[256] Lutetium(III) ion was chosen for this study because it is the smallest lanthanide ion and therefore completes the entire size range of lanthanide ions used in this study. The self-assembly study of **85** in presence of lanthanide ions was pursued by titrating the ligand with $LuCl_3$ in MeOH at a concentration of 1×10^{-5} M ($LuCl_3 \cdot 6H_2O$ was used but to simplify the notation $LuCl_3$ is used through the text to explain the results of the titrations) as was the case in previous titrations.

A sample of 2.5 mL of ligand at 1×10^{-5} M was prepared and titrated against known volumes of standard solutions of $LuCl_3$ between 0 to 9 equivalents to ensure the saturation of all the binding sites of the ligand. As previously, both UV-vis absorption and luminescence spectra were recorded after each addition and the results are shown in Figure 4-37 and appendixes.

The absorption data obtained during the titration were in good agreement with the general trend observed with most of the changes happening during the addition of the first equivalent as shown in the binding isotherm (Figure 4-37C). However, when comparing the amplitudes of changes to the ones obtained during the titration of $LaCl_3$ it is possible to observe that the changes obtained during the addition of $LuCl_3$ are more pronounced suggesting a difference in the binding constants of the species being formed which can be associated to the difference in size as La(III) ions are the largest Ln(III) ions while the Lu(III)ions are the smaller ones and thus are expected to have a higher charge density.

Similarly for the changes observed in the lanthanum chloride titrations, it was possible to see that upon addition of lutetium chloride the λ_{max} in fluorescence spectra (Figure 4-37B, D) shifts from 420 nm to 430 nm with a significant increase in intensity, since the *f* orbital of Lu(III) ion is complete there is no possibility of energy transfer from the ligand to the Lu(III) ions, therefore the energy transfer that is usually taking place with

other emissive lanthanide(III) ions leading to the decrease in the fluorescence intensity is not taking place in this case. Moreover, the coordination of the terpyridine units to La(III) ions restricts their free rotation, again leading to an enhancement of the ligand-centred emission.[219] Further additions of 8 equivalents of Lu(III) ions lead to a λ_{max} shift of another 4 nm concomitantly with an increase in intensity (Figure 4-37).

The fluorescence excitation spectra were also recorded for the full titration of $LuCl_3$ and are shown in the appendix, similarly to La(III) ions the relative intensity of the excitation spectra increased through the entire titration of Lu(III) ions (0 to 9 equivalents) while no obvious shift on the wavelengths of the bands could be observed.

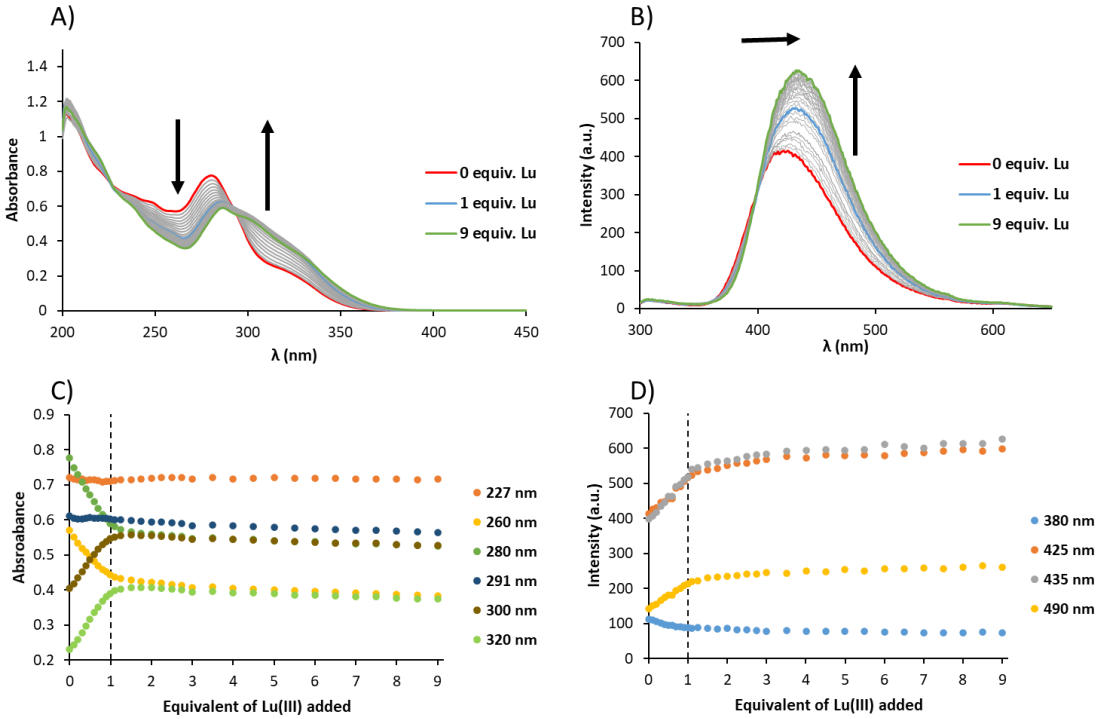

Figure 4-37 Changes in A) the absorption, B) fluorescence spectra of **85** (1×10^{-5} M) upon titrating with $LuCl_3$ (0→9 eq) in MeOH at 22 °C. Experimental C) absorption, D) fluorescence binding isotherms for the complexation of **85** at various wavelengths upon addition of $LuCl_3$.

The analysis of the changes in the absorption spectra using evolving factor analysis suggested the presence of up to five absorbing species and three emissive species in the case of the fluorescence spectra. This difference can be explained by the fact that the evolving factor analysis suggests a maximum of species for the fitting of the data but that it is possible to use less species than suggested for the fit. The fitting of both absorption and fluorescence data obtained from the titration of **85** with $LuCl_3$ solution were successfully carried out to the formation of 1:1 and 3:2 M:L species using non-linear regression analysis software SPECFIT and the results are shown in Figure 4-38. The recalculated absorption spectra (Figure 4-38A) displayed a higher absorbance value for the shoulder at 325 nm for both 1:1

and 3:2 species which is in good agreement with the previous results observed with other lanthanide ions. The good quality of the fit was confirmed by the superposition of the recalculated isotherm with the experimental one. The speciation-distribution diagram obtained for the fitting of the changes in the absorption spectra upon addition of Lu(III) ions reveals that the formation of 1:1 species was the dominant event during the titration, reaching a maximum of 93% after addition of 1.5 equivalents of Lu(III) ions which is similar to that observed with other Ln(III) ions. The 3:2 species are being formed after the addition of 1 equivalent of Lu(III) ions and reached a maximum of 42% after addition of 9 equivalents of $LuCl_3$. The binding constants obtained from the fitting of the absorption data are $\log\beta_{1:1}$ = 6.6 ± 0.1 and $\log\beta_{3:2}$ = 21.9 ± 0.2 for LuL and Lu_3L_2 species respectively.

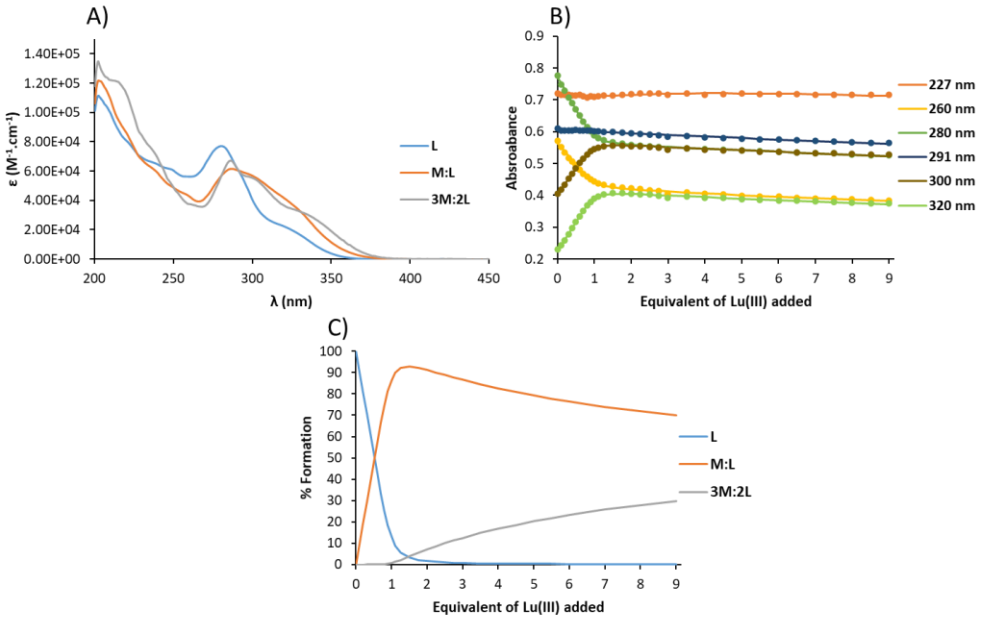

Figure 4-38 A) Recalculated absorption spectra of L, M:L and 3M:2L, B) binding isotherms (dots) and their corresponding fit (line) and C) the corresponding speciation-distribution diagram obtained from the fitting of the UV-vis titration of **85** (1×10^{-5} M) with $LuCl_3$ in MeOH at 22 °C using SPECFIT.

The good fitting of the changes in the fluorescence spectra upon addition of $LuCl_3$ was confirmed by the superposition of the recalculated binding isotherms to the experimental ones (Figure 4-39B). The speciation-distribution diagram obtained (Figure 4-39C) was in a good agreement with the one obtained by fitting of the changes in the fluorescence data. As seen in Figure 4-39C, the formation of 1:1 species reached a maximum of 94% after addition of 1 equivalent of Lu(III) ions. Further addition of $LuCl_3$ led to the formation of Lu_3L_2 species with the simultaneous consumption of LuL species, reaching a maximum of 43% after addition of 9 equivalent of Lu(III) ions. The binding constants obtained from the fitting of the fluorescence data are $\log\beta_{1:1}$ = 7.6 ± 0.5 and $\log\beta_{3:2}$ = 24.2 ± 0.7 for LuL and Lu_3L_2

species respectively. These binding constants are much higher than the ones observed for La(III) while it is close to the binding constants calculated for the mid-size Ln(III) ions such as Sm(III), Gd(III) and Tb(III) ions.

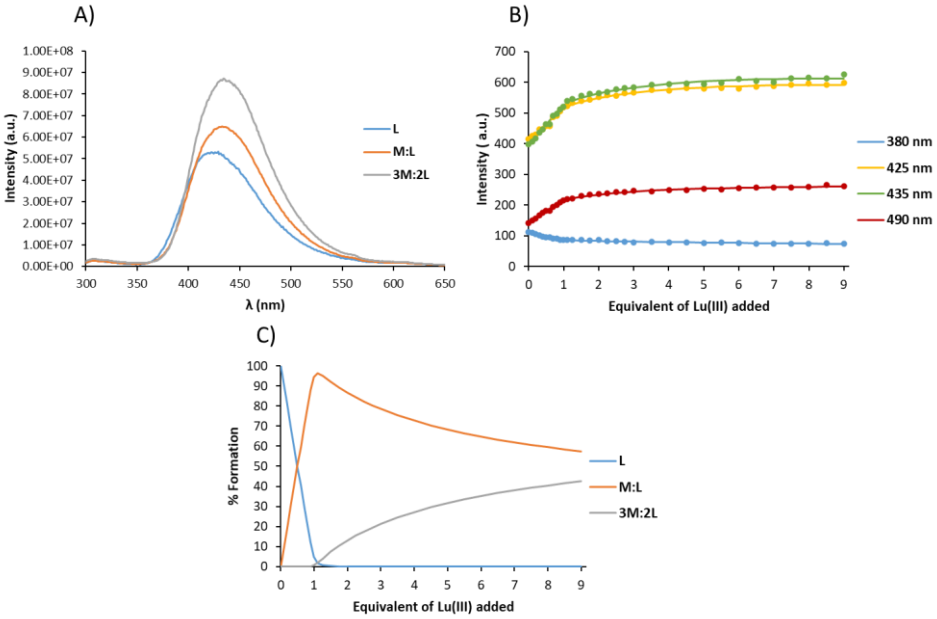

Figure 4-39 A) Recalculated fluorescence spectra of L, M:L and 3M:2L, B) binding isotherms (dots) and their corresponding fit (line) and C) the corresponding speciation-distribution diagram obtained from the fitting of the fluorescence titration of **85** (1×10^{-5} M) with $LuCl_3$ in MeOH at 22 °C using SPECFIT.

The results of the cumulative binding constants obtained from the fitting of the changes in both absorption and fluorescence spectra upon addition of $LuCl_3$ into the solution of **85** were summarised in Table 4-7. The binding constants obtained from fitting of the fluorescence data were significantly higher than the values obtained by fitting of the absorption spectra which is a phenomenon that has been observed previously and explained.

Table 4-7 The summary of the binding constants obtained through fitting the data from absorption and emission titrations of **85** (c= 1×10^{-5} M) with $LuCl_3$ in MeOH at 22 °C using SPECFIT.

	Absorbance		**Fluorescence**	
	$\log\beta_{1:1}$	**$\log\beta_{3:2}$**	**$\log\beta_{1:1}$**	**$\log\beta_{3:2}$**
$LuCl_3$	6.6 ± 0.1	21.9 ± 0.2	7.6 ± 0.5	24.2 ± 0.7

Having determined the binding constants for the formation of 1:1 and 3:2 (M:L) complexes using Lu(III) ions and observed that they are very close to the the mid-size Ln(III) ions but higher than the ones observed for the larger La(III) ions, the titrations and fitting of the data obtained with Yb(III) ions were carried out and are described in the following paragraph.

4.3.9 UV-vis absorption, luminescence and non-linear regression analysis of 85 titrations with $YbCl_3$ in solution

Ytterbium is commonly used in the electron transport layer for photovoltaic cells,[257] and in responsive materials where its capacity of emitting in the NIR is a great advantage for a multitude of applications such as bioimaging and probes.[115,258] The ytterbium(III) ion has been selected for this study as its ionic radius is the second smallest radius and will complement the results obtained for the titrations of Lu(III) ions and will reveal if **85** can sensitise the Yb(III) ions to emit in the NIR region.

The self-assembly study of **85** in the presence of lanthanides ions was pursued by titrating the ligand with $YbCl_3$ in MeOH at a concentration of 1×10^{-5} M ($YbCl_3 \cdot 6H_2O$ was used but to simplify the notation $YbCl_3$). A sample of 2.5 mL of ligand at 1×10^{-5} M was prepared and titrated against known volumes of standard solutions of $YbCl_3$ between 0 to 9 equivalents to ensure the saturation of all the binding sites of the ligand. Both UV-vis absorption and luminescence spectra were recorded after each addition and the results are shown in Figure 4-40. The changes in the absorption spectra through the titration with Yb(III) ions resulted in the same trend as previously observed during the titration of Lu(III) ions. As seen in Figure 4-40B, most of the changes occurred before the addition of 1 equivalent of Yb(III) ions and reach a plateau for the remaining additions of $YbCl_3$.

Through the titration of **85** with $YbCl_3$, the λ_{max} of emission intensity shifted from 420 nm to 430 nm after the addition of 1 equivalent of Yb(III) ions conjointly with a decrease in intensity which was also observed previously with other Ln(III) ions. Addition of the remaining 8 equivalents led to a further shift of λ_{max} to 433 nm with a slight increase in intensity.

Gratifyingly, excitation at 280 nm upon addition of Yb(III) ions resulted in near-infrared Yb(III)-centred emission with a maximum at 975 nm and a shoulder at *ca.* 1010 nm which corresponds to the $^2F_{5/2} \rightarrow {}^2F_{7/2}$ transition (Figure 4-40E). As shown in Figure 4-40F, the intensity for the band at 975 nm increased until the addition of 1 equivalent of $YbCl_3$ and then reached a plateau for the remainder of the titration.

The fluorescence excitation spectra were recorded for the full titration of $YbCl_3$ and are shown in the appendixes, similarly to the fluorescence intensity, the relative intensity of the excitation spectra decreased through the addition of 0 to 1 equivalent of Yb(III) ions and remained relatively constant for the addition of the remaining 8 equivalents of Yb(III) ions while no obvious shift on the wavelengths of the bands could be observed.

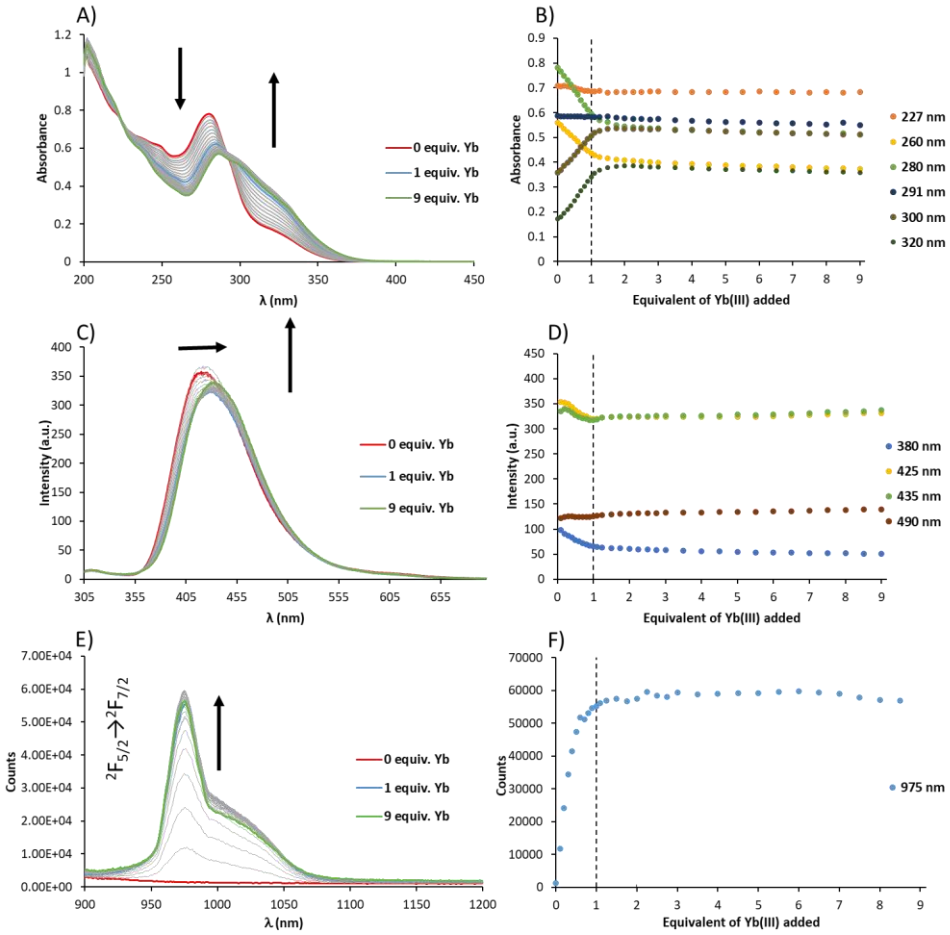

Figure 4-40 Changes in A) the absorption, C) fluorescence, D) Yb(III)-centred emission spectra of **85** (1×10^{-5} M) upon titrating with $YbCl_3$ (0→9 eq) in MeOH at 22 °C. Experimental B) absorption, D) fluorescence and F) Yb(III)-centred emission binding isotherms for the complexation of **85** at various wavelengths upon addition of $YbCl_3$.

The analysis of the changes in the absorption spectra using evolving factor analysis suggested the presence of up to four absorbing species and three emissive species in the case of the fluorescence spectra. The recalculated spectra obtained for the fitting of the absorption data (Figure 4-41A) demonstrate that the 3:2 complex has a much sharper band at 280 nm and a second band at 343 nm which is not displayed in the experimental data, but this error seems to be compensated by the low quantity of 3:2 M:L species formed through the titration as shown in the speciation-distribution diagram on Figure 4-41C. However, the recalculated spectra of the ligand and the YbL complex are in good agreement with the experimental data. The recalculated data for the binding isotherm shown in Figure 4-41B demonstrate an excellent fit to the experimental data. The speciation-distribution diagram obtained for the fitting of absorption data shown that 3:2 species were, as discussed previously, formed in very low quantities and reached a maximum of 6.6% after addition of 9 equivalents of Yb(III) ions. The formation of 1:1 species drastically increases upon addition of the first equivalent of Yb(III) ions and then reached a plateau for the remaining 8 equivalents. The

binding constants obtained for the fit of the absorption changes were $\log\beta_{1:1} = 6.0 \pm 0.1$ and $\log\beta_{3:2} = 19.8 \pm 0.5$. These binding constants appeared to be lower than the binding constants calculated for the mid-size Ln(III) ions such as Sm(III), Eu(III) and Tb(III) ions.

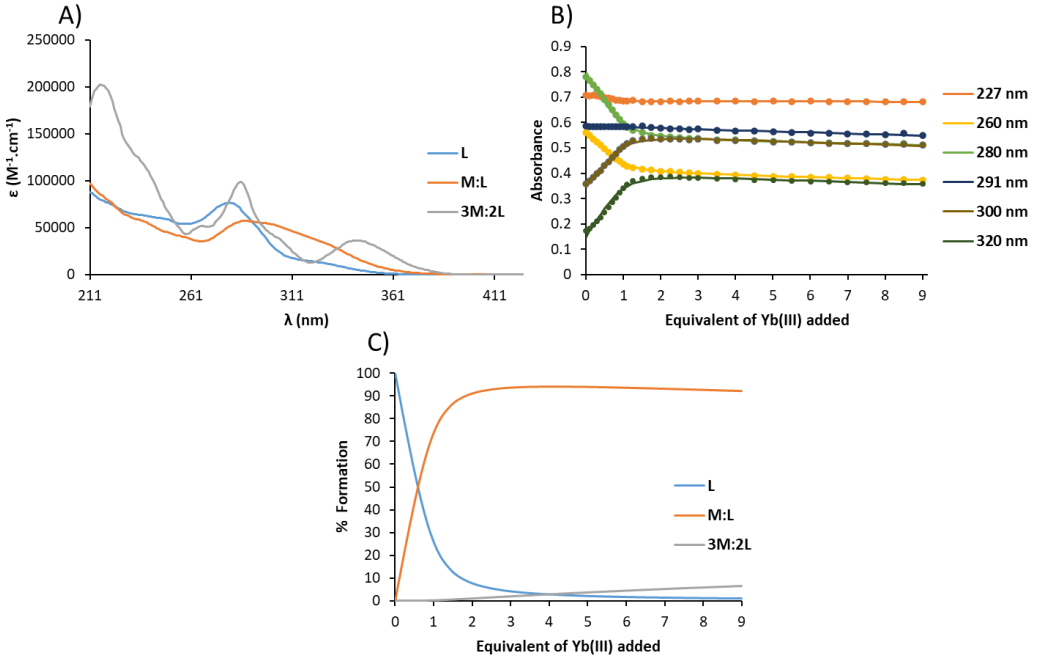

Figure 4-41 A) Recalculated absorption spectra, B) binding isotherms (dots) and their corresponding fit (line) and C) the corresponding speciation-distribution diagram obtained from the fitting of UV-vis titration of **85** (1×10^{-5} M) with $YbCl_3$ in MeOH at 22 °C using SPECFIT.

The recalculated spectra for the fit of fluorescence data were in good agreement with the experimental results, demonstrating that the 1:1 and 3:2 species have a λ_{max} slightly red-shifted from the one of the free ligand which indicates binding of terpyridine centres of **85** to Yb(III) ions (Figure 4-42A). As can be seen in both the experimental and recalculated spectra the fluorescence intensity is decreasing from 0 to 1 equivalent of Yb(III) ions addition suggesting an energy transfer from the ligand to the Yb(III) ion resulting in Yb(III)-centred emission which is further confirmed by the NIR emission measurements. As shown in Figure 4-42B, the recalculated data showed an excellent fit to the experimental binding isotherm ensuring the good quality of the fitting. The speciation-distribution diagram was in good agreement with the one obtained by fitting of the absorption data, showing that the formation of 1:1 species reached a maximum of 98% after addition of 1.25 equivalents of Yb(III) ions. The binding constants obtained by the fit of the fluorescence changes are $\log\beta_{1:1} = 7.3 \pm 0.3$ and $\log\beta_{3:2} = 22.5 \pm 0.5$.

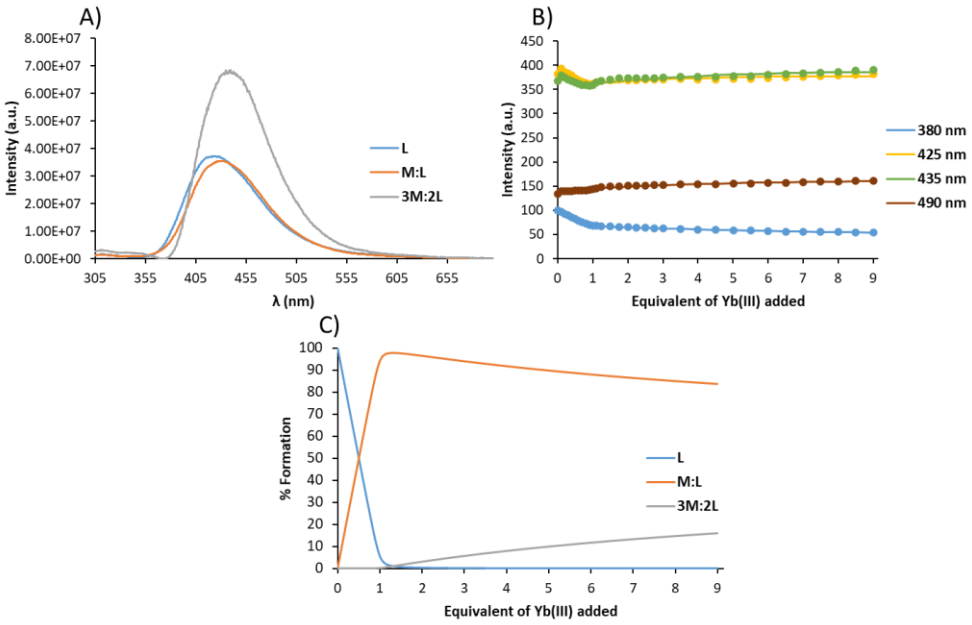

Figure 4-42 A) Recalculated spectra of fluorescence, B) binding isotherms (dots) and their corresponding fit (line) and C) the corresponding speciation-distribution diagram obtained from the fitting of fluorescence titration of **85** (1 × 10–5 M) with $YbCl_3$ in MeOH at 22 °C using SPECFIT.

Non-linear regression analysis of the Yb(III)-centred emission data was also carried out, but several issues could be noticed and will be described here for these analyses. The first one was that the convergence of the fit to the data could only be achieved by setting the ligand as emissive even though it is not emissive in the NIR range. However, the fit confirmed that on the recalculated spectra the ligand was not emissive corresponding to the experimental data (Figure 4-43A). The recalculated spectra for the YbL and Yb_3L_2 species were in a good agreement with the experimental data. The second issue came from the recalculated value for the binding isotherms, as shown in Figure 4-43B, the fit adhered quite well to the experimental values except for the region of 1 equivalent of Yb(III) ions added where the recalculated data spike and despite trying to adjust different parameters such as the baseline, the range of the data analysed and repeating the titrations the spike was always present.

To solve this issue, the fit of the data using a fixed value for the binding constant of one of the species in solution was also attempted and will be described in the next paragraph. The obtained speciation-distribution diagram shown in Figure 4-43C, and describes the formation of 3:2 species as the predominant event, reaching a maximum of 99% after addition of 1.5 equivalents of $YbCl_3$ while the formation of 1:1 species only occurred during the addition of the first 1.5 equivalents. The binding constants obtained by the fit of the Yb(III)-centred emission changes are $\log\beta_{1:1} = 7.9 \pm 0.5$ and $\log\beta_{3:2} = 27.3 \pm 0.6$ for the formation YbL and Yb_3L_2 respectively.

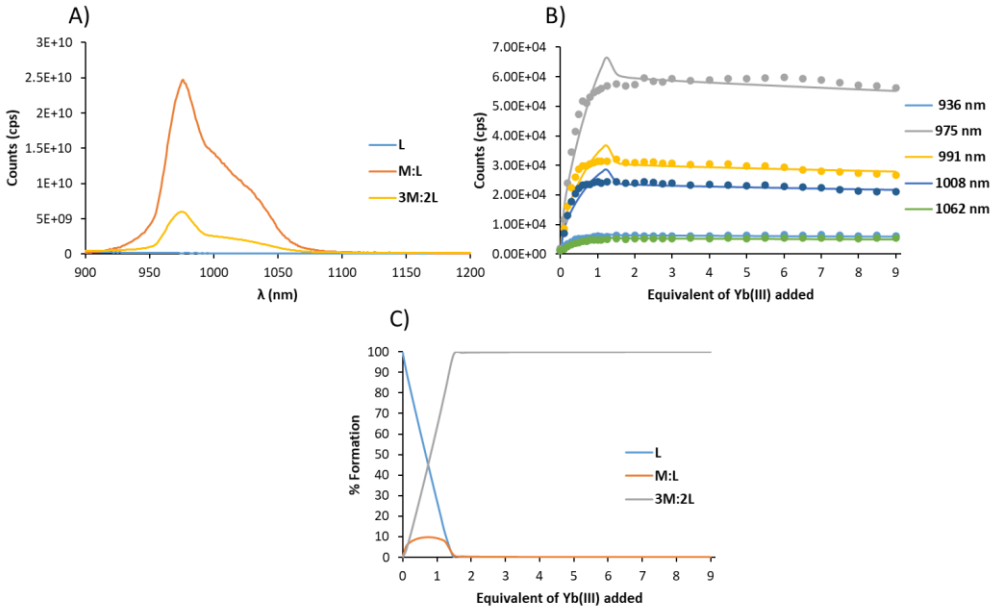

Figure 4-43 A) Recalculated spectra, B) experimental binding isotherms (dots) and their corresponding fit (line) and C) the corresponding speciation-distribution diagram obtained from the fitting of Yb(III)-centred emission titration of **85** (1×10^{-5} M) with $YbCl_3$ in MeOH at 22 °C using SPECFIT.

To investigate the issue encountered during the fitting, another Yb(III)-centred emission titration it was carried out again in similar conditions than previously but fewer data points were taken, only 24 additions of $YbCl_3$ stock solutions were done against 31 additions as the other lanthanide titrations discussed previously. It was thought that since the issue with the fitting was around the 1 equivalent region that by changing the number of additions to reach 1 equivalent of Yb(III) ions in solution could affect the kinetic of the equilibrium between **85** and Yb(III) and hence change the ratio between the species formed and potentially facilitate the fitting.

The possibility of the kinetic effect on the non-linear regression analysis for Yb(III)-centred emission here was also anticipated as NIR emission spectra were recorded on Fluorolog as opposed to a Cary Eclipse for Ln(III) ions emitting in the visible range. This prevented us from recording the spectra with the same rate as for the previously described data. It is worth noting that the difference in the number of additions is comprised between the addition of 0 and 1 equivalent of Yb(III) ions with only four addition to cover the 0 to 1 equivalent range against 10 additions to cover the same range for the longer titrations previously presented.

The changes in the Yb(III)-centred emission can be seen in appendixes and can also be seen from the experimental binding isotherm (dots) in Figure 4-44B, that the increase in intensity is more abrupt than for the longer titration, while after the addition of 1 equivalent

of Yb(III) ions the intensity decreases until the addition of 9 equivalents. It can be seen in the recalculated spectra Figure 4-44A, that the ligand was included as an emissive component to achieve a good fit but that its recalculated spectrum has shown that it is non-emissive confirming the convergence of the fit and experimental data.

The recalculated spectra for the Yb(III)-centred emission of 1:1 and 3:2 species were very similar to the one previously obtained with the first titration and are in good agreement with the experimental data. The binding isotherm (Figure 4-44B) of the recalculated data was in perfect alignment with the experimental data and demonstrate the good quality of the fitting. The speciation-distribution diagram obtained is shown in Figure 4-44C and is closer to the general trend observed with the other lanthanides than the first Yb(III) titration presented previously. The addition of 1 equivalent of Yb(III) ions to the solution of **85** resulted in the formation of 1:1 complexes reaching its maximum of 75% in presence of 1 equivalent of $YbCl_3$ while further addition of Yb(III) ions led to the formation of 3:2 complexes with the simultaneous consumption of the 1:1 species reaching after addition of 9 equivalents of Yb(III) a maximum of 74% of 3:2 species and 26% of 1:1 species. The binding constants obtained for this fitting were $\log\beta_{1:1} = 6.6 \pm 0.1$ and $\log\beta_{3:2} = 23.2 \pm 0.1$ for the formation of YbL and Yb_3L_2 respectively, which appears to be closer to the values observed previously for the other Ln(III) ions.

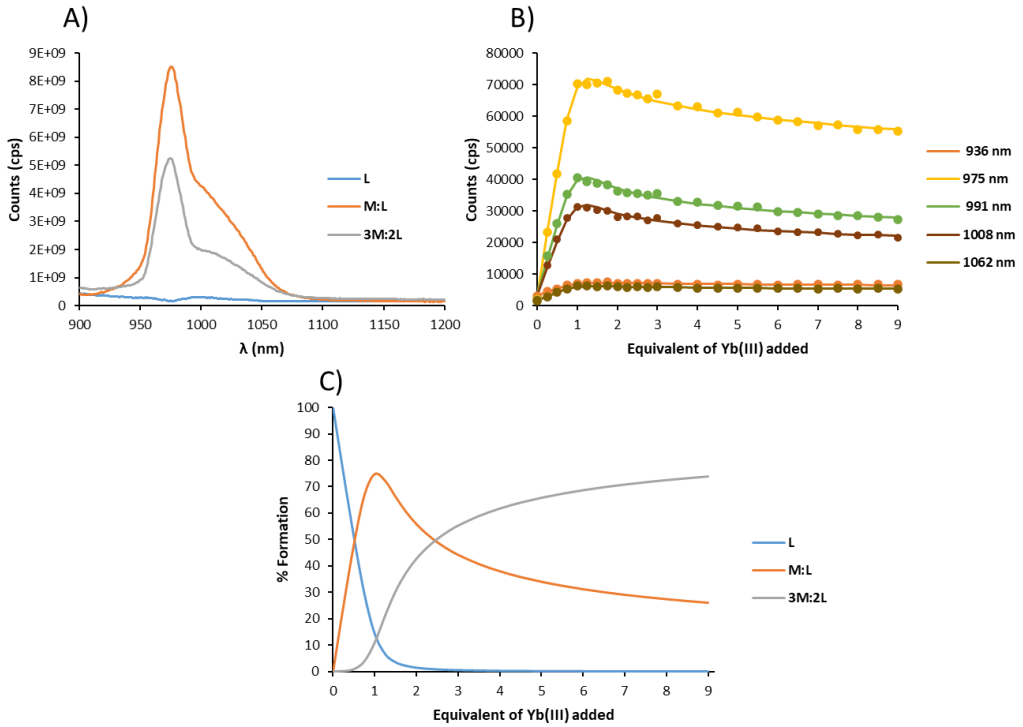

Figure 4-44 A) Recalculated spectra, B) experimental binding isotherms and their corresponding fit, C) speciation-distribution diagram obtained from the fitting of Yb(III)-centred emission titration of **85** (1×10^{-5} M) with $YbCl_3$ in MeOH at 22 °C (25 data points) using SPECFIT.

Using the cumulative binding constants obtained from the shorter titration, it was attempted to apply their values as known for either the 1:1 species or the 3:2 species and determine the binding constant of the other species by non-linear regression analysis for higher data point titration (Figure 4-40C). When fixing the value of the binding constant for the two types of complexes being formed it was possible to observe a clear improvement in the fitting of the corresponding binding isotherm (Figure 4-45B) even though the recalculated data was not perfectly aligned with the experimental data in the region of 1 equivalent, the changes in the recalculated data were much smoother. Moreover, the speciation-distribution diagram (Figure 4-45C) obtained was the same as the one obtained for the shorter titration.

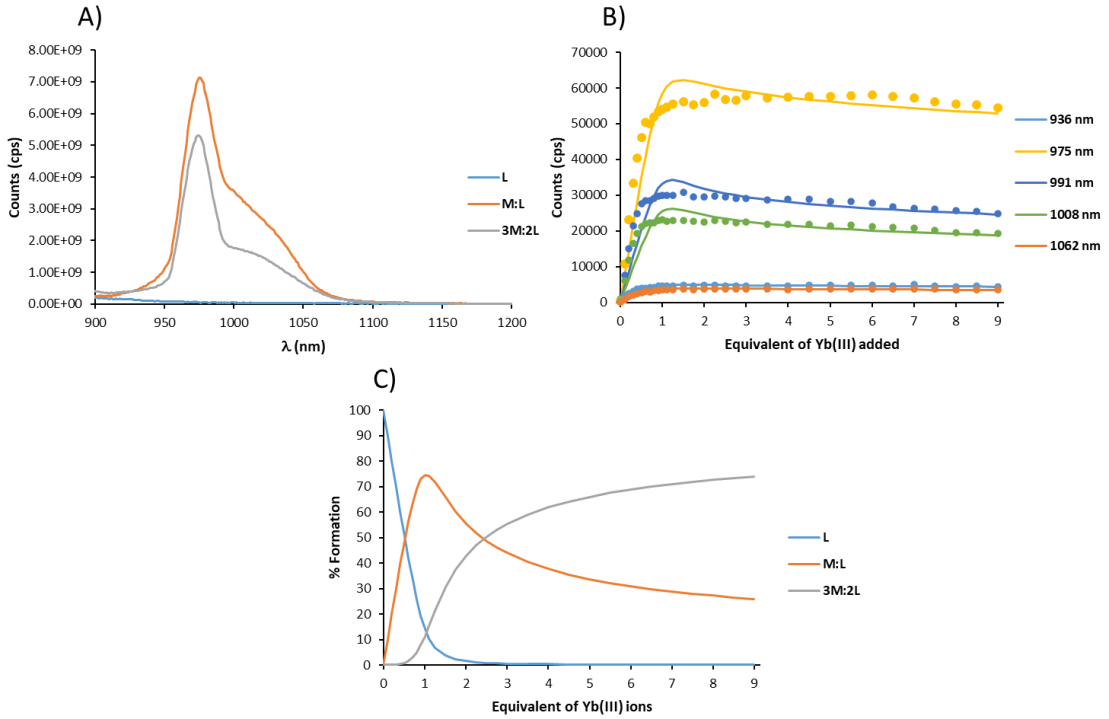

Figure 4-45 A) Recalculated spectra, B) experimental binding isotherms (dots) and their corresponding fit (lines), C) speciation-distribution diagram obtained from the fitting of Yb(III)-centred emission titration of **85** (1×10^{-5} M) with $YbCl_3$ in MeOH at 22 °C using SPECFIT and by fixing both values of the binding constant for 1:1 and 3:2 species.

From these results, it was possible to conclude that the binding constant obtained with the shorter titration does not correspond to a minimum in the process of fitting the longer titration and the kinetic effect involved in the formation of the different species in solution has a significant impact on the result of the fitting.

Another attempt to fit the long titration presented in Figure 4-40 was carried out by using the residual of the previous fit to determine from which data points the discrepancies in the fit could come from and fit the data again after omitting them. This resulted in mainly

reducing the number of data points between 0 to 1 equivalent from originally 11 points to 5. As shown in Figure 4-46, the fitting lead to recalculated spectra which are in good agreement with the previous fits. The recalculated binding isotherms (line in Figure 4-46B) display a much better fit to the experimental binding isotherm, it is still possible to observe a slight spike around 1 equivalent of Yb(III) ions added while the curvature is not as smooth as it is expected. The speciation-distribution diagram is also displaying abrupt changes, but the overall diagram appears smoother than the one obtained with the first fit shown in Figure 4-43C. The maximum formation of 1:1 species is reached after addition of 0.8 equivalents of Yb(III) ions while further addition of $YbCl_3$ drastically increases the formation of 3:2 species with the simultaneous consumption of 1:1 species.

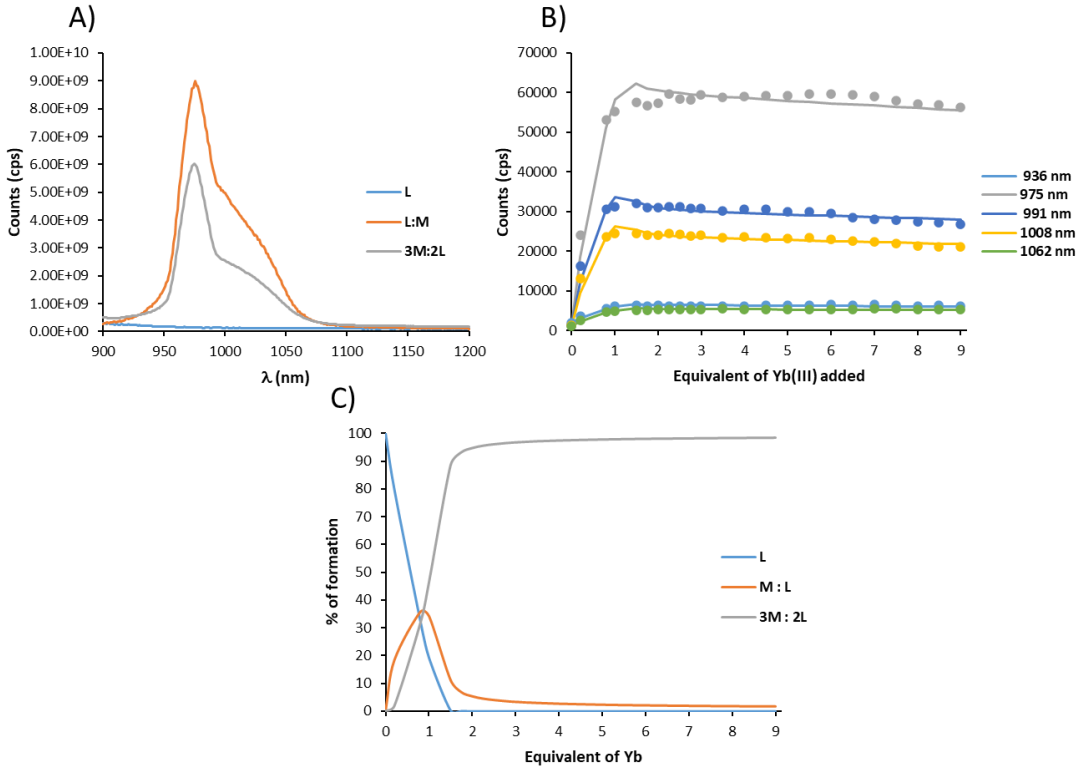

Figure 4-46 A) Recalculated spectra, B) binding isotherms (dots) and their corresponding fit (line), C) speciation-distribution diagram obtained from the fitting of Yb(III)-centred emission titration of **85** (1×10^{-5} M) with $YbCl_3$ in MeOH at 22 °C (using fewer data points from 0 to 1 equivalent) with SPECFIT.

Overall, omitting the data points from the titration data set in order to better understand the non-linear regression analysis for this titration (Figure 4-46C) and specifically the origin of the discrepancy in the fitting according to the residual fit resulted in a significant increase in the quality of the fit compared to the first attempt confirming the kinetic effect occurring in the equilibrium in the range of 0 to 1 equivalent of Yb(III) ions added. However, the quality of this fit was not satisfying and will need further work. The binding constants obtained for this fit are $\log\beta_{1:1} = 7.4 \pm 0.3$ and $\log\beta_{3:2} = 27.3 \pm 0.6$ for the

formation of YbL and Yb_3L_2 respectively. These values obtained were in the expected range and were relatively close to the binding constants obtained for the fitting of lanthanide-centred emission as in the case of Tb(III) and Eu(III) ions but are significantly higher than the values obtained for the fit of the titration using only 21 data points as it can be seen in Table 4-8.

Table 4-8 The summary of the binding constants obtained through fitting the data from the Yb(III)-centred emission titrations of **85** ($c = 1 \times 10^{-5}$ M) with $YbCl_3$ in MeOH at 22 °C using SPECFIT.

	Phosphorescence	
	$\log\beta_{1:1}$	**$\log\beta_{3:2}$**
Short titration	6.6 ± 0.1	23.2 ± 0.1
Long titration	7.9 ± 0.5	30.7 ± 0.9
Long titration modified	7.4 ± 0.3	27.3 ± 0.6

The binding constants obtained through the fitting of the changes in the absorption and fluorescence titrations are summarised in Table 4-9 and will be used for the rest of the study as the quality of these fits was satisfying.

Table 4-9 The summary of the binding constants obtained through fitting the data from absorption and emission titrations of **85** ($c = 1 \times 10^{-5}$ M) with $YbCl_3$ in MeOH at 22 °C using SPECFIT.

	Absorbance		**Fluorescence**	
	$\log\beta_{1:1}$	**$\log\beta_{3:2}$**	**$\log\beta_{1:1}$**	**$\log\beta_{3:2}$**
$YbCl_3$	6.0 ± 0.1	19.8 ± 0.5	7.3 ± 0.3	22.5 ± 0.5

The stoichiometry of the different Yb(III) complexes, their speciation-distribution diagram and their binding constants for the absorption and fluorescence titrations were successfully determined and are slightly lower than the values observed for the mid-sized Ln(III) ions (Sm(III), Eu(III), Gd(III) and Tb(III)). The titrations and fittings of seven Ln(III) ions were carried out, allowing the determination of the binding constants for the formation of 1:1 and 3:2 (M:L) complexes. Following these results, the effect of the size of the Ln(III) ions on these binding constants is discussed in the following paragraph.

4.3.10 Relationship between ionic radii of lanthanide ions and their binding constants

All the previous titrations were successfully carried out and fitted using non-linear regression analysis software SPECFIT. The fitting of the changes in both absorption and emission were successful and allowed us to determine that in all the cases, the addition of Ln(III) ions to a solution of **85** (1×10^{-5} M) in MeOH lead to the formation of 1:1 and 3:2 M:L species as it was previously demonstrated within Gunnlaugsson group,[29] while attempts to fit those changes to the successive formation of 1:1, 2:1 and 3:1 M:L, as demonstrated by Dr. Savyasachi within our research group at a lower concentration, was unsuccessful. The results of the fitting are summarised in Table 4-10 and correspond to the average of the binding constants obtained with at least duplicated titrations and fitting.

Table 4-10 Summary of the cumulative binding constants through fitting the data from absorption and emission titrations of **85** (c= 1×10^{-5} M) with $LnCl_3$ (Ln(III) = La, Sm, Eu, Gd, Tb, Yb, Lu) in MeOH at 22 °C using SPECFIT.

	Absorbance		Fluorescence		Phosphorescence	
	$\log\beta_{1:1}$	$\log\beta_{3:2}$	$\log\beta_{1:1}$	$\log\beta_{3:2}$	$\log\beta_{1:1}$	$\log\beta_{3:2}$
$LaCl_3$	5.5 ± 0.1	20.6 ± 0.2	6.1 ± 0.2	20.0 ± 0.4	Non emissive	
$SmCl_3$	6.8 ± 0.1	22.3 ± 0.3	7.6 ± 0.6	23.6 ± 0.8	4.7 ± 0.5	22.1 ± 0.2
$EuCl_3$	7.5 ± 0.3	25.5 ± 0.6	7.7 ± 0.5	23.4 ± 0.7	6.7 ± 0.1	25.9 ± 0.3
$GdCl_3$	6.5 ± 0.1	20.8 ± 0.5	7.6 ± 0.4	23.9 ± 0.6	Not measured	
$TbCl_3$	6.6 ± 0.3	22.3 ± 0.5	7.7 ± 0.3	23.4 ± 0.5	7.8 ± 0.3	28.5 ± 0.7
$YbCl_3$	6.0 ± 0.1	19.8 ± 0.5	7.3 ± 0.3	22.5 ± 0.5	Issues with fitting	
$LuCl_3$	6.6 ± 0.1	21.9 ± 0.2	7.6 ± 0.5	24.2 ± 0.7	Non emissive	

The formation of 3:2 species was also demonstrated by Bretonnière and co-workers, which successfully crystallized a tripodal tristerpyridine ligand in presence of various Ln(III) ions further supporting the possible formation of 3:2 species where only two terpyridines coordinate the Ln(III) ions.[259] Due to the lack of suitable crystals for single crystal X-ray diffraction, the exact environment of each lanthanide ions is still unclear in our case. Using general knowledge and data collected by the previous studies it was possible to suggest different configurations, however, the models proposed here correspond to a non-exhaustive list, and many more possibilities could be considered. For the formation of 1:1 species, three possibilities depicted in Figure 4-47 seem the most probable. The first one (Figure 4-47A)

corresponds to the Ln(III) ion being coordinated by one terpyridine moiety belonging to the ligand. The second one (Figure 4-47B) corresponds to the Ln(III) ion being coordinated by two terpyridine moieties of the same ligand, leading to the coordination sphere of the lanthanide ion to have 3 coordination sites available. Since Ln(III) ions have already been observed with a coordination sphere of 6 this model seems possible too, but the coordination sphere may be completed with three chloride ions or solvent molecules reaching a coordination number of 9 for Ln(III). More importantly, this configuration has been described previously within the work from the Gunnlaugsson group,[29] for the successive formation of 1:1 and 3:2 species during titration of **85** with Eu(III) ions. The third possibility (Figure 4-47C) correspond to the Ln(III) ion being coordinated by the three terpyridine moieties of the same ligand.

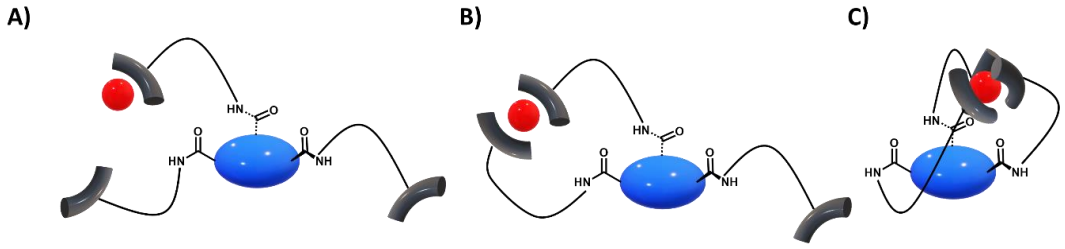

Figure 4-47 Schematic representation of the possible configuration of 1:1 species for LnL complex.

For the formation of 3:2 M:L species, two of the possible configurations are displayed in Figure 4-48. The first option corresponds to the one described previously,[29] which assume that two terpyridine moieties of the same ligand are coordinating one lanthanide ion while the third one is coordinated to another lanthanide ion acting as a linker essentially connecting two 1:1 complexes together through Ln(III) ion with the following formation of 3:2 assembly. The second possibility shown in Figure 4-48B, where the two **85** ligands were stacked on the top of each other, would be in a good agreement with the possibility of the formation of hydrogen bonding with the amide and the carbonyl groups that adorn the benzene ring. Each terpyridine moiety is then engaged in the coordination of a lanthanide ion, which extends the network into the 2D or 3D dimension.

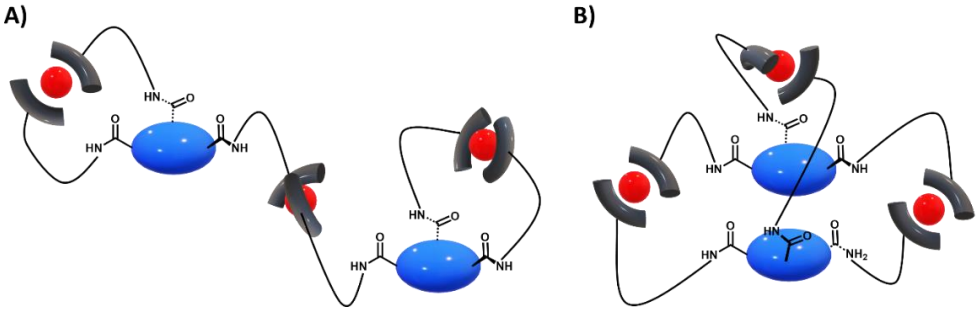

Figure 4-48 Schematic representation of the possible configuration of 3:2 species for Ln_3L_2 complex.

To further understand the coordination environment of the Ln(III) ions during the formation of the complexes, both **85EuCl$_3$** and **85TbCl$_3$** were synthesised according to procedures used in our laboratory to form Ln(III) complexes. **85** was reacted with one equivalent of the desired $LnCl_3$ ions ($EuCl_3$ or $TbCl_3$) under microwave irradiation at 70 °C for 1 hour. The resulting mixture was concentrated to half of its initial volume and ether diffusion led to the precipitation of the desired complex as a cream powder for **85EuCl$_3$** and a white powder for **85TbCl$_3$** in high yields. According to ^{1}H NMR studies (see appendixes), it is possible to observe similar features in the spectra of both **85** and its Eu(III) complex such as the singlet corresponding to the proton of the central core which is shifted from 8.66 ppm for the ligand to 8.70 ppm for the Eu(III) complex, and the protons of the alkane chain appear at a similar position in both spectra. Meanwhile, the signals corresponding to the TPy moieties are significantly broadened due to the paramagnetic nature of Eu(III) ions suggesting successful coordination of the TPy by the Eu(III) ions, which is further confirmed by the apparition of three multiplets between 8.15-7.97 ppm which is in agreement with the previously published results in the case of the titration by ^{1}H NMR of **85** through the addition of Eu(III) ions.[29] In the case of the Tb(III) complex similar features are observed except for the presence of three multiplets between 9.10-8.90 ppm suggesting a different environment between the terpyridine units. The photophysical properties of the complexes are currently being studied in both CD_3OD and MeOH to determine the q values of each complex.

Since it is possible to carry out ^{139}La NMR, a titration of **85** upon the addition of La(III) ion was carried out. The ^{1}H NMR showed in Figure 4-49 (Left) revealed that after the addition of 0.5 equivalent of La(III) ions some of the terpyridine signals are broadened and three multiplets appear between 8.15-7.98 ppm which is in good agreement with the previous observations for the spectroscopy titration of Eu(III) ions.[29] Further addition of La(III) ions did not result in any changes in the NMR spectra.

The ^{139}La NMR showed in Figure 4-49 (Right) reveals the presence of a broad singlet at 229.92 ppm for La(III) ions in 1 equivalent. This broad singlet is further shifted upon addition of La(III) ions to 234.21 ppm when reaching 3 equivalents of La(III). Further additions of La(III) to reach 10 equivalents led to a further shift to 236.97 ppm while the broad singlet is at 241.75 ppm for $LaCl_3$ in CD_3OD. Thus revealing a gradual change in the local environment of the La(III) ion, however, only one signal is observed through the entire titration demonstrating that the coordination environment of the La(III) ions is the same for the different species formed in solution or that the other species present are of negligible

concentration and cannot be observed by the NMR titration. Another explanation could be a fast exchange between the different species which therefore would not be visible by NMR.

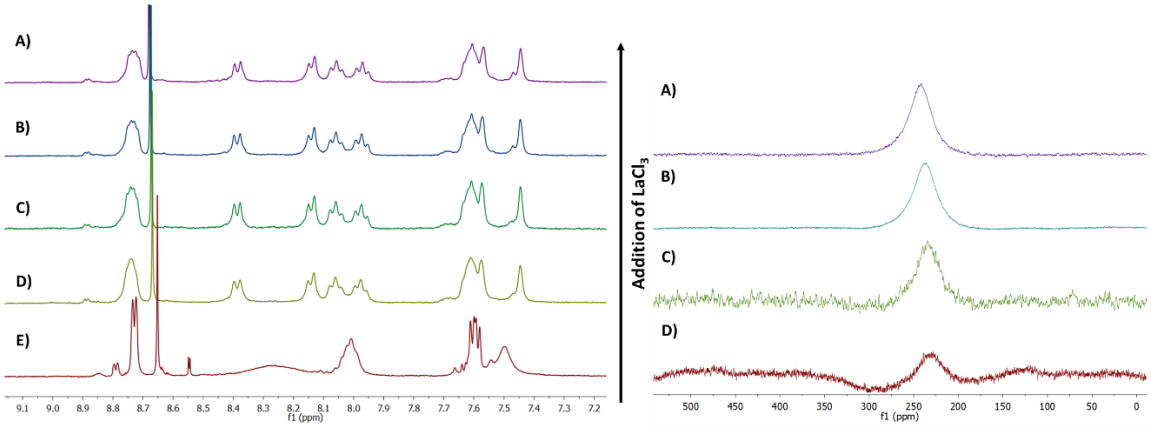

Figure 4-49 (Left) ^{1}H NMR (400 MHz, CD_3OD) of **85** (2.66×10^{-3} M) upon addition of $LaCl_3$ A) 3 eq, B) 2 eq, C) 1 eq, D) 0.5 eq, E) 0eq in CD_3OD. (Right) ^{139}La NMR (56.52 MHz, CD_3OD) of **85** (2.66×10^{-3} M) upon addition of $LaCl_3$ A) $LaCl_3$ alone, B) 10 eq, C) 3 eq, D) 1 eq.

To highlight any potential relationship between the cumulative binding constants $\log\beta_{1:1}$ and $\log\beta_{3:2}$ for the formation of LnL and Ln_3L_2 species in MeOH and the ionic radii of Ln(III) ions, a plot giving $\log\beta_{1:1}$ and $\log\beta_{3:2}$ versus the ionic radii of Ln(III) ions is shown in Figure 4-50. It is possible to see that for the plot of the cumulative binding constants obtained through the fitting of the changes in the absorption spectra, the values obtained for the Eu(III) were the highest ones for both the formation of 1:1 and 3:2 M:L species. However, when using a polynomial trendline of second-order to fit the data obtained, it is clear that the difference in the ionic radii of Ln had a subtle influence on the binding constants. Indeed, the differences in the binding constants obtained through the fitting of the absorption for each lanthanide tested in this chapter are all comprised within a range of 5.5-7.5 and 20.6-25.5 for 1:1 and 3:2 M:L species respectively (Table 4-10), but it is possible to observe a parabolic relationship between the cumulative binding constant and the ionic radii of Ln(III) ions. This trend is further confirmed by the plots of the cumulative binding constant obtained through the fitting of the fluorescence data (Figure 4-50B) where it appears that La(III), which is the largest lanthanide ion, possesses the smallest binding constant. As the ionic radius decreases the corresponding binding constant increases until it reaches a plateau for the Eu(III), Gd(III) and Tb(III) ions. When the ionic radius is further decreasing, for Yb(III) and Lu(III) ions, the binding constant is decreasing again.

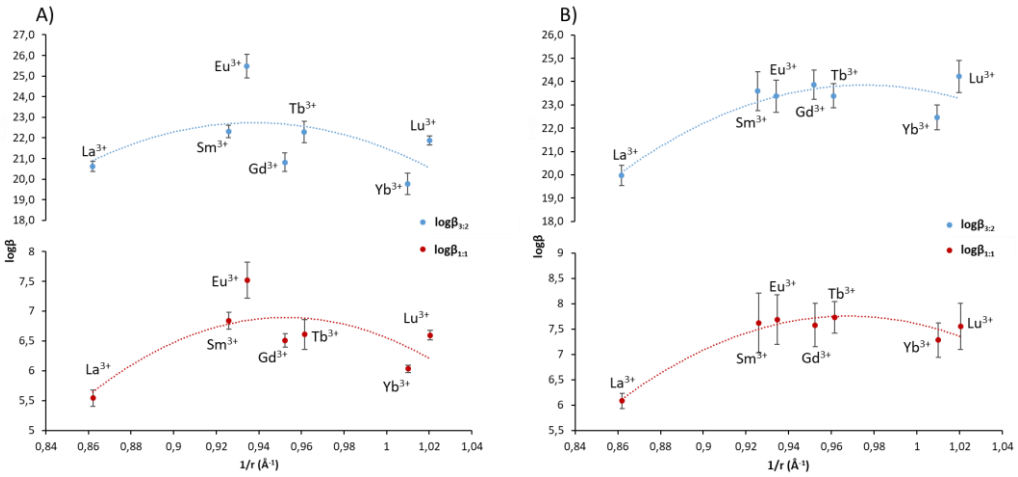

Figure 4-50 Cumulative binding constant $\log_{1:1}$ and $\log_{3:2}$ for LnL and Ln_3L_2 species in MeOH at 22 °C obtained through the fitting of the changes in A) absorption, B) fluorescence given versus the inverse of the ionic radii of Ln(III) ions.[234]

Interestingly, the trend observed deviates from what has been observed by Bünzli and co-workers in the case of the simple 2,2′:6′,2″-terpyridine.[260] In their work the trend observed for the plot of the binding constant of terpyridine in acetonitrile *vs* the inverse of the ionic radii of lanthanide ions corresponds to a straight line with a slight increase in the value of the binding constant as the radius of the lanthanide ions decreases. Bünzli and co-workers have described this behaviour as the classic electrostatic trend, meaning that the smaller lanthanides have a higher binding constant than the larger one.[106] This was further supported by the early work on the 1:1 adducts of 2,2':6',2"-terpyridine with the $LnCl_3$, by C. J. Kepert *et al*. that reported that throughout most of the series, the compounds crystallized as $(TPy)LnCl_3 \cdot xH_2O$ in a monoclinic C_m cell. This means that the only symmetry in the complex corresponds to a single mirror plan with the carbon and nitrogen of the central pyridine in the same plane as the metal and the chlorine. Interestingly they observed a gradual decrease of the number of water molecules observed in the unit cell, starting at 5 with the larger lanthanides (La(III), Ce(III) and Nd(III)), and gradually reducing to four for the mid-sized lanthanides (Sm(III), Eu(III) and Gd(III)) and three for the smaller lanthanides studied (Tb(III), Dy(III), Ho(III) and Er(III)). Thus displaying the effect of the size of the ionic radius on the coordination environment with the TPy being brought closer together and shielding the lanthanide ion from solvent molecules.[261] In the case of our study, the TPy is only functionalised at the 4-position, therefore the overall structure of TPy is not modified nor is its electronic distribution. This implies that the deviation from the trend observed by Bünzli and co-workers is due to three TPy being brought together within one ligand by covalently linking it through diaminopropane to 1,3,5-benzene tricarboxamide and its own

ability to self-assemble even at relatively low concentration in methanol and form supramolecular polymers which presumably preorganised and limit the arrangement of the terpyridine moieties around the Ln(III) ion.

The work carried out by Renaud *et al*. reported the study of a tridentate ligand (**68**) capable of forming triple-helical complexes with Ln(III) ions and that the corresponding stability constants follow the electrostatic trend which is an increase of the binding constant upon decrease of the ionic radius of Ln(III) ions.[137] While the spectroscopic study of the clipped ligand (**74**) demonstrated the opposite trend with its stability constant decreasing as the ionic radius decrease. This was rationalised by the fact that the introduction of a steric constraint created through the formation of the covalent tripod hindered the formation of tighter helical wrapping needed for smaller lanthanides.[140] This observation supports our assumption that the formation of supramolecular polymer preorganise and constrain the positioning of the terpyridine moieties around the Ln(III) ion.

To conclude, ^{1}H NMR and ^{139}La NMR of **85** upon the addition of La(III) ions showed that different species were formed in solution depending on the equivalents of La(III) ions added but that these species possess the same coordination environment. The plot of the determined binding constants *vs* the ionic radii of Ln(III) ions showed a parabolic relationship with the lower binding constants being observed for La(III) ion which is the largest Ln(III) ion while the highest binding constants were observed for the mid-sized Ln(III) ions (Sm (III), Eu(III), Gd(III) and Tb(III)) and the binding constant were decreasing again for the smaller Ln(III) ions (Yb(III) and Lu(III)). These results suggested that the formation of supramolecular polymers preorganise and constrain the positioning of the terpyridine moieties around the Ln(III) ion. To fully understand the environment of the Ln(III) ions in the [Ln**85**]$^{3+}$complexes, ^{1}H and ^{13} C NMR alongside the determination of the q-value of the Eu(III) and Tb(III) and crystallisation of the complexes are necessary. Since the influence of the ionic radius on the cumulative binding constant in solution was demonstrated, it was decided to further study its influence on the properties of the gels formed by **85**.

4.4 Study and Modification of the Properties of Soft-Material

4.4.1 Preparation of gels using 85

Previous studies from our laboratory of **85** have demonstrated that it was possible to form gels using approximatively 0.3 *wt* %, revealing that **85** is a supergelator, which is defined by the ability to form a gel with less than 1 *wt* %, in a mixture of MeOH:H_2O (30:70) upon slow evaporation of the solvent.[29] While Jung *et al.* demonstrated that it was possible to use the same ligand to form gels in a DMSO:H_2O mixture in presence of another tripodal compound to dictate chirality.[26] In the interest of our study, the formation of gel in MeOH: H_2O (30:70) was investigated and successfully demonstrated the reproducibility of the gelation to form 0.3 *wt* % gels. To do so, 3 mg of **85** was dissolved in 0.3 mL of MeOH by gently heating the solution and sonicating it until complete dissolution of the compound. Gentle addition of 0.7 mL of water to the solution of **85** resulted in the formation of gel in a few minutes to a few hours. As the formation of 0.3 *wt* % gel was difficult to achieve and would sometimes result in a very viscous solution, 0.3 *wt* % was considered as the lowest *wt* % achievable with this gelator and therefore the concentration of 3 mg/mL can be defined as the critical gelator concentration (CGC). As described by Kotova and co-workers,[17] crosslinking of the fibres of the supramolecular gel by diffusing *d*-metal through the gel is feasible. To further understand the extent of the modification of the properties of the gel by the diffusion of *d*-metals through it, the diffusion of 3 equivalent of $FeSO_4$ was achieved by preparing a stock solution of $FeSO_4$ in water and drop-casting the calculated amount of solution on the top of the gel. Gratifyingly, it was possible to monitor by the naked eye the diffusion of the Fe(II) ions through the gel.

A similar procedure was used to form 0.6 *wt* % gel by using the same quantities of solvents and 6 mg of **85**, and gelation was observed within a few minutes leading to much more robust soft-material than its 0.3 *wt* % counterpart. To gain an understanding of the extent of the modifications of the gel by diffusion of lanthanide ions and if the subtle difference of the ionic radii between each lanthanide could have an impact on the modification of the gel, the Ln(III) ions previously studied in solution with **85** were diffused through 0.6 *wt* % gels (Figure 4-51).

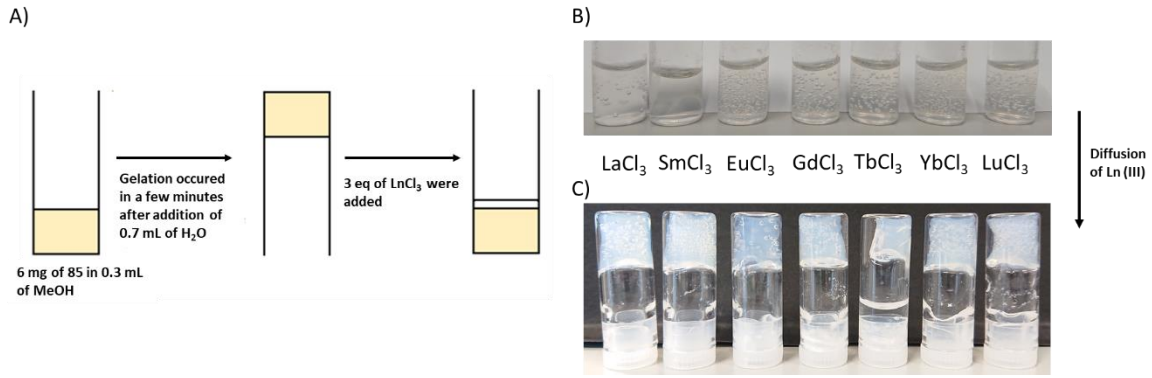

Figure 4-51 A) Schematic representation of the formation of **85** 0.6 *wt* % gel and the diffusion of $LnCl_3$. B) Picture of the 0.6 *wt* % **85** gel before and C) after diffusion of the corresponding $LnCl_3$.

Gratifyingly, the effect on the diffusion of lanthanide ions through the gel could be observed to the naked eye (Figure 4-51B and C). Indeed turbidity appeared and a clear decrease in the size of the gel could be observed. This change in the size could be attributed to the shrinking of the network forming the gel, as an excess of solvent could be removed from the vial 12 hours after the start of the diffusion. To gain further understanding of the properties of the gel, the effect on the properties of the gel by a change in the concentration and by addition of lanthanide ions, rheological study, thermogravimetric analysis (TGA), scanning electron microscopy (SEM) and spectroscopic studies were carried out. The results of these investigations will now be detailed.

4.4.2 Thermogravimetric analysis of 85 gels

Thermogravimetric analysis of the gels is an essential characterisation and reveals the exact weight percentage of solid-state gelator used to form the gel. For this analysis, a little amount of freshly prepared gel was used, and the thermogravimetric analysis was carried out under nitrogen to avoid the formation of metal oxides in presence of *d*- or *f*-metal ion. A typical thermogravimetric analysis profile for the gels discussed in this chapter is shown in Figure 4-52. The initial decrease of mass between 0 and 100 °C accounting for 99.2% of the initial weight of the sample is due to evaporation of the solvents (methanol and water). The insert in Figure 4-52 display the lower part of the *y*-axis (between 0 and 1 wt %) where it is possible to precisely observe the exact weight % of the gel as the first plateau represent the total mass of solid contained in the sample and in this case it is ≈ 0.8%, which can be rationalised by the evaporation of a small quantity of solvent during the gelation process. The other decrease in weight corresponds to the decomposition of the sample and were not analysed further.

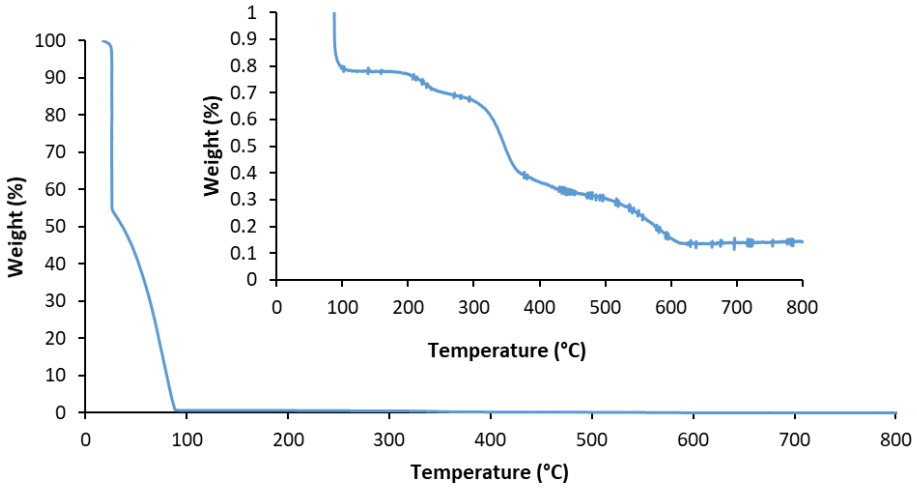

Figure 4-52 TGA thermograph of 0.6 *wt* % gel of **85** (MeOH:H_2O (30:70)), a temperature ramp of 10 °C/min under nitrogen atmosphere. Insert: Zoom on the region of the 0 to 1%.

The 0.3 *wt* % of the **85** gel modified by diffusion of Fe(II) ions leading to the modification of the supramolecular assembly was also analysed by TGA to determine the *wt* % of the solid component within soft material. Similarly to the 0.6 *wt* % gel, the initial decrease of mass between 0 and 100 °C accounting for ≈ 99.5% of the initial weight of the sample is due to evaporation of the solvents (methanol and water). The insert in Figure 4-53 reveals that the *wt* % of the gel is of ≈ 0.5 *wt* % which is relatively close to the theoretical *wt* % of 0.53.

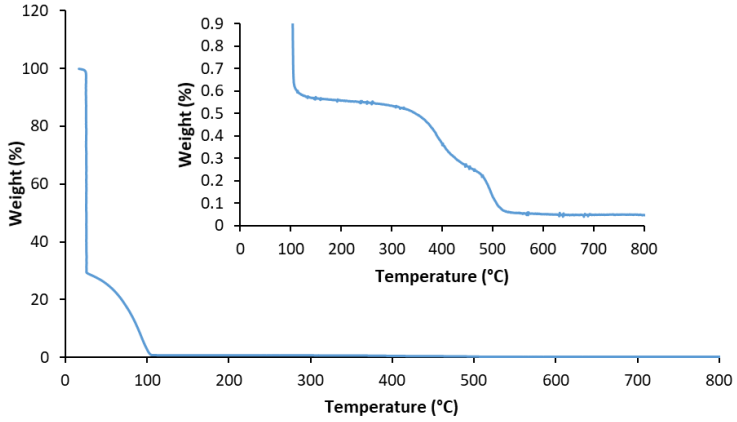

Figure 4-53 TGA thermograph of 0.3 *wt* % gel of **85** modified with Fe(II) ions (MeOH:H_2O (30:70)), a temperature ramp of 20 °C/min under nitrogen atmosphere. Insert: Zoom on the region of the 0 to 1%.

The 0.6 *wt* % gels modified by diffusion of $LnCl_3$ have also been analysed by TGA and has shown in the appendix, they all display a major weight percentage decrease between 0 and 150 °C corresponding to the solvents being evaporated. Interestingly, the temperature range corresponding to the evaporation of the solvents was increased by approximatively 50 °C between the gel formed by the ligand alone and the gels formed with Ln(III) ions. The

second observation is that three of the lanthanide gels (Eu(III), Yb(III) and Lu(III) display only one step in the decomposition of the solid. As shown in Figure 4-54, the *wt* % of each lanthanide gel is ranging between 1.5 and 1.8%, revealing that the shrinking of the network and loss of solvents upon diffusion of Ln(III) ions almost triple the *wt* % of the gels.

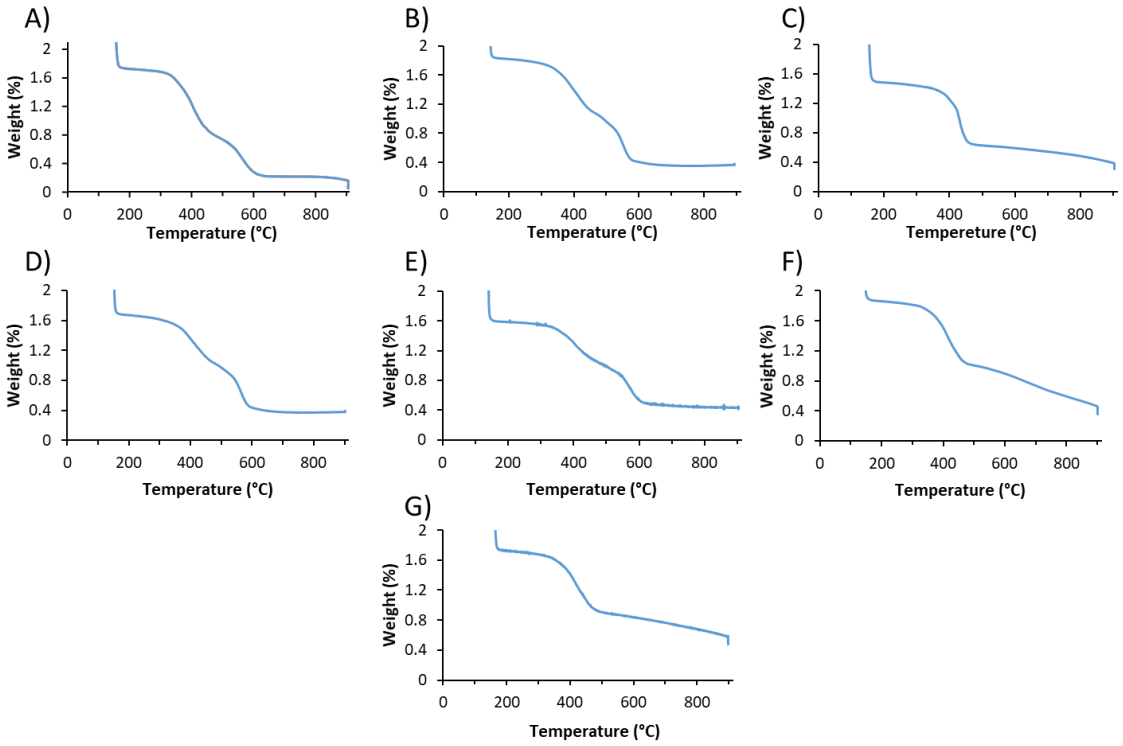

Figure 4-54 TGA thermograph of 0.6 *wt* % **85** gel modified with A) $LaCl_3$, B) $SmCl_3$, C) $EuCl_3$, D) $GdCl_3$, E) $TbCl_3$, F) $YbCl_3$ and G) $LuCl_3$ (MeOH:H_2O (30:70)), a temperature ramp of 10 °C/min under nitrogen atmosphere focused on the region of the 0 to 1.0 *wt* %.

The average values of triplicated measurement of the weight percentage of each gel modified by diffusion of Ln(III) ions are summarised in Table 4-11. It can be concluded from this table that the changes in *wt* % are not closely related to the size of the ionic radii of lanthanide ions. Indeed a random distribution of the *wt* % that varies between 1.57 and 1.79% is observed and demonstrate that a factor such as the size of the ionic radii has a negligible effect compared to the modifications of other factors such as the solubility and the organisation of the species in solution which is taking place upon binding to the Ln(III) ions.

Table 4-11 Summary of the weight % of the gels obtained by diffusion of Ln(III) ions through 0.6 *wt* % **85** gels (MeOH:H_2O (30:70)).

Gels	Weight %	Theoretical Weight %
$LaCl_3$	1.73	1.21
$SmCl_3$	1.75	1.17
$EuCl_3$	1.63	1.25
$GdCl_3$	1.68	1.22
$TbCl_3$	1.57	1.22
$YbCl_3$	1.79	1.20
$LuCl_3$	1.75	1.21

The TGA analysis revealed that the diffusion of Ln(III) ions led to an important increase in the *wt* % of the gels of approximatively 1 % which is higher than the expected *wt* % calculated. This is due to the modifications of the solubility and the organisation of the species in the gel. To analyse further the modifications of the gels, scanning electron microscopy of the gels were carried out and are discussed in the next section.

4.4.3 Scanning electron microscopy on 85 gels

To investigate the extent of the modifications of the gel morphology by diffusion of Ln(III) ions, scanning electron microscopy (SEM) was used to observe the changes. The xerogels of each gel were obtained by adding a small quantity of the gel onto a silicon wafer, leaving the solvent of the sample to evaporate for a few hours and further dry the sample under high vacuum. As the SEM operates under vacuum and requires the samples to be fully dry to avoid evaporation of the solvent in the instrument it was necessary to use the xerogel of the sample, this, of course, implies that the smaller features of the gels would be merged upon drying. Cryo-SEM was the preferred approach for this study to observe the gel in its hydrated form and avoid the merging of the smaller features, but access to this technique was not available at the time of the study. Each sample was finely coated using a gold-palladium target to increase the conductivity of the sample and achieving good quality imaging at high magnification.

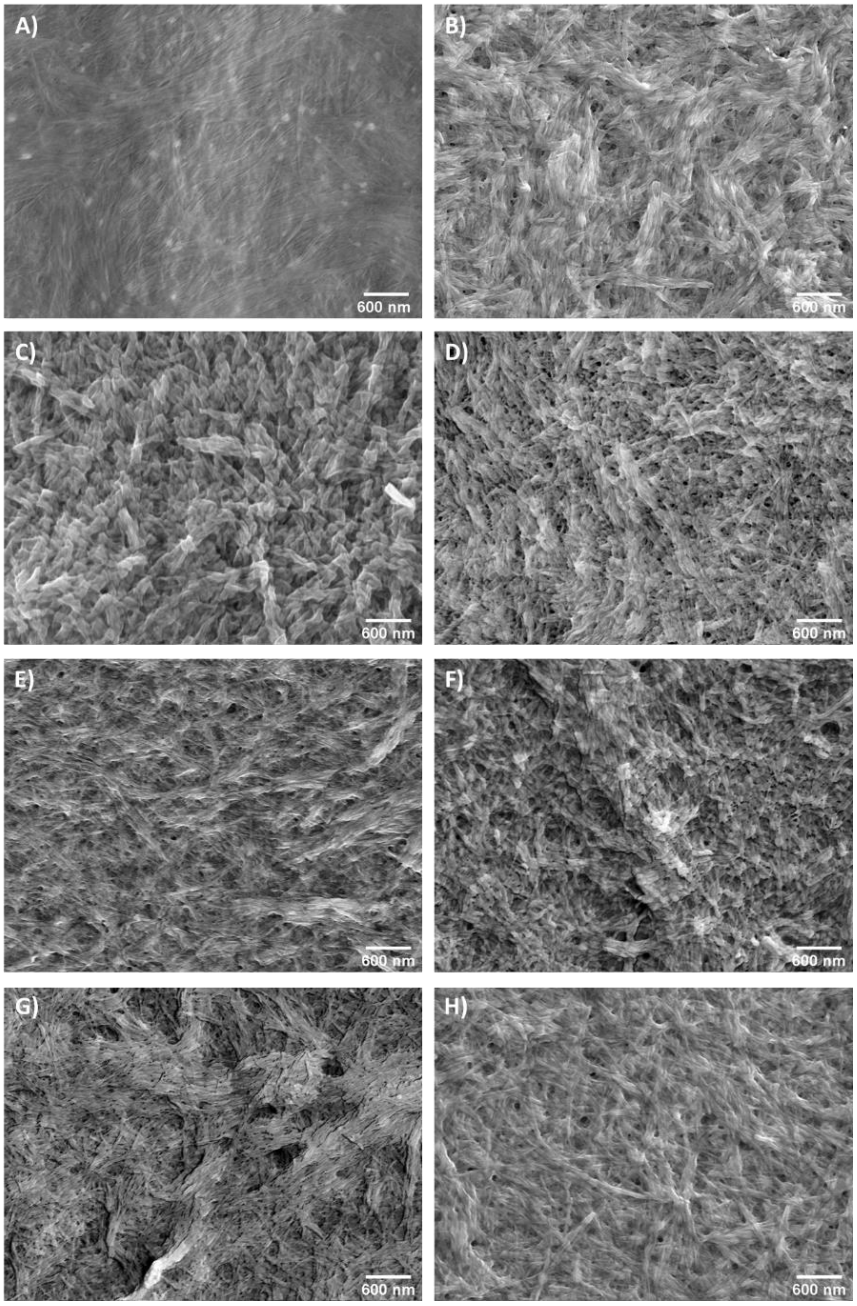

Figure 4-55 SEM images of xerogels of A) **85** (0.6 *wt* %) and modified with B) $LaCl_3$, C) $SmCl_3$, D) $EuCl_3$, E) $GdCl_3$, F) $TbCl_3$, G) $YbCl_3$ and H) $LuCl_3$ at the same magnification (scale bar 600 nm).

The images of the 0.3 *wt* % and 0.6 *wt* % gels are showing a very soft surface with apparent fibres that are not well defined, probably due to the merging of the features upon drying. SEM pictures of the xerogels modified by diffusion of lanthanides are shown in Figure 4-55. It is possible to see that the modification of the gels by diffusion of lanthanides ions resulted in the formation of much bigger and more defined fibres. Interestingly a similar observation was made by Kotova *et al*. with the diffusion of *d*-metals through the gel formed by **85** in MeOH:H_2O leading to the formation of fibres ranging from 40 to 60 nm.[17] Using the image processing programme ImageJ, the width of the fibres observed in the pictures

was measured.[192,193] The measurements demonstrated that the widths of the fibre were ranging from 15 nm to 165 nm, a Gaussian distribution of the fibre width for each gel was obtained and are shown in Figure 4-56.

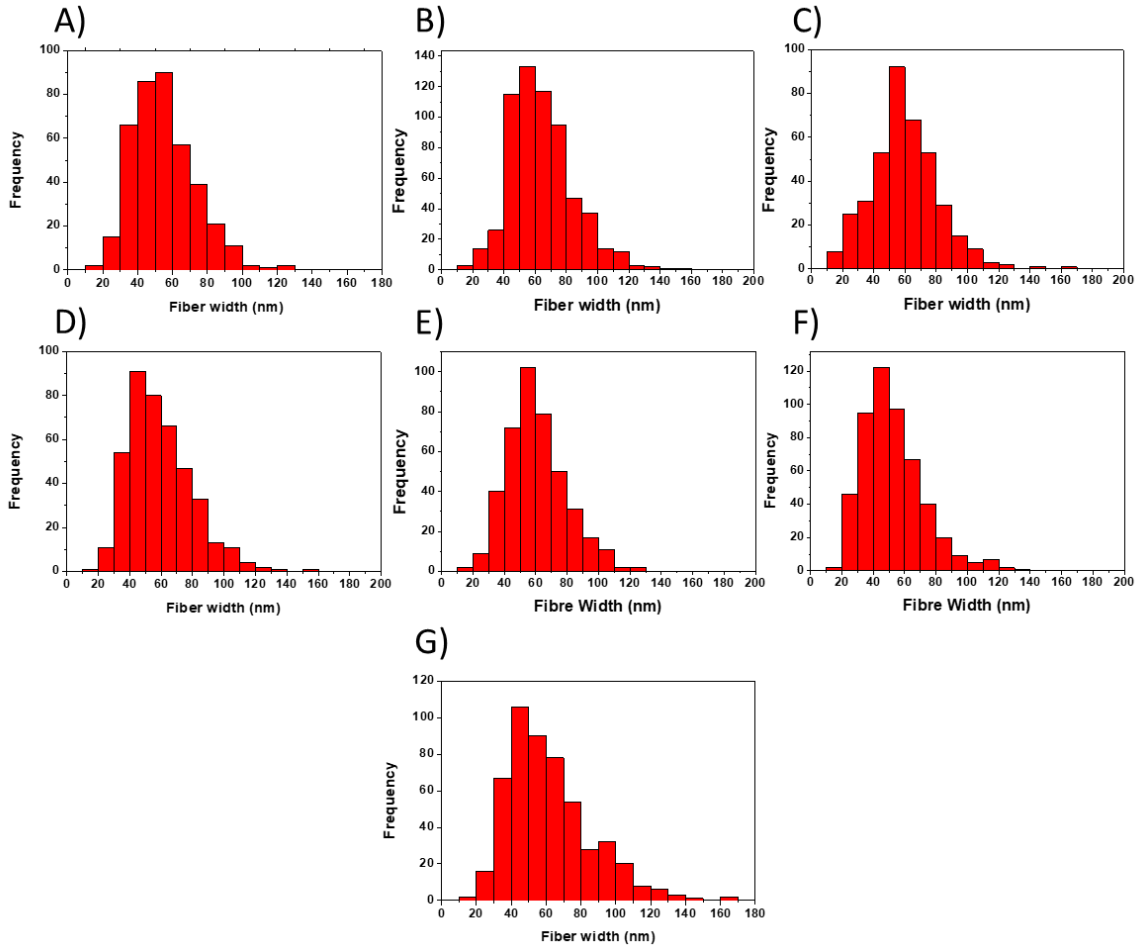

Figure 4-56 Histograms of the size distribution of the fibre widths of xerogel of **85** with A) $LaCl_3$, B) $SmCl_3$, C) $EuCl_3$, D) $GdCl_3$, E) $TbCl_3$, F) $YbCl_3$ and G) $LuCl_3$.

From these histograms, and Table 4-12 summarising the results of the measurements, it is possible to see that the average size of the fibres is comprised in the range of 52-64 nm which is a similar range observed previously for the diffusion of *d*-metal.[17] Interestingly when the gel is formed using the europium complex of **85**, the width of the fibres is only of 20-25 nm,[29] demonstrating a significant difference in the size of the fibres compared to the ones obtained through the diffusion of the metal. However, these observations have to be taken with caution as they are made on fully dry gel samples and therefore smaller features are merged in bigger features.[262] Further studies of the gels using small-angle neutron scattering (SANS) and Cryo-SEM/TEM would be required to accurately measure the fibre size in the wet state.

Table 4-12 Summary of the fibre width measurement of the xerogel of **85** modified by diffusion of Ln(III) ions.

Gels	Number of measurements	Average size (nm)	Minimum (nm)	Maximum (nm)
$LaCl_3$	392	54.8 ± 17.9	15.8	127.4
$SmCl_3$	620	64.1 ± 20.4	16.9	150.0
$EuCl_3$	390	60.0 ± 21.5	11.8	165.0
$GdCl_3$	415	59.5 ± 20.7	16.1	157.2
$TbCl_3$	417	60.7 ± 18.8	18.8	126.4
$YbCl_3$	513	52.6 ± 19.7	15.7	134.7
$LuCl_3$	513	61.6 ± 24.1	16.4	165.9

The SEM analysis revealed that the diffusion of Ln(III) ions led to a significant change in the morphology with the formation of bigger fibres. However, the measurement of the fibres after the modification of the gels did not show a relationship with the size of the lanthanide ion used. To analyse further the modifications of the gels, the rheological study of the gels was carried out and are discussed in the next section.

4.4.4 Rheological study of soft-material formed by 85

All the rheological measurements were carried out in collaboration with Dr. Niamh Willis-Fox and Dr. Ronan Daly in the Institute For Manufacturing (IFM) department of engineers at Cambridge University, United Kingdom. All the rheological measurements were carried out on 1.0 mL gel samples prepared 12 h before the measurement, using an Anton Paar Rheometer: MCR 302 equipped with parallel plates, and to avoid evaporation of solvent during the measurements a solvent trap was used and refilled with solvent if necessary. After placing the sample on the lower plate, the higher plate was lowered slowly to reach a final gap of 0.5 mm. The upper plate is rotated at a fixed frequency and variable amplitude for the amplitude sweep while it is rotated at a fixed amplitude and variable frequency for the frequency sweep. The effect of the rotation of the upper plate on the sample is measured as the strain γ and is plotted in function of time which results in a sinusoidal curve with the strain amplitude γ_A. In the meantime, the force is transferred through the sample to the lower plate and the force required to keep the lower plate in position is measured and is known as the shear stress τ. The plot of τ over time should result in a sinusoidal curve of the shear stress with the amplitude τ_A. For a sample displaying a viscoeslastic behaviour the two

sinusoidal curves will be offset by a phase shift δ which is always between 0° and 90°. From these measurements the complex shear modulus G^* can be calculated using the equation:

$$G^* = \frac{\tau_A}{\gamma_A}$$

With G^* in Pa, the shear-stress amplitude τ_A in Pa and the strain amplitude γ_A is dimensionless. Using the phase shift δ, it is possible to determine the contribution of the solid-like response (G', the storage modulus) and the liquid-like response (G", the loss modulus) to the complex shear modulus using the following equations:

$$G' = G^* cos\delta$$

$$G'' = G^* sin\delta$$

The results of these experiments will be represented by the plot of the storage and loss moduli, G' and G" respectively, in function of a designated variable. All the results presented in this paragraph correspond to the average of the triplicated experiments.

4.4.4.1 Amplitude sweep

To explore the properties of the gel, the storage modulus (G') and loss modulus (G") are measured as function of the shear stress. In this experiment, G' is representative of the energy stored during the test by the gel, in other words, the stiffness (solid-like response) of the gel. While G" corresponds to the energy dissipated during the test, the liquid-like response of the material. The amplitude sweep was measured for both 0.3 *wt* % and 0.6 *wt* % gels at an angular frequency of 1 Hz and the results are shown in Figure 4-57 and are the average of three sets of measurements for each gels. The 0.3 *wt* % gel showed a storage modulus of approximately an order of magnitude higher than its loss modulus. Both moduli displayed a linear response up to 0.1%, after which G" decreases and increases again to become higher than G' at a shear strain of 0.40% and the sample started behaving like a liquid. The yield stress was determined at 0.16% for the 0.3 *wt* % gel while the 0.6 *wt* % gel demonstrated much higher moduli, both an order of magnitude higher than the one demonstrated by the 0.3 *wt* % gel.

These experiments also revealed that G' and G" for the 0.6 *wt* % have a linear response up to 0.0076%, after which G' slowly decreased to become lower than G" at 0.57% of shear strain. The yield stress was determined at 0.06% for the 0.6 *wt* % gel. This demonstrated that the 0.3 *wt* % can sustain higher stress without losing its viscoelastic properties than the 0.6 *wt* % gel. It also showed that the 0.3 *wt* % gel starts to loose its solid-like behaviour later than the 0.6 *wt* % gel, the cross over point between the storage modulus

and the loss modulus happen at 0.59% for 0.6 *wt* % gel while it happens at 0.40% for the 0.3 *wt* % gel.

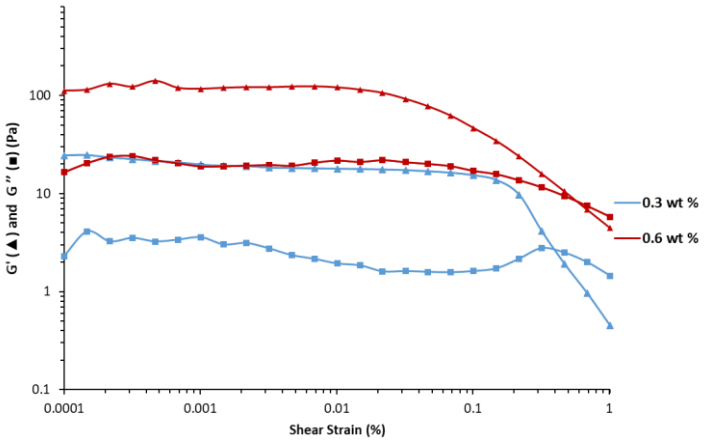

Figure 4-57 Strain sweeps for 0.3 *wt* % (blue) and 0.6 *wt* % (red) gels of **85** (MeOH:H_2O (30:70)), at f = 1 Hz.

As anticipated, the gel modified by the diffusion of Fe(II) ions displayed a drastically enhanced robustness compared to the ligand only gel (Figure 4-58). Its G' and G'' were significantly higher than both the 0.6 *wt* % and 0.3 *wt* % gels formed by **85** alone with G' and G" at 420 and 76 Pa respectively. Both moduli had a perfectly linear relationship with the shear stress up to 0.01% after which G' decreased and became lower than G" at 0.17% of shear strain. The yield stress for the 0.3 *wt* % gel cross-linked with Fe(II) ions was estimated to be 0.05%. These results demonstrated that the modification of the gel by diffusion of Fe(II) ions led to a significantly increased stiffness of the gel network with a larger viscoelastic region and much higher storage and loss moduli. However, the modified gel seems to undergo a transition from solid-like to liquid-like behaviour at a lower strain and thus would tend to flow more easily than the 0.3 *wt* % and 0.6 *wt* % gels formed by the ligand only.

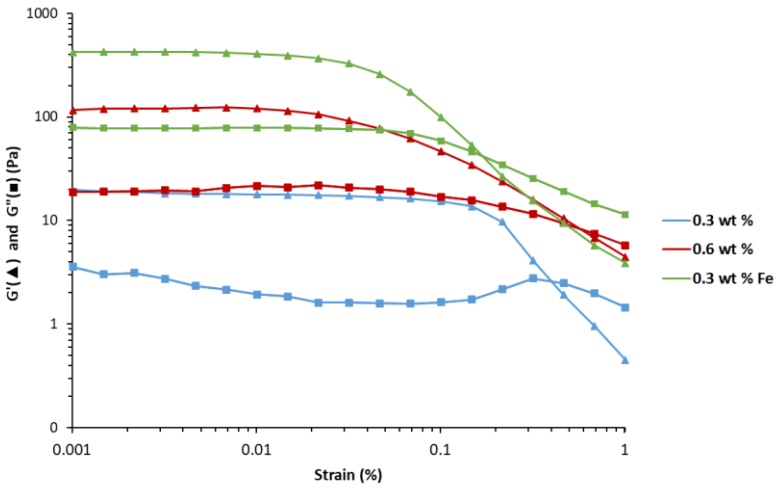

Figure 4-58 Strain sweeps for 0.3 *wt* % (blue), 0.6 *wt* % (red) and 0.3 *wt* % modified with $Fe(SO_4)_2$ (green) gels of **85** (MeOH:H_2O (30:70)), at f = 1 Hz.

The amplitude sweeps were also measured by Dr. Niamh Willis-Fox for both 0.6 *wt* % gel and 0.6 *wt* % gels with La(III) ions diffused through it, at an angular frequency of 10 rad s^{-1} and the results are shown in Figure 4-59. All the data shown in Figure 4-59 were averaged over three consecutive runs on fresh gel samples using serrated parallel plates with a diameter of 25 mm at a gap size of 1 mm. A fresh sample was required for each replicate as once the liquid-like state had been reached beyond the crossover neither gel recovered to their original mechanical properties. These experiments revealed little frequency dependence of the moduli in the linear viscoelastic regime, with a solid-like response (G' > G"), while the yield stress was determined at 0.13% and the cross over point at *ca*. 3.40%. These results demonstrated that the gel formed by the ligand alone is much softer than the one cross-linked with Fe(II) and that the gel cross-linked with La(III) is the more robust one. Indeed the gel modified by the diffusion of La(III) ions displayed a drastically enhanced robustness with G' and G" at 6239 and 980 Pa respectively which is two orders of magnitude higher than the 0.6 *wt* % gel of the ligand alone.

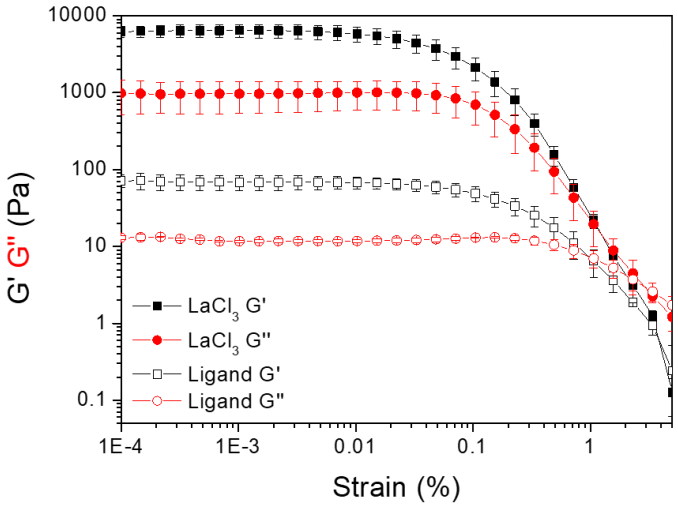

Figure 4-59 Strain sweeps for 0.6 *wt* % and 0.6 *wt* % modified with $LaCl_3$ gels of **85** (MeOH:H_2O (30:70)), at f = 10 rad s^{-1}.

4.4.4.2 Frequency sweep

Since the linear viscoelastic regions of all the gels were established, the study was carried on by a frequency sweep at a strain lower than the yield stress for all the gels. In the case of this experiment, the frequency was varied using a strain of 0.1%. The results of the experiments are shown in Figure 4-60 and it can be seen that G' and G" of the 0.3 *wt* % gel are at 5.2 and 2.4 Pa respectively at 0.1 rad s^{-1}. The moduli displayed a slight increase with the frequency until 12.6 rad s^{-1}, after which both G' and G" strongly increased. This increase is potentially due to the gel inertia, due to the high frequency applied the gel starts to behave

like a viscous liquid and while the frequency of the rotation of the upper plate is increasing, the inertia of the sample induced by the rotation is creating a resistance towards the change of direction of the rotation leading to an increase of the value of the moduli measured.[263] These results are revealing the structural weakness of the gel which appears to be at the lower limit of sensitivity of the rheometer and thus the unusual shape of the modulus when approaching 100 Hz is unreliable. The moduli of the 0.6 *wt* % gels are both much higher than the ones of the 0.3 *wt* % gel with G' at 272 Pa, being 6 orders of magnitude higher than G" at 40 Pa. Both its G' and G" are perfectly linear showing the independence of both the storage modulus and the loss modulus toward the angular frequency revealing the structural robustness of the gel.

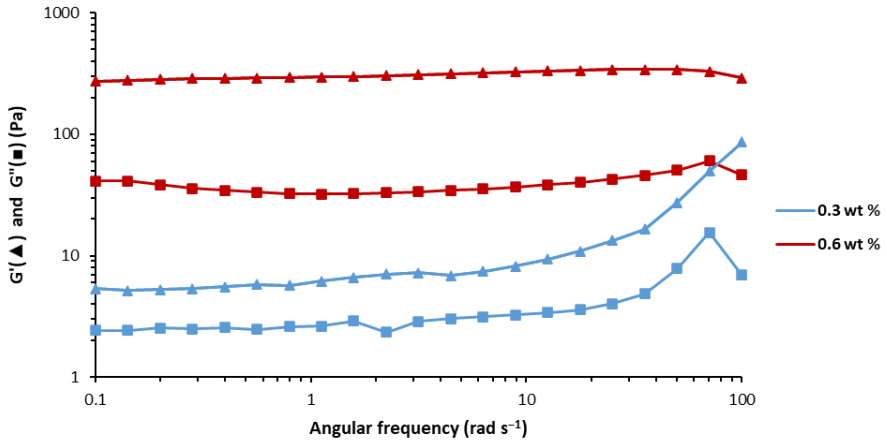

Figure 4-60 Frequency sweep for 0.3 *wt* % (blue) and 0.6 *wt* % (red) gels of **85** (MeOH:H_2O (30:70)), at 0.1% of amplitude strain.

Similarly for the observations made for the amplitude sweep, the 0.3 *wt* % gel modified with Fe(II) ions demonstrated higher values for both moduli than both the 0.3 *wt* % and 0.6 *wt* % gels of **85**, as seen in Figure 4-61. A small increase in the storage and loss moduli was observed as the frequency increased, however, a linear trend was observed for the entire range of frequencies demonstrating that the cross-linking of the fibres with Fe(II) ions resulted in a drastic increase in the robustness of the gel.

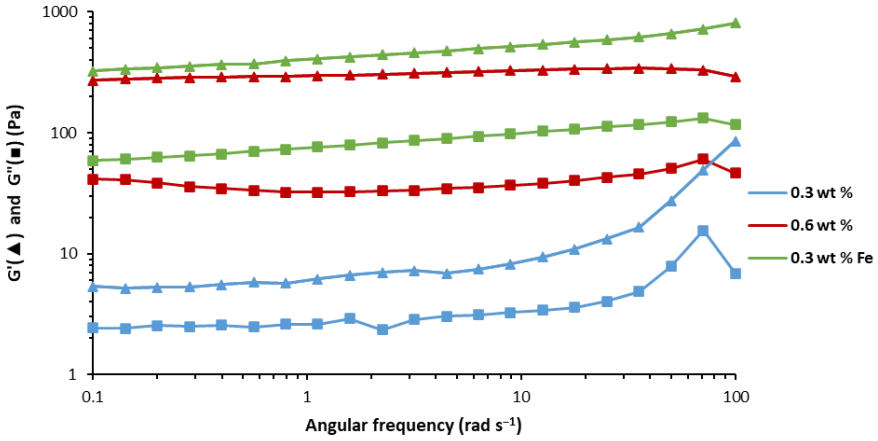

Figure 4-61 Frequency sweep for 0.3 *wt* % (blue), 0.6 *wt* % (red)) and 0.3 *wt* % modified with $FeSO_4$ (green) gels of **85** (MeOH:H_2O (30:70)), at 0.1% of amplitude strain.

The frequency sweeps were also measured by Dr. Niamh Willis-Fox for both 0.6 *wt* % gel and 0.6 *wt* % gels with La(III) ions diffused through it, the frequency was varied using a strain of 0.1% and the results are shown in Figure 4-62. All the data shown in Figure 4-62 were averaged over three consecutive runs on fresh gel samples using serrated parallel plates with a diameter of 25 mm at a gap size of 1 mm. The storage and loss moduli displayed a linear trend for the entire range of frequencies demonstrating that the cross-linking of the fibres with La(III) ions resulted in a drastic increase in the robustness of the gel.

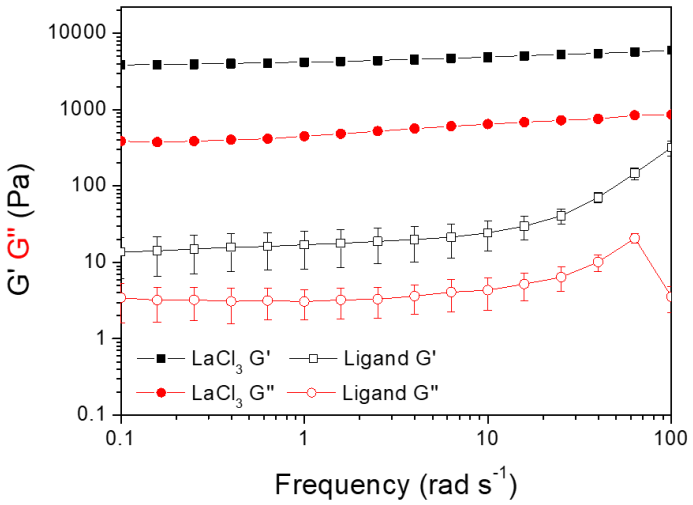

Figure 4-62 Frequency sweep for 0.6 *wt* % and 0.6 *wt* % modified with $LaCl_3$ gels of **85** (MeOH:H_2O (30:70)), at 0.1% of amplitude strain.

Amplitude sweeps along with frequency sweeps were also performed on gels modified with Sm(III), Eu(III), Gd(III), Tb(III), Yb(III) and Lu(III) chloride salts and are shown in the appendices. However, these samples were prepared in Dublin and shipped to Cambridge for the rheological measurements. The gels displayed similar properties to the ones of the 0.6 *wt* % modified with $LaCl_3$, except that each gel displayed lower values of

both moduli than the freshly made $LaCl_3$. Thus revealing that the gels had to be prepared on-site to proceed to the rheological measurement.

4.4.4.3 Recovery test

Since the viscoelastic behaviour of the gels was established and the 0.3 *wt* % gel modified with Fe(II) ions and the 0.6 *wt* % had demonstrated to be structurally robust, the recovery capacities of the gels were examined. To do so each gel was undergoing a series of stress experiments (big amplitude strain) followed by a recovery period (small amplitude strain) and the values of both the storage modulus and the loss modulus were determined. In this study, a strain amplitude of 20% was used to break up the gel, while its recovery was evaluated under a strain amplitude of 1%, with each strain amplitude being applied for 5 minutes. The frequency of the rotation of the plate was set to remain constant during the entire experiment at 1 Hz.

The 0.3 *wt* % gel was the first one to be assessed and the results are shown in the appendixes. Both values of the storage modulus and loss modulus are very low (less than 8 Pa) with some of the points measured being very scattered, moreover G' was always above G" which is fundamentally wrong and could be due to the use of a too high angular frequency for the high-stress phase. It also suggests that the gel did not sustain the recovery test, possibly because of too low concentration of gelator. The combination of these factors made the interpretation of these results impossible and revealed that the 0.3 *wt* % gel is too weak to be evaluated.

The recovery experiment of the 0.6 *wt* % gel was next evaluated under the conditions previously stated and the results are shown in Figure 4-63. The initial storage and loss moduli observed are under a strain amplitude of 20% which is higher than the yield stress, as previously demonstrated and as expected the gel exhibited a fluid-like behaviour (G">G'). But once the strain amplitude was decreased to 0.1% (below the yield stress), G'and G" increased significantly and satisfyingly G'(430 Pa) became significantly higher than G" (48 Pa). Interestingly a small delay in the recovery could be observed but every time a plateau was reached within the 5 minutes of the recovery step. It is also important to note that the gel-sol transition followed by the sol-gel transition was repeated multiple times without showing sign of weakening of the gel demonstrating an excellent thixotropic behaviour.

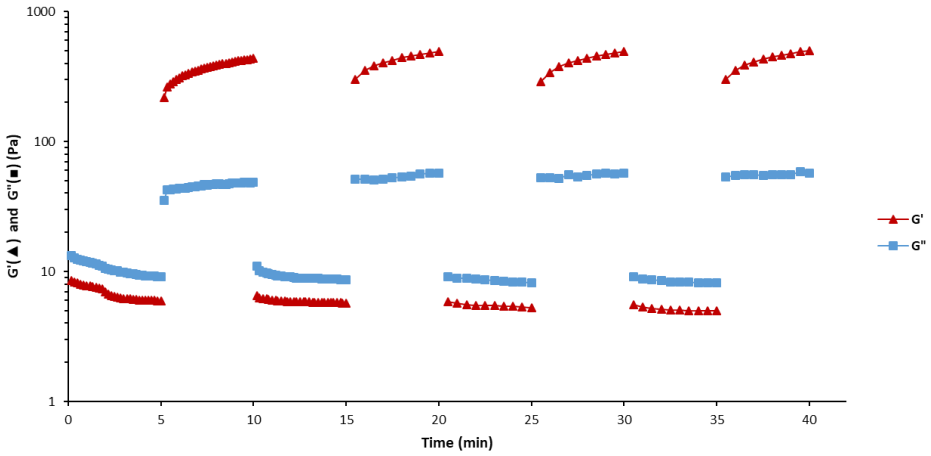

Figure 4-63 Recovery test for 0.6 *wt* % gel with alternating strain amplitudes of 20% and 0.1% at f = 1 Hz.

Interestingly the recovery test carried out on the 0.3 *wt* % gel modified with Fe(II) revealed an improved capacity of the sample to recover its solid-like behaviour (G'>G", more elastic than viscous). As shown in Figure 4-64, under a strain amplitude higher than its yield stress (20% in this case), the gel adopts a liquid-like behaviour (G">G'). Once the strain amplitude is reduced to 0.1% an immediate increase of G' and G" reaching respectively 420 Pa and 72 Pa occured. Similarly to the 0.6 wt % gel, the gel-sol transition followed by the sol-gel transition was repeated multiple times without showing sign of weakening of the gel, demonstrating an excellent thixotropic behaviour. These results demonstrated that the use of metal to cross-link supramolecular polymer allowed the improvement of the structural robustness of the gel and also to decrease the recovery time of thixotropic material.

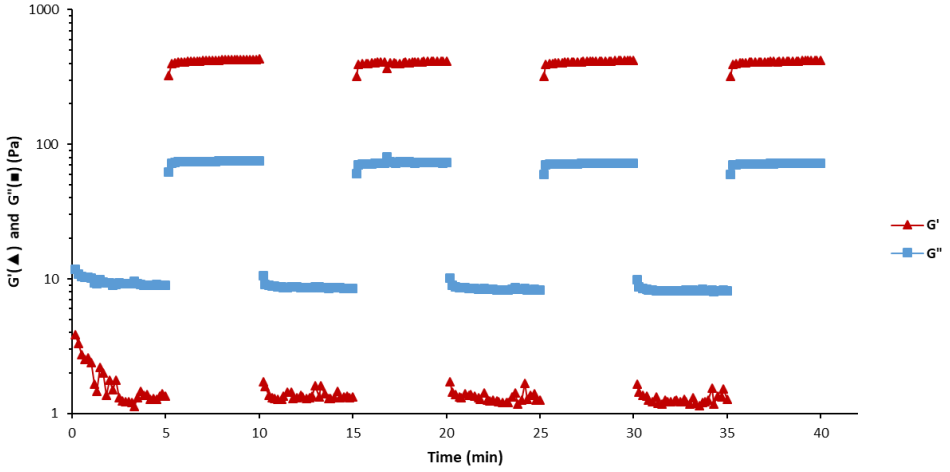

Figure 4-64 Recovery test for 0.3 *wt* % gel modified with Fe(II) ions with alternating strain amplitudes of 20% and 0.1% at f = 1 Hz.

In Figure 4-65, the storage and loss moduli of the gels were measured at 0.1% strain at 1 Hz, following this a shear rate of 100 s^{-1} was applied to damage the gels and the recovery

process was measured at 0.1% strain at 1 Hz. In both cases, once destroyed at 100 s^{-1}, neither recover to their original modulus and subsequent measurements show a much weaker gel.

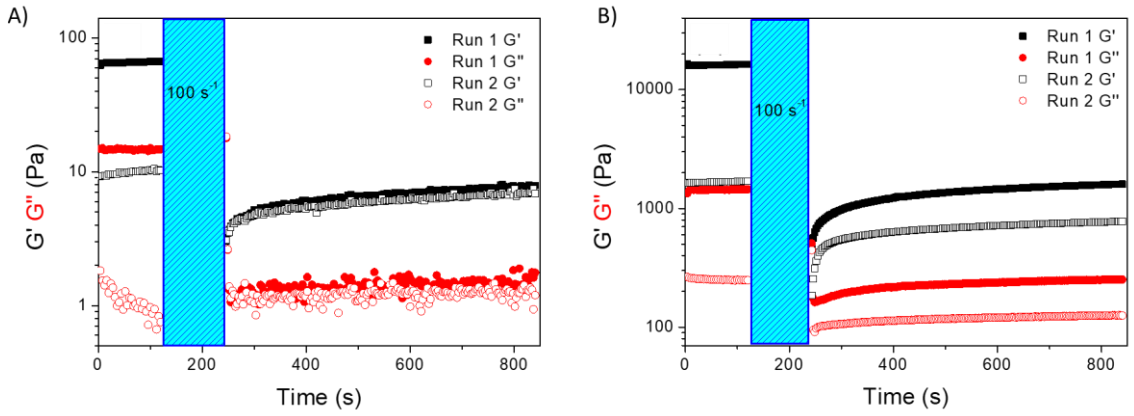

Figure 4-65 Storage (G') and loss (G'') moduli of the A) ligand and B) $LaCl_3$ doped gels recorded at a strain of 0.1% and f = 1 Hz. The blue hatched portion indicated the time during which a rotation at 100 s^{-1} was applied to damage the gels.

The recovery properties of the gels were also tested by imposing alternating strain amplitudes of 100% and 0.1% at a constant 1 Hz oscillation frequency. As shown in Figure 4-66, the ligand gel went from liquid-like ($G'' > G'$) to solid-like ($G' > G''$) behaviour almost instantly with a quick recovery of the original values of the moduli in these two regimes. However, the 0.6 *wt* % gel modified with $LaCl_3$ displayed a different behaviour, while both moduli drastically decreased under the strain amplitude of 100%, the storage modulus never become lower than the loss modulus thus showing that the addition of the metal dopant drastically improves the strength of the gel and does not allow the liquefaction observed for the ligand under the same conditions. Additionally, it is possible to observe that upon the release of the stress, despite displaying quickly higher moduli, the gel never recovered its original moduli and became weaker after each cycle.

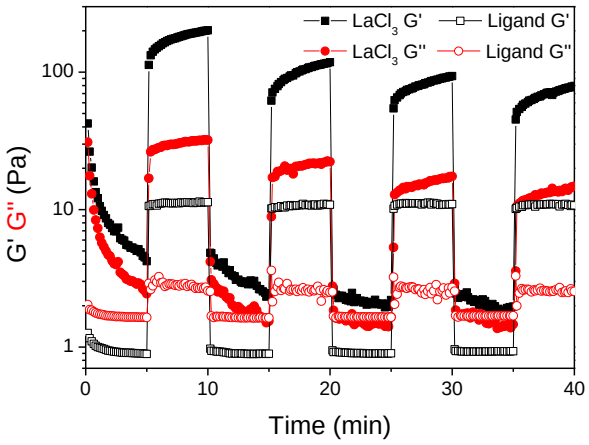

Figure 4-66 Storage (G') and loss (G'') moduli of the ligand gels (0.6 *wt* %) and the gel modified with $LaCl_3$ recorded with alternating strain amplitudes of 100% and 0.1% at f = 1 Hz.

4.5 Formation of Multicomponent Gels

4.5.1 Expanding spectroscopic properties using ruthenium complex $[Ru(phen)_2\mathbf{130}]^{2+}$

There has been an increasing interest for the formation of multicomponent gels, however, different approaches are used depending on the two components being mixed. In some cases, the two components can form gels on their own but cannot form a gel when mixed individually in the same conditions. Also, if only one of components has this capacity the conditions will have to be adapted through trial and error as the addition of the second component can hinder the formation of the overall soft material or disrupt the network and lead to the collapse of the soft material. Similarly, to what has been shown in sections 4.3 and 4.4, the diffusion of ions to cross-link the already existing fibres can lead to modification of the properties of the gel. Hence the idea here was to similarly, diffuse through the gel a second component to extend or modify the properties of the gel. To further explore the potential application of **85** as a matrix to form a multicomponent gel, a ruthenium complex synthesised by Dr. Estelayo-Adrián, namely $[Ru(phen)_2\mathbf{148}]^{2+}$ (Scheme 4-2) was used as the second component. Our interest was drawn to this compound due to its water solubility, its ability to form micelles, its rich spectroscopic properties, and its capacity to form reactive oxygen species upon laser irradiation.[264] Another factor that significantly drew our interest was the possibility of energy transfer from the ruthenium complexes to the Ln(III) ions that emit in the NIR (Yb(III) in this case). Previously, our research group reported the development of a mixed lanthanide-transition-metal complex using neodymium and ytterbium. The study of this complex revealed that upon excitation of the Ru(II) MLCT band, sensitisation of the Yb(III) and Nd(III) centre was occurring leading to NIR emission.[265] This phenomenon was also observed by other groups using ruthenium bipyridine complexes as well as ferrocene.[266] The sensitisation of NIR emitting lanthanides using *d*-metal complexes is an efficient method to avoid the use of high energy UV excitation which can be damaging for biological samples and therefore limit the applications of these complexes in chemical biology. In this study, $[Ru(phen)_2\mathbf{148}]^{2+}$, of which the biological properties were studied by Dr. Estelayo-Adrián,[264] was used to modify the **85** gels as its long alkyl chain could help to stabilise the gel through its diffusion, and explore its capacity to efficiently transfer energy onto the Yb(III) ion excited state leading to an increase in its NIR-emission.

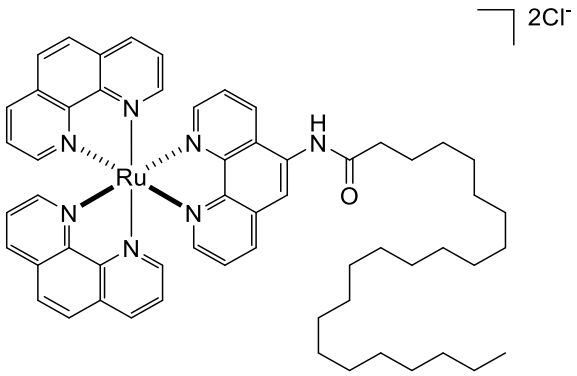

Scheme 4-2 Structure of $[Ru(phen)_2\mathbf{148}]^{2+}$

4.5.1.1 Modification of the gel formed by 85

With the view of preparing the two-component gels, a known quantity (0.1, 0.3 and 0.5 equivalents relative to **85**) of $[Ru(phen)_2\mathbf{148}]^{2+}$ in H_2O was added on the top of the 0.6 *wt* % **85** gels in MeOH:H_2O (30:70). The diffusion was monitored by the naked eye due to the orange colour of $[Ru(phen)_2\mathbf{148}]^{2+}$ originating from the MLCT absorption. $[Ru(phen)_2\mathbf{148}]^{2+}$ complex fully diffused through the gel medium after 96 h (Figure 4-67). Gratifyingly, after the complete diffusion of $[Ru(phen)_2\mathbf{148}]^{2+}$, the resulting two-component gels were still able to hold themselves for 21 h during the inversion test demonstrating that the integration of another component in the gel did not seem to have significantly damaged the fibre network.

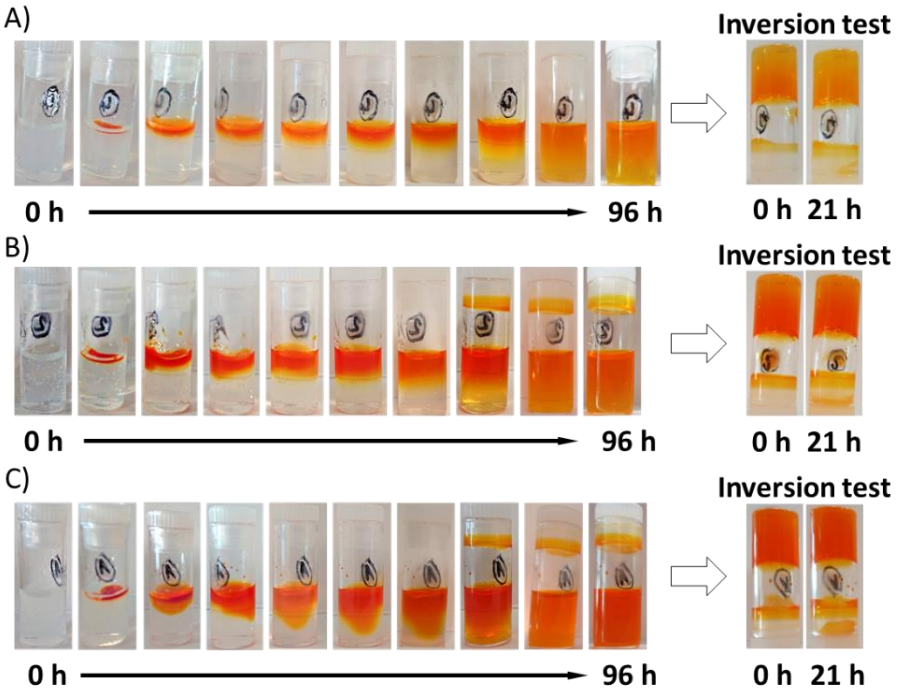

Figure 4-67 Diffusion of A) 0.1, B) 0.3, C) 0.5 equivalents of $[Ru(phen)_2\mathbf{148}]^{2+}$ through 0.6 *wt* % **85** gel (MeOH:H_2O (30:70)) over 96 h with inversion test over 21 h.

The diffusion of $[Ru(phen)_2\mathbf{148}]^{2+}$ was also undertaken in the **85** gel modified with Yb(III) ions. The order of the modification of the gel was also tested, one 0.6 *wt* % gel had first $[Ru(phen)_2\mathbf{148}]^{2+}$ diffused through it leading to the colouration of the gel in orange as previously observed followed by diffusion of 3 equivalents of $YbCl_3$ resulting in the shrinking of the network concomitantly with the loss of solvent and $[Ru(phen)_2\mathbf{148}]^{2+}$. The second order consisted of diffusing 3 equivalents of $YbCl_3$ through the 0.6 *wt* % **85** gel leading to the shrinking of the network as previously observed with the series of lanthanides, followed by addition on the top of the gel of an aqueous solution of $[Ru(phen)_2\mathbf{148}]^{2+}$ leading to the slow diffusion through the metallogel. Due to the difficult synthesis of $[Ru(phen)_2\mathbf{148}]^{2+}$, the second approach was preferred for the remaining experiments to avoid loss of $[Ru(phen)_2\mathbf{148}]^{2+}$ through the shrinking of the network and loss of solvent.

4.5.1.2 Thermogravimetric analysis of the gels

The resulting gels were analysed by thermogravimetric analysis (TGA), before proceeding to the measurements the supernatant that was formed in the case of the diffusion of Yb(III) ions was decanted off, and the results can be seen in Figure 4-68. Diffusion of 0.5 equivalents of $[Ru(phen)_2\mathbf{148}]^{2+}$ in the 0.6 *wt* % gel resulted in the formation of a ≈ 0.7 *wt* % gel while the diffusion of 0.5 equivalent of $[Ru(phen)_2\mathbf{148}]^{2+}$ in the 0.6 *wt* % gel modified with $YbCl_3$ resulted in the formation of 1.9 *wt* % gel. From these results, it appears that the diffusion of $[Ru(phen)_2\mathbf{148}]^{2+}$ through the gels independently of the presence of Yb(III) ions increases the weight percentage by 0.1%.

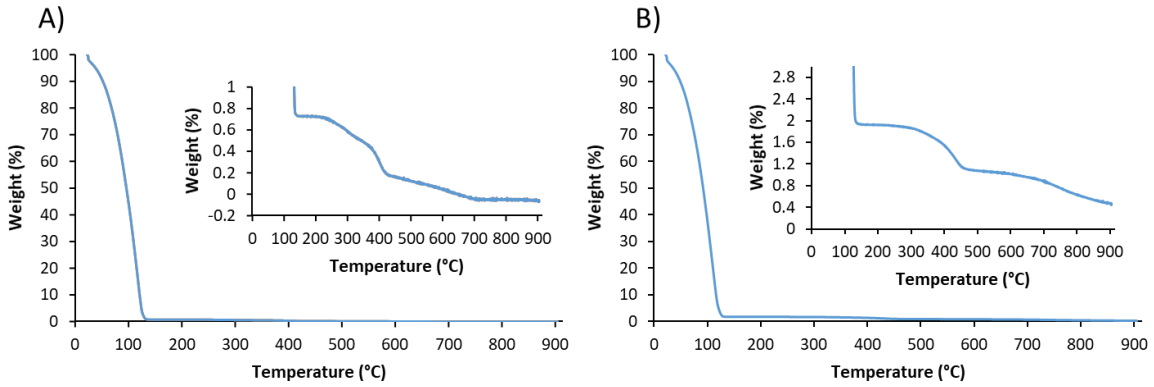

Figure 4-68 TGA thermograph of A) 0.6 *wt* % gel of **85** modified by diffusion of $[Ru(phen)_2\mathbf{148}]^{2+}$, B) 0.6 *wt* % gel of **85** modified by diffusion of $YbCl_3$ followed by diffusion of $[Ru(phen)_2\mathbf{148}]^{2+}$ (MeOH:H_2O (30:70)) with a temperature ramp of 10 °C/min under nitrogen. Inserts represent zoomed-in regions of the 0 to 1% or 3% of the corresponding thermograph.

4.5.1.3 Spectroscopic study of the gels

The spectroscopic properties of the gels were studied by depositing a small quantity of gel on a quartz slide and by spreading it using a second quartz slide. The two slides were then placed into the instrument sample holder, facing the beam in the UV-vis spectrophotometer and at approximatively a 45° angle relative to the beam. The absorption, emission and excitation spectra of a thin layer of **85** gel with 0.5 equivalents of $[Ru(phen)_2\mathbf{148}]^{2+}$ between the two quartz slides are shown in Figure 4-69A, while the ones corresponding to gel with 0.1 and 0.3 equivalents of $[Ru(phen)_2\mathbf{148}]^{2+}$ are shown in the appendixes. The absorption spectra of the gel display three bands at 220, 260 and 450 nm and a shoulder at 317 nm. The two bands at 220 and 260 nm are attributed to the $\pi \rightarrow \pi^*$ intra-ligand bands of $[Ru(phen)_2\mathbf{148}]^{2+}$ while the band at 450 nm corresponds to the $\pi \rightarrow \pi^*$ MLCT band of $[Ru(phen)_2\mathbf{148}]^{2+}$ and are in good agreement with the absorption of the compound in sodium phosphate-buffered aqueous solution.[264] The shoulder at 317 nm belongs to the absorption spectra of **85** and is the only feature visible from the gelator **85**. Upon excitation into the $\pi\pi^*$ MLCT band at 451 nm, a broad emission band is observed between 500 nm and 850 nm with λ_{max} = 610 nm which is slightly blue-shifted (4 nm) compared to the complex in sodium phosphate-buffered aqueous solution but can be rationalised by the difference of polarity of the environment due to the mixture of water and methanol used to form the gel. The excitation spectra of the gel displayed a similar pattern to the absorption with the presence of the three bands and one shoulder.

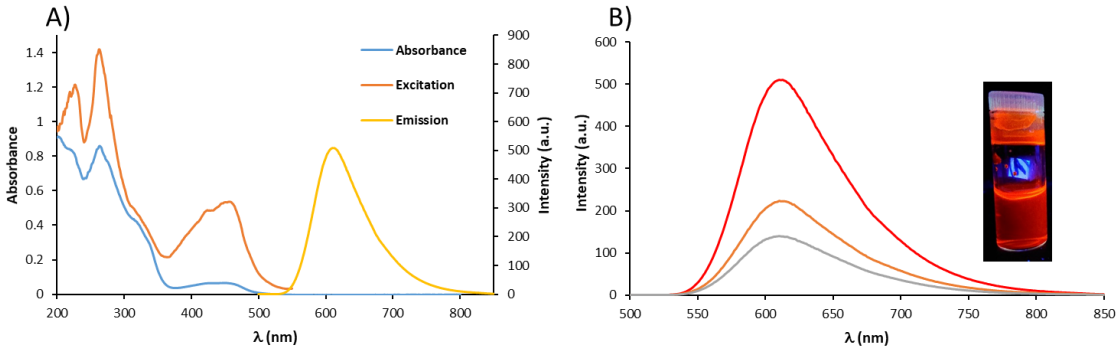

Figure 4-69 A) Absorption (blue), excitation (orange, λ_{em}= 610 nm) and fluorescence (yellow, λ_{ex}= 450 nm) spectra of a thin layer of **85** gel with 0.5 equivalent $[Ru(phen)_2\mathbf{148}]^{2+}$ (MeOH:H_2O (30:70)). B) Fluorescence (red, λ_{ex}= 450 nm) spectra of a thin layer of **85** gel with 0.1 equivalent (grey), 0.3 equivalent (orange) and 0.5 equivalent (red) of $[Ru(phen)_2\mathbf{148}]^{2+}$ diffused through it in MeOH:H_2O (30:70). Insert: Picture of **85** gel with 0.5 equivalents of $[Ru(phen)_2\mathbf{148}]^{2+}$ diffused through it in MeOH:H_2O (30:70) under UV lamp irradiation.

The diffusion of 0.1, 0.3 and 0.5 equivalents of $[Ru(phen)_2\mathbf{148}]^{2+}$ resulted in the emission of the gel to increase up to 5 times, revealing a bright red luminescence under UV

lamp irradiation as shown in the insert in Figure 4-69B. The quantum yield of the gel obtained by diffusion of 0.5 equivalents of $[Ru(phen)_2\mathbf{148}]^{2+}$ was determined by using an integrating sphere and forming the desired gel in a small vial that was directly used for the measurement. The quantum yield was established to be of 5.1% which can be considered the same as the quantum yield of the complex in aqueous solution (4.9%).[264]

4.5.1.4 Scanning electron microscopy on the gels

To investigate the modification of the initial **85** gel morphology by diffusion of $[Ru(phen)_2\mathbf{148}]^{2+}$ and Yb(III) ions into its structure, SEM was used to observe the changes. The xerogels of each gel were obtained by adding a small quantity of the freshly prepared gel onto a silicon wafer, leave the solvent of the sample to evaporate for a few hours and further dry the sample under high vacuum. As the SEM operates under vacuum and requires the samples to be dried and to avoid evaporation of the solvent in the instrument it was necessary to use the xerogel of the sample. As shown in Figure 4-70, the diffusion of 0.5 equivalent of $[Ru(phen)_2\mathbf{148}]^{2+}$ through the 0.6 *wt* % gel did not result in a significant modification of the fibre structure. Indeed the fibres are in the range of 15 to 56 nm with an average value of 26.9 nm with a uniform dispersity and their morphology is very similar to the one of the **85** gel previously observed.

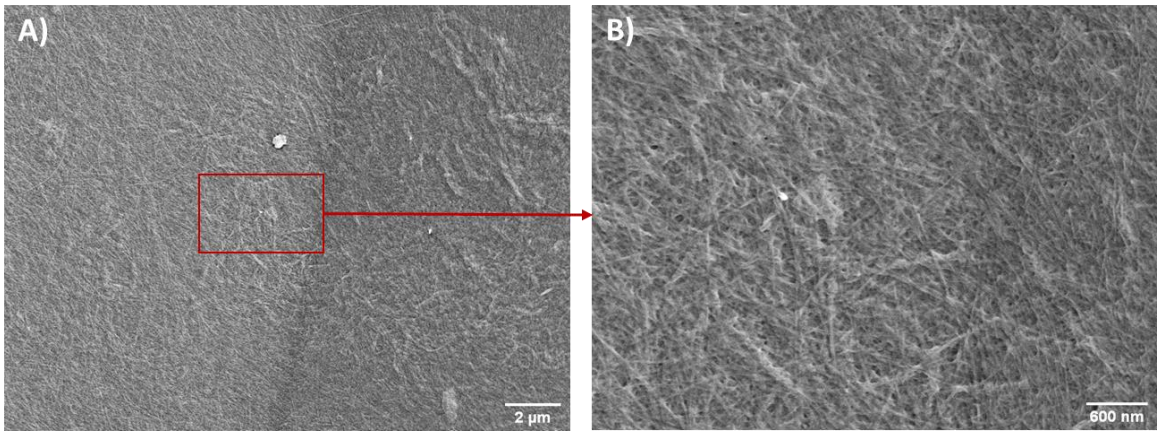

Figure 4-70 SEM pictures of xerogel of **85** with 0.5 equivalent of $[Ru(phen)_2\mathbf{148}]^{2+}$ diffused ($MeOH:H_2O$ (30:70)) with scale bar size of A) 2 µm and B) 600 nm.

The SEM pictures displayed in Figure 4-71 shows the result of the diffusion of $YbCl_3$ followed by the diffusion of $[Ru(phen)_2\mathbf{148}]^{2+}$ through the 0.6 *wt* % gel. It is possible to see that the xerogel was not fully homogeneous, most of the xerogel correspond to pictures A and B which reveal a clear difference with the fibres formed only by diffusion of $[Ru(phen)_2\mathbf{148}]^{2+}$. The fibres formed in this case are much bigger with a size ranging from 25 to 100 nm and an average size of 52.5 nm, they are very similar to the ones observed

during the study of the diffusion of $YbCl_3$ through the 0.6 *wt* % gel formed by **85** which displayed an average size of fibres of 52.6 nm. However, as shown in Figure 4-71C and D the xerogel also had parts where the fibres are less densely packed. These observations were not made during the previous study of diffusion of lanthanide ions and could be attributed to the presence of $[Ru(phen)_2\mathbf{148}]^{2+}$ but since this phenomenon was not observed in the pictures of the gel modified by diffusion of $[Ru(phen)_2\mathbf{148}]^{2+}$ they might be appearing during the drying process of the gel or due to the simultaneous presence of two additives.

The order of diffusion of both lanthanides ion and ruthenium as explained in part 4.5.1.1 was also investigated by SEM. As in one case the Yb(III) ions were first diffused through the gel leading to the shrinking of the network followed by the diffusion of $[Ru(phen)_2\mathbf{148}]^{2+}$.In the other case $[Ru(phen)_2\mathbf{148}]^{2+}$ was diffused first followed by the Yb(III) ions. It revealed that the order of diffusion of both lanthanides ion and ruthenium did not have an influence on the morphology observed on the xerogels (see in the appendixes).

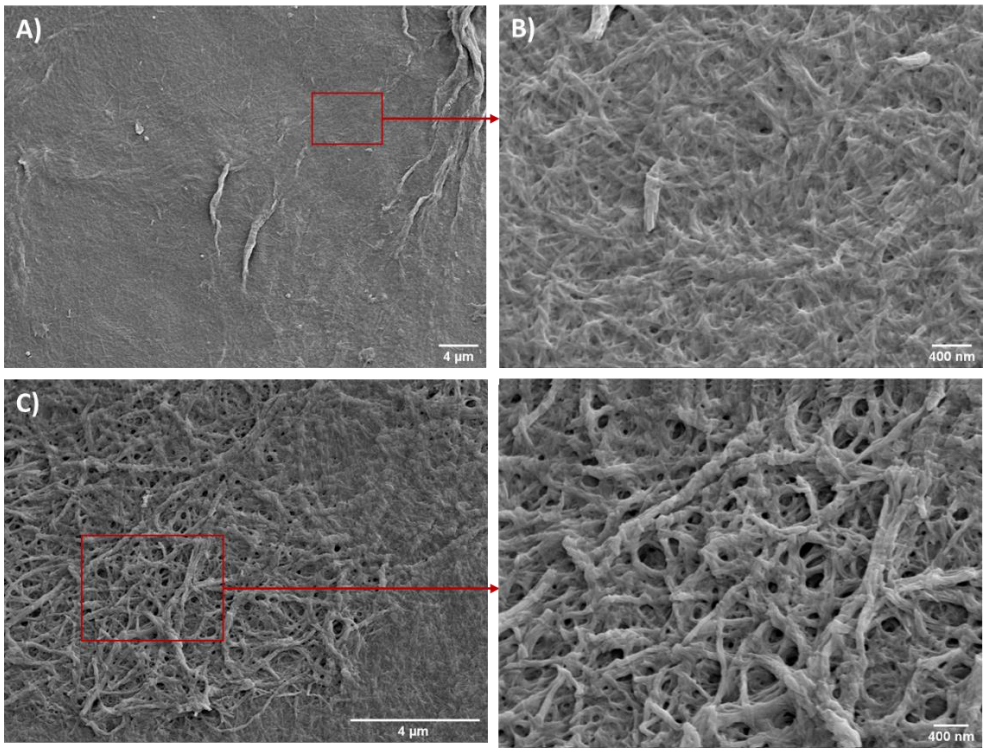

Figure 4-71 SEM pictures of **85** xerogel with $YbCl_3$ followed by $[Ru(phen)_2\mathbf{148}]^{2+}$ diffused through it (MeOH:H_2O (30:70)) with scale bar size of A) 4 µm, B) 400 nm, C) 4 µm and D) 400 nm.

4.6 Conclusions and Future Work

The synthesis and characterisation of **85** were successfully reproduced from data previously reported by our laboratory.[17,21,29] Using ^1H NMR spectroscopy at different temperatures in combination with dilution study of the UV-vis absorption and emission spectra of **85** confirmed the formation of aggregates both in DMSO and MeOH solutions, at higher

concentration (from 25.00×10^{-6} M to 2.58×10^{-6} M in MeOH). The titrations of **85** with $LnCl_3$ (La, Sm, Eu, Gd, Tb, Yb, Lu) were carried out at a concentration where **85** self-assemble (1.0×10^{-5} M) and satisfyingly, lanthanide-centred emission was observed in the case of Sm(III), Eu(III), Tb(III) and Yb(III). The fitting of the spectroscopy data was achieved through the use of non-linear regression analysis software SPECFIT and confirmed the formation of 1:1 and 3:2 M:L stochiometric species upon addition of Ln(III) ions confirming previously obtained results.[29] Interestingly, the binding constants determined through the fitting of the data revealed a parabolic relationship with the ionic radii of the lanthanide and demonstrated the influence of the size of the lanthanide ions on the formation of complexes in a preorganised supramolecular assembly, an effect which was not previously observed when using the simple 2,2′:6′,2″-Terpyridine or the flexible tripod used by Renaud *et al.*[106,140] The formation of gel using different concentrations of **85** was achieved in MeOH:H_2O mixture and the further modification of the gel by addition of *d*- and *f*-metals was carried out by passive diffusion. The aforementioned gels were studied by thermogravimetric analysis to determine their weight percentage and statistical measurement of the fibre width was carried out by using scanning electron microscopy and the image processing program ImageJ.[192,193] These studies did not reveal an influence of the size of the lanthanide ion on the modification of the gel properties. Following this, rheological measurements were carried out on the 0.3 and 0.6 *wt* % gels as well as the 0.3 *wt* % gel modified by diffusion of $FeSO_4$ and the 0.6 *wt* % gel modified by diffusion of $LaCl_3$ demonstrating an important increase in the robustness of the soft material upon increasing the concentration of gelator, while it highlighted the effect of the diffusion of *d*- or *f*-metal acting as a supramolecular glue by cross-linking the fibres and increasing the structural robustness of the gel. Further rheological measurements need to be carried out on the Ln(III)-modified gel as well as Cryo-SEM.

The use of **85** to form multicomponent gels was investigated by means of passive diffusion of $[Ru(phen)_2\mathbf{148}]^{2+}$. It resulted in the modification of the spectroscopic properties of the gel while the morphology appears to be independent of the presence of the complex. Further studies are required to determine whether or not there is an energy transfer from the ruthenium complex to the Yb(III) ion increasing the intensity of the Yb-centred emission and if the gel containing **85** and $[Ru(phen)_2\mathbf{148}]^{2+}$ is capable of forming reactive singlet oxygen species.

Chapter 5— Synthesis and Study of Terpyridine Gelators

5.1 Introduction

As discussed in the introduction, the benzene-1,3,5-tricarboxamide moiety (BTA) is an excellent platform for the formation of supramolecular polymers through the combination of π-π stacking and three-fold hydrogen-bonding interactions. Depending on the desired supramolecular structure, the functionalisation of the arms is of paramount importance,[149] long alkyl chains for liquid-crystals,[267] branched alkyl chain for gelators,[268] bulky substituents for the formation of crystals,[269] *etc*… having been developed to date.

Meijer has shown, as described in the introduction, that the incorporation of a chiral centre into one or more of the arms of BTA can induce a significant influence on the chirality of the overall supramolecular assembly.[148,152,238] To date, one of the only examples of a chiral assembly of BTA functionalised with terpyridine was achieved through the use of the achiral compound **85** and the chiral triacid **86** which were able to serve as a template for the formation of gold nanoparticles to control the organization of such particles.[26] Within the Gunnlaugsson group, Dr. Savyasachi has synthesised several chiral and achiral BTA with the arms composed of an amino acid, an alkyl spacer and a terpyridine as was described previously in this thesis. However, the only BTA able to form gels was the achiral compound **132** while the others displayed the formation of microspheres. This chapter describes the modification of the original tripodal structures designed by the Gunnlaugsson group and synthesised by Dr. Savyasachi with a reduced length of the spacer, by removing the alkyl chain in the aim to improve the gelation ability of the synthesised compounds.

5.2 Synthesis and Characterisation

5.2.1 Core functionalisation

The design of the tris-terpyridine tripodal gelator (**150**) is based on Dr. Savyasachi prior work, who synthesised and studied a family of tris-terpyridine with various amino acids to functionalise the benzene-1,3,5-tricarboxamide (BTA) central core conferring a C_3-symmetry to the molecule, as seen in Chapter 1, thus facilitating the formation of supramolecular polymers, in the aim to study the effect of the chirality induced by the amino acids in the self-assembly along with the effect of the coordination of *d*- and *f*-metals. Despite numerous hydrogen donor and acceptor in the tripods synthesised and studied by Dr. Savyasachi, only one, the glycine derivative, was able to form gels in a mixture of solvent. To improve the gelation capacity of the tripods, the reduction of the propane carbon chain

to a shorter hydrazine moiety was the favoured approach. It was also foreseen that the shortening of the spacer between the chiral moiety and the fluorophore would induce a stronger influence of the chiral moiety on the circular dichroism signal arising from the chromophore. Therefore based on the previous work carried out in the Gunnlaugsson research group, the tris-terpyridine tripodal ligand (**150**) was designed, and the synthesis achieved by carrying out successive modifications of the BTA core, starting by the reaction of the chiral amino-ester with 1,3,5-benzenetricarbonyl trichloride, followed by the saponification of α-tri-ester and the coupling of the resulting tri-acid with three equivalents of 4'-hydrazinyl-2,2':6',2''-terpyridine (**151**) as described in Scheme 5-1.

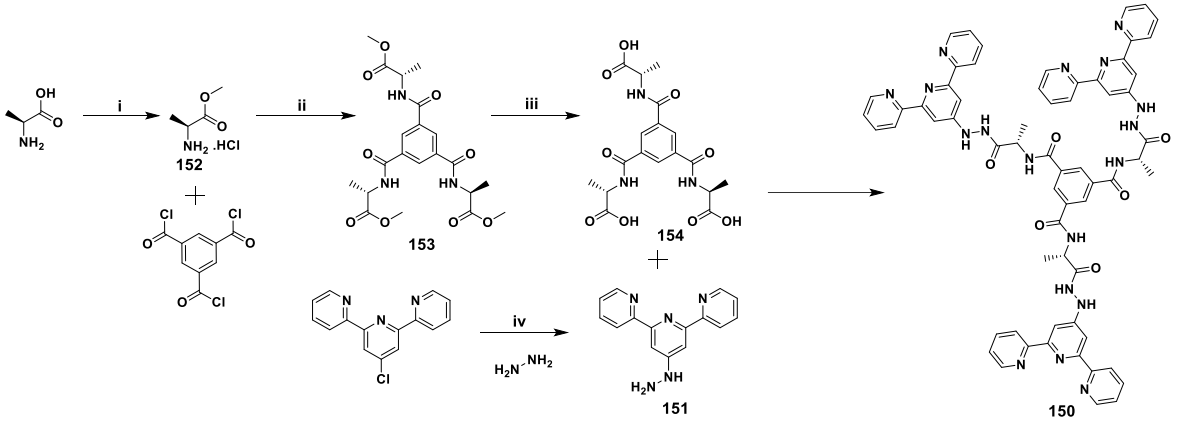

Scheme 5-1 Synthesis of **150** from readily commercially available 4'-chloro-2,2':6',3''-terpyridine, 1,3,5-benzene tricarbonyl trichloride and L-Alanine. i) $SOCl_2$, MeOH, 0 °C to rt, 6 h; ii) 1,3,5-benzenetricarbonyl trichloride, DCM, Et_3N, rt, 18 h, 75%; iii) 2 M NaOH, MeOH, Amberlite IR 120 H^+, 98%; iv) hydrazine monohydrate, 1-butanol, 130 °C, 12 h, 80%.

The 4'-hydrazinyl-2,2':6',2''-terpyridine (**151**) was obtained following a procedure described in the literature,[270] which consisted of refluxing 4'-chloro-2,2':6',2''-terpyridine in the presence of hydrazine monohydrate in warm 1-butanol. The precipitate was isolated by filtration and washed with water giving the desired product as a white solid in 80% yield. The formation of **151** was confirmed by ^{1}HNMR (400 MHz, DMSO-d_6) with the presence of a broad singlet at 4.39 ppm accounting for the terminal NH_2 and by HRMS-ESI where the $[M+H]^+$ fragment was observed at *m/z* = 264.1247.[270]

L-Alanine methyl ester (**152**) was prepared from the commercially available L-Alanine by stirring it in a mixture of thionyl chloride and methanol. Following vacuum distillation, the crude compound was immediately reacted with 1,3,5-benzene tricarbonyl trichloride and trimethylamine in dichloromethane yielding the tri-ester **153** as a white powder in 75% yield. The ^{1}H NMR spectrum confirmed the identity of **153** with a singlet at 8.50 ppm corresponding to the hydrogens of the benzene moiety, the doublet at 1.43 ppm corresponding to the methyl group of the alanine moiety with the quintet of its chiral

hydrogen at 4.52 ppm, and the methyl ester moiety being represented by a singlet at 3.66 ppm (as shown in Figure 5-1A). The high-resolution mass spectroscopy (HRMS) analysis of **153** showed one peak at *m/z* = 466.1833 corresponding to the molecular ion $[M+H]^+$. The IR spectrum of **153** reveals transitions at 3229 cm^{-1} accounting for the secondary amine and at 1745 cm^{-1} corresponding to the stretching of the carbonyl of the ester moiety.

Several reactions conditions were tried to react the commercially available L-Alanine methyl ester hydrochloride with 1,3,5-benzene tricarbonyl trichloride, but it always resulted in a significant drop in yield (to 20%) compared to the reaction with the freshly prepared ester. Hydrolysis of the ester of the 1,3,5-benzene-L-Alanine methyl ester was carried out under basic conditions and Amberlite® IR120 hydrogen form was used, because of its easy separation from the solution, to acidify the mixture giving the tri-acid **154** in stoichiometric amount. As seen in Figure 5-1B, the ^1H NMR spectrum confirmed its identity with a singlet at 8.47 ppm corresponding to the hydrogens of the central benzene moiety; the doublet at 1.42 ppm corresponding to the methyl group of the alanine moiety, with the quintet of its chiral hydrogen at 4.4 ppm, and the disappearance of the methyl ester moiety that previously resonated at 3.66 ppm. The HRMS analysis of **154** showed one peak at *m/z* = 422.1217 corresponding to the molecular ion $[M-H]^-$ (see experimental part). The IR spectrum of **154** showed a peak at 3300 cm^{-1} corresponding to the O-H stretching for the acid and at 1719 cm^{-1} accounting for the stretching of the carbonyl of the acid moiety.

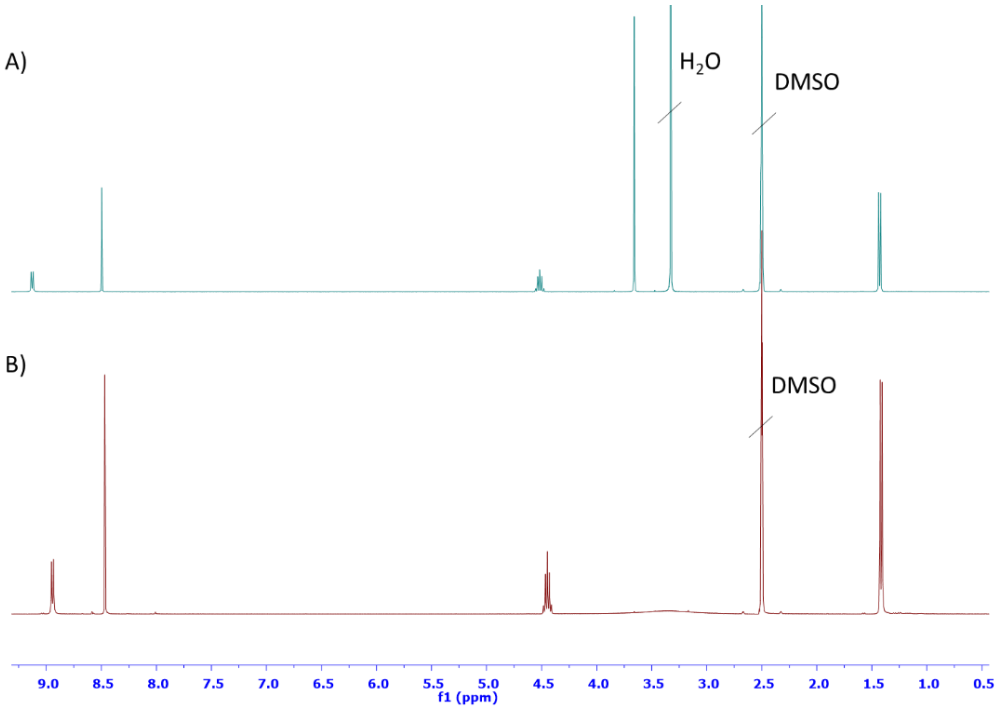

Figure 5-1 The ^1H NMR (400 MHz, DMSO-d_6, ppm) of A) the trimethyl ester **153** and, B) the tri-acid **154**.

The last step corresponding to the coupling between the 4'-hydrazinyl-2,2':6',2''-terpyridine (**151**) and the tri-acid (**154**) was found to be problematic, with combinations of various coupling agents being tested. For example, the coupling between **151** and **154** using EDC.HCl with HOBt, with and without Et_3N, EDC.HCl with DMAP (as well as with and without Et_3N) in different solvent systems (DCM, DCM with few mL of DMF). However, all of these attempts did not result in the formation of the desired product. The reaction was left for lengths of time varying between 2 days and 15 days stirring at room temperature. From these attempts, the conditions showing the most promising results, are the use of EDC.HCl in the presence of DMAP, with the reactants all being dispersed into DCM at 0 °C. The reaction mixture was then left to warm up to room temperature and then the reaction stirred for 15 days. After 15 days the solvent of the reaction was evaporated under reduced pressure and the solid obtained was sonicated until a fine orange powder was obtained. The powder was then filtered, and washed with deionized water followed by ethanol and acetonitrile. The orange powder was then dried and analysed by ^{1}H NMR (DMSO-d_6, 400 MHz). A comparison between the starting material and the compound obtained can be seen in Figure 5-2. It is obvious from the shift of the singlet corresponding to the methyl group (of the chiral centre), now shifted at 1.54 ppm, that the reaction had occurred, but the presence of a second peak perfectly matching the signal of the methyl peak of the starting material at 1.38 ppm demonstrates the presence of uncoupled arm suggesting the presence of potentially three different products the mono-coupled, the bi-coupled and the tri-coupled one. Various TLC conditions were explored with the aim to isolate the desired product, but no successful separation has been achieved to date.

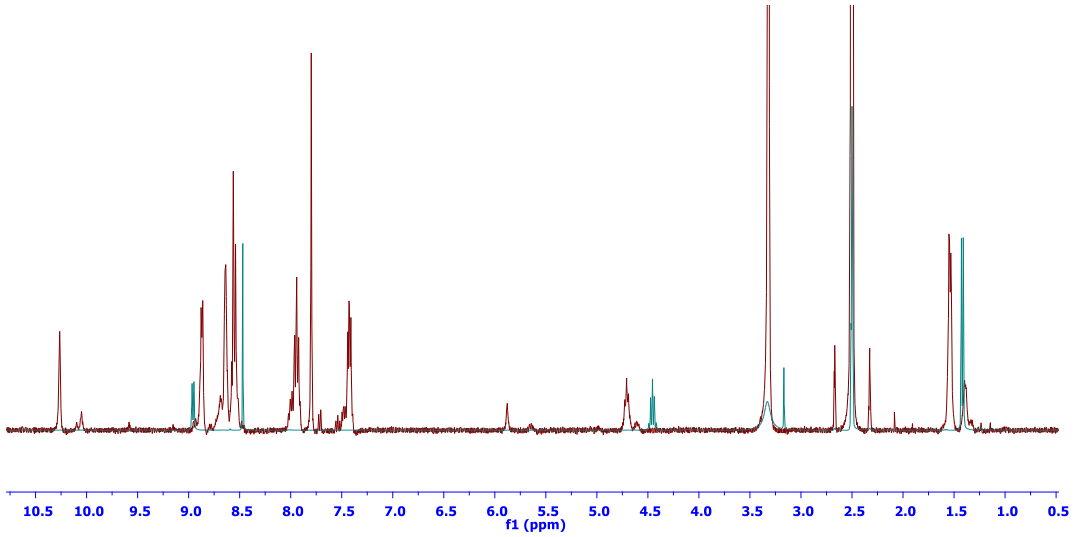

Figure 5-2 The ^{1}H NMR (DMSO-d_6, 400 MHz) between the tri-acid (**154**, green line) and the impure product (**150**, red line).

Because of the difficulties encountered for the last step of the synthesis, an excessively long reaction time (leading to an incomplete reaction and the impossibility to purify the compound), a new synthetic method was to be considered. The design of the new synthetic approach and its results are discussed in the following section.

5.2.2 Synthesis of the arm

Due to the numerous issues described in the previous section for the synthesis of the tripodal molecule **150**, by sequential functionalisation of the central core, a new synthetic method was considered. Instead of functionalising the 3 sites on the core, the reverse approach was considered; starting with the synthesis of the 'arms' (composed of the L-Alanine and hydrazine) which could then be reacted with 4'-chloro-2,2':6',2''-terpyridine as shown in Scheme 5-2.

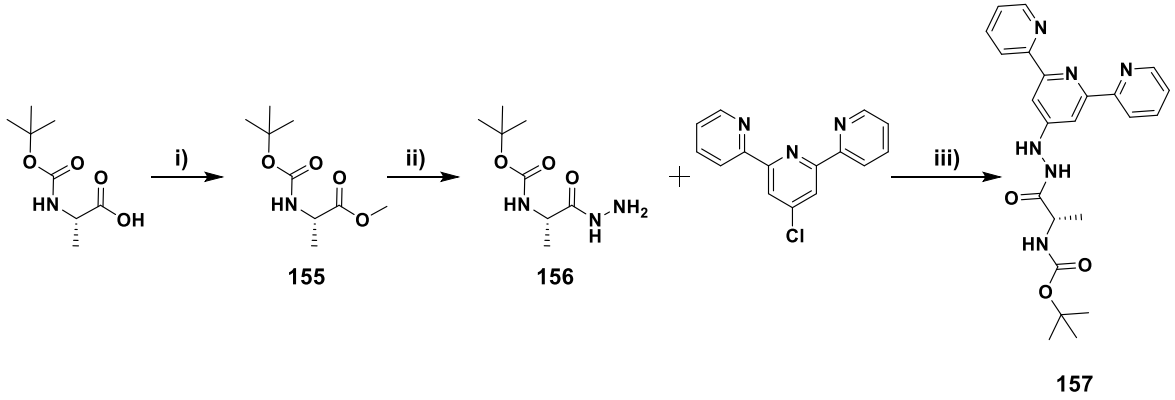

Scheme 5-2 New synthetic scheme to obtain the target molecule **157**, i) CH_3I, Na_2CO_3, DMF, 12h, 59%, ii) hydrazine hydrate, MeOH, 18 h, 79%, iii) 1-butanol, 130 °C, 48h.

The first step consists of the esterification of Boc-L-alanine in **155**. The second step of the synthesis is the coupling between hydrazine monohydrate and Boc-L-alanine methyl ester to form **156** which have been described by Zefirov *et al.*[271] The compound **156** could then be reacted with 4'-chloro-2,2':6',2''-terpyridine following the same procedure used to form **151**.[270] And finally hydrolysis of the Boc protecting group using TFA followed by the reaction of the resulting product with 1,3,5-benzenetricarbonyl trichloride. This final step could be achieved by following similar reaction protocols used in the Gunnlaugsson group. The benefit of this new synthetic approach was that the need of excess arm, used during the last step of the synthesis, can now be easily removed during the workup. Secondly, 1,3,5-benzenetricarbonyl trichloride is much more reactive than the tri-acid **154**, and hence there is no need for the addition of other coupling reagents as was the case above.

The first step was the formation of **155** from the Boc-L-alanine, using methyl iodide. The formation of the ester was confirmed by ^{1}H NMR with the presence of the methyl ester

resonance at 3.72 ppm, while all the other signals were in good agreement with the data found in the literature.[272] The formation of Boc-L-alanine hydrazide (**156**) was carried out by reacting hydrazine hydrate and **155** in methanol, yielding the desired compound in good yield (79%). The successful formation of **156** was confirmed by the presence of the two broad singlets at 7.68 and 3.57 ppm accounting for NH and NH_2 respectively.[271] The following step was the reaction between 4'-chloro-2,2':6',2"-terpyridine and **156**. Similarly to the formation of **151**, the two solids were dissolved in butanol and the mixture was heated at 130 °C for 48 h. The solvent was evaporated under reduced pressure yielding a white solid. The ^{1}H NMR analysis revealed that the solid was only a mixture of the two starting material and that no reaction had occurred.

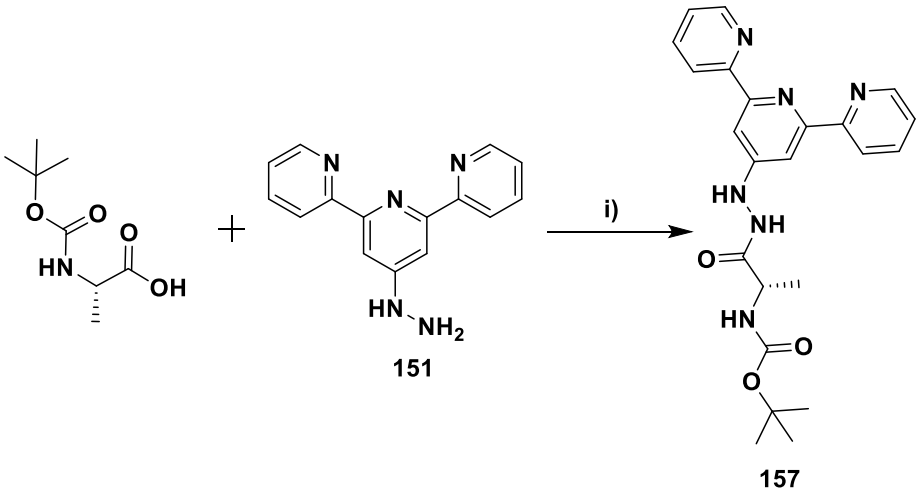

Scheme 5-3 Reaction of Boc-L-alanine with 4'-hydrazinyl-2,2':6',2"-terpyridine, i) EDC.HCl, HOBt, DCM/DMF, 72 h, 23%.

Since the reaction of the 4'-chloro-2,2':6',2"-terpyridine and **156** was not successful, it was decided to attempt the coupling of Boc-L-alanine with **151** (Scheme 5-3). To do so, 1-ethyl-3-(3'-dimethylamino)carbodiimide HCl salt (EDC.HCl) and Hydroxybenzotriazole (HOBt), was used to avoid the formation of unreactive *N*-acylurea, in a mixture of DCM and DMF to ensure that all the starting materials were dissolved. After 3 days of a reaction at room temperature, the solvent was removed under reduced pressure, the solid obtained was dissolved in DCM and washed with water. After evaporation of the solvent under reduced pressure, the ^{1}H NMR of the crude product was obtained and revealed the formation of the desired product. However, it has also shown what seems to be the presence of unreacted **151** (Figure 5-3).

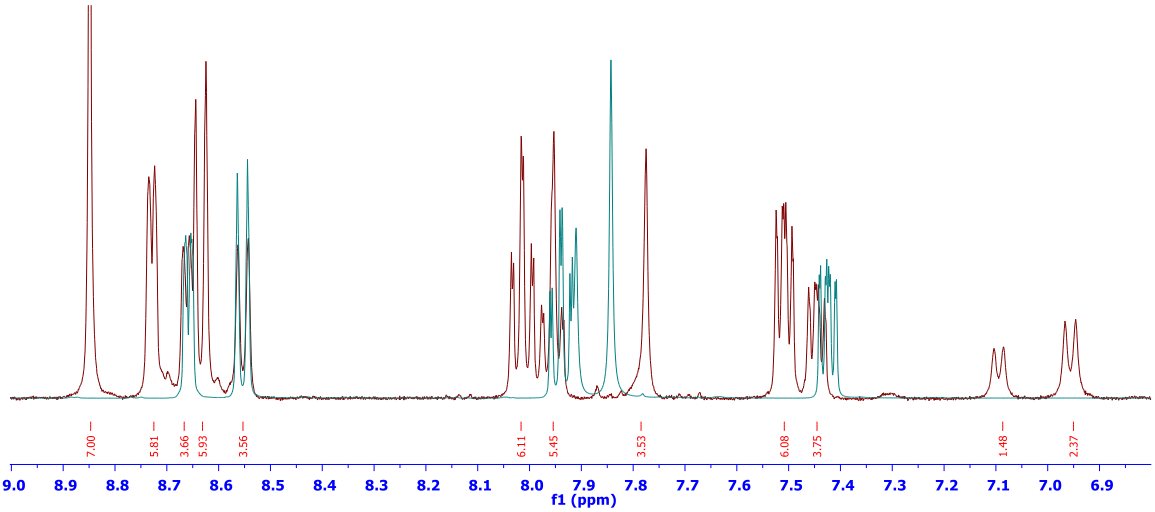

Figure 5-3 The ^{1}H NMR (DMSO-d_6, 400 MHz) between the 4'-hydrazinyl-2,2':6',2"-terpyridine (**151**, green line) and the crude product (**157**, red line).

Various conditions were investigated with the view to separate the unreacted starting material and the desired product by column chromatography. The best results were achieved by using silica and a mixture of DCM:MeOH (95:5) as the eluent. The separation between the first product eluted and the second one was not complete, as seen by ^{1}H NMR shown in Figure 5-4, however, it was possible to isolate the 1st product eluted, and as seen in Figure 5-4A, it appears that the singlet accounting for $H_{3',5'}$ was shifted to 8.85 ppm against 7.86 ppm. It is also possible to observe two doublets in both Figure 5-4B and C that can be attributed to the amide, at 6.96 ppm and 7.09 ppm respectively suggesting that the coupling of the acid occurred at the two different amines of the hydrazine moiety.

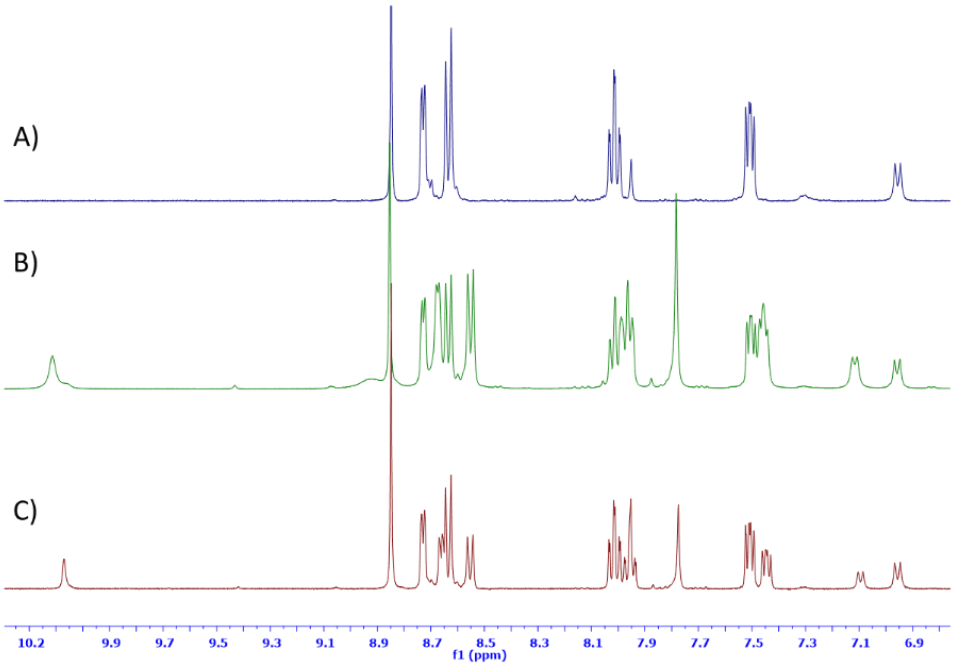

Figure 5-4 The ^{1}H NMR (DMSO-d_6, 400 MHz) of A) 1st product eluted, B) Mixture of 1st and 2nd products eluted and C) crude product (**157**) before the purification by column chromatography.

Investigation of other purification techniques demonstrated that upon reprecipitation from diethyl ether a white solid could be isolated through centrifugation, washing with diethyl ether and drying it under reduced pressure. The characterisation of this material demonstrated the successful formation of **157** as confirmed by HRMS-ESI with the presence of $[M-H]^+$ ion (*m/z* = 435.2139) and by ^{1}H-^{15}N HSQC NMR experiments, revealing the presence of 3 protons at 10.08, 8.85 and 7.10 ppm, respectively, linked to nitrogen atoms (see in the appendix). It was further confirmed with the presence of the quintet at 4.12 ppm assigned to the chiral centre of the alanine moiety and the singlet at 1.38 ppm accounting for the nine protons of the three methyl groups of the tert-Butyloxycarbonyl moiety as seen in Figure 5-5. The full assignment of the target molecule using HMBC and HSQC experiments was carried out and is reported in the experimental section. However, as seen in the expansion of the aromatic region in Figure 5-5, a small impurity corresponding to a terpyridine moiety was still present and it was not possible to remove it with the conventional methods.

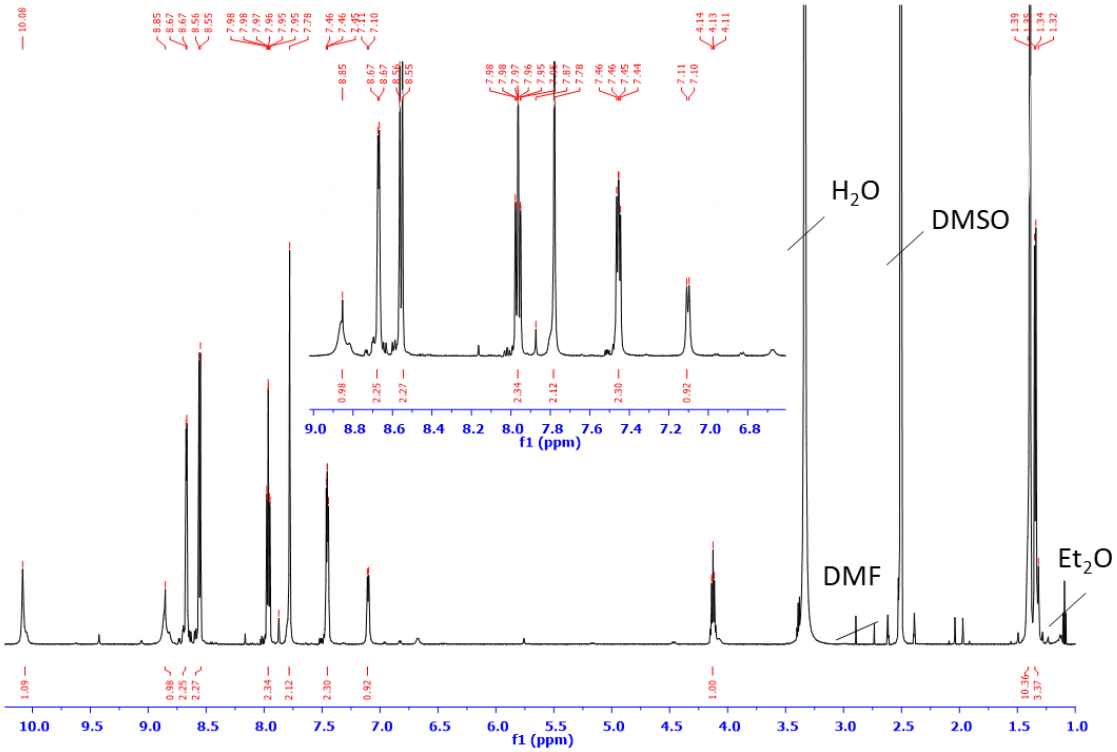

Figure 5-5 The ^{1}H NMR (DMSO-d_6, 600 MHz) of **157** as obtained by precipitation from diethyl ether.

In the hope to facilitate the purification, the removal of the tert-Butyloxycarbonyl moiety by dissolving **157** in DCM and through the addition of TFA was undertaken (Scheme 5-4).

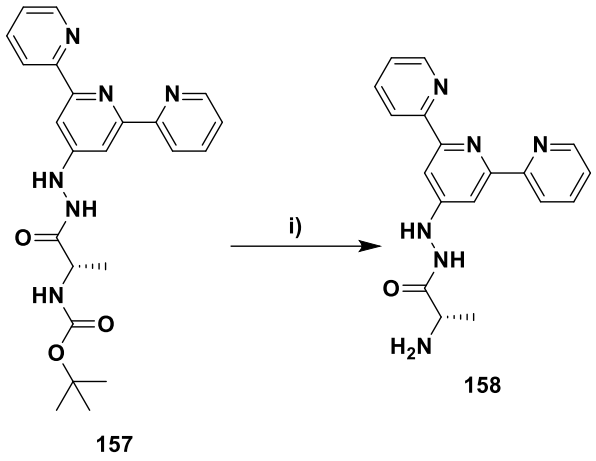

Scheme 5-4 Removal of the tert-Butyloxycarbonyl moiety, i) TFA:DCM (1:2), rt, 4h, 44%.

The successful formation of **158** was confirmed by HRMS-APCI with the presence of $[M-H]^+$ ion (*m/z* = 335.1620) and by ^1H NMR with the clear disappearance of the singlet at 1.38 ppm accounting for the nine protons of the three methyl groups of the tert-Butyloxycarbonyl moiety (see appendix). However, as seen in Figure 5-6, small sets of signals corresponding to the terpyridine precursor can be observed, demonstrating that the impurities observed at the end of the previous reaction are still present. Several combinations of solvents were tested to purify the compound by chromatography but no satisfying separation could be achieved.

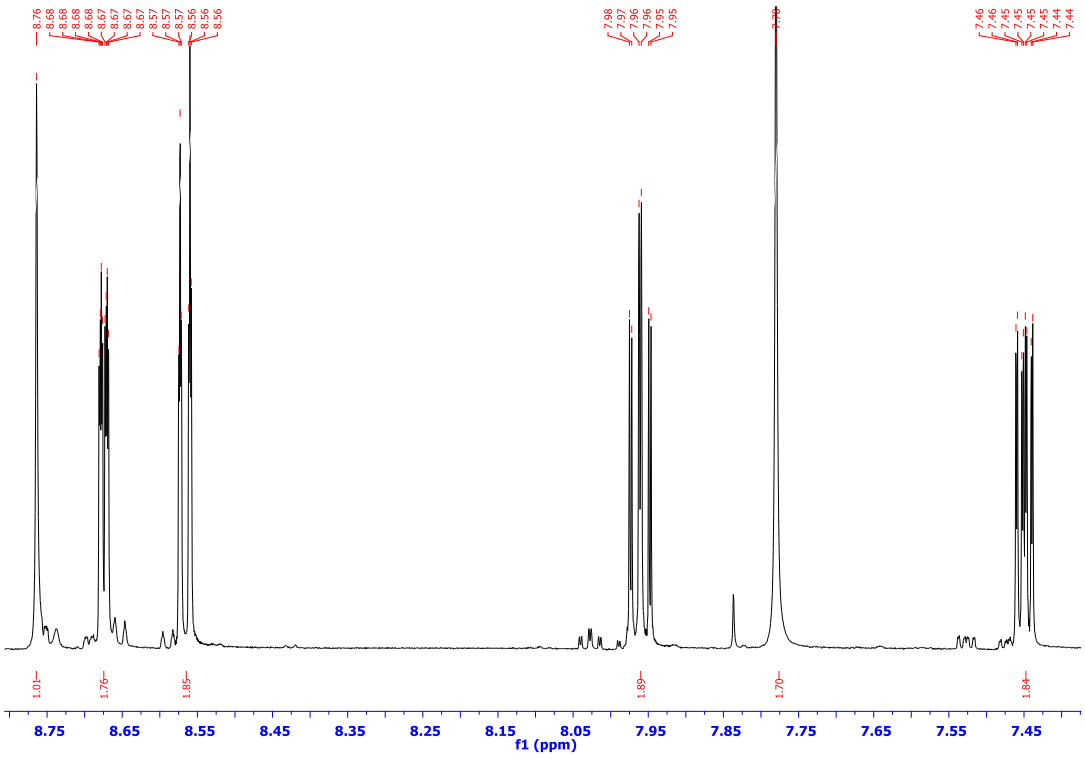

Figure 5-6 The ^1H NMR (DMSO-d_6, 600 MHz) of **158** in the region of 8.95-7.35 ppm.

Due to the low yielding previous step, the tedious workup of the coupling reaction and the price of the 4'-chloro-[2,2';6',2'']terpyridine, it was decided to modify again the target by slightly changing the terpyridine moiety.

5.2.3 Modification of the target molecule

Using 4′-(4-aminophenyl)-2,2′:6′,2″-terpyridine (**111**) which is easily synthesized on a large scale using inexpensive starting material, the target molecule was modified. The synthesis of **111** was discussed in Chapter 2 and detailed in the experimental part. The first step of the synthesis, shown in Scheme 5-5, consisted of the coupling of the Boc-L-alanine to **111** which was carried out using (2-(1*H*-benzotriazol-1-yl)-1,1,3,3-tetramethyluronium hexafluorophosphate (HBTU), HOBt which decreases the possibility of side reaction and *N*,*N*-Diisopropylethylamine (DIPEA) in DMF, yielding the desired product **159**.

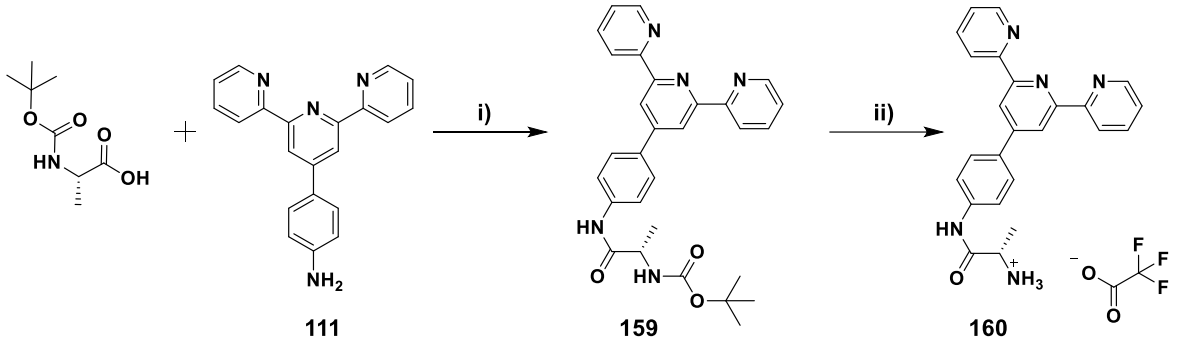

Scheme 5-5 Synthesis of **160**, i) HBTU, HOBt, DIPEA , DMF, 12 h, 66%, ii) DCM:TFA (4:2 mL), 95%.

The overnight reaction gave the desired compound **159** in 66%, and the successful formation of **159** was confirmed by ^{1}H NMR (DMSO-d_6, 600 MHz) with the presence of a singlet integrating to one proton accounting for the newly formed amide at 10.18 ppm and the amide of the Boc moiety at 7.12 ppm (Figure 5-7). This finding was further supported by the ^{1}H-^{15}N HSQC NMR (see in the appendix) and the presence of the quintet integrating to one proton at 4.15 ppm corresponding to the hydrogen of the chiral centre of the alanine moiety. Furthermore, the HRMS-APCI showed the presence of the $[M-H]^+$ ion (*m/z* = 496.2338) again demonstrating the successful formation of **159**. The purity of the product was also evidenced by elemental analysis, demonstrating that the analysed sample corresponds to $C_{29}H_{29}N_5O_3 \cdot 0.25C_4H_8O_2 \cdot 0.1C_6H_{14}$.

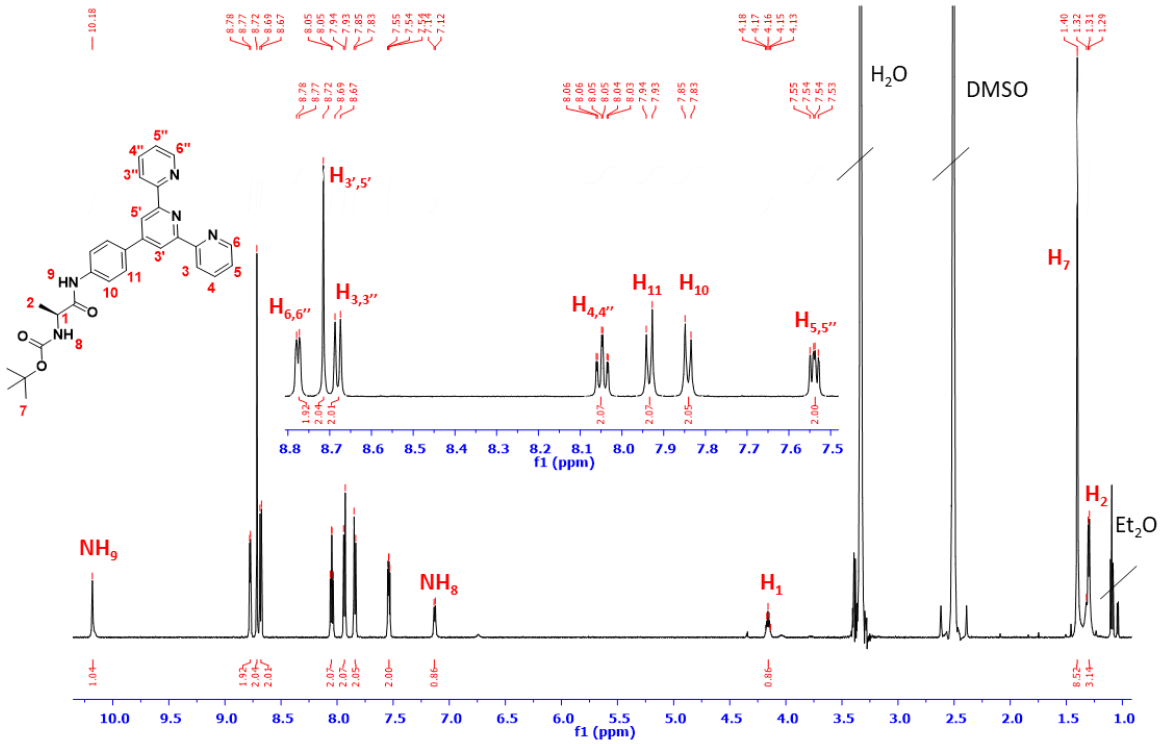

Figure 5-7 The ^{1}H NMR (DMSO-d_6, 600 MHz) of **159**.

Single crystals of X-ray diffraction quality of **159** were obtained by slow diffusion of ether into a DCM solution of **159** and the structures are shown in Figure 5-8. The crystallography in this chapter was carried out and the data solved and refined by Ms Deirdre McAdams and Dr. Brendan Twamley (TCD). The data was solved and refined in the orthorhombic space group $P2_12_12_1$. The central phenyl ring in the molecule was disordered over two orientations with 52:48% occupancy with idealised ring geometry and there is partial solvent occupying the lattice voids as a mixture of diethyl ether (35%) and DCM (15%).

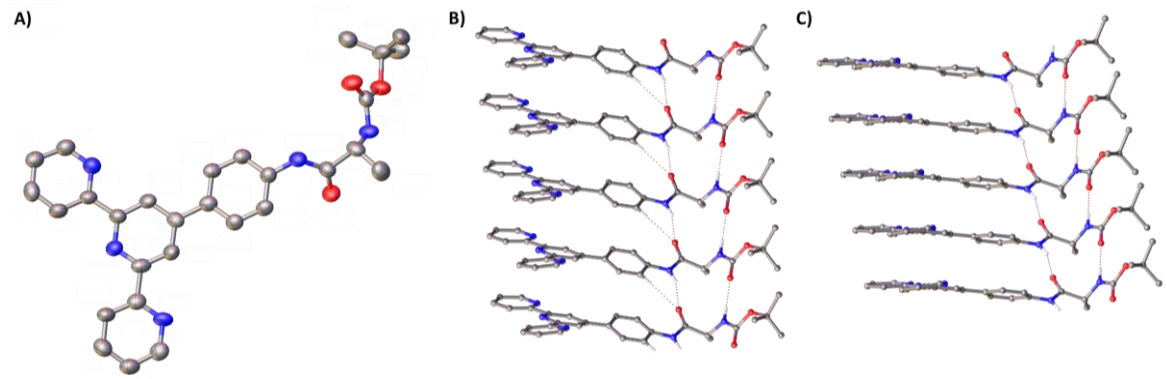

Figure 5-8 A) Molecular structure of **159** showing only one position of the phenyl group and hydrogen are omitted for clarity, with hydrogen bonding drawn for B) the intramolecular hydrogen bonding of the phenyl ring and C) the intermolecular hydrogen bonds only with the phenyl ring in the second position.

The asymmetric unit contains one molecule (Z=4), and as shown in Figure 5-8, the terminal pyridine rings are orientated along with the interanular bond in a *transoid* arrangement which is typically observed for terpyridine moieties with the two terminal rings being slightly off the plan from the central pyridine ring.[177] The interanular C-C bond lengths [1.469(18)-1.499(17) Å], C-C [1.353(18)-1.406(17) Å] and C-N [1.324(15)-1.356(15) Å] in the pyridyl units are comparable with those previously reported for aminophenyl terpyridine.[38,177] The crystal structure also reveals the presence of two sites of hydrogen bonding between neighbouring molecules, N(25)-H(25)···O(27) corresponding to the amide which is the closest to the terpyridine moiety and N(30)-H(30)···O(32) which corresponds to the amide of the Boc group with their N···O distances being of 2.872(12) and 2.986(12) Å respectively and their corresponding N-H···O angles of 159.7 and 177.2°. It was also possible to observe, in one of the orientations of the phenyl ring, an intramolecular hydrogen bond occurring between the hydrogen in the ortho position and the oxygen of the carbonyl group (Figure 5-8B), with a C···O distance of 3.213(16) Å and a C-H···O angle of 130.6°.

The removal of the tert-Butyloxycarbonyl protecting group (shown in Scheme 5-5) was carried out by dissolving **159** in a mixture of DCM:TFA (4:2) and after two hours at rt, the solvent was removed followed by the repetition of the addition of DCM and evaporation under reduced pressure yielding the desired product in the form of a light pink powder as the TFA salt in 95% yield. The successful formation of **160** was confirmed by ^{1}H NMR (DMSO-d_6, 600 MHz) with the disappearance of the singlet integrating for 9 protons accounting for the tert-butyl at 1.40 ppm and the doublet corresponding to the amide of the Boc moiety at 7.12 ppm. This was further confirmed by a shift of the quintet of the chiral hydrogen from 4.15 ppm to 4.06 ppm and the doublet integrating to three protons corresponding to the methyl group from 1.30 ppm to 1.50 ppm and as shown in Figure 5-9.

The presence of a doublet integrating to three protons at 8.23 corresponding to the NH_3, was visible and was further supported by ^{15}N HSQC NMR (see appendix). The successful formation of **160** was also confirmed by HRMS-APCI with the presence of $[M\text{-}TFA]^+$ ion (*m/z* = 396.1820). However, the elemental analysis revealed that the analysed sample was composed of $C_{26}H_{22}F_6N_5O_5 \cdot 0.15CH_2Cl_2 \cdot 0.1\ C_4H_8O_2$ which correspond to **160** with another TFA molecule and some residual solvents.

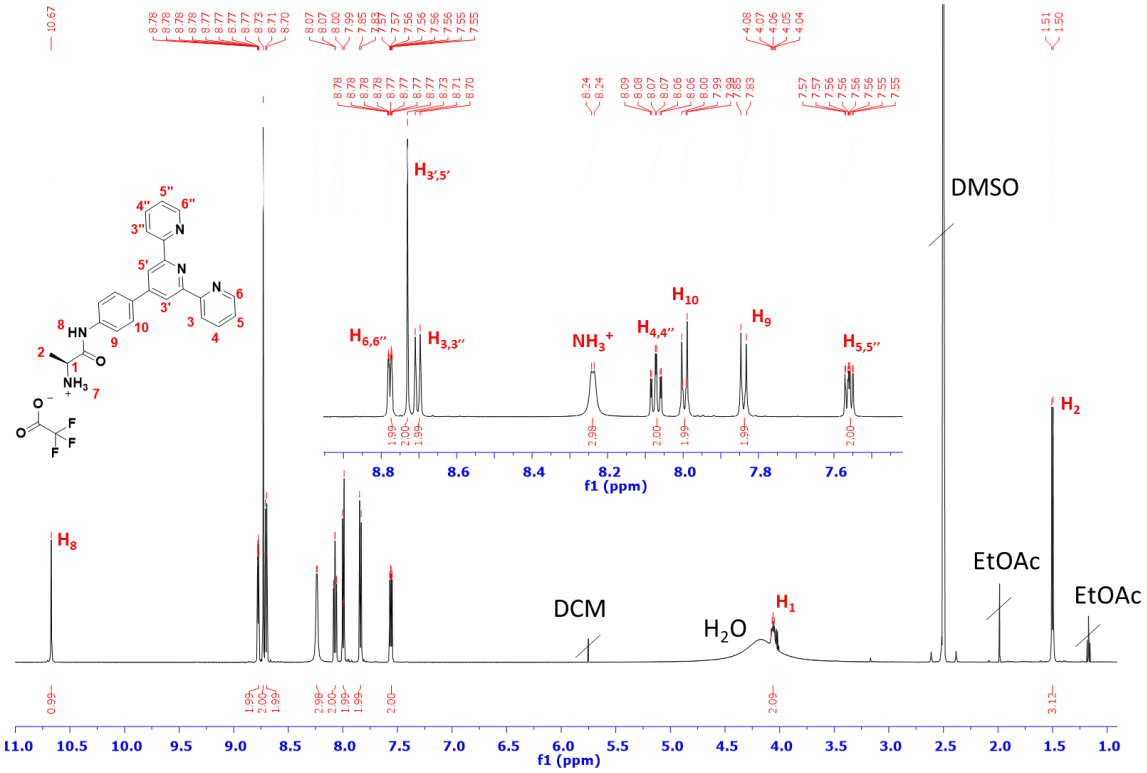

Figure 5-9 The ^{1}H NMR (600 MHz, DMSO-d_6, ppm) of the TFA salt of Alanine-4'-(4-aminophenyl)-2,2':6',2''-terpyridine (**160**).

The next step corresponding to the reaction of **160** with 1,3,5-benzenetricarbonyl trichloride to form **161**, was attempted following the standard procedure consisting of the dropwise addition of 1,3,5-benzenetricarbonyl trichloride to a solution of the amine in DCM in the presence of Et_3N.

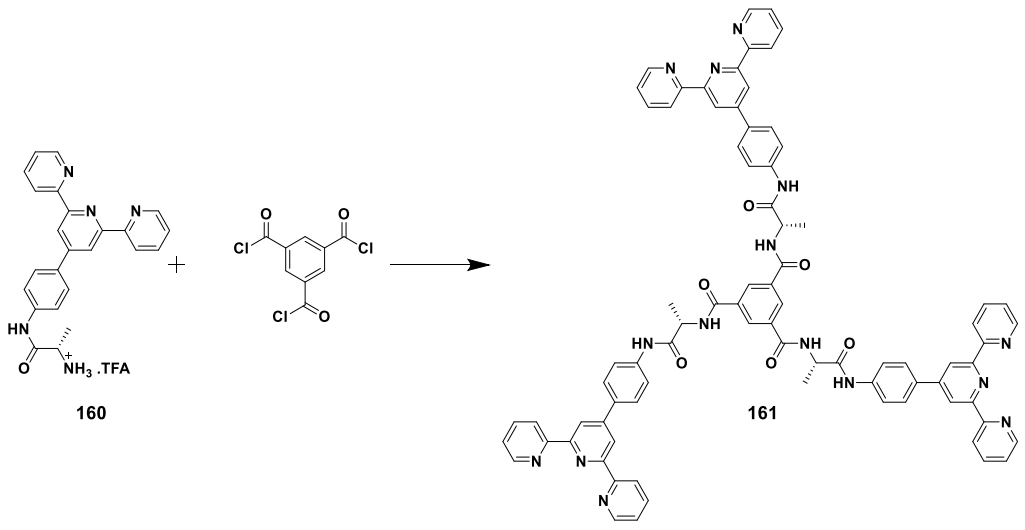

Scheme 5-6 Synthesis of the target molecule **161** from **160** and the commercially available 1,3,5-benzenetricarbonyl trichloride

However, ^{1}H NMR (DMSO-d_6, 400 MHz) of the crude material showed the presence of unreacted **160** with the presence of a singlet at 8.64 ppm, which could be attributed to the

1,3,5-benzenetricarbonyl moiety. After water and base washes, the ^{1}H NMR (DMSO-d_6, 400 MHz) showed the disappearance of the singlet at 8.64 ppm, and the spectrum was very similar to the starting material **160** as shown in Figure 5-10 indicating that the reaction did not occur. The procedure reported by Zhao *et al.*[273] consisting of dissolving the amine in acetone in presence of K_2CO_3 and 1,3,5-benzenetricarbonyl trichloride and heating the mixture at 60 °C overnight. This reaction yielded a red precipitate which was collected by centrifugation of the reaction mixture and was washed with H_2O. The material obtained proved to be insoluble in the most common organic and aqueous solvents used for NMR analysis, thus leading non-conclusive analysis as seen in Figure 5-10E, where the resonances corresponding to the quintet of the chiral centre and the doublet of the methyl group can be distinguished. However, the broad resolution does not allow for further analysis of the aromatic region.

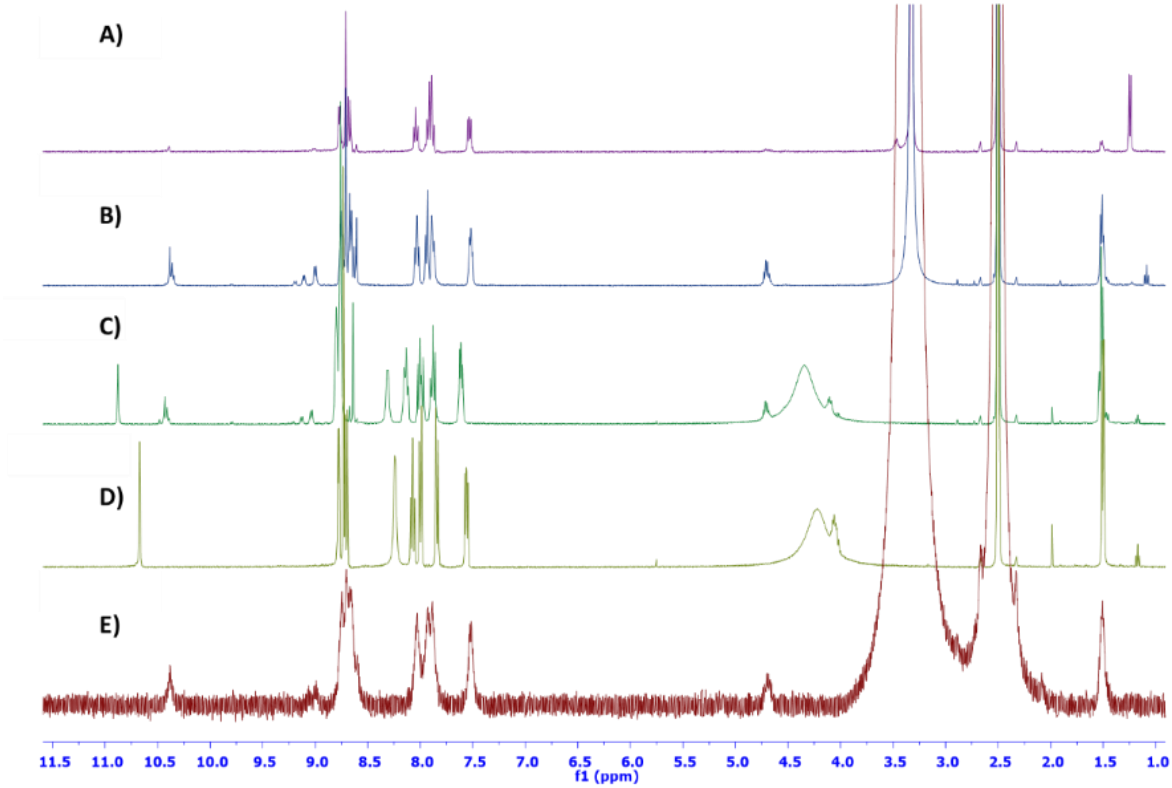

Figure 5-10 The ^{1}H NMR (400 MHz, DMSO-d_6, ppm) of the reaction of **160** with 1,3,5 benzenetricarbonyl trichloride and TEA A) after base wash, B) after water wash, C) crude, D) **160**, E) **160** with 1,3,5 benzenetricarbonyl trichloride and K_2CO_3.

To gain further understanding of the composition of the material formed above, IR of the starting materials, the 1,3,5-benzenetricarbonyl trichloride and **160**, and the material obtained. It can be seen in Figure 5-11 that the strong band at 1746 cm^{-1} corresponding to the $\nu_{C=O}$ of the acyl chloride is not present in the IR spectra of the crude product (**161**) while the presence of strong transition in the region of 1700-1630 cm^{-1} can be attributed to the

$\nu_{C=O}$ of the amides. The broad peak at 3051 cm^{-1} present in the IR spectrum of **160** which corresponds to the $\nu_{C=O}$ of the amine salt is not present in the IR spectrum of the crude product, potentially revealing the formation of the desired compound.

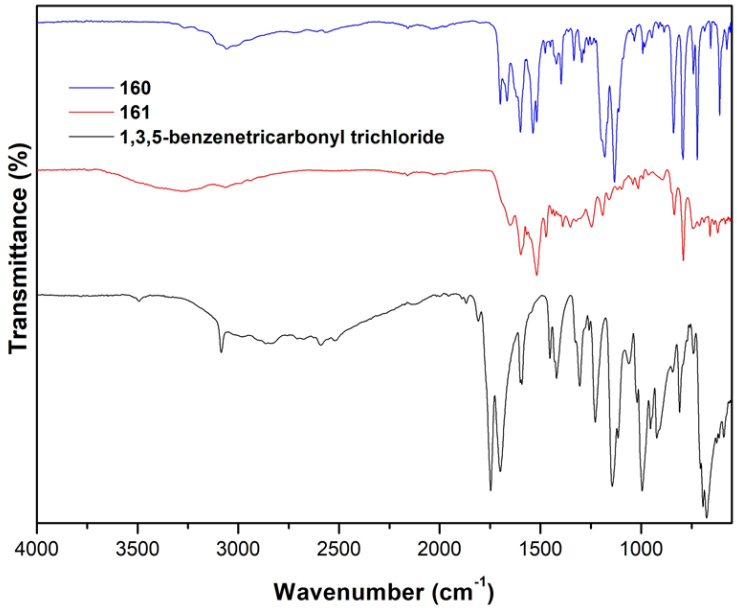

Figure 5-11 FTIR spectrum (550-4000 cm^{-1}) of 1,3,5-benzenetricarbonyl trichloride (black), **160** (blue) and **161** (red).

Due to time constraint, the characterisation of the crude product could not be completed, however as future work mass spectroscopy, solid-state NMR and elemental analysis would need to be carried out to establish the exact structure of the molecule obtained.

5.3 Conclusion

In this chapter, several approaches for the synthesis of the terpyridine tripodal gelator were attempted. The first one consisting of the modification of the 1,3,5-benzenetricarbonyl core to incorporate the spacer, followed by the coupling of the three 4'-hydrazinyl-2,2':6',2"-terpyridine (**151**). While the functionalisation of the central core using L-Alanine methyl ester gave the desired product (**153**) in high yield, the coupling of the three 4'-hydrazinyl-2,2':6',2"-terpyridine (**151**) to the tri-acid (**154**) led to the formation of a mixture of products which could not be separated.

The second approach consisted of the synthesis of the terpyridine with the spacer followed by the reaction of these moieties with the 1,3,5-benzenetricarbonyl trichloride. Firstly, because the synthesis of the terpyridine with the spacer is relatively straight forward and secondly because 1,3,5-benzenetricarbonyl trichloride is very reactive and should be

more efficient to achieve the last step. However, the reaction with the 4'-chloro-2,2':6',2''-terpyridine and **156** did not yield the desired product. While attempting reacting Boc-L-alanine with **151**, the result demonstrated that the coupling was occurring at two different positions. Despite the possibility to achieve a relative separation of the different products through the use of column chromatography, and reprecipitation, some of the terpyridine starting material was still present along with the desired product. As further purification could not be achieved, therefore the target molecule was modified to decrease the possibility of coupling at different positions by using the previously synthesised 4′-(4-aminophenyl)-2,2′:6′,2″-terpyridine (**111**). The change of terpyridine moiety along with coupling reagent led to the successful synthesis of **159** in 66% and was fully characterised, notably through the formation of single crystals suitable for X-ray analysis. While the Boc-deprotection was successful, the elemental analysis demonstrated the presence of remaining TFA. Two different procedures were tested for the formation of the corresponding tripodal molecule and were proven unsuccessful. This could be explained by the presence of the extra TFA in **160** which could have hindered the reactivity with 1,3,5-benzenetricarbonyl trichloride. To solve this issue, the TFA salt and the additional TFA present in the sample could be removed by washing **160** in an aqueous basic solution and extracting the desired amine with an organic solvent. Following this, the reaction with 1,3,5-benzenetricarbonyl trichloride in presence of triethylamine should yield the desired tripodal molecule which could be then used in a variety of studies.

As future work, the completion of the synthesis of the tripodal molecule (**161**), the screening of conditions for the formation of gels using **161**, as well as the spectroscopic study of the self-assembly of **161** in solution should be carried out. The sensitisation of Ln(III)-centred emission could be investigated concomitantly with the emission of lanthanide circularly polarised light. Finally, **160** and other amino acids functionalised terpyridine moieties synthesised following the procedure described in this chapter could be used in the functionalisation of numerous building blocks such as 1,8-naphthalimide, 4-amino-1,8-naphthalimide-Tröger's base or HEMA, which was previously used in the group for the formation of luminescent lanthanide polymers through the incorporation of naphthyl-dipicolinic acid.[222]

Chapter 6— Conclusion

This thesis aimed to synthesise and characterise different building blocks adorned with the 2,2′:6,2″-terpyridine (TPy) motif. The coordination and higher order self-assembly behaviours of these ligands to form discrete *d*- and *f*-metal complexes and larger self-assembled structures was demonstrated using a variety of techniques, and the uses of these materials in different applications was also investigated. The introduction provided an overview of the use of 2,2′:6,2″-terpyridine and 1,8-naphthalimide, with a particular emphasis on 1,8-naphthalimides adorned with coordinating moieties, and the descriptions of the properties of the complexes they formed. Various examples of Tröger's bases were also discussed, exploring the unique features of the bent Tröger's base shape, and how this affects their properties. A summary of the characteristics of Ln(III) ions was provided along with a description of several ligands used for the formation of complexes and sensitisation of Ln(III) ions. This was followed by a review of the work carried out on the effect of the size of the lanthanide radii on the stability constants of the complexes. Finally, several examples of the self-assembly of benzene-1,3,5-tricarboxamide scaffolds were discussed.

Chapter 2 described the synthesis and characterisation of a novel terpyridine covalently attached to a 4-nitro- (**112**) and 4-amino-1,8-napthalimide (**107**). Gratifyingly, crystal structures of the precursors **111** and **112** could be obtained and were described. The ability of **107** to coordinate *d*-metal ions was described and [**107**$_2$($Co(NO_3)_2$)] , [**107**$_2$($FeCl_2$)], [**107**$_2$($Cd(NO_3)_2$)] and [**107**$_2$($Zn(BF_4)_2$)] were fully characterised. The spectroscopic and electrochemical properties of **107** and its corresponding complexes were discussed which highlighted the influence of the metal and the counter ion on the different properties of the complex obtained.

Chapter 3 focused on the uses of two naphthalimide Tröger's bases. The first was the 4′-(4-aminophenyl)-2,2′:6′,2″-terpyridine adorned 4-amino-1,8-naphthalimide Tröger's base (**TBNap-TPy**, **130**) which was synthesised using **107** and fully characterised. The spectroscopic study of **130** in a variety of solvents demonsrtated the ability of **130** to exhibit aggregation induced emission (AIE) in DMSO:H_2O mixtures. The use of **130** as a fluorescent sensor for various nitroaromatics was investigated and it was shown that **130** can discriminate phenolic and non-phenolic nitroaromatics through intermolecular hydrogen bonding with the Tröger's base. In particular, **130** exhibited the highest Stern-Volmer constants for picric acid (PA) and 2,4-dinitrophenol (DNP) ($40.6 \pm 1.7 \times 10^3$ M^{-1} and $25.0 \pm 0.4 \times 10^3$ M^{-1}, respectively). A detailed study was carried out to understand the interactions between **130** and PA *via* a combination of ^{1}H NMR, FT-IR and DFT calculations which demonstrated that intermolecular hydrogen-bonding as well as π-π stacking interactions

were taking place. Competitivity experiments for the selective sensing of PA in the presence of structurally close NACs and various ions revealed the robustness of **130** except in the presence of transition metals which coordinate **130** and quench its emission. The effect of pH was also explored, showing that at acidic pH resulted in a stronger fluorescence quenching while sensing in basic medium resulted in a lower sensitivity. The limit of detection was established to be 20 ppb which is lower than the allowed limit of NACs in drinking water established by the US EPA.[185,201,202]

The second Tröger's base studied in Chapter 3 was a 4-amino-1,8-naphthalimide Tröger's base covalent organic polymer (**131**), which was synthesised and characterised by Asst. Prof. Sankarasekaran from the Gunnlaugsson research group. The spectroscopic study of **131** suspended in water demonstrated that **131** could be used to detect the presence of PA in water by quenching of its fluorescence. Similarly to **130**, **131** showed a high affinity towards PA and 2,4-DNP with Stern-Volmer constants of $32.7 \pm 1.3 \times 10^3\ M^{-1}$ and $17.4 \pm 0.2 \times 10^3\ M^{-1}$, respectively. The robustness of **131** was demonstrated through competitivity experiments for the selective sensing of PA in the presence of structurally related NACs and other ions, which displayed very little effect on the fluorescence sensing. The effect of pH on the sensing mechanism was evaluated: an acidic pH resulted in a slight decrease of fluorescence quenching while, sensing in basic media resulted in a drastic decrease of sensitivity suggesting again that hydrogen-bonding is involved in the sensing mechanism. The mechanism of sensing was investigated through UV-Vis absorption, emission spectroscopy, and DFT, revealing that the inner filter effect accounted for 56% of the quenching while, the remaining 24% was due to a combination of hydrogen bonding interactions and static quenching. The limit of detection was established to be 12 ppb which is lower than the allowed limit of NACs in drinking water established by the US EPA.[185,201,202]

The coordination of **130** to various *d*-metals ($Zn(BF_4)_2$, $Fe(BF_4)_2$ and $Co(BF_4)_2$) was carried out and led to the formation of linear polymers that were fully characterised. Morphological studies of **130** showed that its structure when drop-cast from DMF was highly concentration dependent: bowl-like discs were favoured at 0.5 mg/mL, while spherical aggregates were favoured at concentrations of 1 mg/mL. Morphology studies of [**130**($Zn(BF_4)_2$)] showed that it formed a polymeric, porous network of filaments while [**130**($Fe(BF_4)_2$)] and [**130**($Co(BF_4)_2$)] formed amorphous aggregates. Emission spectroscopy of **130**, [**130**($Zn(BF_4)_2$)], [**130**($Fe(BF_4)_2$)] and [**130**($Co(BF_4)_2$)] in DMF revealed that [**130**($Zn(BF_4)_2$)] is the most luminescent polymer and that the formation of aggregates takes

place in a solution at high concentration. Finally, their cyclic voltammograms were compared to **130** and revealed the influence of the metal ion on their electrochemical properties.

Chapter 4 focused on the synthesis and use of a 1,3,5-benzene tricarboxamide functionalised with terpyridine (**BTA-TPy**, **85**) to generate supramolecular architectures capable of forming soft materials. A combination of ^{1}H NMR, UV-vis absorbption and emission spectroscopic studies of **85** confirmed the formation of aggregates both in DMSO and MeOH solutions at higher concentrations (from 25.00×10^{-6} M to 2.58×10^{-6} M in MeOH). The UV-vis absorbption and emission titrations of **85** with $LnCl_3$ (La, Sm, Eu, Gd, Tb, Yb, Lu) were carried out at a concentration where **85** self-assembles (1.0×10^{-5} M) and, satisfyingly, lanthanide-centred emission was observed in the case of Sm(III), Eu(III), Tb(III) and Yb(III). Using non-linear regression analysis software SPECFIT, the formation of 1:1 and 3:2 M:L stoichiometric species was determined along with there corresponding binding constants. The study of the binding constants revealed a parabolic relationship with the ionic radii of the lanthanides and demonstrated the influence of the size of the lanthanide ions on the formation of the supramolecular assembly, and thus the influence of the preorganisation of the ligand on the formation of Ln(III) complexes.

The formation of gels using **85** and their further modification by diffusion of *d*- and *f*-metals into the gel was carried out. These gels were studied through TGA, SEM and rheology and did not reveal any influence of the size of the lanthanide ion on the modification of the gel properties. However, significant modification of the properties of the gel through passive diffusion of *d*- and *f*-metals was observed, notably with an increase in the width of the fibres, and an important increase in the robustness of the gels, demonstrating that *d*- and *f*-metals act as supramolecular glues by cross-linking the fibres of the gels. The modification of the gel formed by **85** by diffusion of $[Ru(phen)_2\mathbf{148}]^{2+}$ was studied, demonstrating a drastic change in the spectroscopic properties of the gel, while the SEM study demonstrated that the morphology of the gels is independent of the presence of this complex.

Chapter 5 depicted the design and attempted synthesis of a novel 1,3,5-benzenetricarboxamide functionalised with TPy through the use of chiral amino acids as a spacer. Different approaches were discussed along with the synthetic hurdles encountered, leading to the modification of the original design. The successful synthesis of the TFA salt of L-alanine-4'-(4-aminophenyl)-2,2':6',2''-terpyridine (**160**) and its full characterisation are discussed along with the description of the intermediates, with notably the X-ray structure

of **159**. This work establishes a platform for the functionalisation of 4′-(4-aminophenyl)-2,2′:6′,2″-terpyridine with various amino acids.

Chapter 7— Experimental Details

7.1 Materials and Methods

All reagents, solvents, and starting materials and nitroaromatics analytes were purchased from Sigma-Aldrich, Merck, or Fisher Scientific, were of reagent grade and were used as received. Solvents used were HPLC grade unless otherwise stated. Dry solvents were obtained from a solvent purification system (SPS) purchased from Innovative Technology Incorporated.

(***Caution!*** *Nitroaromatic analytes are classified as secondary chemical explosives and should be handled only in small quantity*)

NMR Spectroscopy: All ^{1}H and $^{13}C\{^{1}H\}$ NMR spectra were recorded at 400 MHz and 101.2 MHz respectively using an Agilent Technologies 400-MR NMR spectrometer or a Bruker Spectrospin DPX-400 instrument. NMR spectra were also recorded using a Bruker AV-600 instrument operating at 600.1 MHz for ^{1}H NMR and 150.9 MHz for $^{13}C\{^{1}H\}$. Chemical shifts are reported in ppm with the deuterated solvents as the internal reference. All NMR spectra were carried out at 293 K except when specified. Deuterated solvents [$(CD_3)_2SO$, $CDCl_3$, CD_3OD and CD_3CN] used for NMR analyses were purchased from Sigma-Aldrich or Apollo Scientific. The solid-state CP/MAS ^{13}CNMR spectrum of **TBNap-COP** and **TBNap-TPy** polymers were acquired at 201.1 MHz using a 3.2 mm double resonance MAS probe. The spectrum was acquired under magic angle spinning (MAS) at 20 kHz, if not otherwise specified, using ramped-amplitude cross polarisation, and SPINAL64 decoupling with a ^{1}H-decoupling field of about 80 kHz. A 3 ms contact time and a pulse delay of 5 s were used. Chemical shifts were calibrated setting the ^{13}C low field signal of adamantane to 8.48 ppm.

Infrared Spectroscopy: FT-IR spectra were recorded in the range 4000-550 cm^{-1} on a Perkin-Elmer spectrometer equipped with a universal ATR sampling accessory.

Mass Spectroscopy: Mass spectrometry was carried out using HPLC grade solvents. Electrospray mass spectra were determined on a Micromass LCT spectrometer and high-resolution mass spectra were determined relative to a standard of leucine enkephaline. Maldi-Q-TOF mass spectra were carried out on a MALDI-Q-TOF-premier and high-resolution mass spectrometry was performed using Glu-Fib with an internal reference peak of m/z = 1570.6774.

Thermal Analysis:

Thermal gravimetric analysis was performed on a Perkin Elmer Pyris 1 TGA equipped with an ultra-micro balance with a sensitivity of 0.1 μg. Samples were spread on alumina crucibles and heated under a nitrogen purge flow of 20 ml min^{-1} at a heating rate of 10 °C min^{-1}. The elemental analysis for C, H and N were performed on an Exeter analytical CE-450 elemental analyzer at University College Dublin (UCD). Melting points were determined using an IA9000 digital melting point apparatus.

Scanning Electron Microscopy:

Microscopy analysis of samples by Scanning Electron Microscopy (SEM) was carried out using the facilities of the Advanced Microscopy Laboratory (AML) in Trinity College Dublin. Samples were prepared by drop-casting the sample onto clean silicon wafers. The manually drop cast samples were dried overnight in ambient conditions and under high vacuum for at least 2 hours prior immediately to their imaging. In some cases, samples were coated with a conductive Pd/Au layer using a Cressington 208Hr high-resolution sputter coater, to improve contrast where static charging interfered with the imaging. Low kV SEM was carried out using the Zeiss ULTRA Plus using an SE2 detector.

For Chapter 3: The sample was prepared by drop-casting the DMSO or DMSO/Water mixture (4.79×10^{-5}M) of **TBNap-Tpy** on silica wafers, dried both in ambient conditions and under high-vacuum for few hours, then coated with Pd/Au before the imaging. The samples of **TBNap-Tpy** polymers were prepared by drop-casting the DMF solution (0.5 mg/mL) of the desired polymer on silica wafers, dried both in ambient conditions and under high-vacuum for few hours, then coated with Pd/Au before the imaging.

For Chapter 4: The gels samples were taken using a spatula and gently pressed onto the silica wafers, they were then dried both in ambient conditions and under high-vacuum for few hours, then coated with Pd/Au before the imaging.

Gas Adsorption Studies:

Gas adsorption isotherms were carried out in collaboration with Dr Kevin Byrne of Prof. Wolfgang Schmitt's group in SNIAM, School of Chemistry, Trinity College Dublin. Adsorption measurements were performed volumetrically using a Quantachrome Autosorb-iQ instrument. The temperature was maintained at 278, 293, and 308 (±0.1) K using a circulating Dewar and a refrigerated/heated bath circulator (ISOTEMP 4100 R20, Fischer Scientific), and at 77 K using a liquid nitrogen bath. The as-synthesised compound was

immersed in diethyl ether for 3 days. During the immersion, the diethyl ether was refreshed 5 times with fresh diethyl ether and the resulting solvent exchanged polymer was transferred to a quartz cell. The sample was evacuated under vacuum at 100 °C for 72 hours. BOC gases ultrahigh-purity grade N_2, H_2, and CO_2 were used in all adsorption measurements. The surface area of **TBNap-COP** was calculated by the Brunauer-Emmett-Teller (BET) method.

X-ray crystallography:

X-ray crystallographic data were collected by Dr. Brendan Twamley, Dr. Hannah Dalton or Ms Deirdre McAdams using a Brucker APEX-II Duo dual-source instrument and using graphite-monochromated Mo K α (λ = 0.71073 Å) or microfocus Cu K α (λ = 1.54178 Å) radiation. Datasets were collected using ω and φ scans and the samples were immersed in oil. Brucker APEX suite of programs were used to reduce and process the data.[274] Multi-scan absorption corrections were applied using SADABS[275]. The diffraction data were solved using SHELXT and refined by full-matrix least squares procedures using SHELXL-2015 within the OLEX-2 GUI.[276,277] The functions minimized were $\Sigma w(F^2_o-F^2_c)$, with $w=[\sigma^2(F^2_o)+aP^2+bP]^{-1}$, where $P=[max(F_o)^2+2F^2_c]/3$. All non-hydrogen atoms were refined with anisotropic displacement parameters. All hydrogen atoms were placed in calculated positions and refined with a riding model, with isotropic displacement parameters equal to either 1.2 or 1.5 times the isotropic equivalent of their carrier atoms. In cases where U_{ij} or position restraints were necessary, these were employed as sparingly as possible and only for the purpose of maintaining chemically sensible geometries and ADPs. Hirshfeld d_{norm} surface properties were mapped using CrystalExplorer package (Isovalue 0.5, property ranges 0.5 – 1.0).[278,279]

Photophysical measurements:

UV-visible absorption spectra were recorded in 1 cm quartz cuvettes (Hellma) on a Varian Cary 50 spectrometer at room temperature. Baseline correction was applied for all spectra. The fluorescence measurements were carried out on a Varian Cary Eclipse Fluorimeter equipped with a 1.0 cm path length quartz cell at room temperature. The solvents were all of spectroscopic or HPLC grade.

For Chapter 2: UV-visible absorption spectra were recorded in 1 cm quartz cuvettes (Hellma) on a Varian Cary 50 spectrometer at room temperature. The wavelength range was set from 265 to 650 nm with a scan rate of 300 nm/min. Baseline correction was applied for

all spectra. The setting of the fluorimeter for the luminescence titrations carried out in this chapter are shown in Table 7-1.

Table 7-1 Fluorescence settings for the experiment described in Chapter 2

Mode: Fluorescence	Excitation: 430 nm	Scan range: 450-800 nm
Excitation slit: 2.5 nm	Emission slit: 5 nm	PMT: 600 V
Averaging time: 0.100 s	Scan Rate: 300 nm/min	Data interval: 0.5 nm
Excitation filter: Open	Emission filter: 430-1100 nm	

For Chapter 3: UV-visible absorption spectra were recorded in 1 cm quartz cuvettes (Hellma) on a Varian Cary 50 spectrometer at room temperature. The wavelength range was set from 265 to 650 nm with a scan rate of 300 nm/min. Baseline correction was applied for all spectra. The setting of the fluorimeter for the luminescence titrations carried out in this chapter are shown in Table 7-2.

Table 7-2 Fluorescence settings for the titration described in Chapter 3.

Mode: Fluorescence	Excitation: 388 nm	Scan range: 400-800 nm
Excitation slit:5 nm	Emission slit: 5 nm	PMT: 800 V
Averaging time: 0.100 s	Scan Rate: 300 nm/min	Data interval: 0.5 nm
Excitation filter: Open	Emission filter: 430-1100 nm	

Fluorescence lifetime experiments were carried out on a Horiba Scientific FluoroLog - Modular Spectrofluorometer equipped with Time-Correlated Single Photon Counting (TCSPC) capability.

For Chapter 4: UV-visible absorption spectra were recorded in 1 cm quartz cuvettes (Hellma) on a Varian Cary 50 spectrometer at room temperature. The wavelength range was set from 200 to 450 nm with a scan rate of 600 nm/min. Baseline correction was applied for all spectra. The setting of the fluorimeter for the luminescence titrations carried out in this chapter are shown in Table 7-3.

Table 7-3 Fluorescence settings for the titration described in Chapter 4.

Mode: Fluorescence	Excitation: 280 nm	Scan range: 305-700 nm
Excitation slit: 20 nm	Emission slit: 5 nm	PMT: 600 V
Averaging time: 0.100 s	Scan Rate: 600 nm/min	Data interval: 1 nm
Excitation filter: Auto	Emission filter: 295-1100 nm	

The phosphorescence measurements were carried out on a Varian Cary Eclipse Fluorimeter equipped with a 1.0 cm path length quartz cell at room temperature. The settings of the fluorimeter for the luminescence titrations of $SmCl_3$ are shown in Table 7-4, of $EuCl_3$ are shown in Table 7-5, $GdCl_3$ are shown in Table 7-6 and $TbCl_3$ are shown in Table 7-7.

Table 7-4 Luminescence setting for the titration of $SmCl_3$.

Mode: Phosphorescence	Excitation: 280 nm	Scan range: 540-730 nm
Excitation slit: 20 nm	Emission slit: 5 nm	PMT: 900 V
Averaging time: 0.200 s	Data interval: 1 nm	Excitation filter: Auto
Emission filter: Open	Total decay time: 0.015 s	No of flashes: 1
Delay time: 0.1000 ms	Gate time: 5.000 ms	

Table 7-5 Luminescence settings for the titration of $EuCl_3$.

Mode: Phosphorescence	Excitation: 280 nm	Scan range: 570-720 nm
Excitation slit: 20 nm	Emission slit: 1.5 nm	PMT: 800 V
Averaging time: 0.100 s	Data interval: 0.50 nm	Excitation filter: Auto
Emission filter: Open	Total decay time: 0.020 s	No of flashes: 1
Delay time: 0.1000 ms	Gate time: 5.000 ms	

Table 7-6 Luminescence settings for the titration of $GdCl_3$.

Mode: Phosphorescence	Excitation: 280 nm	Scan range: 300-330 nm
Excitation slit: 20 nm	Emission slit: 10 nm	PMT: 900 V
Averaging time: 0.200 s	Data interval: 1.0 nm	Excitation filter: Auto
Emission filter: Open	Total decay time: 0.015 s	No of flashes : 1
Delay time: 0.1000 ms	Gate time: 5.000 ms	

Table 7-7 Luminescence settings for the titration of $TbCl_3$.

Mode: Phosphorescence	Excitation: 280 nm	Scan range: 460-700 nm
Excitation slit: 20 nm	Emission slit: 1.5 nm	PMT: 720 V
Averaging time: 0.100 s	Data interval: 0.500 nm	Excitation filter: Auto
Emission filter: Open	Total decay time: 0.020 s	No of flashes: 1
Delay time: 0.1000 ms	Gate time: 5.000 ms	

The luminescence titration of $YbCl_3$ were carried out using a Horiba Scientific FluoroLog - Modular Spectrofluorometer equipped with a FluoroHub v2.0 single-photon timing module

using a sub-ns pulsed diode laser. The scan range was set to 900-1200 nm and an Andover Corporation Optical filter P/N: 900Fl I90-50S was used.

The lifetime measurements of the **BTA-TPy** in presence of various lanthanides were carried out along the other titrations on Varian Cary Eclipse Fluorimeter. The setting of the fluorimeter for the lifetime measurements in presence of $EuCl_3$ are shown in Table 7-8. Lifetimes values of Eu(III) ($^5D_0$) excited state were measured in solution in time-resolved mode. The lifetime values are averages of three measurements which were made by monitoring the emission decay of the $^5D_0 \rightarrow {}^7F_2$ transition at 618 nm.

Table 7-8 Settings used for the measurement of Eu(III)-centred luminescence decay.

Mode: Phosphorescence	Excitation: 330 nm	Wavelength monitored: 616 nm
Excitation slit: 20 nm	Emission slit: 20 nm	PMT: 800 V
Excitation filter: Open	Emission filter: Open	Total decay time: 0.020 s
Gate time: 0.015-0.025 ms	Number of cycles: 50	No of flashes: 1
Delay time: 0.0500 ms		

1.7.1 Synthesis and characterisation of compounds described in Chapter 2

(E)-3-(4-Nitrophenyl)-1-(pyridin-2-yl)prop-2-en-1-one)(108):

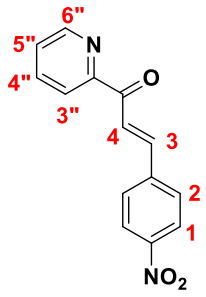

The compound **108** was synthesised according to a procedure reported by Brudvig *et al*. In a 250 mL round-bottomed flask, 2-acetylpyridine (2.2 mL, 19.8 mmol, 1 eq) and nitrobenzaldehyde (3.0 g, 19.8 mL, 1 eq) were dissolved into methanol (40 mL). After cooling the mixture to 0 °C a solution of KOH (1.15 g in 7.5 mL of deionised water) was added dropwise to it. The mixture was stirred at 0 °C for 30 min and further stirred at room temperature for 12 h, during which time a solid precipitated. The precipitate was collected by vacuum filtration and washed with cold methanol. The dried solid was dissolved into the minimum amount of warm chloroform and yellow crystals were formed upon cooling of the solution. The crystals were collected by vacuum filtration and dried under high vacuum (1.835 g, 7.21 mmol, 36%). ^{1}H NMR spectrum was in good agreement with data previously reported in the literature.[280] ^{1}H NMR (400 MHz, $CDCl_3$, ppm): δ 8.76 (1H, d, J = 4.4 Hz, $H_{6"}$), 8.43 (1H, d, J = 16.1 Hz, H_4), 8.27 (2H, d, J = 8.4 Hz, H_2), 8.20 (1H, d, J = 7.8 Hz, $H_{3"}$), 7.94 (1H, m, $H_{4"}$), 7.92 (1H, d, J =15.3 Hz, H_3), 7.86 (2H, d, J = 8.4 Hz, H_1), 7.53 (1H, m, $H_{5"}$).

(1-(2-Oxo-2-(pyridin-2-yl)ethyl)pyridinium iodide (109):

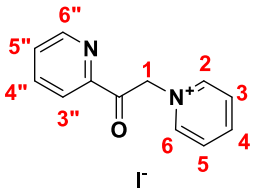

Compound **109** was synthesised using modified procedure previously reported by Brudvig *et al*.[280] 2-acetylpyridine (2.7 mL, 24.07 mmol, 1 eq) and Iodine (6.1 g, 24, 07 mmol, 1 eq) were dispersed in pyridine (14 mL) and the mixture was purged with argon for 15 min, then it was refluxed under argon until the medium crystalised (≈ 40 min). The solid was dissolved in acetonitrile to be loaded on silica. A short silica plug (10 cm) was prepared and the compound was the second yellow band eluted while flushing acetonitrile through the plug. The solvent was evaporated off and the solid was recrystallised from boiling ethanol (≈ 280 mL) as an off-white solid which was dried under high vacuum (5.417 g, 16.6 mmol, 68%). ^{1}H NMR spectrum was in good agreement with data previously reported in the literature.[176] ^{1}H NMR (400 MHz, CD_3CN): δ 8.80 (1H, d, *J* = 4.8 Hz, $H_{6"}$), 8.73 (2H, d, *J* = 6.0 Hz, $H_{2,6}$), 8.64 (1H, t, *J* = 7.9 Hz, H_4), 8.13 (2H, t, *J* = 7.0 Hz, $H_{3,5}$), 8.07 (2H, m, $H_{3",4"}$), 7.74 (2H, t, *J* = 6,0 Hz, $H_{5"}$), 6.41 (2H, s, H_1).

4′-(4-Nitrophenyl)-2,2′:6′,2″-terpyridine(110):

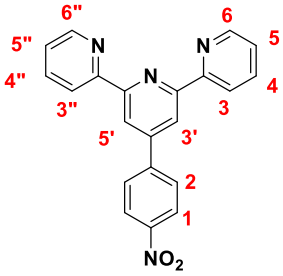

Compound **110** was synthesised according to a procedure reported by Brudvig *et al*. ^{1}H NMR spectrum was in good agreement with data previously reported in the literature.[175,280] In a 250-mL round-bottom flask, **109** (1.71 g, 6.74 mmol, 1 eq), **108** (2.2 g, 6.74 mmol, 1 eq), ammonium acetate (3.64 g, 47.2 mmol, 7 eq), and 100 mL of methanol were added. The mixture was purged with argon for 15 min then refluxed under argon for 4 h, during which time an off-white solid precipitated. After cooling down the mixture to room temperature, the precipitate was collected by vacuum filtration and washed with cold methanol (3 × 50 mL) to give the desired nitrophenyl terpyridine **110** as a white solid. (1.787 g, 5.04 mmol, 75%). ^{1}H NMR (600 MHz, DMSO-d_6, ppm): δ 8.77 (2H, d, *J* = 6.4 Hz, $H_{6",6}$), 8.76 (2H, s, $H_{3',5'}$), 8.67 (2H, d, *J* = 7.9 Hz, $H_{3",3}$), 8.40 (2H, d, *J* = 8.7 Hz, H_1), 8.21 (2H, d, *J* = 8.7 Hz, H_2), 8.05 (2H, t, *J* = 7.9 Hz, $H_{4,4"}$), 7.54 (2H, dd, *J* = 6.9, 5.3 Hz, $H_{5",5'}$).

4′-(4-Aminophenyl)-2,2′:6′,2″-terpyridine(111):

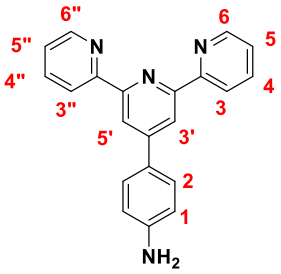

4′-(4-nitrophenyl)-2,2′:6′,2″-terpyridine (**110**) (700 mg, 1.97 mmol) was reduced by catalytic hydrogenation using 10 *wt* % Pd/C (20%, 140 mg) at 3 atm of H_2 in DMF (15 mL) for 24 h. The solution was filtered through a celite plug and washed several times with DMF. The solvent was removed under reduced pressure to isolate **111** (569 mg, 1.75 mmol, 89%) as yellow solid after trituration in diethyl ether. ^{1}H NMR spectrum was in good agreement with data previously reported in the literature.[175,280] ^{1}H NMR (600 MHz, DMSO-d_6, ppm): δ 8.75 (2H, d, *J* = 4.6 Hz, $H_{6",6}$), 8.64 (2H, d, *J* = 8.1 Hz, $H_{3",3}$), 8.62 (2H, s, $H_{3',5'}$), 8.02 (2H, t, *J* = 7.7 Hz, $H_{4",4}$), 7.67 (2H, d, *J* = 8.4 Hz, H_1), 7.50 (2H, m, $H_{5",5}$), 6.74 (2H, d, *J* = 8.4 Hz, H_2), 5.61 (s, 2H, NH_2).

2-[4′-(4-Aminophenyl)-2,2′:6′,2″-terpyridine]-4-nitro-1,8-naphthalimide (NitroNap-TPy, 112):

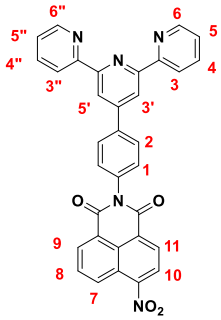

The synthesis of **112** was carried out according to a modified literature procedure.[171] 4′-(4-Aminophenyl)-2,2′:6′,2″-terpyridine (**111**, 200 mg, 0.616 mmol, 1 equiv.) and 4-nitro-1,8-naphthalic anhydride (150 mg, 0.616 mmol, 1 equiv.) were dispersed into acetic acid (15 mL) in a pressure vessel and the reaction mixture was refluxed for 24 h. After cooling the mixture at rt it was poured into H_2O and the solution was basified to pH 6 using KOH leading to the precipitation of a beige solid. The precipitate was filtered and washed several times with water and cold methanol and diethyl ether. The solid was then triturated in ethyl acetate, filtered, and washed with methanol and diethyl ether leading to the pure desired compound (132 mg, 0.204 mmol, 39%). m.p. 307 °C (decomp.). HRMS (MALDI) calculated for $C_{33}H_{20}N_5O_4$ *m/z*= 550.1515 $[M+H]^+$; Found *m/z*= 550.1532. ^{1}H NMR (600 MHz, DMSO-d_6, ppm): δ 8.81 (2H, s, $H_{3',5'}$), 8.79 (2H, d, *J* = 4.9 Hz, $H_{6,6"}$), 8.78 (m, 1H, H_9), 8.70 (2H, d, *J* = 7.9 Hz, $H_{3,3"}$), 8.69 (1H, d, *J* = 7.2 Hz, H_7), 8.66 (1H, d, *J* = 7.9 Hz, H_{11}), 8.61 (1H, d, *J* = 7.9 Hz, H_{10}), 8.15 (1H, dd, *J* = 8.3, 7.2 Hz, H_8), 8.14 (2H, d, *J* = 8.2 Hz, H_1), 8.06 (2H, td, *J* = 7.8, 1.6 Hz, $H_{4,4"}$), 7.66 (2H, d, *J* = 8.3 Hz, H_2), 7.55 (2H, dd, *J* = 7.0, 5.1 Hz, $H_{5,5"}$). ^{13}C{^{1}H} NMR (150.8 MHz, DMSO-d_6, ppm): 163.8 (C=O), 163.0 (C=O), 156.3 (q), 155.4 (q), 149.9 (C_9), 149.8 (q), 149.4 (q), 138.1 (q), 138.0 ($C_{4,4"}$), 137.2 (q), 132.2 (C_7), 130.6 (C_8), 130.6 (C_2), 130.1 (C_{11}), 129.4 ($C_{6,6"}$), 129.3 (q), 128.1 (C_8), 127.8 (q), 125.1 ($C_{5,5"}$), 124.8 (C_{10}), 123.9 (q), 123.4 (q), 121.5 ($C_{3,3"}$), 118.6 ($C_{3',5'}$). IR ν_{max} (neat

sample, cm^{-1}): 3058, 1716, 1673, 1585, 1524, 1214, 1467, 1441, 1415, 1389, 1369, 1344, 1339, 1235, 1193, 1134, 1122, 1077, 1040, 988, 914, 858, 825, 783, 780, 757, 738, 711, 695.

2-[4′-(4-Aminophenyl)-2,2′:6′,2″-terpyridine]-4-amino-1,8-naphthalimide (AminoNap-Tpy, 107):

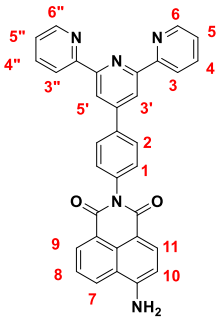

The synthesis of **107** was carried out according to a modified literature procedure.[185] 2-[4′-(4-Aminophenyl)-2,2′:6′,2″-terpyridine]-4-nitro-1,8-naphthalimide (**112**, 122 mg, 0.222 mmol) was reduced by catalytic hydrogenation using 10 *wt* %Pd/C (20%, 25mg) at 3 atm of H_2 in DMF (15 mL) overnight. The mixture was diluted in 60 mL of EtOH, filtered through a celite plug and washed several times with DMF. The solvent was removed under reduced pressure to isolate **107** (110 mg, 0.212 mmol, 95%) as mustard colored solid after trituration in diethyl ether. m.p. 329 °C (decomp). HRMS (ESI^-) calculated for $C_{33}H_{20}N_5O_2$ *m/z* = 518.1622 $[M-H]^-$. Found *m/z* = 518.1616. ^1H NMR (600 MHz, DMSO-d_6, ppm): δ 8.80 (2H, s, $H_{3',5'}$), 8.79 (2H, d, *J* = 4.2 Hz $H_{6,6"}$), 8.70 (2H, d, *J* = 8.0 Hz, $H_{3,3"}$), 8.69 (1H, d, *J* = 8.8 Hz, H_7), 8.47 (1H, d, *J* = 7.1 Hz, H_9), 8.23 (1H, d, *J* = 8.23 Hz, H_{11}), 8.08 (2H, d, *J* = 8.3 Hz, H_2), 8.06 (2H, m, $H_{4,4"}$), 7.71 (1H, t, *J* = 7.8 Hz, H_8), 7.55 (2H, m, $H_{5,5"}$), 7.54 (2H, m, H_1), 6.90 (1H, d, *J* = 8.3 Hz, H_{10}). $^{13}C\{^1H\}$ NMR (150.8 MHz, DMSO-d_6, ppm): 164.1 (C=O), 163.2 (C=O), 155.8 (q), 155.0 (q), 153.0 (q), 149.4 ($C_{6,6"}$), 149.0 (q), 137.9 (q), 137.5 ($C_{4,4"}$), 137.0 (q), 134.1 (C_{11}), 131.2 (C_9), 130.4 (q), 130.3 ($C_{5,5"}$), 129.6 (C_7), 127.4 (C_2), 124.6 (C_1), 124.1(C_8), 122.2 (q), 121.0 ($C_{3,3"}$), 119.6 (q), 118.1 ($C_{3',5'}$), 108.3 (C_{10}), 107.8 (q). IR ν_{max} (neat sample, cm^{-1}): 3470, 3316, 3160, 1690, 1650, 1584, 1518, 1466, 1363, 1345, 1234, 1133, 1130, 990, 914, 887, 822, 793, 772, 740, 694, 659.

[(AminoNap-TPy)$_2$Zn(BF$_4$)$_2$]:

AminoNap-TPy (**107**) (40.6 mg, 0.078 mmol, 2 eq) and $Zn(BF_4)_2.6H_2O$ (13.5 mg, 0.039 mmol, 1 eq) were dispersed in 1 mL of DMF in a sealed vial with a PTFE-lined cap and heated in a dry block heater at 75 °C for 12 h. The mixture was concentrated under reduced pressure, the resulting solid was sonicated in diethyl ether, filtered, and the orange powder obtained was washed with acetonitrile, and ether and dried under high vacuum (49 mg, 0.038 mmol, 98%). m.p. > 300 °C (decomp). Elemental analysis calculated for $C_{66}H_{42}N_{10}O_4ZnB_2F_8 \cdot 1.8DMF \cdot 1.0CH_3CN$: C, 59.27; H, 3.25; N, 10.62; Found: C, 59.43; H, 3.24; N, 10.48. HRMS (ESI) calculated for $C_{66}H_{42}N_{10}O_4Zn$ *m/z* = 551.1335 $[M]^+$. Found *m/z*

= 551.1342. ^{1}H NMR(600 MHz, DMSO-d_6, ppm): δ 9.50 (4H, s, $H_{3',5'}$), 9.20 (4H, d, *J* = 8 Hz, $H_{3,3''}$), 8.72 (2H, d, *J* = 8.3 Hz, H_7), 8.57 (4H, d, *J* = 7.8 Hz, $H_{6,6''}$), 8.51 (2H, d, *J* = 6.9 Hz, H_9), 8.32 (4H, t, *J* = 7.2 Hz, $H_{4,4''}$), 8.27 (2H, d, *J* = 8.1 Hz, H_{11}), 8.01 (4H, d, *J* = 4.4 Hz, H_2), 7.77-7.73 (6H, m, $H_{5,5''}$ and H_8), 7.58 (4 H, s, NH_2), 7.54 (4H, t, *J* = 6.1 Hz, H_1), 6.93 (2H, d, *J* = 8.3 Hz, H_{10}). ^{13}C{^{1}H} NMR (150.8 MHz, DMSO-d_6, ppm):164.1 (C=O), 163.2 (C=O), 154.6 (q), 153.1 (q), 149.6 (q), 147.9 (C_2), 147.8 (q), 141.4 ($C_{4,4''}$), 139.5 (q), 134.9 (q), 134.2 (C_7), 131.3 (C_9), 130.5 ($C_{5,5''}$), 130.4 (q), 129.7 (C_{11}), 128.7 ($C_{6,6''}$), 127.8 (C_1), 124.1 (C_8), 123.6 ($C_{3,3''}$), 122.2 (q), 121.3 ($C_{3',5'}$), 119.6 (q), 108.3 (C_{10}), 107.7 (q). IR ν_{max} (neat sample, cm^{-1}): 3620, 3471, 3360, 3258, 3076, 1682, 1642, 1573, 1528, 1475, 1360, 1230, 1050, 1011, 791, 769.

[(AminoNap-TPy)$_2$Co(NO$_3$)$_2$]:

AminoNap-TPy (**107**, 38.7 mg, 0.0744 mmol, 2 eq) was dissolved in 10 mL of DMF and $Co(NO_3)_2$ (10.8 mg, 0.0372 mmol, 1 eq) were dispersed in 1 mL of DMF in a sealed vial with a PTFE-lined cap and heated in a dry block heater at 75 °C for 12 h. The mixture was concentrated under reduced pressure, the resulting solid was sonicated in diethyl ether, filtered, washed with CH_3CN and ether, and the resulting powder was dried under high vacuum (39 mg, 0.32 mmol, 79%). m.p. > 300 °C (decomp). Elemental analysis calculated for $C_{66}H_{42}N_{12}O_{10}Co \cdot 2.4DMF \cdot 1.6CH_3CN$, 60.74; H, 3.39; N, 13.02; Found: C,60.74; H, 3.27; N, 13.03. HRMS (MALDI) calculated for $C_{66}H_{42}N_{10}O_4Co$ *m/z* = 1097.2722 $[M]^+$. Found *m/z* = 1097.2708. IR ν_{max} (neat sample, cm^{-1}): 3548, 3415, 3347, 3243, 3057, 1677, 1637, 1613, 1571, 152, 1474, 1358, 1337, 1306, 1236, 821, 793, 773, 750.

[(AminoNap-TPy)$_2$Cd(NO$_3$)$_2$]:

AminoNap-TPy (**107**, 41.8 mg, 0.0804 mmol, 2 eq) was dispersed in 1 mL of DMF and a solution of $Cd(NO_3)_2$ (12.4 mg in 175 µL of DMF, 0.0402 mmol, 1 eq) was added to a sealed vial with a PTFE-lined cap and heated in a dry block heater at 75 °C for 12 h. The mixture was concentrated under reduced pressure, the resulting solid was sonicated in diethyl ether and filtered and the powder was dried under high vacuum (41 mg, 0.032 mmol, 80%). m.p. > 300 °C (decomp). Elemental analysis calculated for $C_{66}H_{42}N_{12}O_{10}Cd \cdot 0.9DMF \cdot 0.8Et_2O$: C, 60.28; H, 3.53; N, 12.9; Found: C,60.14; H, 3.26; N, 12.79. HRMS (MALDI) calculated for $C_{66}H_{42}N_{10}O_4Cd$ *m/z* = 1152.2449 $[M]^+$. Found *m/z* = 1152.2424. ^{1}H NMR (400 MHz, DMSO-d_6, ppm): δ 9.12 (3H, s, H_{TPy}), 8.99 (3H, s, H_{TPy}), 8.70 (2H, d, *J* = 8.9 Hz, H_7), 8.59 (2H, s, H_{TPy}), 8.48 (2H, d, *J* = 6.7 Hz, H_9), 8.33 (3H, s, H_{TPy}), 8.25 (4H, d, *J* = 8.3 Hz,

H_{11}+H_{TPy}), 7.72 (2H, t, *J* = 7.8 Hz, H_8), 7.64 (7H, d, *J* = 8.0 Hz, H_{TPy}), 7.55 (4H, s, NH_2), 6.91 (2H, d, *J* = 8.4 Hz, H_{10}). $^{13}C\{^1H\}$ NMR (101 MHz, DMSO-d_6, ppm): δ 164.1 (C=O), 163.2 (C=O), 153.0, 149.5 (C_{TPy}), 134.1 ($C_{11/TPy}$), 131.2 (C_9), 130.3 (C_{TPy}), 129.7(C_7), 128.2 (C_{TPy}), 124.1 (C_8), 122.22, 119.6, 108.3 (C_{10}), 107.7. IR ν_{max} (neat sample, cm^{-1}): 3412, 3351, 3241, 3103, 3058, 1637, 1570, 1528, 1475, 1357, 1331, 1302, 1235, 1012, 791, 769.

[(AminoNap-TPy)$_2$FeCl$_2$]:

AminoNap-TPy (**107**, 40.2 mg, 0.077 mmol, 2 eq) and $FeCl_2$ (7.69 mg, 0.0386 mmol, 1 eq) were dispersed in 1 mL of DMF in a sealed vial with a PTFE-lined cap and heated in a dry block heater at 75 °C for 12 h. The mixture was concentrated under reduced pressure, the resulting solid was sonicated in diethyl ether filtered and the brown powder obtained was dried under high vacuum (36 mg, 0.0308 mmol, 80%). m.p. > 300 °C (decomp). Elemental analysis calculated for $C_{66}H_{42}N_{10}O_4FeCl_2 \cdot 1.6DMF \cdot 2H_2O$: C, 63.02; H, 3.63; N, 10.62; Found: C,62.78; H, 3.60; N, 10.91 HRMS (ESI) calculated for $C_{66}H_{42}FeN_{10}O_4$ *m/z* = 547.1365 $[M]^+$. Found *m/z* = 547.1376. ^1H NMR(400 MHz, DMSO-d_6, ppm): δ 9.80 (4H, br, H_{TPy}), 9.15 (4H, br, H_{TPy}), 8.73 (6H, br, H_{TPy}), 8.53 (2H, br, H_7), 8.29 (2H, br, H_9), 8.08 (4H, br), 7.81 (6H, br), 7.65 (4H, br), 7.33 (4H, br), 7.24 (4H, br), 6.95 (2H, br, H_{10}). IR ν_{max} (neat sample, cm^{-1}): 3347, 3232, 3053, 1685, 1637, 1576, 1528, 1365, 1235, 786, 772, 755.

1.7.2 Synthesis and characterisation of compounds described in Chapter 3

Bis-2-[4′-(4-aminophenyl)-2,2′:6′,2″-terpyridine]-4-amino-1,8-naphthalimide-[b,f][1,5]-diazocine (TBNap-TPy, 130):

The synthesis of **130** was carried out according to modified literature procedure.[185] 2-[4′-(4-aminophenyl)-2,2′:6′,2″-terpyridine]-4-amino-1,8-naphthalimide (**107**, 200 mg, 0.385 mmol, 1 equiv.) and paraformaldehyde (17.3 mg, 0.577 mmol, 1.5 equiv.) were flushed with argon. Trifluoroacetic acid (4 mL) was added at 0 °C and the resulting solution was stirred at room temperature overnight under inert atmosphere. The mixture was added dropwise to a solution of aqueous ammonia at 0 °C. DCM was added and the organic phase was washed with saturated $NaHCO_3$ solution followed by H_2O. The organic phase was dried over $NaSO_4$ and the solvent was removed under reduced pressure. The solid was triturated in diethyl ether and isolated *via* filtration as an orange solid (125 mg, 0.116 mmol, 77%). m.p. 308 °C (decomp.). Elemental analysis calculated for $C_{69}H_{42}N_{10}O_4 \cdot 0.13CH_3Cl \cdot 0.01DMF \cdot 1.9H_2O$: C, 73.79; H, 4.12; N,

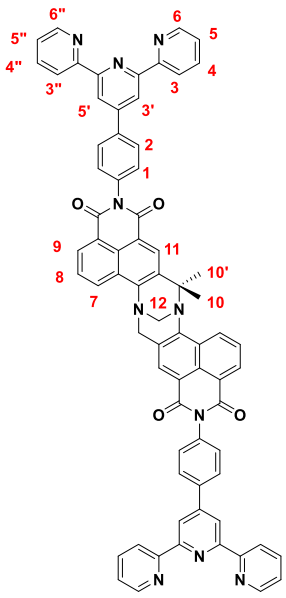

12.45; Found: C,73.80; H, 3.84; N, 12.35. HRMS (MALDI) calculated for $C_{69}H_{43}N_{10}O_4$ *m/z*= 1075.3469 $[M+H]^+$ Found *m/z*= 1075.3445. ^{1}H NMR (600 MHz, DMSO-d_6, ppm): δ 8.79 (2H, d, *J* = 8.79 Hz, H_9), 8.77 (4H, m, $H_{6,6"}$), 8.77 (4H, s, $H_{3',5'}$), 8.69 (4H, d, *J* = 7.9 Hz, $H_{3,3"}$), 8.52 (2H, d, *J* = 7.2 Hz, H_7), 8.19 (2H, s, H_{11}), 8.06 (4H, m, H_2), 8.05 (4H, m, 4H, $H_{4,4"}$), 8.00 (2H, t, *J* = 7.9 Hz, H_8), 7.54 (8H, m, H_1 and $H_{5,5"}$), 5.23 (2H, d, *J* = 17.6 Hz, H_{10}), 4.79 (2H, s, H_{12}), 4.74 (2H, d, *J* = 17.6Hz, $H_{10'}$). ^{13}C{^{1}H} NMR (150.8 MHz, DMSO-d_6, ppm): δ 163.7 (C=O), 163.2 (C=O), 155.8, 154.9, 149.4 ($C_{6,6"}$), 149.3, 148.9, 137.5 ($C_{4,4"}$), 137.3, 137.2, 130.7 (C_{11}), 130.4 (C_7), 130.2 ($C_{1/5,5"}$), 129.4 (C_9), 128.0, 127.5 (C_2), 127.2 (C_8), 126.8, 126.2, 124.6 ($C_{1/5,5"}$), 123.0, 121.0 ($C_{3,3"}$), 118.2 ($C_{3',5'}$), 118.1, 64.9 (C_{12}), 56.9 (C_{10}). IR ν_{max} (neat sample, cm^{-1}): 3063, 1705, 1665, 1584, 1567, 1512, 1467, 1459, 1404, 1369, 1339, 1301, 1240, 1177, 1127, 1087, 1034, 991, 928, 891, 830, 815, 783, 774, 737, 688, 659.

[(TBNap-TPy)$_2$Zn(BF$_4$)$_2$]:

TBNap-TPy (**130**, 42.1 mg, 0.0391 mmol, 1 eq) was dissolved in 1 mL of DMF and a solution of $Zn(BF_4)_2.6H_2O$ (250,7 µL, 0.0391 mmol, 1 eq) was added to the first solution in a sealed vial with a PTFE-lined cap and heated in a dry block heater at 80 °C for 48 h. The mixture was concentrated under reduced pressure, the resulting solid was sonicated in diethyl ether and filtered, washed with small quantities of DCM, MeOH and diethyl ether and the yellow powder was dried under high vacuum (isolated yield: 50 mg,calculated for the monomeric unit 97%). m.p. >300 °C (decomp.). Elemental analysis calculated for the repeating unit $[C_{69}H_{42}N_{10}O_4B_2F_8Zn]\cdot 1.7CH_2Cl_2\cdot 0.5DMF$·: C, 58.00; H, 3.29; N, 9.84; Found: C,58.04; H, 3.03; N, 9.79. ^{1}H NMR (600 MHz, DMSO-d_6, ppm): δ 9.47 (4H, s), 9.15 (4H, m), 8.88-8.70 (4H, m), 8.59 (2H, s), 8.54 (4H, m), 8.31 (2H, s), 8.25 (4H, m), 8.08 (3H, s), 7.99 (4H, m), 7.75 (4H, s), 7.53 (4H, m), 5.29 (2H, br), 4.78 (4 H, br). ^{13}C{^{1}H} NMR (150.8 MHz, DMSO-d_6, ppm): δ 163.8 (C=O), 163.2 (C=O), 149.6, 147.9, 147.7, 141.4, 138.7, 135.4, 130.8, 130.4, 130.3, 129.5, 128.8, 128.1, 127.8, 127.3, 126.3, 123.6, 123.0, 121.4, 118.2. IR ν_{max} (neat sample, cm^{-1}): 3606 w (br), 3218 w (br), 3069 w (br), 2924 w, 1703 m, 1659 s, 1595 s, 1571 s, 1551 m, 1513 m, 1476 m, 1369 s, 1242 m, 1033 s, 1013 s, 785 s.

[(TBNap-TPy)$_2$Fe(BF$_4$)$_2$]:

TBNap-TPy (**130**, 40.2 mg, 0.0373 mmol, 1 eq) and Fe(BF$_4$)$_2$.6H$_2$O (12.6 mg, 0.0373 mmol, 1 eq) were dissolved in 1 mL of DMF in a sealed vial with a PTFE-lined cap and heated in a dry block heater at 80 °C for 48 h. The mixture was concentrated under reduced pressure, the resulting solid was sonicated in diethyl ether and filtered, washed with small quantities of DCM, CH$_3$CN and diethyl ether and the purple amorphous solid was dried under high vacuum (isolated yield: 45 mg, calculated for the monomeric unit 92%). m.p. >300 °C (decomp.). Elemental analysis calculated for the repeating unit [C$_{69}$H$_{42}$N$_{10}$O$_4$B$_2$F$_8$Fe]·1.8CH$_2$Cl$_2$ 0.2CH$_3$CN 0.3DMF·: C, 58.21; H, 3.27; N, 9.88; Found: C,58.12; H, 3.00; N, 9.82. ^{1}H NMR (600 MHz, DMSO-d$_6$, ppm): δ 9.75 (4H, s), 9.07 (4H, m), 8.89 (2H, s), 8.79-8.61 (8H, m), 8.29-8.23 (2H, m), 8.06 (7H, m), 7.80 (4H, m), 7.55 (1H, m), 7.31 (4H, s), 7.22 (4H, m), 5.31 (2H, m), 4.80 (2H, m). IR ν_{max} (neat sample, cm^{-1}): 3588 w (br), 3072 w, 1703 m, 1662 s, 1594 s, 1459 w, 1403 w, 1340 s, 1241 m, 1178 w, 1051 s, 1031 s, 784 s.

[(TBNap-TPy)$_2$Co(BF$_4$)$_2$]:

TBNap-TPy (**130**, 41.6 mg, 0.0386 mmol, 1 eq) was dissolved in 1 mL of DMF in a sealed vial with a PTFE-lined cap, a DMF solution of Co(BF$_4$)$_2$.6H$_2$O (249.1 μL, 0.0386 mmol, 1 eq) was added in a sealed vial with a PTFE-lined cap and the mixture was heated in a dry block heater at 80 °C for 48 h. The mixture was concentrated under reduced pressure, the resulting solid was sonicated in diethyl ether and filtered, washed with small quantities of DCM, CH$_3$CN and diethyl ether and the red amorphous solid was dried under high vacuum (isolated yield: 46 mg, calculated for the monomeric unit 96%). m.p. >300 °C (decomp.). Elemental analysis calculated for the repeating unit [C$_{69}$H$_{42}$N$_{10}$O$_4$B$_2$F$_8$Co]·2CH$_2$Cl$_2$ 0.3CH$_3$CN 0.2DMF·: C, 57.64; H, 3.23; N, 9.77; Found: C, 57.40; H, 2.97; N, 9.78. ^{1}H NMR (400 MHz, DMSO-d$_6$, ppm): δ 86.76, 50.75, 36.37, 35.77, 31.40, 13.71 (6H, m), 10.20 (6H, m), 9.36 (3H, m), 9.24 (4H, m), 8.97 (9H, m), 8.54 (5H, m), 5.80 (2H, m), 5.35 (4H, m). IR ν_{max} (neat sample, cm^{-1}): 3611 w (br), 3071 w (br), 1702 m, 1660 s, 1595 s, 1571 m, 1513 w, 1474 m, 1402 m, 1351 s, 1302 w, 1242 m, 1051 s, 1033 s, 1014 s, 785 s, 774 s.

1.7.3 Synthesis and characterisation of compounds described in Chapter 4

_N_-[2,2';6',2'']terpyridin-4'-yl-propane-1,3-diamine (149):

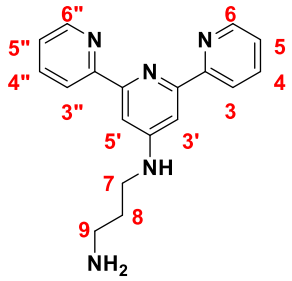

The synthesis was carried out according to a slight modification of the already existing procedure.[29] 4'-Chloro-[2,2';6',2'']terpyridine, (0.575 g, 2.14 mmol, 1 eq) was suspended in 1,3-diamino propane (5.4 mL, 64.3 mmol, 30 eq). Upon heating a yellow solution was observed through solubilisation of all the reactant. The reaction was heated at 125 °C for 12 h. After cooling to room temperature, ice cold H_2O (35mL) was added and a white precipitate was formed. DCM (75 mL) were added to the mixture and extracted in a separating funnel. The aqueous phase was further extracted with an aliquot of DCM (50 mL). The organic phases were combined and washed with deionised water (3×75 mL). The organic layer was dried over Na_2SO_4, filtered and the solvent removed under reduced pressure to yield a white solid (0.511 g, 1.67 mmol, 78%). m.p. 308 °C (decomp.). HRMS (ESI) calculated for $C_{18}H_{20}N_5$ *m/z* = 306.17132 $[M+H]^+$ Found *m/z* = 306.1732. ^{1}H NMR (400 MHz, $CDCl_3$, ppm): δ 8.66 (2H, ddd, *J* = 4.8, 1.8, 0.9 Hz, $H_{6,6"}$), 8.60 (2H, dt, *J* = 8.0, 1.0 Hz, $H_{3,3"}$), 7.82 (2H, dt, *J* = 7.7, 1,8 Hz, $H_{4,4"}$), 7.66 (2H, s, $H_{3',5'}$), 7.29 (2H, ddd, *J* = 7.5, 4.8, 1.2 Hz, $H_{5,5"}$), 5.09 (1H, t, *J* = 4.8 Hz, NH), 3.46 (2H, dd, *J* = 11.9, 6.6 Hz, H_7), 2.90 (2H, t, *J* = 6.6 Hz, H_8), 1.82 (2H, quint., *J* = 6.6 Hz, H_9).

Benzene-1,3,5-tricarboxamide tris-{[3-([2,2';6',2'']terpyridin-4'-ylamino)-propyl] (85):

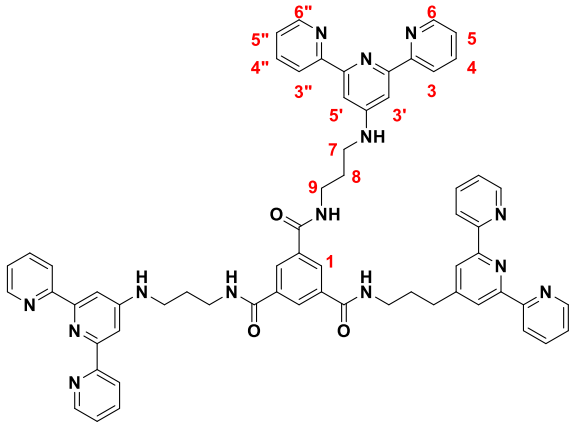

N-[2,2';6',2'']terpyridin-4'-yl-propane-1,3-diamine (**149**, 52 mg, 0.170 mmol, 3 eq) was dissolved in dry DCM (10 mL) and stirred for few minutes in an ice bath. 1,3,5 benzenetricarbonyl trichloride (15 mg, 0.0565 mmol, 3 eq) was dissolved in dry DCM (15 mL) and added in the first solution dropwise. A milky mixture was formed upon the addition and it was let to stir at room temperature overnight. A white precipitate was filtered by gravity, was washed with DCM and then was dried to recovers an off-white solid (57 mg, 0.0532 mmol, 94%). m.p. 220-224 °C. Elemental analysis calculated for $C_{63}H_{57}N_{15}O_3$ 1.3 NaCl CH_2Cl_2 2 H_2O: C, 60.57; H,5.00; N, 16.55; Found: C, 60.28; H, 5.03;

N, 16.74. ^{1}H NMR (400 MHz, DMSO-d_6 at 80 °C , ppm): δ 8.94 (1H, t, *J* = 5.5 Hz, NH), 8.79 (2H, d, *J* = 4.4 Hz, $H_{6,6"}$), 8.67 (1H, s, H_1), 8.38 (2H, s, br, $H_{3,3"}$), 8.06 (2H, dtd, *J* = 7.9, 1.1 Hz, $H_{4,4"}$), 7.70 (2H, s, $H_{3',5'}$), 7.62 (2H, dd, *J* = 7.1, 5,1 Hz, $H_{5,5"}$), 3.66 (2H, t, *J* = 6.1 Hz, H_9), 3.52 (2H, dd, *J* = 11.9, 6.1 Hz, H_7), 2.03 (2H, q, *J* = 6.5 Hz, H_8). ^{1}H NMR (400 MHz, DMSO-d_6, ppm): δ 9.14 (1H, t, *J* = 5.0 Hz, NH) , 8.78 (2H, m, H_{terpy}) , 8.71 (1H, s, H_1), 8.60 (1H, s, br, H_{terpy}), 8.08 (3H, s, br, H_{terpy}), 7.66 (4H, s, br, H_{terpy}), 3.65 (2H, s, br, H_9), 3.47 (2H, q, *J* = 6.1 Hz, H_7), 1.98(2H, q, *J* = 6.4 Hz, H_8). IR ν_{max} (neat sample, cm^{-1}): 3410 br, 3238 m, 3099 w, 3053 w, 2933 w, 2868 w, 1637s, 1584 s, 1528 s, 1467 s, 1444 s, 1291 m, 1265 m, 1248 m, 1160 m, 1097 m, 1089 m, 1071 m,996 m, 856 m, 788 s, 739 s.

Complex 85-Eu:

Benzene-1,3,5-tricarboxylic acid tris-{[3-([2,2';6',2'']terpyridin-4'-ylamino)-propyl]-amide}(**85**, 10.6 mg, 9.88 μmol, 1 eq) was dissolved in 10 mL of MeOH and a solution of $EuCl_3$ (230.7 μL, 9.88 μmol, 1 eq) was added to it. The mixture was heated in a sealed vial under microwave irradiation at 70 °C for 1 h. The mixture was cooled to room temperature and concentrated to a third of its initial volume. Ether diffusion led overnight to the formation of a beige precipitate, the solution was decanted off and another 10 mL of diethyl ether was added, the solid was sonicated, and centrifuged. The supernatant was decanted off and the solid was dried under high vacuum (12 mg, 9.1 μmol, 91%). ^{1}H NMR (400 MHz, CD_3OD, ppm): δ 8.74 (2H, s, br), 8.70 (1H, s), 8.39 (2H, d, *J* = 7.8 Hz), 8.06 (4H, m, *J* = 33.5, 27.5, 7.3 Hz), 7.61 (4H, m), 7.44 (1H, s), 3.69 (2H, t, *J* = 7.1 Hz), 3.64 (2H, t, *J* = 6.1 Hz), 2.12 (2H, dt, *J* = 13.1, 6.7 Hz). IR ν_{max} (neat sample, cm^{-1}): 3450 sh, 3234 s, 3056 s, 2937 sh, 2867 sh, 1627 s, 1587 s,1526 s, 1467 s,1439 s, 1292 m, 1265 m, 1248 m, 1162 w, 1089 w, 995 m, 787 s.

Complex 85-Tb:

Benzene-1,3,5-tricarboxylic acid tris-{[3-([2,2';6',2'']terpyridin-4'-ylamino)-propyl]-amide}(**85**, 25.6 mg, 23.8 μmol, 1 eq) was dissolved in 10 mL of MeOH and a solution of $TbCl_3$ (253.5 μL, 23.8 μmol, 1 eq) was added to it. The mixture was heated in a sealed vial under microwave irradiation at 70 °C for 1 h. The mixture was cooled to room temperature and concentrated to a third of its initial volume. Ether diffusion led overnight to the formation of a white precipitate, the solution was decanted off and another 10 mL of diethyl ether was added, the solid was sonicated, and centrifuged. The supernatant was decanted off and the solid was dried under high vacuum (31 mg, 23.1 μmol, 97%).^{1}H NMR (400 MHz, CD_3OD,

ppm): δ 9.10-8.90 (2H, m), 8.76 (3H,m, br), 8.56 (1H, s, br), 8.42 (2H, s), 8.19-8.00 (6H, m), 7.61-7.48 (6H, m), 3.57 (2H, s, br), 3.06 (2H, t, *J* = 7.6 Hz), 2.04 (2H, quint., *J* = 7.8 Hz). IR ν_{max} (neat sample, cm^{-1}): 3368 sh, 3235 m, 3059 m, 2944 sh, 2883 sh, 1620 s, 1582 s, 1533 m, 1470 m, 1439 m, 1292 m, 1248 m, 1161 w, 1089 w, 997 m, 852 w, 790 s.

1.7.4 Synthesis and characterisation of compounds described in Chapter 5

4'-Hydrazinyl-2,2':6',2''-terpyridine (151):

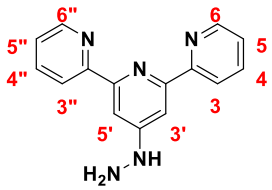

This compound was synthesised according to literature methods.[270] 4'-chloro-2,2':6',3"-terpyridine (600 mg, 2.24 mmol 1.0 eq.) was dissolved in warm 1-butanol (12 mL), hydrazine monohydrate (8 ml, 256,8 mmol, 114 eq.) was added dropwise and stirred for 12 h at reflux (130 °C). The mixture was cooled down to room temperature and a white precipitate formed. The precipitate was filtered yielding a white solid that was washed with water. The product was dried under high vacuum (475 mg, 1.80 mmol, 80%). Melting point 198 °C. HRMS-ESI (*m/z*): calculated for $C_{15}H_{14}N_5$ 264.1243; found 264.1247 $[M+H]^+$. ^{1}H NMR (400 MHz, DMSO-d_6, ppm): δ 8.66 (2H, ddd, *J* = 4.8, 1.7, 0.8 Hz, $H_{6,6''}$), 8.56 (2H, td, *J* = 7.9, 0.9 Hz, $H_{3,3''}$), 7.94(2H, td, *J* = 7.6, 1.8 Hz, $H_{4,4''}$), 7.92 (1H, s, N-H), 7.85 (2H, s, $H_{3',5'}$), 7.43 (2H, ddd, *J* = 7.6, 4.8, 1.2 Hz, $H_{5,5''}$), 4.39 (2H, s, NH_2). $^{13}C\{^1H\}$ NMR (100 MHz, DMSO-d_6): δ 158.8 (q), 156.1 (q), 154.6 (q), 148.8 ($C_{6,6''}$), 136.9 ($C_{4,4''}$), 123.7 ($C_{5,5''}$), 120.5 ($C_{3,3''}$), 102.8 ($C_{3',5'}$). IR ν_{max} (neat sample, cm^{-1}): 3324, 3275, 3180, 3050, 2985, 1643, 1604, 1582, 1561, 1463, 1443, 1400, 1227, 1044, 983, 862, 728, 657.

(*S*,*S*,*S*)-Tris-alanine-trimethylester-benzene-1,3,5-tricarboxamide (153):

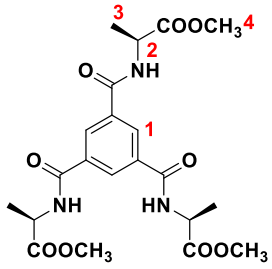

The compound was synthesised according to reference and analysis of the compound were in agreement with the data obtained in the literature.[233] *S*-Alanine (2.00 g, 22.44 mmol, 4 eq) was suspended in CH_3OH (50 mL) at 0 °C. $SOCl_2$ (16.4 mL, 224.4 mmol, 40 eq) was added to the solution and the mixture was allowed to warm up to room temperature and left stirring for 6 h. CH_3OH and $SOCl_2$ were removed under reduced pressure leading to a solid (*S*-Alanine methyl ester hydrochloride). The crude compound (3.133 g, 22.4 mmol, 4 eq) was dissolved in CH_2Cl_2 (100 mL) and cooled in an ice bath to 0 °C, triethylamine (6.25 mL, 44.9 mmol, 8 eq) was added to the solution, followed by the addition of 1,3,5-benzenetricarbonyl trichloride (1.70 g, 5.61 mmol, 1 eq). The mixture was warmed up to room temperature and left to stir for 12 h.

Completion of the reaction was monitored by silica TLC using CH_2Cl_2: CH_3OH (94:6). Once the reaction was completed, the mixture was diluted with CH_2Cl_2 and washed with 1 M HCl, $NaHCO_3$ sat. solution and H_2O. The organic phase was dried over Na_2SO_4, filtered and evaporated under reduced pressure. The solid was purified using silica column chromatography using CH_2Cl_2: CH_3OH (95:5) as a mobile phase to yield **153** as the pure compound (1.95 g, 4.189 mmol, 75%). m. p. 290 °C, literature 290 °C.[233] ^{1}H NMR (400 MHz, DMSO-d_6, ppm): δ 9.13 (3H, d, *J* = 6.9 Hz, NH), 8.50 (3H, s, H_1), 4.52 (3H qnt, *J* = 7.3 Hz, H_2), 3.66 (9H, s, H_4), 1.43 (9H, d, *J* = 7.3 Hz, H_3).

1,3,5-benzenealanine (154):

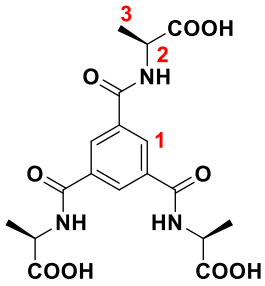

The compound was synthesised according to reference and analysis of the compound were in agreement with the data obtained in the literature.[233] **153** (220 mg, 0.472 mmol, 1 eq) was suspended in CH_3OH (5 mL) and the mixture was cooled to 0 °C using an ice bath. An aqueous solution of 2 M NaOH (2.39 mL, 4.72 mmol, 10 eq) was added to the mixture and let to stir at room temperature for 12 h. The mixture was diluted using 30 mL of MeOH and 10 mL of H_2O. NaOH was neutralized by adding Amberlite IR 120 H^+ resin until the pH reaches 6.5. The resin was filtered and washed with MeOH (2 × 50 mL), the solvent was evaporated under reduced pressure yielding the desired product as a white powder (197 mg, 0.465 mmol, 98%). m.p.220 °C, literature 220 °C.[233] ^{1}H NMR (400 MHz, DMSO-d_6, ppm): δ 8.95 (3H, d, , *J* = 7.2 Hz, NH), 8.47 (3H,s , H_1), 4.45 (3H, qnt, *J* = 7.2 Hz, H_2), 1.42 (9H, d, *J* = 7.2 Hz, H_3).

Boc-L-alanine methyl ester (155):

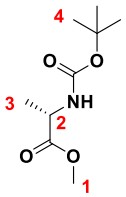

This compound was synthesised according to a slight modification of the procedure found in the literature and ^{1}H NMR was in agreement with the data in the literature.[272] Boc-L-alanine (5.00 g, 26.4 mmol, 1 eq) was dissolved in DMF (40 mL), Na_2CO_3 (5.98 g, 55.5 mmol, 2.1 eq) was added, followed by a dropwise addition of methyl iodide (6.91 mL, 110.9 mmol, 4.2 eq). The solution was stirred at room temperature for 15 h and the solvent was evaporated under reduced pressure. The residue was dissolved in EtOAc (100 mL). The organic layer was washed with brine, then water, dried over $MgSO_4$ and the solvent was evaporated under reduced pressure. The yellow oil was purified by column chromatography using silica as the stationary phase and DCM:MeOH (99:1) as the mobile phase. The solvent was evaporated under reduced pressure

yielding a yellow oil that formed crystals after a few hours in the fridge (3.182 g, 15.6 mmol, 59%). ^{1}H NMR (400 MHz, $CDCl_3$, ppm): δ 5.05 (1H, s, NH), 4.30 (1H, qnt, *J* = 6.7 Hz, H_2), 3.72 (3H, s, H_1), 1.42 (9H, s, H_4), 1.36 (1H, d, *J* = 7.2 Hz, H_3).

Boc-L-Alanine hydrazide (156):

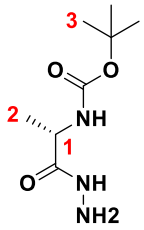

This compound was synthesised according to a slight modification of the procedure found in the literature and ^{1}H NMR was in agreement with the data in the literature.[271] Boc-L-alanine methyl ester (1,03 g, 4.92 mmol, 1 eq) was dissolved into 10 mL of MeOH and hydrazine hydrate was added slowly to the mixture. The solution was stirred at room temperature for 18 h. The solvent was evaporated under reduced pressure and the resulting product was sonicated in diethyl ether yielding a white powder that was filtered and dried under high vacuum (0.796 g, 3.91 mmol, 79%). ^{1}H NMR (400 MHz, $CDCl_3$, ppm): δ 7.68 (1H, br s, N<u>H</u>-NH_2), 5.05 (1H, d, *J* = 6.7 Hz, NH), 4.16 (1H, qnt, *J* = 7.2 Hz, H_1), 3.57 (2H, br s, NH-N<u>H</u>$_2$), 1.43 (9H, s, H_3), 1.36 (3H, d, *J* = 7.2 Hz, H_2).

Boc-L-alanine hydrazine-2,2':6',2''-terpyridine (157):

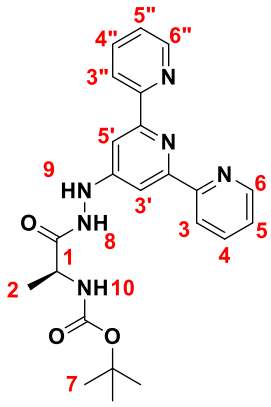

Boc-L-alanine (419 mg, 2.215 mmol, 1 eq), EDC.HCl (509 mg, 2.65 mmol, 1.2 eq) and HOBT (358 mg, 2.65 mmol, 1.2 eq) were suspended in DCM and 2 mL DMF was added to dissolve all the solids, the solution was cooled to 0 °C in an ice bath. 4'-hydrazinyl-2,2':6',2"-terpyridine (**151**, 700 mg, 2.65 mmol, 1.2 eq) was dissolved in a DCM:DMF mixture (13:8 mL) was slowly added to the first solution. The mixture turned yellow during the addition and was further stirred at 0 °C for 30 min, then allowed to warm up at room temperature and stirred for 72 h. The solvent was evaporated under reduced pressure and the crude solid was purified by column chromatography using silica as the stationary phase and DCM:MeOH (95:5) as the mobile phase. The desired product is the second one to be eluted however a good separation with the first compound eluted is not possible. All the fraction containing the desired compound are collected, the solvent is removed under reduced pressure and diethyl ether is added to the crude solid yielding the formation of a yellow solution and a white precipitate. The solid is collected by centrifugation and further washed with a small quantity of diethyl ether. The white solid is dried under reduced pressure (217 mg, 0.499 mmol, crude yield 23%). HRMS (ESI) calculated for $C_{23}H_{27}N_6O_3$ *m/z* = 435.2139

$[M+H]^+$ Found *m/z* = 435.2138. ^{1}H NMR (600 MHz, DMSO-d_6, ppm): δ 10.08 (1H, s, H_8), 8.85 (1H, s, H_9) 8.67 (2H, d, *J* = 4.2 Hz, $H_{6,6"}$), 8.56 (2H, d, *J* = 7.8 Hz, $H_{3,3"}$), 7.96 (2H, td, *J* = 7.8, 1.7 Hz, $H_{4,4"}$), 7.78 (2H, s, $H_{3',5'}$), 7.45 (2H, dd, *J* = 6.7, 5.0 Hz, $H_{5,5"}$), 7.10 (1H, d, *J* = 7.1 Hz, H_{10}), 4.13 (1H, qnt, *J* = 7.1 Hz, H_1), 1.39 (9H, s, H_7), 1.35 (3H, d, *J* = 7.1 Hz, H_2). ^{13}C{^{1}H} NMR (151 MHz, DMSO): δ 172.9 (C=O), 156.9(q), 155.6 (q), 155.1(q), 149.1 ($C_{6,6"}$), 137.1 ($C_{4,4"}$), 124.1 ($C_{5,5"}$), 120.7($C_{3,3"}$), 103.6 ($C_{3,5'}$), 78.1 (q), 48.5 (C_1), 28.2 (C_7), 18.1 (C_2).

L-Alanine hydrazine-2,2':6',2''-terpyridine (158):

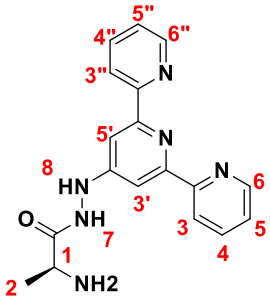

Boc-L-alanine hydrazine-2,2':6',2"-terpyridine (**157**), 100 mg, 0.230 mmol) was suspended in 4 mL of DCM, the solution was cooled to 0 °C in an ice bath and the addition of 2 mL of TFA to the flask resulted in the formation of a clear solution. The solution was warmed up to room temperature and was stirred for 4 h. In a 250 mL RBF, 200 mL of 25% aqueous ammonia was stirred in an ice bath and the reaction mixture was added dropwise. The solution was extracted with 250 mL of DCM, the organic layer was washed with 100 mL of $NaHCO_3$ sat. solution, followed by (3 × 100 mL) of H_2O. The organic phase was dried over $MgSO_4$, filtered and the solvent was evaporated under reduced pressure yielding an off-white solid (34 mg, 0.101 mmol, crude yield 44%). HRMS (APCI) calculated for $C_{18}H_{19}N_6O$ *m/z* = 335.1614 $[M+H]^+$ Found *m/z* = 335.1620. ^{1}H NMR (600 MHz, DMSO-d_6, ppm): δ 8.76 (1H s,H_8), 8.67 (2H, ddd, *J* = 4.7, 1.7, 0.9 Hz, $H_{6,6"}$), 8.57 (2H, dt, *J* = 8.0, 1.0 Hz, $H_{3,3"}$), 7.96 (2H, td, *J* = 7.7, 1,8 Hz, $H_{4,4"}$), 7.78 (2H, s, $H_{3',5'}$), 7.45 (2H, ddd, *J* = 7.5, 4.7, 1.2 Hz, $H_{5,5"}$), 3.47 (1H, q, *J* = 6.9 Hz, H_1), 1.27 (3H, d, *J* = 6.9 Hz, H_2). ^{13}C{^{1}H} NMR (151 MHz, DMSO-d_6, ppm): δ 176.2 (C=O), 157.4 (q), 156.1 (q), 155.6 (q), 149.6 ($C_{6,6"}$), 137.6 ($C_{4,4"}$), 124.5 ($C_{5,5"}$), 121.2 ($C_{3,3"}$),104.0($C_{3',5'}$), 49.7 (C_1), 22.4 (C_2).

Boc-L-alanine-4'-(4-aminophenyl)-2,2':6',2''-terpyridine (159):

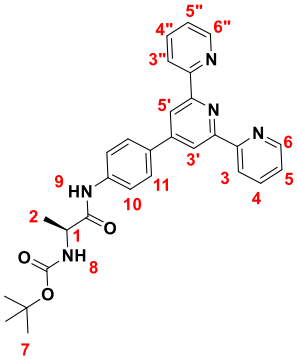

Boc-L-alanine (1.46 g, 7.71 mmol, 5 eq), HBTU (2.92 g, 7.71 mmol, 5 eq) and HOBT (1.04g, 7.71 mmol, 5 eq) and DIPEA (1.34 mL, 7.71 mmol, 5 eq) were dissolved in DMF (10 mL), the solution was cooled to 0 °C in an ice bath and stirred for 30 min. 4′-(4-aminophenyl)-2,2′:6′,2″-terpyridine (**111**, 500 mg, 1.54 mmol, 1 eq) was added to the mixture. The solution turned yellow during the was further stirred at 0 °C for 30 min, then allowed to warm up

at room temperature and stirred for 12 h. The solvent was evaporated under reduced pressure yielding a yellow oil, water (200 mL) was added to it producing the formation of a yellow precipitate. The aqueous phase was extracted using DCM (200 mL) and the organic phase was washed using a saturated aqueous solution of $NaHCO_3$ (2×200 mL) leading to the aqueous phase to become white, followed by water (2×200 mL). The organic phase was dried over Na_2SO_4 and the solvent was removed under reduced pressure yielding to a yellow oil. Successive addition of diethyl ether, sonication and evaporation of the solvent under reduced pressure yielded a white solid. The solid was dissolved in the minimum amount of warm ethyl acetate, the solution was cool down in an ice bath and cold hexane was added to the solution, leading to the precipitation of an off-white solid. The solid was filtered and the reprecipitation was carried out a second time yielding the desired product as an off-white solid. (506 mg, 1.02 mmol, 66%). m.p. 202-204 °C. HRMS (APCI) calculated for $C_{29}H_{30}N_5O_3$ *m/z* = 496.2343 $[M+H]^+$ Found *m/z* = 496.2338. ^1H NMR (600 MHz, DMSO-d_6, ppm): δ 10.18 (1H, s, NH_9), 8.77 (2H, d, *J* = 4.0 Hz, $H_{6,6"}$), 8.71 (2H, s, $H_{3',5'}$), 8.67 (2H, d, *J* = 7.9 Hz, $H_{3",3}$), 8.04 (2H, td, *J* = 7.7, 1.7 Hz, $H_{4,4"}$), 7.93 (2H, d, *J* = 8.6 Hz, H_{11}), 7.83 (2H, d, *J* = 8.6 Hz, H_{10}), 7.53 (2H dd, *J* = 6.9, 5.1 Hz, $H_{5,5"}$), 7.12 (1H, d, *J* = 7.1 Hz, NH_8), 4.15 (1H, qnt, *J* = 7.1 Hz, H_1), 1.40 (9H, s, H_7), 1.30 (3H, d, *J* = 7.1 Hz, H_2). $^{13}C\{^1H\}$ NMR (151 MHz, DMSO-d_6, ppm): δ 172.2 (C=O), 155.5 (q), 155.2 (q), 155.0 (q), 149.4 ($C_{6,6"}$), 148.9 (q), 140.5 (q), 137.5 ($C_{4,4"}$), 131.8 (q), 127.4 (C_{11}), 124.5 ($C_{5,5"}$), 120.9 ($C_{3,3"}$), 119.7 (C_{10}), 117.4 ($C_{3',5'}$), 78.1 (q), 64.9 (q), 50.5 (C_1), 28.2 (C_7), 17.9 ($C_{4,4"}$).

L-Alanine-4'-(4-aminophenyl)-2,2':6',2''-terpyridine trifluoroacetate (160):

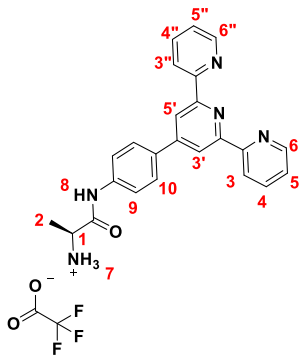

Boc-L-alanine-4'-(4-aminophenyl)-2,2':6',2''-terpyridine (**159**, 468 mg, 0.944 mmol) was dissolved in DCM:TFA (4:2 mL) and stirred at room temperature for 2 h. The solvent mixture was evaporated under reduced pressure, using a base trap and a cold trap, leading to the formation of an orange oil. DCM (20 mL) was added to the oil, after sonication the solvent was removed under reduced pressure, this operation was repeated 4 times leading to the formation of a light pink powder. The powder was triturated in warm ethyl acetate, filtered, and dried under high vacuum, yielding the desired product as the TFA salt in the form of a light pink solid. (457 mg, 0.897 mmol, 95%). m.p. 229-231 °C. HRMS (APCI) calculated for $C_{24}H_{22}N_5O$ *m/z* = 396.1818 $[M-TFA]^+$ Found *m/z* = 396.1820. ^1H NMR (600 MHz, DMSO-d_6, ppm): δ 10.67 (1H, s, NH_8), 8.78 (2H, ddd, *J* = 4.8, 1.6, 0.7 Hz, $H_{6,6"}$), 8.73

(2H, s, $H_{3',5'}$), 8.70 (2H, d, *J* = 7.9 Hz, $H_{3,3''}$), 8.24 (3H, d, *J* = 4.1 Hz, NH_3), 8.07 (2H, td, *J* = 7.7, 1.8 Hz, $H_{4,4''}$), 8.00 (2H, d, *J* = 8.7 Hz, H_{10}), 7.84 (2H, d, *J* = 8.7 Hz, H_9), 7.56 (2H, ddd, *J* = 7.4, 4.8, 1.0 Hz, $H_{5,5''}$), 4.09 – 4.03 (1H, m, H_1), 1.50 (3H, d, *J* = 7.0 Hz, H_2). $^{13}C\{^1H\}$ NMR (151 MHz, DMSO-d_6, ppm): δ 168.5 (C=O), 158.2 (q), 158.0 (q), 155.5 (q), 154.7 (q), 149.2 ($C_{6,6''}$), 148.9 (q), 139.5 (q), 137.8 ($C_{4,4''}$), 132.7 (q), 127.7 (C_{10}), 124.7 ($C_{5,5''}$), 121.1 ($C_{3,3''}$), 120.1 (C_9), 117.6 ($C_{3,5'}$), 49.2 (C_1), 17.1 (C_2).

Chapter 8— References

1. Cram, D. J. *Angew. Chem. Int. Ed. Engl.* **1988**, *27*, 1009-1020.
2. Pedersen, C. J. *J. Am. Chem. Soc.* **1967**, *89*, 7017-7036.
3. Lehn, J.-M. *Science* **1985**, *227*, 849-856.
4. Lehn, J. M. *Angew. Chem. Int. Ed. Engl.* **1988**, *27*, 89-112.
5. Chakrabarty, R.; Mukherjee, P. S.; Stang, P. J. *Chem. Rev.* **2011**, *111*, 6810-6918.
6. Banerjee, S.; Bright, S. A.; Smith, J. A.; Burgeat, J.; Martinez-Calvo, M.; Williams, D. C.; Kelly, J. M.; Gunnlaugsson, T. *J. Org. Chem.* **2014**, *79*, 9272-9283.
7. Banerjee, S.; Veale, E. B.; Phelan, C. M.; Murphy, S. A.; Tocci, G. M.; Gillespie, L. J.; Frimannsson, D. O.; Kelly, J. M.; Gunnlaugsson, T. *Chem. Soc. Rev.* **2013**, *42*, 1601-1618.
8. de Silva, A. P.; McCaughan, B.; McKinney, B. O. F.; Querol, M. *Dalton Trans.* **2003**, 1902-1913.
9. Beves, J. E.; Blight, B. A.; Campbell, C. J.; Leigh, D. A.; McBurney, R. T. *Angew. Chem. Int. Ed.* **2011**, *50*, 9260-9327.
10. Dietrich-Buchecker, C. O.; Sauvage, J. P.; Kintzinger, J. P. *Tetrahedron Lett.* **1983**, *24*, 5095-5098.
11. Nierengarten, J. F.; Dietrich-Buchecker, C. O.; Sauvage, J. P. *J. Am. Chem. Soc.* **1994**, *116*, 375-376.
12. Bissell, R. A.; Córdova, E.; Kaifer, A. E.; Stoddart, J. F. *Nature* **1994**, *369*, 133-137.
13. Fletcher, S. P.; Dumur, F.; Pollard, M. M.; Feringa, B. L. *Science* **2005**, *310*, 80-82.
14. Kudernac, T.; Ruangsupapichat, N.; Parschau, M.; Maciá, B.; Katsonis, N.; Harutyunyan, S. R.; Ernst, K.-H.; Feringa, B. L. *Nature* **2011**, *479*, 208-211.
15. Zhang, H.; Fan, X.; Suo, R.; Li, H.; Yang, Z.; Zhang, W.; Bai, Y.; Yao, H.; Tian, W. *Chem. Commun.* **2015**, *51*, 15366-15369.
16. Frank, M.; Johnstone, M. D.; Clever, G. H. *Chem. Eur. J.* **2016**, *22*, 14104-14125.
17. Kotova, O.; Daly, R.; dos Santos, C. M. G.; Kruger, P. E.; Boland, J. J.; Gunnlaugsson, T. *Inorg. Chem.* **2015**, *54*, 7735-7741.
18. Kotova, O.; Comby, S.; Lincheneau, C.; Gunnlaugsson, T. *Chem. Sci.* **2017**, *8*, 3419-3426.
19. Martínez-Calvo, M.; Kotova, O.; Möbius, M. E.; Bell, A. P.; McCabe, T.; Boland, J. J.; Gunnlaugsson, T. *J. Am. Chem. Soc.* **2015**, *137*, 1983-1992.
20. Meazza, L.; Foster, J. A.; Fucke, K.; Metrangolo, P.; Resnati, G.; Steed, J. W. *Nat. Chem.* **2012**, *5*, 42.
21. Daly, R.; Kotova, O.; Boese, M.; Gunnlaugsson, T.; Boland, J. J. *ACS Nano* **2013**, *7*, 4838-4845.
22. Poynton, F. E.; Hall, J. P.; Keane, P. M.; Schwarz, C.; Sazanovich, I. V.; Towrie, M.; Gunnlaugsson, T.; Cardin, C. J.; Cardin, D. J.; Quinn, S. J.; Long, C.; Kelly, J. M. *Chem. Sci.* **2016**, *7*, 3075-3084.
23. Hofmeier, H.; Schubert, U. S. *Chem. Soc. Rev.* **2004**, *33*, 373-399.

24. Fallahpour, R.-A. *Synthesis* **2003**, *2003*, 0155-0184.
25. Gao, Y.; Rajwar, D.; Grimsdale, A. C. *Macromol. Rapid Commun.* **2014**, *35*, 1727-1740.
26. Jung, S. H.; Jeon, J.; Kim, H.; Jaworski, J.; Jung, J. H. *J. Am. Chem. Soc.* **2014**, *136*, 6446-6452.
27. Hwang, S.-H.; Moorefield, C. N.; Fronczek, F. R.; Lukoyanova, O.; Echegoyen, L.; Newkome, G. R. *Chem. Commun.* **2005**, 713-715.
28. Schultz, A.; Cao, Y.; Huang, M.; Cheng, S. Z. D.; Li, X.; Moorefield, C. N.; Wesdemiotis, C.; Newkome, G. R. *Dalton Trans.* **2012**, *41*, 11573-11575.
29. Kotova, O.; Daly, R.; dos Santos, C. M. G.; Boese, M.; Kruger, P. E.; Boland, J. J.; Gunnlaugsson, T. *Angew. Chem. Int. Ed.* **2012**, *51*, 7208-7212.
30. Constable, E. C. *Chem. Soc. Rev.* **2007**, *36*, 246-253.
31. Dobrawa, R.; Ballester, P.; Saha-Möller, C. R.; Würthner, F. 4. In *Metal-Containing and Metallosupramolecular Polymers and Materials*; American Chemical Society: 2006; Vol. 928, 43-62.
32. Schubert, U.; Winter, A.; Newkome, G. *Terpyridine-based Materials* **2011**, 65-127.
33. Ghosh, B. N.; Topić, F.; Sahoo, P. K.; Mal, P.; Linnera, J.; Kalenius, E.; Tuononen, H. M.; Rissanen, K. *Dalton Trans.* **2015**, *44*, 254-267.
34. Sauvage, J. P.; Collin, J. P.; Chambron, J. C.; Guillerez, S.; Coudret, C.; Balzani, V.; Barigelletti, F.; De Cola, L.; Flamigni, L. *Chem. Rev.* **1994**, *94*, 993-1019.
35. Medlycott, E. A.; Hanan, G. S. *Chem. Soc. Rev.* **2005**, *34*, 133-142.
36. Maestri, M.; Armaroli, N.; Balzani, V.; Constable, E. C.; Thompson, A. M. C. *Inorg. Chem.* **1995**, *34*, 2759-2767.
37. Tu, S.; Jia, R.; Jiang, B.; Zhang, J.; Zhang, Y.; Yao, C.; Ji, S. *Tetrahedron* **2007**, *63*, 381-388.
38. Liu, B.; Zhang, Q.; Ding, H.; Hu, G.; Du, Y.; Wang, C.; Wu, J.; Li, S.; Zhou, H.; Yang, J.; Tian, Y. *Dyes Pigm.* **2012**, *95*, 149-160.
39. Hecker, C. R.; Gushurst, A. K.; McMillin, D. R. *Inorg. Chem.* **1991**, *30*, 538-541.
40. Winkler, J. R.; Netzel, T. L.; Creutz, C.; Sutin, N. *J. Am. Chem. Soc.* **1987**, *109*, 2381-2392.
41. Fang, Y.-Q.; Taylor, N. J.; Hanan, G. S.; Loiseau, F.; Passalacqua, R.; Campagna, S.; Nierengarten, H.; Dorsselaer, A. V. *J. Am. Chem. Soc.* **2002**, *124*, 7912-7913.
42. Wolpher, H.; Johansson, O.; Abrahamsson, M.; Kritikos, M.; Sun, L.; Åkermark, B. *Inorg. Chem. Commun.* **2004**, *7*, 337-340.
43. Passalacqua, R.; Loiseau, F.; Campagna, S.; Fang, Y. Q.; Hanan, G. S. *Angew. Chem.* **2003**, *115*, 1646-1649.
44. Biswas, A.; Mukhopadhyay, S.; Singh, R. S.; Kumar, A.; Rana, N. K.; Koch, B.; Pandey, D. S. *ACS Omega* **2018**, *3*, 5417-5425.
45. Rupp, M. T.; Auvray, T.; Shevchenko, N.; Swoboda, L.; Hanan, G. S.; Kurth, D. G. *Inorg. Chem.* **2021**, *60*, 292-302.

46. Rajah, D.; Pfrunder, M. C.; Chong, B. S. K.; Ireland, A. R.; Etchells, I. M.; Moore, E. G. *Dalton Trans.* **2021**, *50*, 7400-7408.
47. Wild, A.; Winter, A.; Schlütter, F.; Schubert, U. S. *Chem. Soc. Rev.* **2011**, *40*, 1459-1511.
48. Jennifer, S. J.; Thomas Muthiah, P. *Chem. Cent. J.* **2013**, *7*, 139.
49. Culshaw, J. L.; Cheng, G.; Schmidtmann, M.; Hasell, T.; Liu, M.; Adams, D. J.; Cooper, A. I. *J. Am. Chem. Soc.* **2013**, *135*, 10007-10010.
50. Grepioni, F.; d'Agostino, S.; Braga, D.; Bertocco, A.; Catalano, L.; Ventura, B. *J. Mater. Chem. C* **2015**, *3*, 9425-9434.
51. Chai, W.; Jin, R. *J. Mol. Struct.* **2016**, *1103*, 177-182.
52. Duke, R. M.; Veale, E. B.; Pfeffer, F. M.; Kruger, P. E.; Gunnlaugsson, T. *Chem. Soc. Rev.* **2010**, *39*, 3936-3953.
53. Qian, X.; Zhu, Z.; Chen, K.; Yin, Q.; Zhu, G. *Mater. Chem. Phys.* **1989**, *23*, 335-339.
54. Shen, L.; Lu, X.; Tian, H.; Zhu, W. *Macromolecules* **2011**, *44*, 5612-5618.
55. Pardo, A.; Martin, E.; Poyato, J. M. L.; Camacho, J. J.; Braña, M. F.; Castellano, J. M. *J. Photochem. Photobiol. A* **1987**, *41*, 69-78.
56. Brana, M. F.; Castellano, J. M.; Moran, M.; Emling, F.; Kluge, M.; Schlick, E.; Klebe, G.; Walker, N. *Arzneimittelforschung* **1995**, *45*, 1311-1318.
57. Chanh, T. C.; Lewis, D. E.; Allan, J. S.; Sogandares-Bernal, F.; Judy, M. M.; Utecht, R. E.; Matthews, J. L. *AIDS Res. Hum. Retrovir.* **1993**, *9*, 891-896.
58. Chanh, T. C.; Lewis, D. E.; Judy, M. M.; Sogandares-Bernal, F.; Michalek, G. R.; Utecht, R. E.; Skiles, H.; Chang, S. C.; Matthews, J. L. *Antivir. Res.* **1994**, *25*, 133-146.
59. Wang, H.; Wu, H.; Xue, L.; Shi, Y.; Li, X. *Org. Biomol. Chem.* **2011**, *9*, 5436-5444.
60. Langdon-Jones, E. E.; Williams, C. F.; Hayes, A. J.; Lloyd, D.; Coles, S. J.; Horton, P. N.; Groves, L. M.; Pope, S. J. A. *Eur. J. Inorg. Chem.* **5279**, *2017*, 5279-5287.
61. Johnson, K. R.; de Bettencourt-Dias, A. *Inorg. Chem.* **2019**, *58*, 13471-13480.
62. Gupta, K.; Patra, A. K. *Eur. J. Inorg. Chem.* **2018**, *2018*, 1882-1890.
63. Tröger, J. *J. Prakt. Chem.* **1887**, *36*, 225-245.
64. Spielman, M. A. *J. Am. Chem. Soc.* **1935**, *57*, 583-585.
65. Sergeyev, S. *Helv. Chim. Acta* **2009**, *92*, 415-444.
66. Wagner, E. C. *J. Am. Chem. Soc.* **1935**, *57*, 1296-1298.
67. Miller, T. R.; Wagner, E. C. *J. Am. Chem. Soc.* **1941**, *63*, 832-836.
68. Rúnarsson, Ö. V.; Artacho, J.; Wärnmark, K. *Eur. J. Org. Chem.* **2012**, *2012*, 7015-7041.
69. Prelog, V.; Wieland, P. *Helv. Chim. Acta* **1944**, *27*, 1127-1134.
70. Larson, S. B.; Wilcox, C. S. *Acta Crystallogr. Sect. C* **1986**, *42*, 224-227.
71. Sucholeiki, I.; Lynch, V.; Phan, L.; Wilcox, C. S. *J. Org. Chem.* **1988**, *53*, 98-104.

72. Cudero, J.; Pardo, C.; Ramos, M.; Gutierrez-Puebla, E.; Monge, A.; Elguero, J. *Tetrahedron* **1997**, *53*, 2233-2240.
73. Vande Velde, C. M. L.; Tylleman, B.; Zeller, M.; Sergeyev, S. *Acta Crystallogr. B.* **2010**, *66*, 472-481.
74. Weber, E.; Müller, U.; Worsch, D.; Vögtle, F.; Will, G.; Kirfel, A. *J. Chem. Soc., Chem. Commun.* **1985**, 1578-1580.
75. Arribas, C. S.; Wendt, O. F.; Sundin, A. P.; Carling, C.-J.; Wang, R.; Lemieux, R. P.; Warnmark, K. *Chem. Commun.* **2010**, *46*, 4381-4383.
76. Pardo, C.; Sesmilo, E.; Gutiérrez-Puebla, E.; Monge, A.; Elguero, J.; Fruchier, A. *J. Org. Chem.* **2001**, *66*, 1607-1611.
77. Mosca, L.; Čejka, J.; Dolenský, B.; Havlík, M.; Jakubek, M.; Kaplánek, R.; Král, V.; Anzenbacher, P. *Chem. Commun.* **2016**, *52*, 10664-10667.
78. Talianová, V.; Bříza, T.; Krčová, L.; Dolenský, B.; Králová, J.; Martásek, P.; Král, V.; Havlík, M. *Bioorg. Chem.* **2020**, *94*, 103447.
79. Jeon, Y. M.; Armatas, G. S.; Kim, D.; Kanatzidis, M. G.; Mirkin, C. A. *Small* **2009**, *5*, 46-50.
80. Yuan, C.-X.; Tao, X.-T.; Ren, Y.; Li, Y.; Yang, J.-X.; Yu, W.-T.; Wang, L.; Jiang, M.-H. *J. Phys. Chem. C* **2007**, *111*, 12811-12816.
81. Yuan, C.-X.; Tao, X.-T.; Wang, L.; Yang, J.-X.; Jiang, M.-H. *J. Phys. Chem. C* **2009**, *113*, 6809-6814.
82. Yuan, C.; Xi, H.; Tao, X. *Inorg. Chem. Commun.* **2017**, *86*, 145-149.
83. Deprez, N. R.; McNitt, K. A.; Petersen, M. E.; Brown, R. G.; Lewis, D. E. *Tetrahedron Lett.* **2005**, *46*, 2149-2153.
84. Zhao, Y.; Chen, K.; Yildiz, E. A.; Li, S.; Hou, Y.; Zhang, X.; Wang, Z.; Zhao, J.; Barbon, A.; Yaglioglu, H. G.; Wu, H. *Chem. Eur. J.* **2020**, *26*, 3591-3599.
85. Bünzli, J.-C. G. In *Kirk-Othmer Encyclopedia of Chemical Technology* 2013, 1-43.
86. Yen, W. M.; Shionoya, S.; Yamamoto, H. *Phosphor handbook, second edition*, 2006.
87. Kuriki, K.; Koike, Y.; Okamoto, Y. *Chem. Rev.* **2002**, *102*, 2347-2356.
88. Sessoli, R.; Powell, A. K. *Coord. Chem. Rev.* **2009**, *253*, 2328-2341.
89. Nagae, H.; Aoki, R.; Akutagawa, S.-n.; Kleemann, J.; Tagawa, R.; Schindler, T.; Choi, G.; Spaniol, T. P.; Tsurugi, H.; Okuda, J.; Mashima, K. *Angew. Chem. Int. Ed.* **2018**, *57*, 2492-2496.
90. You, W.; Tu, D.; Li, R.; Zheng, W.; Chen, X. *Nano Res.* **2019**, *12*, 1417-1422.
91. Kumar, P.; Nagpal, K.; Gupta, B. K. *ACS Appl. Mater. Interfaces* **2017**, *9*, 14301-14308.
92. Biju, S.; Gallo, J.; Bañobre-López, M.; Manshian, B. B.; Soenen, S. J.; Himmelreich, U.; Vander Elst, L.; Parac-Vogt, T. N. *Chem. Eur. J.* **2018**, *24*, 7388-7397.
93. Sun, L.; Wei, R.; Feng, J.; Zhang, H. *Coord. Chem. Rev.* **2018**, *364*, 10-32.

94. Xu, J.; Gulzar, A.; Yang, P.; Bi, H.; Yang, D.; Gai, S.; He, F.; Lin, J.; Xing, B.; Jin, D. *Coord. Chem. Rev.* **2019**, *381*, 104-134.
95. Nonat, A. M.; Charbonnière, L. J. *Coord. Chem. Rev.* **2020**, *409*, 213192.
96. Aletti, A. B.; Gillen, D. M.; Gunnlaugsson, T. *Coord. Chem. Rev.* **2018**, *354*, 98-120.
97. Cotton, S. *Lanthanide and actinide chemistry*; John Wiley & Sons, 2013.
98. Bünzli, J.-C. G. *J. Coord. Chem.* **2014**, *67*, 3706-3733.
99. Bünzli JC.G., E. S. V. In *Lanthanide Luminescence. Springer Series on Fluorescence (Methods and Applications)*; Hänninen P., H. H., Ed.; Springer, Berlin, Heidelberg: Berlin, 2010; Vol. vol 7.
100. Carnall, W. T.; Fields, P. R.; Rajnak, K. *J. Chem. Phys.* **1968**, *49*, 4412-4423.
101. Carnall, W. T.; Fields, P. R.; Rajnak, K. *J. Chem. Phys.* **1968**, *49*, 4447-4449.
102. Carnall, W. T.; Fields, P. R.; Rajnak, K. *J. Chem. Phys.* **1968**, *49*, 4450-4455.
103. Bünzli, J.-C. G.; Piguet, C. *Chem. Soc. Rev.* **2005**, *34*, 1048-1077.
104. Binnemans, K. *Coord. Chem. Rev.* **2015**, *295*, 1-45.
105. Bünzli, J.-C. G.; Eliseeva, S. V. *Chem. Sci.* **2013**, *4*, 1939-1949.
106. Bünzli, J.-C. G.; Piguet, C. *Chem. Rev.* **2002**, *102*, 1897-1928.
107. Weissman, S. I. *J. Chem. Phys.* **1942**, *10*, 214-217.
108. Heffern, M. C.; Matosziuk, L. M.; Meade, T. J. *Chem. Rev.* **2014**, *114*, 4496-4539.
109. Eliseeva, S. V.; Bünzli, J.-C. G. *Chem. Soc. Rev.* **2010**, *39*, 189-227.
110. Kleinerman, M. *J. Chem. Phys.* **1969**, *51*, 2370-2381.
111. Kropp, J. L.; Windsor, M. W. *J. Chem. Phys.* **1963**, *39*, 2769-2770.
112. Horrocks, W. D.; Sudnick, D. R. *Acc. Chem. Res.* **1981**, *14*, 384-392.
113. Horrocks, W. D.; Sudnick, D. R. *J. Am. Chem. Soc.* **1979**, *101*, 334-340.
114. Bünzli, J.-C. G. *Coord. Chem. Rev.* **2015**, *293-294*, 19-47.
115. Bradberry, S. J.; Savyasachi, A. J.; Martinez-Calvo, M.; Gunnlaugsson, T. *Coord. Chem. Rev.* **2014**, *273-274*, 226-241.
116. Kovacs, D.; Phipps, D.; Orthaber, A.; Borbas, K. E. *Dalton Trans.* **2018**, *47*, 10702-10714.
117. Parker, D.; Williams, J. A. G. *J. Chem. Soc., Perkin Trans. 2* **1996**, 1581-1586.
118. Kovacs, D.; Lu, X.; Mészáros, L. S.; Ott, M.; Andres, J.; Borbas, K. E. *J. Am. Chem. Soc.* **2017**, *139*, 5756-5767.
119. Alonso, M. a.-T.; Brunet, E.; Juanes, O.; Rodríguez-Ubis, J.-C. *J. Photochem. Photobiol. A* **2002**, *147*, 113-125.
120. Kostova, I.; Momekov, G.; Stancheva, P. *Met.-Based Drugs* **2007**, *2007*, 015925.
121. Guzmán-Méndez, Ó.; González, F.; Bernès, S.; Flores-Álamo, M.; Ordóñez-Hernández, J.; García-Ortega, H.; Guerrero, J.; Qian, W.; Aliaga-Alcalde, N.; Gasque, L. *Inorg. Chem.* **2018**, *57*, 908-911.

122. Li, R.-f.; Li, R.-h.; Liu, X.-f.; Chang, X.-h.; Feng, X. *RSC Adv.* **2020**, *10*, 6192-6199.
123. Di Pietro, S.; Gautier, N.; Imbert, D.; Pécaut, J.; Mazzanti, M. *Dalton Trans.* **2016**, *45*, 3429-3442.
124. Yang, H.; Wang, A.; Zhang, L.; Zhou, X.; Yang, G.; Li, Y.; Zhang, Y.; Zhang, B.; Song, J.; Feng, Y. *New J. Chem.* **2017**, *41*, 15173-15179.
125. Kim, C.; Kim, K. Y.; Lee, J. H.; Ahn, J.; Sakurai, K.; Lee, S. S.; Jung, J. H. *ACS Appl. Mater. Interfaces* **2017**, *9*, 3799-3807.
126. Davis, D.; Carrod, A. J.; Guo, Z.; Kariuki, B. M.; Zhang, Y.-Z.; Pikramenou, Z. *Inorg. Chem.* **2019**, *58*, 13268-13275.
127. Kulpe, S., Seidel, I., Szulewsky, K., & Kretschmer, G. *Acta Crystallogr. B* **1982**, *38(11)*, 2813–2817.
128. Izatt, R. M.; Lamb, J. D.; Christensen, J. J.; Haymore, B. L. *J. Am. Chem. Soc.* **1977**, *99*, 8344-8346.
129. Massaux, J.; Desreux, J. F.; Delchambre, C.; Duyckaerts, G. *Inorg. Chem.* **1980**, *19*, 1893-1896.
130. Bünzli, J. C. G.; Pilloud, F. *Inorg. Chem.* **1989**, *28*, 2638-2642.
131. Piguet, C.; G. Bünzli, J.-C. *Chem. Soc. Rev.* **1999**, *28*, 347-358.
132. Almasio, M.-C.; Arnaud-Neu, F.; Schwing-Weill, M.-J. *Helv. Chim. Acta* **1983**, *66*, 1296-1306.
133. Massaux, J.; Desreux, J. F. *J. Am. Chem. Soc.* **1982**, *104*, 2967-2972.
134. Grenthe, I. *J. Am. Chem. Soc.* **1961**, *83*, 360-364.
135. Ouali, N.; Bocquet, B.; Rigault, S.; Morgantini, P. Y.; Weber, J.; Piguet, C. *Inorg. Chem.* **2002**, *41*, 1436-1445.
136. Renaud, F.; Piguet, C.; Bernardinelli, G.; Bünzli, J.-C. G.; Hopfgartner, G. *Chem. Eur. J.* **1997**, *3*, 1660-1667.
137. Renaud, F.; Piguet, C.; Bernardinelli, G.; Bünzli, J.-C. G.; Hopfgartner, G. *Chem. Eur. J.* **1997**, *3*, 1646-1659.
138. Piguet, C.; Williams, A. F.; Bernardinelli, G.; Buenzli, J. C. G. *Inorg. Chem.* **1993**, *32*, 4139-4149.
139. Petoud, S.; Bünzli, J.-C. G.; Renaud, F.; Piguet, C.; Schenk, K. J.; Hopfgartner, G. *Inorg. Chem.* **1997**, *36*, 5750-5760.
140. Renaud, F.; Piguet, C.; Bernardinelli, G.; Bünzli, J.-C. G.; Hopfgartner, G. *J. Am. Chem. Soc.* **1999**, *121*, 9326-9342.
141. de Gennes, P. G. *Rev. Mod. Phys.* **1992**, *64*, 645-648.
142. Segarra-Maset, M. D.; Nebot, V. J.; Miravet, J. F.; Escuder, B. *Chem. Soc. Rev.* **2013**, *42*, 7086-7098.
143. Alemán, J. V.; Chadwick, A. V.; He, J.; Hess, M.; Horie, K.; Jones, R. G.; Kratochvíl, P.; Meisel, I.; Mita, I.; Moad, G.; Penczek, S.; Stepto, R. F. T. In *Pure Appl. Chem.* 2007; Vol. 79, p 1801.
144. Maeda, H. *Chem. Eur. J.* **2008**, *14*, 11274-11282.
145. Konieczynska, M. D.; Grinstaff, M. W. *Acc. Chem. Res.* **2017**, *50*, 151-160.
146. Morita, C.; Kawai, C.; Kikuchi, A.; Imura, Y.; Kawai, T. *J Oleo Sci* **2012**, *61*, 707-713.

147. Curtius, T. *J. Prakt. Chem.* **1915**, *91*, 39-102.
148. Stals, P. J. M.; Everts, J. C.; de Bruijn, R.; Filot, I. A. W.; Smulders, M. M. J.; Martín-Rapún, R.; Pidko, E. A.; de Greef, T. F. A.; Palmans, A. R. A.; Meijer, E. W. *Chem. Eur. J.* **2010**, *16*, 810-821.
149. Cantekin, S.; de Greef, T. F. A.; Palmans, A. R. A. *Chem. Soc. Rev.* **2012**, *41*, 6125-6137.
150. Jana, P.; Schmuck, C. *Chem. Eur. J.* **2017**, *23*, 320-326.
151. Blomenhofer, M.; Ganzleben, S.; Hanft, D.; Schmidt, H.-W.; Kristiansen, M.; Smith, P.; Stoll, K.; Mäder, D.; Hoffmann, K. *Macromolecules* **2005**, *38*, 3688-3695.
152. Cantekin, S.; Balkenende, D. W. R.; Smulders, M. M. J.; Palmans, A. R. A.; Meijer, E. W. *Nat. Chem.* **2010**, *3*, 42.
153. Brunsveld, L.; Vekemans, J. A. J. M.; Hirschberg, J. H. K. K.; Sijbesma, R. P.; Meijer, E. W. *Proc. Natl. Acad. Sci. U. S. A.* **2002**, *99*, 4977-4982.
154. Desmarchelier, A.; Raynal, M.; Brocorens, P.; Vanthuyne, N.; Bouteiller, L. *Chem. Commun.* **2015**, *51*, 7397-7400.
155. Greciano, E. E.; Calbo, J.; Buendía, J.; Cerdá, J.; Aragó, J.; Ortí, E.; Sánchez, L. *J. Am. Chem. Soc.* **2019**, *141*, 7463-7472.
156. Jung, S. H.; Kwon, K.-Y.; Jung, J. H. *Chem. Commun.* **2015**, *51*, 952-955.
157. Jung, S. H.; Kim, K. Y.; Lee, J. H.; Moon, C. J.; Han, N. S.; Park, S.-J.; Kang, D.; Song, J. K.; Lee, S. S.; Choi, M. Y.; Jaworski, J.; Jung, J. H. *ACS Appl. Mater. Interfaces* **2017**, *9*, 722-729.
158. Hou, Z.; Li, P.; Wang, H.-Y.; Li, Z.; Li, H. *Dyes Pigm.* **2017**, *147*, 429-435.
159. Wang, H.-Y.; Ding, Z.-J.; Li, Z.; Zhang, Y.; Li, H. *Colloid. Polym. Sci.* **2018**, *296*, 53-58.
160. Gunnlaugsson, T.; Kruger, P. E.; Lee, T. C.; Parkesh, R.; Pfeffer, F. M.; Hussey, G. M. *Tetrahedron Lett.* **2003**, *44*, 6575-6578.
161. Duke, R. M.; Gunnlaugsson, T. *Tetrahedron Lett.* **2007**, *48*, 8043-8047.
162. Veale, E. B.; Gunnlaugsson, T. *J. Org. Chem.* **2008**, *73*, 8073-8076.
163. Gunnlaugsson, T.; Lee, T. C.; Parkesh, R. *Org. Biomol. Chem.* **2003**, *1*, 3265-3267.
164. Parkesh, R.; Clive Lee, T.; Gunnlaugsson, T. *Org. Biomol. Chem.* **2007**, *5*, 310-317.
165. Duke, R. M.; Gunnlaugsson, T. *Tetrahedron Lett.* **2011**, *52*, 1503-1505.
166. Saha, D.; Das, S.; Bhaumik, C.; Dutta, S.; Baitalik, S. *Inorg. Chem.* **2010**, *49*, 2334-2348.
167. Elmes, R. B. P.; Gunnlaugsson, T. *Tetrahedron Lett.* **2010**, *51*, 4082-4087.
168. Ryan, G. J.; Quinn, S.; Gunnlaugsson, T. *Inorg. Chem.* **2008**, *47*, 401-403.
169. Veale, E. B.; Kitchen, J. A.; Gunnlaugsson, T. *Supramol. Chem.* **2013**, *25*, 101-108.

170. Kitchen, J. A.; Martinho, P. N.; Morgan, G. G.; Gunnlaugsson, T. *Dalton Trans.* **2014**, *43*, 6468-6479.
171. Lovitt, J. I.; Hawes, C. S.; Lynes, A. D.; Haffner, B.; Möbius, M. E.; Gunnlaugsson, T. *Inorg. Chem. Front.* **2017**, *4*, 296-308.
172. Hawes, C. S.; Lynes, A. D.; Byrne, K.; Schmitt, W.; Ryan, G.; Möbius, M. E.; Gunnlaugsson, T. *Chem. Commun.* **2017**, *53*, 5989-5992.
173. Elmes, R. B. P.; Erby, M.; Bright, S. A.; Williams, D. C.; Gunnlaugsson, T. *Chem. Commun.* **2012**, *48*, 2588-2590.
174. Durrell, A. C. L., Gonghu; Koepf, Matthieu; Young, Karin J.;Negre, Christian F A; Allen, Laura J.; McNamara, William R.;Song, Hee Eun;Batista, Victor S.;Crabtree, Robert H.; Brudvig, Gary W. *J. Catal.* **2014**, *310*, 37-44.
175. Mondal, P. C.; Manna, A. K. *New J. Chem.* **2016**, *40*, 5775-5781.
176. Wang, J.; Pappalardo, M.; Keene, F. *Aust. J. Chem.* **1995**, *48*, 1425-1436.
177. Ghosh, B. N.; Puttreddy, R.; Rissanen, K. *Polyhedron* **2020**, *177*, 114304.
178. D. Storrier, G.; B. Colbran, S.; C. Craig, D. *J. Chem. Soc., Dalton Trans.* **1997**, 3011-3028.
179. Elgrishi, N.; Rountree, K. J.; McCarthy, B. D.; Rountree, E. S.; Eisenhart, T. T.; Dempsey, J. L. *J. Chem. Educ.* **2018**, *95*, 197-206.
180. Kershaw Cook, L. J.; Tuna, F.; Halcrow, M. A. *Dalton Trans.* **2013**, *42*, 2254-2265.
181. Peter Atkins, P.; De Paula, J. *Atkins' physical chemistry*; OUP Oxford, 2014.
182. Veale, E. B.; Frimannsson, D. O.; Lawler, M.; Gunnlaugsson, T. *Org. Lett.* **2009**, *11*, 4040-4043.
183. Veale, E. B.; Gunnlaugsson, T. *J. Org. Chem.* **2010**, *75*, 5513-5525.
184. Murphy, S.; Bright, S. A.; Poynton, F. E.; McCabe, T.; Kitchen, J. A.; Veale, E. B.; Williams, D. C.; Gunnlaugsson, T. *Org. Biomol. Chem.* **2014**, *12*, 6610-6623.
185. Shanmugaraju, S.; Dabadie, C.; Byrne, K.; Savyasachi, A. J.; Umadevi, D.; Schmitt, W.; Kitchen, J. A.; Gunnlaugsson, T. *Chem. Sci.* **2017**, *8*, 1535-1546.
186. Shanmugaraju, S.; McAdams, D.; Pancotti, F.; Hawes, C. S.; Veale, E. B.; Kitchen, J. A.; Gunnlaugsson, T. *Org. Biomol. Chem.* **2017**, *15*, 7321-7329.
187. Shanmugaraju, S.; Hawes, C. S.; Savyasachi, A. J.; Blasco, S.; Kitchen, J. A.; Gunnlaugsson, T. *Chem. Commun.* **2017**, *53*, 12512-12515.
188. Caruso, F.; Rossi, M.; Benson, A.; Opazo, C.; Freedman, D.; Monti, E.; Gariboldi, M. B.; Shaulky, J.; Marchetti, F.; Pettinari, R.; Pettinari, C. *J. Med. Chem.* **2012**, *55*, 1072-1081.
189. Shanmugaraju, S.; la Cour Poulsen, B.; Arisa, T.; Umadevi, D.; Dalton, H. L.; Hawes, C. S.; Estalayo-Adrián, S.; Savyasachi, A. J.; Watson, G. W.; Williams, D. C.; Gunnlaugsson, T. *Chem. Commun.* **2018**, *54*, 4120-4123.
190. Havlik, M.; Kral, V.; Kaplanek, R.; Dolensky, B. *Org. Lett.* **2008**, *10*, 4767-4769.

191. Song, P.; Sun, S.-g.; Zhou, P.-w.; Liu, J.-y.; Xu, Y.-q.; Peng, X.-j. *Chin. J. Chem. Phys.* **2010**, *23*, 558-564.
192. Rueden, C. T.; Schindelin, J.; Hiner, M. C.; DeZonia, B. E.; Walter, A. E.; Arena, E. T.; Eliceiri, K. W. *BMC Bioinformatics* **2017**, *18*, 529.
193. Schneider, C. A.; Rasband, W. S.; Eliceiri, K. W. *Nat. Methods* **2012**, *9*, 671-675.
194. Aletti, A. B.; Blasco, S.; Aramballi, S. J.; Kruger, P. E.; Gunnlaugsson, T. *Chem* **2019**, *5*, 2617-2629.
195. Wyman, J. F.; Serve, M. P.; Hobson, D. W.; Lee, L. H.; Uddin, D. E. *J. Toxicol. Environ. Health* **1992**, *37*, 313-327.
196. Meher, N.; Iyer, P. K. *Nanoscale* **2017**, *9*, 7674-7685.
197. Kumar, A.; Chae, P. S. *Sens. Actuators B Chem.* **2017**, *240*, 1-9.
198. Cao, X.; Zhao, N.; Lv, H.; Ding, Q.; Gao, A.; Jing, Q.; Yi, T. *Langmuir* **2017**, *33*, 7788-7798.
199. Kim, S. K.; Lim, J. M.; Pradhan, T.; Jung, H. S.; Lynch, V. M.; Kim, J. S.; Kim, D.; Sessler, J. L. *J. Am. Chem. Soc.* **2014**, *136*, 495-505.
200. Shanmugaraju, S.; Joshi, S. A.; Mukherjee, P. S. *J. Mater. Chem.* **2011**, *21*, 9130-9138.
201. Nagarkar, S. S.; Joarder, B.; Chaudhari, A. K.; Mukherjee, S.; Ghosh, S. K. *Angew. Chem. Int. Ed.* **2013**, *52*, 2881-2885.
202. Shanmugaraju, S.; Umadevi, D.; Savyasachi, A. J.; Byrne, K.; Ruether, M.; Schmitt, W.; Watson, G. W.; Gunnlaugsson, T. *J. Mater. Chem. A* **2017**, *5*, 25014-25024.
203. Kaur, S.; Gupta, A.; Bhalla, V.; Kumar, M. *J. Mater. Chem. C* **2014**, *2*, 7356-7363.
204. Lin, Q.; Guan, X.-W.; Fan, Y.-Q.; Wang, J.; Liu, L.; Liu, J.; Yao, H.; Zhang, Y.-M.; Wei, T.-B. *New J. Chem.* **2019**, *43*, 2030-2036.
205. Valeur, B.; Berberan-Santos, M. N. In *Molecular Fluorescence* 2012, 141-179.
206. Tanwar, A. S.; Hussain, S.; Malik, A. H.; Afroz, M. A.; Iyer, P. K. *ACS Sensors* **2016**, *1*, 1070-1077.
207. Li, J. H. Q. L. Z. In *Aggregation-Induced Emission: Fundamentals and Applications, Volumes 1 and 2* 2013, 127-153.
208. Zhao, Y.; Truhlar, D. G. *Theor. Chem. Acc.* **2008**, *120*, 215-241.
209. Frisch, M. J.; Trucks, G. W.; Schlegel, H. B.; Scuseria, G. E.; Robb, M. A.; Cheeseman, J. R.; Scalmani, G.; Barone, V.; Petersson, G. A.; Nakatsuji, H.; Li, X.; Caricato, M.; Marenich, A. V.; Bloino, J.; Janesko, B. G.; Gomperts, R.; Mennucci, B.; Hratchian, H. P.; Ortiz, J. V.; Izmaylov, A. F.; Sonnenberg, J. L.; Williams; Ding, F.; Lipparini, F.; Egidi, F.; Goings, J.; Peng, B.; Petrone, A.; Henderson, T.; Ranasinghe, D.; Zakrzewski, V. G.; Gao, J.; Rega, N.; Zheng, G.; Liang, W.; Hada, M.; Ehara, M.; Toyota, K.; Fukuda, R.; Hasegawa, J.; Ishida, M.; Nakajima, T.; Honda, Y.; Kitao, O.; Nakai, H.; Vreven, T.; Throssell, K.; Montgomery Jr., J. A.; Peralta, J. E.; Ogliaro, F.; Bearpark, M. J.; Heyd, J. J.; Brothers, E. N.; Kudin, K. N.; Staroverov, V. N.; Keith, T. A.; Kobayashi, R.; Normand, J.; Raghavachari, K.; Rendell, A. P.; Burant, J. C.;

Iyengar, S. S.; Tomasi, J.; Cossi, M.; Millam, J. M.; Klene, M.; Adamo, C.; Cammi, R.; Ochterski, J. W.; Martin, R. L.; Morokuma, K.; Farkas, O.; Foresman, J. B.; Fox, D. J. *Gaussian 16 Rev. C.01* Wallingford, CT, 2016.
210. Walker, M.; Harvey, A. J. A.; Sen, A.; Dessent, C. E. H. *J. Phys. Chem. A* **2013**, *117*, 12590-12600.
211. Ma, S.; Zhou, H.-C. *Chem. Commun.* **2010**, *46*, 44-53.
212. Ma, L.; Abney, C.; Lin, W. *Chem. Soc. Rev.* **2009**, *38*, 1248-1256.
213. Babu, H. V.; Bai, M. G. M.; Rajeswara Rao, M. *ACS Appl. Mater. Interfaces* **2019**, *11*, 11029-11060.
214. Kaleeswaran, D.; Murugavel, R. *J. Chem. Sci.* **2018**, *130*, 1.
215. Sang, N.; Zhan, C.; Cao, D. *J. Mater. Chem. A* **2015**, *3*, 92-96.
216. Delente, J. M.; Umadevi, D.; Shanmugaraju, S.; Kotova, O.; Watson, G. W.; Gunnlaugsson, T. *Chem. Commun.* **2020**.
217. Tanwar, A. S.; Adil, L. R.; Afroz, M. A.; Iyer, P. K. *ACS Sensors* **2018**, *3*, 1451-1461.
218. Chen, S.; Yu, Y.-L.; Wang, J.-H. *Anal. Chim. Acta* **2018**, *999*, 13-26.
219. Albrecht, C. *Anal. Bioanal. Chem.* **2008**, *390*, 1223-1224.
220. Brown, D. H.; Nuttall, R. H.; McAvoy, J.; Sharp, D. W. A. *J. Chem. Soc. A* **1966**, 892-896.
221. McCarney, E. P.; Byrne, J. P.; Twamley, B.; Martínez-Calvo, M.; Ryan, G.; Möbius, M. E.; Gunnlaugsson, T. *Chem. Commun.* **2015**, *51*, 14123-14126.
222. Bradberry, S. J.; Dee, G.; Kotova, O.; McCoy, C. P.; Gunnlaugsson, T. *Chem. Commun.* **2019**, *55*, 1754-1757.
223. Bradberry, S. J.; Byrne, J. P.; McCoy, C. P.; Gunnlaugsson, T. *Chem. Commun.* **2015**, *51*, 16565-16568.
224. Kotova, O.; Comby, S.; Pandurangan, K.; Stomeo, F.; O'Brien, J. E.; Feeney, M.; Peacock, R. D.; McCoy, C. P.; Gunnlaugsson, T. *Dalton Trans.* **2018**, *47*, 12308-12317.
225. Barry, D. E.; Kitchen, J. A.; Pandurangan, K.; Savyasachi, A. J.; Peacock, R. D.; Gunnlaugsson, T. *Inorg. Chem.* **2020**, *59*, 2646-2650.
226. Galanti, A.; Kotova, O.; Blasco, S.; Johnson, C. J.; Peacock, R. D.; Mills, S.; Boland, J. J.; Albrecht, M.; Gunnlaugsson, T. *Chem. Eur. J.* **2016**, *22*, 9709-9723.
227. Barry, D. E.; Kitchen, J. A.; Mercs, L.; Peacock, R. D.; Albrecht, M.; Gunnlaugsson, T. *Dalton Trans.* **2019**, *48*, 11317-11325.
228. Molloy, J. K.; Nonat, A. M.; O'Brien, J. E.; Brougham, D. F.; Gunnlaugsson, T. *Supramol. Chem.* **2020**, *32*, 373-382.
229. Lynes, A. D.; Hawes, C. S.; Ward, E. N.; Haffner, B.; Mobius, M. E.; Byrne, K.; Schmitt, W.; Pal, R.; Gunnlaugsson, T. *CrystEngComm* **2017**, *19*, 1427-1438.
230. Lynes, A. D.; Hawes, C. S.; Byrne, K.; Schmitt, W.; Gunnlaugsson, T. *Dalton Trans.* **2018**, *47*, 5259-5268.
231. Lynes, A. D. Supramolecular soft materials and structural studies of a series of BTA and pyridine-dicarboxamide derivatives with various d-metal ions. Trinity College Dublin, 2018.

232. Fukuda, Y.; Nakao, A.; Hayashi, K. *J. Chem. Soc., Dalton Trans.* **2002**, 527-533.
233. Savyasachi, A. J. Luminescent Self-assembled Supramolecular Polymers and Microspheres Based on Benzene-1,3,5-tricarboxamide (BTA) Derivatives. University of Dublin Trinity College, 2017.
234. Shannon, R. *Acta Crystallogr. Sect. A* **1976**, *32*, 751-767.
235. Hewitt, S. H.; Macey, G.; Mailhot, R.; Elsegood, M. R. J.; Duarte, F.; Kenwright, A. M.; Butler, S. J. *Chem. Sci.* **2020**, *11*, 3619-3628.
236. He, G.; Guo, D.; He, C.; Zhang, X.; Zhao, X.; Duan, C. *Angew. Chem. Int. Ed.* **2009**, *48*, 6132-6135.
237. Kulkarni, C.; Meijer, E. W.; Palmans, A. R. A. *Acc. Chem. Res.* **2017**, *50*, 1928-1936.
238. Smulders, M. M. J.; Schenning, A. P. H. J.; Meijer, E. W. *J. Am. Chem. Soc.* **2008**, *130*, 606-611.
239. Gampp, H.; Maeder, M.; Meyer, C. J.; Zuberbu¨hler, A. D. *Talanta* **1985**, *32*, 257-264.
240. Gampp, H.; Maeder, M.; Meyer, C. J.; Zuberbühler, A. D. *Talanta* **1985**, *32*, 1133-1139.
241. Gampp, H.; Maeder, M.; Meyer, C. J.; Zuberbühler, A. D. *Talanta* **1985**, *32*, 95-101.
242. Gampp, H.; Maeder, M.; Meyer, C. J.; Zuberbühler, A. D. *Talanta* **1986**, *33*, 943-951.
243. Law, G.-L.; Man, C.; Parker, D.; Walton, J. W. *Chem. Commun.* **2010**, *46*, 2391-2393.
244. Nasso, I.; Bedel, S.; Galaup, C.; Picard, C. *Eur. J. Inorg. Chem.* **2008**, *2008*, 2064-2074.
245. Law, G.-L.; Pal, R.; Palsson, L. O.; Parker, D.; Wong, K.-L. *Chem. Commun.* **2009**, 7321-7323.
246. Shuvaev, S.; Kotova, O.; Utochnikova, V.; Vaschenko, A.; Puntus, L.; Baulin, V.; Kuzmina, N.; Tzivadze, A. *Inorg. Chem. Commun.* **2012**, *20*, 73-76.
247. Melo, L. L. L. S.; Castro, G. P.; Gonçalves, S. M. C. *Inorg. Chem.* **2019**, *58*, 3265-3270.
248. Lo, W.-S.; Zhang, J.; Wong, W.-T.; Law, G.-L. *Inorg. Chem.* **2015**, *54*, 3725-3727.
249. Lunstroot, K.; Nockemann, P.; Van Hecke, K.; Van Meervelt, L.; Görller-Walrand, C.; Binnemans, K.; Driesen, K. *Inorg. Chem.* **2009**, *48*, 3018-3026.
250. Janghouri, M.; Amini, M. M. *J. Electron. Mater.* **2018**, *47*, 2761-2767.
251. Ugale, A.; Kalyani, T. N.; Dhoble, S. J. In *Lanthanide-Based Multifunctional Materials*; Martín-Ramos, P., Ramos Silva, M., Eds.; Elsevier: 2018, 59-97.
252. Caravan, P.; Ellison, J. J.; McMurry, T. J.; Lauffer, R. B. *Chem. Rev.* **1999**, *99*, 2293-2352.

253. Tliha, M.; Mathlouthi, H.; Lamloumi, J.; Percheron-Guegan, A. *J. Alloys Compd.* **2007**, *436*, 221-225.
254. Schweizer, T.; Samson, B. N.; Hector, J. R.; Brocklesby, W. S.; Hewak, D. W.; Payne, D. N. *Infrared Phys. Technol.* **1999**, *40*, 329-335.
255. Gupta, S. K.; Zuniga, J. P.; Abdou, M.; Thomas, M. P.; De Alwis Goonatilleke, M.; Guiton, B. S.; Mao, Y. *Chem. Eng. J.* **2020**, *379*, 122314.
256. Shukla, A. K.; Kumar, U. *J. Med . Phys.* **2006**, *31*, 13-21.
257. Kim, G. M.; Oh, I. S.; Lee, A. N.; Oh, S. Y. *J. Mater. Chem. A* **2014**, *2*, 10131-10136.
258. Zhang, L.-Y.; Hou, Y.-J.; Pan, M.; Chen, L.; Zhu, Y.-X.; Yin, S.-Y.; Shao, G.; Su, C.-Y. *Dalton Trans.* **2015**, *44*, 15212-15219.
259. Bretonnière, Y.; Mazzanti, M.; Wietzke, R.; Pécaut, J. *Chem. Commun.* **2000**, 1543-1544.
260. Mürner, H.-R.; Chassat, E.; Thummel, R. P.; Bünzli, J.-C. G. *J. Chem. Soc., Dalton Trans.* **2000**, 2809-2816.
261. Kepert, C.; Lu, W.; Skelton, B.; White, A. *Aust. J. Chem.* **1994**, *47*, 365-384.
262. Mears, L. L. E.; Draper, E. R.; Castilla, A. M.; Su, H.; Zhuola; Dietrich, B.; Nolan, M. C.; Smith, G. N.; Doutch, J.; Rogers, S.; Akhtar, R.; Cui, H.; Adams, D. J. *Biomacromolecules* **2017**, *18*, 3531-3540.
263. Ewoldt, R. H.; Johnston, M. T.; Caretta, L. M. In *Complex Fluids in Biological Systems: Experiment, Theory, and Computation*; Spagnolie, S. E., Ed.; Springer New York: New York, NY, 2015, 207-241.
264. Adrian, S. E. Photophysical and Biological Profiling of Ruthenium(II) Polypyridyl Complex-based Systems. Trinity College, The University of Dublin, 2019.
265. Sénéchal-David, K.; Pope, S. J. A.; Quinn, S.; Faulkner, S.; Gunnlaugsson, T. *Inorg. Chem.* **2006**, *45*, 10040-10042.
266. Klink, S. I.; Keizer, H.; Hofstraat, H. W.; van Veggel, F. C. J. M. *Synth. Met.* **2002**, *127*, 213-216.
267. Stals, P. J. M.; Smulders, M. M. J.; Martín-Rapún, R.; Palmans, A. R. A.; Meijer, E. W. *Chem. Eur. J.* **2009**, *15*, 2071-2080.
268. Shikata, T.; Ogata, D.; Hanabusa, K. *J. Phys. Chem. B* **2004**, *108*, 508-514.
269. Kristiansen, M.; Smith, P.; Chanzy, H.; Baerlocher, C.; Gramlich, V.; McCusker, L.; Weber, T.; Pattison, P.; Blomenhofer, M.; Schmidt, H.-W. *Cryst. Growth Des.* **2009**, *9*, 2556-2558.
270. Lowe, G.; Droz, A. S.; Vilaivan, T.; Weaver, G. W.; Tweedale, L.; Pratt, J. M.; Rock, P.; Yardley, V.; Croft, S. L. *J. Med. Chem.* **1999**, *42*, 999-1006.
271. Matveeva, E.; Kolesnikova, I.; Zefirov, N. *Russ. Chem. Bull.* **2011**, *60*, 248.
272. Jahns, C.; Hoffmann, T.; Müller, S.; Gerth, K.; Washausen, P.; Höfle, G.; Reichenbach, H.; Kalesse, M.; Müller, R. *Angew. Chem. Int. Ed.* **2012**, *51*, 5239-5243.

273. Zhang, Y.; Wang, Q.; Xiao, Y.-J.; Han, J.; Zhao, X.-L. *Polyhedron* **2012**, *33*, 127-136.
274. Apex-3 *Brucker-AXS Inc*, 2016.
275. *SADABS, Brucker-AXS Inc 2016*.
276. Dolomanov, O. V.; Bourhis, L. J.; Gildea, R. J.; Howard, J. A. K.; Puschmann, H. *J. Appl. Crystallogr.* **2009**, *42*, 339-341.
277. Sheldrick, G. *Acta Crystallogr. Sect. C* **2015**, *71*, 3-8.
278. McKinnon, J. J.; Jayatilaka, D.; Spackman, M. A. *Chem. Commun.* **2007**, 3814-3816.
279. Spackman, M. A.; Jayatilaka, D. *CrystEngComm* **2009**, *11*, 19-32.
280. Durrell, A. C. L., Gonghu; Koepf, Matthieu; Young, Karin J.;Negre, Christian F A; Allen, Laura J.; McNamara, William R.;Song, Hee Eun;Batista, Victor S.;Crabtree, Robert H.; Brudvig, Gary W. *J. Catal.* **2014**, *310*, 37-44.

Appendices

Data to Support Chapter 2

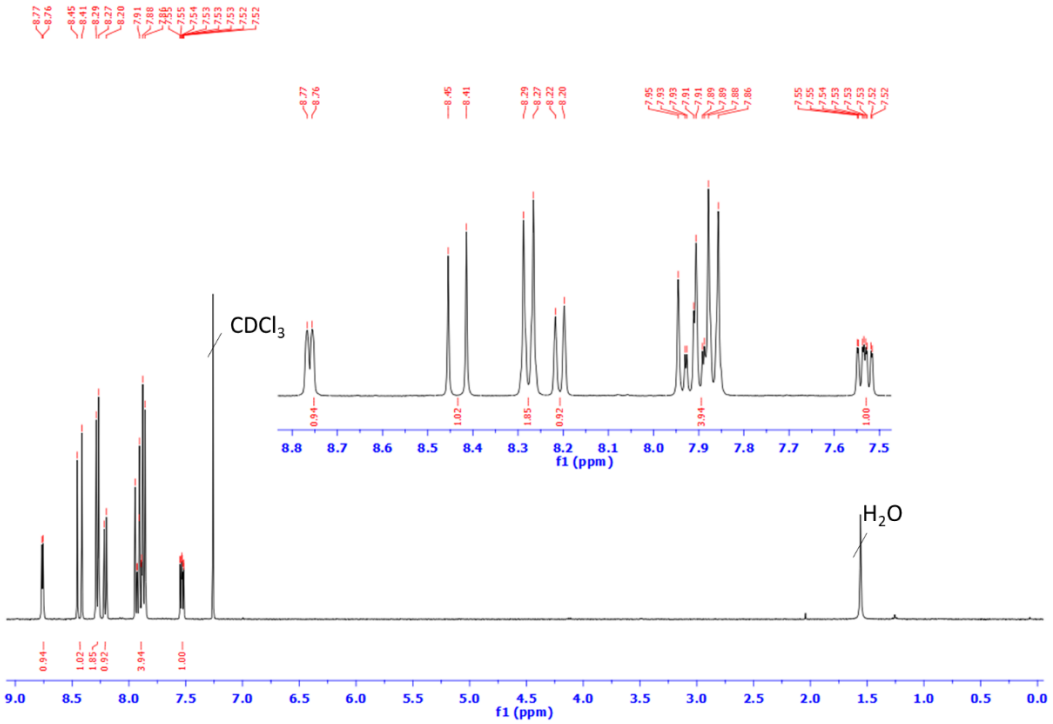

Figure A. 1 ^{1}H NMR ($CDCl_3$, 400 MHz) of **108** with inset of the highlighted aromatic region.

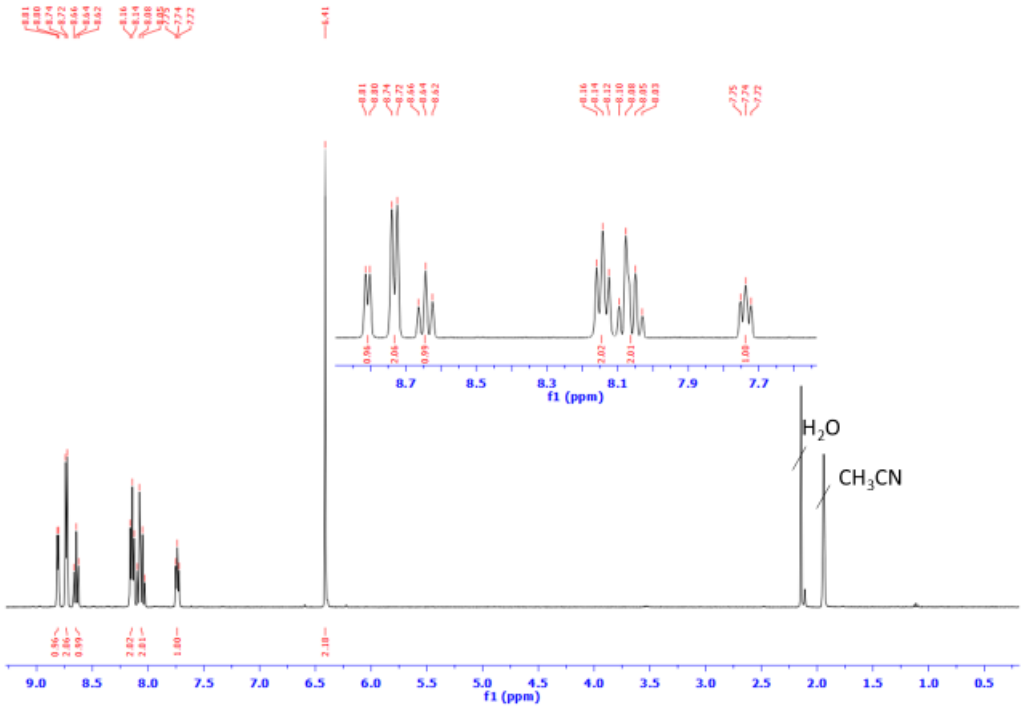

Figure A. 2 ^{1}H NMR (CD_3CN, 400 MHz) of **109** with inset of the highlighted aromatic region.

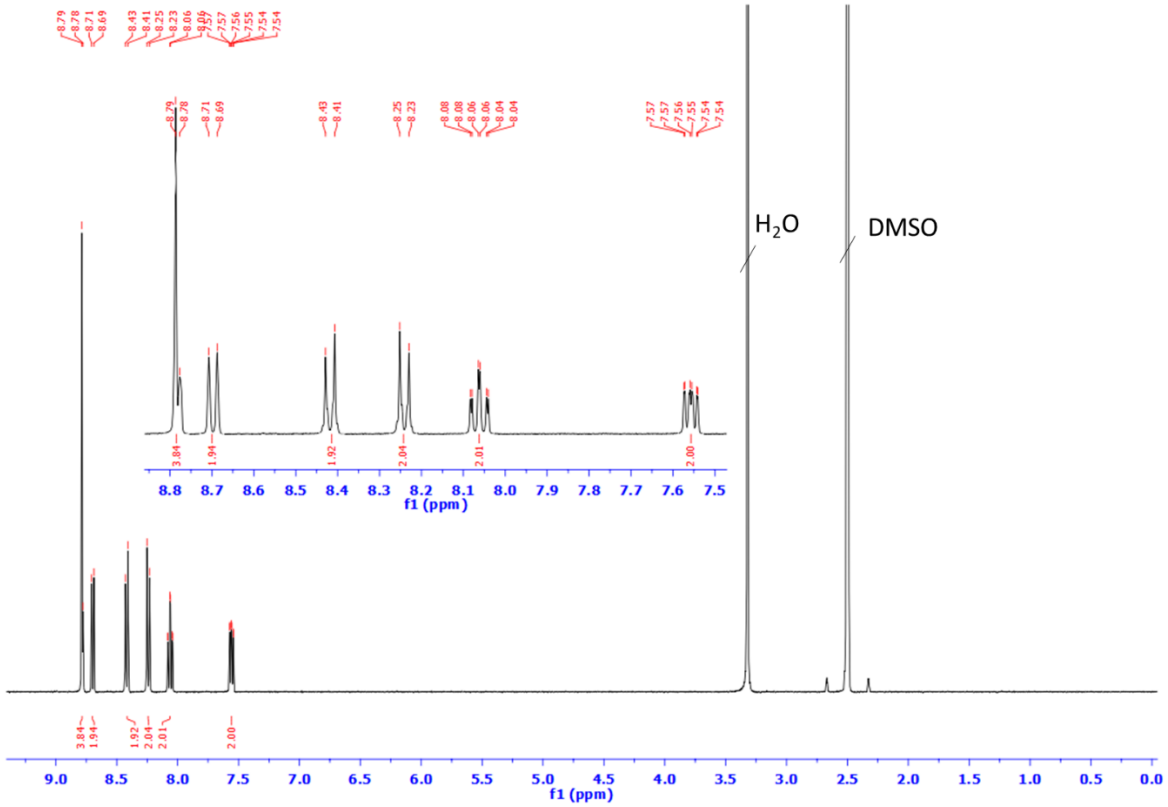

Figure A. 3 ^{1}H NMR (DMSO-d_6, 400 MHz) of **110** with inset of the highlighted aromatic region.

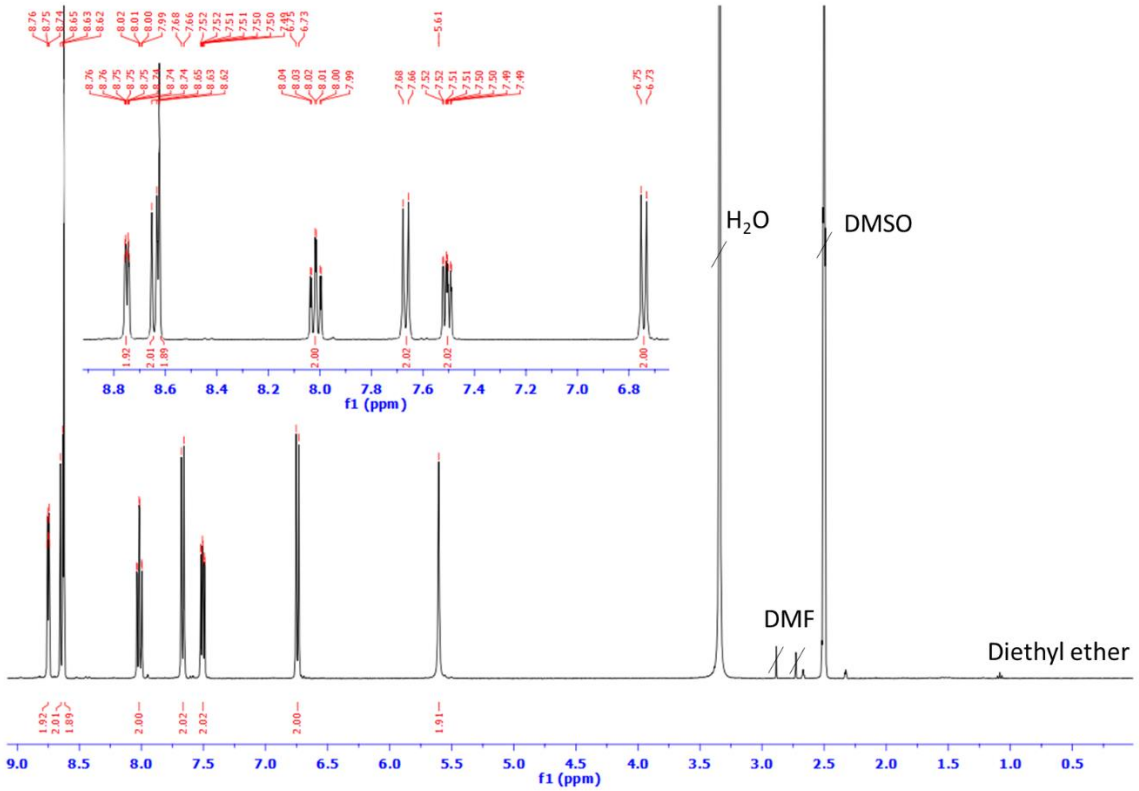

Figure A. 4 ^{1}H NMR (DMSO-d_6, 400 MHz) of **111** with inset of the highlighted aromatic region.

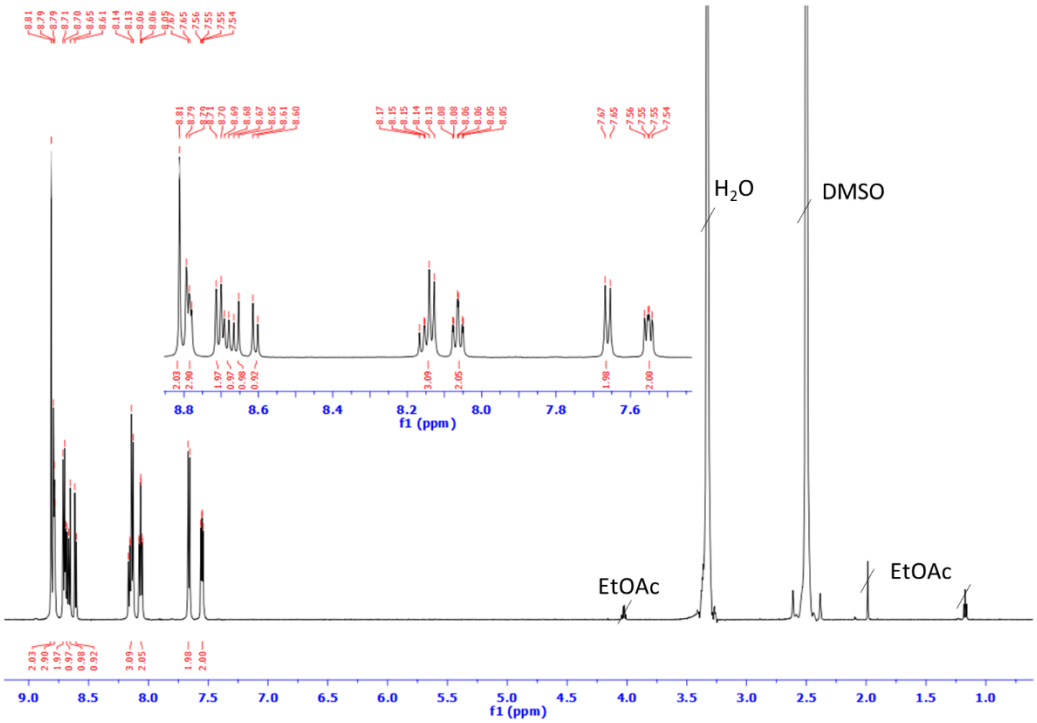

Figure A. 5 ^{1}H NMR (DMSO-d_6, 600 MHz) of **112** with inset of the highlighted aromatic region.

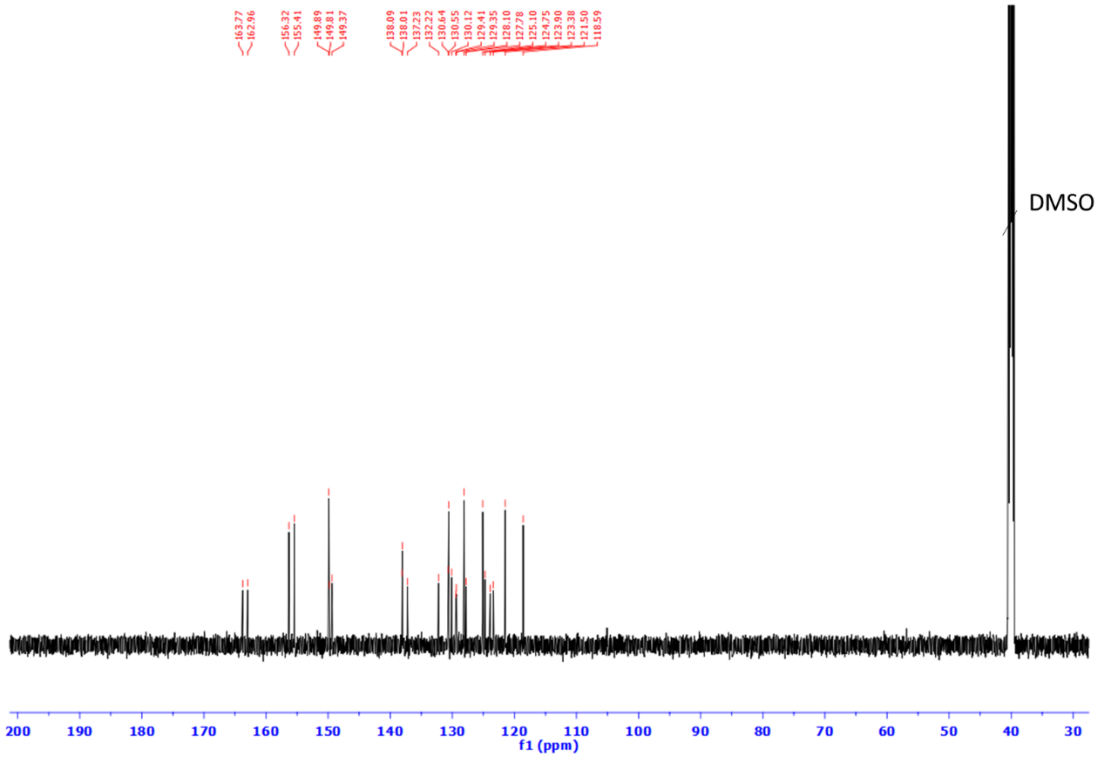

Figure A. 6 ^{13}C{^{1}H} NMR (DMSO-d_6, 151 MHz) of **112**.

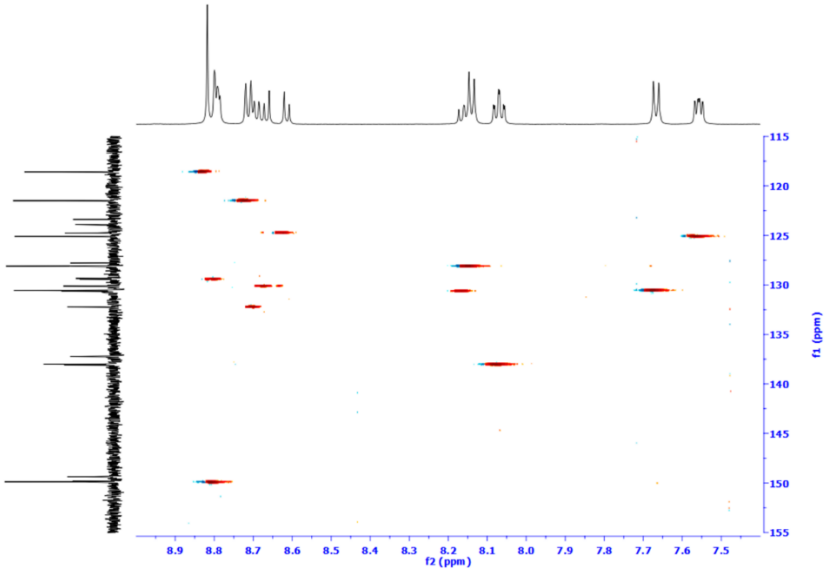

Figure A. 7 HSQC NMR (DMSO-d_6) of **112**.

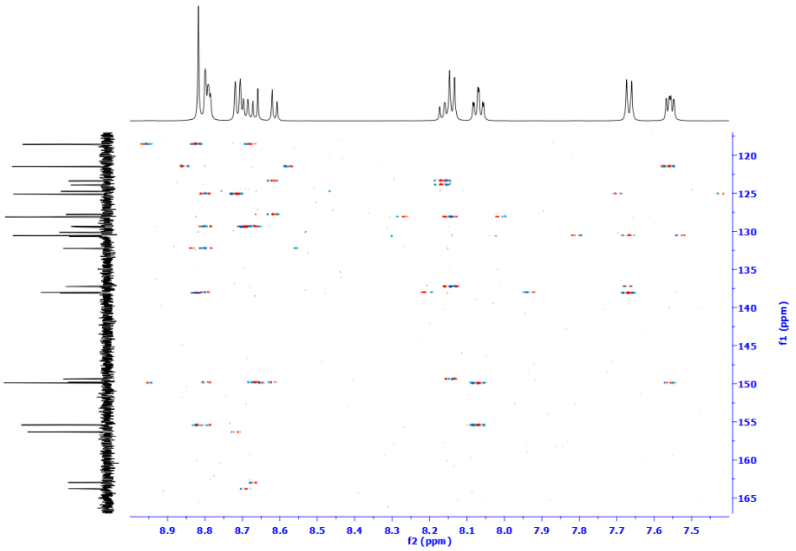

Figure A. 8 HMBC NMR (DMSO-d_6) of **112**.

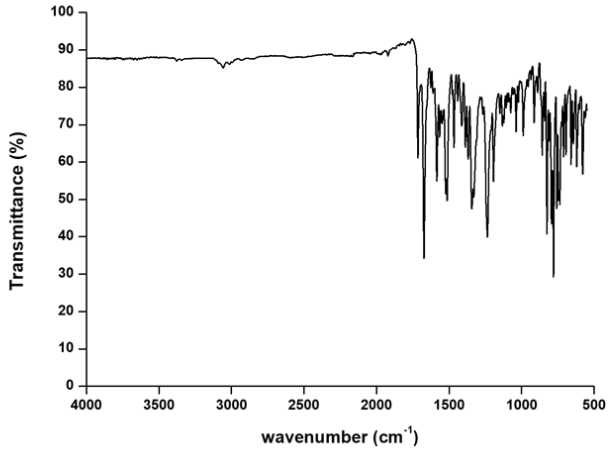

Figure A. 9 IR spectra of **112**.

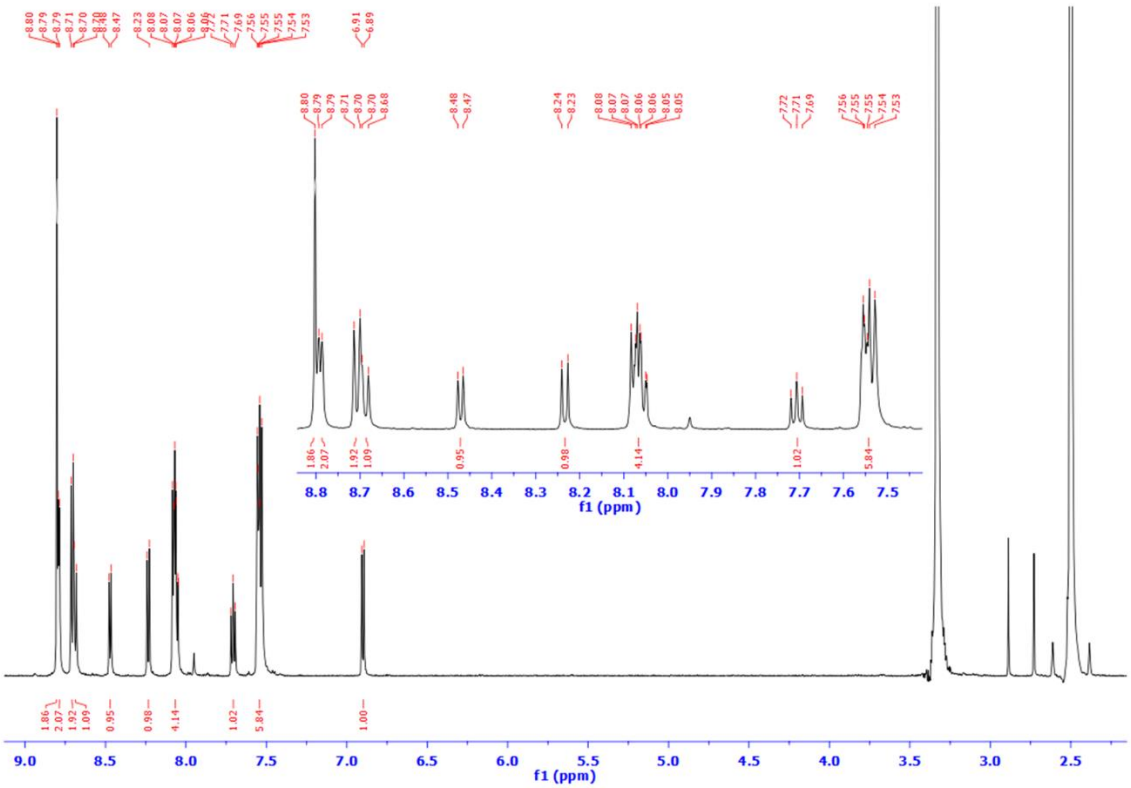

Figure A. 10 ^{1}H NMR (DMSO-d$_6$, 600 MHz) of **107** with inset of the highlighted aromatic region.

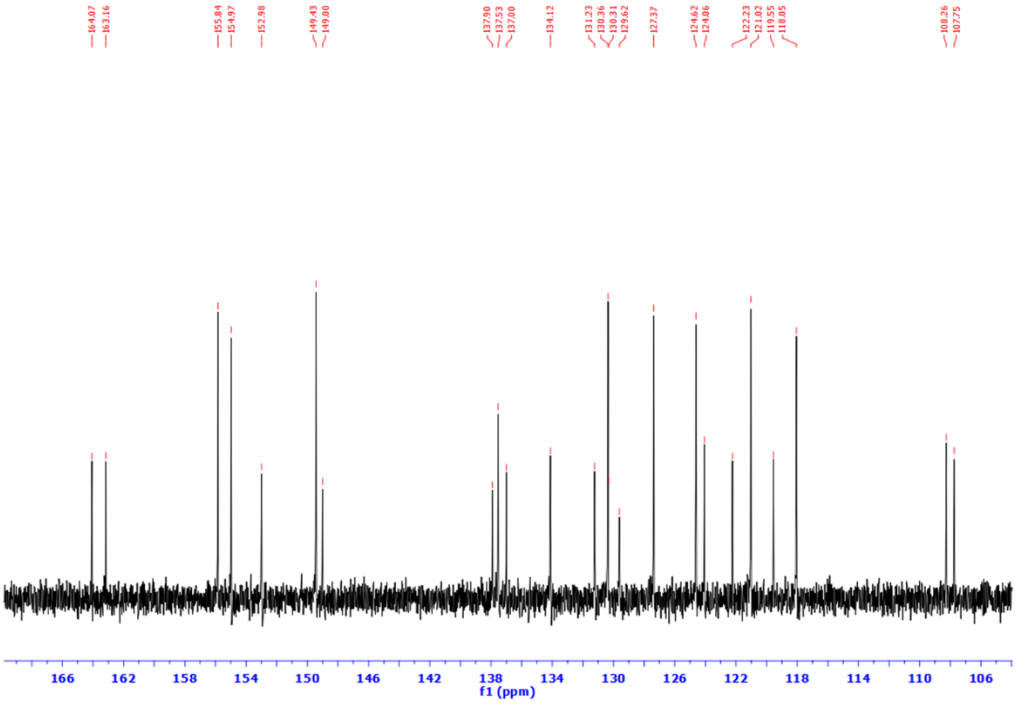

Figure A. 11 ^{13}C{^{1}H} NMR (DMSO-d$_6$, 151 MHz) of **107**.

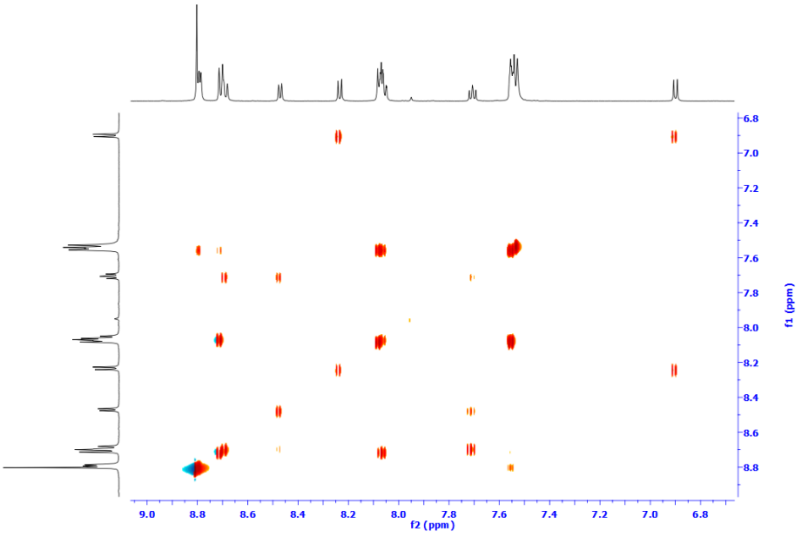

Figure A. 12 HH COSY NMR(DMSO-d_6) of **107**.

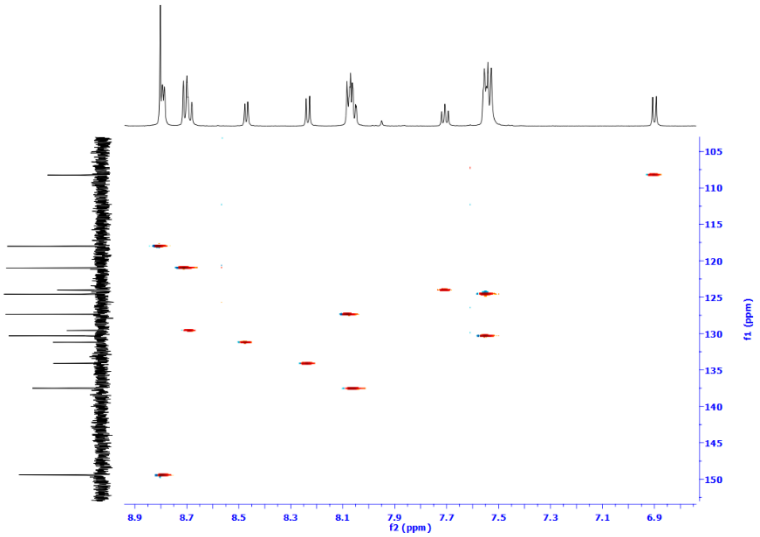

Figure A. 13 HSQC NMR(DMSO-d_6) of **107**.

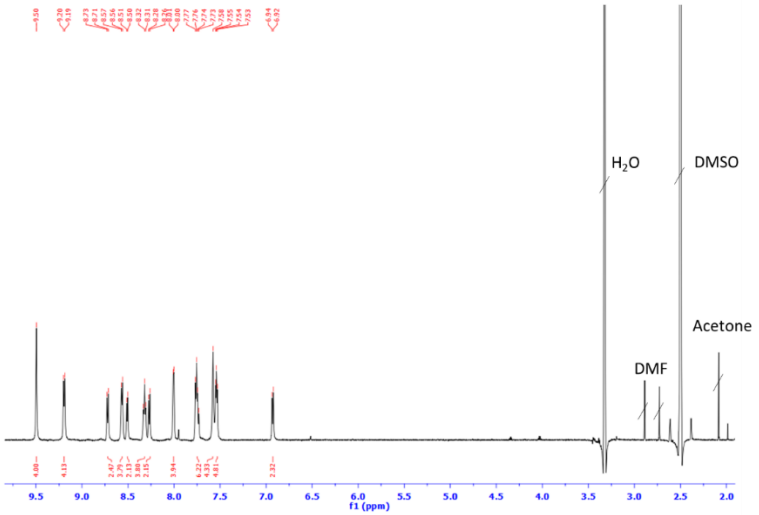

Figure A. 14 ^{1}H NMR (DMSO-d_6, 600 MHz) of [**107**$_2$**(**Zn$(BF_4)_2$)].

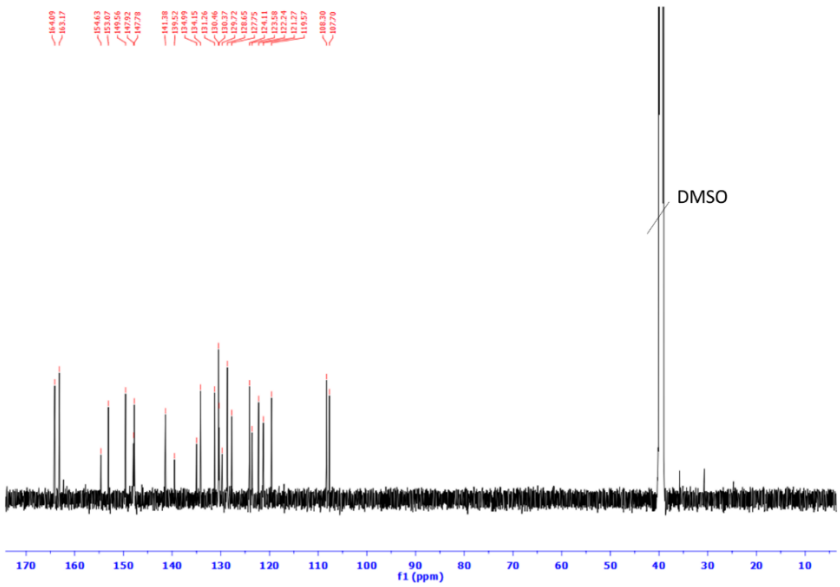

Figure A. 15 $^{13}C\{^{1}H\}$ NMR (DMSO-d_6, 151 MHz) of [**107**$_2$**(**$Zn(BF_4)_2$)].

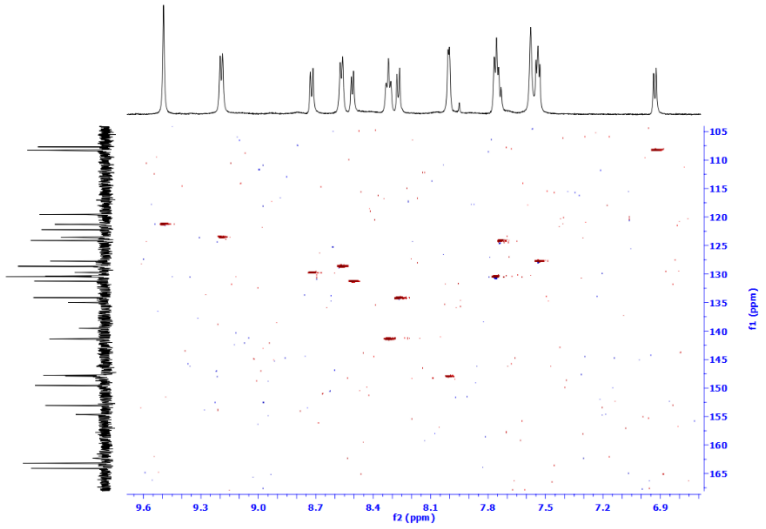

Figure A. 16 HSQC NMR(DMSO-d_6) of [**107**$_2$**(**$Zn(BF_4)_2$)].

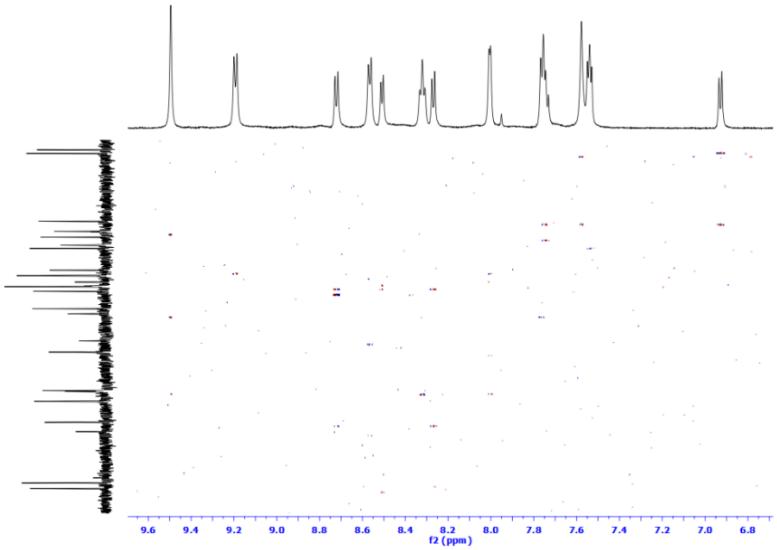

Figure A. 17 HMBC NMR (DMSO-d_6) of [**107**$_2$**(**$Zn(BF_4)_2$)].

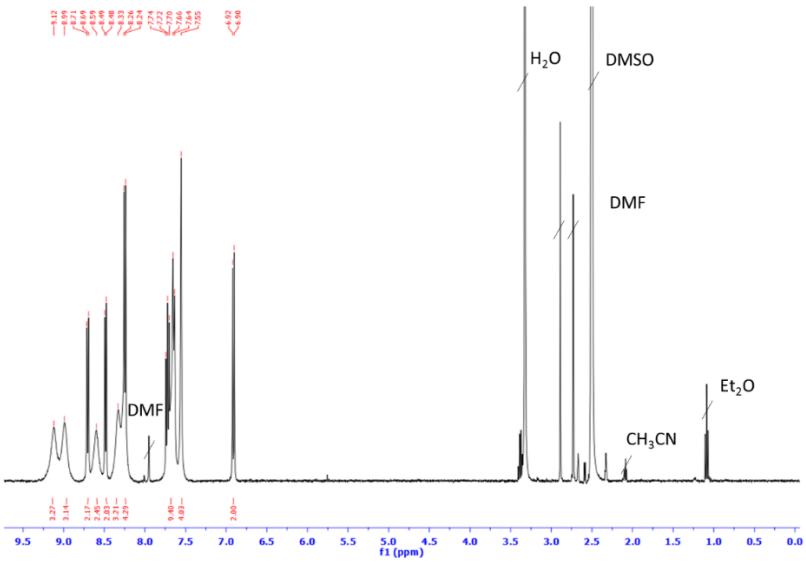

Figure A. 18 ^{1}H NMR (DMSO-d$_6$, 400 MHz) of [**107**$_2$**(**Cd(NO$_3$)$_2$)].

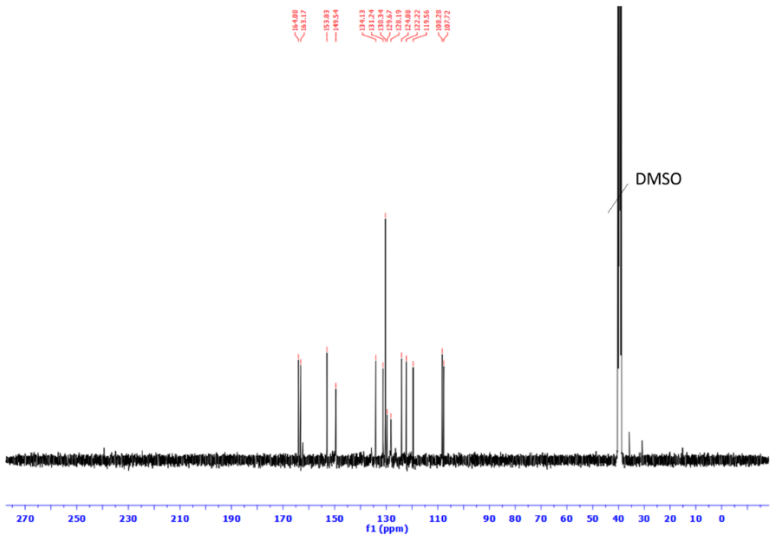

Figure A. 19 ^{13}C{^{1}H} NMR (DMSO-d$_6$, 101 MHz) of [**107**$_2$**(**Cd(NO$_3$)$_2$)].

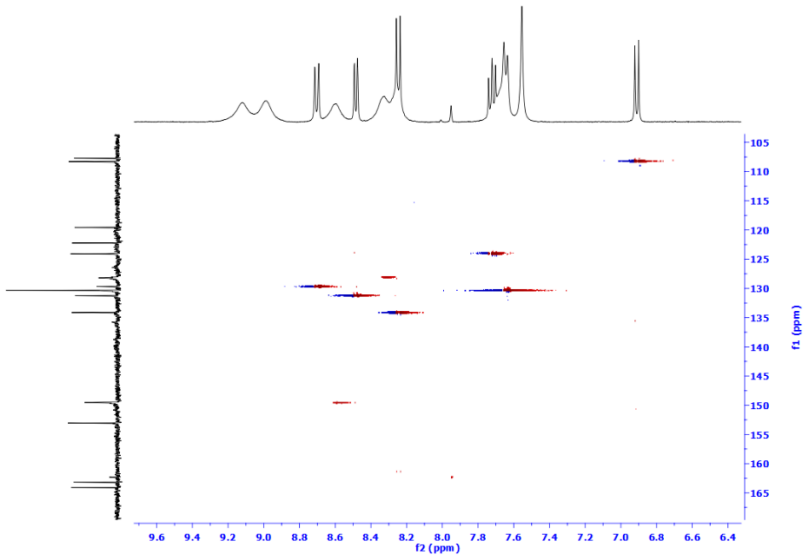

Figure A. 20 HSQC NMR(DMSO-d$_6$) of [**107**$_2$**(**Cd(NO$_3$)$_2$)].

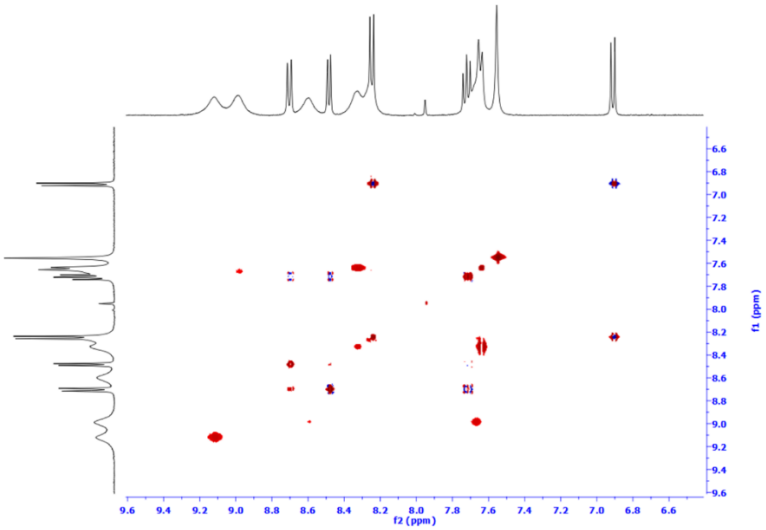

Figure A. 21 TOCSY NMR(DMSO-d_6) of [**107**$_2$(Cd(NO_3)$_2$)].

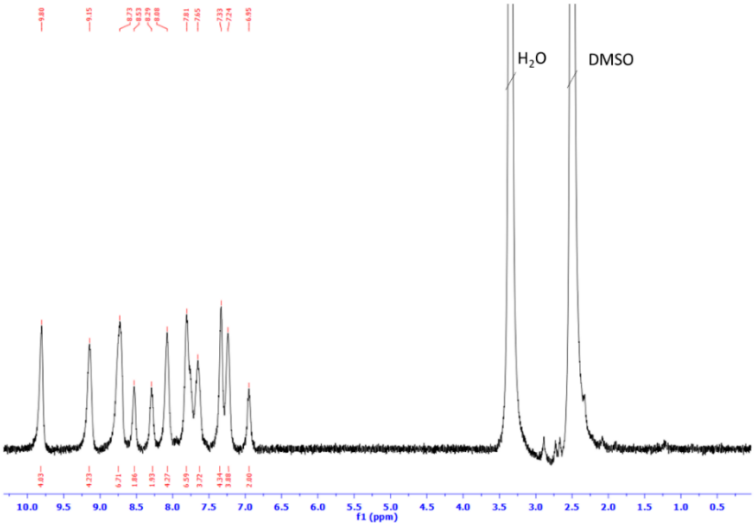

Figure A. 22 ^{1}H NMR (DMSO-d_6, 400 MHz) of [**107**$_2$($FeCl_2$)].

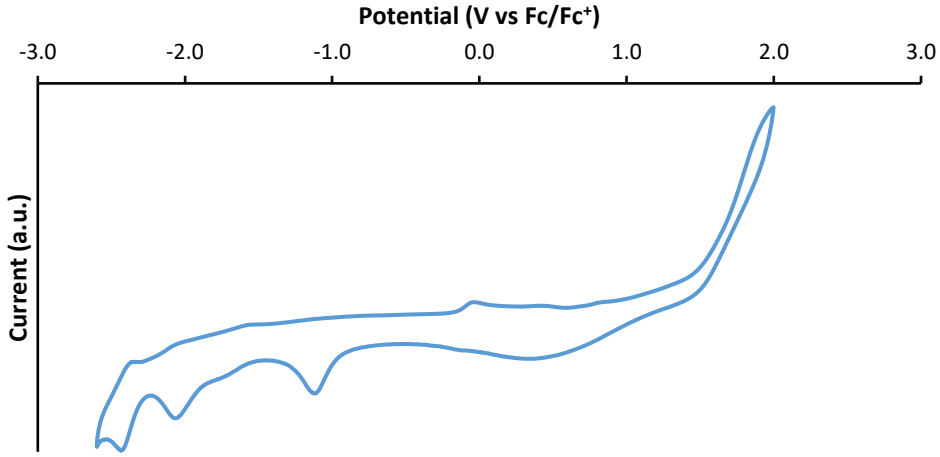

Figure A. 23 Voltammogram of [**107**$_2$($Co(NO_3)_2$)] under N_2 at 100 mV/s, scanned in the negative direction in 0.1 M [NBu_4][PF_6] CH_3CN solution. The Fc/Fc^+ couple was used as an internal standard and the voltammogram is referenced against this couple.

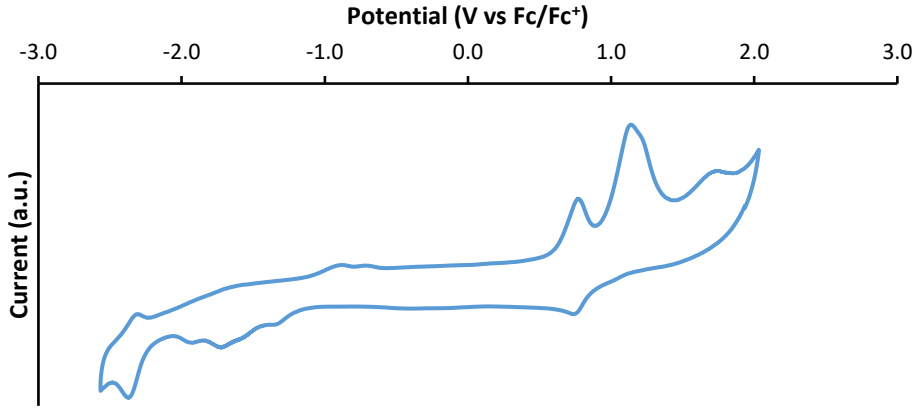

Figure A. 24 Voltammogram of [**107**$_2$($FeCl_2$)] under N_2 at 100 mV/s, scanned in the negative direction in 0.1 M [NBu_4][PF_6] CH_3CN solution. The Fc/Fc^+ couple was used as an internal standard and the voltammogram is referenced against this couple.

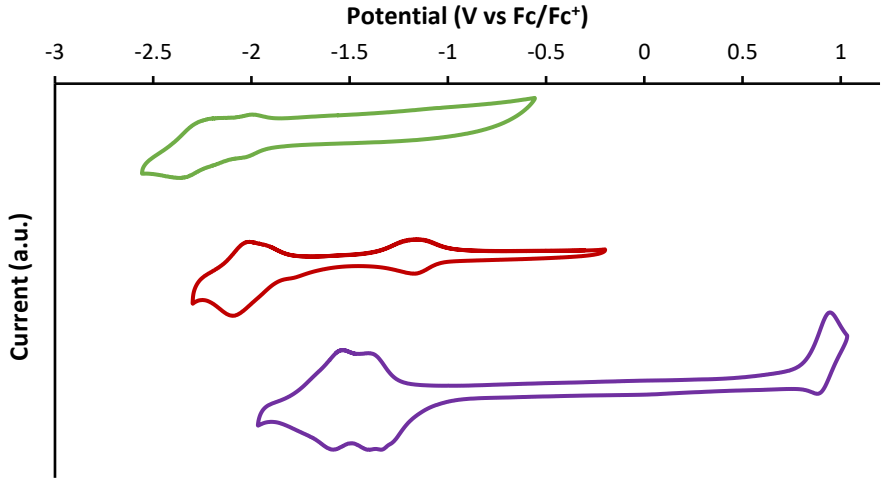

Figure A. 25 Voltammograms of [**107**$_2$($Zn(BF_4)_2$)] (green), [**107**$_2$($Co(NO_3)_2$)] (red) and [**107**$_2$($FeCl_2$)] (purple) under N_2 at 100 mV/s, scanned in the negative direction in 0.1 M [NBu_4][PF_6] CH_3CN solution. The Fc^+/Fc couple was used as an internal standard.

Table A. 1 Crystal and refinement parameters for structures of **111** and **112**.

Identification code	TCD1415 (**111**)	HLD058a_1 (**112**)
Empirical formula	$C_{21}H_{16}N_4$	$C_{33}H_{19}N_5O_4$
Formula weight	324.38	549.53
Temperature/K	100(2)	100.0
Crystal system	orthorhombic	monoclinic
Space group	$Pca2_1$	$P2_1/c$
a/Å	11.3168(8)	17.2408(17)
b/Å	17.3318(14)	6.8189(8)
c/Å	7.9224(6)	21.288(2)
α/°	90	90
β/°	90	90.835(7)
γ/°	90	90
Volume/Å^3	1553.9(2)	2502.4(4)
Z	4	4
ρ_{calc}g/cm^3	1.387	1.459
μ/mm^{-1}	0.085	0.809
F(000)	680.0	1136.0
Crystal size/mm^3	0.202 × 0.137 × 0.108	0.33 × 0.05 × 0.03
Radiation	MoKα (λ = 0.71073)	Cu Kα (λ = 1.54178)
2Θ range for data collection/°	5.922 to 52.902	5.126 to 125.418
Index ranges	$-14 \leq h \leq 14$, $-21 \leq k \leq 21$, $-9 \leq l \leq 9$	$-19 \leq h \leq 19$, $-7 \leq k \leq 7$, $-23 \leq l \leq 24$
Reflections collected	20838	33300
Independent reflections	3191 [R_{int} = 0.1411, R_{sigma} = 0.0682]	3995 [R_{int} = 0.0890, R_{sigma} = 0.0657]
Data/restraints/parameters	3191/3/235	3995/0/407
Goodness-of-fit on F^2	1.041	1.086
Final R indexes [I>=2σ (I)]	R_1 = 0.0507, wR_2 = 0.0894	R_1 = 0.0612, wR_2 = 0.1635
Final R indexes [all data]	R_1 = 0.0952, wR_2 = 0.1051	R_1 = 0.0792, wR_2 = 0.1753
Largest diff. peak/hole / e Å^{-3}	0.19/-0.21	0.22/-0.25
Flack parameter	-3.5(10)	

Data to support Chapter 3

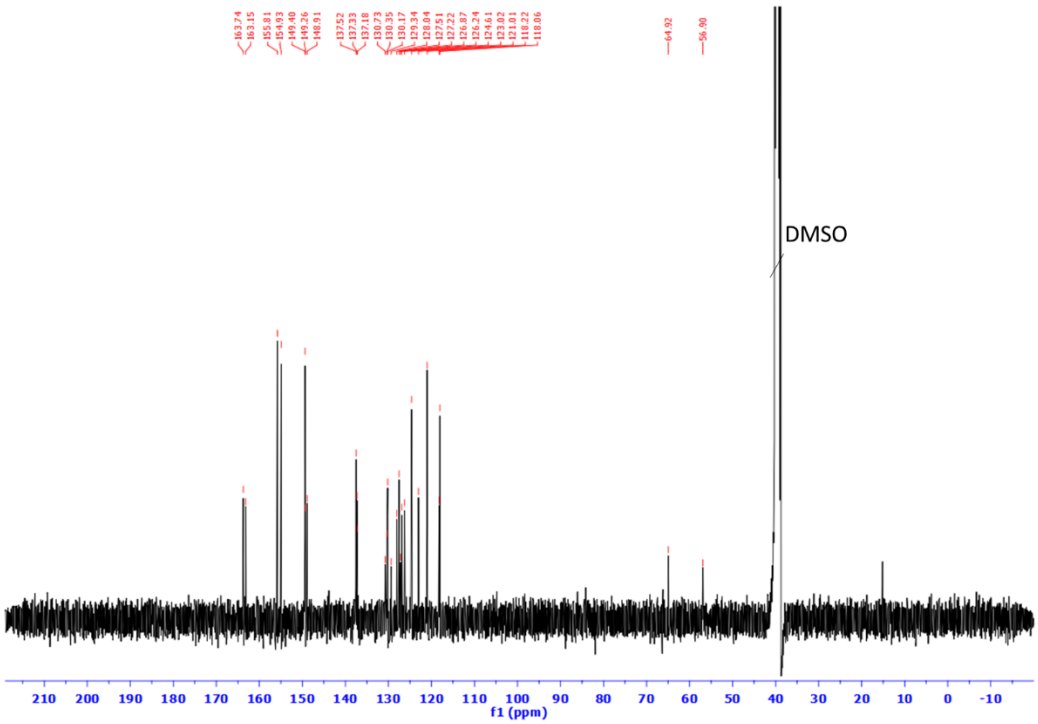

Figure A. 26 $^{13}C\{^{1}H\}$ NMR (DMSO-d_6, 151 MHz) of **130**.

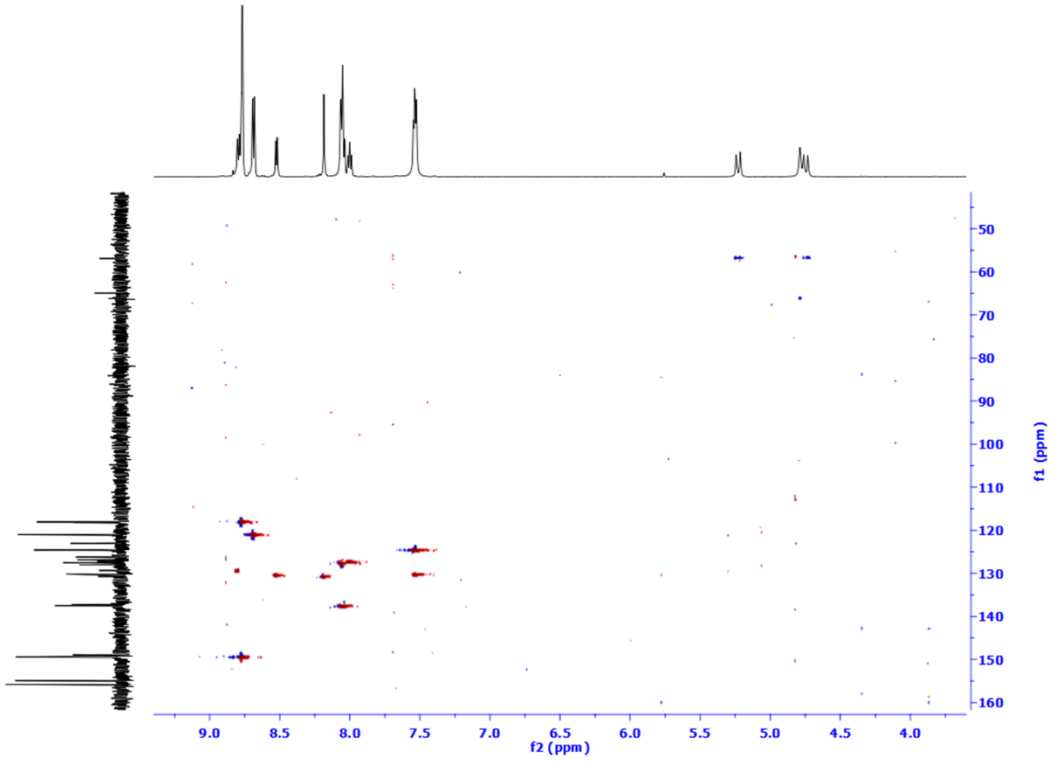

Figure A. 27 HSQC NMR(DMSO-d_6) of **130**.

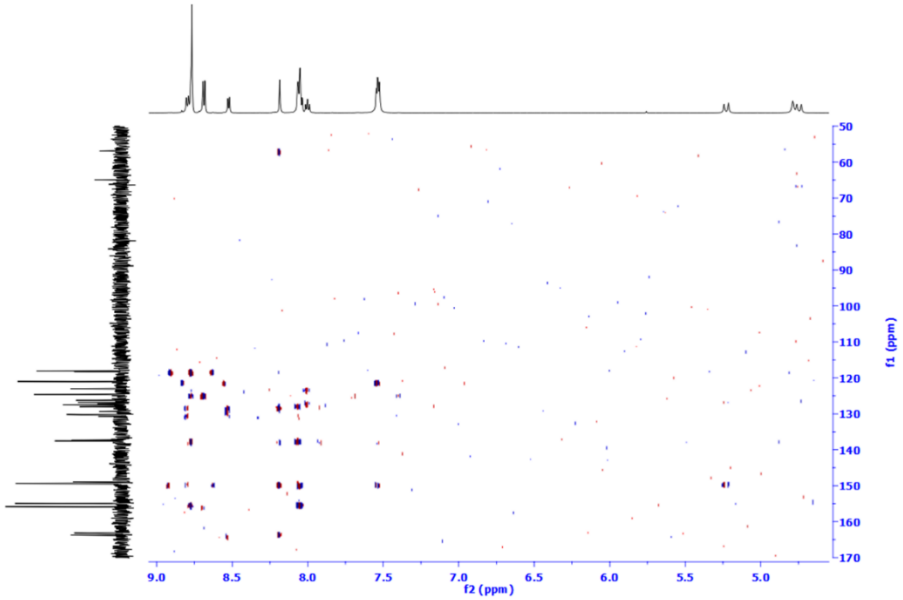

Figure A. 28 HMBC NMR (DMSO-d_6) of **130**.

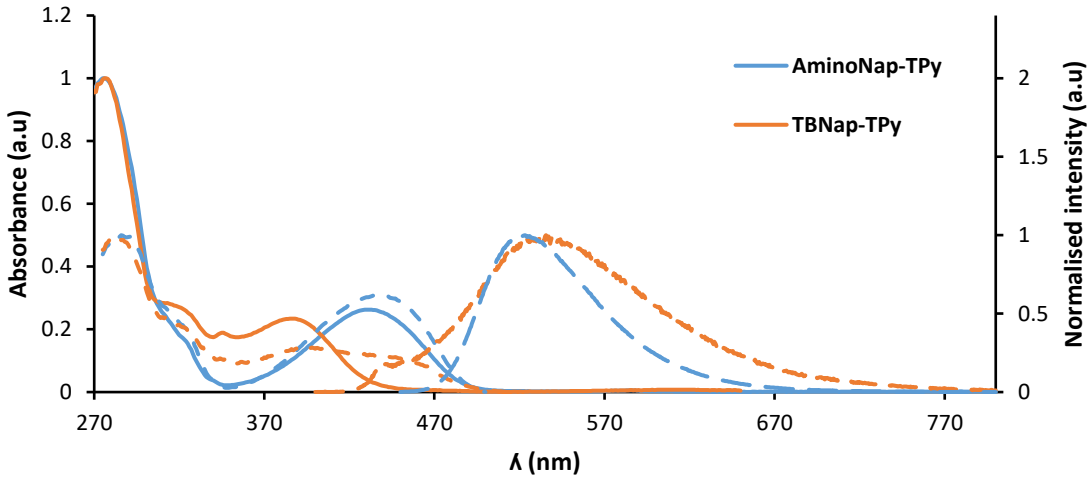

Figure A. 29 Normalised absorption (—), emission (– – –, λ_{exc} = 430 nm for **AminoNap-TPy** (**107**), λ_{exc} = 388 nm for **TBNap-TPy** (**130**) and excitation (- - -, λ_{em} = 520 nm for **AminoNap-TPy** (**107**), λ_{em} = 540 nm for **TBNap-TPy** (**130**) in DMF.

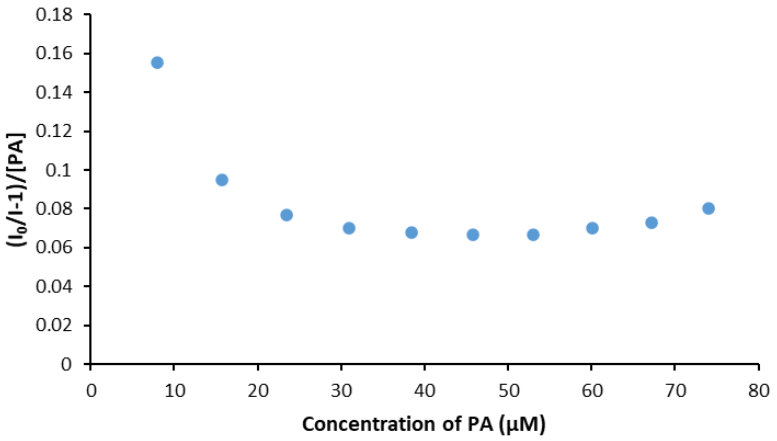

Figure A. 30 (I_0/I-1)/[PA] against the concentration of PA for the change of intensity of **130**.

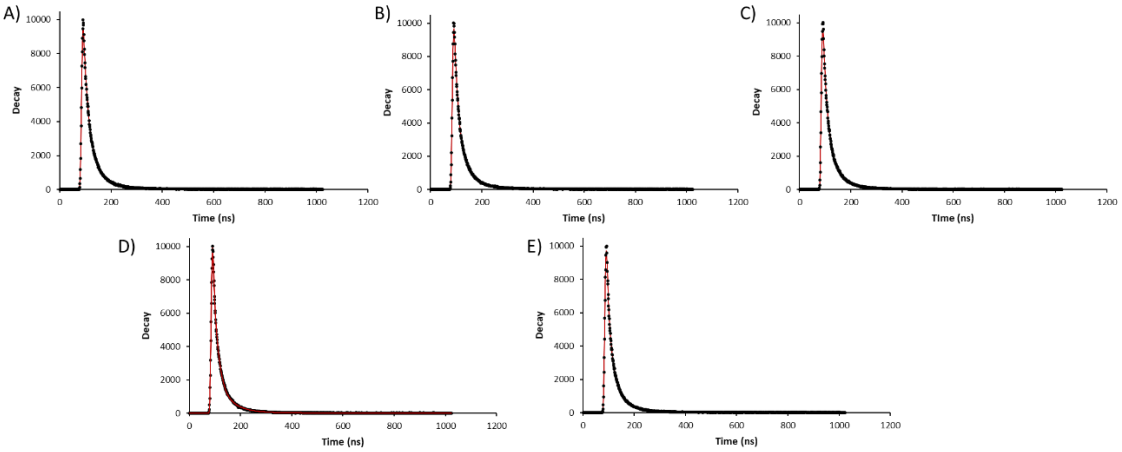

Figure A. 31 Luminescence lifetime decay (•) and fit (—) to a bi-exponential decay of **130** in the presence of A) 0 µM, B) 23.4 µM,, C) 45.8 µM, D) 60.2 µM, and E) 74.1 µM.

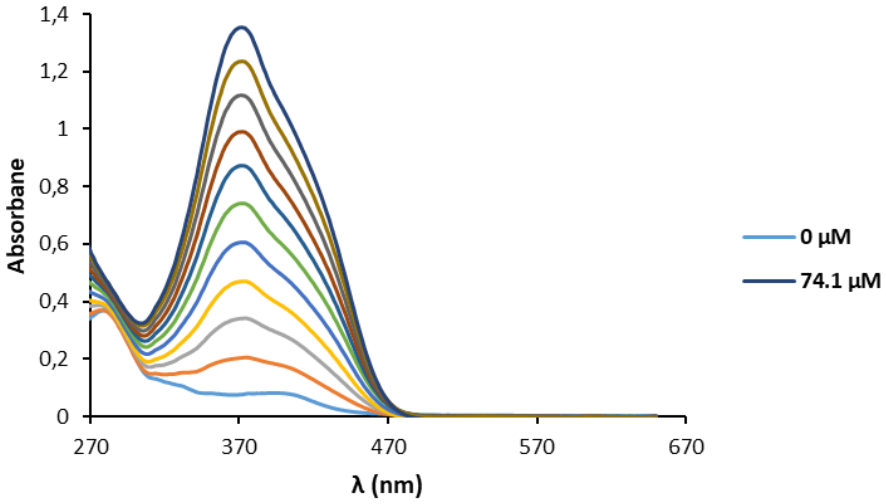

Figure A. 32 The absorption spectra of **130** upon the addition of PA.

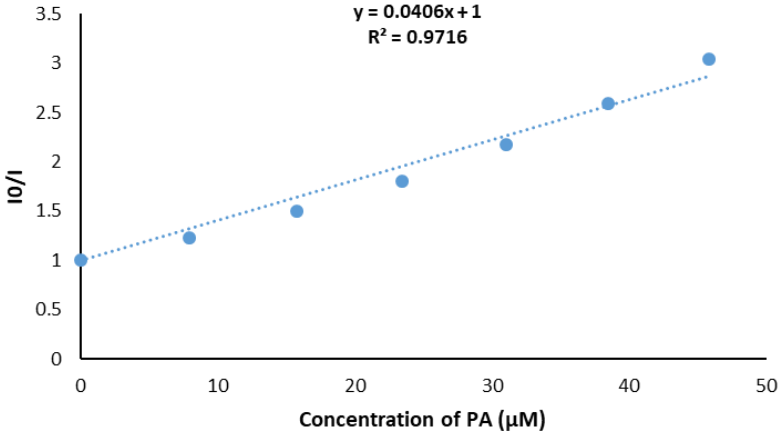

Figure A. 33 Linear fitting of the Stern-Volmer plots for the quenching of **130** in presence of low concentrations of PA

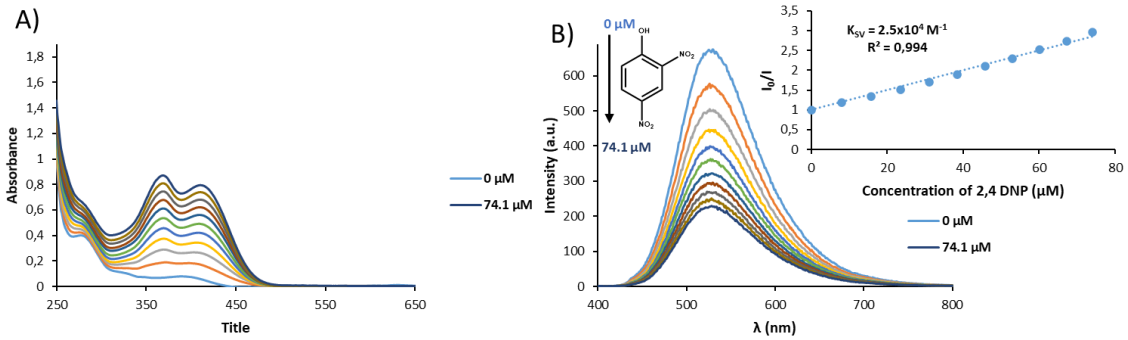

Figure A. 34 Changes in A) absorption and B) fluorescence spectra of **130** upon addition of 2,4-DNP in DMSO:H_2O (70:30) and insert: the corresponding Stern-Volmer plot.

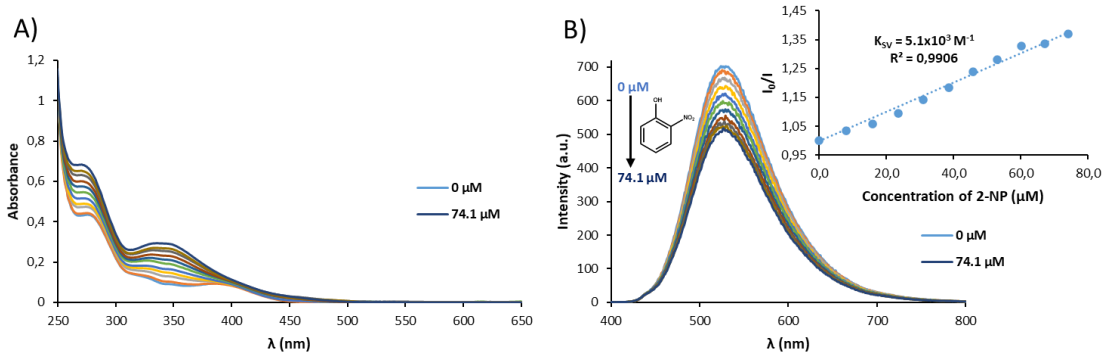

Figure A. 35 Changes in A) absorption and B) fluorescence spectra of **130** upon addition of 2-NP in DMSO:H_2O (70:30) and insert: the corresponding Stern-Volmer plot.

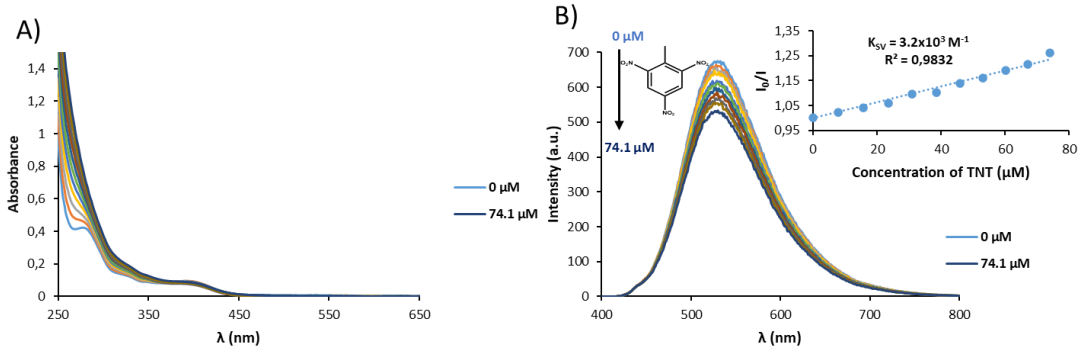

Figure A. 36 Changes in A) absorption and B) fluorescence spectra of **130** upon addition of TNT in DMSO:H_2O (70:30) and insert: the corresponding Stern-Volmer plot.

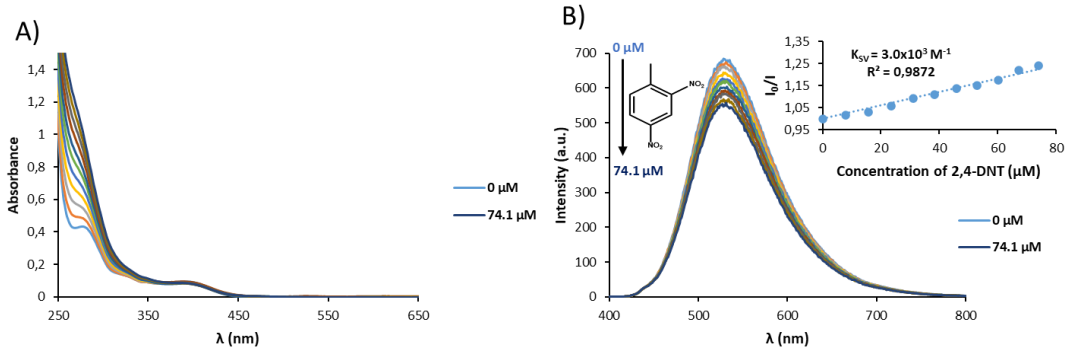

Figure A. 37 Changes in A) absorption and B) fluorescence spectra of **130** upon addition of 2,4-DNT in DMSO:H_2O (70:30) and insert: the corresponding Stern-Volmer plot.

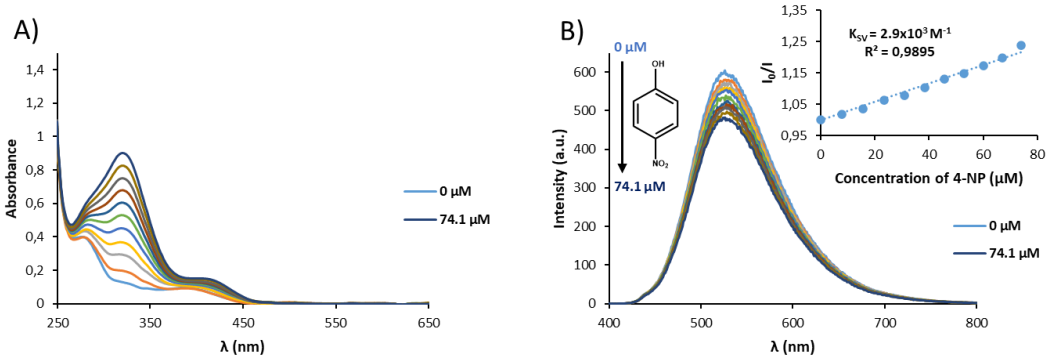

Figure A. 38 Changes in A) absorption and B) fluorescence spectra of **130** upon addition of 4-NP in DMSO:H_2O (70:30) and insert: the corresponding Stern-Volmer plot.

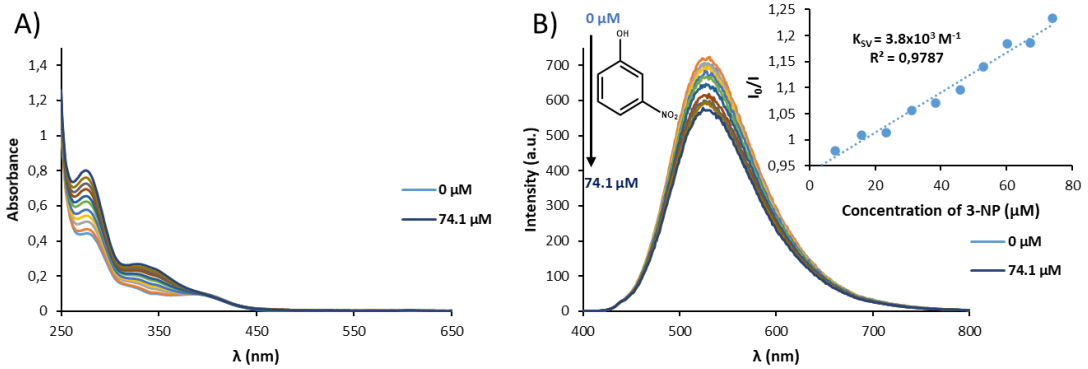

Figure A. 39 Changes in A) absorption and B) fluorescence spectra of **130** upon addition of 3-NP in DMSO:H_2O (70:30) and insert: the corresponding Stern-Volmer plot.

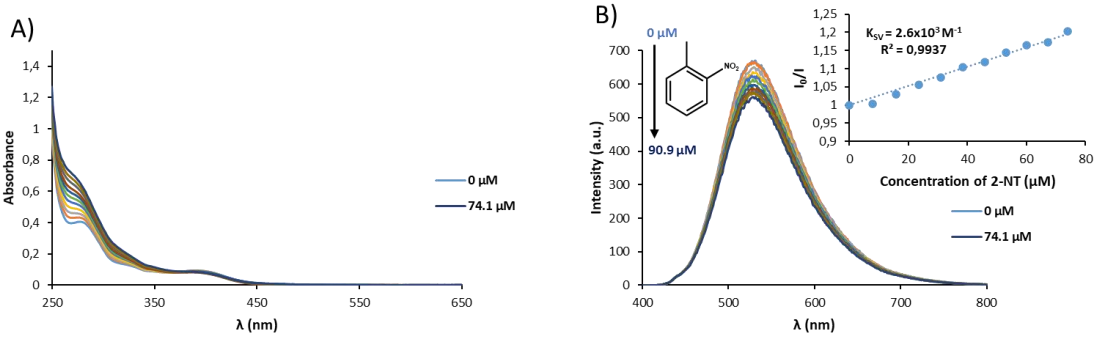

Figure A. 40 Changes in A) absorption and B) fluorescence spectra of **130** upon addition of 2-NT in DMSO:H_2O (70:30) and insert: the corresponding Stern-Volmer plot.

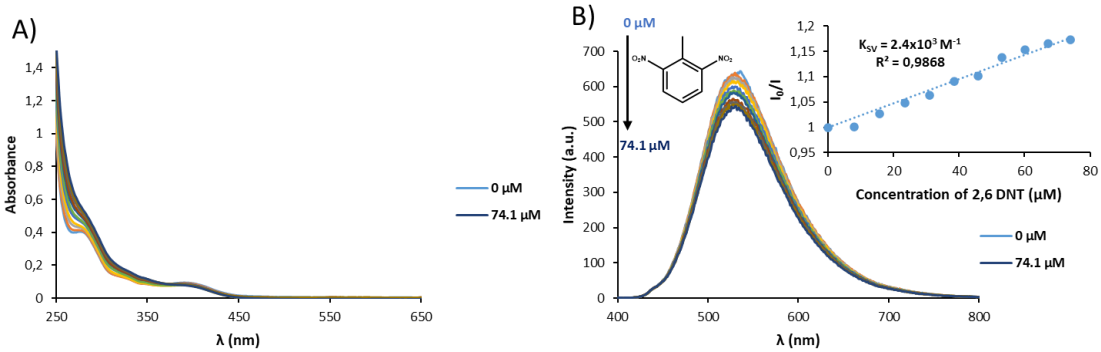

Figure A. 41 Changes in A) absorption and B) fluorescence spectra of **130** upon addition of 2,6-DNT in DMSO:H_2O (70:30) and insert: the corresponding Stern-Volmer plot.

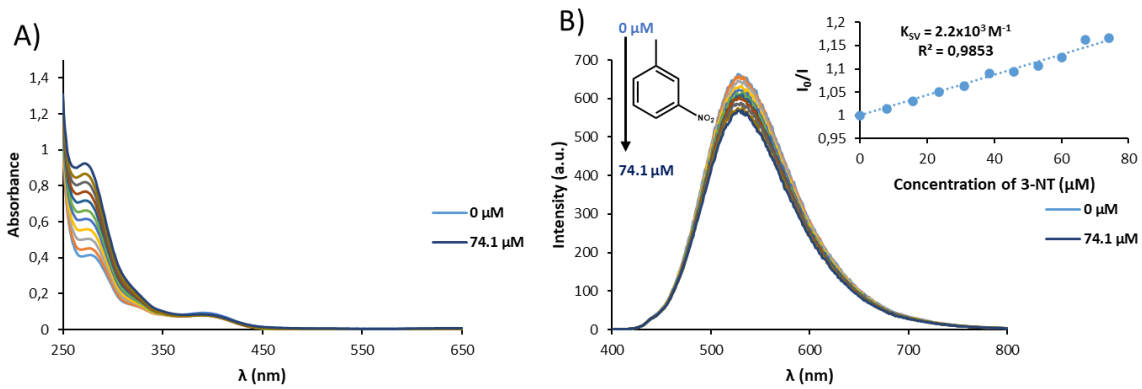

Figure A. 42 Changes in A) absorption and B) fluorescence spectra of **130** upon addition of 3-NT in DMSO:H_2O (70:30) and insert: the corresponding Stern-Volmer plot.

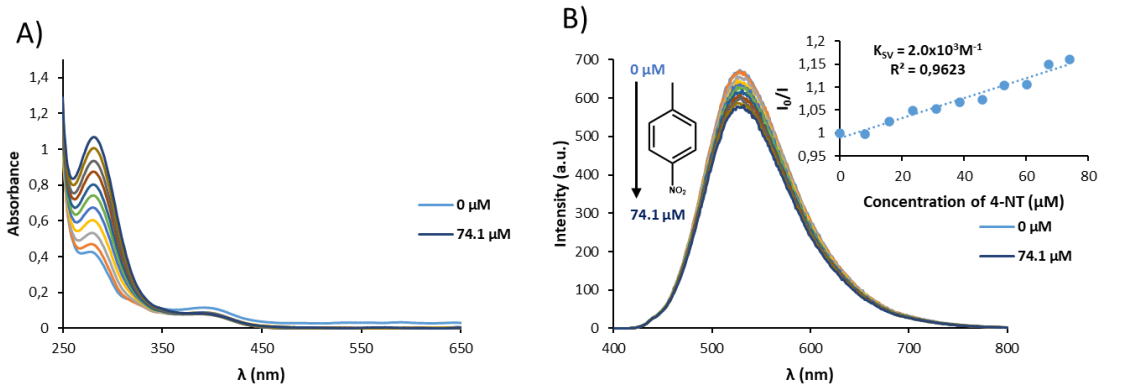

Figure A. 43 Changes in A) absorption and B) fluorescence spectra of **130** upon addition of 4-NT in DMSO:H_2O (70:30) and insert: the corresponding Stern-Volmer plot.

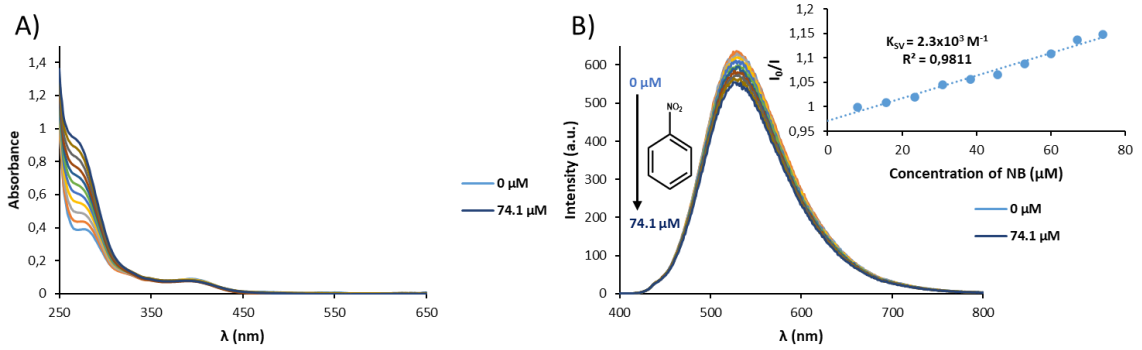

Figure A. 44 Changes in A) absorption and B) fluorescence spectra of **130** upon addition of NB in DMSO:H_2O (70:30) and insert: the corresponding Stern-Volmer plot.

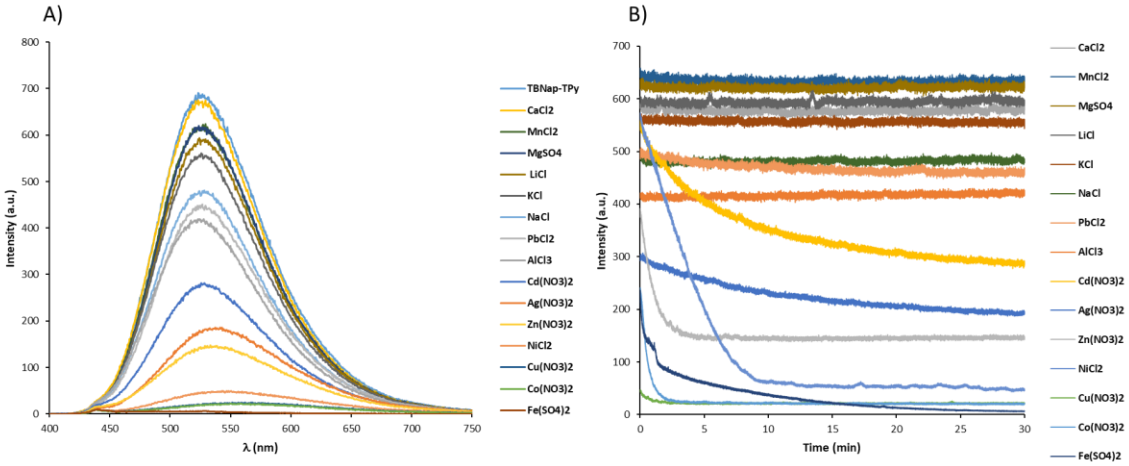

Figure A. 45 A) Fluorescence spectra (λ_{ex} = 388 nm) of **130** in presence of various ions in DMSO:H_2O (70%:30%) and B) Stability of the fluorescence intensity at 540 nm over 30 minutes in presence of various ions in DMSO:H_2O (70%:30%).

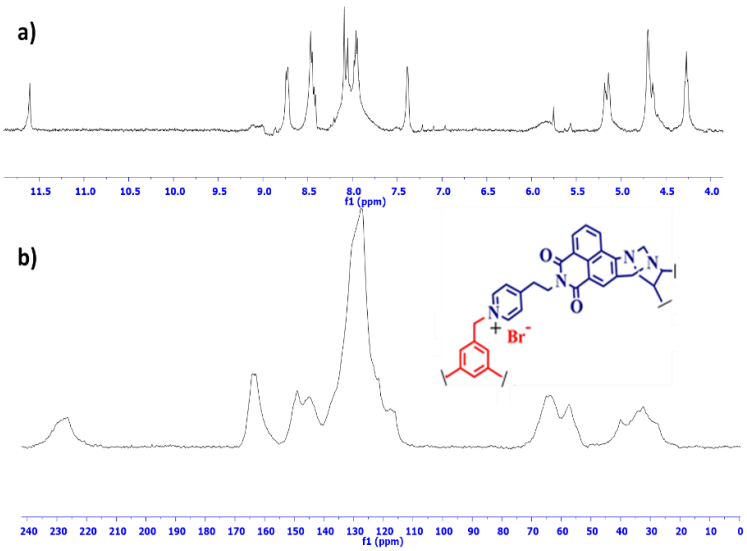

Figure A. 46 a) ^{1}H NMR spectra (in DMSO-d_6, 400 MHz) and b) solid-state CP-MAS ^{13}C-NMR (800 MHz) spectra of polymer **131**.

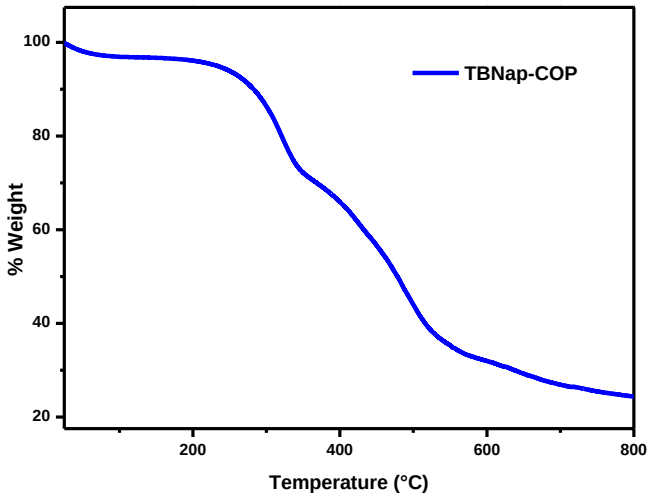

Figure A. 47 Thermogravimetric analysis of as-synthesised **TBNap-COP** (**131**) measured under N_2.

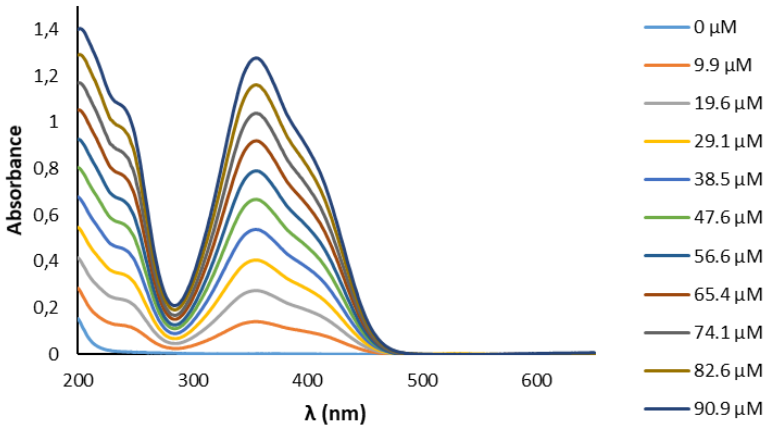

Figure A. 48 Absorption of **131** dispersed in water in the presence of PA (0- 90.9µM).

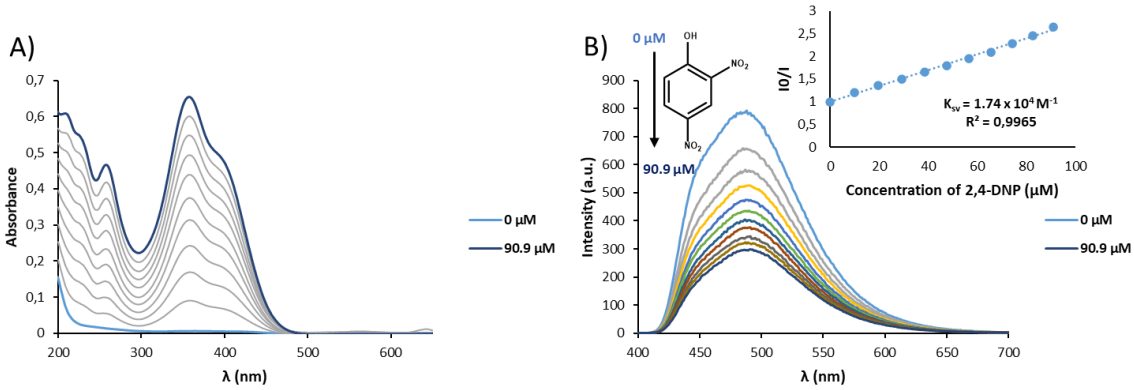

Figure A. 49 Changes in A) absorption and B) fluorescence spectra of **131** upon addition of 2,4-DNP in DMSO:H_2O (70:30) and insert: the corresponding Stern-Volmer plot.

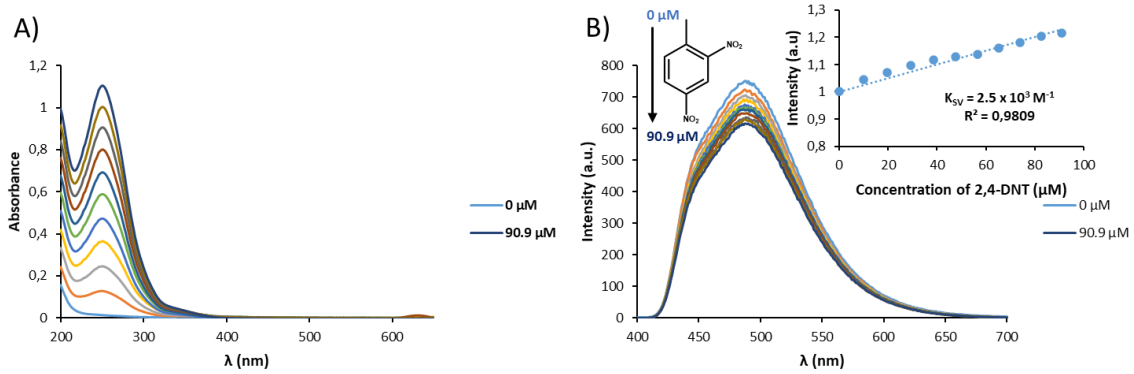

Figure A. 50 Changes in A) absorption and B) fluorescence spectra of **131** upon addition of 2,4-DNT in DMSO:H_2O (70:30) and insert: the corresponding Stern-Volmer plot.

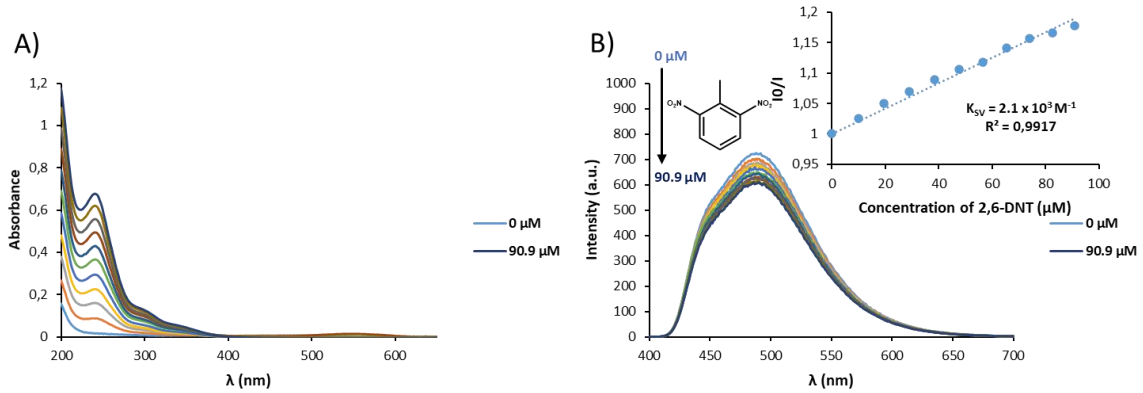

Figure A. 51 Changes in A) absorption and B) fluorescence spectra of **131** upon addition of 2,6-DNT in DMSO:H_2O (70:30) and insert: the corresponding Stern-Volmer plot

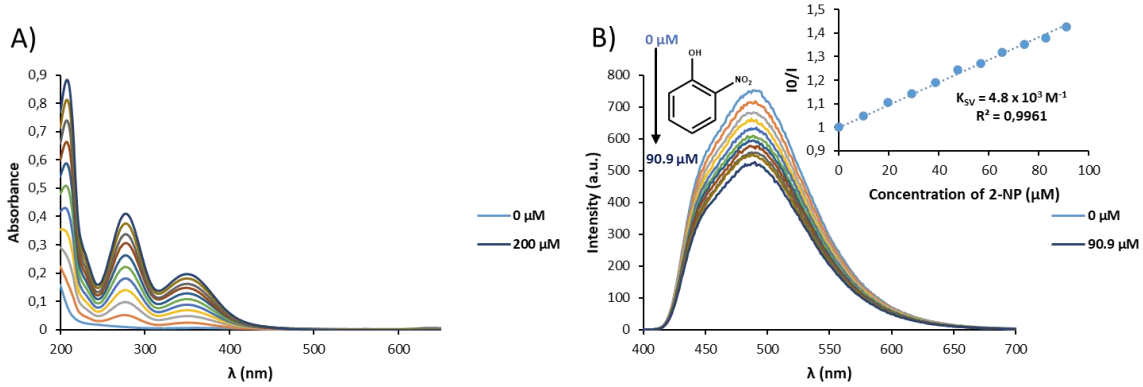

Figure A. 52 Changes in A) absorption and B) fluorescence spectra of **131** upon addition of 2-NP in DMSO:H_2O (70:30) and insert: the corresponding Stern-Volmer plot

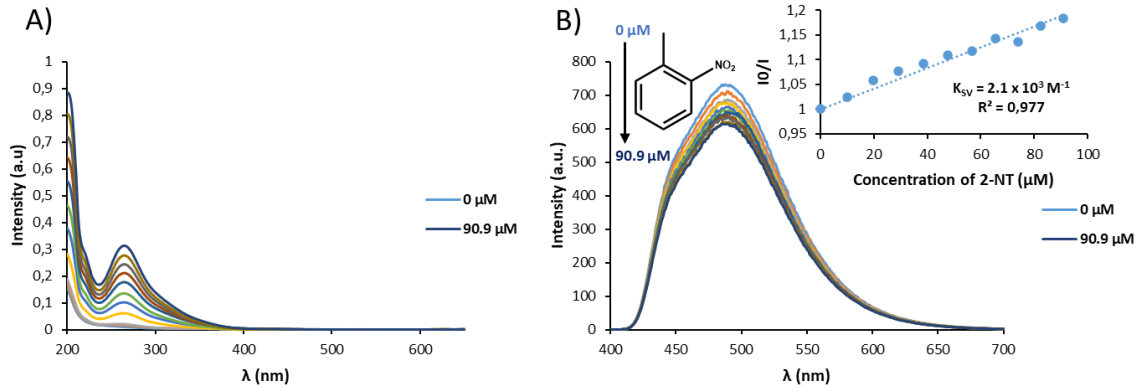

Figure A. 53 Changes in A) absorption and B) fluorescence spectra of **131** upon addition of 2-NT in DMSO:H_2O (70:30) and insert: the corresponding Stern-Volmer plot

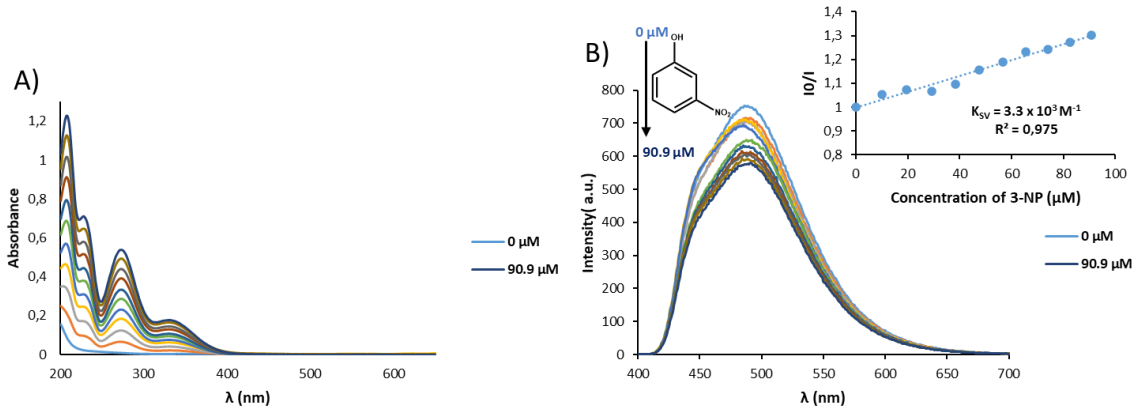

Figure A. 54 Changes in A) absorption and B) fluorescence spectra of **131** upon addition of 3-NP in DMSO:H_2O (70:30) and insert: the corresponding Stern-Volmer plot

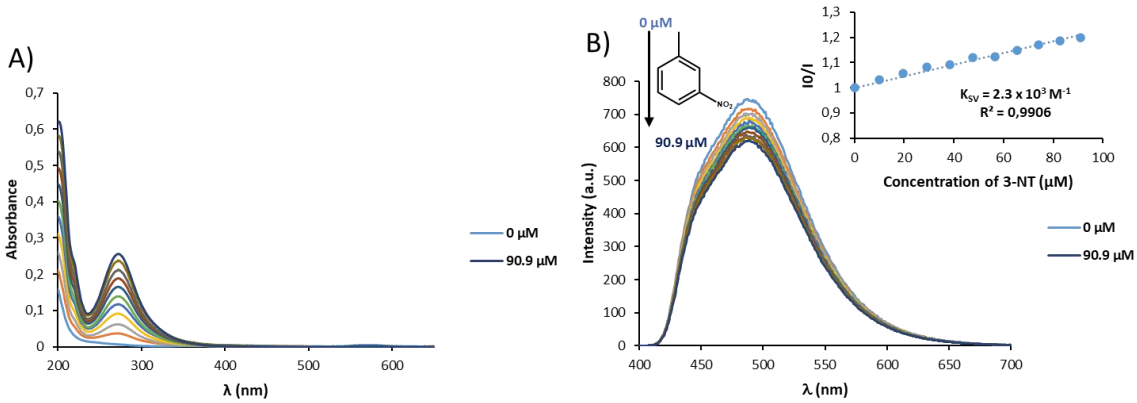

Figure A. 55 Changes in A) absorption and B) fluorescence spectra of **131** upon addition of 3-NT in DMSO:H_2O (70:30) and insert: the corresponding Stern-Volmer plot

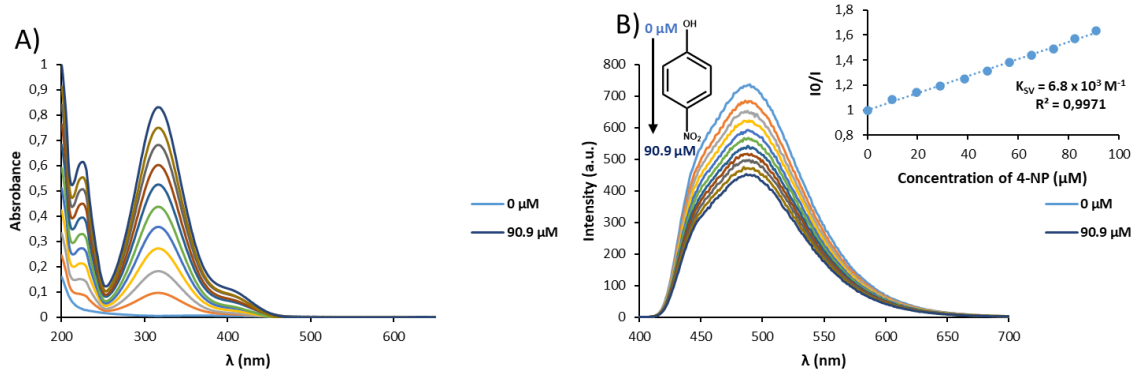

Figure A. 56 Changes in A) absorption and B) fluorescence spectra of **131** upon addition of 4-NP in DMSO:H_2O (70:30) and insert: the corresponding Stern-Volmer plot

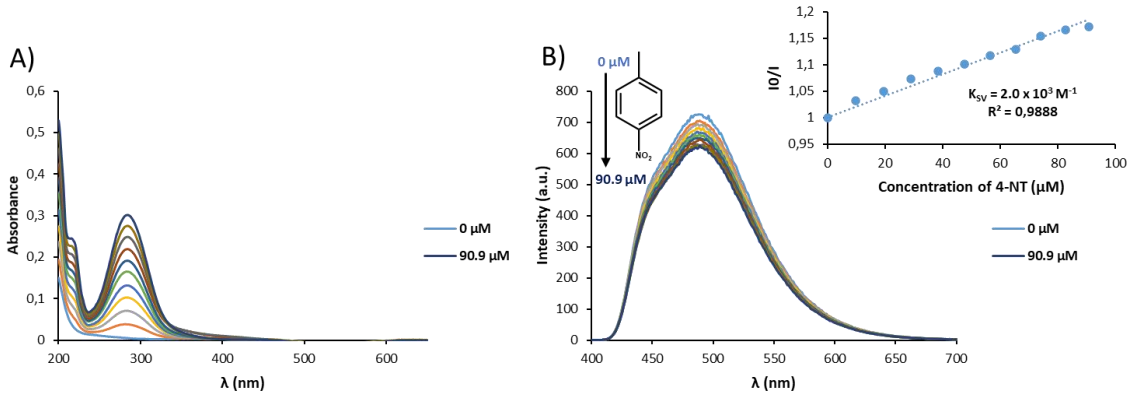

Figure A. 57 Changes in A) absorption and B) fluorescence spectra of **131** upon addition of 4-NT in DMSO:H_2O (70:30) and insert: the corresponding Stern-Volmer plot

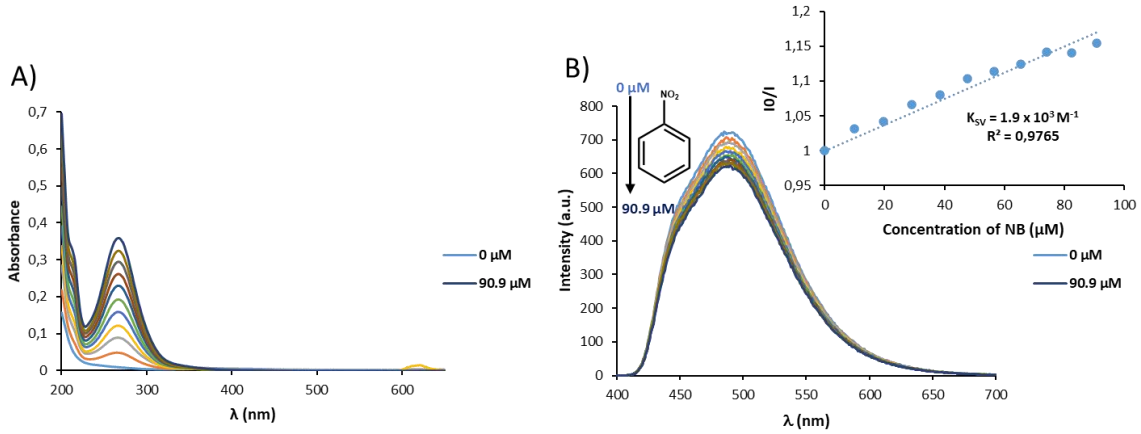

Figure A. 58 Changes in A) absorption and B) fluorescence spectra of **131** upon addition of NB in DMSO:H_2O (70:30) and insert: the corresponding Stern-Volmer plot

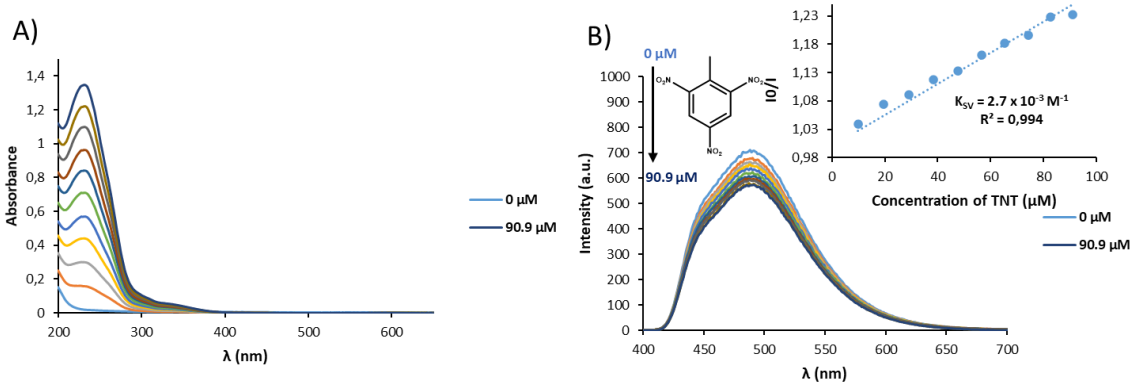

Figure A. 59 Changes in A) absorption and B) fluorescence spectra of **131** upon addition of TNT in DMSO:H_2O (70:30) and insert: the corresponding Stern-Volmer plot

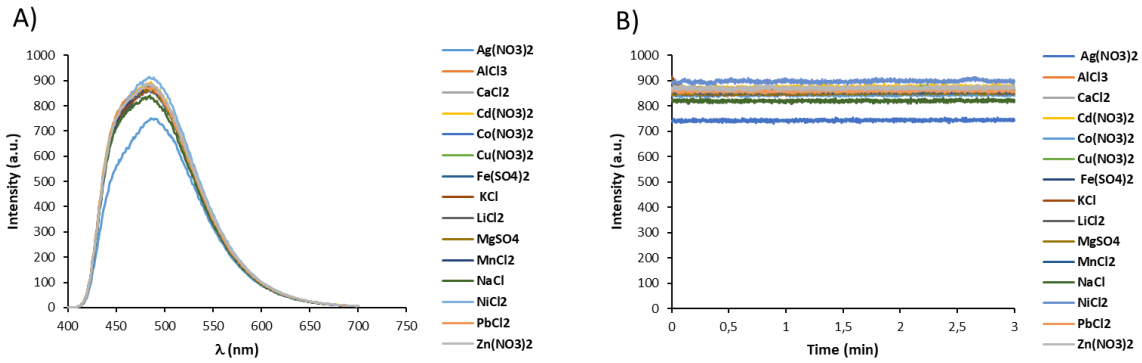

Figure A. 60 A) Fluorescence spectra (λ_{ex} = 370 nm) of **131** in presence of various ions H_2O and B) Stability of the fluorescence intensity at 490 nm over 30 minutes in presence of various ions in H_2O.

Table A. 2Calculations of IFE corrections for quenching of **131** by PA in water.

PA (µM)	A_{exc}	A_{em}	I_{obs}	I_{cor}	I_{cor}/I_{obs} (Correction factor)	QE observed (%)	QE corrected (%)
0	0.00262723	-0.0006124	717.28	718.95	1.00232236	0	0
9.9	0.12723678	-0.0018669	583.55	674.16	1.15527383	18.64	6.23
19.6	0.24932219	-0.0027291	483.95	642.83	1.32830121	32.53	10.59
29.1	0.37135878	-0.0004526	429.71	658.61	1.53268572	40.09	8.39
38.5	0.49208191	0.00015174	346.21	610.18	1.76245009	51.73	15.13
47.6	0.60843909	-0.0021552	289.34	581.49	2.00974947	59.66	19.12
56.6	0.72451133	-0.0019623	259.87	597.08	2.29760055	63.77	16.95
65.4	0.84227675	0.00044404	218.02	575.25	2.63852004	69.60	19.99
74.1	0.95255655	-0.0034949	188.04	560.77	2.98215904	73.78	22.00
82.6	1.06368828	0.00043002	162.45	553.06	3.40454556	77.35	23.07
90.9	1.17172909	0.00046459	141.82	546.82	3.85564322	80.23	23.94

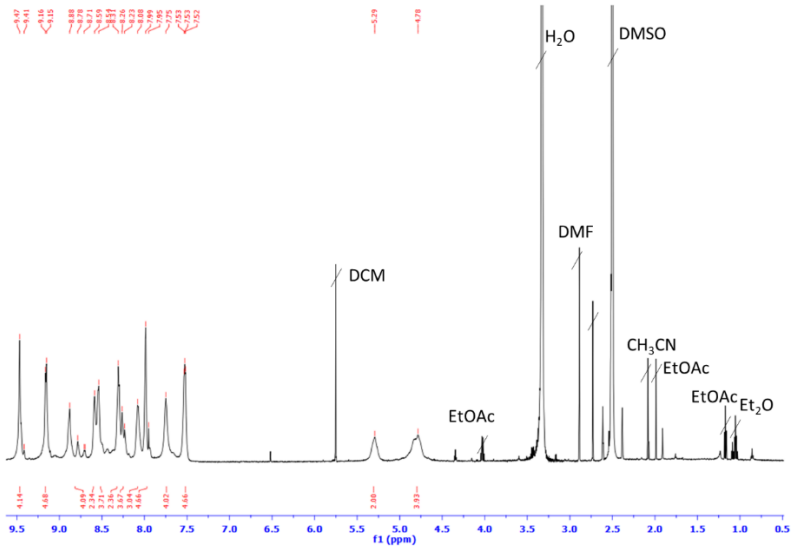

Figure A. 61 ^{1}H NMR (DMSO-d_6, 600 MHz) of [(**130**)$_2$Zn$(BF_4)_2$].

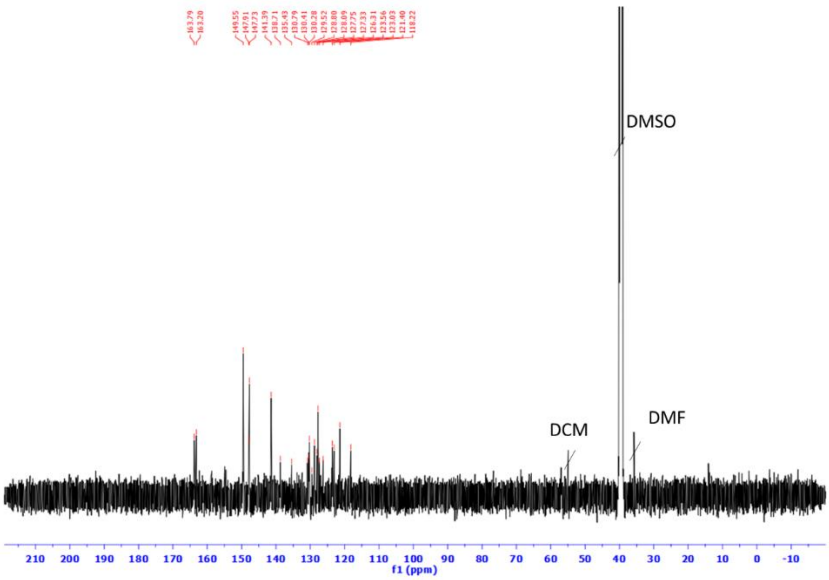

Figure A. 62 $^{13}C\{^{1}H\}$ NMR (DMSO-d_6, 151 MHz) of [(**130**)$_2$Zn$(BF_4)_2$].

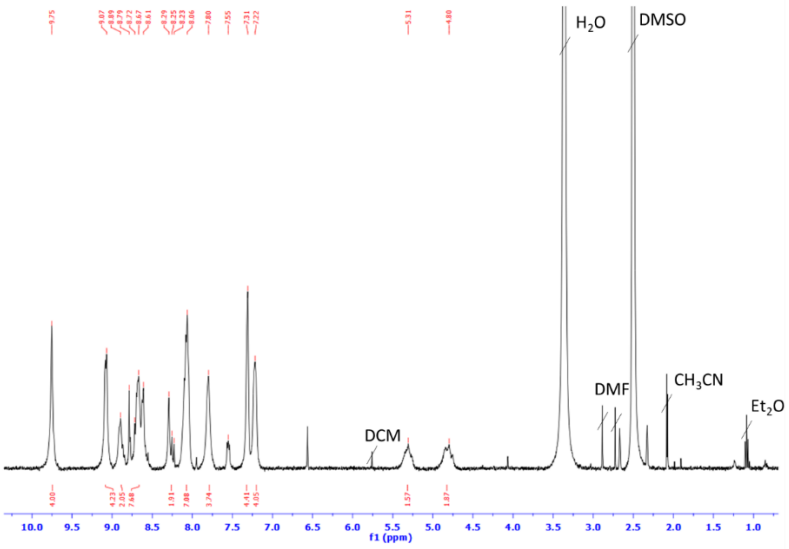

Figure A. 63 ^{1}H NMR (DMSO-d_6, 600 MHz) of [(**130**)$_2$Fe$(BF_4)_2$].

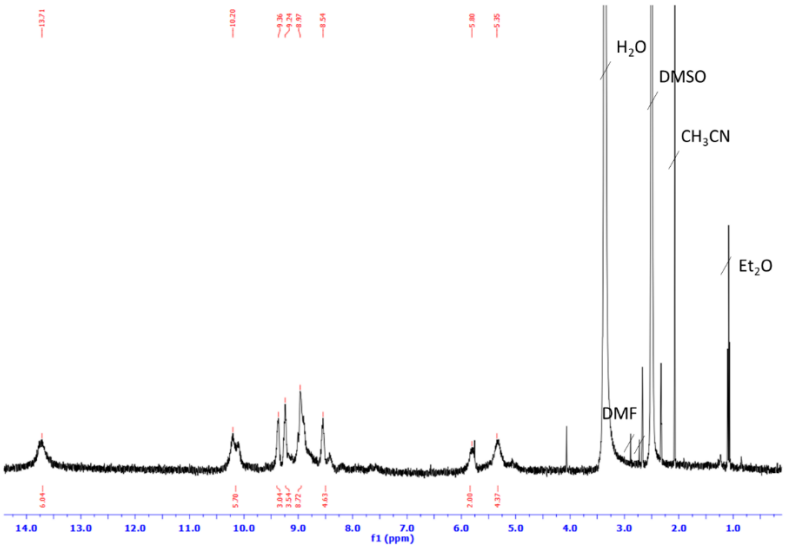

Figure A. 64 ^{1}H NMR (DMSO-d_6, 400 MHz) of [(**130**)$_2$Co$(BF_4)_2$].

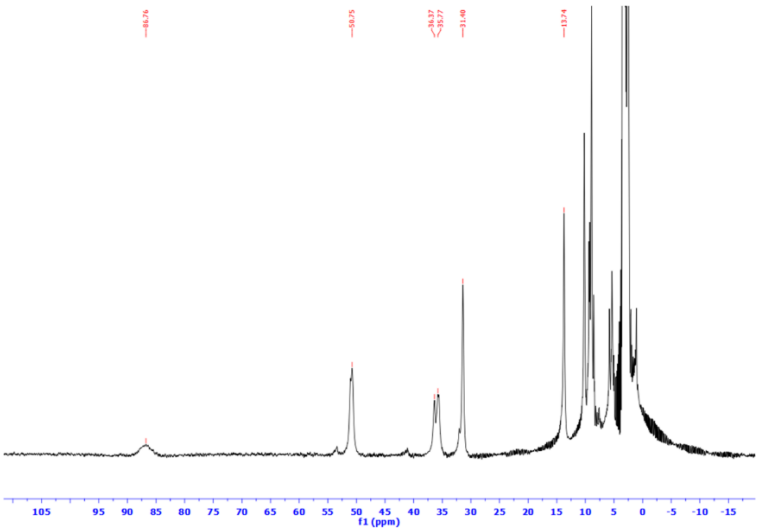

Figure A. 65 ^{1}H NMR (DMSO-d_6, 400 MHz) of [(**130**)$_2$Co(BF$_4$)$_2$] with a longer range.

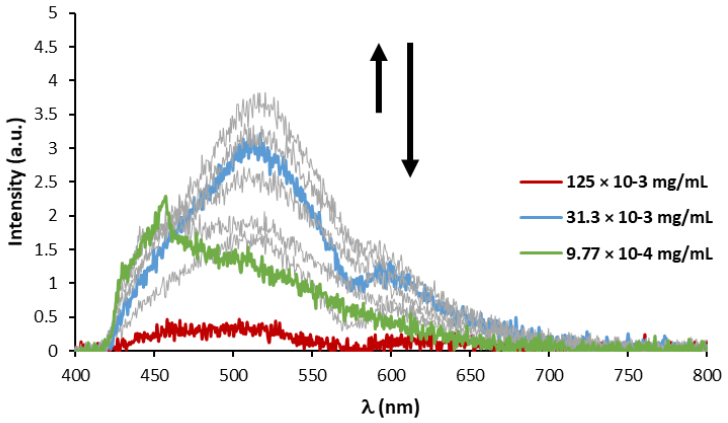

Figure A. 66 Changes in the emission (λ_{ex} = 380 nm) spectra of [(**130**)$_2$Fe(BF$_4$)$_2$] in DMF upon dilution.

Data to support Chapter 4

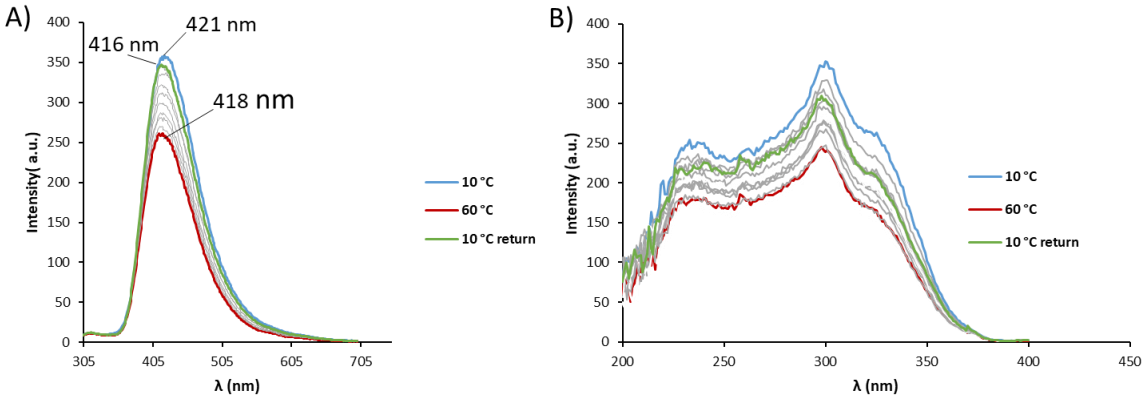

Figure A. 67 Changes in A) the fluorescence (λ_{ex} = 280 nm) and B) excitation (λ_{em} = 420 nm) spectra of **85** (c = 1.0 × 10^{-5} M) in MeOH in the function of the temperature.

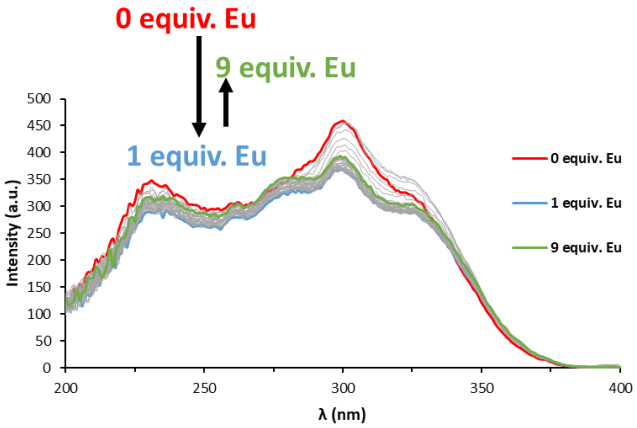

Figure A. 68 Changes in the excitation fluorescence spectrum (λ_{em}= 420 nm) of **85** (1 × 10^{-5} M) upon titrating with $EuCl_3$ (0→9 eq) in MeOH at 22 °C.

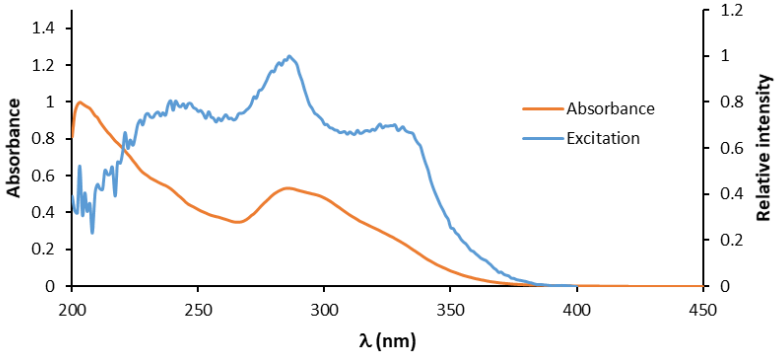

Figure A. 69 Comparison of absorption spectra (orange) and excitation spectra of the phosphorescence (λ_{em} = 618 nm) of **85** (1 × 10^{-5} M) after addition of 9 eq of Eu(III) ions in MeOH at 22 °C.

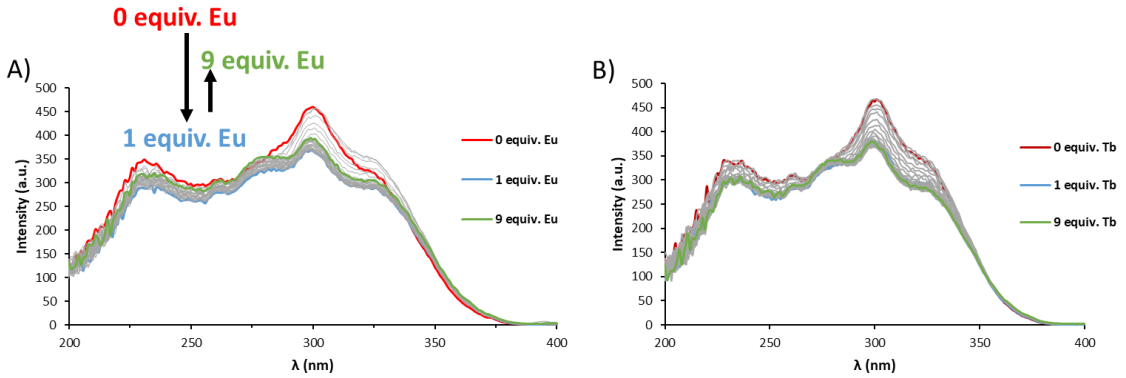

Figure A. 70 Changes in the excitation fluorescence spectra (λ_{em} = 420 nm) of **85** (1 × 10^{-5} M) upon titrating with A) $EuCl_3$ (0→9 eq) and B) $TbCl_3$ (0→9 eq) in MeOH at 22 °C.

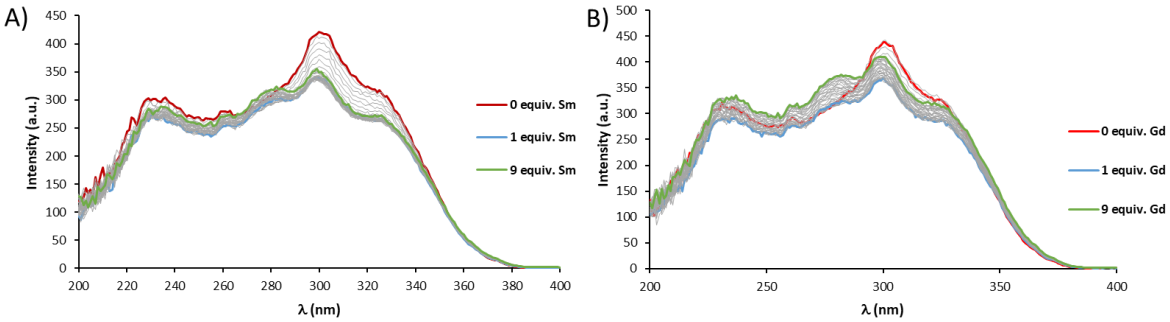

Figure A. 71 Changes in the excitation fluorescence spectra (λ_{em} = 420 nm) of **85** (1 × 10^{-5} M) upon titrating with A) $SmCl_3$ (0→9 eq) and B) $GdCl_3$ (0→9 eq) in MeOH at 22 °C.

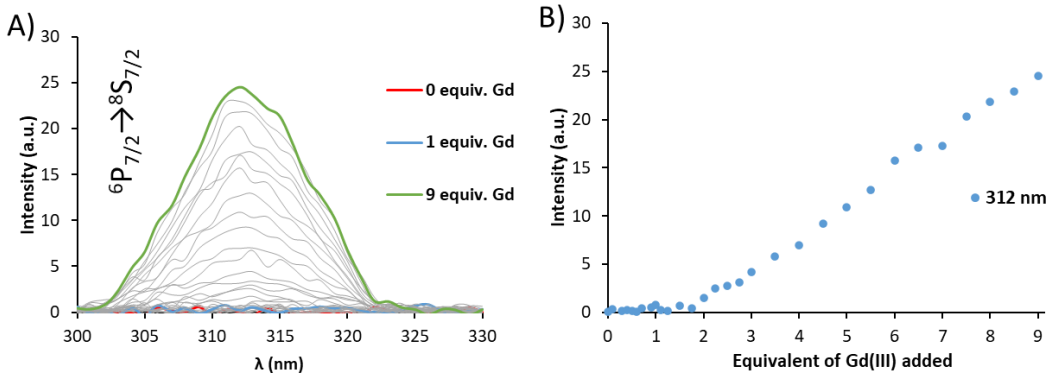

Figure A. 72 Changes in A) the Gd(III)-centred emission spectra of **85** (1 x 10^{-5} M) upon titrating with $GdCl_3$ (0→9 eq) in MeOH at 22 °C. B) Experimental Gd(III)-centred emission binding isotherms for the complexation of **85** at 312 nm upon addition of $GdCl_3$.

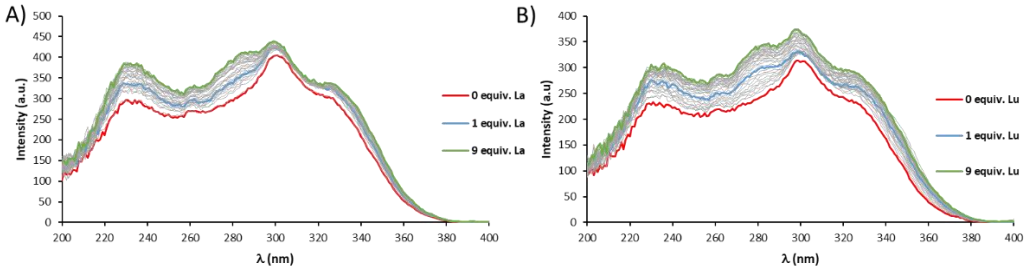

Figure A. 73 Changes in the excitation fluorescence spectra (λ_{em} = 420 nm) of **85** (1 × 10^{-5} M) upon titrating with A) $LaCl_3$ (0→9 eq) and B) $LuCl_3$ (0→9 eq) in MeOH at 22 °C.

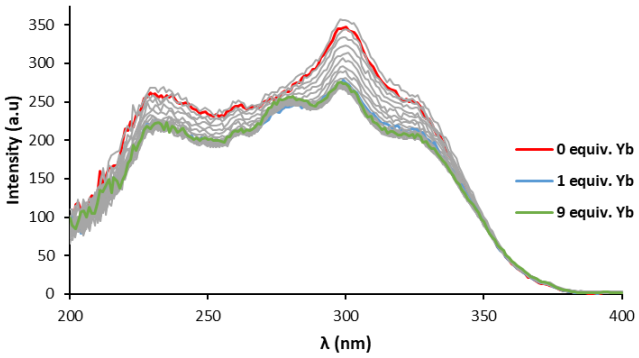

Figure A. 74 Changes in the excitation fluorescence spectra (λ_{em} = 420 nm) of **85** (1×10^{-5} M) upon titrating with $YbCl_3$ (0→9 eq) in MeOH at 22 °C.

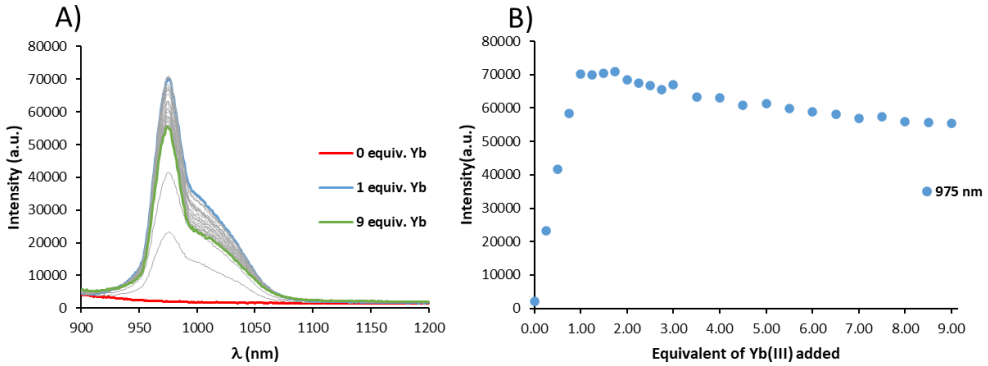

Figure A. 75 A)Change in Yb(III)-centred emission spectra of **85** (1×10^{-5} M) upon titrating with $YbCl_3$ (0→9 eq) in MeOH at 22 °C. Experimental Yb-centred emission binding isotherms for the complexation of **85** at various wavelengths upon addition of $YbCl_3$.

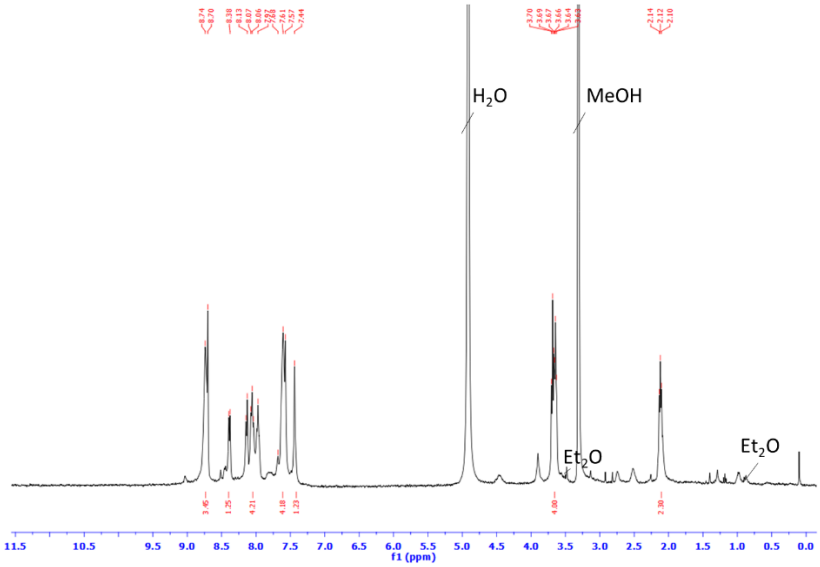

Figure A. 76 ^{1}H NMR (400 MHz, CD_3OD) of **85-EuCl$_3$** complex.

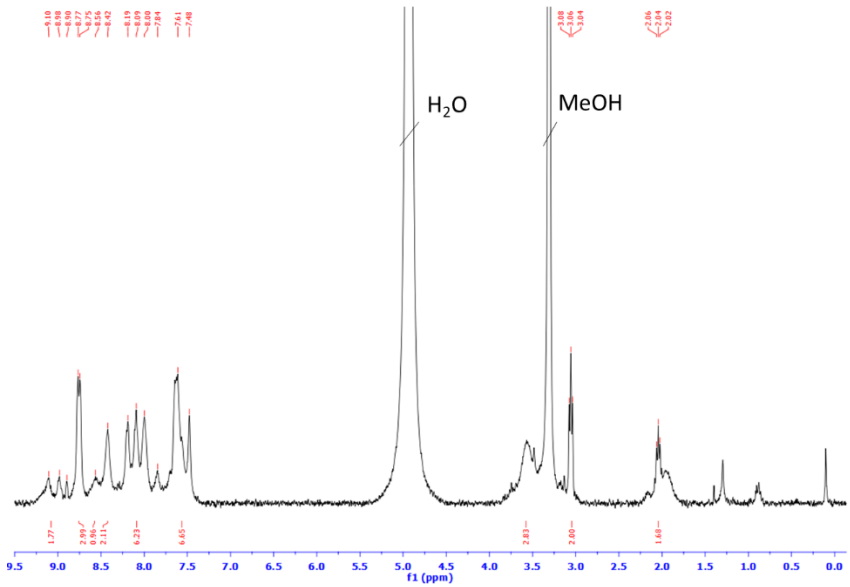

Figure A. 77 ^{1}H NMR (400 MHz, CD_3OD) of **85-TbCl$_3$** complex.

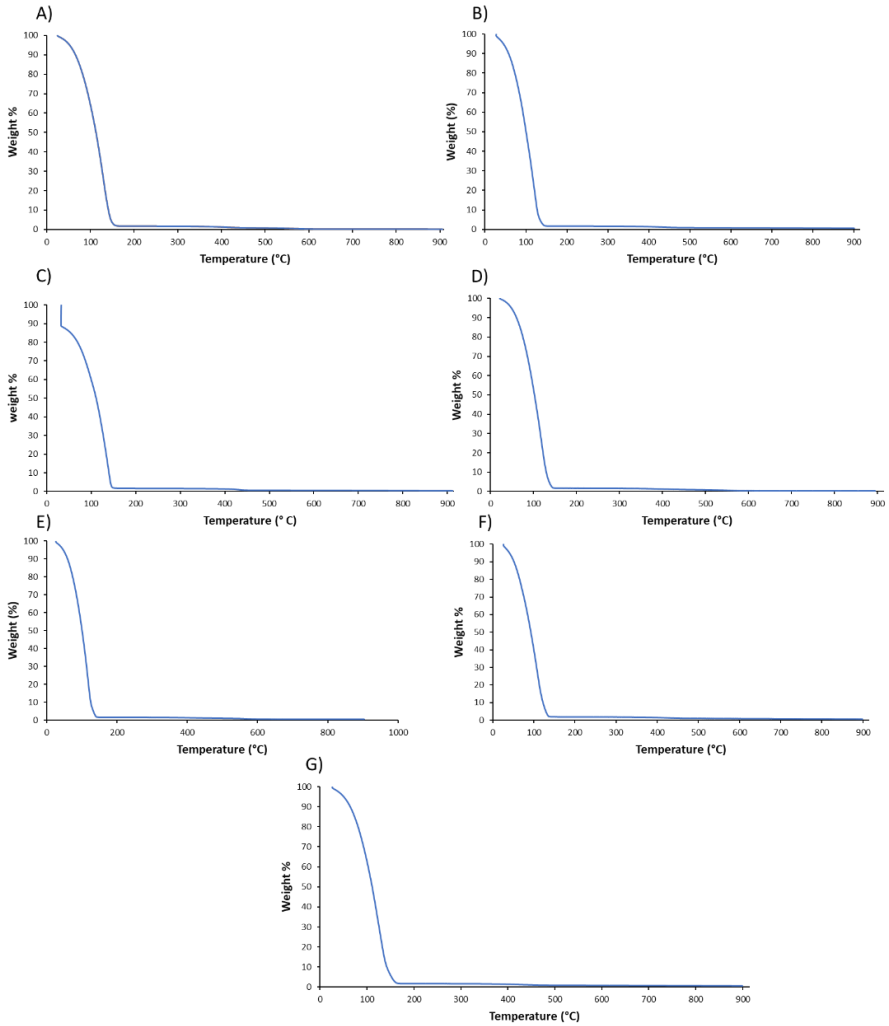

Figure A. 78 TGA thermograph of 0.6 *wt* % **85** gel modified with A) $LaCl_3$, B) $SmCl_3$, C) $EuCl_3$, D) $GdCl_3$, E) $TbCl_3$, F) $YbCl_3$ and G) $LuCl_3$ ($MeOH:H_2O$ (30:70)), a temperature ramp of 10 °C/min under nitrogen atmosphere.

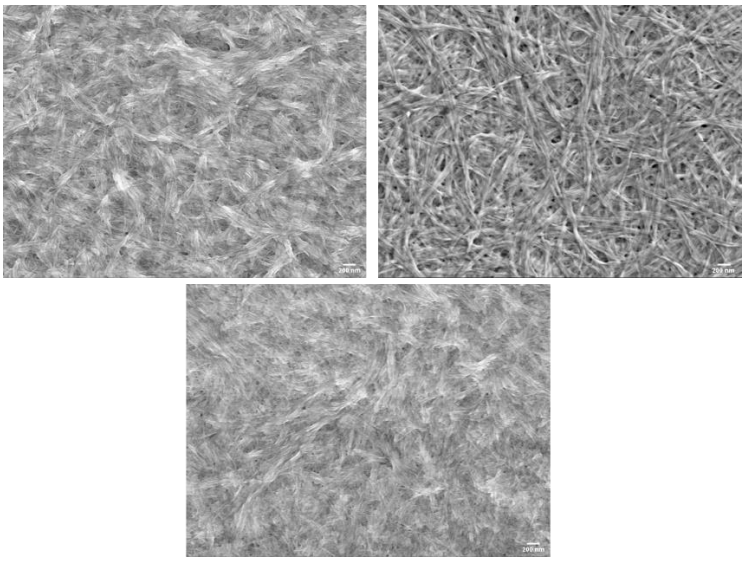

Figure A. 79 SEM images of xerogels modified with $LaCl_3$ at the same magnification (scale bar 200 nm).

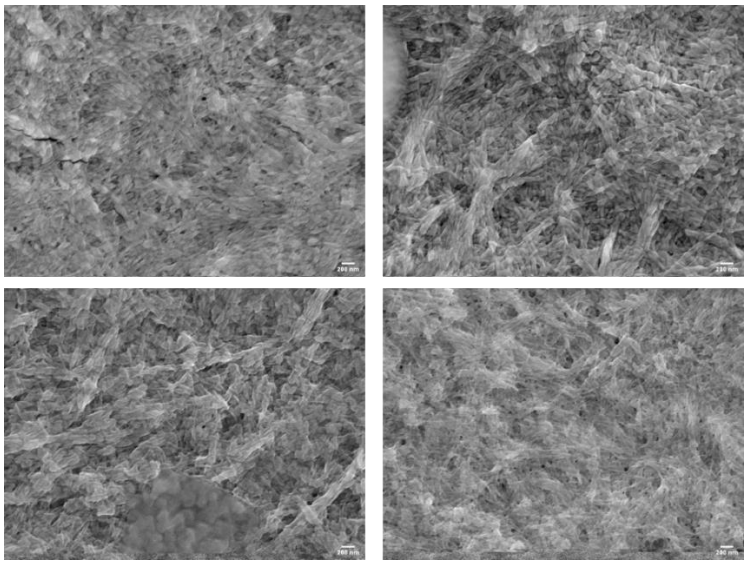

Figure A. 80 SEM images of xerogels modified with $SmCl_3$ at the same magnification (scale bar 200 nm).

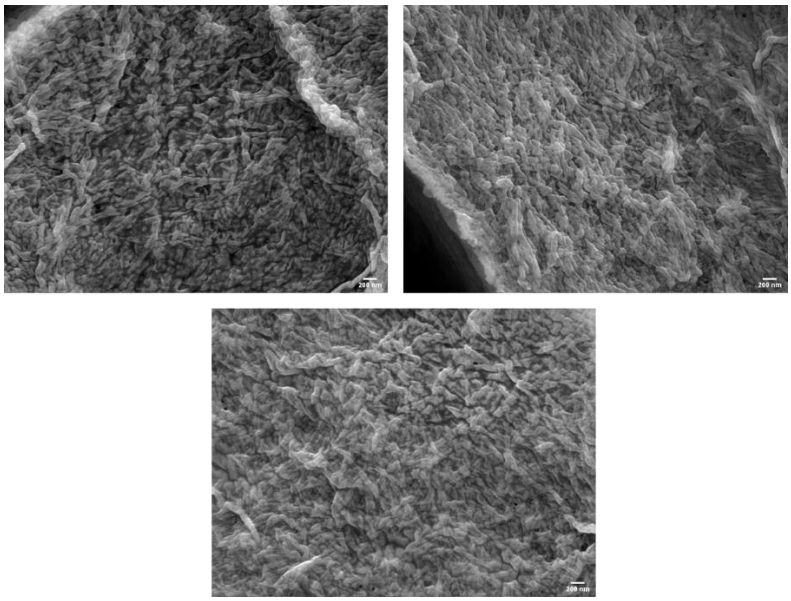

Figure A. 81 SEM images of xerogels modified with $EuCl_3$ at the same magnification (scale bar 200 nm).

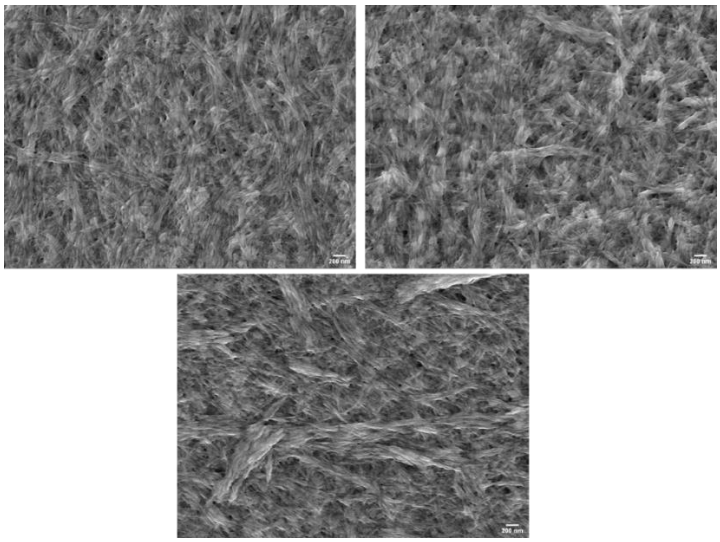

Figure A. 82 SEM images of xerogels modified with $GdCl_3$ at the same magnification (scale bar 200 nm).

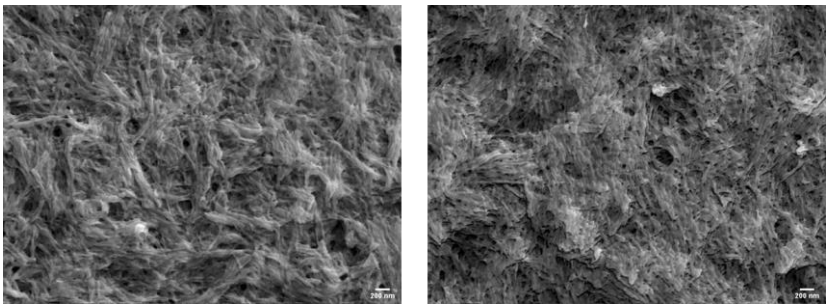

Figure A. 83 SEM images of xerogels modified with $TbCl_3$ at the same magnification (scale bar 200 nm).

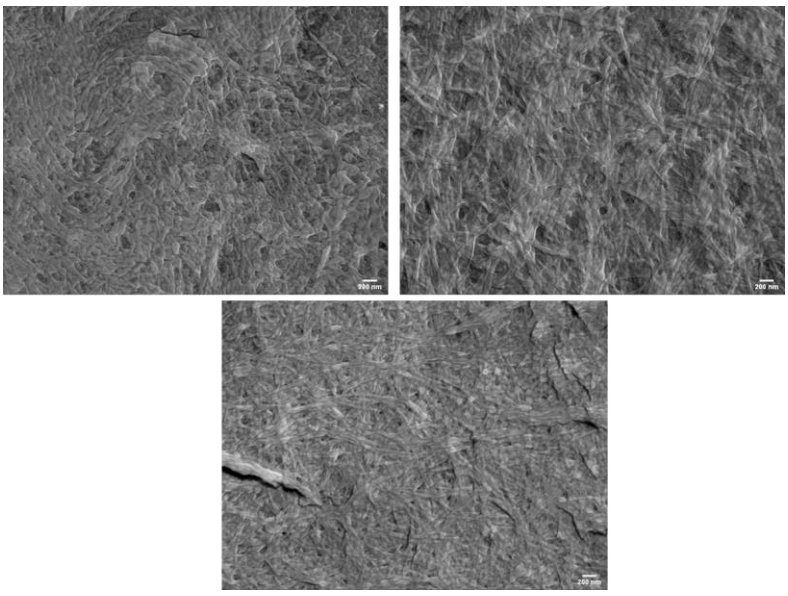

Figure A. 84 SEM images of xerogels modified with $YbCl_3$ at the same magnification (scale bar 200 nm).

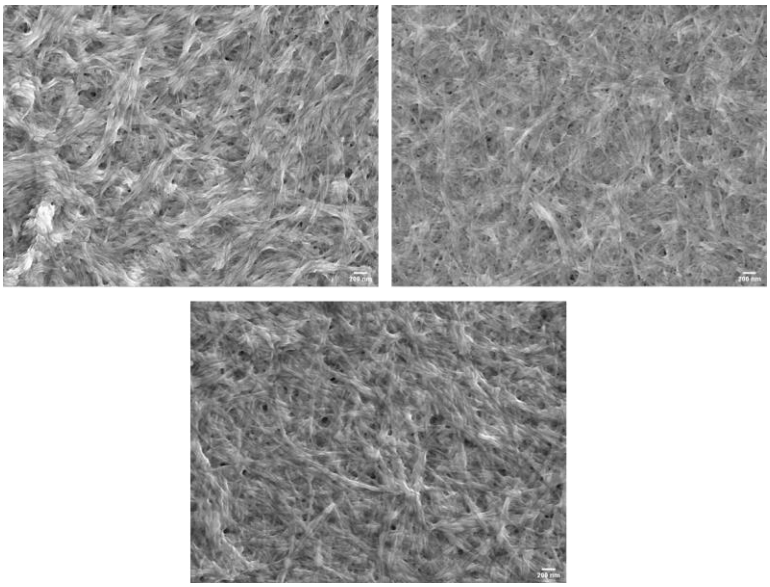

Figure A. 85 SEM images of xerogels modified with $LuCl_3$ at the same magnification (scale bar 200 nm).

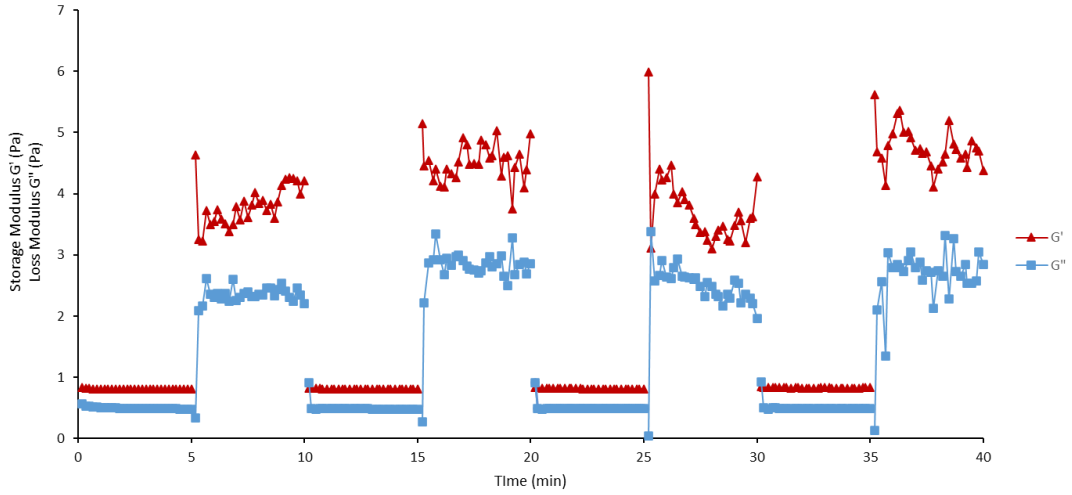

Figure A. 86 Recovery test for 0.3 wt % gel with alternating strain amplitudes of 20% and 0.1% at f = 1 Hz.

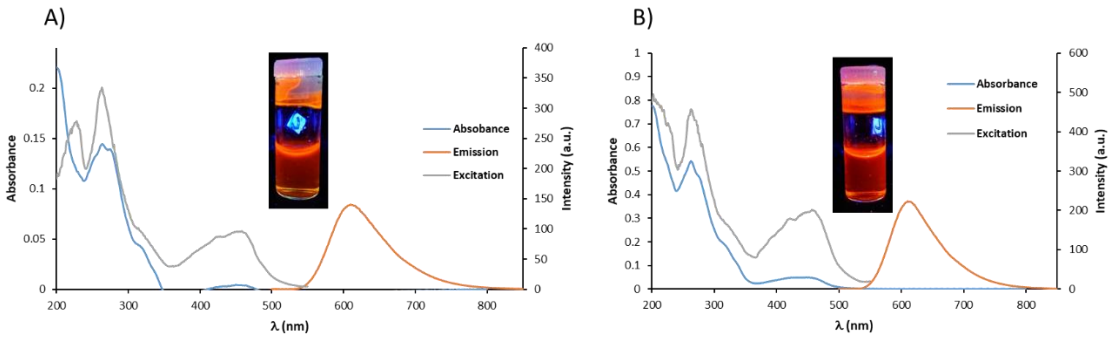

Figure A. 87 Absorption (blue), excitation (orange, λ_{em}= 610 nm) and fluorescence (red, λ_{ex}= 450 nm) spectra of a thin layer of **85** gel with A) 0.1 and B) 0.3 equivalent of $[Ru(phen)_2\mathbf{148}]^{2+}$ in MeOH:H_2O (30:70). Insert: Picture of the corresponding **85** gel with $[Ru(phen)_2\mathbf{148}]^{2+}$ diffused through it in MeOH:H_2O (30:70) under UV lamp irradiation.

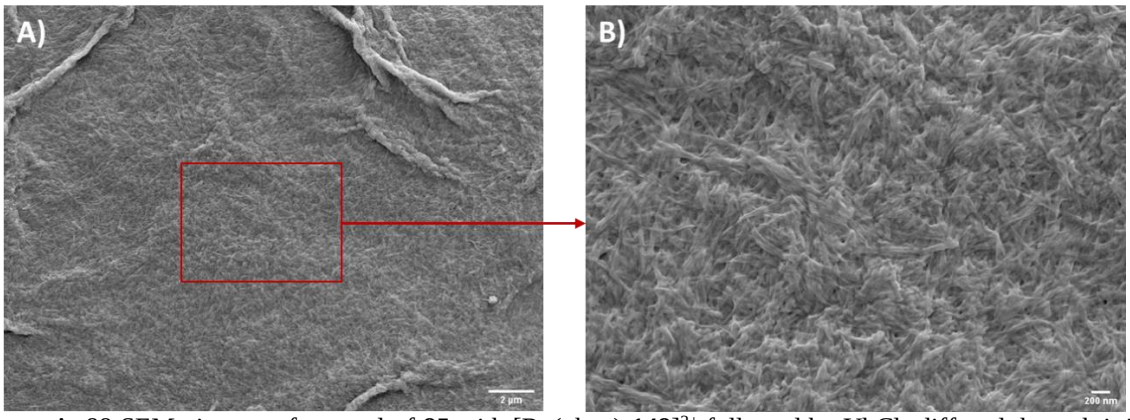

Figure A. 88 SEM pictures of xerogel of **85** with $[Ru(phen)_2$**148**$]^{2+}$ followed by $YbCl_3$ diffused through it in MeOH:H_2O (30:70) with scale bar size of A) 2 µm, B) 200 nm, C) 2 µm and D) 200 nm.

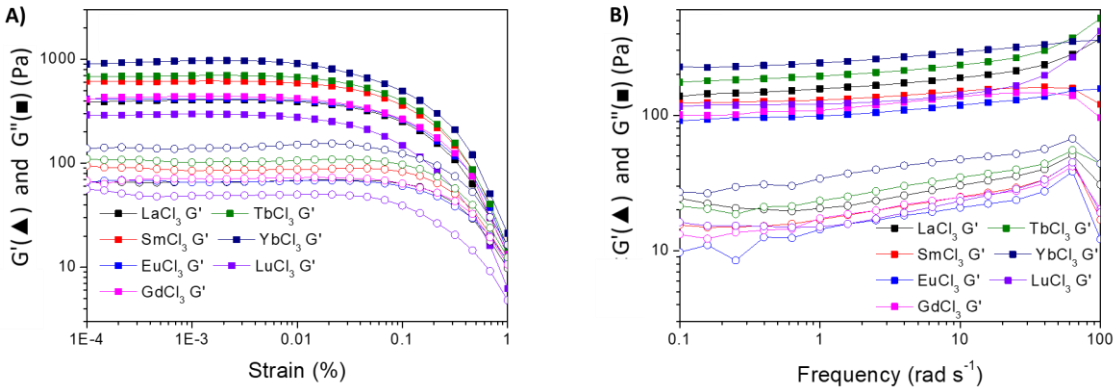

Figure A. 89 A) Strain sweeps for 0.6 *wt* % modified with $LnCl_3$ gels of **85** (MeOH:H_2O (30:70)), at f = 10 rad s^{-1}. B) Frequency sweep for 0.6 *wt* % modified with $LnCl_3$ gels of **85** (MeOH:H_2O (30:70)), at 0.1% of amplitude strain.

Table A. 3 Eigen Vectors obtained through non-linear regression analysis of titrations of **85** with various Ln(III) ions presented in Chapter 4.

LnCl3.6H2O	Absorbance				Fluorescence				Phosphorescence			
	Eigen Value	Square Sum	Residual	Prediction	Eigen Value	Square Sum	Residual	Prediction	Eigen Value	Square Sum	Residual	Prediction
LaCl3.7H2O	1.34E+03	8.07E+00	3.17E-02	Data Vector	7.72E+08	6.64E+05	7.69E+00	Data Vector				
	8.00E+00	7.30E-02	3.02E-03	Data Vector	6.26E+05	3.78E+04	1.83E+00	Data Vector				
	4.89E-02	2.41E-02	1.73E-03	Data Vector	6.97E+03	3.08E+04	1.66E+00	Probably Noise				
	1.29E-02	1.12E-02	1.18E-03	Possibly Data	2.24E+03	2.86E+04	1.60E+00	Probably Noise				
	2.51E-03	8.70E-03	1.04E-03	Probably Noise								
SmCl3	1 1.745E+03	7.51E+00	3.06E-02	Data Vector	1 3.219E+09	3.53E+06	1.14E+01	Data Vector	1 4.728E+05	1.42E+03	4.81E-01	Data Vector
	2 7.433E+00	7.87E-02	3.13E-03	Data Vector	2 3.344E+06	1.89E+05	2.64E+00	Data Vector	2 7.456E+02	6.70E+02	3.31E-01	Data Vector
	3 5.630E-02	2.24E-02	1.67E-03	Data Vector	3 1.596E+05	2.97E+04	1.04E+00	Data Vector	3 6.035E+01	6.10E+02	3.16E-01	Probably Noise
	4 9.403E-03	1.30E-02	1.27E-03	Probably Noise	4 5.155E+03	2.45E+04	9.49E-01	Probably Noise	4 4.522E+01	5.65E+02	3.04E-01	Probably Noise
	5 4.006E-03	8.99E-03	1.06E-03	Probably Noise	5 2.300E+03	2.22E+04	9.04E-01	Probably Noise				
					6 1.507E+03	2.07E+04	8.73E-01	Probably Noise				
					7 1.276E+03	1.95E+04	8.45E-01	Probably Noise				
EuCl3	1 1.563E+03	6.91E+00	2.93E-02	Data Vector	1 3.460E+09	3.89E+06	1.21E+01	Data Vector	1 3.999E+05	1.98E+03	4.54E-01	Data Vector
	2 6.853E+00	5.35E-02	2.58E-03	Data Vector	2 3.855E+06	3.72E+04	1.18E+00	Data Vector	2 1.119E+03	8.64E+02	3.00E-01	Data Vector
	3 2.545E-02	2.81E-02	1.87E-03	Data Vector	3 7.210E+03	3.00E+04	1.06E+00	Probably Noise	3 4.377E+02	4.26E+02	2.10E-01	Data Vector
	4 1.040E-02	1.76E-02	1.48E-03	Probably Noise	4 5.297E+03	2.47E+04	9.64E-01	Probably Noise	4 5.374E+01	3.73E+02	1.97E-01	Probably Noise
	5 5.256E-03	1.24E-02	1.24E-03	Probably Noise	5 1.821E+03	2.29E+04	9.28E-01	Probably Noise	5 3.044E+01	3.42E+02	1.89E-01	Probably Noise
	6 4.265E-03	8.12E-03	1.01E-03	Probably Noise					6 2.392E+01	3.18E+02	1.82E-01	Probably Noise
	7 2.099E-03	6.03E-03	8.67E-04	Probably Noise								
GdCl3	1 1.672E+03	8.41E+00	3.24E-02	Data Vector	1 7.711E+08	7.31E+05	7.59E+00	Data Vector				
	2 8.329E+00	8.34E-02	3.22E-03	Data Vector	2 7.023E+05	2.84E+04	1.50E+00	Data Vector				
	3 4.927E-02	3.42E-02	2.06E-03	Data Vector	3 2.481E+03	2.60E+04	1.43E+00	Probably Noise				
	4 1.761E-02	1.66E-02	1.44E-03	Possibly Data	4 1.761E+03	2.42E+04	1.38E+00	Probably Noise				
	5 6.151E-03	1.04E-02	1.14E-03	Probably Noise								
	6 3.614E-03	6.80E-03	9.21E-04	Probably Noise								
	7 1.934E-03	4.87E-03	7.79E-04	Probably Noise								
TbCl3	1 1.495E+03	1.17E+01	3.82E-02	Data Vector	1 8.869E+08	7.58E+06	1.73E+01	Data Vector	1 4.075E+07	5.97E+04	1.97E+00	Data Vector
	2 1.159E+01	9.94E-02	3.52E-03	Data Vector	2 7.442E+06	1.39E+05	2.34E+00	Data Vector	2 5.229E+04	7.40E+03	6.94E-01	Data Vector
	3 6.062E-02	3.88E-02	2.20E-03	Data Vector	3 1.186E+05	2.01E+04	8.92E-01	Data Vector	3 5.536E+03	1.87E+03	3.48E-01	Data Vector
	4 1.806E-02	2.07E-02	1.61E-03	Data Vector	4 7.481E+03	1.26E+04	7.07E-01	Data Vector	4 8.744E+02	9.93E+02	2.54E-01	Data Vector
	5 7.845E-03	1.29E-02	1.27E-03	Possibly Data	5 2.143E+03	1.05E+04	6.44E-01	Probably Noise				
	6 4.869E-03	8.02E-03	1.00E-03	Possibly Data	6 1.086E+03	9.40E+03	6.10E-01	Probably Noise				
	7 3.250E-03	4.77E-03	7.71E-04	Probably Noise	7 7.271E+02	8.68E+03	5.86E-01	Probably Noise				
	8 9.612E-04	3.81E-03	6.89E-04	Probably Noise	8 5.857E+02	8.09E+03	5.65E-01	Probably Noise				
	9 8.180E-04	2.99E-03	6.10E-04	Probably Noise								
YbCl3	1 1.204E+03	1.27E+01	4.30E-02	Data Vector	1 4.692E+08	1.17E+06	6.80E+00	Data Vector				
	2 1.261E+01	1.33E-01	4.40E-03	Data Vector	2 1.162E+06	8.09E+03	5.65E-01	Data Vector				
	3 1.256E-01	7.78E-03	1.06E-03	Data Vector	3 2.885E+03	5.21E+03	4.54E-01	Possibly Data				
	4 5.857E-03	1.93E-03	5.29E-04	Data Vector	4 4.776E+02	4.73E+03	4.32E-01	Probably Noise				
	5 8.646E-04	1.06E-03	3.93E-04	Possibly Data	5 3.807E+02	4.35E+03	4.14E-01	Probably Noise				
	6 3.485E-04	7.12E-04	3.22E-04	Probably Noise	6 3.097E+02	4.04E+03	3.99E-01	Probably Noise				
	7 2.943E-04	4.18E-04	2.47E-04	Probably Noise								
LuCl3	1 1.247E+03	8.81E+00	3.31E-02	Data Vector	8.952E+08	1.69E+06	1.23E+01	Data Vector				
	8.719E+00	9.49E-02	3.44E-03	Data Vector	2.681E+03	1.68E+06	4.89E-01	Data Vector				
	6.937E-02	2.55E-02	1.78E-03	Data Vector	2.681E+03	8.47E-07	8.69E-06	Data Vector				
	4 8.833E-03	1.67E-02	1.44E-03	Data Vector	1.608E-07	6.86E-07	7.82E-06	Probably Noise				
	5 5.918E-03	1.08E-02	1.16E-03	Data Vector								
	6 4.042E-03	6.73E-03	9.16E-04	Possibly Data								
	2.354E-03	4.38E-03	7.39E-04	Probably Noise								
	1.065E-03	3.31E-03	6.42E-04	Probably Noise								
	9 7.891E-04	2.52E-03	5.61E-04	Probably Noise								
	5.870E-04	1.94E-03	4.91E-04	Probably Noise								

Table A. 4 Sigma Y values obtained for the fitting of the titrations **85** with various Ln(III) ions presented in Chapter 4.

	Absorbance	Fluorescence	Phosphorescence
	Sigma Y	Sigma Y	Sigma Y
$LaCl_3$	2.68E-03	2.232	Non-emissive
$SmCl_3$	3.51E-03	3.205	8.40E-01
$EuCl_3$	2.45E-03	3.112	4.20E-01
$GdCl_3$	3.95E-03	1.82E+00	Not measured
$TbCl_3$	4.57E-03	2.2	8.46E-01
$YbCl_3$	3.99E-03	1.482	Issues with fitting
$LuCl_3$	2.85E-03	2.977	Non-emissive

Data to Support Chapter 5

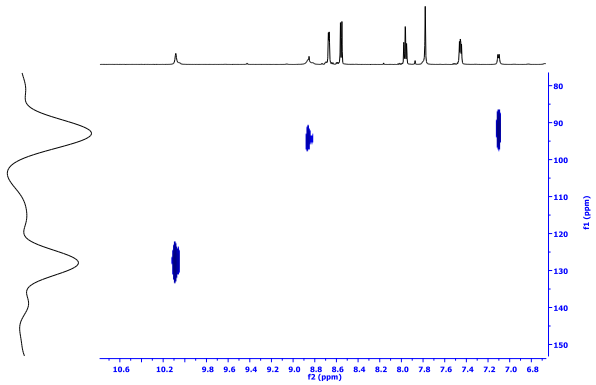

Figure A. 90 ^{1}H-^{15}N HSQC NMR (DMSO-d_6) of **157**.

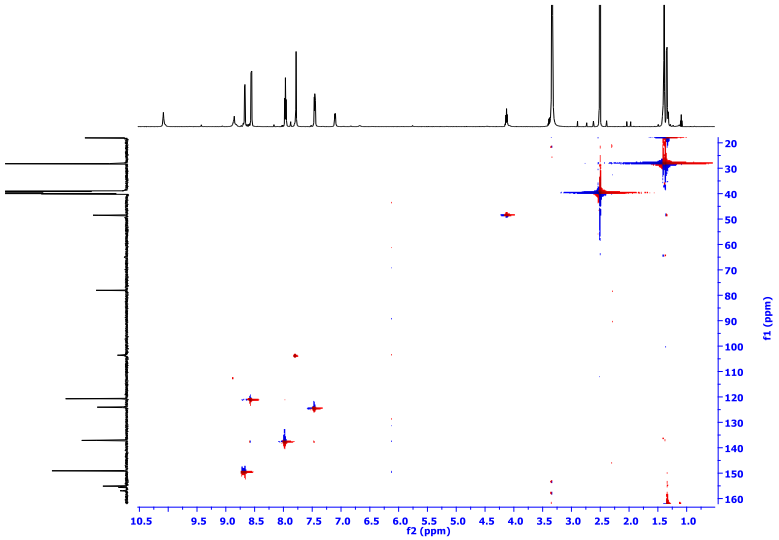

Figure A. 91 ^{1}H-^{13}C HSQC NMR (DMSO-d_6, 600 MHz) of **157**.

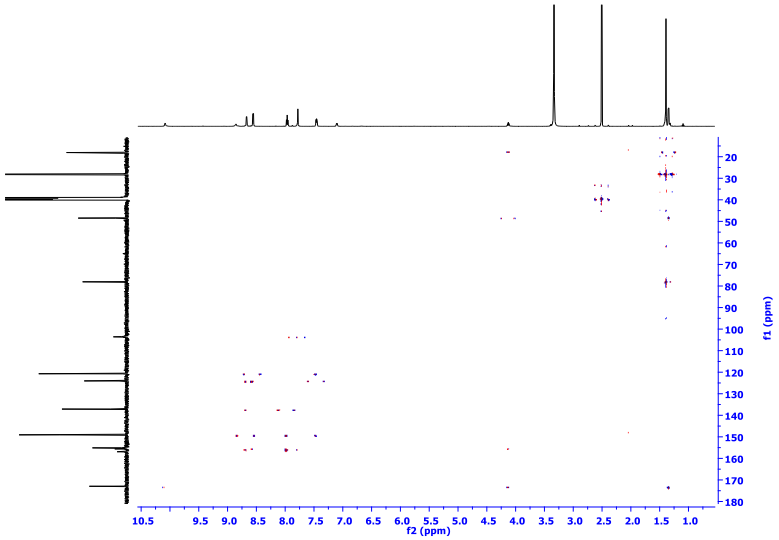

Figure A. 92 HMBC NMR (DMSO-d_6, 600 MHz) of **157**.

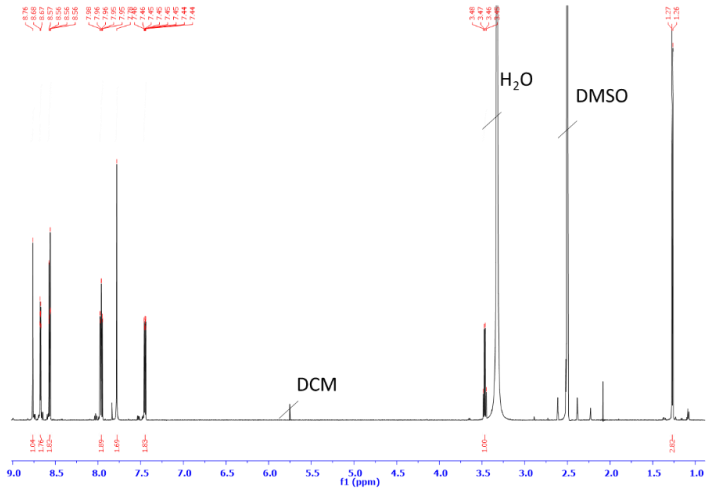

Figure A. 93 ^{1}H NMR (DMSO-d$_6$, 600 MHz) of **158**.

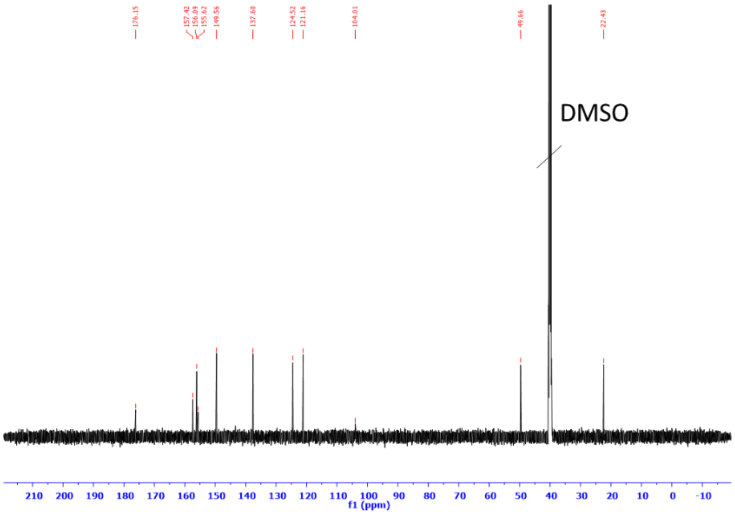

Figure A. 94 ^{13}C{^{1}H} NMR (DMSO-d$_6$, 151 MHz) of **158**.

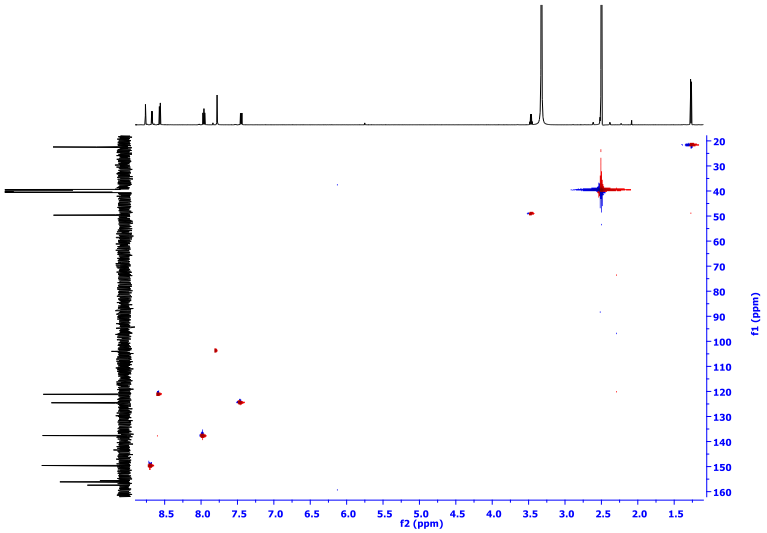

Figure A. 95 ^{1}H-^{13}C HSQC NMR (DMSO-d$_6$) of **158**.

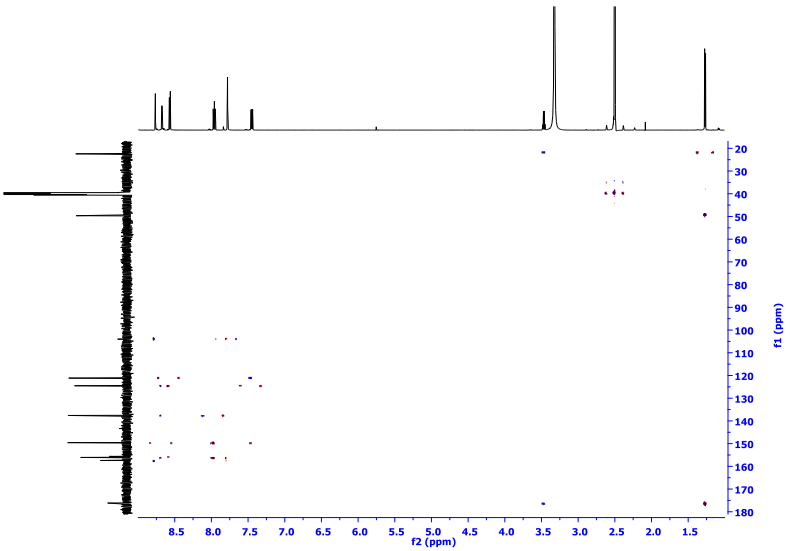

Figure A. 96 HMBC NMR (DMSO-d_6) of **158**.

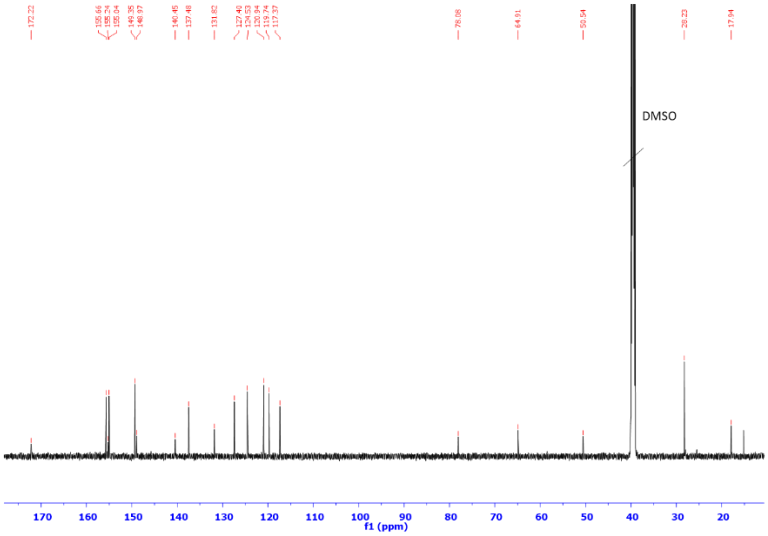

Figure A. 97 $^{13}C\{^{1}H\}$ NMR (DMSO-d_6, 151 MHz) of **159**.

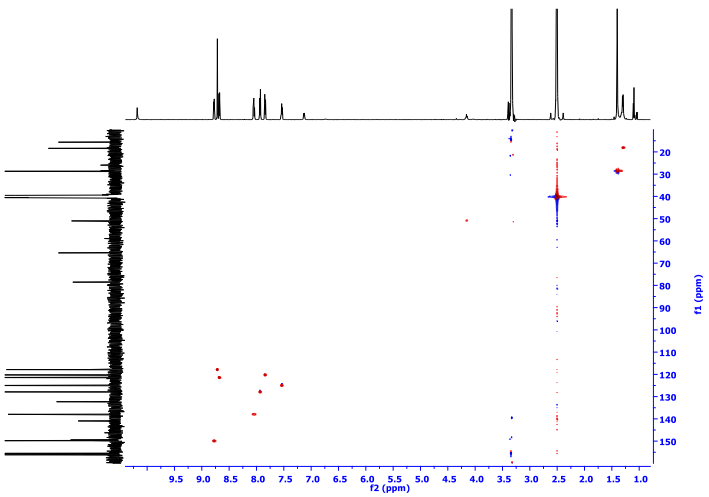

Figure A. 98 ^{1}H-^{13}C HSQC NMR (DMSO-d_6) of **159**.

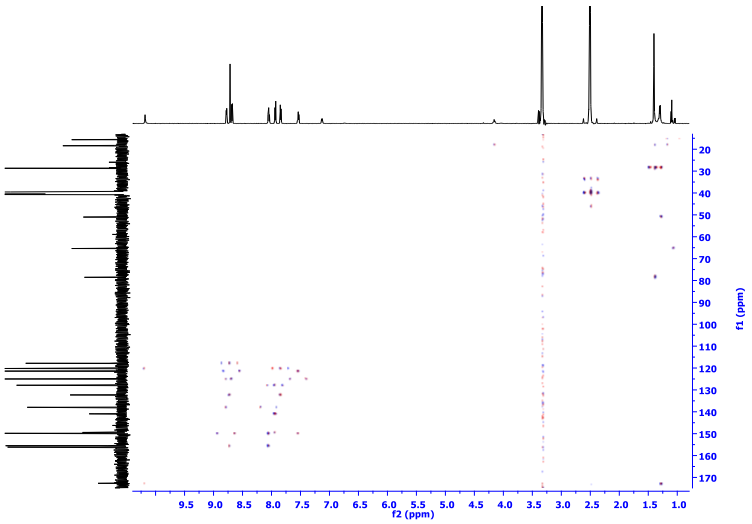

Figure A. 99 HMBC NMR (DMSO-d_6) of **159**.

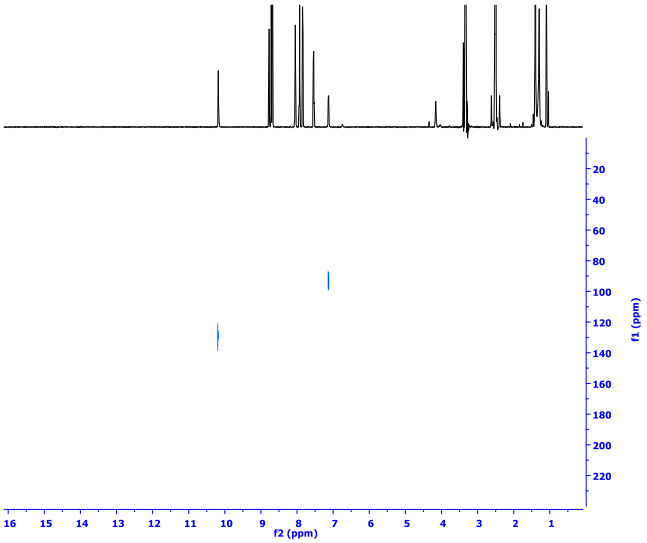

Figure A. 100 ^{1}H-^{15}N HSQC NMR (DMSO-d_6) of **159**.

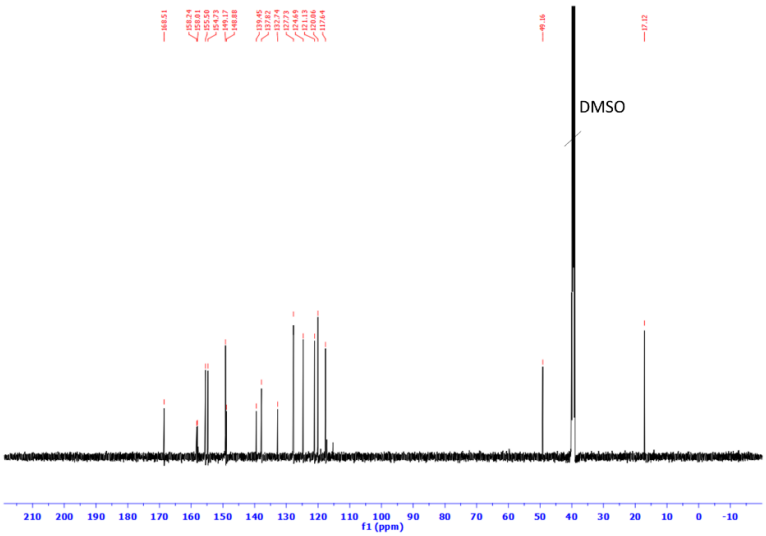

Figure A. 101 $^{13}C\{^{1}H\}$ NMR (DMSO-d_6, 151 MHz) of **160**.

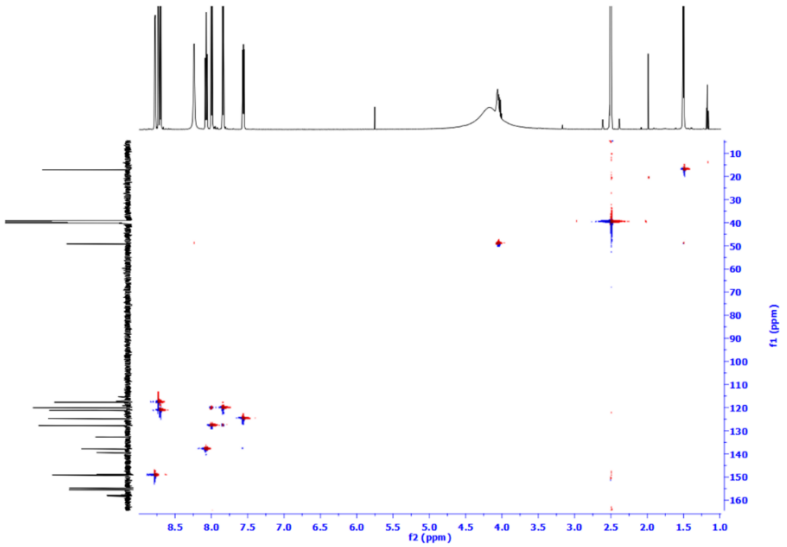

Figure A. 102 ^{1}H-^{13}C HSQC NMR (DMSO-d_6) of **160**.

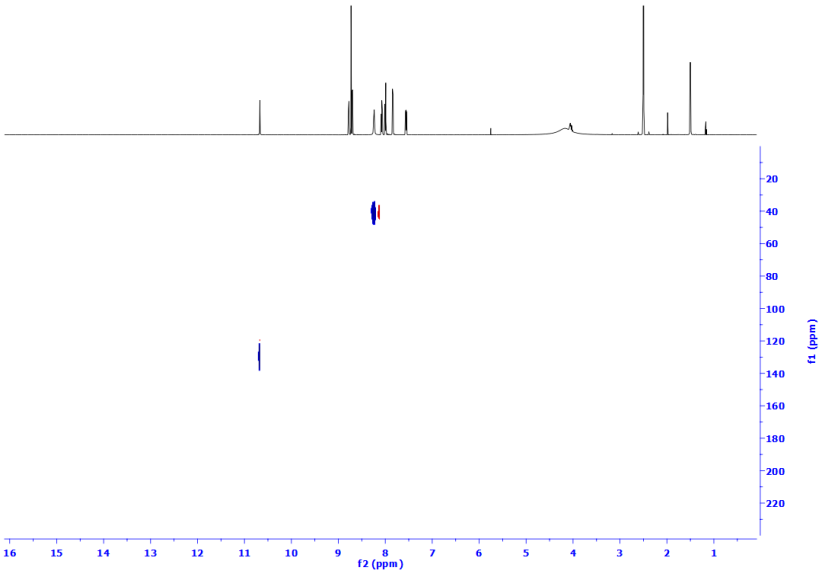

Figure A. 103 ^{1}H-^{15}N HSQC NMR (DMSO-d_6) of **160**.

Table A. 5 Crystal data and structure refinement for **159**.

Identification code	tcd1380 (**159**)
Empirical formula	$C_{29.25}H_{29.5}Cl_{0.5}N_5O_3$
Formula weight	516.80
Temperature/K	100(2)
Crystal system	orthorhombic
Space group	$P2_12_12_1$
a/Å	5.054(4)
b/Å	16.915(11)
c/Å	32.94(2)
α/°	90
β/°	90
γ/°	90
Volume/Å^3	2816(3)
Z	4
ρ_{calc}g/cm^3	1.219
μ/mm^{-1}	1.072
F(000)	1090.0
Crystal size/mm^3	0.19 × 0.02 × 0.02
Radiation	Cu Kα (λ = 1.54178)
2Θ range for data collection/°	5.366 to 108.97
Index ranges	$-3 \leq h \leq 5$, $-17 \leq k \leq 17$, $-34 \leq l \leq 34$
Reflections collected	8446
Independent reflections	3447 [R_{int} = 0.0914, R_{sigma} = 0.1556]
Data/restraints/parameters	3447/284/419
Goodness-of-fit on F^2	1.024
Final R indexes [I>=2σ (I)]	R_1 = 0.0979, wR_2 = 0.2373
Final R indexes [all data]	R_1 = 0.1441, wR_2 = 0.2748
Largest diff. peak/hole / e Å^{-3}	0.68/-0.28
Flack parameter	0.3(4)

Publications

Organic & Biomolecular Chemistry

PAPER

View Article Online
View Journal | View Issue

Cite this: *Org. Biomol. Chem.*, 2019, **17**, 2116

Glycosylated naphthalimides and naphthalimide Tröger's bases as fluorescent aggregation probes for Con A†

Elena Calatrava-Pérez, [a] Jason M. Delente,[a] Sankarasekaran Shanmugaraju,[a] Chris S. Hawes, [b] Clive D. Williams,[c] Thorfinnur Gunnlaugsson *[a] and Eoin M. Scanlan *[a]

Received 29th November 2018,
Accepted 20th December 2018

DOI: 10.1039/c8ob02980f

rsc.li/obc

Herein we report the synthesis of fluorescent, glycosylated 4-amino-1,8-naphthalimide (**Nap**) **1**, and the related 1,8-naphthalimides Tröger's bases (**TBNap**) **2** and **3**, from 1,8-naphthalic anhydride precursors, the α-mannosides being introduced through the use of CuAAC mediated 'click' chemistry. We investigate the photophysical properties of these probes in buffered solution and demonstrate their ability to function as fluorescent probes for Concanavalin A (Con A) lectin. We show that both the **Nap** and **TBNap** structures self-assemble in solution. The formation of the resulting supramolecular structures is driven by head-to-tail π–π stacking and extended hydrogen bonding interactions of the Nap and the triazole moieties. These interactions give rise to spherical nano-structures (*ca.* 260 nm and 100 nm, for **1** and **3**, respectively), which interact with the Con-A protein, the interaction being probed by using both luminescent and Scanning Electron Microscopy imaging as well as dynamic light scattering measurements. Finally, we show that these supramolecular assembles can be used as luminescent imaging agents, through confocal fluorescence imaging of HeLa cells of the per-acetylated version **2**.

Introduction

The development of small-molecule targeted fluorescent probes and sensors remains an area of intensive research interest,[1–3] particularly for use in live-cell analysis and imaging as high-resolution fluorescence imaging[4,5] techniques have advanced significantly in recent times.[6] Applications of such probes include ion-sensing,[7] subcellular imaging[8] and protein tracking[9] amongst other supramolecular applications.[10] However, significant challenges in the development of such probes arise because many molecular probes/sensors can be cytotoxic, give rise to immunogenic response, and are prone to enzymatic degradation.[11] For real time imaging in cells, insufficient water solubility and lack of targeting ability for specific proteins and enzymes remain a major obstacle.[12,13] We have recently demonstrated the real time monitoring of enzymatic activities in competitive media using enzyme targeting luminescent probes.[11] We have also shown that enzymatic activation (*e.g.* hydrolysis), coupled with the use of fluorescent therapeutics, that have been structurally modified to be selectively recognised by a specific enzyme, can be employed in the generation of so called '*pro-probes*'. These are 'probes' or 'bioconjugates', that only become active *in vivo* upon enzymatic triggered release of the therapeutic cargo; the release/delivery being probed by the emission from the cargo itself within cells.[11,14] Herein, we extend this strategy towards the use of proteins as the targeting carriers;[15] by developing the glycosylated 4-amino-1,8-aphthalimide (**Nap**) **1** and the a 9,18-methano-1,8-naphthalimide-[*b*,*f*][1,5]diazocine ring fused, or Tröger's base based 4-amino-1,8-naphthalimide (**TBNap**) structure **2**, Scheme 1, as fluorescent targeted Concanavalin A (Con A) lectin probes.

Lectins are proteins which specifically recognise and bind to carbohydrates.[16] Lectins are involved in a wide range of biological processes; including regulation of cell adhesion, modulation of protein levels in blood, immune and inflammatory processes, glycoprotein synthesis and the promotion of cell–cell interactions.[17] Lectins have important therapeutic applications in cancer treatment, and are biomarkers for disease and autophagy inducers.[18,19] It is thus not surprising that

[a]*School of Chemistry and Trinity Biomedical Sciences Institute (TBSI), Trinity College Dublin, The University of Dublin, Dublin 2, Ireland. E-mail: gunnlaut@tcd.ie, eoin.scanlan@tcd.ie; http://thorrigunnlaugsson.wordpress.com, http://chemistry.tcd.ie/staff/academic/SCANLAE*

[b]*School of Chemical and Physical Sciences, Keele University, Keele ST5 5BG, UK*

[c]*School of Biochemistry and Immunology and Trinity Biomedical Sciences Institute (TBSI), Trinity College Dublin, The University of Dublin, Dublin 2, Ireland*

†Electronic supplementary information (ESI) available. CCDC 1866499. For ESI and crystallographic data in CIF or other electronic format see DOI: 10.1039/c8ob02980f

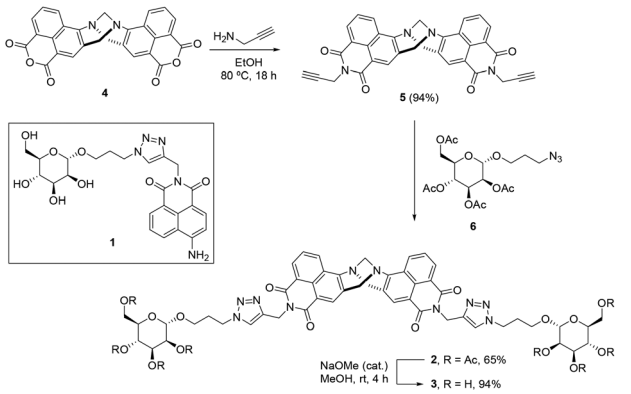

Scheme 1 The structure of **Nap 1**, and the synthetic strategy for the preparation of **TBNap 3** from the **TB** anhydride **4** and the precursor **2**.

lectin recognition is a topical area of research within supramolecular and medicinal chemistry.[17]

Con A is a lectin protein belonging to the legume-type family that preferably binds to α-linked mannosides, but it is also able to bind α-glucosides. With this in mind we designed probe **1**, which consists of a single α-mannoside unit covalently linked to a **Nap**, Scheme 1. Above pH 7, Con A is presented as a tetramer; where each subunit is separated *ca.* 72 Å apart.[20] However, at mildly acidic pH, *e.g.* 4.5–5.5, Con A adopts a di-meric structure. Each monomer contains two metal binding sites for Ca^{2+} and Mn^{2+} ions, which need to be occupied for the sugar binding to take place.[21] In addition to the **Nap** derivative, we developed a divalent system by synthesising the bis α-mannoside **TBNap** derivative **2**, Scheme 1., in order to directly compare the interactions of the mono- *vs.* a divalent probe with Con A. In this article, we present the results from our investigation in the use of **1** and **2** as fluorescent aggregation probes for lectins in solution and compatibility *in vitro* with human cervical cancer cells.

Results and discussion

Design of Nap and TBNap based lectin probes

Using CuAAC chemistry, the **Nap** and **TBNap** probes **1** and **2**, were synthesised as Con A targeted lectin probes; both being synthesised from their corresponding 1,8-naphthalic anhydride structures. **Naps** are well documented fluorophores, possessing internal charge transfer excited state (ICT), that have been extensively used in the development of florescent sensor for ions and molecules, and in medicinal chemistry.[22,23] In contrast to these, the **TBNaps**, are bi-naphthalimide systems, that we have recently developed the application of in significant detail; including their application as anticancer drugs, cellular imaging agents and in MOFs and coordination compounds and polymers, *etc.*[24,25]

Like **Naps**, **TBNaps**, also possess ICT excited state characters, though to lesser extent. Due to the methano-1,5-diazocine ring (N–CH_2–N), the two naphthalimide components of the **TBNaps** units are almost orthogonal to each other, with dihedral angles ranging from 90 to 104°; thus making the **TBNaps** a highly desirable recognition motive for biomolecules.[24,25] With this in mind, both the **Naps** and the **TBNaps** were fully characterised using a range of photophysical techniques, their photophysical as well as their bioavailability properties were investigated.

Synthesis and photophysical analysis of 1–3

Mannosyl-naphthalimide conjugate **1** was prepared according to the reported literature procedures. 4-Nitro-1,8-napthalic anhydride and propargylamine, were first reacted together, followed by conjugation to the per-*O*-acylated mannoside derivative **6** using CuAAC mediated click chemistry under microwave assisted conditions. A reduction of this intermediate, to give the 4-amino analogue, using Pd/C and H_2 at 2 atm., followed by deprotection of the mannose unit, gave **1** in good yield.[11,26] The structure was fully characterised as shown in ESI.†

We have developed many examples **TBNaps** whereby imide end functionalised 3- or the 4-amino-1,8-naphthalimides are reacted with formaldehyde under acidic conditions. This normally results in the formation of the desired **TBNaps**. Unfortunately, this strategy did not work in this case, and the desired compound **3** was difficult to isolate in high purity or yield. Consequently, we moved towards synthesising **3** using an alternative route, based on the use of the TB anhydride **4**, Scheme 1, which was recently developed in our laboratory, and structurally fully charatesised.[27] The anhydride, can be formed in a signal step *via* nucleophilic substitution reaction from a single common 'synthon', a 5-dimethyl-isophthalate based **TBNap** (bis-[*N*-(5-dimethyl-isophthalate)]-9,18-methano-1,8-naphthalimide [*b*,*f*][1,5]diazocine), upon treatment with aqueous KOH. The anhydride was reacted with propargylamine in refluxing ethanol to furnish the dialkyne compound **5** in 94% yield. Compound **5** was then reacted under CuAAC conditions in the presence of per-*O*-acylated mannoside derivative **6**, displaying an alkylazide group at the anomeric position to furnish the protected product **2** in 65% yield. Treatment of **2** under Zemplén conditions furnished the desired product **3** in 98% yield. Both compounds **2** and **3** were characterised (*cf.* Experimental and ESI†) using conventional methods, including both NMR and HRMS. The ^{1}H NMR of **2** (400 MHz, DMSO-d_6) indicated that some aggregation or self-assembly formation occurred in solution, with several broad resonances assigned to the aromatic protons, while the protons assigned to the diazocine moiety appeared as well resolved set of signals between 5.5–5.0 ppm. The HRMS (MALDI) of **1–3** gave the accurate mass for $[M + H]^+$; which in the case of **3**, was found to be m/z = 1063.38054, for $C_{51}H_{55}N_{10}O_{16}$.

Photophysical characterisation of 1–3

Amino-naphthalimides such as **1** have push–pull based intramolecular charge transfer (ICT) based photophysical properties. Their absorption and fluorescence emission spectra are therefore broad and occur within the UV-Vis and the visible regions, possessing moderately large Stokes shift, as

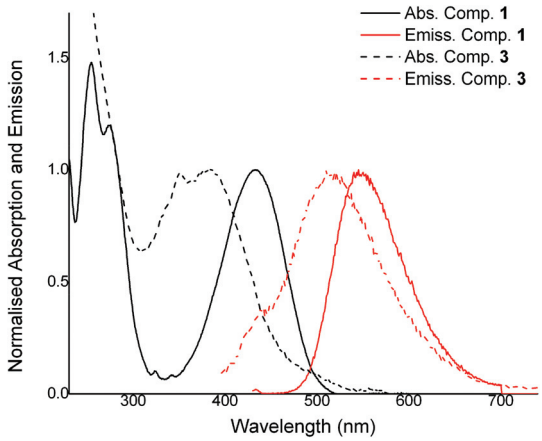

Fig. 1 Normalised absorption and emission spectra for **1** (black solid and black dotted) and **3** (red solid and red dotted).

shown in Fig. 1. Naps also normally possess reasonable lifetimes and quantum yields (Φ_F). The photophysical characterisation of both **1** and **3** was carried in phosphate buffered saline (PBS) solution. Probe **1** displayed an absorption band centred *ca.* 430 nm (ε = 12 300 M^{-1} cm^{-1}) characteristic of the intramolecular charge transfer (ICT) process, and a fluorescence emission with its maximum at 530 nm upon excitation at λ_{max} at 433 nm. The Φ_F was also measured as under these conditions as 11% (see ESI† for details). The fluorescence excitation spectrum mirrored that seen in the absorption spectrum (see ESI†). In the case of **3**, a broad absorption band centred at 380 nm (ε = 9000 M^{-1} cm^{-1}), with a shoulder *ca.* 350 nm was observed. The emission spectra of **3** showed a band centred at 510 nm. Therefore, both the absorption and emission spectra of the **1** are 50 nm blue-shifted with respect to **3**. This blue-shift is due to the substitution of the 4-amino group, reducing the ICT (the push–pull) process. In a similar manner, the per-*O*-acetylated mannose **2**, was also investigated and the UV-Vis absorption and emission spectra matched that observed for **3**.

Self-assembly formation in solution and solid-state analysis of 7

As the **Naps** are known to take part in 'head-to-tail' aggregation through π–π interactions, aggregation studies were undertaken in solution, where both the absorption and the fluorescence emission were monitored for **1** and **3**. It is also well known that sugars and short carbohydrates can self-assemble into higher order structures. These studies were carried out in pH 7.2 DPBS (Dulbecco's phosphate-buffered saline), by varying the concentrations of these two structures between 1×10^{-6} to 1×10^{-4} M. While the absorption spectrum (see ESI†) was not significantly affected, and the Beer–Lambert plot gave a linear slope, the florescence emission of both compounds was significantly affected at concentrations greater than 5×10^{-5} M in the case of **3**. For both systems, the emission was quenched at elevated concentrations, Fig. 2.

In the case of **3**, no significant changes were observed in the λ_{max}, but for the **TBNap 1**, the aggregation seem to be

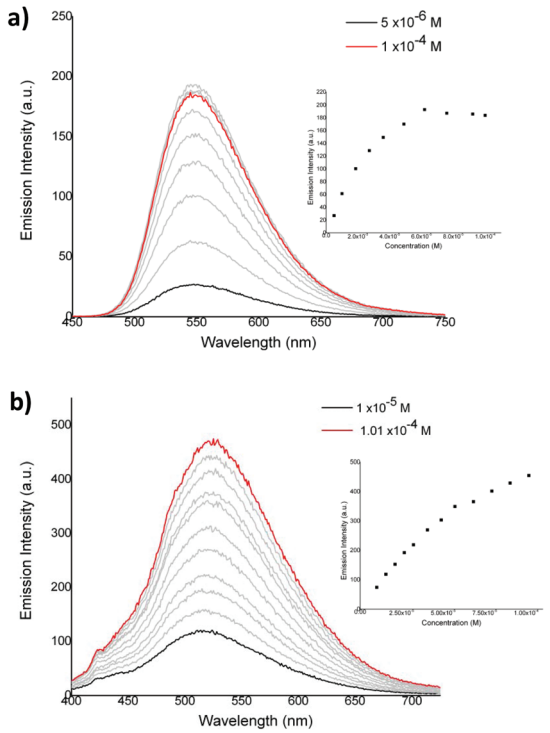

Fig. 2 Changes in the fluorescence emission of (a) **1** and (b) **3** in DPBS at room temperature upon changing the concentrations of these two structures between 1×10^{-6} to 1×10^{-4} M. Inset: The changes in the emission intensity at λ_{max} as a function of increasing concentration of **1** and **3**, respectively.

occurring at slower rate, while being concomitantly causing blue shift in the λ_{max}. The quenching is characteristic of naphthalimides π–π stacking interactions, in addition to hydrogen bonding interactions between the imide and the 4-amino moieties of stacked **Naps** 'dimers'.[23c] These interactions giving rise the formation of columns of such stacked structures, which are often stabilised by solvent interactions, such as hydrogen bonding to interstitial water protons. In the case of **1** and **3**, we anticipated that these supramolecular interactions would be further aided by the mannoside moieties, which would be expected to take part in the formation of higher order self-assembly formations, through extended and multiple intermolecular hydrogen bonding interactions.

We have in the past characterised such 'head-to-tail' interactions both in solution as well as in the solid-state; these normally showing a clear hydrogen bonding interaction between the amino group of the **Nap** moiety.[23c] However, attempts to crystallise either **1** or **3** on all occasions did not result in the formations of crystals suitable for solid state crystallographic analysis. We were however, able to obtain crystals of the **Nap** structure **7**, Fig. 3, which is structurally related to **1**, with the exception that the mannoside moiety is missing. This 'model' compound was previously synthesised in our laboratory by subjecting a glycosylated **Nap** 'pro-probe' to the glycosidase enzymes β-galactosidase, which rapidly hydrolysed the glycosidic bond, concomitantly releasing **7** into cancer cells.[11] **7**, and

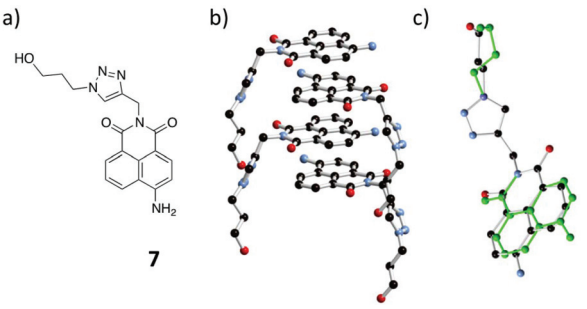

Fig. 3 (a) Chemical structure of compound **7**. (b) The X-ray crystal structure formed in H_2O, and the extended π–π interactions, and (c) the two disordered orientations of the naphthalimide and alcohol fragments (minor conformer shown in green).

is a good model of **1**, as it allows us gain inside into the various supramolecular interactions occurring at the **Nap** and the triazole moieties.

The structure of **7** is shown in Fig. 3a, as well as the packing in the solid state in Fig. 3b.[33] As can be seen in Fig. 3b, the **Naps** display π–π stacking interactions, being arranged with a near-120° rotation between the major axes of each successive **Nap**. This orientation is different to what we have observed before, where a true head-to-tail orientation is typically observed. These interactions give rise to stacked columns; the chains are bent to shroud the exterior of the columns and engage in hydrogen bonding interactions with neighbouring groups.

There are three types of hydrogen bond donor in the compound: the amine and alcohol groups and the triazole C–H group. The alcohol and imide oxygen atoms and one triazole nitrogen atom act as hydrogen bond acceptors. The **Nap** molecules interact further with a molecule of water, shared between four **Nap** molecules, forming hydrogen-bonding interactions with the terminal alcohol. One could envisage that such interactions could be potentially greater for **1** and **3**, given the number of additional hydrogen bonding acceptors/donors available. As the more directional interactions take place at the peripheries of the molecule, substantial crystallographic disorder is observed on the core atoms. This is related to the tendency of the central **Naps** to orient across two positions related by rotation (Fig. 3c), with a distribution 2 : 1 or 1 : 1 for the two unique residues. It is clear from these results that the **Nap** structures can partake in self-assembly processes, that could result in the formation of higher-order materials, and that this could potentially affect their biological applications. As **1** and **3** were developed as fluorescent probes for Lectin protein, we set out to investigate both the affinity of this binding interaction, through the use of fluorescent titrations, as well as how this would affect the 'material' nature of **1** and **3** using Scanning Electron Microscopy (SEM) imaging.

Con A binding studies

In order to investigate if the **Nap** compounds could function as molecular probes for lectin proteins, we evaluated the changes in their luminescent properties upon addition of Con A to solutions of **1** and **3**. Based on our investigation above, we postulated that following addition of Con A, the carbohydrate–lectin binding interactions would occur and potentially disrupt aggregates resulting in significant changes in the fluorescence. As a qualitative test, 0.1 equivalents of Con A were initially added to a 1×10^{-4} M solution of **1** and **3**, respectively, Fig. 4a and b, in pH 7.2 DPBS solution, in the presence of 0.1 mM $MnCl_2$ and 0.1 mM $CaCl_2$ at 25 °C. In the case of **1**, the fluorescence was enhanced significantly upon the addition of Con A, highlighting its ability to interact with Con A, and function as a lectin probe.

In contrast to this, the fluorescence intensity for **3** decreased at λ_{em} = 510 nm but a new shoulder appeared at 450 nm. This could possibly be due to the presence of the Tröger's base moiety, which places the two **Naps** part almost orthogonal. We have observed similar effect upon binding Ru(II) polypyridyl based **TBNap** upon binding to DNA.[25] Similarly, we analysed the binding of **2** to Con A. However, no changes were observed in the fluorescence emission, indicating that acetylated version was unable to bind to the protein in the same manner as **3** (see ESI†). Having established that both compounds **1** and **3**, interacted with Con A, a titration of **1** and **3** (1×10^{-4} M) with Con A was undertaken (using final concentrations of Con A between 10^{-6} and 10^{-4} M). Here, significant changes were observed in the emission of **1**, which was enhanced. The changes in the ICT band at 535 nm are shown in Fig. 4c as a function of emission enhancement $(F - F_0)$ where it is clear that the most significant changes occur at low concentrations of Con A; the emission showing a linear trend upon addition of Con A, until 9×10^{-5} M, after which a saturation point is reached. In a similar manner, the changes in the emission of **3** was monitored. While no significant changes were observed in the λ_{max} at 510 nm, changes were observed at 450 nm shoulder, which also demonstrated a linear enhance-

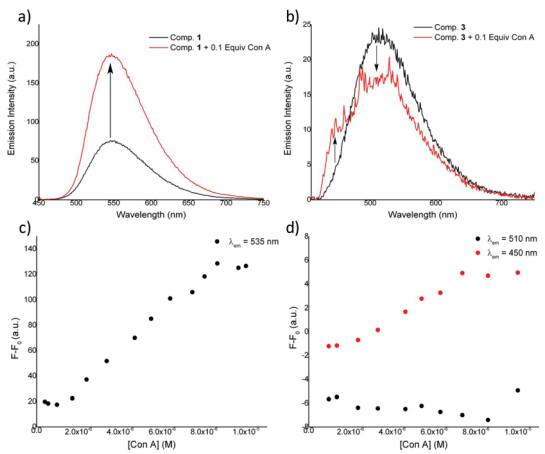

Fig. 4 Changes in the fluorescence emission intensity of **1** (a and c) and **3** (b and d), respectively, upon addition of 0.1 equiv. of Con A and varying concentrations of Con A. In pH 7.2 DPBS solution, in the presence of 0.1 mM $MnCl_2$ and 0.1 mM $CaCl_2$ at 25 °C.

ment occurred within the same concentration window as that seen for **1**, namely, between 2×10^{-6} and 8×10^{-5} M of Con A. The titrations also showed that below 1 μM Con A concentration, no changes were observed, Fig. 4c and d. Unfortunately, we were unable to accurately determine the binding affinity for these interactions.

Binding selectivity

Encouraged by the positive results obtained with **1**, we set out to investigate the effect of the Con A binding under varying conditions, and the results are summarised in Fig. 5. As can be seen in Fig. 5, the addition of Con A (0.1 equivalents) led to a *ca.* 70% increase in the fluorescent intensity of **1**. The addition of two-fold excess of α-D-mannose (compare to Con A) did not affect the emission properties. This could indicate that the probe was fully bound at this concentration. Similarly, no further quenching was observed for **3** upon addition of α-D-mannose at this concentration. In a separate experiment, the probes were incubated with de-natured Con A (heated at 80 °C for 30 min), and no relevant changes in the fluorescent emission were observed, demonstrating that only a specific binding interaction between Con A and the two probes induces a change in the luminescence.

To further validate the binding interactions, the probes were treated with 0.1 equiv. of Bovine Serum Albumin (BSA). Albumin is a prevalent macromolecular transporter protein found in the blood stream due to its capacity to bind and carry small molecules. Significantly, no changes were observed in the luminescence of **1** and **3** in the presence of BSA, demonstrating that the fluorescence changes observed are exclusively due to the selective binding with Con A. Following this experiment, Con A (0.1 equiv.) was added to this mixture to investigate if the presence of BSA would interfere with binding seen above. Gratifyingly, the fluorescence changes followed the same trend as the experiment conducted in the absence of BSA, highlighting that lectin–carbohydrate binding remains efficient in the presence of other macromolecules. This is an important finding in view of these compounds having application as molecular probes *in vitro*.

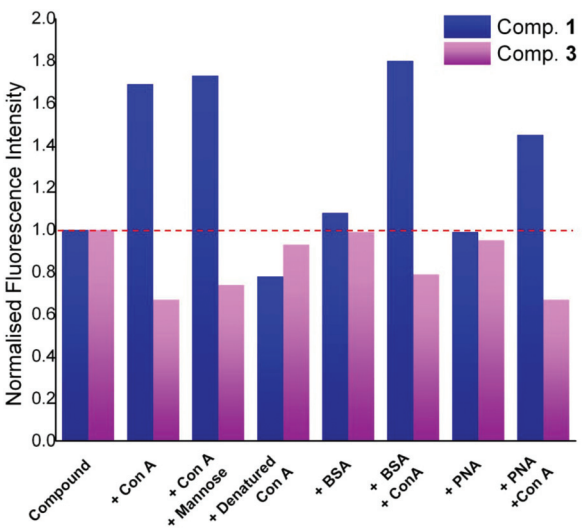

Fig. 5 Normalised fluorescence intensity of **1** (blue) and **3** (magenta) in the presence of different biomolecules, in pH 7.2 DPBS solution, in the presence of 0.1 mM $MnCl_2$ and 0.1 mM $CaCl_2$ at 25 °C.

We repeated this experiment using another relevant lectin Peanut Agglutinin (PNA) which preferably binds to β-Gal-(1–3)-β-GalNAc units, and identical, non-bonding, behaviour was observed for both **1** and **3**. Therefore the changes in the luminescence are clearly only due to the selective binding between the α-mannosides probes and Con A. Finally, as a negative control, two structurally related **Naps**, that have previously developed in our laboratory,[11] possessing a β-galactoside (**Gal-Nap**) and β-Lactoside (**Lac-Nap**) moiety instead of the mannose site employed here, as well as **2**, were treated with Con A (0.1 equiv.) under identical conditions as described above. Importantly, only negligible changes were observed in the fluorescence intensity of all of these probes (see ESI†) upon addition of Con A. We believe that this demonstrates that the aggregation of **1** and **3** is significantly affected upon binding to Con A. As we were unable to accurately determining the binding constants for the interaction of **1** and **3** for Con A, we set out to probe if the nanostructure (*e.g.* the morphology of self-assembly structure of **1** and **3**) would be affected upon binding to Con A. This elucidation was carried out by using SEM imaging.

Morphology studies

The self-assembly or aggregation of **1** and **3** was observed above in solution. To investigate further the material nature of these assembles, pH 7.2 DPBS solution of **1** and **3** were drop casted onto silicon wafer, dried in air and imaged using SEM. The results are shown in Fig. 6 (see also ESI†). From this imaging, it is clear that both **1** and **3** form particles; these being of *ca.* 260 nm and 100 nm average size, Fig. 6a and b, for **1** and **3** respectively (it is also possible to see some salt formation, due to the buffer from which these were casted from). These images further support out findings above that both the **Nap** and the **TBNaps** form self-assembly structures in solutions. The changes in the morphology of both of our probes when interacting with Con A, was next carried out. The SEM images of these are shown in Fig. 6c and d; the samples being formed in identical manner except in the presence of 0.2 equivalents of Con A, and 0.1 mM $MnCl_2$ and 0.1 mM $CaCl_2$, followed by drop casting and drying in air. It is clear form Fig. 6c and d, that the presence of the Con A. and the salts has significant effect on the morphology of both **1** and **3**. While some indications of the presence of the nanospheres can be seen for **1**, it is clear that significant aggregation has occurred in the present of the protein, and as above, in the presence of salts. However, SEM imaging of the protein itself (drop casted from buffered ionic solutions), demonstrated the formation of thick films which lack the morphology seen in Fig. 6c (see ESI†).

Similarly, the morphology of the **TBNap 3** in the present of Con A is significantly different to the self-assembly of **3** alone;

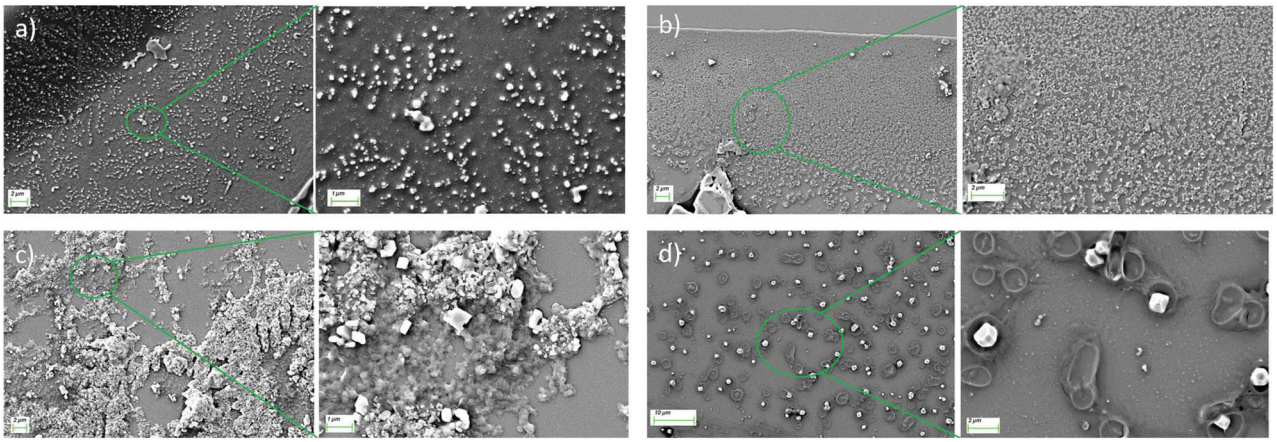

Fig. 6 SEM images of **1** before (a) and after addition of 0.1 equiv. of Con A (c) and **3** before (b) and after addition of 0.1 equiv. of Con A (d), showing significant morphological changes that demonstrate the binding with Con A, after drop-casting from buffered pH 7.2 solutions of these compounds. The formation of salts is also visible in these images.

the presence of larger aggregates is observed that seem to consist of spherical structures, some of which seem to indicate a 'collapsed' hallow-spheres. These results provided further evidence that these structures do interact with Con A resulting in changes in their morphological features. To probe if the DPBS buffer had an effect on the morphology of both probes, the samples were prepared in pure deionised water, and the resulting solution of **1** and **3** drop casted onto silicon wafer, dried in air followed by few hours under vacuum and imaged using SEM (see ESI†). Gratifyingly, the two samples showed similar morphology to that seen for samples prepared in DPBS demonstrating that the buffer did not influence the morphology of both probes and that the changes observed previously are due to the presence of Con A. This observation was also supported by DLS measurement that were carried out on **3** in both the absence and presence of **Con A** in DPBS buffer. Here, the DLS showed that the average size of the aggregates in solution for the **3** alone was similar to that seen in the SEM, while these were almost ten times the size upon interacting with Con A (see ESI†).

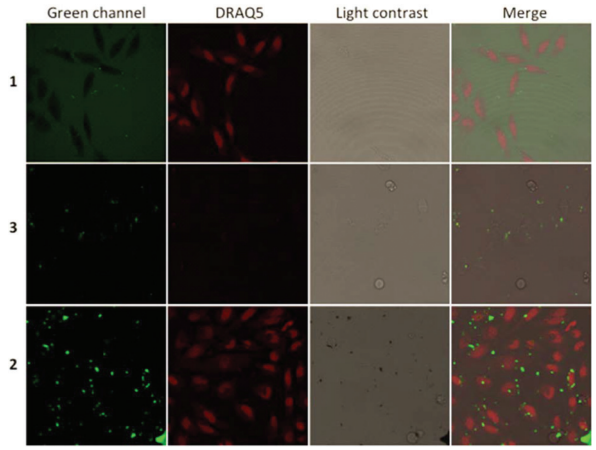

Fig. 7 Confocal images of HeLa cells treated with compound 1 (50 μM, first row), compound **3** (50 μM, second row) and compound **2** (50 μM, third row) after 24 h incubations. Compounds were excited by a 405 nm argon laser, emission 450–550 nm, DRAQ5 was excited by a 633 nm red helium–neon laser, emission >650 nm. *Compound **3** was not incubated with DRAQ5 as it quenched its fluorescence emission.

Biological evaluation

Having demonstrated that **1** and **3** could interact with lectin proteins, and that no interaction was seen with proteins such as BSA (Fig. 5), we investigated the biological scope of **1–3** *in vitro* using human cervical cancer cells (HeLa). We have previously performed uptake studies of **1** across various cell lines where no uptake was observed, even after long incubation times (24 h) (Fig. 7, first row). However, **3** was shown to localize within the cytosol of the HeLa cells (Fig. 7, second row) within 24 h; possibly due to the greater lipophilicity of **3** *vs.* **1**. However, compound **3** was not shown to be toxic, with IC_{50} values >100 μM (evaluated *via* Alamar Blue assay). Longer incubation times (72 h), also resulted in IC_{50} that were greater than 100 μM, therefore it can be concluded that **3** could be used safely *in vitro*. To support this rationale, compound **2** was also evaluated *in vitro*, as the protected mannose units make it even more lipophilic and therefore more prone to cellular uptake. Incubation in HeLa cells (Fig. 7, third row) showed a greater uptake than either **1** or **3**. However, due to its high hydrophobicity it was observed to form aggregates in aqueous solution. Interestingly, short times of incubation (of *ca.* 1 h) showed larger aggregates that are more challenging for cellular uptake, and these aggregates interact with the cell membrane (see ESI†). After longer times (24 h), the aggregates reduce in size and are increasingly accumulated within the cells. Confocal imaging analysis through the use of *Z*-stacks images proved that the smaller aggregates were indeed located inside the cells whereas the larger ones only interact with the cell membrane (see ESI†).

Conclusions

Two structurally related glyconaphthalimide probes were prepared and their photophysical and self-assembly properties investigated. Their ability to function as fluorogenic molecular probes for lectin binding was studied and it was demonstrated that carbohydrate–lectin interactions resulted in a disruption of aggregation that resulted in significant changes in fluorescence. Binding studies in the presence of non-lectin proteins demonstrated that changes in the luminescence arise from selective binding interactions between the α-mannosides probes and Con A and highlight the potential of these probes for *in vitro* and *in vivo* applications. The monovalent **1** probe was found to be superior to **3** for lectin detection although **3** more readily underwent cellular uptake in HeLa cells. Detailed morphology studies further confirmed the disruption of aggregates upon carbohydrate–lectin binding interactions. This proof of principle opens novel avenues for molecular probe design using naphthalimide derivatives. We are currently investigating the use of **TBNap** structures as supramolecular synthons for the formation of self-assemble in solutions for applications in chemical biology.

Experimental

Materials and methods

Unless otherwise stated; all commercial chemicals were obtained from Sigma-Aldrich or Fluka and used without further purification. Deuterated solvents for NMR use were purchased from Apollo. Dry solvents were distilled under Argon and dried over 4 Å molecular sieves prior to use. Solvents for synthesis purposes were used at GPR grade. NMR spectra were recorded on Bruker DPX-400 Advance spectrometers, operating at 400.13 MHz and 600.1 MHz for ^{1}H NMR; 100.6 MHz and 150.9 MHz for ^{13}C-NMR. Shifts are referenced to the internal solvent signals.[1] NMR data were processed using Mestrenova software. HRMS spectra were measured on a Micromass LCT electrospray TOF instrument with a WATERS 2690 autosampler and methanol/acetonitrile as carrier solvent. Melting points were determined using a Stuart Scientific Melting point was determined using an Electrochemical IA9000 digital melting point apparatus in an unsealed capillary tube and are incorrect. Infrared spectra were recorded on a PerkinElmer Spectrum One FT-IR Spectrometer equipped with a Universal ATR sampling accessory. Carbohydrate positions are named 1 to 6, starting the count in the anomeric position.

UV/Vis measurements

UV-visible absorption spectra and optical density were recorded by means of a Varian CARY 50 spectrophotometer. Solutions were measured in 3 cm (10 mm × 10 mm) cuvettes. The wavelength range was 200–600 nm with a scan rate of 300 nm min^{-1}. The solvents employed were HPLC or spectrophotometric grade.

Fluorescence measurements

Fluorescence measurements were made with a Varian Carey Eclipse Fluorimeter equipped with a 1.0 cm path length quartz cell. The solvents used were of HPLC grade. The concentrations of the compounds under investigation were the same as those used for the UV-visible absorption measurements.

Cell culture

HeLa cells were grown in Dulbecco's Modified Eagle Medium (Glutamax) supplemented with 10% fetal bovine serum, 1% penicillin/streptomycin and 0.2% of plasmocin at 37 °C in a humidified atmosphere of 5% CO_2.

Alamar blue viability assay

HeLa cells were seeded at a density of 2.5×10^4 cells per well in 96-well plates and treated with the indicated compounds for 24 or 72 h. Alamar blue (22 μl) was then added to each well and incubated at 37 °C in the dark for 4 h. Plates were then read on a fluorescence plate reader (SpectraMax Gemini, Molecular Devices) with excitement and emission wavelengths of 544 nm and 590 nm, respectively. Experiments were performed in triplicate on three independent days with activity expressed as percentage cell viability compared to vehicle treated controls. All data points (expressed as means ± S.E.M.) were analysed using GRAPHPAD Prism (Graphpad software Inc., San Diego, CA).

Confocal microscopy

Cells were seeded at a density of 5×10^4 cells per dish in glass bottom wells and leave to grow for 24 h. Before treatment cell media was replaced by phenol-red free media and cells were incubated with compounds (50 μM) for 1 and 24 h, respectively. Cells were stained with DRAQ5 (red nuclear stain), followed by viewing using Leica SP8 STED confocal microscopy with a 40× oil immersion lens. Image analysis was performed using Leica Application Suite software. Compounds were excited by a 405 nm argon laser, emission 450–550 nm, DRAQ5 was excited by a 633 nm red helium–neon laser, emission >650 nm. Images are representative of three independent experiments.

Scanning electron microscopy

The morphology of the samples were studied using a Carl Zeiss Ultra SEM with an SE2 or in-lens detector in the Advanced Microscopy Laboratory, CRANN, Trinity College Dublin, with the samples deposited on silicon wafers with a thick silicon dioxide layer. Prior to imaging, all samples were coated with a conductive layer of Pd/Au using a Cressington 208Hr high-resolution sputter coater.

X-ray crystallography

The diffraction data were collected on a Bruker APEX-II Duo dual-source instrument using microfocus Cu-Kα radiation (λ = 1.5405 Å) using ω and φ scans. A single crystal was mounted on Mitegen micromounts in NVH immersion oil, and maintained at a temperature of 100 K using a Cobra cryostream.

The diffraction data were reduced and processed using the Bruker APEX suite of programs.[28] Multi-scan absorption corrections were applied using SADABS.[29] The data were solved using the Intrinsic Phasing routine in SHELXT. Although the chiral space group $P2_12_12$ gave the best statistics and most appropriate structure model, no chirality information is assumed and the structure was refined as a racemic twin with full-matrix least squares procedures using SHELXL-2015 within the OLEX-2 GUI.[30–32] All non-hydrogen atoms were refined with anisotropic displacement parameters. All hydrogen atoms were placed in calculated positions and refined with a riding model, with isotropic displacement parameters equal to either 1.2 or 1.5 times the isotropic equivalent of their carrier atoms. Due to the severe disorder in the naphthalimide fragments of both unique molecules, DFIX, SADI and RIGU restraints and EADP constraints were necessary to maintain reasonable chemical geometries and U_{ij} tensors, particularly where atoms from both fragments were closely overlapping. Occupancies of the individual conformers were determined with free variable refinement and then fixed to sensible fractional values. Specific collection and refinement strategies are further outlined in the combined crystallographic information file (cif) under the _refine_special_details heading. CCDC 1866499.†

Crystal data for compound **7** ($C_{36}H_{35}N_{10}O_{6.5}$, M = 711.74 g mol^{-1}): orthorhombic, space group $P2_12_12$ (no. 18), a = 17.0714(12) Å, b = 27.849(2) Å, c = 6.8249(3) Å, V = 3244.7(4) Å^3, Z = 4, T = 100.0 K, μ(CuKα) = 0.859 mm^{-1}, D_{calc} = 1.457 g cm^{-3}, 21 933 reflections measured (6.072° ≤ 2Θ ≤ 137.048°), 5941 unique (R_{int} = 0.0536, R_{sigma} = 0.0544) which were used in all calculations. The final R_1 was 0.0754 ($I > 2\sigma(I)$) and wR_2 was 0.2039 (all data).

Synthetic procedures

Bis-(*N*-(1-(3-(2′,3′,4′,6′-tetra-*O*-acetyl-α-D-mannopyranosyloxy)propyl)-1*H*-1″,2″,3″-triazol-4″-yl)methyl)-9,18-methano-1,8-naphthalimide-[*b*,*f*][1,5]diazocine (2). Compound **5** (28 mg, 0.05 mmol, 1 equiv.), compound **1** (45 mg, 0.1 mmol, 2 equiv.) and Cu(BF$_4$)(MeCN)$_4$ (10 mg, 0.03 mmol, 0.3 equiv.) were dissolved in DMF (5 mL) in a microwave vial. The reaction mixture was stirred for 2 h at 115 °C in a microwave reactor. The solvent was removed *in vacuo* and the crude product dissolved in a mixture of MeOH/CH_2Cl_2 (1 : 2) and filtered through a plug of Celite® to remove the copper catalyst. The filtrate was concentrated *in vacuo* and purified by SiO_2 column chromatography. The product was obtained as an orange wax (40 mg, 66%). **^{1}H** (799.7 MHz, $CDCl_3$): 8.69 (bs, 2H, H–Ar), 8.62 (d, J = 11.4 Hz, 2H, H–Ar), 8.13 (s, 2H, H–Ar), 8.03 (s, 2H, H–Ar), 7.86 (s, 2H, H–Ar), 7.61 (s, 2H), 5.42 (bs, 3H), 5.27–5.24 (m, 4H, CH_2), 5.21 (bs, 1H), 5.14 (app t, 2H, N–CH_2), 4.76 (s, 2H, H-1), 4.66–4.64 (m, 2H), 4.61–4.56 (m, 2H), 4.43–4.39 (m, 2H), 4.38–4.34 (m, 2H), 4.20–4.35 (m, 2H), 4.05 (d, J = 12.6 Hz, 2H), 3.96–3.92 (s, 2H), 3.71–3.67 (s, 2H), 3.40–3.35 (s, 2H), 2.14, 2.06, 2.05, 1.99 (s, 24H, $OCOCH_3$), (2 × CH_2 buried under $OCOCH_3$). **^{13}C** (201.1 MHz, $CDCl_3$): 153.6, 133.5 (C–Ar), 129.8 (C–Ar), 100.4 (C-1), 71.9, 71.6 (C–CH_2), 71.3, 69.6, 68.5 (C–CH_2), 67.3, 67.2, 65.0, 59.7 (C-16), 59.6, 39.2, 37.8, 34.1, 33.7, 33.6, 23.6, 23.5, 23.4, 23.3, 22.4 (7C, $OCOCH_3$). ν_{max} (ATR)/cm^{-1}: 789, 1051 (C–N), 1229 (C–N), 1373, 1597 (ar. C–C), 1659 (C═O), 1747, 2923. **HRMS** (m/z – MALDI): found: 1421.4504, ([M + Na]$^+$. $C_{67}H_{70}N_{10}O_{24}Na$, required: 1421.4462).

Bis-(*N*-(1-(3-(α-D-mannopyranosyloxy)propyl)-1*H*-1′,2′,3′-triazol-4′-yl)methyl)-9,18-methano-1,8-naphthalimide-[*b*,*f*][1,5]diazocine (3). Compound **2** (40 mg, 0.028 mmol, 1 equiv.) was dissolved in MeOH/NaOMe (5 mL, 0.4 equiv.). After stirring for 4 h at rt, DOWEX® 50WX8-200 ion exchange resin was added to the mixture until a neutral pH was measured. The reaction mixture was filtered and the filtrate concentrated *in vacuo*. Yielding the desired product as an orange powder (28 mg, 98%). **M.p:** 120.5–122.0 °C (decomposition). **^{1}H** (400 MHz, d-TFA): 9.05 (d, J = 8.0 Hz, 2H, H–Ar), 8.99 (d, J = 7.2 Hz, 2H, H–Ar), 8.84 (s, 2H, H–Ar), 8.65–8.59 (m, 2H, H–Ar), 8.36 (s, 2H, H–Ar), 5.96 (s, 2H, H–Ar), 5.93–5.87 (m, 4H, CH_2, H–Ar), 5.83 (s, 2H, N–CH_2), 5.32–5.29 (m, 2H), 5.28–5.25 (m, 2H), 5.22 (s, 2H), 5.00–4.94 (s, 6H), 4.55–4.39 (m, 2H), 4.55–4.29 (m, 2H), 4.19–4.08 (m, 4H), 3.81–3.75 (m, 2H). ν_{max} (ATR)/cm^{-1}: 980, 1100, 1490 (ar. C–C), 1750 (C═O), 3410 (OH/NH_2). **HRMS** (m/z – ESI): found: 1063.38054, ([M + H]$^+$. $C_{51}H_{55}N_{10}O_{16}$, required: 1063.3792).

Bis-[*N*-(1-propargyl)]-9,18-methano-1,8-naphthalimide-[*b*,*f*][1,5]diazocine (5). Compound **4** (100 mg, 0.21 mmol, 1 equiv.) was reacted with propargylamine (35 μL, 0.54 mmol, 2.5 equiv.) in EtOH (10 mL) at 80 °C for 16 h. After this time, the reaction mixture was filtered through Celite and washed with cold EtOH leaving an orange solid (108 mg, 94%). **M.p:** 292–294 °C (decomposition). **^{1}H** (400 MHz, $CDCl_3$): 8.72 (d, J = 8.4 Hz, 2H, H–Ar), 8.65 (d, J = 7.2 Hz, 2H, H–Ar), 8.14 (s, 2H, H–Ar), 7.88 (app t, 2H, H–Ar), 5.15 (d, J = 16.9 Hz, 1H, N–CH_2), 4.88 (s, 4H, H-2), 4.68 (s, 2H, N–CH_2–N), 4.59 (d, J = 16.9 Hz, 2H, N–CH_2). **^{13}C** (100 MHz, CDCl3): 163.2, 162.6, 150.0, 131.6, 131.1, 131.0, 127.9, 127.78, 127.4, 126.9, 122.5, 117.8, 79.8, 73.4, 66.4, 56.5, 31.2, 29.4, 19.0. ν_{max} (ATR)/cm^{-1}: 1033, 1661 (C═O), 1340 (ar. C–C), 2935 (CCH). **HRMS** (m/z – MALDI): found: 537.1578, ([M + Na]$^+$. $C_{33}H_{54}N_{10}O_{16}Na$, required: 537.15557).

Conflicts of interest

There are no conflicts to declare.

Acknowledgements

We thank the Irish Research Council (IRC) (GOIPD/2013/442 to S. S., and GOIPD/2015/446 to C. S. H.) and Science Foundation Ireland (SFI PI Award 13/IA/1865 to T. G.) and (SFI CDA Award 15/CDA/3310 to E. M. S.) for the financial support.

Notes and references

1 (*a*) D. Wu, A. C. Sedgwick, T. Gunnlaugsson, E. U. Akkaya, J. Yoon and T. D. James, *Chem. Soc. Rev.*, 2017, **46**, 7105–

7123; (*b*) S. Erbas-Cakmak, S. Kolemen, A. C. Sedgwick, T. Gunnlaugsson, T. D. James, J. Yoon and E. U. Akkaya, *Chem. Soc. Rev.*, 2018, **47**, 2228–2248.

2 (*a*) B. Daly, J. Ling and A. P. de Silva, *Chem. Soc. Rev.*, 2015, **44**, 4203–4211; (*b*) A. P. de Silva, H. Q. N. Gunaratne, T. Gunnlaugsson, A. J. M. Huxley, C. P. McCoy, J. T. Rademacher and T. E. Rice, *Chem. Rev.*, 1997, **97**, 1515–1566; (*c*) W. Guan, W. Zhou, J. Lu and C. Lu, *Chem. Soc. Rev.*, 2015, **44**, 6981–7009; (*d*) E. B. Veale and T. Gunnlaugsson, *Annu. Rep. Prog. Chem.*, 2010, **106**, 376; (*e*) H. N. Kim, Z. Guo, W. Zhu, J. Yoon and H. Tian, *Chem. Soc. Rev.*, 2011, **40**, 79–93; Z. Guo, S. Park, J. Yoon and I. Shin, *Chem. Soc. Rev.*, 2014, **43**, 16–29.

3 (*a*) F. E. Poynton, S. A. Bright, S. Blasco, D. C. Williams, J. M. Kelly and T. Gunnlaugsson, *Chem. Soc. Rev.*, 2017, **46**, 7706–7756; (*b*) R. T. K. Kwok, C. W. T. Leung, J. W. Y. Lam and B. Z. Tang, *Chem. Soc. Rev.*, 2015, **44**, 4228–4238.

4 V. García-López, F. Chen, L. G. Nilewski, G. Duret, A. Aliyan, A. B. Kolomeisky, J. T. Robinson, G. Wang, R. Pal and J. M. Tour, *Nature*, 2017, **548**, 567–572.

5 C. Moylan, E. M. Scanlan and M. O. Senge, *Curr. Med. Chem.*, 2015, **22**, 2238–2348.

6 (*a*) S. H. Hewitta and S. J. Butler, *Chem. Commun.*, 2018, **54**, 6635–6647; (*b*) I. V. Kolesnichenko and E. V. Anslyn, *Chem. Soc. Rev.*, 2017, **46**, 2385–2390.

7 (*a*) P. A. Gale and C. Caltagirone, *Coord. Chem. Rev.*, 2018, **354**, 2–27; (*b*) A. B. Aletti, D. M. Gillen and T. Gunnlaugsson, *Coord. Chem. Rev.*, 2018, **354**, 98–120; (*c*) Z. Xu, K.-H. Baek, H. N. Kim, J. Cui, X. Qian, D. R. Spring, I. Shin and J. Yoon, *J. Am. Chem. Soc.*, 2010, **132**, 601–610.

8 (*a*) L. Fang, G. Trigiante, C. J. Kousseff, R. Crespo-Otero, M. P. Philpott and M. Watkinson, *Chem. Commun.*, 2018, **54**, 9619–9622; (*b*) X. Sun, Q. Xu, G. Kim, S. E. Flower, J. P. Lowe, J. Yoon, J. S. Fossey, X. Qian, S. D. Bull and T. D. James, *Chem. Sci.*, 2014, **5**, 3368–3373; X. Jia, Q. Chen, Y. Yang, Y. Tang, R. Wang, Y. Xu, W. Zhu and X. Qian, *J. Am. Chem. Soc.*, 2016, **138**, 10778–10781; (*c*) D. T. Shi, D. Zhou, Y. Zang, J. Li, G. R. Chen, T. D. James, X.-P. He and H. Tian, *Chem. Commun.*, 2015, **51**, 3653–3655.

9 (*a*) H. M. Burke, T. Gunnlaugsson and E. M. Scanlan, *Chem. Commun.*, 2015, **51**, 10576–10588; (*b*) Z.-R. Dai, G.-B. Ge, L. Feng, J. Ning, L.-H. Hu, Q. Jin, D.-D. Wang, X. Lv, T.-Y. Dou, J.-N. Cui and L. Yang, *J. Am. Chem. Soc.*, 2015, **137**, 14488–14495.

10 (*a*) J. I. Lovitt, C. S. Hawes, A. D. Lynes, B. Haffner, M. E. Mobius and T. Gunnlaugsson, *Inorg. Chem. Front.*, 2017, **4**, 296; (*b*) C. S. Hawes, A. D. Lynes, K. Byrne, W. Schmitt, G. Ryan, M. E. Möbius and T. Gunnlaugsson, *Chem. Commun.*, 2017, **53**, 5989–5992; (*c*) C. S. Hawes, K. Byrne, W. Schmitt and T. Gunnlaugsson, *Inorg. Chem.*, 2016, **55**, 11570–11582; (*d*) S. Mukherjee and P. Thilagar, *Chem. – Eur. J.*, 2014, **20**, 8012–8023.

11 E. Calatrava-Perez, S. A. Bright, S. Achermann, C. Moylan, M. O. Senge, E. B. Veale, D. C. Williams, T. Gunnlaugsson and E. M. Scanlan, *Chem. Commun.*, 2016, **52**, 13086–13089.

12 Examples where such targeting has been achieved: (*a*) D. Wu, S. Cheung, R. Daly, H. Burke, E. M. Scanlan and D. F. O'Shea, *Eur. J. Org. Chem.*, 2014, 6841; (*b*) Y. Fu, J. Zhang, H. Wang, J.-L. Chen, P. Zhao, G.-R. Chen and X.-P. He, *Dyes Pigm.*, 2016, **133**, 372–379; (*c*) M. H. Lee, J. H. Han, P.-S. Kwon, S. Bhuniya, J. Y. Kim, J. L. Sessler, C. Kang and J. S. Kim, *J. Am. Chem. Soc.*, 2012, **134**, 1316–1322; (*d*) R. Daly, G. Vaz, A. M. Davies, M. O. Senge and E. M. Scanlan, *Chem. – Eur. J.*, 2012, **18**, 14671–14679; (*e*) O. B. Locos, C. C. Heindl, A. Corral, M. O. Senge and E. M. Scanlan, *Eur. J. Org. Chem.*, 2010, 1026–1028.

13 (*a*) X. Jia, Y. Yang, Y. Xu and X. Qian, *Pure Appl. Chem.*, 2014, **86**, 1237–1246; (*b*) Z. Xu, L. Xu, J. Zhou, Y. Xu, W. Zhu and X. Qian, *Chem. Commun.*, 2012, **48**, 10871.

14 H.-L. Zhang, X.-Li Wei, Y. Zang, J.-Y. Cao, S. Liu, X.-P. He, Q. Chen, Y.-T. Long, J. Li, G.-R. Chen and K. Chen, *Adv. Mater.*, 2013, **25**, 4097–4101.

15 S. Cecioni, A. Imberty and S. Vidal, *Chem. Rev.*, 2015, **115**, 525–561.

16 T. J. Tymoczko, J. M. Berg and L. Stryer, *Biochemistry*, W H Freeman, 5th edn, 2002, ISBN-10: 0-7167-3051-0.

17 T. Yau, X. Dan, C. Ng and T. Ng, *Molecules*, 2015, **20**, 3791.

18 (*a*) J. M. Benito, M. Gómez-García, C. Ortiz Mellet, I. Baussanne, J. Defaye and J. M. García Fernández, *J. Am. Chem. Soc.*, 2004, **126**, 10355–10363; (*b*) V. Wittmann and R. J. Pieters, *Chem. Soc. Rev.*, 2013, **42**, 4492–4503.

19 P. N. Kanellopoulos, K. Pavlou, A. Perrakis, B. Agianian, C. E. Vorgias, C. Mavrommatis, M. Soufi, P. A. Tucker and S. J. Hamodrakas, *J. Struct. Biol.*, 1996, **116**, 345–355.

20 H. M. Burke, T. Gunnlaugsson and E. M. Scanlan, *Org. Biomol. Chem.*, 2016, **14**, 9133–9145.

21 M. Matsui and Y. Ebara, *Bioorg. Med. Chem. Lett.*, 2012, **22**, 6139–6143.

22 (*a*) R. M. Duke, E. B. Veale, F. M. Pfeffer, P. E. Kruger and T. Gunnlaugsson, *Chem. Soc. Rev.*, 2010, **39**, 3936–3953; (*b*) S. Banerjee, E. B. Veale, C. M. Phelan, S. A. Murphy, G. M. Tocci, L. J. Gillespie, D. O. Frimannsson, J. M. Kelly and T. Gunnlaugsson, *Chem. Soc. Rev.*, 2013, **42**, 1601–1618; (*c*) S. Banerjee, J. A. Kitchen, S. A. Bright, J. E. O'Brien, D. C. Williams, J. M. Kelly and T. Gunnlaugsson, *Chem. Commun.*, 2013, **49**, 8522–8524.

23 (*a*) K. Jobe, C. H. Brennan, M. Motevalli, S. M. Goldup and M. Watkinson, *Chem. Commun.*, 2011, **47**, 6036–6038; (*b*) J. Pancholi, D. J. Hodson, K. Jobe, G. A. Rutter, S. M. Goldup and M. Watkinson, *Chem. Sci.*, 2014, **5**, 3528–3535; (*c*) J. A. Kitchen, P. N. Martinho, G. G. Morgan and T. Gunnlaugsson, *Dalton Trans.*, 2014, **43**, 6468–6479; (*d*) E. B. Veale, J. A. Kitchen and T. Gunnlaugsson, *Supramol. Chem.*, 2013, **25**, 101–108; (*e*) E. Tamanini, A. Katewa, L. M. Sedger, M. H. Todd and M. Watkinson, *Inorg. Chem.*, 2009, **48**, 319; (*f*) E. Tamanini, K. Flavin, M. Motevalli, S. Piperno, L. A. Gheber, M. H. Todd and M. Watkinson, *Inorg. Chem.*, 2010, **49**, 3789; (*g*) F. Lupo, S. Gentile, F. P. Ballistreri, G. A. Tomaselli, M. E. Fragala

and A. Gulino, *Analyst*, 2010, **135**, 2273; (*h*) T. Gunnlaugsson, M. Glynn, G. M. Tocci, P. E. Kruger and F. M. Pfeffer, *Coord. Chem. Rev.*, 2006, **250**, 3094; (*i*) R. M. Duke and T. Gunnlaugsson, *Tetrahedron Lett.*, 2007, **48**, 8043; (*j*) T. Gunnlaugsson, M. Nieuwenhuyzen, L. Richard and V. Thoss, *Tetrahedron Lett.*, 2001, **42**, 4725; (*k*) T. Gunnlaugsson, B. Bichell and C. Nolan, *Tetrahedron Lett.*, 2002, **43**, 4989.

24 (*a*) E. B. Veale, D. O. Frimannsson, M. Lawler and T. Gunnlaugsson, *Org. Lett.*, 2009, **11**, 4040–4043; (*b*) E. B. Veale and T. Gunnlaugsson, *J. Org. Chem.*, 2010, **75**, 5513–5525; (*c*) S. Banerjee, S. A. Bright, J. A. Smith, J. Burgeat, M. Martinez-Calvo, D. C. Williams, J. M. Kelly and T. Gunnlaugsson, *J. Org. Chem.*, 2014, **79**, 9272–9283; (*d*) S. Murphy, S. A. Bright, F. E. Poynton, T. McCabe, J. A. Kitchen, E. B. Veale, D. C. Williams and T. Gunnlaugsson, *Org. Biomol. Chem.*, 2014, **12**, 6610–6623.

25 (*a*) S. Shanmugaraju, B. la Cour Poulsen, T. Arisa, D. Umadevi, H. L. Dalton, C. S. Hawes, S. Estalayo-Adrian, A. J. Savyasachi, G. W. Watson, D. C. Williams and T. Gunnlaugsson, *Chem. Commun.*, 2018, **54**, 4120–4123; (*b*) R. B. P. Elmes, M. Erby, S. A. Bright, D. C. Williams and T. Gunnlaugsson, *Chem. Commun.*, 2012, **48**, 2588–2590.

26 K. Hanaoka, Y. Muramatsu, Y. Urano, T. Terai and T. Nagano, *Chem. – Eur. J.*, 2010, **16**, 568–572.

27 S. Shanmugaraju, D. McAdams, F. Pancotti, C. S. Hawes, E. B. Veale, J. A. Kitchen and T. Gunnlaugsson, *Org. Biomol. Chem.*, 2017, **15**, 7321–7329.

28 *Bruker APEX-3*, Bruker-AXS Inc., Madison, WI, 2016.

29 *Bruker DIFFRAC.EVA*, Bruker-AXS Inc., Madison, WI, 2016.

30 *SADABS*, Bruker-AXS Inc., Madison, WI, 2016.

31 G. M. Sheldrick, *Acta Crystallogr., Sect. A: Found. Adv.*, 2015, **71**, 3–8.

32 G. M. Sheldrick, *Acta Crystallogr., Sect. C: Struct. Chem.*, 2015, **71**, 3–8.

33 O. V. Dolomanov, L. J. Bourhis, R. J. Gildea, J. A. K. Howard and H. Puschmann, *J. Appl. Crystallogr.*, 2009, **42**, 339–341.

Volume 55 | Number 81 | 18 October 2019 | Pages 12115–12268

ChemComm

Chemical Communications

rsc.li/chemcomm

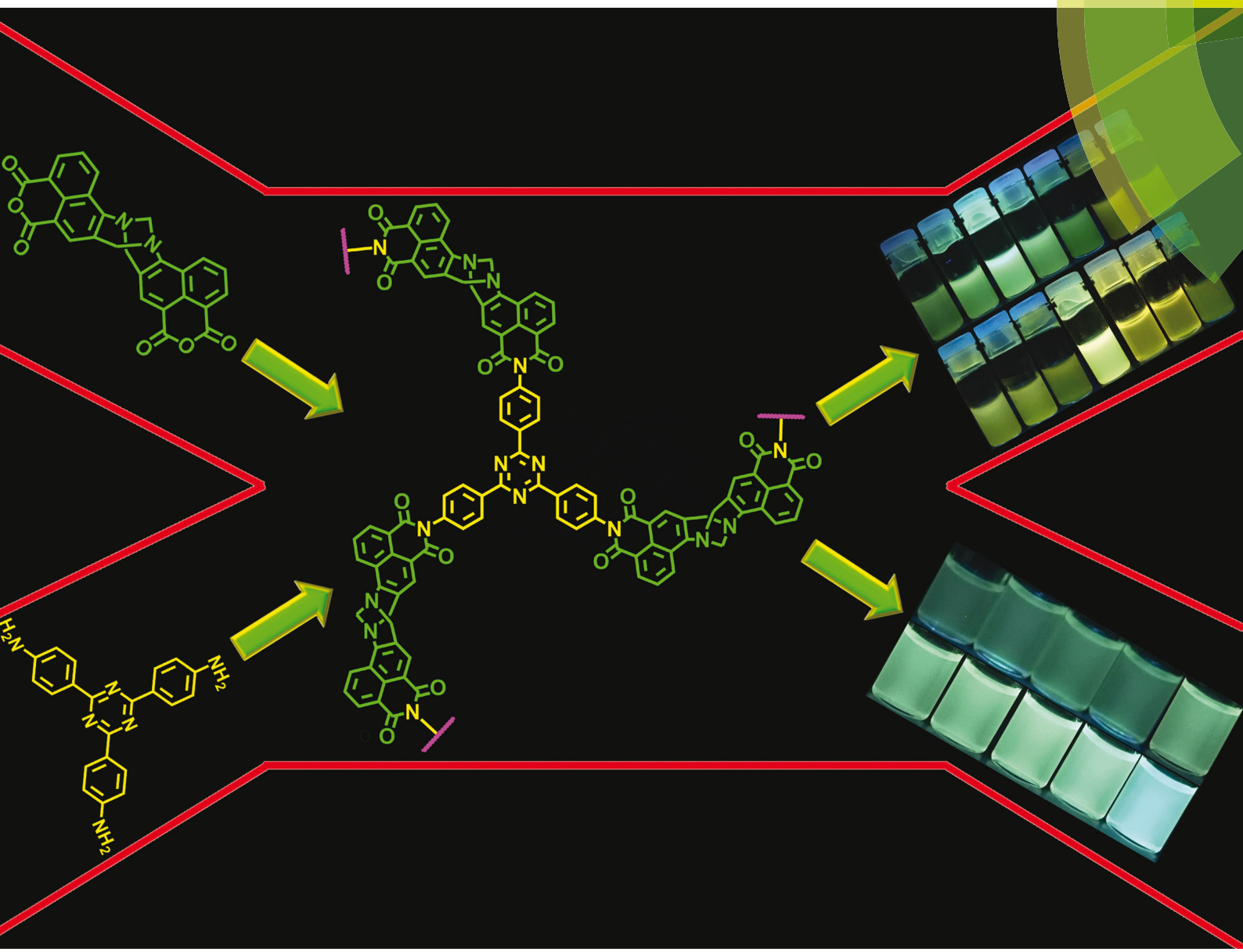

ISSN 1359-7345

ROYAL SOCIETY OF CHEMISTRY | Celebrating IYPT 2019

COMMUNICATION

Sankarasekaran Shanmugaraju, Thorfinnur Gunnlaugsson *et al.*

"Turn-on" fluorescence sensing of volatile organic compounds using a 4-amino-1,8-naphthalimide Tröger's base functionalised triazine organic polymer

ChemComm

COMMUNICATION

View Article Online
View Journal | View Issue

Cite this: *Chem. Commun.*, 2019, 55, 12140

Received 19th July 2019,
Accepted 9th September 2019

DOI: 10.1039/c9cc05585a

rsc.li/chemcomm

"Turn-on" fluorescence sensing of volatile organic compounds using a 4-amino-1,8-naphthalimide Tröger's base functionalised triazine organic polymer†

Sankarasekaran Shanmugaraju, *[ab] Deivasigamani Umadevi, [c] Luis M. González-Barcia, [a] Jason M. Delente, [ad] Kevin Byrne, [c] Wolfgang Schmitt, [c] Graeme W. Watson [c] and Thorfinnur Gunnlaugsson *[ad]

The 4-amino-1,8-naphthalimide Tröger's base functionalized triazine covalent organic polymer TB-TZ-COP was synthesised and employed as a "turn-on" fluorescent and a colorimetric sensor for the discriminative sensing of volatile organic compounds; the TB-TZ-COP displaying the largest fluorescent enhancement and high sensitivity for 1,4-dioxane, a harmful environmental pollutant classified as a Group 2B carcinogen.

Discovery of suitable chemosensors for the fast and selective sensing of hazardous substances and organic pollutants has attracted increasing attention in recent years to mitigate environmental pollution.[1,2] Among the various known pollutants, the volatile organic compounds (VOCs) have become a major source of environmental contaminants due to their mass use in manufacturing industries, as well as in scientific research laboratories.[3] The continuous exposure to VOCs is toxic to human health, causing a wide range of serious inflictions and chronic diseases like asthma, kidney failure, neurological damage, cystic fibrosis, and cancer.[4,5] Therefore, the design and the development of suitable chemical sensors for VOCs is highly desirable for the betterment of human health and to get rid of environmental pollution.[6] Several sophisticated instrumental techniques are currently available for VOCs detection and analysis, including gas-chromatography, high-performance liquid chromatography, ion chromatography, and mass spectrometry.[3,4,6,7] Despite the high selectivity, the real-time use of these traditional techniques is limited due to their expensive apparatuses, lack of portability, time-consuming detection process, and complicated instrument standardization.[6,7] Recently, fluorescence quenching/enhancement-based sensing has become an effective and alternative detection method to the above, owing to its simplicity, high sensitivity, easy visualization and short response time;[1,2,8,9] where the initial emission intensity of the fluorophore is perturbed, in one way or the other, by the presence of analytes.[10] A wide variety of fluorescent sensors have been developed and used for the detection of VOCs through fluorescence quenching based mechanism; however, background interference has been known to limits their practical use.[11] Furthermore, their real-life application has also been restricted due to low sensitivity, non-reusability and lack of specificity among VOCs.[12] Hence, there currently exists a need for developing alternative analytical/sensing methods for VOCs. In general, the use of '*turn-on*' (also known as 'switch-on') fluorescence sensing is particularly appealing because the sensing event can be easily detected, sometimes, even by the naked eye.[13] However, unlike 'turn-off' sensing, which can simply operate *via* static or dynamic quenching mechanisms, the design of *turn-on* fluorescence sensing, is more challenging.[14] We thus considered if the use of solvatochromic fluorescent sensing, might be a simple and an effective alternative and an effective approach for the discriminative sensing of VOCs.[15,16] With this in mind, we set out to develop an efficient fluorescent sensor suitable for selective and discriminative sensing of structurally related-VOCs, based on amino-1,8-naphthalimide Tröger's bases (**TBNaps**).

Over the past few years, we are interested in developing novel luminescent structures and materials of 3- and 4-amino-**TBNaps** motifs for their application in supramolecular material and medicinal chemistry.[17] **TBNaps** are fascinating chiral cleft-shaped supramolecular scaffolds (with *ca.* 90° angle between the two **Nap** structures) that are strongly colored and fluorescent due to their internal charge-transfer (ICT) excited state transition; which are solvent polarity dependent.[2,17] Furthermore, **TBNaps** display significant Strokes shifts in different solvents and thus they can be used as a potential luminescent sensor for the

[a] *School of Chemistry and Trinity Biomedical Sciences Institute (TBSI), Trinity College Dublin, The University of Dublin, Dublin 2, Ireland. E-mail: gunnlaut@tcd.ie*
[b] *Chemistry, Indian Institute of Technology Palakkad (IITPKD), Palakkad 678557, Kerala, India. E-mail: shanmugam@iitpkd.ac.in*
[c] *School of Chemistry and Centre for Research on Adaptive Nanostructures and Nanodevices (CRANN), Trinity College Dublin, The University of Dublin, Dublin 2, Ireland*
[d] *Advanced Materials and BioEngineering Research Center (AMBER), Trinity College Dublin, Dublin 2, Ireland*

† Electronic supplementary information (ESI) available: Experimental details, synthesis and characterisation details (FTIR, TGA, powder diffraction and SEM) fluorescence studies and computational details. See DOI: 10.1039/c9cc05585a

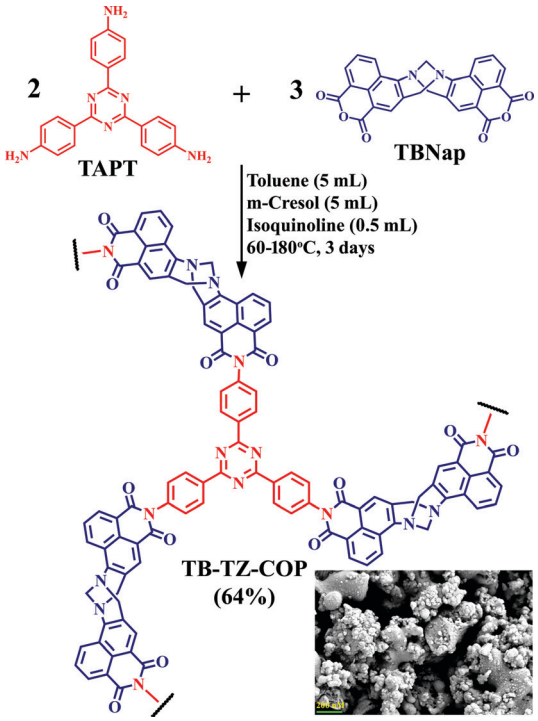

Scheme 1 Synthesis of polyimide **TB-TZ-COP** (inset: FESEM image of as-synthesized polymer).

discriminative sensing of structurally similar VOCs of varied polarity. Here we report the synthesis and fluorescence sensing properties of a new **TBNap** functionalized triazine covalent organic polymer, **TB-TZ-COP**, Scheme 1. We foresaw that the polyimide part of **TB-TZ-COP** would structurally facilitate the solvent polarity dependent emission properties, and thus **TB-TZ-COP** could act as a potential fluorescence sensor for the discriminative sensing of volatile organic pollutants.[2,9]

The polyimide **TB-TZ-COP** was synthesized using a one-step metal-free polycondensation reaction, Scheme 1, between triazine-based triamine (**TAPT**, 2.0 eq.) and the 4-amino-1,8-naphthalic anhydride derived Tröger's base (**TBNap**, 3.0 eq.) in a mixture of toluene and *m*-cresol as a reaction medium and isoquinoline as a catalyst under a stepwise increase of the reaction temperature (for details see ESI†).[18,19] The **TB-TZ-COP** polymer was isolated as a bright yellow solid and was found to be insoluble in common organic solvents. The successful formation of **TB-TZ-COP** was fully characterized at the molecular level by using CP/MAS ^{13}C-NMR and FT-IR spectroscopy. The solid-state ^{13}C-NMR spectrum of **TB-TZ-COP** showed the expected characteristic carbonyl carbon resonances at 164 ppm, which is slightly down-field shifted (~2 ppm) compared to the **TBNap** monomer due to the imide ring formation (ESI†).[19,20] The signal corresponding to the triazine unit was clearly observed at 171 ppm, while the two CH_2 carbon resonances of Tröger's base linkage were located at 67 and 57 ppm.[20] The chemical shifts corresponding to the other aromatic carbons were observed as a hampered overlapping signal in the range of 118 to 150 ppm (ESI†). In the FT-IR spectrum, the appearance of a new broad band at 1353 cm^{-1} corresponding to the stretching vibration of C–N–C linkage of the imide ring and the complete disappearance of NH_2 stretching vibrations around 3314 cm^{-1} of **TAPT** monomer confirms the successful formation of polyimide network in the isolated material (ESI†).[21] The characteristics carbonyl symmetric and asymmetric stretching vibrations of six-membered imide ring were observed at 1707 cm^{-1} and 1666 cm^{-1}, respectively. The FT-IR spectra also showed several intense bands at 1240 cm^{-1} and 1503 cm^{-1} accounting for C–N and N–C–N stretching, respectively which confirms the successful incorporation of Tröger's base and triazine functional groups into the isolated material (ESI†). The elemental analysis of **TB-TZ-COP** indicated that the calculated elemental composition is consistent with the experimentally measured values. The thermogravimetric analysis (TGA) under N_2 atmosphere showed an initial weight loss of ~4% at low temperature due to the loss of trapped solvent molecules and the desolvated **TB-TZ-COP** was stable up to 410 °C, indicating its high thermal stability (ESI†). The powder X-ray diffraction (PXRD) measurement shows that **TB-TZ-COP** was amorphous in nature (ESI†). The morphology of **TB-TZ-COP**, as observed by FESEM, is composed of particles with a rough surface and in a disorganized pattern (Scheme 1 and ESI†). The surface area and porosity of **TB-TZ-COP** were verified by N_2 adsorption isotherm. The N_2 uptake measurement at 77 K of activated **TB-TZ-COP** displayed steep and reversible adsorption of 139 cm^3 g^{-1} at 1 bar (ESI†). The Brunauer–Emmett–Teller (BET) surface was calculated to be 198 m^2 g^{-1}. The DFT pore size distribution confirms the presence of microporosity. Notably, the uptake capacity of **TB-TZ-COP** for CO_2 was moderate while the uptake capacity for H_2 was almost negligible (ESI†). The presence of high surface area and micropores suggests that **TB-TZ-COP** can, in addition to the surface interactions, efficiently adsorb the analytes inside the voids space and thus it can show superior sensing capability.[2]

Having successfully synthesized and characterized **TB-TZ-COP**, we next looked into the fluorescence sensing characteristics of **TB-TZ-COP** towards VOCs. These experiments were performed by dispersing **TB-TZ-COP** in various common organic solvents with varying polarities, such as toluene, CH_2Cl_2, THF, acetone, CH_3OH, CH_3CH_2OH, CH_3CN, diethyl ether, glycol, 1,4-dioxane, DMF, DMSO and then measured the fluorescence emission intensity of **TB-TZ-COP** in these solvents. As expected, the suspension of **TB-TZ-COP** displayed different fluorescent emission characteristics in these solvents and thus discriminative sensing ability for the rapid detection of VOCs (Fig. 1). Notably, the suspension of **TB-TZ-COP** in 1,4-dioxane displayed a dramatic enhancement in the fluorescence intensity in comparison to other organic solvents tested for. Furthermore, the discriminative sensing ability of **TB-TZ-COP** was found to be highly sensitive and reversible.

The emission intensity in H_2O was used as a reference to determine the relative number-fold emission enhancement of **TB-TZ-COP** in different organic solvents. The fluorescent study results implied that **TB-TZ-COP** was capable of discriminatively sense VOCs through a change in the **TBNap** fluorescence intensity, either *via* luminescent quenching or through luminescent enhancement (Fig. 1A). As alluded to above, then among different VOCs, the largest emission enhancement of 44% was observed at 502 nm for 1,4-dioxane, while THF, showed a moderate fluorescence

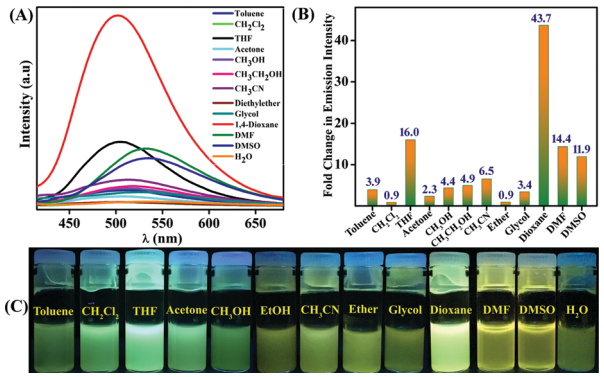

Fig. 1 (A) The emission spectra (λ_{ex} = 360 nm) of **TB-TZ-COP** in different solvents and (B) corresponding fold change in emission intensity with respect to its emission in H_2O. (C) Photograph of **TB-TZ-COP** dispersed in different solvents taken under UV light illumination (λ_{ex} = 365 nm).

enhancement (~16%) upon exciting at 360 nm. In high polar solvents such as DMF and DMSO, **TB-TZ-COP** displayed an average emission enhancement, which was significantly red-shifted to around 534 nm with a large Stokes shift; this shift is accompanied by **TBNap** spectral broadening. This can be accounted for because the excited state of the **TBNap** fluorophore is more stabilized in highly polar solvents than the ground state due to increasing the non-radiative transition of excited molecules.[16] Notably, the suspension of **TB-TZ-COP** in other organic solvents displayed almost no to weak fluorescence emission intensity. As depicted in Fig. 1B, the descending order of relative fold-change in emission enhancement of **TB-TZ-COP** are as following: 1,4-dioxane > THF > DMF > DMSO > CH_3CN > CH_3CH_2OH > CH_3OH > toluene > glycol > acetone > CH_2Cl_2 ≃ diethyl ether. This results clearly demonstrate the discriminative sensing ability of **TB-TZ-COP** towards the closely related VOCs. Gratifyingly, this discriminative fluorescence sensing was also being clearly visible to the naked eye as it appears from Fig. 1C.

We further performed Density Functional Theory (DFT) calculations using Gaussian 09[22] on our system to elucidate the reasons for the observed discriminative fluorescence sensing. One monomer unit of **TB-TZ-COP** as a representative fragment was considered for optimization. We also modelled all the VOCs considered in this study. Geometry optimization was done using DFT by employing the hybrid M062X functional and 6-311G(d,p) basis set.[23] The highest occupied molecular orbital (HOMO) and the lowest unoccupied molecular orbital (LUMO) energies of the **TB-TZ-COP** and the VOCs were calculated. It has been suggested that the fluorescent enhancement may be due to the energy transfer from the VOCs to **TB-TZ-COP**; this classically will only happen when the LUMO of the analyte is higher in energy than the corresponding LUMO of the sensor.[20] Gratifyingly, the LUMO energies of all the analytes tested for were comparatively higher (see ESI,† Table S1) than that determined computationally for **TB-TZ-COP** which would facilitate the energy transfer that gives rise to the fluorescence emission. While this would be in support of the observed emission enhancement (of 44%) for 1,4-dioxane, which has the highest LUMO energy value for the solvents studied, it would not account entirely for the observed order of enhancement seen for the other VOCs. Hence, the energy transfer phenomenon might not be the sole mechanism for the observed emission enhancements, and in fact, alternative and weak interaction might also be operating between **TB-TZ-COP** and the VOCs, which would further contribute to the observed luminescence enhancement. It has been shown that 1,4-dioxane exhibit significant intermolecular interactions with the solute, especially with aromatic molecules.[24] Because of this, we set out to investigate the fluorescent sensing of 1,4-dioxane more thoroughly using **TB-TZ-COP**.

Despite its hazardous nature, 1,4-dioxane is still used as a solvent in a variety of practical application, and the solvent is considered as an environmental pollutant and classified as group 2B carcinogens by US EPA. It is also used as a stabilizer for the organochloride transport and as a precursor in various manufacturing industries.[25] In general, 1,4-dioxane is synthesized *via* the condensation reaction of ethylene glycol (Fig. 2A).[26] Hence, having a sensor that can distinguish between glycol and 1,4-dioxane is practically useful. The fluorescence emission intensity of polymer **TB-TZ-COP** in glycol, 1,4-dioxane, and their mixture were thus assessed. As shown in Fig. 2C, the emission intensity of **TB-TZ-COP** in glycol increased linearly with an increasing percentage volume ratio of 1,4-dioxane. This enhancement was also accompanied by a significant blue-shift of ~22 nm in the fluorescence emission, assigned to the decrease in the polarity of the resulting solvent mixture. Furthermore, the effect was also clearly visible to the naked eye as is evident from Fig. 2B. Further analysis demonstrated fast emission response times, and a linear relationship between the observed emission enhancement and the concentrations of 1,4-dioxane in glycol; both demonstrating that **TB-TZ-COP** could be employed for the quantitative determination of specific VOCs mixtures (see ESI†). In fact, quantitative analysis of the emission enhancement profile

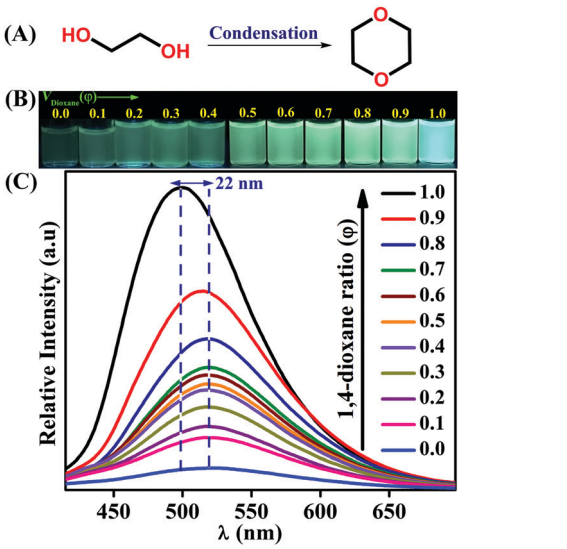

Fig. 2 (A) The reaction scheme for the condensation of glycol to 1,4-dioxane. (C) Emission spectra of **TB-TZ-COP** in glycol/1,4-dioxane mixture with different volume ratio of 1,4-dioxane and (B) corresponding photographs taken under UV light illumination (λ_{ex} = 365 nm).

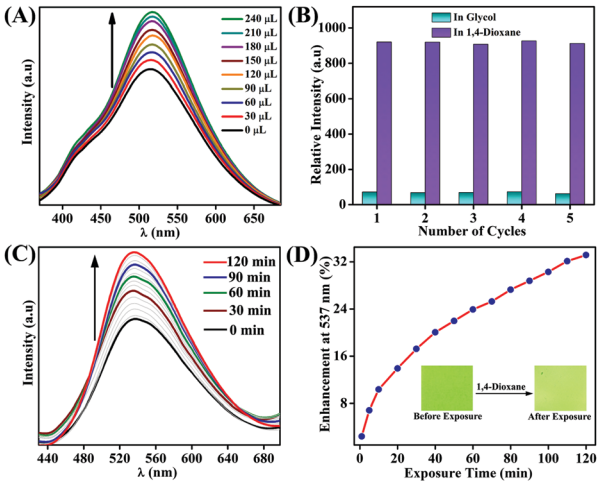

Fig. 3 (A) Change in emission intensity of **TB-TZ-COP** upon addition of dioxane (µL) in glycol. (B) Recycling test in glycol and in dioxane. (C) Emission spectra of thin film of **TB-TZ-COP** upon exposure to the dioxane vapours and (D) its corresponding enhancement efficiency plot (inset: photograph of thin film of **TB-TZ-COP** before and after exposure to dioxane vapours).

did demonstrate that **TB-TZ-COP** could detect 1,4-dioxane in glycol at as low levels as 22.2 ppm (Fig. 3A and ESI†).[11]

To meet the practical application of the **TB-TZ-COP** polymer as a reversible fluorescence sensor, we next verified the reproducibility of the sensing process of **TB-TZ-COP** towards 1,4-dioxane. The emission intensity of **TB-TZ-COP** in both glycol and 1,4-dioxane was first recorded, and after each measurement, the polymer was isolated by centrifugation and subsequently reused in the next emission study (cycle). As shown in Fig. 3B, the emission intensity of **TB-TZ-COP** in glycol (cyan bar) and 1,4-dioxane (violet bar), was retained even after five cycles of repetitions. This study demonstrates the excellent reproducibility, the recyclability sensing and the high photostability of **TB-TZ-COP** over several sensing cycles. To further explore the vapor phase sensing propensity of **TB-TZ-COP**, the emission intensity of a freshly made thin film of **TB-TZ-COP** exposed to the saturated vapours of 1,4-dioxane was monitored as a function of exposure time. As can be seen in Fig. 3C, the initial emission intensity of **TB-TZ-COP** at 537 nm increased dramatically upon exposing the film to the saturated vapours of 1,4-dioxane at room temperature, indicating the strong binding interactions between analytes and polymer. For instance, the emission was enhanced by 17% after just 30 minutes of exposure time; reaching 33% within 120 minutes, as demonstrated in Fig. 3D. Furthermore, a noticeable visual colour change was observed upon exposing the film to 1,4-dioxane vapours, as presented as an inset in Fig. 3D, demonstrating the potential application of **TB-TZ-COP** as a naked eye sensor for both solution and vapor phase detection of VOCs.

In summary, we have synthesized a new **TBNap** functionalized triazine covalent organic polymer, **TB-TZ-COP**, and demonstrated its application in the discriminative fluorescence sensing of VOCs. Notably, the ability of **TB-TZ-COP** to distinguish between structurally and chemically close related VOCs, such as glycol and 1,4-dioxane, was demonstrated. Such a system is highly attractive, the sensing being achieved in both solution and in the vapor phase using thin films using either colorimetric or fluorescent sensing. We are currently exploring the properties of such sensors in greater detail.

We thank the Irish Research Council for postdoctoral fellowships (GOIPD/2013/442 to SS and GOIPD/2015/290 to DU) and Science Foundation Ireland (SFI PI Award 13/IA/1865 to TG). We also thank Dr M. Ruether for carrying out NMR analysis of the monomer and polymer developed herein. All computational calculations were performed using the Lonsdale supercomputers at Trinity Centre for High-Performance Computing (TCHPC).

Conflicts of interest

There are no conflicts to declare.

Notes and references

1 D. Wu, A. C. Sedgwick, T. Gunnlaugsson, E. U. Akkaya, J. Yoon and T. D. James, *Chem. Soc. Rev.*, 2017, **46**, 7105–7123.
2 S. Shanmugaraju, C. Dabadie, K. Byrne, A. J. Savyasachi, D. Umadevi, W. Schmitt, J. A. Kitchen and T. Gunnlaugsson, *Chem. Sci.*, 2017, **8**, 1535–1546.
3 R. Atkinson and J. Arey, *Chem. Rev.*, 2003, **103**, 4605–4638.
4 K. Vellingiri, P. Kumar and K.-H. Kim, *Nano Res.*, 2016, **9**, 3181–3208.
5 L. Mølhave, B. Bach and O. F. Pedersen, *Environ. Int.*, 1986, **12**, 167–175.
6 T. Kida, K. Suematsu, K. Hara, K. Kanie and A. Muramatsu, *ACS Appl. Mater. Interfaces*, 2016, **8**, 35485–35495.
7 D. S. Moore, *Rev. Sci. Instrum.*, 2004, **75**, 2499–2512.
8 Y. Cui, Y. Yue, G. Qian and B. Chen, *Chem. Rev.*, 2012, **112**, 1126–1162.
9 S. Shanmugaraju, S. A. Joshi and P. S. Mukherjee, *J. Mater. Chem.*, 2011, **21**, 9130–9138; S. Shanmugaraju and P. S. Mukherjee, *Chem. Commun.*, 2015, **51**, 16014–16032.
10 B. McLaughlin, E. M. Surender, G. D. Wright, B. Daly and A. P. de Silva, *Chem. Commun.*, 2018, **54**, 1319–1322; A. J. Savyasachi, D. F. Caffrey, K. Byrne, G. Tobin, B. D'Agostino, W. Schmitt and T. Gunnlaugsson, *Front. Chem. Sci. Eng.*, 2019, **13**, 171–184.
11 D. Ma, B. Li, Z. Cui, K. Liu, C. Chen, G. Li, J. Hua, B. Ma, Z. Shi and S. Feng, *ACS Appl. Mater. Interfaces*, 2016, **8**, 24097–24103; J. Zhou, H. Li, H. Zhang, H. Li, W. Shi and P. Cheng, *Adv. Mater.*, 2015, **27**, 7072–7077.
12 R. Goswami, S. C. Mandal, B. Pathak and S. Neogi, *ACS Appl. Mater. Interfaces*, 2019, **11**, 9042–9053.
13 S. Erbas-Cakmak, S. Kolemen, A. C. Sedgwick, T. Gunnlaugsson, T. D. James, J. Yoon and E. U. Akkaya, *Chem. Soc. Rev.*, 2018, **47**, 2228–2248.
14 Y. Tang, D. Lee, J. Wang, G. Li, J. Yu, W. Lin and J. Yoon, *Chem. Soc. Rev.*, 2015, **44**, 5003–5015; P. Mani, A. A. Ojha, V. S. Reddy and S. Mandal, *Inorg. Chem.*, 2017, **56**, 6772–6775; L. Guao and D. Cao, *J. Mater. Chem. C*, 2015, **3**, 8490–8494.
15 L. Dai, D. Wu, Q. Qiao, W. Yin, J. Yin and Z. Xu, *Chem. Commun.*, 2016, **52**, 2095–2098; C. J. Chang, T. Gunnlaugsson and T. D. James, *Chem. Soc. Rev.*, 2015, **44**, 4176–4178.
16 R. M. Duke, E. B. Veale, F. M. Pfeffer, P. E. Kruger and T. Gunnlaugsson, *Chem. Soc. Rev.*, 2010, **39**, 3936–3953.
17 E. B. Veale, D. O. Frimannsson, M. Lawler and T. Gunnlaugsson, *Org. Lett.*, 2009, **11**, 4040–4043; E. B. Veale and T. Gunnlaugsson, *J. Org. Chem.*, 2010, **75**, 5513–5525.
18 Y. Luo, B. Li, L. Liang and B. Tan, *Chem. Commun.*, 2011, **47**, 7704–7706.
19 Q. Fang, Z. Zhuang, S. Gu, R. B. Kaspar, J. Zheng, J. Wang, S. Qiu and Y. Yan, *Nat. Commun.*, 2014, **5**, 4503.
20 Y. Liao, J. Weber and C. F. J. Faul, *Macromolecules*, 2015, **48**, 2064–2073; J. Dong, A. K. Tummanapelli, X. Li, S. Ying, H. Hirao and D. Zhao, *Chem. Mater.*, 2016, **28**, 7889–7897.
21 S. Shanmugaraju, D. Umadevi, A. J. Savyasachi, K. Byrne, M. Ruether, W. Schmitt, G. W. Watson and T. Gunnlaugsson, *J. Mater. Chem. A*, 2017, **5**, 25014–25024.
22 M. J. Frisch, *et al.*, *GAUSSIAN 09*, Gaussian Inc., Wallingford, CT, 2009.
23 Y. Zhao and D. Truhlar, *Theor. Chem. Acc.*, 2008, **120**, 215–241.
24 A. K. Nain, N. Chaudhary, Ankita, J. Gupta and P. Chandra, *J. Chem. Thermodyn.*, 2017, **108**, 145–161.
25 A. Abe, *Sci. Total Environ*, 1999, **227**, 41–47.
26 A. J. Heuvelsland, *Method for Producing 1,4-Dioxane*, US 4764626, 1988.

ChemComm

COMMUNICATION

View Article Online
View Journal | View Issue

Cite this: *Chem. Commun.*, 2020, **56**, 2562

Received 29th October 2019,
Accepted 27th January 2020

DOI: 10.1039/c9cc08457f

rsc.li/chemcomm

Aggregation induced emission (AIE) active 4-amino-1,8-naphthalimide-Tröger's base for the selective sensing of chemical explosives in competitive aqueous media†

Jason M. Delente,[ab] Deivasigamani Umadevi,[c] Sankarasekaran Shanmugaraju,[*d] Oxana Kotova,[a] Graeme W. Watson[c] and Thorfinnur Gunnlaugsson[*ab]

The 4-amino-1,8-naphthalimide-Tröger's base fluorophore, TBNap-TPy, adorned with phenyl-terpyridine moiety was synthesised and assessed for its aggregation-induced emission (AIE) behaviour. TBNap-TPy was further employed as a fluorescent sensor for the discriminative sensing of π-electron-deficient nitroaromatic; the TBNap-TPy displaying the largest fluorescence quenching with high selectivity for picric acid, a harmful environmental pollutant widely used in the dye industries.

Supramolecular chemistry has been used to form dynamic and intricate structures and materials demonstrating various properties ranging from gelators,[1] bioimaging agents,[2] and luminescent sensors,[3] to name a few. Fluorescence 'on–off' and 'off–on' switching systems are highly attractive chemosensors due to their simplicity of uses, high sensitivity and fast response time.[3] Recently, the phenomenon of aggregation-induced emission (AIE) and aggregation-induced emission enhancement (AIEE), has been developed for use in chemical sensing and bio-imaging.[4] Unlike many fluorophores, which often suffer from aggregation-caused quenching (ACQ), the common strategy for designing AIE or AIEE fluorophores is to functionalise the fluorophore with bulky substituents or a long branched chains with the aim of restraining intramolecular rotation, which will lead to the loss of excited energy only through radiative pathway.[5] Many examples of fluorophores have been shown to achieve AIE/AIEE sensors such as pentacenequinone,[6] tetraphenylethene,[7] anthracene,[8] hexaphenylsiloles.[9] Naphthalimide (**Nap**) based fluorescence sensors have attracted substantial attention in fluorescence sensing,[10] and have recently been shown to be candidates for use in AIE based systems.[2,3] Poly-nitroaromatic compounds (NACs) are secondary chemical explosives and are used widely as pigments in various dye and textile industries.[11–13] While several examples of fluorescent sensors for NACs exists, there currently exist the need to develop a suitable and reliable fluorescence sensor for the trace detection of NACs in competitive media.[12,13] By taking advantage of the AIE design, luminescent sensors have recently been developed that are able to compete with the metal–organic framework (MOF) and coordination polymers for sensing of NACs.[13] These AIE examples have shown both good sensibility and selectivity, as well as enabling such sensing in more competitive aqueous media.[6,11,14] Recently, using 4-amino-1,8-naphthalimide Tröger's base motifs (**TBNaps**), we have developed a variety of materials for the discriminative detection of NACs such as picric acid (PA), including organic polymers and coordination networks.[13,15] We have shown that these structures are able to sense PA with both high sensitivity and selectivity where the sensing action was monitored through observing the luminescent 'on–off' and 'off–on' switching properties in water.

The **Nap** derived **TBNaps** are novel and highly versatile supramolecular building blocks that we have been developing over the last decade.[2,13,16] Due to the almost orthogonal orientation between the two **Nap** fluorophores [caused by the chiral cleft-shaped diazocine ring (Tröger's bases) unit] in **TBNaps**, we have shown, through the use of solid-state crystallography, that the **TBNaps** can give rise to variety of solid-state stacking interactions; the nature of which is dictated by (a) the structural unit incorporated at the imide site and (b) the solvent media. With the aim of capitalising on this aggregation property of the **TBNaps** we set out to (i) develop the first examples of AIE based **TBNaps**, and (ii) demonstrate their applications in fluorescence AIE sensing. Herein, we present our result into the use of **TBNap-TPy**, the phenyl-terpyridine, and 4-amino-1,8-naphthalimide based

[a] *School of Chemistry and Trinity Biomedical Sciences Institute, Trinity College Dublin, The University of Dublin, Dublin 2, Ireland. E-mail: gunnlaut@tcd.ie*
[b] *AMBER (Advanced Materials and Bioengineering Research) Centre, Trinity College Dublin, The University of Dublin, Dublin 2, Ireland*
[c] *School of Chemistry and Centre for Research on Adaptive Nanostructures and Nanodevices (CRANN), Trinity College Dublin, The University of Dublin, Dublin-2, Ireland*
[d] *Chemistry, Indian Institute of Technology Palakkad (IITPKD), Kerala, India. E-mail: shanmugam@iitpkd.ac.in*

† Electronic supplementary information (ESI) available: Experimental details, synthesis and characterisations details (multinuclear NMR, IR, HRMS), fluorescence studies and computational calculations. See DOI: 10.1039/c9cc08457f

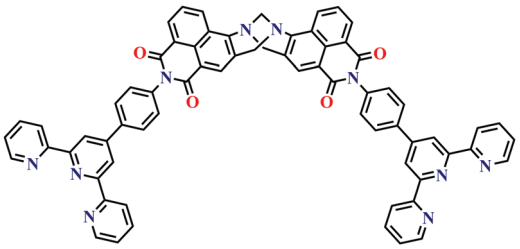

Fig. 1 Structure of **TBNap-TPy** fluorophore studied herein.

Tröger's base, as an AIE based sensor for NACs. During the design of **TBNap-TPy**, we anticipated that by incorporating phenyl-terpyridine (TPy) moieties, being π-electron-rich, into the **TBNap** framework (*e.g.* Fig. 1) would: (i) enhance the sensing propensity of the **TBNap** towards π-electron-deficient NAC,[15] and (ii) in counter-solvents, lead to hindering in the molecular free-rotation of the TPy rings, which would enable AIE.

The **TBNap-TPy** was synthesised from the commercially available acetylpyridine, 4-nitrobenzaldehyde, and 4-nitro-1,8-naphthalic anhydride, in few steps. Formation of 4′-(4-nitrophenyl)-2,2′:6′,2″-terpyridine was achieved following the procedure described by Brudvig *et al.*[17] while the formation of the desired Tröger's base **TBNap-TPy** was carried out using methods developed in our laboratory (see full details in ESI†).[15,16] The successful formation of **TBNap-TPy** was demonstrated by HRMS and elemental analysis (see ESI†). The ^{1}H NMR in DMSO-d_6 confirmed the formation of the Tröger's base moiety with the presence of the two well-defined doublets at 5.23 and 4.74 ppm corresponding to the methylene protons of the diazocine ring (see ESI†).[16] The IR spectrum of **TBNap-TPy** reveals two peaks at 1705 cm^{-1} and 1665 cm^{-1} accounting for the carbonyl groups on the naphthalimide moieties and a strong signal at 1240 cm^{-1} due to C–N stretching of the Tröger's base unit.[13]

The luminescence behaviour of **TBNap-TPy** in solution was studied with the use of various organic solvents and mixtures of organic-aqueous solutions. In general, the results demonstrated the presence of a red shift of the emission spectrum upon increasing polarity which is an indicator of the presence of internal charge transfer (ICT) state due to the push–pull nature of the donating amine and the withdrawing imide. This is typical for amino-**Naps** and we demonstrated the same for the **TBNaps**, though the diazocine ring reduces the strength of the push–pull interactions leading to a small blue shift in the **TBNap** emission *vs.* the **Nap** emission (see ESI†).[16] The discussion below will, due to the nature of the work, focuses on these properties in DMSO and mixed DMSO–H_2O solutions. The electronic absorption spectra of the ligands in DMSO (see ESI†) was dominated by ligand-centred π → π* transitions centred at 278 nm (ε = 98 919 ± 388 cm^{-1} M^{-1}), 319 nm (ε = 27 929 ± 146 cm^{-1} M^{-1}), 346 nm (ε = 18 864 ± 142 cm^{-1} M^{-1}), and the ICT Tröger's base band centred at 388 nm (ε = 21 303 ± 134 cm^{-1} M^{-1}).[16,18] As we had anticipated, then upon adding deionized H_2O to the DMSO solutions, an enhancement in the fluorescence was observed, due to enhanced aggregation of **TBNap-TPy** and the 'switching on' effect of the AIE; the effect is clearly visible even to the naked eye as demonstrated in Fig. 2. We studied this effect further by measuring the changes in the

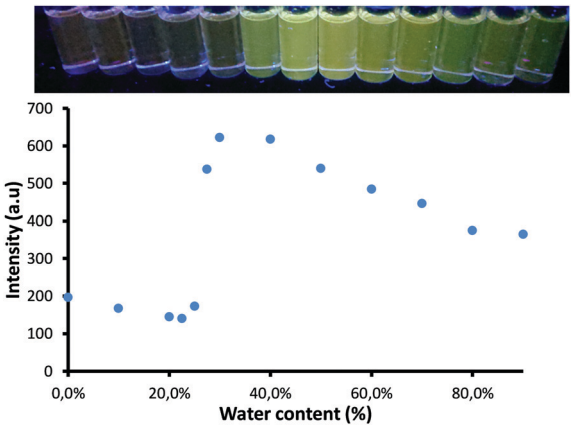

Fig. 2 Intensity plot of **TBNap-TPy** (c = 4.6 × 10^{-6} M) in DMSO upon addition of water. Inset: Visible colour changes observed under UV lamp (ex. 360 nm).

absorbance, fluorescence and excitation spectrum of **TBNap-TPy** (c = 4.6 × 10^{-6} M) at the various percentage of H_2O in DMSO (see full details in ESI†). All the work was carried out in triplicates and found to be fully reproducible. In the absorbance spectrum, no significant changes were observed in the ground state upon the addition of H_2O compared to that seen in DMSO. In contrast, the fluorescence excitation spectrum exhibited a significant shift from 450 nm to 400 nm for the ICT transition when the H_2O content was changed from 20 → 40%.[19] These changes reflecting the **TBNap-TPy** aggregation in the more polar protic solution. Upon excitation of the ICT band in DMSO, broad fluorescence emission was observed with λ_{max} at 530 nm. Upon the addition of H_2O, no significant shifts were seen in the λ_{max}. However, a significant 3-fold enhancement was observed in the emission intensity (see ESI† and Fig. 2.), with maximum intensity being observed at 30% H_2O. Once the water content increased beyond this, the emission intensity slowly decreased, stabilising between 80–90% of H_2O as demonstrated in Fig. 2. To gain further insight into the aggregation effects and their associated morphological features, we employed FE-SEM to probe the aggregate formation at various DMSO:H_2O fractions. As can be seen in Fig. 3, the FE-SEM analysis demonstrates the formation of amorphous aggregates with the presence of a random distribution of spherical particles. As the water content increased, the number of spherical aggregates increased, becoming the predominant structural feature when the water content reaches 30%. The spherical aggregates have a size ranging from 48 nm to 300 nm. Upon increasing the water content above 30% the spherical aggregates are destroyed, forming amorphous aggregates that demonstrate the influence of the solvent on the self-assembly of **TBNap-TPy**.[1]

Having established the optimum emission properties for **TBNap-TPy** in the H_2O–DMSO mixture, we next investigated the potential application of this system as a luminescent sensor for pollutants in water, such as PA, which was used as a prototype of NACs, where the changes in the ICT emission of **TBNap-TPy** were monitored. PA is extensively used in industry, and is considered as environmental pollutants and potentially toxic to living organisms.[12,13] It has a high solubility in water (~14 g L^{-1}), and as such is stored and transported in water across the world.[15] The continuous exposure to saturated

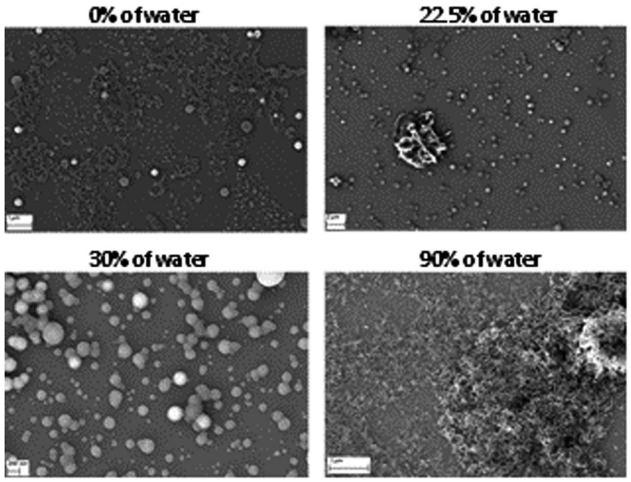

Fig. 3 Scanning electron microscopy images of **TBNap-TPy** at various percentage content of water in DMSO.

vapours of PA can cause severe and un-repairable health issues like liver and kidney failure and neurological damages and as such it is a highly desirable target for chemosensing in competitive media.[11,13–15] The changes in the ICT centered emission of **TBNap-TPy** upon increasing concentration of PA are shown in Fig. 4. As can be seen, no significant changes in λ_{max} were observed, while significant quenching in the **TBNap** fluorescence was observed between 0–74.1 μM of PA. The observed significant fluorescence quenching clearly indicates a strong interaction between PA and aggregated state of **TBNap-TPy**. The quenching propensity was thus next analyzed using the Stern–Volmer equation. The results are shown as an inset in Fig. 4, showing a slight upward curvature upon increasing PA concentrations, which could indicate that both static and dynamic quenching occurred.[13a] Nevertheless, the linear region of these changes was fitted to a Stern–Volmer plot and gave $K_{sv} = 4.06 \pm 0.4 \times 10^4\ M^{-1}$, which is comparable to what has been observed for similar systems.[13a]

Density functional theory (DFT) analysis was performed using the M06-2X/6-311G(d,p)[20] method to understand the interactions between **TBNap-TPy** and PA using the model system (see ESI†). All the calculations were done by using Gaussian 09 package.[21] The frontier molecular orbital calculations show that the HOMO is more localized in the Troger's base and naphthalene region while the LUMO is more localized in the imide region of **TBNap** (ESI†). This confirms that **TBNap** moiety is electron-rich. The structure of

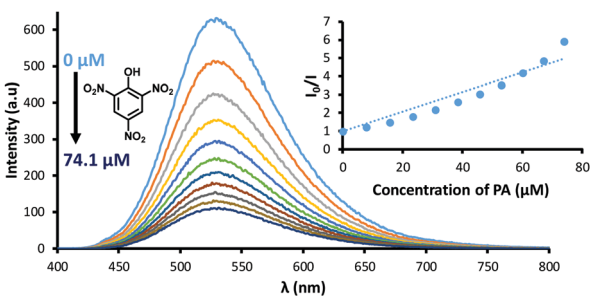

Fig. 4 Fluorescence quenching of **TBNap-TPy** upon addition of PA. Inset: The corresponding Stern–Volmer plot for the quenching.

TBNap-TPy indicates five possible sites ($-N_{Tröger's}$, $-C{=}O_{imide}$, $-N_{imide}$, $-N_{Py1}$, $-N_{Py2}$) where **TBNap-TPy** could interact with PA (ESI†). Our calculations showed that PA exhibits intermolecular interactions at $-N_{Tröger's}$, $-C{=}O_{imide}$, $-N_{Py1}$, and $-N_{Py2}$ sites with binding energies 8.45, 15.90, 23.87 and 18.46 kcal mol^{-1}, respectively. The optimized geometries indicate hydrogen-bond interactions at the $-N_{Tröger's}$, and $-N_{Py1}$ sites and a combination of hydrogen-bonding and π–π stacking type of interactions at the $-C{=}O_{imide}$, $-N_{Py1}$ sites (ESI†). No such stable interaction was observed at the $-N_{imide}$ site. The higher binding energies observed at the TPy moieties are in good agreement with the observed enhanced sensing propensity of **TBNap** adorned with TPy moieties. To substantiate this experimentally, a ^1H NMR titration study between **TBNap-TPy** and PA was carried out, which shows a significant downfield shift for proton resonances of TPy moiety upon the gradual addition of PA, while the proton resonance of **TBNap** showed no to little changes (ESI†). This substantiates our assumption that TPy moiety forms strong π-stacking interactions with PA. We further analyzed the FT-IR spectra of PA and **TBNap-TPy** before and after mixing with PA (ESI†). In the FTIR spectrum of PA after mixing with **TBNap-TPy**, the peak corresponding to the –OH stretching of PA was completely disappeared confirming the existence of strong intermolecular hydrogen-bonding interactions between **TBNap-TPy** and PA.[15]

To demonstrate the mechanism of fluorescence quenching, the time-resolved fluorescence decay at different concentrations of PA was recorded, and the temperature dependence quenching in the **TBNap-TPy** emission in the presence of PA was analyzed. Both the time-resolved decay of **TBNap-TPy** in DMSO and in the 70 : 30 DMSO–H_2O mixture were fitted to bi-exponential decay, which showed that upon addition of PA, the excited state lifetimes were decreasing respectively from 2.52 ns to 1.85 ns for τ_1, and 7.44 ns to 6.20 ns for τ_2; this revealing the interaction of PA to **TBNap-TPy** in the excited state (see ESI†).[13a] These measurements were shown to be fully reproducible. The temperature dependence experiment in presence of 38.5 μM of PA also revealed that the quenching efficiency was 59% at 24.5 °C, being dramatically increased to 70% at 45 °C (ESI†). This can be accounted by two phenomena; (i) enhancement in dynamic quenching upon raising the temperature, due to enhanced rate of collision between **TBNap-TPy** and PA, and (ii) to the potential destruction of the **TBNap-TPy** emissive aggregates.[5,13a] We also found that the extent of fluorescence quenching was highly dependents on the solution pH (ESI†). In acidic pH = 2.4, the quenching efficiency was high ($K_{SV} = 11.3 \times 10^4\ M^{-1}$), but in basic medium (pH = 11) the efficiency was decreased considerably ($K_{SV} = 2.1 \times 10^4\ M^{-1}$) likely due to the lack of intermolecular hydrogen-bonding interactions at alkaline pH.[15]

In order to be used as an AIE sensor for PA in aqueous media, it was necessary to demonstrate that **TBNap-TPy** possessed a good selectivity and sensitivity. The selectivity of **TBNap-TPy** was evaluated by carrying out fluorescence titrations separately using other NACs such as 2,4-DNP, 2-NP, 3-NP, 4-NP, TNT, 2,4-DNT, 2,6-DNT, 2-NT, 3-NT, 4-NT and NB and determining their corresponding Stern–Volmer constant (see ESI†). These titrations revealed that highest quenching efficiency was indeed obtained

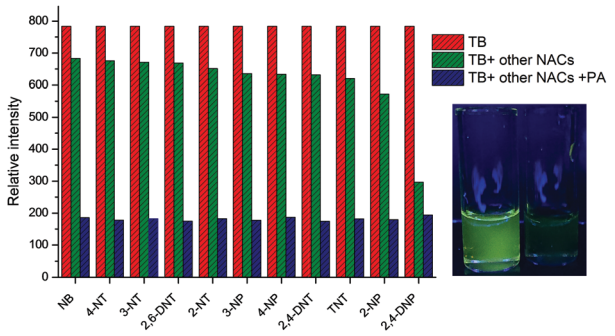

Fig. 5 Competitive selective affinity of **TBNap-TPy** (c = 4.6 × 10^{-6} M) towards different nitroaromatics in the presence of PA (74.1 μM) in DMSO–H_2O (70–30%) mixture. Inset: Visible colour changes observed before (left) and after (right) addition of PA (74.1 μM).

for PA with 83% (at endpoint) quenching in the AIE intensity; this being followed by 2,4-DNP which gave rise to 66% quenching at the same concentration. Furthermore, the analysis of these changes using the Stern–Volmer equation showed linear regression from which K_{sv} was determined (see details in ESI†). From this screening, it can be deduced that the phenolic-nitroaromatics (PA, 2,4-DNP, 2-NP, 3-NP, 4-NP) exhibited the highest quenching efficacy, which can be explained by the phenol group being able to form stronger intermolecular interactions with the Lewis basic nitrogen of the terpyridine and Tröger's base motifs.[13,15] The selectivity of **TBNap-TPy** towards phenolic nitroaromatics, and more specifically PA was further confirmed by performing competitive fluorescence studies, where a concentration of 74.1 μM of each of the NACs was added to a solution of **TBNap-TPy** (green bar, Fig. 5). This was followed by the addition of 74.1 μM of PA. The results (shown as blue bars in Fig. 5) clearly showed that in all cases to the **TBNap-TPy** emission was further quenched upon the addition of PA; which confirmed the high selectivity of **TBNap-TPy** towards PA. Furthermore, **TBNap-TPy** also displayed a strong binding affinity for PA in presence of various common ions except for a few transition metal cations such as Ni^{2+}, Co^{2+}, Cu^{2+} and Fe^{2+} showed a significant fluorescence quenching likely due to the metal–ligand chelation effect (see ESI†).[1] Gratifyingly, the PA quenching could also be seen with the naked eye under a UV lamp irradiation as demonstrated as an insert in Fig. 5. A sensitivity experiment was also carried out. The results (see ESI†) showed that the **TBNap-TPy** AIE response could be affected by PA even at 20 ppb concentration. Moreover, this level of sensitivity is under the allowed limit of NACs in drinking water established by the US EPA.[13,15] The response time towards PA was also evaluated at different PA concentrations; the results showing that upon addition of PA, the emission changes had equilibrated within a minute (see ESI†); the response time being independent of the concentration of PA employed. These overall results demonstrate that **TBNap-TPy** could potentially be used as a fluorescent AIE sensor for the on-site detection of PA.

In summary, we have synthesized **TBNap-TPy**, a 4-amino-1,8-naphthalimide Tröger's base functionalized with phenyl-terpyridine. We have shown the ability of this system to give rise to AIE in aqueous DMSO mixture. Taking advantage of this property we further demonstrated the fluorescent sensing of various NACs, where the selective sensing of PA and 2,4-DNP was demonstrated; the detection of PA being particularly selective.

We thank the Irish Research Council (IRC) for a postdoctoral fellowship (GOIPD/2015/290 to DU), Science Foundation Ireland (SFI PI Award 13/IA/1865 to TG) and the AMBER Centre for financial support, and Advanced Microscopy Laboratory-CRANN for the SEM analysis. All computation calculations were performed using the Lonsdale super computers-Trinity Centre for High-Performance Computing.

Conflicts of interest

There are no conflicts to declare.

Notes and references

1 A. J. Savyasachi, O. Kotova, S. Shanmugaraju, S. J. Bradberry, G. M. Ó'Máille and T. Gunnlaugsson, *Chem*, 2017, **3**, 764.
2 S. Erbas-Cakmak, S. Kolemen, A. C. Sedgwick, T. Gunnlaugsson, T. D. James, J. Yoon and E. U. Akkaya, *Chem. Soc. Rev.*, 2018, **47**, 2228.
3 P. Gopikrishna, N. Meher and P. K. Iyer, *ACS Appl. Mater. Interfaces*, 2018, **10**, 12081.
4 Z. He., C. Ke and B. Z. Tang, *ACS Omega*, 2018, **3**, 3267–3277.
5 J. H. Q. L. Z. Li, *Aggregation-Induced Emission: Fundamentals and Applications, vol. 1–2*, 2013, pp. 127–153.
6 S. Kaur, A. Gupta, V. Bhalla and M. Kumar, *J. Mater. Chem. C*, 2014, **2**, 7356.
7 Y. Dong, J. W. Y. Lam, A. Qin, J. Liu, Z. Li, B. Z. Tang, J. Sun and H. S. Kwok, *Appl. Phys. Lett.*, 2007, **91**, 011111.
8 H. Lu, B. Xu, Y. Dong, F. Chen, Y. Li, Z. Li, J. He, H. Li and W. Tian, *Langmuir*, 2010, **26**, 6838.
9 G. He, H. Peng, T. Liu, M. Yang, Y. Zhang and Y. Fang, *J. Mater. Chem.*, 2009, **19**, 7347.
10 R. Puglisi, A. Pappalardo, A. Gulino and G. Trusso Sfrazzetto, *ACS Omega*, 2019, **4**, 7550.
11 (*a*) N. Meher and P. K. Iyer, *Nanoscale*, 2017, **9**, 7674; (*b*) X. Cao, N. Zhao, H. Lv, Q. Ding, A. Gao, Q. Jing and T. Yi, *Langmuir*, 2017, **33**, 7788.
12 (*a*) S. Shanmugaraju, S. A. Joshi and P. S. Mukherjee, *J. Mater. Chem.*, 2011, **21**, 9130; (*b*) S. K. Kim, J. M. Lim, T. Pradhan, H. S. Jung, V. M. Lynch, J. S. Kim, D. Kim and J. L. Sessler, *J. Am. Chem. Soc.*, 2014, **136**, 495.
13 (*a*) S. Shanmugaraju, C. Dabadie, K. Byrne, A. J. Savyasachi, D. Umadevi, W. Schmitt, J. A. Kitchen and T. Gunnlaugsson, *Chem. Sci.*, 2017, **8**, 1535; (*b*) S. S. Nagarkar, B. Joarder, A. K. Chaudhari, S. Mukherjee and S. K. Ghosh, *Angew. Chem., Int. Ed.*, 2013, **52**, 2881.
14 Q. Lin, X.-W. Guan, Y.-Q. Fan, J. Wang, L. Liu, J. Liu, H. Yao, Y.-M. Zhang and T.-B. Wei, *New J. Chem.*, 2019, **43**, 2030.
15 S. Shanmugaraju, D. Umadevi, A. J. Savyasachi, K. Byrne, M. Ruether, W. Schmitt, G. W. Watson and T. Gunnlaugsson, *J. Mater. Chem. A*, 2017, **5**, 25014.
16 (*a*) S. Shanmugaraju, C. S. Hawes, A. J. Savyasachi, S. Blasco, J. A. Kitchen and T. Gunnlaugsson, *Chem. Commun.*, 2017, **53**, 12512; (*b*) E. B. Veale and T. Gunnlaugsson, *J. Org. Chem.*, 2010, **75**, 5513.
17 A. C. Durrell, G. Li, M. Koepf, K. J. Young, C. F. A. Negre, L. J. Allen, W. R. McNamara, H. E. Song, V. S. Batista, R. H. Crabtree and G. W. Brudvig, *J. Catal.*, 2014, **310**, 37.
18 P. Song, S.-g. Sun, P.-w. Zhou, J.-y. Liu, Y.-q. Xu and X.-j. Peng, *Chin. J. Chem. Phys.*, 2010, **23**, 558.
19 R. M. Duke and T. Gunnlaugsson, *Tetrahedron Lett.*, 2011, **52**, 1503.
20 Y. Zhao and D. G. Truhlar, *Theor. Chem. Acc.*, 2008, **120**, 215.
21 M. J. Frisch, *et al.*, *Gaussian 09*, Gaussian Inc., Wallingford, CT, 2009, see the ESI† for full citation.

Organic & Biomolecular Chemistry

ROYAL SOCIETY OF CHEMISTRY

COMMUNICATION

View Article Online
View Journal | View Issue

Cite this: *Org. Biomol. Chem.*, 2020, **18**, 3475

Received 7th January 2020,
Accepted 16th April 2020

DOI: 10.1039/d0ob00033g

rsc.li/obc

Fluorescent supramolecular hierarchical self-assemblies from glycosylated 4-amino- and 4-bromo-1,8-naphthalimides†

Elena Calatrava-Pérez,[a] Stefan Acherman,[a] Lucas Stricker,[a] Gavin McManus,[b] Jason Delente,[a,c] Amy D. Lynes,[a] Adam F. Henwood,[a] June I. Lovitt,[a] Chris S. Hawes,[a,d] Kevin Byrne,[a] Wolfgang Schmitt,[a,c,e] Oxana Kotova,[a] Thorfinnur Gunnlaugsson *[a,c,e] and Eoin M. Scanlan *[a,e]

An investigation into the self-assembly of two 4-amino- and a 4-bromo-1,8-naphthalimide (Nap) based structures (1–3) possessing an appended glycan unit, from protic polar media, is presented. The results demonstrate the formation of complex hierarchical luminescent aggregates, wherein the morphologies, sizes and spherical structures were highly dependent on both the media and the Nap structure. Upon cleaving the native glycosidic bond, using an enzyme, the structure/morphology of the self-assembly of 3 in buffered solution was significantly transformed.

The 1,8-naphthalimide (**Nap**) structure has rich and tuneable photophysical properties which have been extensively capitalised on in the development of colorimetric and luminescent sensors and probes.[1,2] Due to their ease of functionalization, the **Nap** moieties have also found application in the development of molecular logic gates and sensors,[3] in the investigation into electron transfer and energy processes,[4] and other related photoactive devices.[5] Their applications in medicinal chemistry, where their properties as DNA targeting and anticancer agents, have been utilised for targeted luminescent cellular imaging agents and as enzymatic probes, have been particularly researched in recent times.[6,7] In contrast to this, the use of **Naps** in the development of functional supramolecular self-assembly structures has been less researched. Nevertheless, like their related naphthalene di-imide (NDI) structures, which are known to aggregate through hydrogen bonding, π–π, n–π, and other weak interactions, **Naps** (depending on their substitution patterns and functionalities) have been shown to self-assemble in an analogous manner, even at low (*e.g.* μM) concentrations.[8,9] We have been actively developing examples of various self-assemblies,[10c] including **Nap** structures for use in many of the applications listed above, and recently began to investigate the self-assembly properties of various functional **Nap** structures in solution,[10] the solid-state,[11] and in the generation of soft responsive and healable materials[12] in a more focused manner. Others have also commenced such investigations; works include that of Olson and collaborators,[13] who have recently developed **Nap**-pyridinium structures that can be used in printable materials, Kitchen *et al.*,[14] who have developed coordination **Nap** networks, self-assembly monolayers, films, and coordination polymers, and Hawes *et al.*,[15] who have developed **Nap** based mechanically interlocked and healable coordination compounds. Other works include that of Jing *et al.*,[16] Chang *et al.*,[17] and Yi *et al.*,[18] who have demonstrated that the **Nap** structures can give rise to a variety of supramolecular self-assembly structures possessing different degrees of morphologies, including those of soft materials. Concomitantly, we have developed glycosylated functionalised 4-amino-**Nap** structures as glycosidase specific prodrugs, cellular imaging agents,[19] and as luminescent probes for the Con A lectin protein.[20] It was during these investigations that it became apparent to us that the **Nap** structures were prone to aggregate into higher order structures, and we set out to investigate if and how such self-assembly formation could be controlled, particularly in competitive media. To this end, we have recently developed responsive and healable **Nap**-gels.[12] Herein we discuss the results from our investigation into the use of glycosylated 4-amino (**1** and **2**) and 4-bromo-1,8-**Nap** (**3**) structures (Fig. 1), where we demonstrate that, depending on the media and the nature of the chemical structure, higher order, luminescent self-assemblies form that visually mimic the structure of larger biological matter. We

[a]*School of Chemistry, Trinity College Dublin, The University of Dublin, Dublin 2, Ireland. E-mail: gunnlaut@tcd.ie, scanlae@tcd.ie*
[b]*School of Biochemistry and Immunology, Trinity Biomedical Sciences Institute (TBSI), Trinity College Dublin, Dublin-2, Ireland*
[c]*The AMBER (Advanced Materials and BioEngineering Research) Centre, Trinity College Dublin, The University of Dublin, Dublin 2, Ireland*
[d]*School of Chemical and Physical Sciences, Keele University, Keele ST5 5BG, UK*
[e]*Synthesis and Solid State Pharmaceutical Centre (SSPC), Ireland*

†Electronic supplementary information (ESI) available: General experimental synthetic and additional photophysical details. CCDC 1968851–1968853. For ESI and crystallographic data in CIF or other electronic format see DOI: 10.1039/d0ob00033g

also demonstrate that chemical transformation using glycosidase enzymes allowed for the modification of their morphology under physiological conditions upon cleaving the native glycosidic bond.[21,22]

The synthesis of **1–3** was achieved in a facile and high-yielding manner. Compounds **1** and **2**, based on the 4-amino-**Nap** motif and which only differ in the nature of the glycan unit, were originally synthesised and subsequently employed at low μM concentrations as luminescent imaging 'pro-probes'.[20] The 4-bromo-**Nap 3** was synthesised in a similar manner (see ESI†), starting with a condensation reaction between 4-bromo-1,8-naphthalic anhydride and propargyl amine in refluxing EtOH (97% yield). This was followed by using a copper catalyzed azide–alkyne (CuAAC) 'click' ligation with 1-*O*-(3-azidopropyl)-β-D-galactopyranoside in DMF under microwave irradiation using $[(CH_3CN)_4Cu]BF_4$ to furnish **3** in 44% yield. The low yield is attributed to challenging purification caused by aggregation of the **Nap** moieties. The compound was characterized using conventional methods (see ESI†); both the ^{1}H (400 MHz, DMSO-d_6) and the ^{13}C NMR (100 MHz, DMSO-d_6) spectra were consistent with the desired product, while the HRMS (ESI^+) gave 599.073311, which was assigned to $[M + Na]^+$. Some of these compounds were also characterized in other solvent media, such as in deuterated water and methanol. In the case of **1**, it was necessary to both heat and apply sonication to ensure full solubilisation in CD_3OD. All the compounds were subjected to enzymatic liberation in buffered solutions, which showed the successful transformation of the 'free' glycan product (see ESI, Scheme S1† for **3**; where **1** and **2** give the common product **4**, while **3** gives **5**) upon cleaving the native glycosidic bond. All the compounds were also photophysically analysed in a variety of solvents; both **1** and **2** (see ESI† for **1**) exhibited green emission due to the strong internal charge transfer (ICT) character [λ_{Absmax} = 433 ($\log \varepsilon$ = 6500), λ_{Fmax} = 550, q = 13% for **1**; λ_{Absmax} = 433 ($\log \varepsilon$ = 12 000), λ_{Fmax} = 550, q = 11.5% for **2** when measured in water] of the 4-amino-**Nap** 'push–pull' character. The aggregation was also observed in polar protic solvents where both the absorption and the emission spectrum did not increase linearly as a function of increasing concentration; the absorption spectra following the Beer–Lambert Law from 0 → 0.6 mM, after which, a decrease was seen, while the emission spectrum was dramatically quenched above 0.2 mM concentration (see ESI†). In comparison, for **3**, the absorption and the emission properties occur at higher energy due to the lack of electron-donating character of the Br-substituent (this also affects the quantum yield, thought this was not determined for **3**); the emission being blue shifted *vs.* **1** and **2**.[23] However, the Br-Nap derivatives studied have an absorption tail that extends into the visible region which allowed us to observed (see below) the self-assembly using confocal fluorescence microscopy (see ESI†).

While the assignment of the ^{1}H NMR was in accordance with the desired structure, the tendency of the **Nap** systems to aggregate in solution, mainly driven by π–π interactions, was evident at room temperature, with the formation of orange coloured assemblies being observed. Furthermore, the presence of the glycan unit modifies the **Nap** self-assembly arrangement further, due to the larger amount of hydrogen bonding interactions. While we were unable to crystallographically analyze **1** or **2**, we recently showed that **4** (see structure in ESI†) gives rise to such π–π packing, where each of the **Nap** moieties are offset at 120° to each other, while the triazole units also partake in intermolecular hydrogen bonding interactions (see ESI†).[20] Microscopic analysis, using the soft imaging technique Helium-Ion Beam (HIB) microscopy, showed these self-assemblies or aggregates to be microspheres, Fig. 2. From the HIB imaging, it was observed that the microspheres were of approximately 100–150 μm diameter and were formed by networks of fibres that were on average 2–5 μm of length; these being further intertwined to form a hierarchical self-assembled 3D material. Interestingly, these microspheres formed a porous material with the largest pores visible by microscopy to be approximately 10 μm in diameter and myriad smaller inter-particle distances. By using the Brunauer–Emmett–Teller theory (BET), the surface area of the material was found to be 87 $m^2\ g^{-1}$ (R^2 = 0.9887) (see ESI†).[6a] This was in agreement with a second method used, Dubin–Radushkevich (DR), which gave 84.8 $m^2\ g^{-1}$ (R^2 = 0.9998) (see ESI†). These methods indicated that the surface area of the pores was approximately 85 $m^2\ g^{-1}$.

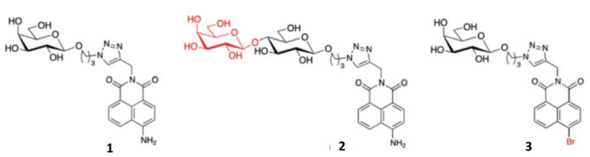

Fig. 1 The glycosylated **Nap**-structures employed in the current study.

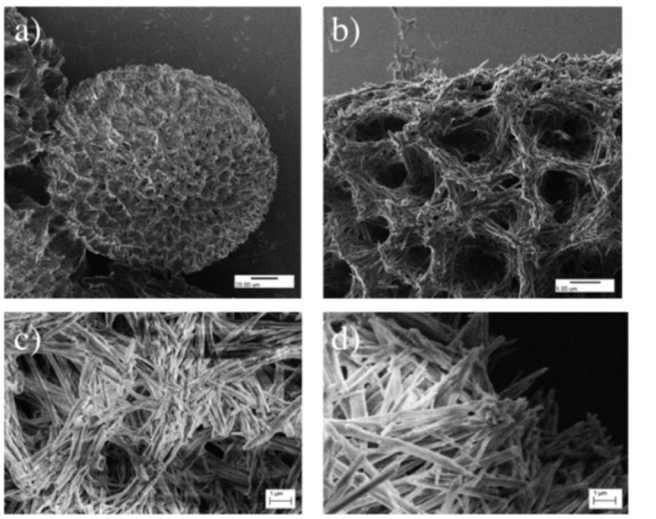

Fig. 2 Helium-Ion Beam (HIB) microscopy images pf glycosylated microspheres formed from **1** in deuterated methanol. (a) Bar is 50 μm. (b) Bar is 5 μm. (c and d) Bar is 1 μm.

Confocal fluorescence microscopy (λ_{exc} = 405 nm, λ_{em} = 500–550 nm) confirmed that these materials were luminescent after transferring the samples to silicon plates and drying overnight, Fig. 3a, demonstrating the formation of fluorescent supramolecular hierarchical self-assemblies. Our investigation, however, showed that these assemblies were not formed arbitrarily, but rather their formation depended on specific conditions such as time, temperature, and concentrations. Furthermore, while the spheres constructed from **1** maintained their appearance (and size between 80–100 μm) in solution, upon longer drying a partial or complete loss of their structural integrity occurred, as demonstrated in the SEM and the confocal imaging studies presented in Fig. 3b and c, respectively. Consequently, we investigated the effect of employing different drying times (1–7 days) and different temperatures (22 °C and 65 °C) to elucidate these effects on the stability of the isolated hierarchical self-assemblies (it is worth pointing out that for consistency, we used NMR tubes to grow these particles, independent of the nature of the solvent systems used). Unfortunately, no improvement was observed upon varying these parameters, and the structural integrity of the spheres was disrupted upon drying. This would indicate the critical role the solvent plays in the self-assembly process and in the overall stability of the 3D structure. We have also investigated the effect of solvents, such as H_2O or EtOAc. In all cases self-assembly formation was observed; however, these solvents did not generate the regular shaped spheres shown in Fig. 2.

Because of this, we next investigated **2** in an analogous manner, with a view to probing what role the carbohydrate fragment (with the β-D-lactose moiety instead of β-D-galactose) had on the self-assembly process. Here, the formation of aggregates was also observed in solvents such as CD_3OD and CH_3OH and, again, spherical luminescent aggregates were observed, Fig. 4. As can be seen in Fig. 4a, confocal studies demonstrated that these aggregates were not formed from fibrous assemblies of the same type as observed for **1**, but instead **2** aggregated to form "boomerang-shape" structures. Further SEM analysis confirmed the hierarchical self-assembly formation as consisting of fibers of *ca.* 2 μm length. This is not surprising, as the carbohydrate units would be expected to modulate the shape of the aggregates due to their different capacities to participate in hydrogen bonding and exhibit different degrees of solvation. With this in mind, we thus investigated the aggregation of **3** under identical conditions to that above.

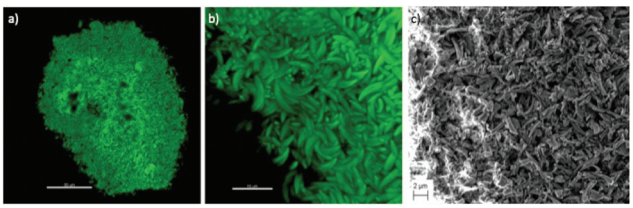

Fig. 4 (a) Confocal fluorescence images of **2** isolated from deuterated methanol and dried overnighted: (a) Bar is 50 μm. (b) Bar is 10 μm. (c) SEM image of **2** upon isolation from deuterated methanol. Bar is 2 μm. See ESI† for other magnifications.

Unlike that seen for **1**, in the case of **3** large aggregates were formed within 16 hours in alcohol solution that, upon isolation from the media, maintained their 3D structure. As for **1** and **2**, these were also fluorescent both in solution and in the solid state, the latter being evident upon imaging using confocal fluorescence microscopy, Fig. 5a. As before, these consisted of fibrous networks, similar to those observed for **1**. Upon isolation of these, the particles were subjected to heating and/or sonication in MeOH, after which they were left to stand at room temperature. As before, the formation of aggregates was observed, Fig. 5b, which were isolated and imaged. Unlike that seen for **1** and **2**, the integrity of these spheres was maintained indicating that the substitution pattern of the **Nap** unit ($-NH_2$ *vs.* –Br) also plays a major part herein. This we confirmed by carrying out X-ray crystallographic analysis on several alkyl-4-bromo-**Nap** mimic structure (see the results in ESI†), that lacked both triazole and glycan moieties, and on compound **4** discussed above (see structure

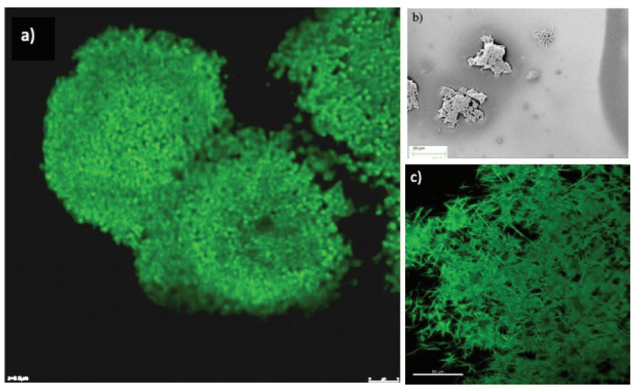

Fig. 3 (a) Confocal fluorescence image of the microspheres formed of **1** in deuterated methanol solution. (b) SEM images of particles formed upon drying on silica surface (λ_{exc} = 405 nm, λ_{em} = 500–550 nm). Bar is 20 μm. (C) Fluorescence microscopic image of **1** upon isolation and drying (λ_{exc} = 405 nm, λ_{em} = 500–550 nm). Bar is 50 μm.

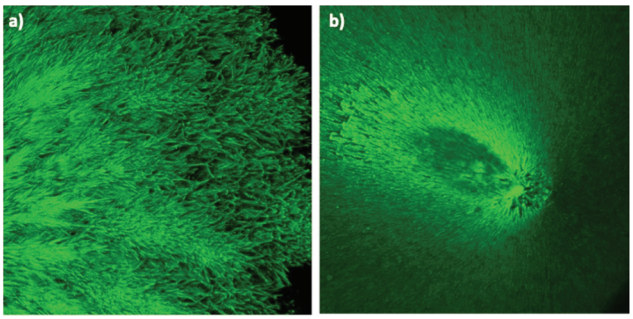

Fig. 5 Confocal fluorescence images of **3**. (a) Upon isolation from deuterated methanol. (b) Sample of **3** that was isolated, re-dissolved, and subject to both heating and sonication and left to stand for 12 hours before imaging.

and packing in ESI†). From these results it is clear that the π–π stacking dominates, and that in most cases these 4-bromo-**Naps** stack through offset head-to-tail fashion. Others have seen similar head-to tail structures for 4-bromo-**Nap** structures in the solid-state.[23] The one exception is where an octyl-chain was employed, which seem to lead to additional favorable hydrophobic interactions with offset head-to-head stacking observed. Hence, based on these analyses, one can infer that the spherical aggregates are the results of extended π–π stacking interactions from the **Nap**-moieties, with the carbohydrate moieties facing away from these in helical fashion depending on the degree of tiling between the stacked **Nap** structures. The glycan units can form strong hydrogen bonding interactions with both the polar protic media and through intermolecular glycan–glycan interactions.[22]

Having demonstrated that compound **3** formed spherical-like aggregates in alcoholic solutions, and that these were replicable, the formation of similar aggregates in a more competitive and biologically relevant solvent system was undertaken. Compound **3** was thus dissolved in pH 7.2 phosphate-buffered saline (PBS) solution, and after 12 h similar spheres as those shown in Fig. 5b were formed. However, these were softer than those produced from pure alcoholic solution and, despite careful decanting of the mother liquor and drying of the isolated aggregates overnight (at room temperature), attempts to move them onto SiO_2 and other surfaces on all occasions disrupted their structure. Other attempts to remove the solvent by gently heating unfortunately caused the spheres to swell and re-dissolve in the PBS buffer solution. However, it is worth pointing out that heating at or below 30 °C did not change the morphology of these shapes. Because of this, confocal fluorescence microscopy imaging of the aggregates formed from **3** was carried out on their 'wet' (not fully dried) state. As can be seen in Fig. 6a, the confocal imaging of **3** showed the formation of spheres with an average diameter of 90 μm, which is complimentary to that seen for **1** and **2** above, and as for **1**, these were formed from the self-assembly of linear fibers into the hierarchical structure.

The results for **1–3** clearly demonstrate that bio-conjugated **Nap** structures can give rise to rich self-assembled formations

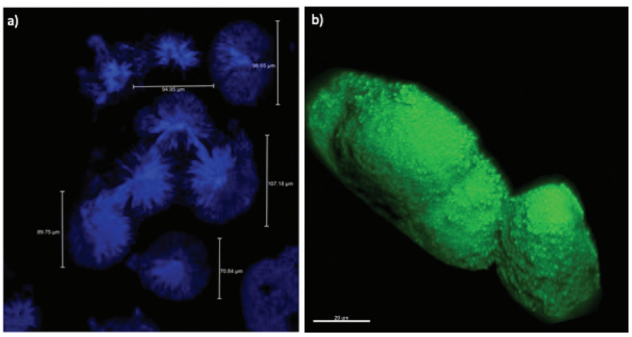

Fig. 6 Confocal fluorescence microscopy images: (a) **3** in PBS buffer after 16 h. Each of the bars is between 80–100 μm. (b) After the incubation of **3** in new PBS buffer media consisting of 1 U of β-galactosidase at 30 °C for 16 h. The bar is 20 μm.

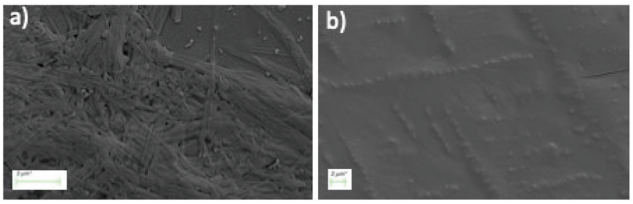

Fig. 7 SEM images of **3** in PBS buffer drop cased onto silica, before (a), and after (b) treatment with 1 U of β-galactosidase. Each bar is 2 μm.

that, in the case of **1–3** in competitive hydrogen bonding media, manifest as spherical hierarchical self-assemblies. Given that these structures can all be post-synthetically altered upon cleaving the native glycoside linkage using endogenous enzymes, this process could potentially be used to alter the morphology of the self-assembled materials *in situ*. We thus decided to investigate this using the most robust example **3**.

The spheres formed from **3** were isolated and incubated in new media consisting of 1 U (catalytic unit) of β-galactosidase at 30 °C for 16 h in PBS buffer. In parallel, an identical experiment was carried out under the same experimental conditions except without the presence of the enzyme. In the control experiment, no morphological changes were observed, with the isolated particles looking identical to that shown in Fig. 6a. However, as can be seen from Fig. 6b, β-galactosidase treatment of the preformed spheres of **3** resulted in loss of their morphological features, transformed them into amorphous aggregates. The confocal images of this material clearly reveal there are no longer any fibrous hierarchical self-assembly structures. Instead the transformation of these into an amorphous material, Fig. 6b was observed. To gain further insight of the morphological changes occurring upon enzymatic hydrolysis, SEM images were recorded before and after the enzymatic treatment. As shown in Fig. 7, the SEM images of compound **3** before enzymatic treatment clearly show the presence of fibers network, while after enzymatic treatment the material was converted to non-spherical soft matter, with the presence of PBS salt also being observed. This would confirm that the glycan moieties play an important role in modulating the overall supramolecular interactions of these structures, and that the formation of the hierarchical self-assemblies is highly dependent on synergistic interactions, the most prominent being π–π stacking and hydrogen bonding interactions within the same media. We are currently evaluating the application of these systems further, and in particular, the supramolecular self-assembly formations of 4-bromo-**Nap** structures in greater detail.

Conflicts of interest

There are no conflicts to declare.

Acknowledgements

We thank Science Foundation Ireland (SFI PI Award 13/IA/1865) for financial support, and Dr J. E. O'Brien, M. Reuther

and G. Hessman for their help with NMR and HRMS. We also thank CRANN/AML facilities at TCD for access to HIB and SEM infrastructure.

Notes and references

1 (*a*) D. Wu, A. C. Sedgwick, T. Gunnlaugsson, E. U. Akkaya, J. Yoon and T. D. James, *Chem. Soc. Rev.*, 2017, **46**, 7105–7123; (*b*) S. Erbas-Cakmak, S. Kolemen, A. C. Sedgwick, T. Gunnlaugsson, T. D. James, J. Yoon and E. U. Akkaya, *Chem. Soc. Rev.*, 2018, **47**, 2228–2248; (*c*) T. Gunnlaugsson, M. Glynn, G. M. Tocci, P. E. Kruger and F. M. Pfeffer, *Coord. Chem. Rev.*, 2006, **250**, 3094; (*d*) H. N. Kim, Z. Guo, W. Zhu, J. Yoon and H. Tian, *Chem. Soc. Rev.*, 2011, **40**, 79–93; (*e*) Z. Guo, S. Park, J. Yoon and I. Shin, *Chem. Soc. Rev.*, 2014, **43**, 16–29; (*f*) A. P. de Silva, H. Q. N. Gunaratne, T. Gunnlaugsson, C. P. McCoy, P. R. S. Maxwell, J. T. Rademacher and T. E. Rice, *Pure Appl. Chem.*, 1996, **68**, 1443–1448.

2 (*a*) R. M. Duke, E. B. Veale, F. M. Pfeffer, P. E. Kruger and T. Gunnlaugsson, *Chem. Soc. Rev.*, 2010, **39**, 3936–3953; (*b*) S. Banerjee, E. B. Veale, C. M. Phelan, S. A. Murphy, G. M. Tocci, L. J. Gillespie, D. O. Frimannsson, J. M. Kelly and T. Gunnlaugsson, *Chem. Soc. Rev.*, 2013, **42**, 1601–1618; A. P. de Silva, T. Gunnlaugsson and T. E. Rice, *Analyst*, 1996, **121**, 1759–1762.

3 (*a*) B. Daly, J. Ling and A. P. de Silva, *Chem. Soc. Rev.*, 2015, **44**, 4203–4211; (*b*) A. P. de Silva, H. Q. N. Gunaratne, T. Gunnlaugsson, A. J. M. Huxley, C. P. McCoy, J. T. Rademacher and T. E. Rice, *Chem. Rev.*, 1997, **97**, 1515–1566; (*c*) W. Guan, W. Zhou, J. Lu and C. Lu, *Chem. Soc. Rev.*, 2015, **44**, 6981–7009; (*d*) E. B. Veale and T. Gunnlaugsson, *Annu. Rep. Prog. Chem.*, 2010, **106**, 376; (*e*) F. E. Poynton, S. A. Bright, S. Blasco, D. C. Williams, J. M. Kelly and T. Gunnlaugsson, *Chem. Soc. Rev.*, 2017, **46**, 7706–7756.

4 (*a*) D. Collado, P. Remon, Y. Vida, F. Najera, P. Sen, U. Pischel and E. Perez-Inestrosa, *Chem. – Asian J.*, 2014, **9**, 797–804; (*b*) D. Gosztola, M. P. Niemczyk, W. Svec, Aa. S. Lukas and Mi. R. Wasielewski, *J. Phys. Chem. A*, 2000, **104**, 6545–6551; (*c*) E. B. Veale and T. Gunnlaugsson, *J. Org. Chem.*, 2008, **73**, 8073–7076; (*d*) T. E. Rice and A. P. de Silva, *Chem. Commun.*, 1999, 163–164.

5 (*a*) P. Gopikrishna, N. Meher and P. K. Iyer, *ACS Appl. Mater. Interfaces*, 2018, **10**, 12081–12111; (*b*) Z. Chen, D. Wu, X. Han, Y. Nie, J. Yin, G.-A. Yu and S. H. Liu, *RSC Adv.*, 2014, **4**, 63985–63988; (*c*) S. Mukherjee and P. Thilagar, *Chem. – Eur. J.*, 2014, **20**, 9052–9062; (*d*) S. Mukherjee and P. Thilagar, *Phys. Chem. Chem. Phys.*, 2014, **16**, 20866–20877; (*e*) X. Cao, L. Meng, Z. Li, Y. Mao, H. Lan, L. Chen, Y. Fan and T. Yi, *Langmuir*, 2014, **30**, 11753–11760.

6 (*a*) S. Shanmugaraju, D. Umadevi, L. M. Gonzalez-Barcia, J. M. Delente, K. Byrne, W. Schmitt, G. W. Watson and T. Gunnlaugsson, *Chem. Commun.*, 2019, **55**, 12140–12143; (*b*) M. Martínez-Calvo, S. A. Bright, E. B. Veale, A. F. Henwood, D. C. Williams and T. Gunnlaugsson, *Front. Chem. Sci. Eng.*, 2020, **14**, 61–75; (*c*) S. Shanmugaraju, B. la Cour Poulsen, T. Arisa, D. Umadevi, H. L. Dalton, C. S. Hawes, S. Estalayo-Adrian, A. J. Savyasachi, G. W. Watson, D. C. Williams and T. Gunnlaugsson, *Chem. Commun.*, 2018, **54**, 4120–4123; (*d*) G. J. Ryan, R. B. P. Elmes, M.-L. Erby, F. E. Poynton, D. C. Williams, S. J. Quinn and T. Gunnlaugsson, *Dalton Trans.*, 2015, **44**, 16332–16344; (*e*) S. Shanmugaraju, C. Dabadie, K. Byrne, A. J. Savyasachi, D. Umadevi, W. Schmitt, J. A. Kitchen and T. Gunnlaugsson, *Chem. Sci.*, 2017, **8**, 1535–1546; (*f*) T. Gunnlaugsson, B. Bichell and C. Nolan, *Tetrahedron Lett.*, 2002, **43**, 4989–4992.

7 (*a*) X. Ao, S. A. Bright, N. C. Taylor and R. B. P. Elmes, *Org. Biomol. Chem.*, 2017, **15**, 6104–6108; (*b*) T. Jia, C. Fu, C. Huang, H. Yang and N. Jia, *ACS Appl. Mater. Interfaces*, 2015, **7**, 10013–10021; (*c*) M. H. Lee, J. H. Ha, P.-S. Kwon, S. Bhuniya, J. Y. Kim, J. L. Sessler, C. Kang and J. S. Kim, *J. Am. Chem. Soc.*, 2012, **134**, 1316–1322; (*d*) L. Dong, Y. Zang, D. Zhou, X.-P. He, G.-R. Chen, T. D. James and J. Li, *Chem. Commun.*, 2015, **51**, 11852–11855; S. Tan, H. Yin, Z. Chen, X. Qian and Y. Xu, *Eur. J. Med. Chem.*, 2013, **62**, 130–138; (*e*) D.-T. Shi, D. Zhou, Y. Zang, J. Li, G.-R. Chen, T. D. James, X.-P. He and H. Tian, *Chem. Commun.*, 2015, **51**, 3653–3655; (*f*) S. Mukherjee and P. Thilagar, *Chem. Commun.*, 2013, **49**, 7292–7294.

8 (*a*) L. K. Kumawat, A. A. Abogunrin, M. Kickham, J. Pardeshi, O. Fenelon, M. Schroeder and R. B. P. Elmes, *Front. Chem.*, 2019, **7**, 354; (*b*) J. I. Lovitt, C. S. Hawes and T. Gunnlaugsson, *CrystEngComm*, 2019, **21**, 207–217; (*c*) A. Das and S. Ghosh, *Chem. Commun.*, 2016, **52**, 6860–6872; (*d*) N. Ponnuswamy, G. Pantos, M. Smulders and J. Sanders, *J. Am. Chem. Soc.*, 2012, **134**, 566–573; (*e*) M.-Y. Yeh, C.-T. Huang, T.-S. Lai, F.-Y. Chen, N.-T. Chu, D. T-H. Tseng, S.-C. Hung and H.-C. Lin, *Langmuir*, 2016, **32**, 7630–7638; (*f*) A. K. Srivastava, A. Singh and L. Mishra, *J. Phys. Chem. A*, 2016, **120**, 4490–4504.

9 (*a*) A. W. H. Ng and H. Y. Au-Yeung, *Chem. – Asian J.*, 2019, **14**, 1602–1612; (*b*) S. L. Suraru and F. Würthner, *Angew. Chem., Int. Ed.*, 2014, **53**, 7428–7448; (*c*) G. M. Prentice, L. Emmett, V. Luxami and G. D. Pantos, in *Naphthalenediimide and its Congeners: From Molecules to Materials*, ed. G. D. Pantos, RSC Publishing, Cambridge, 2017, ch. 1.; (*d*) N. Sakai, J. Mareda, E. Vauthey and S. Matile, *Chem. Commun.*, 2010, **46**, 4225–4237; (*e*) R. S. K. Kishore, O. Kel, N. Banerji, D. Emery, G. Bollot, J. Mareda, A. Gomez-Casado, P. Jonkheijm, J. Huskens, P. Maroni, M. Borkovec, E. Vauthey, N. Sakai and S. Matile, *J. Am. Chem. Soc.*, 2009, **131**, 11106–11116.

10 (*a*) S. Banerjee, S. A. Bright, J. A. Smith, J. Burgeat, M. Martinez-Calvo, D. C. Williams, J. M. Kelly and T. Gunnlaugsson, *J. Org. Chem.*, 2014, **79**, 9272–9283; (*b*) S. Murphy, S. A. Bright, F. E. Poynton, T. McCabe, J. A. Kitchen, E. B. Veale, D. C. Williams and T. Gunnlaugsson, *Org. Biomol. Chem.*, 2014, **12**, 6610–6623;

(*c*) A. B. Aletti, S. Blasco, S. J. Aramballi, P. E. Kruger and T. Gunnlaugsson, *Chem*, 2019, **5**, 2617–2629.

11 (*a*) S. Shanmugaraju, B. la Cour Poulsen, T. Arisa, D. Umadevi, H. L. Dalton, C. S. Hawes, S. Estalayo-Adrian, A. J. Savyasachi, G. W. Watson, D. C. Williams and T. Gunnlaugsson, *Chem. Commun.*, 2018, **54**, 4120–4123; (*b*) C. S. Hawes, A. D. Lynes, K. Byrne, W. Schmitt, G. Ryan, M. E. Möbius and T. Gunnlaugsson, *Chem. Commun.*, 2017, **53**, 5989–5992; (*c*) C. S. Hawes, K. Byrne, W. Schmitt and T. Gunnlaugsson, *Inorg. Chem.*, 2016, **55**, 11570–11582.

12 (*a*) J. I. Lovitt, C. S. Hawes, A. D. Lynes, B. Haffner, M. E. Möbius and T. Gunnlaugsson, *Inorg. Chem. Front.*, 2017, **4**, 296–308; (*b*) T. Gunnlaugsson, C. P. McCoy, R. J. Morrow, C. Phelan and F. Stomeo, *Arkivoc*, 2003, **7**, 216–228.

13 Y. Ni, Z. Sun, Y. Wang, H. F. Nour, A. C.-H. Sue, N. S. Finney, K. K. Baldridge and M. A. Olson, *J. Mater. Chem. C*, 2019, **7**, 7399–7410.

14 (*a*) I. D. Welsh, D. Draper, J. Kim, J. A. Kitchen and J. R. Allison, *Chem. – Asian J.*, 2019, **14**, 1221–1229; (*b*) B. Carter, R. J. Laverick, D. J. Wales, S. O. Akponasa, A. J. Scott, T. D. Keene and J. A. Kitchen, *Cryst. Growth Des.*, 2017, **17**, 5129–5144; (*c*) J. A. Kitchen, N. Zhang, A. B. Carter, A. J. Fitzpatrick and G. G. Morgan, *J. Coord. Chem.*, 2016, **69**, 2024–2037; (*d*) J. A. Kitchen, P. N. Martinho, G. G. Morgan and T. Gunnlaugsson, *Dalton Trans.*, 2014, **43**, 6468–6479.

15 C. S. Hawes, K. Byrne, W. Schmitt and T. Gunnlaugsson, *Mater. Chem. Front.*, 2018, **2**, 1366–1373.

16 (*a*) X. Cao, Q. Ding, N. Zhao, A. Gao and Q. Jing, *Sens. Actuators, B*, 2018, **256**, 711–720; (*b*) X. Cao, N. Zhao, H. Lv, Q. Ding, A. Gao, Q. Jing and T. Yi, *Langmuir*, 2017, **33**, 7788–7798.

17 X. Cao, N. Zhao, A. Gao, Q. Ding, Y. Li and X. Chang, *Langmuir*, 2018, **34**, 7404–7415.

18 (*a*) M. Zhang, S. Sun, X. Yu, Xi. Cao, Y. Zou and T. Yi, *Chem. Commun.*, 2010, **46**, 3553–3555; (*b*) Z. Ma, P. Zhang, X. Yu, H. Lan, Y. Li, D. Xie, Ji. Lib and T. Yi, *J. Mater. Chem. B*, 2015, **3**, 7366–7371; (*c*) X. Yu, D. Xie, H. Lan, Y. Li, X. Zhen, J. Ren and T. Yi, *J. Mater. Chem. C*, 2017, **5**, 5910–5916.

19 E. Calatrava-Perez, S. A. Bright, S. Achermann, C. Moylan, M. O. Senge, E. B. Veale, D. C. Williams, T. Gunnlaugsson and E. M. Scanlan, *Chem. Commun.*, 2016, **52**, 13086–13089.

20 E. Calatrava-Pérez, J. M. Delente, S. Shanmugaraju, C. S. Hawes, C. D. Williams, T. Gunnlaugsson and E. M. Scanlan, *Org. Biomol. Chem.*, 2019, **17**, 2116–2125.

21 (*a*) H. M. Burke, T. Gunnlaugsson and E. M. Scanlan, *Chem. Commun.*, 2015, **51**, 10576–10588; (*b*) H. M. Burke, T. Gunnlaugsson and E. M. Scanlan, *Org. Biomol. Chem.*, 2016, **14**, 9133–9145.

22 C. Moylan, E. M. Scanlan and M. O. Senge, *Curr. Med. Chem.*, 2015, **22**, 2238–2348.

23 B. Ventura, A. Bertocco, D. Braga, L. Catalano, S. d'Agostino, F. Grepioni and P. Taddei, *J. Phys. Chem. C*, 2014, **118**, 18646–18658.

SUPRAMOLECULAR CHEMISTRY
2020, VOL. 32, NO. 9, 508–517
https://doi.org/10.1080/10610278.2020.1825715

Taylor & Francis
Taylor & Francis Group

Hyper-crosslinked 4-amino-1,8-naphthalimide Tröger's base containing pyridinium covalent organic polymer (COP) for discriminative fluorescent sensing of chemical explosives

Jason M. Delente[a,b], Deivasigamani Umadevi[c], Kevin Byrne[c], Wolfgang Schmitt[b,c], Graeme W. Watson[c], Thorfinnur Gunnlaugsson[a,b] and Sankarasekaran Shanmugaraju[d]

[a]School of Chemistry and Trinity Biomedical Sciences Institute, Trinity College Dublin, The University of Dublin, Ireland; [b]AMBER (Advanced Materials and Bioengineering Research) Centre, Trinity College Dublin, The University of Dublin, Ireland; [c]School of Chemistry and Centre for Research on Adaptive Nanostructures and Nanodevices (CRANN), Trinity College Dublin, The University of Dublin, Ireland; [d]Discipline of Chemistry, Indian Institute of Technology Palakkad, Kerala, India

ABSTRACT

A new hyper-crosslinked 4-amino-1,8-naphthalimide Tröger's base containing pyridinium covalent organic polymer, **TBNap-COP**, was synthesised and employed as a 'turn-off' fluorescent chemosensor for nitroaromatic explosives. **TBNap-COP** was synthesised in quantitative yield using a one-step nucleophilic substitution reaction between a dipyridyl scaffold (**TBNap**, bis-[N-(2-(pyridine-4-yl)ethyl)]-9,18-methano-1,8-naphthalimide-[b,f][1,5]diazocine) and 1,3,5-tris(bromomethyl)benzene by heating in DMF for 3 days. The formation and phase-purity of **TBNap-COP** were fully characterised by using various spectroscopic and microscopy analyses. The suspension of **TBNap-COP** in water showed strong fluorescence emission characteristics owing to the 'push-pull' based ICT transition and it was used as a fluorescent sensor for discriminative detection of nitroaromatic explosives. **TBNap-COP** displayed selective fluorescence quenching responses for phenolic-nitroaromatics, with particularly high sensitivity for picric acid which is a powerful secondary chemical explosive and a harmful environmental pollutant widely used in the dye industries.

ARTICLE HISTORY
Received 11 August 2020
Accepted 11 September 2020

KEYWORDS
Organic polymers; Tröger's base; 1,8-naphthalimide; fluorescence; chemosensing; nitroaromatics

Introduction

The development of suitable sensors and probes for fast and reliable identification of chemical explosives at trace-level is necessary to combat terrorism, improve homeland security, and to eliminate environmental pollution [1,2]. Nitroaromatic compounds (NACs), such as 2,4,6-trinitrotoluene (TNT) and the related 2,4,6-trinitrophenol also known as picric acid (PA), are classified as powerful secondary chemical explosives because of their high detonation velocity [3]. Due to their low-cost preparation and easy transportation, NACs are used as the primary component in various known chemical explosives [4,5]. For example, Tritonal is a well-known chemical explosive made up of 80% TNT and 20% aluminium powder [3–5]. However, apart from their use as a powerful chemical explosive, many of these electron-deficient structures have other 'chemical' roles and functions, for instance in chemical biology, where agents such as 2,4-dinitrophenol (DNP) can inhibit adenosine triphosphate (ATP) production in cells [6]. Hence, many NACs can have high acute toxicity. Other NACs, such as the aforementioned PA, are also extensively used as a reagent in the pharmaceutical industry and as a yellow pigment in the dye industry [2–5]. This makes PA highly available and accessible, which is concerning. PA is a very common reagent, being environmental contaminant and toxic to living organisms [3–5,7]. Because of its extensive use, and high solubility in water (~14 $g.L^{-1}$), PA and its derivatives can easily contaminate groundwater and soils, exposing humans and animals/life-stocks [5,7]. In fact, continuous exposure to saturated vapours of PA can cause severe eye irritation and headaches, while prolonged exposure results in serious and irreversible health issues like liver and kidney failure, and neurological damage [3–5,7]. Hence, there is a need to develop a suitable and reliable sensor for the trace detection of NACs. Various techniques for detection are currently used but are often very expensive and have limited portability, making them impractical for on-site detection [8]. Therefore, researchers have directed their efforts towards fluorescence sensors representing

CONTACT Thorfinnur Gunnlaugsson gunnlaut@tcd.ie School of Chemistry, Trinity Biomedical Sciences Institute and AMBER (Advanced Material and Bioengineering Research) Centre, Trinity College Dublin, the University of Dublin, Dublin 2, Ireland; Shanmugaraju Sankarasekaran shanmugam@iitpkd.ac.in Department of Chemistry, Indian Institute of Technology, Palakkad, Kerala, India
Supplemental data for this article can be accessed here.

a low-cost sensing method with high sensitivity and selectivity and are often synonym of portable devices for on-site detections [1–7], and this is an area we have been developing in recent times [9,10].

A wide variety of fluorophores have been used, ranging from purely organic molecules to inorganic and hybrid compounds such as tetraphenylethenes [11], pentacenequinones [12], carbazoles [13], pyrene [14], calixarene [15], Tröger's base [16], 1,8-naphthalimides [17], quantum dots [18], metal-organic frameworks (MOFs) [19], and covalent organic polymers [20]. Amongst the plethora of sensors created, polymer-based sensors are advantageous because of their enhanced sensitivity caused by the signal amplification effect and recyclability [21]. Covalent organic polymers (COPs) are a class of porous polymers gaining significant interest as chemosensors for the trace detection of environmental pollutants and hazardous substances [22]. Like MOFs, COPs are also composed of repeating motifs but only contain organic functional groups, usually leading to materials that are lighter than MOFs, as they are mainly composed of light elements (C, H, N, O) [23]. COPs are also generally very robust as they are principally composed of C-C and C-N bonds [24]. In a similar fashion to MOFs, it is possible to control the pore size and therefore, the surface area of the polymer [25]. Most COPs synthesised are used for gas storage and catalysis; however, the luminescent properties of these materials, combined with the ability to tune their pore sizes, make them ideal candidates for sensing applications [26].

Using electron-rich, conjugated fluorophores as one of the COP building blocks leads to the formation of large π-conjugated networks, which are capable of acting as excellent electron donors that exhibit increased sensitivity towards electron acceptor analytes such as nitroaromatics [9,21,25,26]. Taking into account these considerations, and knowledge gained from previous results from our laboratory showing that 4-amino-1,8-naphthalimide-Tröger's base (**TBNaps**) can discriminatively detect chemical explosives with high sensitivity [9,10], we report herein a novel hyper-crosslinked 4-amino-1,8-naphthalimide-Tröger's base functionalised pyridinium covalent organic polymer **TBNap-COP**. Our approach is based on three factors: (i) By using a **TBNap** moiety we take advantage of the presence of the Lewis basic nitrogen's of the Tröger's base motif, which should lead to good selectivity and sensitivity towards phenolic nitroaromatics particularly for PA; (ii) By using 1,3,5-trimethyl benzene as the linking point between each **TBNap** this should lead to a hyper-crosslinked polymeric system, which could potentially further increase the sensitivity by providing additional binding sites; (iii) The presence of positively charged pyridinium ions and the bromide anions should help to solvate the polymer, countering any π-π stacking interactions taking place, and thus facilitating the formation of a very stable fine suspension of **TBNap-COP** in water. As we expected **TBNap-COP** exhibited enhanced fluorescence emission when dispersed in water. However, as we demonstrate here, the screening of the solution of structurally close-related NACs resulted in significant quenching in the **TBNap-COP** emission, the largest quenching response being observed for PA, which also displayed a discriminative sensing propensity towards phenolic NACs over non-phenolic NACs.

Experimental section

Materials and methods

All reagents, solvents, starting materials, and nitroaromatic analytes were purchased from Sigma-Aldrich, Merck, or Fisher Scientific and were of reagent grade and were used as received. Solvents used were HPLC grade unless otherwise stated. Deuterated solvent ($(CD_3)_2SO$) used for NMR analyses was purchased from Sigma-Aldrich or Apollo Scientific. The monomer **TBNap** was synthesised according to the previously published procedure [27,28]. (Caution! Nitroaromatic analytes are classified as secondary chemical explosives and should be handled only in small quantity).

The elemental analysis for C, H, and N was performed on an Exeter analytical CE-450 elemental analyser.

FT-IR spectra were recorded in the range 4000–550 cm^{-1} on a Perkin-Elmer spectrometer equipped with a universal ATR sampling accessory.

The solution-phase ^1H NMR spectra were recorded at 400 MHz using an Agilent Technologies 400-MR NMR spectrometer. Chemical shifts are reported in ppm with the deuterated solvents as the internal reference. All NMR spectra were carried out at 293 K. The ^{13}C NMR spectra of precursors were acquired in DMSO-d_6 at 100.55 MHz at 25°C.

The solid-state CP/MAS ^{13}CNMR spectrum of **TBNap-COP** was acquired at 201.1 MHz using a 3.2 mm double-resonance MAS probe. The spectrum was acquired under magic angle spinning (MAS) at 20 kHz, if not otherwise specified, using ramped-amplitude cross-polarisation, and SPINAL64 decoupling with a ^1H-decoupling field of about 80 kHz. A 3 ms contact time and a pulse delay of 5 s were used. Chemical shifts were calibrated setting the ^{13}C low field signal of adamantane to 8.48 ppm.

Mass spectrometry was carried out using HPLC grade solvents. Electrospray mass spectra were determined on a Micromass LCT spectrometer and high-resolution mass

spectra were determined relative to a standard of leucine enkephaline. MaldiQ-TOF mass spectra were carried out on a MALDI-Q-TOF-premier and high-resolution mass spectrometry was performed using Glu-Fib with an internal reference peak of *m/z* 1570.6774.

Morphology of **TBNap-COP** was imaged using field emission scanning electron microscopy (FE-SEM) with an SE2 on the in-lens detector. The sample was prepared by drop-casting the aqueous suspension (1 mg in 100 µL of Millipore water) of as-synthesised **TBNap-COP** on silica wafers, then coated with Au and dried under vacuum before the imaging.

UV-visible absorption spectra were recorded in 1 cm quartz cuvettes (Hellma) on a Varian Cary 50 spectrometer. Baseline correction was applied for all spectra.

Emission spectra were recorded on a Varian Cary Eclipse Fluorimeter. The temperature was kept constant throughout the measurements at 298 K by using a thermostatic unit block.

Synthesis of pyridinium polymer TBNap-COP

A mixture of monomers *bis*-[N-(2-(pyridine-4-yl)ethyl)]-9,18-methano-1,8-naphthalimide-[*b,f*] [1,5]diazocine (**TBNap**, 150 mg, 0.22 mmol, 3.0 eq.) and 1,3,5-Tris(bromomethyl) benzene (53 mg, 0.15 mmol, 2.0 eq.) was taken in a Pyrex tube along with 50 mL of DMF. Then, the mixture was heated under stirring at 100°C for 3 days. The formed heavy precipitate was isolated by vacuum filtration and then the precipitate was washed extensively with DCM (2 × 50 mL), CH_3OH (2 × 50 mL) and diethyl ether (1 × 50 mL) to remove the unreacted monomers and oligomers. Finally, the solid was dried under high vacuum for 6 hours to isolate the expected pyridinium covalent organic polymer **TBNap-COP** as bright yellow powder (68%). Elemental analysis (%) calculated for the repeating unit $[C_{141}H_{108}Br_6N_{18}O_{12}].3CH_2Cl_2.4CH_3OH.DMF$: C, 56.99; H, 4.33; N, 8.36; found: C, 56.79, H, 4.18, N, 8.45; FT-IR (υ cm^{-1}): 3371, 2972, 1691, 1654, 1595, 1570, 1511, 1458, 1402, 1376, 1342, 1300, 1259, 1231, 1169, 1151, 1126, 1090, 1053, 921, 870, 785, 759, 693; ^{1}H NMR (400 MHz, $(CD_3)_2SO$) *d* 11.61 (4 H, s, pyridyl-H), 8.75–8.72 (2 H, d, *J* = 8.0 Hz, Ar-H), 8.48–8.46 (2 H, d, *J* = 8.0 Hz, Ar-H), 8.10 (2 H, s, Ar-H), 8.06 (3 H, s, Ph-H), 7.99–7.95 (2 H, t, *J* = 8.0 Hz, Ar-H), 7.40 (4 H, s, pyridyl-H), 5.19–5.15 (2 H, d, *J* = 16.0 Hz, N-CH_2), 4.71 (8 H, m, N-CH_2, Ph-CH_2), 4.66 (2 H, s, N-CH_2), 4.29–4.26 (4 H, t, *J* = 12.0 Hz, CH_2-CH_2), 3.00–2.97 (4 H, t, *J* = 12.0 Hz, CH_2-CH_2).

Gas uptake measurements

All the gas (N_2, H_2, and CO_2) adsorption measurements were carried out using a Quantachrome Autosorb IQ automated gas sorption analyser. The as-synthesised **TBNap-COP** was immersed in diethyl ether for 3 days. During the immersion, the diethyl ether was refreshed 5 times with fresh diethyl ether and the resulting solvent exchanged polymer was transferred to a quartz cell. The sample was evacuated under vacuum at 100°C for 72 hours. BOC gases ultrahigh-purity grade N_2, H_2, and CO_2 were used in all adsorption measurements. The surface area of **TBNap-COP** was calculated by the Brunauer-Emmett-Teller (BET) method.

Preparation of the stock solution

10 mg of **TBNap-COP** was placed in a 10 mL standard measuring flask and 100 mL of respective solvents were added to it. Then, the mixture was sonicated for 30 minutes and aged for 72 h to get a uniform suspension for spectroscopic studies. The desired quantity of each of the nitroaromatics was dissolved into 2 mL of EtOH and then 18 mL of deionised water was slowly added to the solution.

Fluorescence titration experiments

200 µL of the suspension of **TBNap-COP** in water was taken in a quartz cuvette and 1800 µL of water was added to it. During the fluorescence titration, 1 mM solution of different nitroaromatic explosives was added (0.0 µM — 90.9 µM) in an incremental fashion (20 µL each addition) to a 2 mL aqueous suspension of **TBNap-COP**. The emission intensity was monitored after each addition. For all the fluorescence titration experiments, the excitation wavelength was 380 nm and the emission spectra were recorded in the range of 400–800 nm. The percentage of quenching efficiency was calculated from the following equation:

$$Quenching\ efficiency(\%) = (I_0 - I)/I_0 \times 100$$

Where I_0 is the initial emission intensity of **TBNap-COP** in H_2O and I is the intensity after the addition of the analyte.

Results and discussion

Synthesis and characterisation of TBNap-COP

As shown in Scheme 1, the polymer**TBNap-COP** was readily synthesised in quantitative yield (68%) using **TBNap** and the commercially available 1,3,5-tris-(bromomethyl)benzene by heating in DMF for 3 days.

The successful formation of **TBNap-COP** was confirmed by ^{1}H NMR, solid-state CP-MAS ^{13}C NMR, FT-IR, and elemental analysis. The ^{1}H NMR spectrum in DMSO-d_6 revealed the presence of the Tröger's base

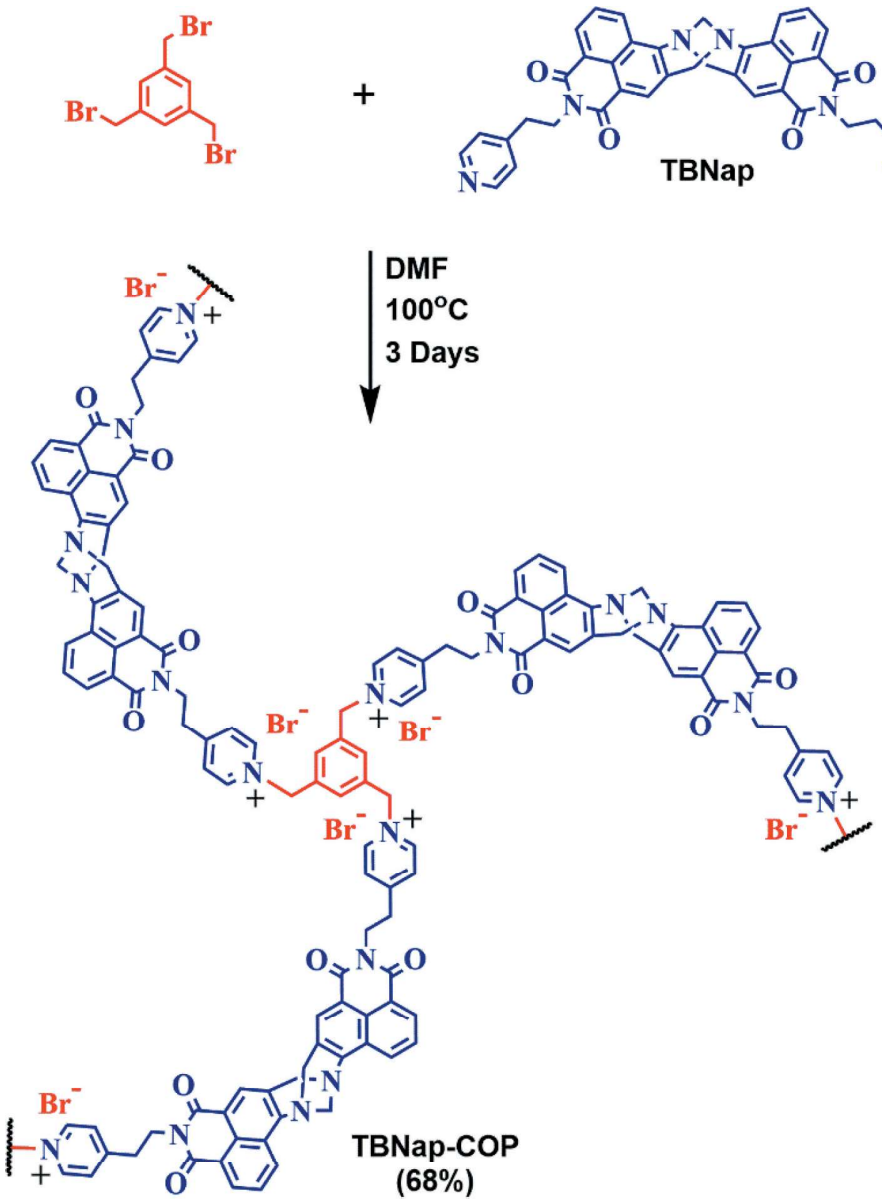

Scheme 1. Synthesis of pyridinium covalent organic polymer TBNap-COP.

moiety with the doublet at 5.19 ppm and the merged singlet and doublet at 4.71–4.66 ppm accounting for the methylene protons of the diazocine ring (Figure S1) [9,10,27]. Notably, the pyridyl ^{1}H signals of **TBNap-COP** are significantly down-field shifted (~3.14 ppm) upon quaternization. The solid-state CP-MAS ^{13}C-NMR spectrum further confirmed the presence of the **TBNap** unit, with a resonance at 164 ppm corresponding to the carbonyl groups, and two further resonances at 64 ppm and 57 ppm ascribed to the CH_2 of the diazocine ring (Figure S1) [9,10]. The FT-IR spectrum of **TBNap-COP** showed two signals at 1691 cm^{-1} and 654 cm^{-1} corresponding to the carbonyl (C = O) groups of the naphthalimide moiety, two strong transitions at 1259 cm^{-1} and 1231 cm^{-1} accounting for the C-N stretching of the diazocine ring of the Tröger's base (Figure S2) [9,10,24]. Thermogravimetric analysis (TGA) of **TBNap-COP** under N_2 showed a weight loss of 4% at 200°C, representing the loss of solvent trapped within the polymeric network. **TBNap-COP** was found to be stable up to ~270°C, demonstrating good thermal stability (Figure S3). The powder X-ray diffraction (PXRD) measurement confirmed that **TBNap-COP** is an amorphous solid (Figure S4), which was further supported by the scanning electron microscopy, where the solid forms aggregate with a random distribution of pores of various sizes (Figure 1). The gas uptake capacity of the as-synthesised polymer was investigated and the

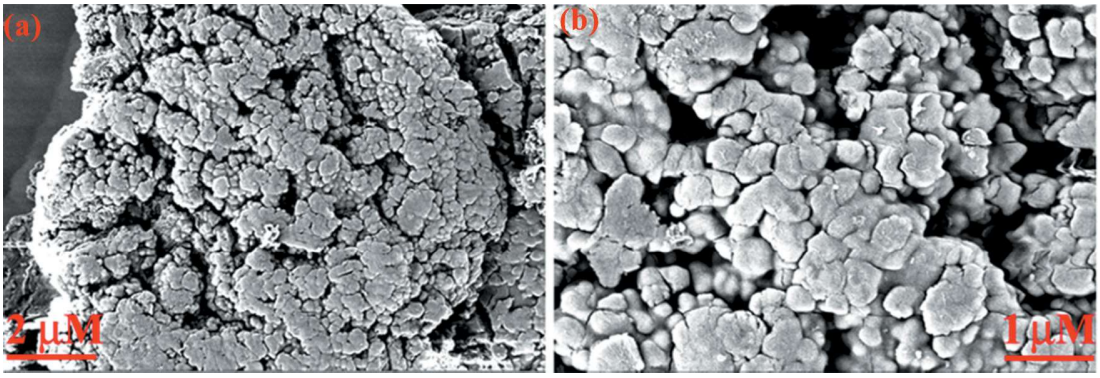

Figure 1. (a) Scanning electron microscopy image and (b) an enlarged image of the as-synthesised polymer **TBNap-COP.**

N_2 adsorption isotherm demonstrated reversible adsorption at 77 K of 55 cm^3/g at 1 bar and the Brunauer-Emmett-Teller (BET) surface area was calculated to be 65 m^2/g (Figure S5-S6). In addition to this study, the CO_2 adsorption was also studied but was found to be negligible.

Fluorescence sensing studies of TBNap-COP

Having successfully synthesised and characterised it, we then assessed the spectroscopic properties of **TBNap-COP**, particularly concerning its use as a fluorescence sensor for NACs by carrying out spectroscopic titrations in competitive aqueous media. The **TBNap-COP** showed the appearance of typical internal charge transfer (ICT, due to the push-pull nature of the naphthalimide moieties in the **TBNap** structure) transition with an absorption maxima in the visible region around λ_{max} = 366 nm, and a broad emission band with λ_{max} at *ca.* 490 nm in water (Figure S7). To demonstrate the ability of **TBNap-COP** for sensing NACs, we performed a fluorescence titration study of **TBNap-COP** with PA as a prototype of NACs. As shown in Figure 2, the initial emission intensity of **TBNap-COP** decreased progressively upon the incremental addition (20→200 µL) of PA (1 mM) solution in water. Except for a strong fluorescence quenching, no other significant spectral changes (such as a shift in λ_{max}) were observed. As it is shown in the inset of Figure 2, it is also possible to visually observe the quenching of the **TBNap-COP** fluorescence upon UV (λ = 360 nm) irradiation, making **TBNap-COP** a good candidate for visual detection of PA. The observed change in emission intensity was further analysed by fitting the titration data to the classical Stern-Volmer equation ($I_0/I = 1 + K_{sv}[Q]$), from which the Stern-Volmer constant (K_{SV}) was determined. The quenching of the fluorescence upon the addition of PA follows a linear trend for the lower concentration while at higher concentration the curve rises exponentially signifying that a super-amplified quenching effect operates at higher concentration of PA (Inset in Figure 2). Therefore, the Stern-Volmer binding constant, $K_{SV} = 32.7 \pm 1.34 \times 10^3\ M^{-1}$, was determined at lower concentrations of PA, demonstrating the higher binding propensity of **TBNap-COP** and the obtained K_{SV}

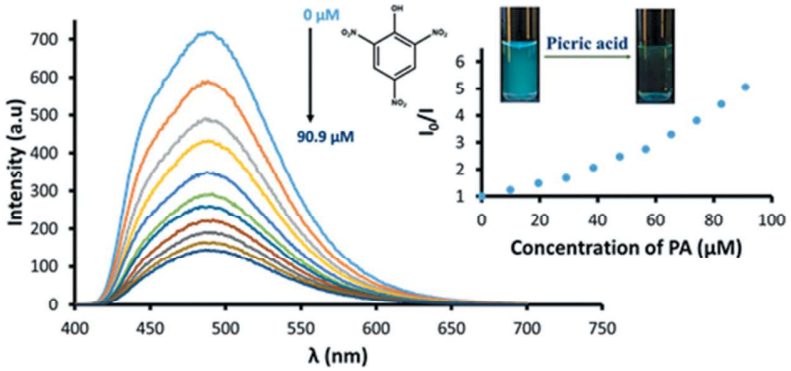

Figure 2. Fluorescence quenching of **TBNap-COP** upon the addition of PA (inset: its corresponding non-linear Stern-Volmer plot and visual colour change before and after the addition of PA under UV lamp).

is comparable to that which has been observed for similar systems (see Table S1).

Mechanism of fluorescence quenching

The obtained non-linear Stern-Volmer plot suggests that the fluorescence quenching could be the results of several mechanisms taking place: (i) energy transfer from the excited donor to an acceptor through a non-radiative pathway, (ii) the inner filter effect (IFE) due to the spectral overlap between the absorbance spectra of PA and the excitation spectra of **TBNap-COP**, (iii) the formation of hydrogen bonding interaction between the Lewis basic nitrogen of the Tröger's base and the hydroxy group of PA leading to the formation of a charge-transfer complex resulting in drastic quenching of emission intensity [9,10,24]. As seen in the superposition of the normalised absorbance spectrum of PA and the excitation and emission spectra of **TBNap-COP** (Figure S8), the inner filter effect is taking place and absorb part of the excitation light. However, this superposition also highlights a spectral overlap between the absorbance spectrum of PA and the emission spectrum of **TBNap-COP** confirming the possibility of energy transfer from the excited **TBNap-COP** to PA [1,2,9]. To estimate the participation of the IFE through the entire titration, the IFE correction was calculated using the equation:

$$I_{corr} = I_{obs} \times 10^{(A_{ex}+A_{em})/2}$$

Where I_{corr} is the corrected fluorescence intensity, I_{obs} the measured maximum intensity, A_{ex} and A_{em} correspond to the absorbance values of **TBNap-COP** in presence of PA at the excitation wavelength and the maxima of emission, respectively [29,30].

The value for I_{corr} can be found in Table S2 and was used to determine the contribution of the IFE to the quenching efficiency. The contribution of the IFE was determined to be responsible for ~56% of the observed quenching efficiency in presence of 90.9 µM of PA (Figure S9). Thus, demonstrating that the inner filter effect is not the only mechanism responsible for the quenching of the emission intensity of **TBNap-COP** and that the remaining 24% of fluorescence quenching involves other mechanisms. The obtained non-linear Stern-Volmer plot suggests that the observed fluorescence quenching is presumably due to the combination of IFE and either static or dynamic quenching. This can be confirmed by analysing the time-resolved fluorescence decay profile of **TBNap-COP** before and after the addition of PA. These fluorescence decay measurements data of **TBNap-COP** in water were best fitted to a bi-exponential decay, from which excited state life-times (τ_1 and τ_2) of 3.97 ns and 10.61 ns, were determined, respectively. Upon the incremental addition of PA, the initial life-time of **TBNap-COP** decreased to 3.16 ns and 9.98 ns for τ_1 and τ_2, respectively, (Figure 3). This demonstrates that PA is forming a complex with the excited state of **TBNap-COP** and that therefore dynamic quenching is taking place at higher concentrations of PA [9,10]. We also carried out temperature-dependent emission studies. These experiments demonstrated an increase in the quenching efficiency upon increasing the temperature, due to the enhanced

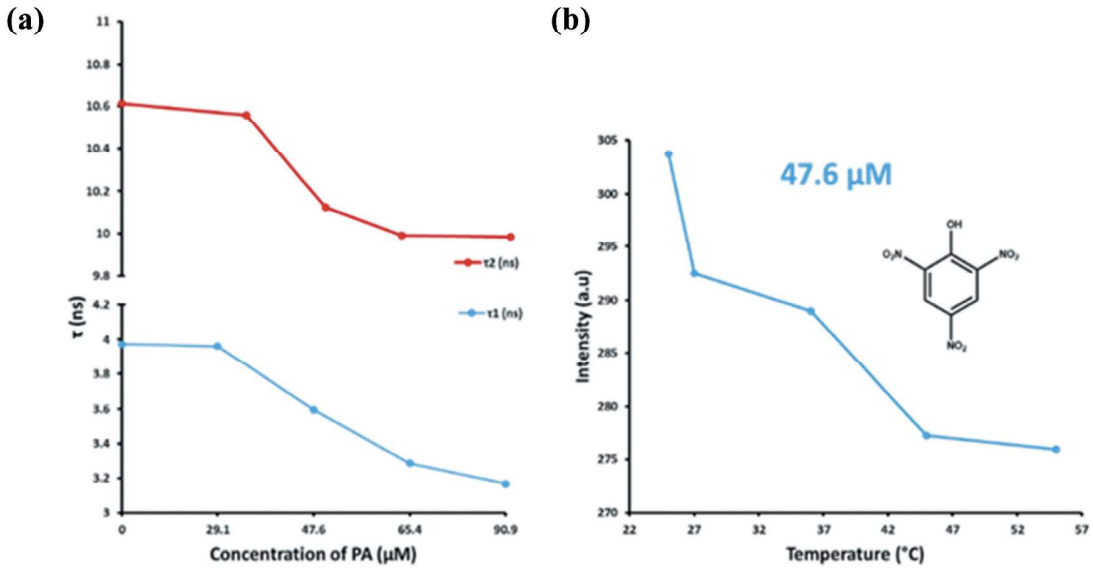

Figure 3. (a) Fluorescence decay profiles of **TBNap-COP** upon addition of PA (0 – 90.9 µM) and (b) its temperature-dependent emission profile in the presence of PA (47.6 µM).

molecular collision, of PA (47.6 μM) from 57% at 25°C to 61% at 55°C further confirming that the observed fluorescence quenching follows the dynamic quenching mechanism at higher NACs concentration (Figure 3) [9,10]. Furthermore, in the UV-vis absorption titrations studies, a significant increase in the absorption intensity of **TBNap-COP** upon the gradual mixing of PA was observed. However, no significant changes in the absorption maxima (λ_{max}) or no new peak were seen in the absorption spectra, which eliminate the possibility of ground-state charge transfer (CT) complexation between **TBNap-COP** and PA; this results further supported that PA forms a complex with the excited state **TBNap-COP** (Figure S10).

Theoretical study

To further understand the mechanism of excited-state charge transfer between **TBNap-COP** and picrate anion, theoretical calculations were undertaken by employing density functional theory (DFT). One monomer unit was considered as a model to represent the polymer. Geometry optimisations were performed using the M06-2X12 hybrid functional of Truhlar and Zhao with the 6–31 + G(d) basis set [31]. All the calculations were utilised in the Gaussian 09 package [32]. Figure 4 depicts the optimised geometry and the frontier orbitals of PA, the picrate anion, and the **TBNap-COP** model system. The highest occupied molecular orbital (HOMO) of **TBNap-COP** was mainly located on the Tröger's base moiety and the lowest unoccupied molecular orbital (LUMO) density was more localised in the pyridinium moiety. The energy of the HOMO and the LUMO of the **TBNap-COP** model systems are −10.548 eV and −5.704 eV, respectively. The HOMO and LUMO of the picrate anion are −4.490 eV and 1.351 eV, respectively. This would suggest that charge transfer can occur from the HOMO of the picrate anion to the LUMO of **TBNap-COP** and supports the proposed excited-state charge-transfer quenching mechanism [33,34].

Selectivity and competitive studies

To explore the selectivity of **TBNap-COP** towards NACs, similar fluorescence titration studies, under identical experimental conditions, were performed with various interfering nitroaromatics. These studies revealed a differential fluorescence quenching responses of **TBNap-COP** for different NACs and thus, structurally similar nitro explosives can be discriminated based on their quenching propensity. As it is shown in Figure 5(a), upon the incremental addition (20→200 μL) of different NACs (1 mM) in an aqueous suspension of **TBNap-COP**, a strong fluorescence quenching was observed for PA,

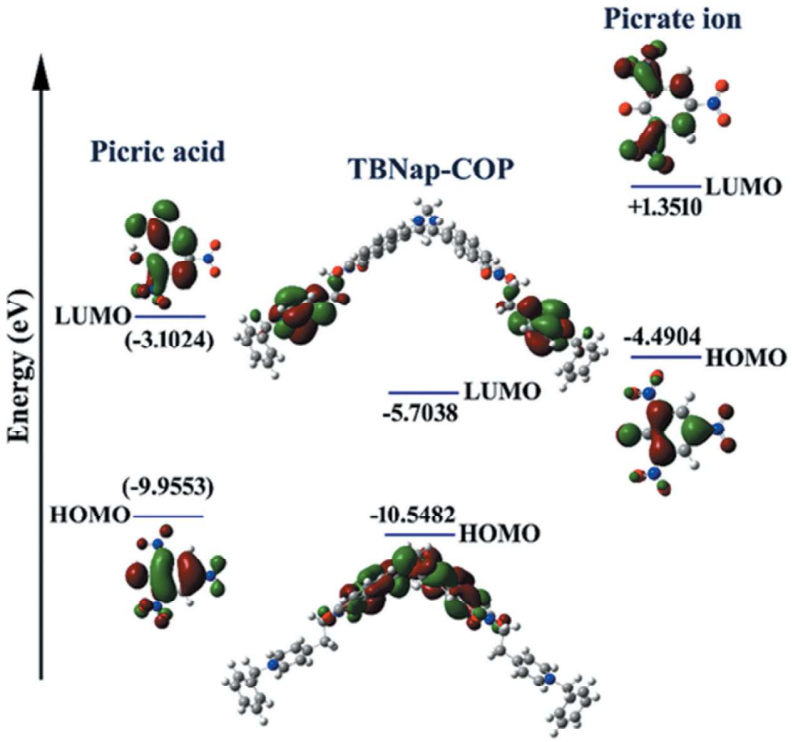

Figure 4. Pictorial representation of the charge transfer phenomena occurring from the HOMO of picrate ion to the LUMO of **TBNap-COP.**

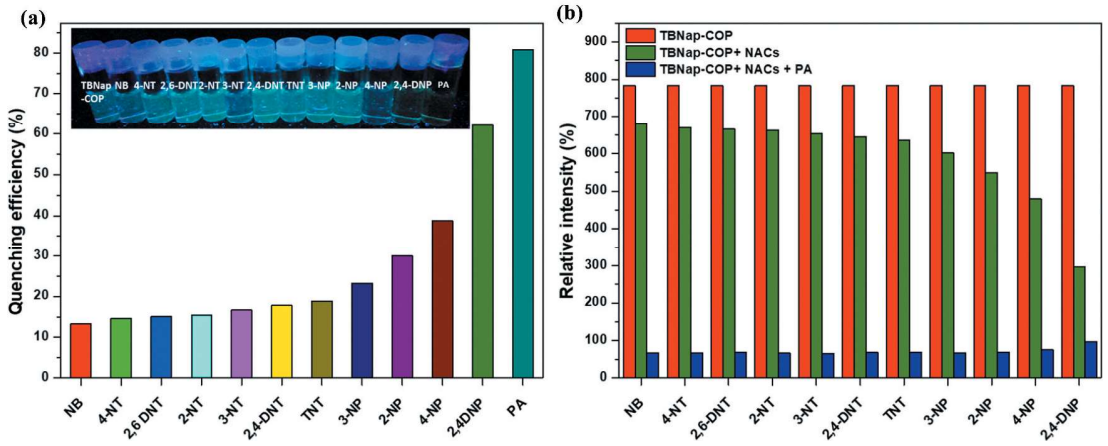

Figure 5. (a) Fluorescent quenching of **TBNap-COP** observed upon addition of different NACs (Insert: observed visual colour change before and after the addition of PA under UV lamp). (b) Competitive selective binding of **TBNap-COP** towards different NACs in the presence of PA in water.

2,4-dinitrophenol (2,4-DNP) and 4-nitrophenol (4-NP) with a quenching efficiency of 80%, 62%, and 39%, respectively. The highest quenching efficiency for PA is due to its more electron-deficient nature. The fluorescence titration experiments, which were shown to be fully reproducible, also highlighted the capacity of **TBNap-COP** to discriminate phenolic nitroaromatics over non-phenolic nitroaromatics. The observed discriminative fluorescence sensing is also being seen by visual colour changes as is given in Figure 5(a). The changes in the **TBNap-COP** emission upon the addition of different NACs are presented in Figure S11-S21. The Stern-Volmer constant for the other NACs titrations were also determined using the same method and are summarised in Table S3. From the analysis of the titration data, the order of decreasing quenching efficiency was determined as being: PA > 2,4-DNP > 4-NP > 2-NP > 3-NP > TNT > 2,4-DNT > 3-NT > 2-NT > 2,6-DNT > 4-NT > NB; being in a similar order to that seen previously for such systems [9,10]. These results demonstrate the high selectivity and discriminative sensing ability of **TBNap-COP** for phenolic-nitroaromatics over other interfering non-phenolic analytes. This favoured binding affinity is ascribed to the Lewis basic nitrogens of the Tröger's base moiety, interacting strongly with the acidic hydroxy groups of the phenolic-nitroaromatics in the sensing process [9,10,24].

To further validate the potential of **TBNap-COP** to act as a selective sensor, a competitive sensing experiment/titrations were performed in competitive media, where to an aqueous suspension of **TBNap-COP** (red bar), 90.9 μM of each of the NAC tested above was added (green bar) and the emission spectra were recorded (Figure 5(b)). This was then followed by the addition of 90.9 μM of PA (blue bar), and the emission spectra were recorded. A strong quenching of emission intensity of **TBNap-COP** (in presence of NACs) was observed after the addition of PA. To demonstrate the high selectivity of **TBNap-COP** for PA further, a similar competitive study was performed in the presence of group-I and transitions metal ions commonly present in water. **TBNap-COP** showed the highest binding propensity for PA in the presence of these different metal cations (Figure S22) demonstrating the ability of **TBNap-COP** to selectively detect the presence of PA in aqueous media in co-existence of other structurally similar and potentially competing analytes. The influence of pH on the sensing propensity was also investigated and it showed sensitivity to pH (Figure S23). Indeed, in acidic conditions (pH = 2.3), the binding capacity was slightly decreased (K_{SV} = 2.35 ± 0.05 × 10^4 M^{-1}), but in basic medium (pH = 11.7) the capacity is drastically decreased (K_{SV} = 1.86 ± 0.06 × 10^4 M^{-1}) presumably due to the diminished intermolecular interactions, as proposed earlier, between **TBNap-COP** and NACs at alkaline pH [9,10,24].

Sensitivity and response time

One important parameter for on-site detection/sensing is a fast time of response, which corresponds to how long the system needs to be exposed to an analyte before the detection takes place. The time of response of **TBNap-COP** was tested in the presence of PA at different concentrations, and this experiment demonstrated that the maximum quenching response is reached within one minute of contact time with PA.

Thus, **TBNap-COP** can be an excellent sensor for the fast detection of NACs (Figure S24). To find out the sensitivity of **TBNap-COP** for NAC detection, the limit of detection was estimated at natural pH. The sensitivity experiment showed that the fluorescence of **TBNap-COP** was affected by a quantity as low as 12 ppb of PA, making this system a very sensitive and selective sensor for PA (Figure S25). Moreover, this level of sensitivity is below the allowed limit of NACs in drinking water established by the US EPA [6,7,11,12].

Conclusion

In summary, we have synthesised a new **TBNap** functionalised pyridinium covalent organic polymer and demonstrated its uses as a fluorescent sensor for NACs. More importantly, it was demonstrated that **TBNap-COP** exhibited a rapid fluorescence quenching response for PA exposure and was able to selectively sense PA, even in the presence of other competing analytes. This system has proven to be very sensitive towards traces of PA, making it an ideal candidate for on-site detection of PA. We are currently developing the application of **TBNap-COP** further to design a practically feasible sensor system.

Acknowledgments

We thank the Irish Research Council (IRC) (GOIPD/2015/290 to D. U.), Science Foundation Ireland (SFI PI Award 13/IA/1865 to TG and 13/IA/1896 to WS) and European Research Council (CoG SUPRAMOL 2014–647719 to WS) and Science and Engineering Research Board (EMEQ Award EEQ/2018/000799 to SS) for financial support. Computational calculations were performed using the Lonsdale supercomputing at Trinity Centre for High-performance Computing (TCHPC). We thank Drs J. E. O'Brien, M. Reuther, and G. Hessman for NMR and MS analysis. SEM analysis was performed at the AMBER Center and the CRANN Advanced Microscopy Laboratory (AML), TCD.

Disclosure statement

There are no conflicts to declare.

Funding

This work was supported by the H2020 European Research Council [CoG SUPRAMOL 2014–647719 to W.S.]; Science and Engineering Research Board [EMEQ Award EEQ/2018/000799 to SS].

ORCID

Jason M. Delente http://orcid.org/0000-0002-8889-5798

References

[1] Sun X, Wang Y, Lei Y. Fluorescence based explosive detection: from mechanisms to sensory materials. Chem Soc Rev. **2015**;44:8019–8061.
[2] Chhatwal M, Mittal R, Gupta RD, et al. Sensing ensembles for nitroaromatics. J Mater Chem C. **2018**;6 (45):12142–12158.
[3] Shanmugaraju S, Mukherjee PS. Self-assembled discrete molecules for sensing nitroaromatics. Chem–Eur J. **2015**;21(18):6656–6666.
[4] Kartha KK, Sandeep A, Praveen VK, et al. Detection of nitroaromatic explosives with fluorescent molecular assemblies and π-gels. Chem Rec. **2015**;15(1):252–265.
[5] Shanmugaraju S, Mukherjee PS. π-Electron rich small molecule sensors for the recognition of nitroaromatics. Chem Commun. **2015**;51(89):16014–16032.
[6] Grundlingh J, Dargan PI, El-Zanfaly M, et al. 2,4-Dinitrophenol (DNP): a weight loss agent with significant acute toxicity and risk of death. J Med Toxicol. **2011**;7(3):205–212.
[7] Shanmugaraju S, Joshi SA, Mukherjee PS. Fluorescence and visual sensing of nitroaromatic explosives using electron rich discrete fluorophores. J Mater Chem. **2011**;21(25):9130–9138.
[8] Moore DS. Instrumentation for trace detection of high explosives. Rev Sci Instrum. **2004**;75(8):2499–2512.
[9] Shanmugaraju S, Dabadie C, Byrne K, et al. A supramolecular Troger's base derived coordination zinc polymer for fluorescent sensing of phenolic-nitroaromatic explosives in water. Chem Sci. **2017**;8 (2):1535–1546.
[10] Delente JM, Umadevi D, Shanmugaraju S, et al. Aggregation induced emission (AIE) active 4-amino-1,8-naphthalimide-Tröger's base for the selective sensing of chemical explosives in competitive aqueous media. Chem Commun. **2020**;56(17):2562–2565.
[11] Chandrasekaran Y, Venkatramaiah N, Patil S. Tetraphenylethene-based conjugated fluoranthene: a potential fluorescent probe for detection of nitroaromatic compounds. Chem–Eur J. **2016**;22 (15):5288–5294.
[12] Kaur S, Gupta A, Bhalla V, et al. Pentacenequinone derivatives: aggregation-induced emission enhancement, mechanism and fluorescent aggregates for superamplified detection of nitroaromatic explosives. J Mater Chem C. **2014**;2(35):7356–7363.
[13] Kartha KK, Sandeep A, Nair VC, et al. A carbazole–fluorene molecular hybrid for quantitative detection of TNT using a combined fluorescence and quartz crystal microbalance method. Phys Chem Chem Phys. **2014**;16 (35):18896–18901.
[14] Gupta SK, Kaleeswaran. D, Nandi S, et al. Bulky isopropyl group loaded tetraaryl pyrene based azo-linked covalent organic polymer for nitroaromatics sensing and CO_2 adsorption. ACS Omega. **2017**;2(7):3572–3582.
[15] Lee YH, Liu H, Lee JY, et al. Dipyrenylcalix[4]arene-a fluorescence-based chemosensor for trinitroaromatic explosives. Chem Eur J. **2010**;16(20):5895–5901.
[16] Mosca L, Čejka J, Dolenský B, et al. Bowl-shaped Tröger's bases and their recognition properties. Chem Commun. **2016**;52(70):10664–10667.

[17] Meher N, Iyer PK. Pendant chain engineering to fine-tune the nanomorphologies and solid state luminescence of naphthalimide AIEEgens: application to phenolic nitro-explosive detection in water. Nanoscale. **2017**;9(22):7674–7685.
[18] Wang J, Yang Y, Sun G, et al. A convenient and universal platform for sensing environmental nitro-aromatic explosives based on amphiphilic carbon dots. Environ Res. **2019**;177:108621–108628.
[19] Banerjee D, Hu Z, Li J. Luminescent metal–organic frameworks as explosive sensors. Dalton Trans. **2014**;43 (28):10668–10685.
[20] Guo L, Cao D. Color tunable porous organic polymer luminescent probes for selective sensing of metal ions and nitroaromatic explosives. J Mater Chem C. **2015**;3 (33):8490–8494.
[21] Yang J-S, Swager TM. Fluorescent porous polymer films as TNT chemosensors: electronic and structural effects. J Am Chem Soc. **1998**;120(46):11864–11873.
[22] Zhang S, Yang Q, Wang C, et al. Porous organic frameworks: advanced materials in analytical chemistry. Adv Sci. **2018**;5:1801116–1801144.
[23] Suresh VM, Bonakala S, Atreya HS, et al. Amide functionalized microporous organic polymer (Am-MOP) for selective CO_2 sorption and catalysis. ACS Appl Mater Interfaces. **2014**;6(7):4630–4637.
[24] Shanmugaraju S, Umadevi D, Savyasachi AJ, et al. Reversible adsorption and storage of secondary explosives from water using a Tröger's base-functionalised polymer. J Mater Chem A. **2017**;5 (47):25014–25024.
[25] Guan X, Chen F, Fang Q, et al. Design and applications of three dimensional covalent organic frameworks. Chem Soc Rev. **2020**;49(5):1357–1384.
[26] Xu Y, Jin S, Xu H, et al. Conjugated microporous polymers: design, synthesis and application. Chem Soc Rev. **2013**;42(20):8012–8031.
[27] Banerjee S, Bright SA, Smith JA, et al. Supramolecular approach to enantioselective DNA recognition using enantiomerically resolved cationic 4-Amino-1,8-naphthalimide-based Tröger's bases. J Org Chem. **2014**;79(19):9272–9283.
[28] Shanmugaraju S, McAdams D, Pancotti F, et al. One-pot facile synthesis of 4-amino-1,8-naphthalimide derived Tröger's bases *via* a nucleophilic displacement approach. Org Biomol Chem. **2017**;15(35):7321–7329.
[29] Tanwar AS, Adil LR, Afroz MA, et al. Inner filter effect and resonance energy transfer based attogram level detection of nitroexplosive picric acid using dual emitting cationic conjugated polyfluorene. ACS Sens. **2018**;3 (8):1451–1461.
[30] Chen S, Yu Y-L, Wang J-H. Inner filter effect-based fluorescent sensing systems: A review. Anal Chim Acta. **2018**;999:13–26.
[31] Zhao Y, Truhlar DG. The M06 suite of density functionals for main group thermochemistry, thermochemical kinetics, noncovalent interactions, excited states, and transition elements: two new functionals and systematic testing of four M06-class functionals and 12 other functionals. Theory Chem Acc. **2008**;120:215–241.
[32] Frisch MJ, Trucks GW, Schlegel HB, et al., 2009.
[33] Roy B, Bar AK, Gole B, et al. Fluorescent Tris-imidazolium sensors for picric acid explosive. J Org Chem. **2013**;78 (3):1306–1310.
[34] Tanwar A, Meher N, Adil LR, et al. Stepwise elucidation of fluorescence based sensing mechanisms considering picric acid as a model analyte. Analyst. **2020**;145 (14):4753–4767.